Single Particle Characterisation of Atmospheric Aerosol Particles in Remote, Rural, and Urban Locations of Central Europe

Einzelpartikelcharakterisierung von atmosphärischen Aerosolpartikeln an abgelegenen, ländlichen und städtischen Standorten in Mitteleuropa

Zur Erlangung des akademischen Grades einer

DOKTORIN DER NATURWISSENSCHAFTEN

von der KIT–Fakultät für

Bauingenieur-, Geo- und Umweltwissenschaften

des Karlsruher Instituts für Technologie (KIT)

genehmigte

DISSERTATION

von

M. Sc. Xiaoli Shen

aus Fujian, China

Tag der mündlichen Prüfung: 05.07.2019

Referent: Prof. Dr. Stefan Norra

Korreferent: Prof. Dr. Thomas Leisner

Karlsruhe, den 08.07.2019

Erklärung

Hiermit erkläre ich, dass ich die vorliegende Dissertation, abgesehen von der Benutzung der angegebenen Hilfsmittel, selbständig verfasst habe.

Alle Stellen, die gemäß Wortlaut oder Inhalt aus anderen Arbeiten entnommen sind, wurden durch Angabe der Quelle als Entlehnungen kenntlich gemacht.

Diese Dissertation liegt in gleicher oder ähnlicher Form keiner anderen Prüfungsbehörde vor.

Karlsruhe den 08.07.2019

Xiaoli Shen

There are some great mottos and people to guide my way in science.

I keep them in mind and can always be back to the right track.

Mottos

Wenn du es nicht einfach erklären kannst,

hast du es nicht gut genug verstanden.

——Albert Einstein

Every science begins as philosophy and ends as art;

it arises in hypothesis and flows into achievement.

——Will Durant

Acknowledgements

Abstract

Chemical composition and mixing state of aerosol particles are of current scientific interest, due to their impact on visibility and air quality, human and ecosystem health, as well as weather and climate. Despite their importance, big knowledge gaps still exist regarding the interaction of anthropogenic and biogenic emission for formation and aging of aerosols, as well as the impact of mixing and transport. Aerosol mass spectrometry is a powerful tool to provide near real-time information of chemical composition and internal mixing of even individual aerosol particles.

As a basis to measure aerosols in aerosol and cloud chambers and at characteristic locations of central Europe, it was my aim to determine detection efficiencies of a mass spectrometer for single particle identification and quantification. By comparing measurement and model results, I aimed to determine sources, to understand the evolution of ambient aerosols, to evaluate a transport model, and to investigate the role of particle composition for its ice nucleation ability.

Consequently, I determined the measurement capabilities of the relatively new laser ablation aerosol particle time-of-flight mass spectrometer (LAAPTOF), by characterising its overall detection efficiency (ODE) ranging from ~0.01% to ~5% for various particle types in the size range 200 nm to 2.5 µm, and by obtaining 32 laboratory-based reference spectra of the most important atmospherically relevant particles. Based on these reference spectra, I identified characteristic particle classes for field measurements with much higher reliability than usual Fuzzy clustering methods. With this precise particle identification and the ODE for this instrument, I developed a new method to estimate particle mass without the need of a reference instrument. The resulting total particle mass measured by LAAPTOF showed a correlation coefficient >0.6 with independent results from an aerosol mass spectrometer (AMS) for more than 85% of a six-week campaign at a rural site. Although, the LAAPTOF total mass values only account for 23% to 68% of the AMS total mass, this new analysis method leads to much more realistic particle type fractions than usual mass spectrometric analysis methods.

During a six-week measurement campaign in winter 2017 at the remote mountain site Jungfraujoch (3571 m a.s.l.) in Switzerland, I identified nine characteristic particle types, more than I observed at rural or urban locations. Besides common types, e.g., aged soot, aged sea salts, secondary inorganics, and aged biomass burning particles, also dust and phosphate containing particles were

identified. Hence, the aerosols contain particles from various sources reaching the location by long-range transport in the free troposphere, but also from the more polluted boundary layer.

During the measurement campaign at the rural site in the upper Rhine valley near Karlsruhe in summer 2016, I found six different periods dominated by seven different characteristic particle types. The major ones were aged sea salt and biomass burning and soil dust like particles, contributing on average 36% (± 27%) und 30% (± 18%) to the $PM_{2.5}$ mass measured by the LAAPTOF, respectively. I verified that aged sea salt particles originated from the Atlantic Ocean more than 800 km away. With detailed transport modelling (COSMO-ART), I identified an industrial point source in Karlsruhe for elevated concentrations in particle number. For a 3-day episode with high organic mass concentrations, the comparison of the trace gases and particle composition measured to those predicted by the model showed very good agreements in trends and amplitudes. However, the model underestimates the organic mass concentrations by a factor of 2.3 and the total particle number by an order of magnitude. The latter being most likely due to missing nucleation processes in the model. I showed that the missing organic mass may be caused by an underestimated regional background or a combination of missing VOC sources and oxidation mechanisms e.g., for night-time chemistry. My model analysis shows how complex interactions of biogenic and anthropogenic aerosol sources as well as transport pattern can explain three subsequent days with high organic concentrations caused by sources in Karlsruhe (day 1), by mixed emissions from Stuttgart and forests (day 2), as well as night-time chemistry (day 2&3).

During two measurement campaigns in summer 2017 and winter 2018 in the urban background of the city of Stuttgart in Germany, I identified six particle types in summer, similar to those in the Rhine valley with organics dominating. For the winter period particle numbers increased by a factor of seven with nitrate containing particles being the most abundant.

Furthermore, I showed during several aerosol and cloud chamber campaigns at KIT and a campaign at MIT, how the particle chemical composition, e.g., of soil dust particles or of aged organic particles affects their ice nucleation ability.

This dissertation is an example how the combination of laboratory, field, and transport model studies can improve the quality of scientific results, helps to understand complex interactions in the real atmosphere, and allows the validation and improvement of models.

Zusammenfassung

Die chemische Zusammensetzung und der Mischungszustand von Aerosolpartikeln sind aufgrund ihrer Bedeutung für Sichtweite und Luftqualität, die Gesundheit von Menschen, den Schutz von Ökosystemen sowie für Wetter und Klima von aktuellem, wissenschaftlichen Interesse. Trotz ihrer Bedeutung bestehen nach wie vor große Wissenslücken über das Zusammenspiel von anthropogenen und biogenen Emissionen zur Bildung und Alterung von Aerosolen sowie über die Auswirkungen von Mischungs- und Transportprozessen. Die Aerosolmassenspektrometrie ist ein leistungsstarkes Werkzeug, um nahezu in Echtzeit Informationen über die chemische Zusammensetzung und den Mischungszustand selbst einzelner Aerosolpartikel bereitzustellen.

Um die Grundlage für die Messung von Aerosolen in Aerosol- und Nebelkammern und an charakteristischen Orten Mitteleuropas zu schaffen, war es mein Ziel, die Detektionseffizienz eines Massenspektrometers zur Einzelpartikelidentifikation und -quantifizierung zu bestimmen. Durch den Vergleich von Messungen und Modellresultaten wollte ich Partikelquellen bestimmen, die Entwicklung der Umgebungsaerosole verstehen, ein Transportmodell bewerten und die Rolle der Partikelzusammensetzung für ihre Eiskeimfähigkeit untersuchen.

Hierzu habe ich die Messmöglichkeiten des relativ neuen Laserablations-Aerosolpartikel-Flugzeitmassenspektrometers (LAAPTOF) bestimmt, indem ich seine Gesamtdetektionseffizienz (ODE) im Bereich von ~0,01% bis ~5% für verschiedene Partikeltypen im Größenbereich von 200 nm bis 2,5 µm charakterisiert und 32 Referenzspektren der wichtigsten atmosphärisch relevanten Partikel gemessen habe. Basierend auf diesen Referenzspektren identifizierte ich charakteristische Partikelklassen für Feldmessungen mit wesentlich höherer Zuverlässigkeit als übliche Fuzzy-Clustermethoden. Mit dieser präzisen Partikelidentifikation und der ODE habe ich eine neue Methode entwickelt, um die Masse einzelner Partikel ohne Referenzinstrument zu schätzen. Die resultierende Gesamtpartikelmasse, gemessen mit LAAPTOF, zeigte eine Korrelation von >0,6 mit unabhängigen Ergebnissen eines Aerosol-Massenspektrometers (AMS) für mehr als 85% einer sechs-wöchigen Kampagne an einem ländlichen Standort. Obwohl die LAAPTOF-Gesamtmassenwerte nur 23% bis 68% der AMS-Gesamtmasse ausmachen, führt diese neue Analysemethode zu wesentlich realistischeren Partikeltypanteilen als herkömmliche Massenspektrometeranalysen.

Während einer sechswöchigen Messkampagne im Winter 2017 auf dem Jungfraujoch (3571 m ü.d.M.) in der Schweiz habe ich neun charakteristische Partikeltypen identifiziert; deutlich mehr als an ländlichen oder städtischen Standorten. Neben den gängigen Partikeltypen, wie z.B. gealterter Ruß, gealterte Meersalze, sekundäre anorganische Verbindungen und gealterte Biomasseverbrennungspartikel, wurden auch Stäube und phosphathaltige Partikel identifiziert. Die Aerosole an der Bergstation enthalten somit Partikel aus verschiedensten Quellen, die in der freien Troposphäre über große Distanzen transportiert werden, aber auch Partikel aus der stärker verschmutzten Grenzschicht.

Während der Messkampagne an einem ländlichen Standort am Oberrhein nördlich von Karlsruhe fand ich im Sommer 2016 sechs verschiedene Zeiträume mit insgesamt sieben unterschiedlichen charakteristischen Partikeltypen. Dazu gehörten gealtertes Meersalz, Biomasseverbrennung und bodenstaubähnliche Partikel, die durchschnittlich 36% ($\pm$ 27%) und 30% ($\pm$ 18%) zu der mit dem LAAPTOF gemessenen PM$_{2,5}$-Masse beitrugen. Ich konnte zeigen, dass gealterte Meersalzpartikel aus dem mehr als 800 km entfernten Atlantik stammen. Mit einer detaillierten Transportmodellierung (COSMO-ART) konnte ich in Karlsruhe eine industrielle Punktquelle als Ursache für erhöhte Partikelanzahlkonzentrationen identifizieren. Für eine dreitägige Episode mit hohen organischen Massenkonzentrationen zeigte der Vergleich der gemessenen Spurengase und Partikelzusammensetzung mit den entsprechenden Modellvorhersagen sehr gute Übereinstimmungen in Trends und Amplituden. Das Modell unterschätzte jedoch die organischen Massenkonzentrationen um den Faktor 2,3 und die Gesamtpartikelzahl um eine Größenordnung. Letzteres ist höchstwahrscheinlich darauf zurückzuführen, dass im Modell ein Teil der Nukleationsprozesse fehlt. Ich konnte aufzeigen, dass die fehlende organische Masse durch einen unterschätzten regionalen Hintergrund oder eine Kombination aus fehlenden VOC-Quellen und Oxidationsmechanismen, z.B. für die Nachtchemie, verursacht werden kann. Meine Modellanalyse zeigt, wie komplexe Wechselwirkungen zwischen biogenen und anthropogenen Aerosolquellen sowie dem Transport drei aufeinander folgende Tage mit hohen organischen Konzentrationen erklären können. Tatsächlich stammen diese Aerosole sowohl aus Quellen in Karlsruhe (Tag 1), von Emissionen aus Stuttgart und Wäldern (Tag 2) sowie aus Nachtchemie (Tag 2&3).

In zwei Messkampagnen im Sommer 2017 und im Winter 2018 im urbanen Hintergrund (Unterer Schlossgarten) der Stadt Stuttgart habe ich für den Sommer sechs Partikeltypen identifiziert,

ähnlich denen im Rheintal, wobei auch die organischen Komponenten dominierten. Im Winter stieg die Partikelzahl um den Faktor Sieben, wobei nitrathaltige Partikel am häufigsten vorkamen.

Weiterhin konnte ich in mehreren Aerosol- und Nebelkammerkampagnen am KIT und einer Kampagne am MIT zeigen, wie die chemische Zusammensetzung, z.B. von Bodenstaubpartikeln oder gealterten organischen Partikeln, die Eiskeimfähigkeit dieser Partikel beeinflusst.

Diese Dissertation ist ein Beispiel dafür, wie die Kombination von Laborexperimenten, Feldmessungen und Transportmodellierung die Qualität wissenschaftlicher Ergebnisse verbessert. Zudem erlaubt es komplexe Wechselwirkungen in der realen Atmosphäre zu verstehen und ermöglicht die Validierung und Verbesserung von Modellen.

Table of Contents

List of Figures

List of Tables

1 Context of this dissertation

Atmospheric aerosols affect visibility and air quality, human and ecosystem health, as well as weather and climate change (Seinfeld and Pandis, 2006). Aerosols' composition and mixing states are of scientific interest, as they are related to their properties and influence all aerosol effects (Burkholder et al., 2017; Pöschl, 2005). However, the knowledge gaps in the physicochemical complexity of aerosol particles and limitations of instruments hinder the assessment for aerosols impacts on various aspects. Furthermore, such complexity also impedes particle source apportionment, which is a prerequisite for local and global environmental policy. Detailed introduction of these issues follows in section 1.1. In this context, this dissertation aims to contribute to a better understanding of the complexity of composition and sources of atmospheric aerosols as well as the roles of chemical transformations and transport processes. To achieve this goal, I aim to do comprehensive analysis of the chemical composition, mixing states, and sources of atmospheric aerosols by using complementary mass spectrometry (on both single particle and bulk measurements) and transport modelling. The specific research objectives are in section 1.2.

This dissertation is based on the cumulation of nine scientific publications (all are research articles). I am the first author for three (2 accepted and 1 submitted) of them. The methodology is described in section 1.3, including the major tools of mass spectrometers (LAAPTOF and HR-TOF-AMS, hereafter AMS), an aerosol and cloud chamber (AIDA), and a transport model (COSMO-ART); as well as their application in the laboratory, field, and model studies. I used the LAAPTOF by systematic characterising its performance and developing a new method for single particle identification and mass quantification. This way it could be used together with a complementary mass spectrometer (AMS), for the quantitative interpretation of ambient data. Furthermore, I used transport modelling (COSMO-ART) to track the origin and evolution of ambient aerosols. Most of the results are within the aforementioned scientific publications and shown in section 2 with the corresponding abstracts (full articles of first author and co-authored publications are in the Appendix B and C, respectively). Section 2 shows also yet unpublished results that are important for this work. Combining complementary information of chemical composition, size, mixing states, emissions, aging, and transport of the atmospheric aerosols is a prerequisite to understand the full complexity of atmospheric aerosols in central Europe.

1.1 Introduction

Atmospheric aerosols evolve on time scales from seconds to days including processes like nucleation, coagulation, coating, chemical transformation, and cloud processing leading to complex external and internal mixtures. The following sections explain the role of aerosol particles in our atmosphere, the actual mass spectrometric methods available to characterise the aerosol particles, and model tools used to identify their sources and transformations.

1.1.1 Atmospheric aerosol particles
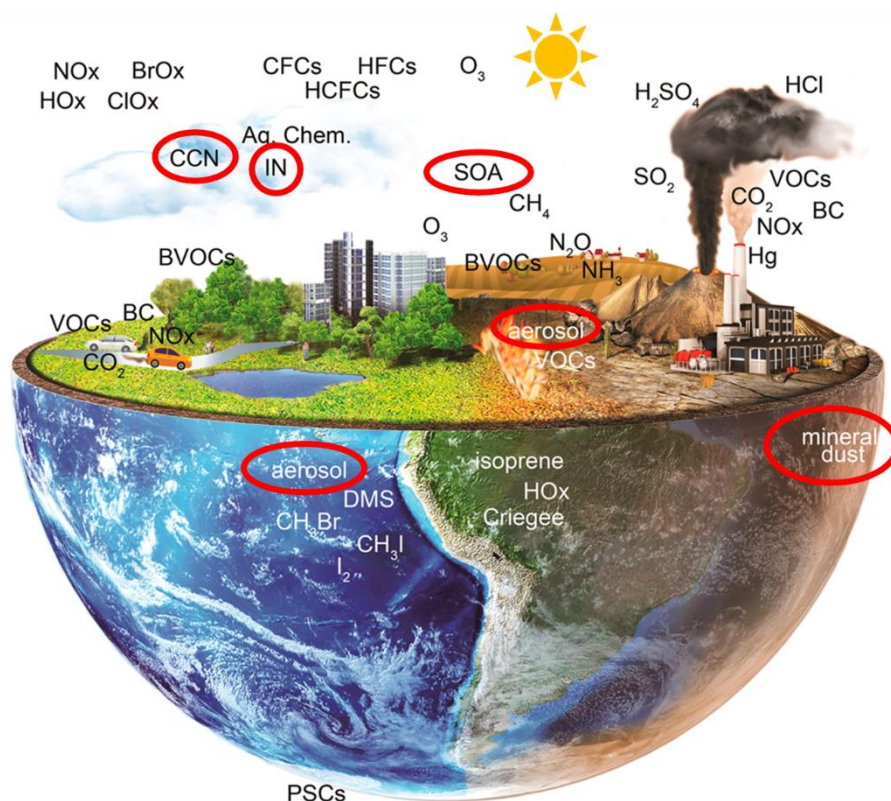
Figure 1: A chemical view of the atmosphere highlighting biogenic and anthropogenic emissions sources and key atmospheric trace gases and aerosol particles. This is adapted with permission from Figure 1 in Burkholder et al. (2017). © 2017, American Chemical Society.

Atmospheric aerosol particles are major components in the atmosphere (Figure 1). High particle loadings can reduce the visibility in both local and regional scale, and thus affects transportation safety (Watson, 2002). The visibility degradation is also suggested to be the most perceived impact of air pollution (Seinfeld and Pandis, 2006). Epidemiological studies have reported that mortality

from cardiopulmonary disease and lung cancer increased under persistent high particle loading above 10–20 mg m^{-3} (Dockery et al., 1993; Dominici et al., 2006; Pope et al., 2002). Aerosols can also have adverse effect on ecosystem, such as water eutrophication and land acidification (Bytnerowicz and Fenn, 1996). Furthermore, aerosol particles modify atmospheric radiative fluxes, e.g., most particles have cooling effect while soot particles have a warming effect. In general, particles with a size larger than 50 nm can serve as cloud condensation nuclei (CCN), and some of them can be activated to form ice crystals, namely served as ice nuclei (IN). These processes influence cloud formation, cloud radiative properties and the initiation of precipitation, and thereby have further impact on weather and climate change (Fuzzi et al., 2015; Pöschl, 2005; Seinfeld and Pandis, 2006; Zhang et al., 2015). However, the direct and indirect impacts of aerosols on the Earth's radiation budget are still highly uncertain (IPCC, 2013). It is reported that the impact of natural and anthropogenic aerosols on the atmosphere on global and regional scale is not well understood. In addition, the scientific basis for the development of dedicated strategies for improved air quality is still rather weak (IPCC, 2013). Therefore, more field and laboratory experiments are needed, including single particle characterization, to advance our understanding of aerosol and cloud processes and to improve the quality of their parameterizations in regional transport and global climate models.

There are various types of atmospheric aerosol particles, such as mineral dust, sea salt, soot, and organic aerosol particles. They are originating from biogenic and/or anthropogenic emission sources (primary aerosol particles), as well as particles (secondary particles), which are formed in the atmosphere (e.g. nitrate, sulfate, organic) by oxidation of precursor gases (e.g. NO_x, SO_2, volatile organic compounds VOC) (Burkholder et al., 2017; Tsigaridis et al., 2006; Zhang et al., 2015). Except for newly formed particles (~3 to 5 nm) that exist for seconds, the lifetime of ambient aerosol particles ranges from hours to several days (Pöschl, 2005). During their lifetime, the chemical composition of the aerosol particles is continuously evolving by coagulation, cloud processing, and chemical reactions. For example, they can be coated with secondary inorganic (e.g., sulfates, nitrates, and ammonium) and secondary organic compounds (Fuzzi et al., 2015; Seinfeld and Pandis, 2006; Usher et al., 2003; Zhang et al., 2015). Therefore, aerosol particles can have complex internal and external mixing states. They often consist of various components, including inorganic and organic species and ranging from volatile to refractory species (Pratt and Prather, 2012). As a result, the optical properties, hygroscopicity, toxicity, as well as the ice

nucleation abilities of the aerosol particles can vary significantly, and thus influence their impact on visibility, air quality, health, weather and climate. However, large knowledge gaps still exist with respect to the spatial and temporal variation of particle composition, the internal/external mixing state of organic and inorganic components, and their mutual interaction in the aerosols (Jimenez et al., 2009; Murphy et al., 2006; Schill and Tolbert, 2013; Zhang et al., 2007). Moreover, the inorganic fraction contains a limited number of relatively well-characterized major components, which are strongly influenced by anthropogenic emissions. The organic fraction contains a complex mixture of substances from both anthropogenic and biogenic emissions. This makes it difficult to distinguish and to trace them to their primary source and/or secondary formation pathway. The aforementioned issues underscore the importance of measuring aerosol chemical composition and mixing state, as well as their changes on short timescales, which can be realized by on-line and real-time mass spectrometry.

1.1.2 Aerosol mass spectrometry

On-line and real-time mass spectrometry is widely used to provide size and chemical information of aerosol particles with high temporal resolution, typically minutes (Nash et al., 2006; Pratt and Prather, 2012; Sullivan and Prather, 2005). Many variations of aerosol mass spectrometers have been developed, differing in sampling inlets, desorption and ionization methods, and mass analysers. Two major instrument types are aerosol mass spectrometer (AMS) and single particle mass spectrometer (singe-particle MS), corresponding to bulk and single-particle measurements, respectively (Pratt and Prather, 2012). In the last decade, the AMS (Aerodyne, Inc.) has found very broad application leading to a good overview of non-refractory tropospheric aerosol mass composition (e.g., ammonium, nitrate, sulfate, chloride, and organics) near ground level (Canagaratna et al., 2007). In contrast, much fewer singe-particle MS instruments have been in use and only very few became commercially available (ATOFMS, TSI Inc.). However, they can measure both non-refractory and refractory species and mixing state on single particle basis, and identify various ambient particle types, e.g., dust, sea salt, soot, and biomass burning particles (Murphy, 2007; Noble and Prather, 2000; Pratt and Prather, 2012). With the recently commercially available novel singe-particle MS (LAAPTOF, AeroMegt GmbH) more single particle data should become available in the near future. This will complement the bulk data measured by AMS and allows quantitative interpretation of internal and external mixing of the aerosol particles (Gemayel

et al., 2017; Gunsch et al., 2018; Healy et al., 2013; Jeong et al., 2011; Shen et al., 2019a; Zhou et al., 2016).

Singe particle mass spectrometry commonly uses high-energy laser pulse for particle desorption and ionization (LDI). This strong ionization method allows measuring nearly all particulate components. However, it cannot interact with the entire particle. In addition, the LDI mechanisms are quite complex, including charge and proton transfer, as well as ion-molecule reactions that may occur in the plume with many collisions. Therefore, the resulting ion fragments/clusters are susceptible to LDI matrix effects (Murphy, 2007; Reilly et al., 2000; Reinard and Johnston, 2008; Thomson et al., 1997; Zenobi and Knochenmuss, 1998). These make the analytical approach quite challenging: 1) the LDI matrix effects may obscure the particle composition, resulting in some mass spectroscopic signature peaks that may not directly reflect the primary composition of the particles. Therefore, particle type identification becomes one critical issue. 2) Quantification of individual particles' mass and chemical composition cannot be directly provided by single-particle MS measurement, due to the aforementioned incomplete ionization of the entire particle.

Great effort has been put into solving such issues. In field measurements, a single-particle MS can generate a large number of spectra (thousands to millions). Therefore, several clustering algorithms, such as fuzzy k-means, fuzzy c-means (modification of k-means), ART-2a neural network, hierarchical clustering algorithms, and machine learning algorithms, have been applied for grouping the single particle spectra in order to reduce the complexity (Christopoulos et al., 2018; Reitz et al., 2016). This is the common aim among source apportionment methods. The grouped spectra can reflect the major particle types/classes in the ambient. Regarding the particle class identification, different peak ratios pairs were used, such as Ca_2O^+/Ca^+ vs. CaO^+/Ca^+ for calcium-containing dust (Gallavardin et al., 2008), and CN^-/CNO^- vs. PO_3^-/PO_2^- for primary biological aerosol particles (Zawadowicz et al., 2017). Besides, marker peak thresholds (Köllner et al., 2017), natural isotopic signatures (Lu et al., 2018), combination of peak area and peak shift ratio (Marsden et al., 2018) and ternary sub-composition systems such as $(Al+Si)^+–K^+–Na^+$ (Marsden et al., 2019) were used as well. However, the complex particle and LDI matrix cannot be completely overcome by these methods. Regarding the particle mass quantification, an explicit field-based scaling approach was developed (Allen et al., 2000), improved (Qin et al., 2006; Wenzel et al., 2003), and are widely used (Allen et al., 2006; Bein et al., 2006; Fergenson et al.,

2001; Gunsch et al., 2018; May et al., 2018). This approach is based on the comparison with co-located more quantitative particle measurement to obtain continuous particle mass concentrations as a function of particle size. For the quantification of particle composition, the similar scaling method was used by considering the relative sensitivity factors (RSFs) for different particulate species (Gemayel et al., 2016; Gross et al., 2000; Healy et al., 2013; Jeong et al., 2011; Zhou et al., 2016). It should be noted that such field-based scaling methods strongly rely on the availability of a reference instrument. The aforementioned particle identification and quantification issues call for further improvement of the methodology for single particle data analysis.

1.1.3 Aerosol source apportionment and transport modelling

As mentioned above, the complex particle composition and mixing states make it difficult to track their primary source and/or secondary formation. For single particle data, clustering algorithms are applied to group the spectra, which is useful for identify major particle classes in the ambient aerosol and thus gives a hint of their origin (Reitz et al., 2016), e.g., NaCl rich particles might originate from the sea. Positive matrix factorization (PMF; Paatero, 1997; Paatero and Tapper, 1994) is commonly used for AMS data classification, resulting in different types of organic aerosols (OA), e.g., hydrocarbon-like organic aerosol (HOA) and cooking-related organic aerosol (COA) (Canonaco et al., 2013; Canonaco et al., 2015; Crippa et al., 2014; Zhang et al., 2011).. However, these methods can only provide indirect source information, and cannot address the questions, as follows: Were the aerosols formed locally or did they undergo regional/global transport? Were they transported vertically or horizontally? What is the transport time? These can be answered with the help of transport models.

Some questions about potential source regions for the particles can already be answered with models calculating back trajectories like Hybrid Single-Particle Lagrangian Integrated Trajectory (HYSPLIT; Stein et al., 2015). However, more complex scenarios require transport models including detailed meteorology, accurate emission data, and a good parameterisation of aerosol particles and trace gases. One of such type of models is COSMO-ART (stands for Consortium for small-scale modelling -aerosols and reactive trace gases; Vogel et al., 2009) and its successor ICON-ART (ICON stands for ICOsahedral Nonhydrostatic; Rieger et al., 2015; Weimer et al., 2017), which can give temporal and spatial (regional or global) information of the aerosols. In

addition, the comparison between model simulations and field observations can assist model evaluation, identifying and potentially improving weaknesses e.g., missing sources or mechanisms in the model. Some attempts also use specific emission characteristics like element or isotope ratios in single particle mass spectra to facilitate source identification at the measurement sites. This method is employed, e.g., by a single particle mass spectrometer network in China.

The combination of laboratory experiments, field measurements, and transport modelling will give comprehensive information, including the particle size, composition, sources, mixing states and aging, as well as the complex transformation processes, and thus help to advance the understanding of atmospheric aerosols.

1.2 Research objectives

Accurate assessment of aerosol effects on air quality, health, weather and climate requires a better understanding of their sources, composition, and evolution. To achieve this a better understanding of the internal (inside a single particle) and external (among different single particles) mixing state of the aerosol particles as well as the identification and quantification of particle types is required. I want to approach this goal by combining a new single particle mass spectrometer with an aerosol mass spectrometer allowing quantitative bulk particle analysis in laboratory experiments and at characteristic field locations. The first step with the new single particle mass spectrometer is to quantify its measurement capabilities. In addition, reference mass spectra to identify typical atmospheric aerosol types or sources need to be measured as the corresponding marker ions are likely instrument specific. On this basis, I want to apply the mass spectrometers in comprehensive field studies to generate aerosol data sufficient to compare to and to validate a, state of the art transport model, to determine particle types for different regions, as well as the impact of particle composition on their ice nucleation ability. This leads to the following objectives:

1) Assess the reliability and determine the measurement capabilities of a relatively new single particle mass spectrometer, the LAAPTOF. Determine its overall detection efficiencies for different characteristic types of particles for the maximum size range possible ($PM_{2.5}$), and to obtain references spectra for most of the atmospherically relevant particle types including pure compounds and complex mixtures.

2) Develop a new methodology to improve single particle identification and achieve single particle quantification in mass. Both can be achieved by systematic lab work, and by making use of aerosol and cloud chamber studies with different target particle types and aging experiments, as well as larger data sets from field measurements.

3) Determine typical or characteristic aerosol concentrations, compositions, particle types, and mixing states by combination of two aerosol mass spectrometers (LAAPTOF & AMS) in field measurements at representative remote, rural, and urban locations in central Europe. The two complementary tools will be used to characterize ambient particles from clean areas such as remote mountain sites (free troposphere), to moderately polluted rural boundary layer, and to polluted urban background sites. This objective and the aforementioned two will complement each other.

4) Determine sources and evolution of ambient aerosols, and evaluate the regional transport model COSMOS-ART, by comparing field measurements and transport model results. Specify the relative importance of chemical transformations and transport processes for the local aerosol characteristics. These objectives will be achieved in collaboration with the model developers.

5) Investigate the impact of aerosol particle composition on their ice nucleation ability, based on dedicated aerosol chamber and field studies.

1.3 Methodology

To achieve my objectives I used mainly two complementary mass spectrometers: a laser ablation aerosol particle time-of-flight mass spectrometer (LAAPTOF, AeroMegt GmbH) and a high-resolution time-of-flight aerosol mass spectrometer (HR-ToF-AMS, Aerodyne Inc.). They provide real time information on size and chemical compositions for individual particles and bulk samples, respectively. Laboratory work was mainly performed at the aerosol and cloud chamber facility AIDA (Aerosol Interaction and Dynamics in the Atmosphere; http://www.imk-aaf.kit.edu) but also at the aerosol chamber facility of MIT (http://krollgroup.mit.edu/research.htm). Apart from that, I learned to use the transport model COSMO-ART (consortium for small scale modelling–aerosols and reactive trace gases), partially developed by modellers at IMK-TRO at KIT, to identify aerosol sources and to understand aerosol transport and transformations.

1.3.1 Analytical methods

The LAAPTOF is a single particle mass spectrometer that measures refractory and non-refractory species. It has been commercially available for a short time. It was assessed and applied for atmospheric aerosol studies in recent publications (Ahern et al., 2016; Gemayel et al., 2016; Gemayel et al., 2017; Marsden et al., 2018; Marsden et al., 2016; Marsden et al., 2019; Ramisetty et al., 2018; Reitz et al., 2016; Shen et al., 2018; Shen et al., 2019a). The LAAPTOF used in this dissertation was delivered in April 2015. As shown in Figure 2, aerosols are sampled with a flowrate of ~80 cm^3 min^{-1} via an aerodynamic lens (ADL, LPL-2.5, AeroMegt GmbH) at ambient pressure. In front of the ADL mounts an orifice with a diameter of 100 µm. Aerosol particles in a size range between 70 nm and 2500 nm d_{va} are focused and then accelerated in the ADL. The transmission efficiency is close to 100% for particles with diameters of 100 nm to 2 µm d_{va}. In the vacuum, they pass through the particle time-of-flight (PTOF) chamber/detection chamber with two detection/sizing laser beams (λ = 405 nm, continuous wave, 40mW). Once the detection lasers successively detect a single particle, its d_{va} is calculated from its time of flight and recorded. After detection by the rear laser, an excimer/ionization laser pulse can be triggered for a one-step desorption/ionization of the refractory and non-refractory species of the particle. The parameters of the excimer laser (ATLEX-S, ATL Lasertechnik GmbH) are as follows: λ = 193 nm; pulse

duration: 4 to 8 ns; maximum pulse energy: 8 mJ; beam diameter: 300 μm; power density: ~10^9 Wcm^{-2}. A laser pulse energy of 3 to 4 mJ was used for all the measurements in this dissertation. The resulting cations and anions are analysed by a bipolar time-of-flight mass spectrometer (BTOF-MS; TOFWERK AG; mass resolution of m/Δm=~ 600 to 800 at 184 Th; mass range: mass to charge ratio=1 up to ~2000 Th) with unit mass resolution. Thus, for each individual particle two mass spectra of positive and negative ions are generated.
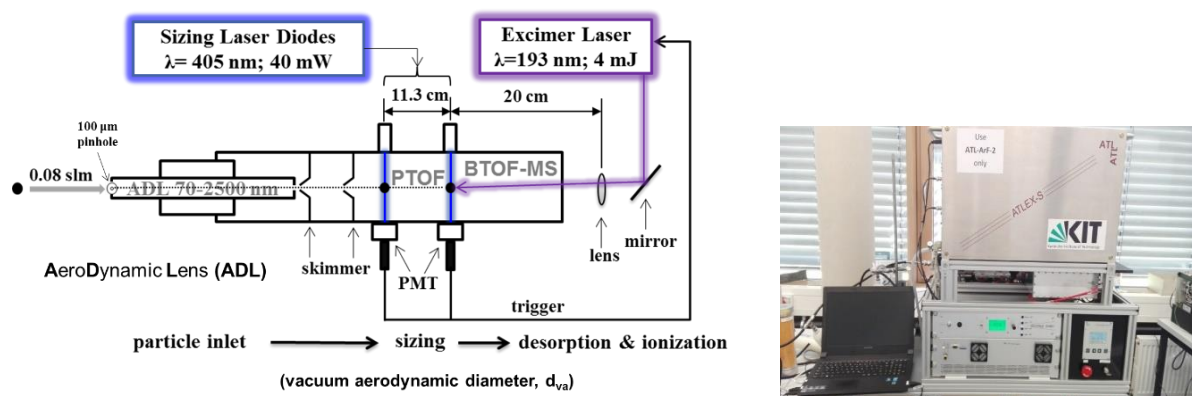
Figure 2: Schematic and photo of the LAAPTOF instrument. PTOF stands for particle time-of-flight, BTOF-MS strands for bipolar time-of-flight mass spectrometer, and PMT stands for photomultiplier tube. The instrument is running under step-down decreasing low-pressure system: from the ambient pressure 1 atm (760 Torr), decreases to 5 Torr in ADL with inlet open (10^{-1} Torr when inlet is closed), and reaches 10^{-7} Torr in BTOF-MS region.

The description mentioned above is suitable for the operation in the environment under atmospheric pressure (1 atm). At lower pressure, the particle size determined will become larger than that at 1 atm. In order to obtain the right size information, a pinhole with larger size should be used to compensate the lower pressure and a new size calibration is required. For instance, a 120 µm pinhole was used at the Jungfraujoch site with an atmospheric pressure of 650 mbar.

In LAAPTOF operation, there are four modes for triggering excimer/ionization laser. The most commonly used one is both lasers mode as mentioned above, namely front and rear detection lasers are used for triggering and sizing.

It should be noted that there are spectrum-to-spectrum mass peak shifts (jitter), especially in the positive spectra. This is mainly due to variance in the position of particle–excimer laser interaction, which complicates mass calibration and cannot be corrected with the existing AeroMegt IGOR software of the LAAPTOF instrument. Such peak shifting might be avoided with delayed ion

extraction, namely implementing a pulsed extraction system to store the ions for a certain time and then extract them into the BTOF-MS region.

Single particle data analysis**.** A large amount of data has been generated during the chamber and field campaigns. Therefore, efficient procedures (e.g. software tools) for data analysis are required. I am continuously working on improvement of existing software while doing such analysis. The single data analysis is done via the Igor LAAPTOF data analysis software (version 1.0.2, AeroMegt GmbH). As mentioned above, there is a peak shifting (jitter) problem with the LAAPTOF mass spectra. The original mass calibration procedure in the manual is inadequate for a big data set. Therefore, I have improved the method and the corresponding modified procedure is described in my 1st first author paper (Shen et al., 2018) for my PhD study. Furthermore, I have successfully written a set of new Igor procedures to make better use of the laboratory-based reference spectra to interpret the field data, as the target/reference-oriented classification method can also realize the selection of specific particles classes. This method is described in detail in my Shen et al. (2018) and has been applied for analysis of field data in my 2nd first author paper (Shen et al., 2019a).

The HR-ToF-AMS is used to provide quantitative information with respect to mass concentrations of non-refractory species, such as ammonium, nitrate, sulfate, chloride, and organic compounds with high time resolution and sensitivity (DeCarlo et al., 2006). Similar as the LAAPTOF, aerosols are sampled with a flowrate of ~84 cm^3 min^{-1} via an ADL, which allows to focus and accelerate particles in the size range of 80 to 2500 nm d_{va}. The resulting particle beam passes through a PTOF/sizing chamber where particles' size is determined and recorded. As shown in Figure 3, at the entrance of the PTOF chamber there is a chopper, which is moving between open, blocked, and chopping positions and serves as the starting time point. After the PTOF region, the particles enter hit a target heated to 600°C to vaporise the non-refractory particle compounds. The resulting vapours are ionized and split into fragments by electron impact with an energy of 70 eV, from a tungsten filament. The positive ions generated are extracted into a ToF mass spectrometer. Ion movements have two modes: V and W modes, corresponding to lower and higher mass resolution (~2500 for V; 4500 to 5000 for W). It is important to note that, particles can bounce off the heater. The bouncing effect leads to an underestimation of mass concentrations. Therefore, a collection efficiency (CE, the product of net particle transmission and detection efficiency) is used for

correction (Canagaratna et al., 2007). The default value of CE is 0.5 for field studies (Canagaratna et al., 2007; Middlebrook et al., 2012). However, it should be noted that the CE is dependent on particle composition and phase of the particles (Bahreini et al., 2005). In this dissertation, composition dependent CEs were used to correct the AMS data for this measurement campaign. The result is similar as that generated by using a CE = 0.5.
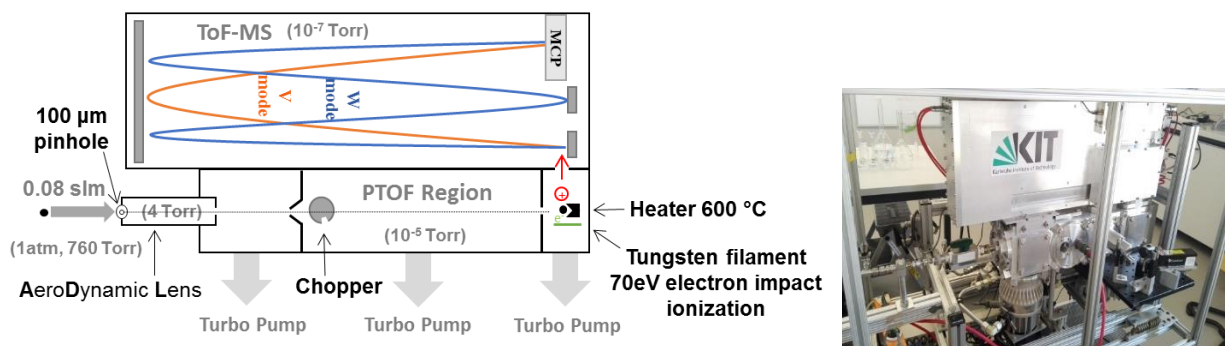
Figure 3: Schematic and photo of the high-resolution time-of-flight mass spectrometer (HR-TOF-MS). PTOF stands for particle time-of-flight and MCP stands for micro-channel plate detector. The instrument is running under step-down decreasing low-pressure system: from the ambient pressure 1 atm (760 Torr), decreases to 4 Torr in ADL with inlet open (10^{-1} Torr when inlet is closed), to 10^{-5} Torr in PTOF region and reaches 10^{-7} Torr in TOF-MS region.

The LAAPTOF and AMS have similar components, including ADL inlet, PTOF region for sizing, ionization region, and TOF-MS for analysing ion fragments. The ADL inlet allows forming a narrow particle beam and initial pressure reduction. The total pressure drop inside the mass spectrometers are both of about 8 orders of magnitude. The major difference between these two instruments are: 1) LAAPTOF measures single particles, while AMS measures particulate species in bulk. 2) LAAPTOF is using laser ablation (laser desorption and ionization, LDI), while AMS is using thermal vaporization (600 °C) and electron impact ionization. As a result, LAAPTOF can measure both non-refractory and refractory species, while AMS can only measure non-refractory ones. 3) The excimer laser cannot interact with the entire particle; therefore, LAAPTOF cannot provide direct quantitative information regarding the mass of particle and particulate species. However, AMS can do quantitative measurements for the non-refractory species in the particles. 4) LAAPTOF has bipolar TOF-MS that allows analysing both cations and anions, while AMS can only measure fragment cations but with higher mass resolution. The main common features and differences between these two mass spectrometers are summarized in Table 1.

Table 1: Comparison between LAAPTOF and HR-TOF-AMS

	LAAPTOF	HR-TOF-AMS
Instrument components	ADL Inlet − sizing region − ionization region − TOF-MS − MCP Detector − Computer	
Sizing method	Two detection laser beams	Chopper as the starting time
Ionization method	Laser ablation	Electron impact ionization
TOF-MS type	Bipolar; measures cations and anions	Only measure cations
Samples	Fragments from individual particles	Fragments from bulk samples
Analysis of non-refractory species	Both can measure e.g. organic, sulfate, nitrate, ammonium, and chloride	
Analysis of refractory species	Yes, it measures e.g. dust, sea salt, and soot	No
Quantification in particle mass	No	Yes

1.3.2 Aerosol and cloud chambers
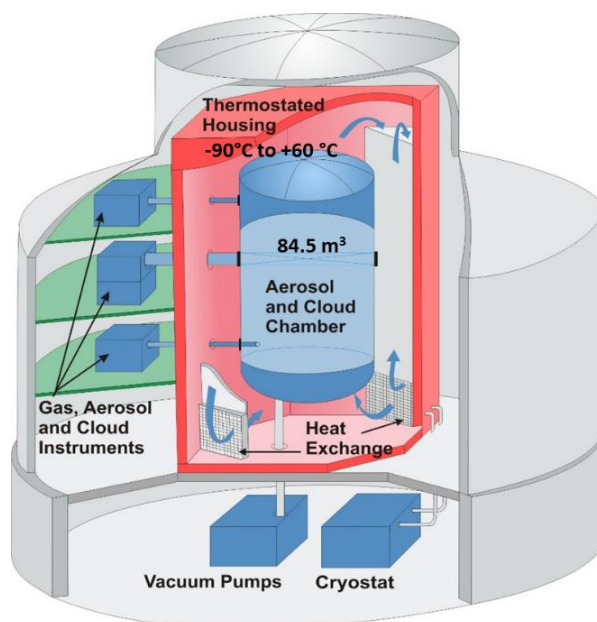
Figure 4: Schematic view of the AIDA facility, adapted from http://www.imk-aaf.kit.edu/304.php.

Main part of the experimental work of my PhD study was carried out using the AIDA (stands for Aerosol Interaction and Dynamics in the Atmosphere) chamber facility (Figure 4) at IMK-AAF (http://www.imk-aaf.kit.edu). This facility allows experiments under relevant atmospheric conditions on timescales of up to several days. Aerosol experiments are carried out in the 84.5 m^3 aluminium vessel that can be operated under a wide range of atmospherically relevant temperatures (60 − -90 °C), pressures (1 − 1000 hPa), and relative humidities (0 − >100%). The AIDA campaigns covering comprehensive research topics on aerosol formation and chemical aging process, aerosol-

cloud interactions, the direct and indirect effects of aerosols on climate, weather, and the environment (Cziczo et al., 2009; Donahue et al., 2012; Mohler et al., 2005; Mohler et al., 2006; Saathoff et al., 2009; Wagner et al., 2009). The AIDA facility can also be used as a platform for testing and intercomparison of measurement techniques for e.g., water vapour, soot, and ice nucleation (DeMott et al., 2018; DeMott et al., 2011; Fahey et al., 2014; Laborde et al., 2012). The combination of its size, temperature range, and comprehensive trace gas, aerosol, and cloud instrumentation makes it a unique facility for air pollution, weather, and climate research. In this dissertation, I have made use of several AIDA campaigns with different research topics on aerosols, which provided a good opportunity to characterize different atmospherically relevant samples, such as secondary organic aerosols with and without seeds, soil dust, and sea salt particles. The AMS or the LAAPTOF are typically connected to the chamber via stainless steel tubes of 4 mm inner diameter.

During my research visit at the MIT I used the 7.5 m^3 Teflon aerosol chamber (http://krollgroup.mit.edu/research.htm) for aerosol aging experiments and characterised the chemical composition of atmospheric particles with the single particle mass spectrometer PALMS of my host group (Prof. Daniel Cziczo's group; http://cziczogroup.scripts.mit.edu/wp/).

1.3.3 Transport model COSMO-ART
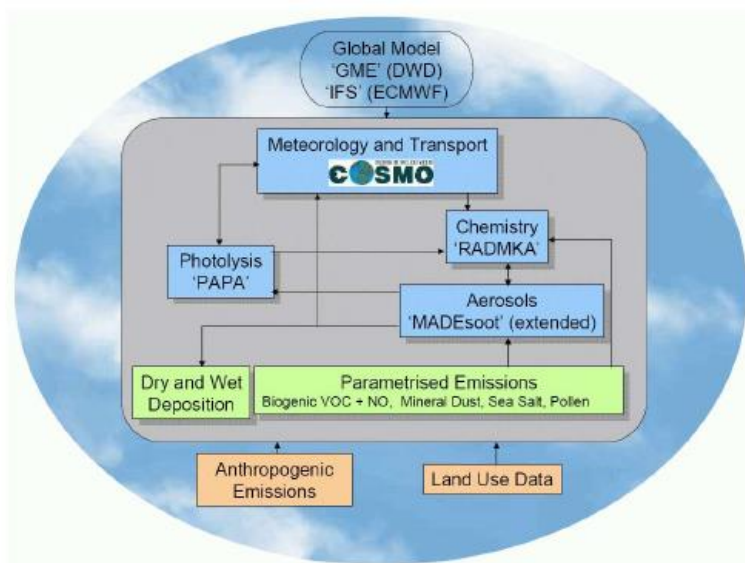
Figure 5: Schematic of the transport model system COSMO-ART © Vogel et al. (2009).

Transport models are useful tools to study aerosol particle sources, transport, and transformation, since they can predict temporal and spatial atmospheric composition. The transport model COSMO-ART (Figure 5) is a fully online coupled model system, covering the continental to the regional scale (Vogel et al., 2009). The online coupling allows calculating the interactions of gases and aerosols with the same spatial and temporal resolution for all scalars, such as temperature, gas and aerosol particle concentrations. COSMO-ART is the extended version of the operational weather forecast model COSMO (Baldauf et al., 2011) of the German weather service (Deutscher Wetterdienst, DWD), and continuously improved by IMK-TRO modellers (http://www.imk-tro.kit.edu/english/3509.php). The extension allows online calculation the transport of reactive trace gases and aerosols as well as their interaction with the atmosphere. The version used in this dissertation is COSMO5.1-ART3.1, which includes the treatment of secondary aerosols, emissions of soot, mineral dust, sea salt, and biological species such as pollen grains, physical processes such as coagulation, condensation, dry deposition and sedimentation, as well as the treatment of washout in a consistent way. Based on the actual aerosol loading, the corresponding photolysis frequencies and radiative fluxes can be calculated efficiently with newly developed methods. According to the simulated radiative fluxes and temperatures, as well as the land use data, the hourly biogenic emissions are calculated online (Vogel et al., 1995). The pre-calculated anthropogenic emissions includes traffic emissions, large point and area sources such as industrial and households' areas. The emission data used in this dissertation is based on the work by (Backes et al., 2016; Bieser et al., 2011). In addition, the large amount of model output data (netcdf files with four dimensions) were handled with dedicated Python scripts.

Apart from the major tools mentioned above, I also used the following instruments. A nebulizer (ATM 221, Topas GmbH) was used for generating aerosol particles. A propane burner (RSG miniCAST; Jing Ltd.) was used for generating soot. A scanning mobility particle sizer (SMPS, TSI GmbH) system including a condensation particle counter (CPC) and a differential mobility analyser (DMA 3080) was used for measuring particle size distributions. In the field measurements, particle mass (total suspended particulate, PM_{10}, and $PM_{2.5}$) was obtained with an optical particle counter (OPC; FIDAS, PALAS GmbH). An Aethalometer (AE33-7, Magee Scientific Co.) was used for black carbon measurements. Trace gases sensors (O_3, O341M, Environment SA; SO_2, AF22M, Environment SA; NO_2, AS32M, Environment SA; CO_2, NGA2000, Rosemont Inc.) and a weather sensor (WS700, Lufft GmbH) were used as well.

1.3.4 Laboratory, field, and model studies

In this work, I have made use of comprehensive information from laboratory experiments, field measurements, and modelling, aiming to better understand the chemical composition, mixing state, sources, and aging of aerosol particles. The LAAPTOF is one of the most important but was not yet well-determined tool, and therefore I have done dedicated laboratory experiments to access its reliability, determine its performance and to obtain references spectra for particles consisting of atmospherically relevant components, from pure compounds to complex mixtures. Afterwards, the LAAPTOF together with the AMS were deployed to investigate the formation, aging, and ice nucleation of secondary organic aerosols (SOA) in AIDA chamber. In addition, I participated in several chamber studies at KIT and MIT to determine the potential impact of the chemical composition of single aerosol particles on their ice nucleation behaviour. The AIDA campaigns were also used for characterization of selected atmospherically relevant aerosol samples and aging processes. Moreover, I took part in four field measurements and characterized the chemical compositions of the ambient aerosol particles from a relatively clean mountain site to a polluted urban background site with both complementary mass spectrometers AMS and LAAPTOF. In the last year of my PhD study, I learned to use the COSMO-ART model in order to understand transformations of ambient aerosols. Colleagues from the group of Bernhard Vogel (IMK-TRO) supported me significantly not only with teaching but also by providing emission data and in discussions about interpretation of the model results. The timeline of the corresponding activities is shown in Figure 6. More details of the performed laboratory, field, and model studies will be given in the following sub-sections 1.3.4.1, 1.3.4.2, and 1.3.4.3, respectively.

2015
- AIDA Campaign SOA15 (Oct to Nov)
- Determination of measurement capabilities of LAAPTOF (since Nov)

2016
- AIDA Campaign SOIL02 (Mar)
- Field Campaign TRAM01 (Jul to Aug)
- AIDA Campaign SOA16c (Oct)
- AIDA Campaign SOOT18 (May)
- AIDA Campaign PLANTS01b (Sep)
- AIDA Campaign Ocean02 (Dec)

2017
- Field Campaign INUIT-CLACE (Jan to Feb)
- Field Campaign Stuttgart01 (Jul to Aug)
- AIDA Campaign SOA17 (Nov)
- AIDA Campaign CAINIC01 (Dec)

2018
- Field Campaign Stuttgart02 (Feb to Mar)
- SOA Ice Nucleation Project at MIT (Apr to May)
- AIDA Campaign SOA18 (Nov)
- AIDA Campaign TXDUST01 (Oct)
- COSMO-ART modelling (since Apr)

2019
- COSMO-ART modelling
- Finalizing data analysis
- Finalizing thesis
- Finalizing publications

AIDA simulation chamber
84.5 m³

Summer
TRAM01 Rural site

INUIT-CLACE Jungfraujoch Mountain site

Stuttgart 01 & 02 Urban site
Summer / Winter

Figure 6: Timeline of my PhD work. The major activities are shown in bold, including determination of the measurement capabilities of the LAAPTOF, AIDA chamber campaigns, field campaigns, and COSMO-ART modelling.

1.3.4.1 Laboratory experiments

Determination of the LAAPTOF measurement capabilities. In order to find the ideal settings and setup, and to assess the reliability of this instrument and prepare it for its deployment at the chamber and in the field, I did alignment and calibrations for the LAAPTOF by using various particle types with different size and optical properties in the lab. Afterwards, I did systematic experiments to characterize its overall detection efficiency (ODE). In order to better understand the spectral performance of the LAAPTOF, and more importantly, better interpret the ambient data, I measured various atmospherically relevant aerosol particles in the lab: particles consist of pure compounds, such as NH_4NO_3, $NaCl$, K_2SO_4, polystyrene latex particles (PSL) and some mixtures of them, as well as soot particles. I have also measure more complex samples, such as SOA, soil

dust, plant debris, sea salt, and fly ash particles, during various AIDA chamber studies. The resulting 32 reference spectra have been uploaded to a database publicly available in electronic format via the EUROCHAMP DATA CENTER – Library of Analytical Resources of the EU project EUROCHAMP-2020 (https://data.eurochamp.org/). The corresponding methods and results have been published as my 1st first author paper for my PhD study (Shen et al., 2018), and shown in section 2.1. I also presented this work as a poster at the European Aerosol Conference in 2017 (EAC 2017), and won the "Best Poster Award".

Apart from that, I also took part in a project to explore femtosecond (fs) laser ablation in the LAAPTOF, aiming to assess whether the fs laser with high power densify leads to a more complete ionization of the entire particle and thus improve quantitative abilities of single particle mass spectrometer. In this project, supported the experimental set-up in the lab and the measurements of the single aerosol particles. The corresponding results have been published in my co-authored paper (Ramisetty et al., 2018), shown in section 2.1.

Aerosol and cloud chamber campaigns. I have participated in a total of 10 AIDA chamber campaigns with investigations on secondary organic aerosols (SOA), soil dust, plant debris, sea salt, soot, and fly ash particles. The major AIDA campaigns I participated were organised by our group are the ones related to SOA: SOA15, 16c, 17, and 18. SOA15 and 16c aimed to investigate SOA formation and chemical aging processes, as well as its ice nucleation abilities for different temperatures and relative humidity (RH); SOA17 focused on better understanding of urban and rural aerosol interaction. During these three campaigns, I was operating the LAAPTOF and AMS, did the calibrations for the instruments and data analysis. During SOA18, I was mainly offering technical support and teaching two new PhD students in operating different instruments, such as aerosol mass spectrometer and scanning mobility particle sizer, and corresponding theory, as well as data analysis skills.

SOA15 results are shown in section 2.4 and 2.5, corresponding to two publications (Huang et al., 2018; Wagner et al., 2017), both of which I co-authored. I used SOA reference spectra obtained from SOA16c in my 1st first author publication (Shen et al., 2018). SOA17 results have been mentioned in my 2nd first author publication (Shen et al., 2019a), and discussed in more detail in section 2.4, as well as in my 3rd first author publication (Shen et al., 2019b; submitted).

Another important campaign is SOIL02 in 2016. That was my first time to deploy the LAAPTOF at the AIDA chamber facility. I aimed to compare the chemical composition of different soil dust particles with their ice nucleating behaviour. Positive and negative ion mass spectra were recorded typically for several hundred individual particles of each dust type before and after cloud expansion experiments in the temperature range 228−260 K. I have done all the LAAPTOF data analysis, and the major results are shown in section 2.5. I have presented this work as a poster at EAC 2016 and a talk in EAC2017 as the first author.

Regarding the other AIDA campaigns, they mainly focused on the ice nucleation abilities of the aerosol particles. I took the opportunity to do chemical characterization of many different particle types and obtained corresponding reference spectra, which I made publicly available via the EUROCHAMP DATA CENTER.

The various reference spectra and their potential use in single particle mass spectrometry are discussed in my 1st first author publication (Shen et al., 2018).

SOA ice nucleation project at MIT by using PALMS and SPIN. I was a visiting student in Prof. Daniel J. Cziczo's group at the Massachusetts Institute of Technology (MIT) from April 21 to June 13, 2018. During my stay, I have participated in a laboratory study on ice nucleation of SOA. The SOA were formed in a 7.5 m^3 Teflon chamber or potential aerosol mass oxidation flow reactor (PAM, Aerodyne), characterized with a single particle mass spectrometer, PALMS (strands for Particle Analysis by Laser Mass Spectrometry) and an AMS. After aerosol characterization, the aerosol was introduced to the SPIN (stands for the SPectrometer for Ice Nuclei; Droplet Measurement Technologies, Boulder, CO) to quantify the nucleation efficiency of the ice nucleating particles (Garimella et al., 2016). In this project, I was working on characterization of the particles by using the PALMS. My tasks included alignment and operation of the instrument as well as data analysis. I will co-author one or more publications related to this work.

1.3.4.2 Field campaigns

I have participated in four field measurement campaigns and characterised particles in different environments. These were particles from the relatively clean free troposphere at a remote mountain site on the Jungfraujoch in Switzerland, particles from anthropogenic (industrial and urban) and biogenic sources at a rural site in the upper Rhine valley, and particles from urban sources at an urban background site in downtown Stuttgart.

Remote mountain site Jungfraujoch. From January 16th to February 23rd 2017, I took part in the field campaign, INUIT-CLACE-2017, at Jungfraujoch (JFJ) station, a high alpine research station 3500 m above sea level (a.s.l.) in Switzerland. The JFJ research station is one of the rare stations in the world, which allows direct sampling in ice or mixed phase clouds. The station is equipped with inlets required to probe the total, interstitial, and residual aerosol particles. INUIT-CLACE-2017 campaign focused on quantification of the ice nucleation behaviour of the total aerosol particles, and determination of the impact of single particle chemical composition on the ice nucleation behaviour of the aerosol particles collected in ice and mixed phase clouds at the Jungfraujoch. During the campaign, I was operating LAAPTOF that belongs to KIT, measured single particle size and composition aiming to characterize the aerosol particles and investigate clouds particle residuals. My tasks included experimental setup, alignment and calibration for the instrument, data acquisition during the campaign, and data analysis. In addition, I also helped collect the aerosol particles from the total aerosol inlet on filters for subsequent analysis of the ice nucleating ability of the particles with an immersion freezing method in the laboratory.

I have already finished the single particle data analysis and will use the data in my 4th first author publication for PhD study. This paper will focus on the comparison of particle types identified at different measurement sites from relatively clean to more polluted environment (from remote mountain to rural to urban). I will also co-author one or more publications related to this work.

Rural site in the upper Rhine valley. From July 26th to September 1st, 2016, I have taken part in a field campaign TRAM01 to analyse the chemical composition and mixing state of individual aerosol particles by using LAAPTOF, to quantify the refractory organic and inorganic aerosol compounds by using AMS, for comparison with the associated trace gases and meteorological

conditions. Aim of this campaign is to study the nature and to identify possible sources of aerosol particles in Leopoldshafen, a rural site about 12 km north of the city of Karlsruhe.

I used one-day LAAPTOF data obtained in TRAM01 as an example to compare classical fuzzy clustering and a reference-spectra-based classification method in my 1st first author publication for my PhD study (Shen et al., 2018). I used all of the LAAPTOF data obtained in TRAM01 as a test case to quantify particle mass contributions based on chemically and size-resolved ODE for this instrument, without a need of a reference instrument. This has been shown in section 2.2, corresponding to my 2nd first author publication (Shen et al., 2019a), and I presented it as a poster at American Geographical Conference (AGU) 2018. In order to find out the sources for the particles, I also did model simulations that will be mentioned in section 1.3.4.3. Comprehensive measurement and model results have been used and discussed in my 3rd first author publication that has been submitted. Another companion paper that I co-authored, focusing on night-time organonitrate contributions to particle growth, has been published (Huang et al., 2019a) and shown in section 2.3.2.

Urban background site in downtown Stuttgart. I have participated in two measurement campaigns taking place in the city centre of Stuttgart (unterer Schlossgarten). One was in summer time from July 5th to August 17th, 2017; and the second in wintertime from Feb 5th to March 5th 2018. I aimed to characterize the chemical composition and mixing state of the ambient aerosol particles at a polluted urban site, determine the most important processes and timescales for transformation of properties of urban aerosols relevant for air quality and climate. In these two campaigns, I analyzed the chemical composition of individual aerosol particles by using LAAPTOF, measured the organic and inorganic species on refractory aerosol particles by using AMS and measured the associated trace gases and meteorological conditions.

Part of the corresponding results are published (Huang et al., 2019b; in review), which I co-authored. This is shown in section 2.3.3. Besides, I will use the Stuttgart data in my 4th first author publication for my PhD study, by comparing particle types and mixing state observed at the different measurement locations.

1.3.4.3 Model studies

In order to determine the origin and evolution of ambient aerosol particles, I used the regional transport model COSMO-ART in close cooperation with the model developers at IMK-TRO (http://www.imk-tro.kit.edu) since March 2018. I employed the COSMO-ART model to simulate a specific episode of the TRAM01 field campaign, with corresponding transport and transformation of biogenic and anthropogenic aerosols including urban and industrial pollution. With the input data provided by the modellers, I did all model runs including the basic model runs for five days and all the model sensitivity tests, such as with and without biogenic emissions, doubled biogenic emissions, and varied boundary conditions. All the output netcdf (.nc) data with four dimensions were analysed with Phython scripts which I created.

The combination of COSMO-ART modelling and field measurement has proven to be very useful for source apportionment and understanding of the complex transformation processes of atmospheric aerosols, which is the focal point of my 3rd first author publication (Shen et al., 2019b; submitted) that is shown in section 2.3.2. Some of the model results have been published as video files at KIT open data (https://doi.org/10.5445/IR/1000094401) to illustrate the complex aerosol transport dynamics.

2 Results and discussions

According to my research objectives, I have performed the laboratory, filed, and model work as aforementioned. This leads to three first author publications (2 have been published, 1 has been submitted) and five co-authored publications (4 published, 1 in review). In this section, I summarize the major results of my PhD work, from technical (section 2.1) to methodological (section 2.2) to scientific (section 2.3 and 2.4) aspects. For this purpose, I show the abstracts of the publications together with an authorship statement and two or three major plots. My three first author publications are in section 2.1, 2.2, and 2.3.2, respectively, together with the co-authored publications that fit into the corresponding topics. Besides, some other important results that have not yet been published are shown as well.

2.1 Measurement capabilities of the single particle mass spectrometer

The measurement capabilities of the relatively new single particle mass spectrometer, LAAPTOF, were determined by systematic laboratory experiments and field measurements. The instrument performance, reference spectra, and classification of atmospheric samples are published in my first author paper (Shen et al., 2018). Another publication I co-authored, has verified the difficulties in quantitative measurement of single particles. This quantification problem could not be solved by replacing the original nanosecond excimer laser with a femtosecond laser with higher laser power density and shorter laser pulse length (Ramisetty et al., 2018). In the following, my 1st first author publication and this co-authored publication are shown successively, with their titles, authors, journal, authorship statement and abstract, respectively. Two major plots from my first author publication are shown as well.

First author publication title: Laser ablation aerosol particle time-of-flight mass spectrometer (LAAPTOF): Performance, reference spectra and classification of atmospheric samples.

Authors: <u>Xiaoli Shen,</u> Ramakrishna Ramisetty, Claudia Mohr, Wei Huang, Thomas Leisner, and Harald Saathoff

Journal: Atmospheric Measurement Techniques 11, 2325–2343, 2018

Authorship statement: This peer-reviewed scientific journal article was written by me, based on the systematic determination of the LAAPTOF measurement capabilities and measurements of the aerosol particles both in the lab and in the ambient. I did alignment and calibration for the LAAPTOF, measured the particles samples, did all the data analysis, developed a method for classification by using reference spectra, and produced all figures.

Ramakrishna Ramisetty helped to characterize the LAAPTOF and to measure some of the particle samples. Claudia Mohr provided technical and scientific support for characterizing the LAAPTOF as well as data analysis, and for interpretation and discussion of the results. Wei Huang provided scientific support for interpretation and discussion of the results. Thomas Leisner gave general advices and comments for this paper. Harald Saathoff provided technical and scientific support for characterizing the LAAPTOF, as well as suggestions for the data analysis, interpretation, and discussion. All authors contributed to the final text.

Abstract: The laser ablation aerosol particles time-of-flight mass spectrometer (LAAPTOF, Aeromegt GmbH) is able to identify the chemical composition and mixing state of individual aerosol particles, and thus is a tool for elucidating their impacts on human health, visibility, ecosystem and climate. The overall detection efficiency (ODE) of the instrument we use was determined to range from ~(0.01 ± 0.01)% to ~(4.23 ± 2.36)% for polystyrene latex (PSL) in the size rage of 200 to 2000 nm, ~(0.44 ± 0.19)% to ~(6.57 ± 2.38)% for ammonium nitrate (NH_4NO_3), and ~(0.14 ± 0.02)% to ~(1.46 ± 0.08)% for sodium chloride (NaCl) particles in the size rage of 300 to 1000 nm. Reference mass spectra of 32 different particle types relevant for atmospheric aerosol (e.g. pure compounds NH_4NO_3, K_2SO_4, NaCl, oxalic acid, pinic acid, and pinonic acid; internal mixtures of e.g. salts, secondary organic aerosol, and metallic core-organic shell particles; more complex particles such as soot and dust particles) were determined. Our results show that internally mixed aerosol particles can result in spectra with new clusters of ions, rather than simply a combination of the spectra from the single components. An exemplary one-day ambient data set was analysed by both classical Fuzzy clustering and a reference spectra based classification method. Resulting identified particle types were generally well correlated. We show how a combination of both methods can greatly improve the interpretation of single particle data in field measurements.

Major plots: The following plots show the overall detection efficiency determined for the single particle mass spectrometer and the correlation matrix between reference spectra and particle classes obtained by fuzzy clustering of the mass spectra.
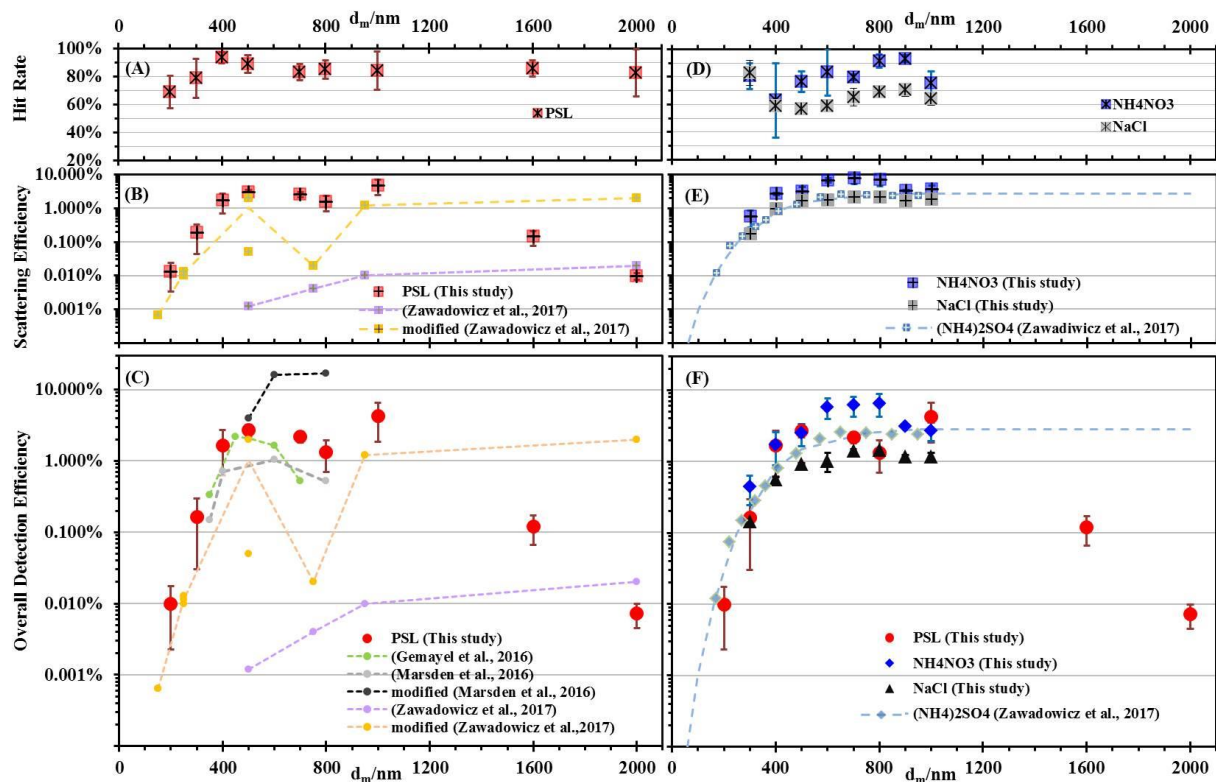
Figure 7: Hit rate (HR, panel A and D), scattering efficiency (SE, panel B and E), and overall detection efficiency (ODE, panel C and F) for PSL, ammonium nitrate (NH$_4$NO$_3$) and sodium chloride (NaCl) salt particles as a function of mobility diameter, d$_m$. Aerosol particles in this study were generated from a nebulizer and size-selected by DMA. In panel (B) and (E), optical counting efficiencies (OCE) for PSL and ammonium sulphate ((NH$_4$)$_2$SO$_4$) at the detection beam from the study by Zawadowlcz et al. (2017), corresponding to the SE defined in this study, are plotted for comparison. In panel (C) and (F), ODE for PSL and salt particles from other studies are plotted for comparison. In this figure, dashed lines are used only for guiding the eyes. Reproduced from Shen et al. (2018) (Figure 2, Appendix B.1).
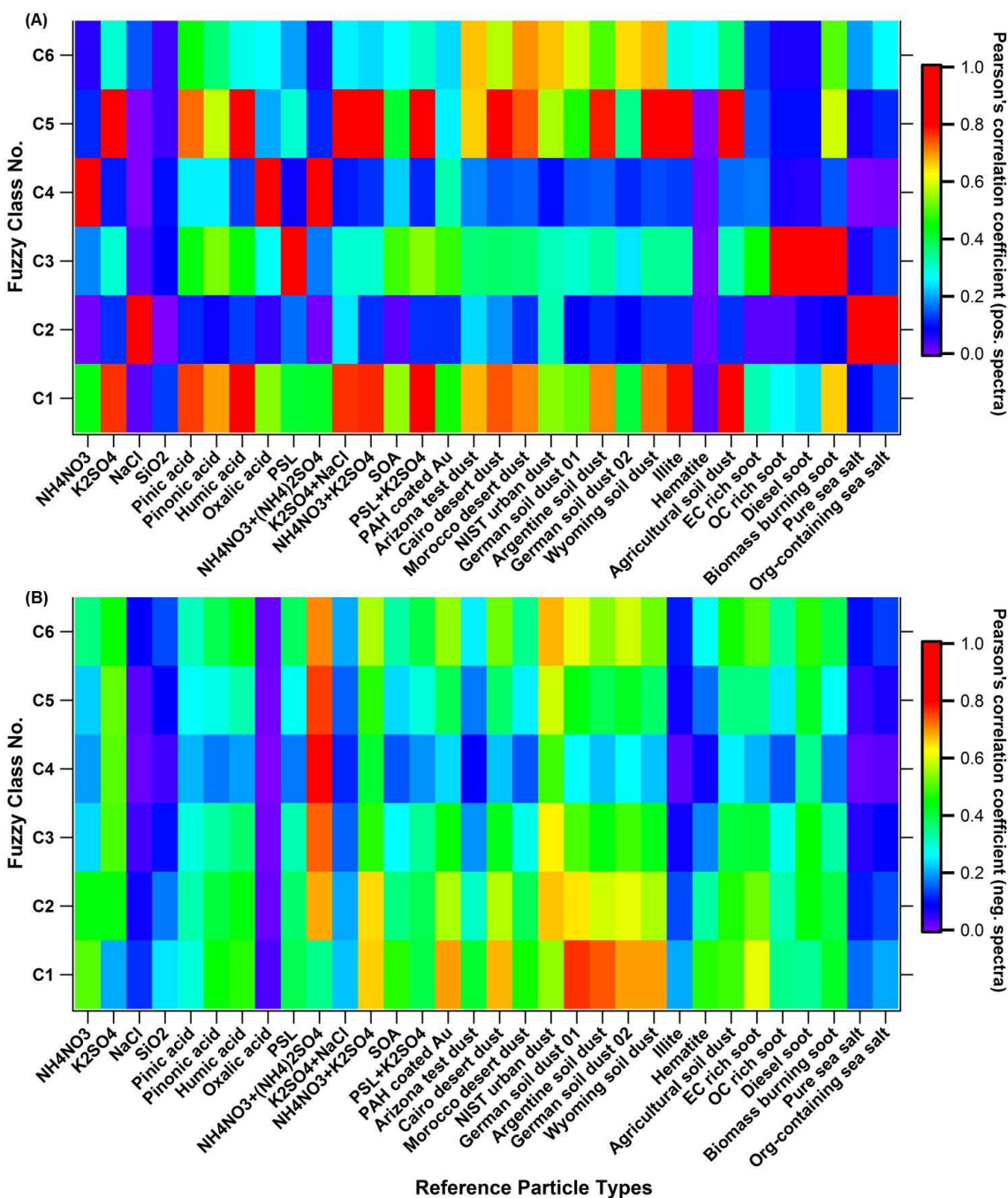
Figure 8: Correlation between Fuzzy classification results (6 classes, C1 to C6) and laboratory-based reference spectra. Panel (A) and (B) are the correlation results for the positive and negative spectra, respectively. The six classes are class 1 "More aged/mixed"; class 2 "Sodium rich"; class3: "Aged soot"; class 4 "Secondary inorganic rich"; class 5 "Potassium rich"; class 6 "Calcium rich". PAH is short for poly(allylamine hydrochloride), biomass burning soot is the lignocellulosic char from chestnut wood. Reproduced from Shen et al. (2018) (Figure 9, Appendix B.1).

The full article is reprinted in Appendix B.1. © Shen et al. (2018)

Co-author publication title: Exploring femtosecond laser ablation in single-particle aerosol mass spectrometry

Authors: Ramakrishna Ramisetty, Ahmed Abdelmonem, **<u>Xiaoli Shen,</u>** Harald Saathoff, Thomas Leisner, and Claudia Mohr

Journal: Atmospheric Measurement Techniques 11, 4345–4360, 2018

Authorship statement: This peer-reviewed scientific journal article is based on a project for investigation of femtosecond laser implementation in the single particle mass spectrometer. I have supported the experimental set-up in the lab and the measurements of the single aerosol particles. I contributed to the scientific discussions and the interpretation of the results, especially the mass spectra analysis.

Abstract: Size, composition, and mixing state of individual aerosol particles can be analysed in real time using single particle mass spectrometry (SPMS). In SPMS, laser ablation is the most widely used method for desorption and ionization of particle components, often realizing both in one single step. Excimer lasers are well suited for this task due to their relatively high power density (10^7–10^{10} W cm^{-2}) in nanosecond (ns) pulses at ultraviolet (UV) wavelengths and short triggering times. However, varying particle optical properties and matrix effects make a quantitative interpretation of this analytical approach challenging. In atmospheric SPMS applications, this influences both the mass fraction of an individual particle that is ablated, as well as the resulting mass spectral fragmentation pattern of the ablated material. The present study explores the use of shorter (femtosecond, fs) laser pulses for atmospheric SPMS. Its objective is to assess whether the higher laser power density of the fs laser leads to a more complete ionization of the entire particle and higher ion signal and thus improvement in the quantitative abilities of SPMS. We systematically investigate the influence of power density and pulse duration on airborne particle (polystyrene latex, SiO_2, NH_4NO_3, NaCl, and custom-made core-shell particles) ablation and reproducibility of mass spectral signatures. We used a laser ablation aerosol time-of-flight single-particle mass spectrometer (LAAPTOF, AeroMegt GmbH), originally equipped with an excimer laser (wavelength 193 nm, pulse width 8 ns, pulse energy 4 mJ), and coupled it to an fs laser (Spectra Physics Solstice-100F ultrafast laser) with similar pulse energy but longer wavelengths (266 nm with 100 fs and 0.2 mJ, 800 nm with 100 fs and 3.2 mJ). We successfully

coupled the free firing fs laser with the single-particle mass spectrometer employing the fs laser light scattered by the particle to trigger mass spectra acquisition. Generally, mass spectra exhibit an increase in ion intensities (factor 1 to 5) with increasing laser power density (~10^9 to ~10^{13} Wcm^{-2}) from ns to fs laser. At the same time, fs-laser ablation produces spectra with larger ion fragments and ion clusters as well as clusters with oxygen, which does not render spectra interpretation more simple compared to ns-laser ablation. The idea that the higher power density of the fs laser leads to a more complete particle ablation and ionization could not be substantiated in this study. Quantification of ablated material remains difficult due to incomplete ionization of the particle. Furthermore, the fs laser application still suffers from limitations in triggering it in a useful time frame. Further studies are needed to test potential advantages of fs- over ns-laser ablation in SPMS.

The full article is reprinted in Appendix C.1. © Ramisetty et al. (2018).

2.2 Improvement of single particle identification and quantification

Improving the single particle identification and quantification with the new LAAPTOF instrument was one of my major objectives during the first part of my PhD work. Aside from identification of specific particles, the quantification of particles in terms of characteristic types and in mass concentrations is a long lasting open problem for single particle mass spectrometry in general. Therefore, I developed a methodology to achieve quantitative results based on ambient single particle data. Such that the single particle measurement results can be used to compare with/complement the bulk measurements by other quantitative instrument such as the AMS. Based on the laboratory-derived overall detection efficiency of the LAAPTOF that I determined and reference spectra that I obtained (refer to section 2.1), as well as the big data set from the field measurement TRAM01, I have successfully improved the particle identification method and estimated particle mass without a need of a reference instrument in the field. In the following, this first author publication is shown with the title, authors, journal, authorship statement, abstract, and two major plots.

First author publication title: Understanding of atmospheric aerosol particles with improved particle identification and quantification by single particle mass spectrometry

Authors: <u>**Xiaoli Shen,**</u> Harald Saathoff, Wei Huang, Claudia Mohr, Ramakrishna Ramisetty, and Thomas Leisner

Journal: Atmospheric Measurement Techniques 12, 2219–2240, 2019

Authorship statement: This peer-reviewed scientific journal article was written by me. It is based on the laboratory-derived instrument sensitivity and the data set obtained from field measurement campaign TRAM01. I determined the laboratory based overall detection efficiency of the LAAPTOF, obtained all the reference spectra in the lab. During the field campaign, I operated LAAPTOF and AMS, did alignments and calibration for these two instruments, did all the LAAPTOF data analysis, developed the methodology, and produced all figures.

Harald Saathoff organized the campaign and provided suggestions for the data analysis, interpretation, and discussion. Wei Huang operated AMS during the whole campaign and did AMS

Abstract: Single particle mass spectrometry (SPMS) is a widely used tool to determine chemical composition and mixing state of aerosol particles in the atmosphere. During a six-week field campaign in summer 2016 at a rural site in the upper Rhine valley near Karlsruhe city in southwest Germany, $\sim$3.7 $\times$ 10^5 single particles were analysed by a laser ablation aerosol particle time-of-flight mass spectrometer (LAAPTOF). Combining fuzzy classification, marker peaks, typical peak ratios, and laboratory-based reference spectra, seven major particle classes were identified. With the precise particle identification and well characterized laboratory-derived overall detection efficiency (ODE) for this instrument, particle similarity can be transferred into corrected number and mass fractions without a need of a reference instrument in the field. Considering the entire measurement period, "Aged biomass burning and soil dust like particles" dominated the particle number (45.0% number fraction) and mass (31.8% mass fraction); "Sodium salts like particles" were the second lowest in number (3.4%), but the second dominating class in terms of particle mass (30.1%). This difference demonstrates the crucial role of particle number counts correction for mass quantification using SPMS data. Using corrections for size and chemically-resolved ODE, the total mass of the particles measured by LAAPTOF accounts for 23–68% of the total mass measured by an aerosol mass spectrometer (AMS) depending on the measurement periods. These two mass spectrometers show a good correlation (correlation coefficient $\gamma > 0.6$) regarding total mass for more than 85% of the measurement time, indicating non-refractory species measured by AMS may originate from particles consisting of internally mixed non-refractory and refractory components. In addition, specific relationships of LAAPTOF ion intensities and AMS mass concentrations for non-refractory compounds were found for specific measurement periods, especially for the fraction of org/(org+nitrate). Furthermore, our approach allows assigning the non-refractory compounds measured by AMS to different particle classes. Overall AMS-nitrate was mainly arising from sodium salts like particles, while aged biomass burning particles were dominant during events with high organic aerosol particle concentrations.

Major plots: The following plots show the strong improvement of the particle class fractions determined using the newly developed methodology and the comparison of the mass concentrations determined based on single particle analysis with bulk reference measurements.
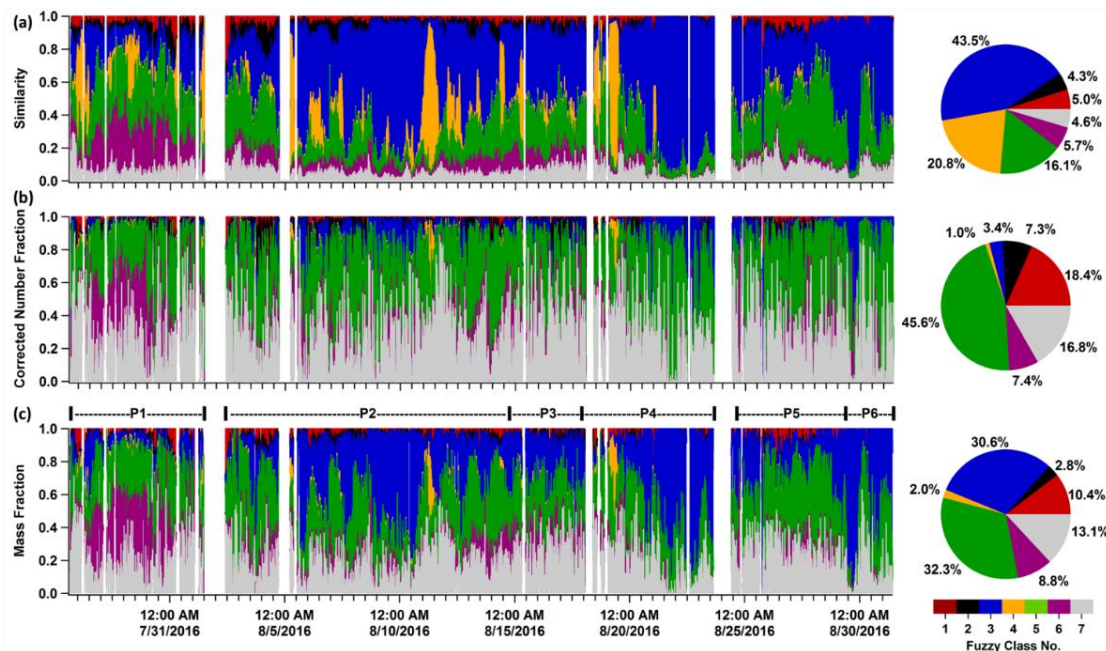
Figure 9: Time series of the similarity, corrected number fraction, and mass fraction of seven major particle classes and the corresponding pie charts for total fractions. Note that, the correction shown here is based on a chemically or particle class resolved ODE. The seven classes are class 1 (c1) "Calcium-Soil"; c2 "Aged soot"; c3: "Sodium salts"; c4 "Secondary inorganics-Amine"; c5 "Biomass burning-Soil"; c6 "Biomass burning-Organosulfate"; and c7 "Mixed/aged-Dust". In panel (c), 6 periods have been marked. Reproduced from Shen et al. (2019a) (Figure 4, Appendix B.2).
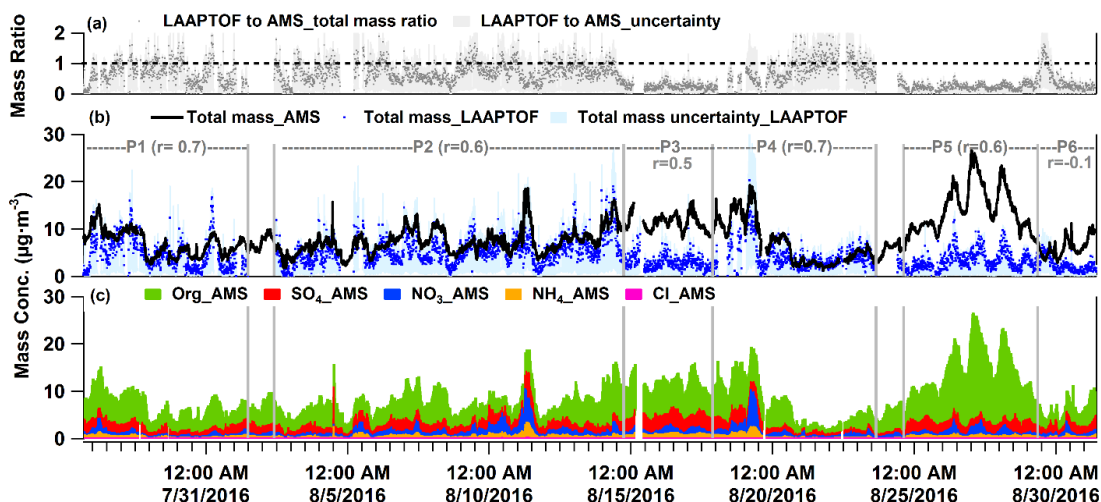
Figure 10: Time series of (a) total mass ratio of LAAPTOF to AMS data, (b) LAAPTOF total mass and AMS total mass (c) mass concentrations of particulate compounds measured by AMS. In panel (b) r is the Pearson's correlation coefficient between LAAPTOF and AMS results. Reproduced from Shen et al. (2019a) (Figure 6, Appendix B.2).

The full article is reprinted in Appendix B.2. © Shen et al. (2019a)

2.3 Composition and sources of ambient aerosol particles

The work on the determination of the LAAPTOF performance and reference mass spectra (section 2.1) and the improvement of single particle identification and quantification (section 2.2) is the important base for subsequent research. I have participated in four field campaigns at a relatively clean remote mountain site, a rural area, and a polluted urban area, in order to investigate the chemical compositions, mixing states, particle classes, and potential sources of atmospheric aerosols in different environments, and to determine their common features and differences. The overview of the LAAPTOF measurements in different field campaigns is summarized in Table 2. The corresponding results are shown in the following sub-sections. My 3rd first author publication is described in section 2.3.2

Table 2: Overview of the LAAPTOF measurements at four different field sites

	INUIT-CLACE_Jungfraujoch	TRAM01_rural	Stuttgart01_Summer	Stuttgart02_Winter
Start date	2017-01-22	2016-07-26	2017-07-05	2018-02-05
End date	2017-02-22	2016-08-31	2017-08-16	2018-03-05
Total measurement days	28	37	42	28
Total particles detected	$\sim 10 \times 10^3$	$\sim 28 \times 10^3$	$\sim 2 \times 10^6$	$\sim 8 \times 10^6$
Averaged trigger rate (particles/min)	~3	~23	~30	~210
Spectra obtained	42 404	377 936	265 759	analysis ongoing

2.3.1 Free troposphere at the Jungfraujoch mountain site

During the INUIT-CLACE-2017 campaign at the Jungfraujoch research station, I measured with the LAAPTOF instrument size as well as mass spectra for a total of 42404 single particles from January 22nd to February 22nd 2017. Most of them were measured using the total aerosol inlet. Fuzzy clustering analysis of the total mass spectra identified nine different particle classes. Some of these classes showed up almost every day, e.g., particles containing potassium (K), sulfate and nitrate (assigned to aged biomass burning particles); particles containing elemental carbon (EC) and sulfate (assigned to aged soot); and particles containing sodium (Na) salts (assigned to aged sea salt). The particle classes observed vary with particle size. As shown in Figure 11 , the following particle classes dominate the submicron size range (< 1µm d_{va}): biomass burning particles, and aged soot particles, as well as secondary inorganics particles. For sizes above 1 µm,

aged sea salt particles as well as Ca–chloride–nitrate particles have the largest number fraction. In addition, a particle class combining many of the different chemical components was observed and can be attributed to more aged/mixed aerosol particles.
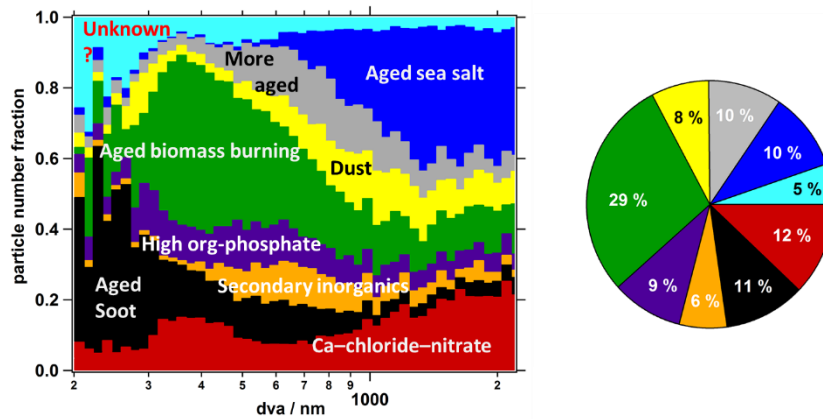
Figure 11: Size resolved number fraction for seven particle classes measured during the field campaign INUIT-CLACE-2017 from January 22nd to February 22nd 2016, based on fuzzy classification according to fuzzy c-means clustering algorithm. Particle size shown here is vacuum aerodynamic diameter (d$_{va}$).

For many measurement periods, the LAAPTOF data can be compared to another single particle mass spectrometer ALABAMA (Aircraft-based Laser Ablation Aerosol Mass Spectrometer; Max Planck Institute, Mainz) for validation of the single particle sizing and chemical characterization. For some cloud events, the LAAPTOF was characterising the total aerosol, while the ALABAMA was measuring ice residual particles using the ice counter flow virtual impactor (ICE-CVI), which is the complementary information. The data allow comparing the chemical composition of the total aerosol particles with the ice crystal residuals and may help determine the impact of chemical composition on the ice nucleation behaviour of the aerosol particles collected in clouds at the Jungfraujoch. The corresponding data analysis is still ongoing.

2.3.2 Rural site in the upper Rhine valley

In rural area of the upper Rhine valley, high particle number concentrations (similar to downtown Karlsruhe) were frequently observed by particle counters on board a tram wagon (www.aero-tram.kit.edu) intersecting the city (Hagemann et al., 2014). In order to study the chemical nature and possible sources of the particles, a stationary measurement campaign TRAM01 campaign was conducted in summer 2016. Among a total of ~3.7 $\times$ 10^5 single particles, seven major particle classes have been well identified in my 2nd first author paper (Shen et al., 2019a). Their representative mass spectra are shown in Figure 12. The size resolved number fraction for particle

classes based on the fuzzy c-means clustering algorithm is given in Figure 13. Similarly as the particles at the Jungfraujoch, aged soot particles, secondary inorganics rich, and aged sea salt particles dominate the size ranges of <400 nm, 400 nm to 1 μm, and >1 μm d_{va}, respectively.
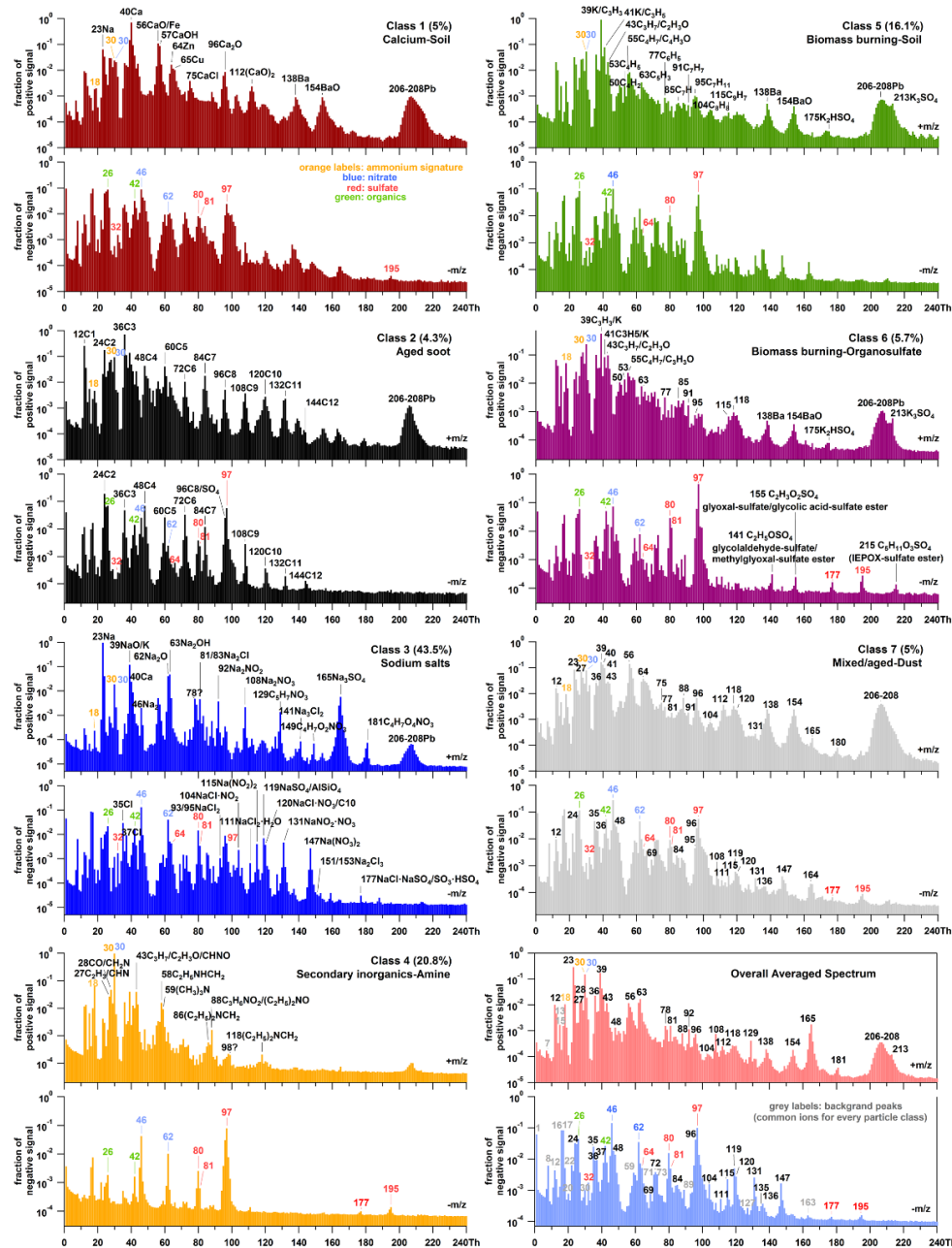
Figure 12: Representative mass spectra of seven particle classes measured during the field campaign TRAM01, based on fuzzy classification according to fuzzy c-means clustering algorithm, and averaged spectrum of total ~3.7 × 10^5 single particles measured. The percentage in each pair of spectra gives us information about the similarity of the total aerosol particles to different classes. Black labels represent the ions characteristic for different classes. The red, blue, and orange labels represent the signatures for sulfate (32 S^-, 64 SO_2^-, 80 SO_3^-, 81 HSO_3^-, 97 HSO_4^-, 177 SO_3HSO_4^-, and 195 HSO_4H_2SO_4^-), nitrate (30 NO^+, 46 NO_2^-, and 62 NO_3^-) and ammonium (18 NH_4^+ and 30 NO^+). The green labels represent the organic compounds (26 C_2H_2/CN^- and 42 C_2H_2O/CNO^-). In the overall averaged spectrum, grey labels represent the background fragments (common ions) that exist for every particle class. Reproduced from Shen et al. (2019a) (Figure 2 Appendix B.2).

Figure 13 : Size resolved number fraction for seven particle classes measured during the field campaign TRAM01 from July 26ᵗʰ to August 31ˢᵗ, 2016, based on fuzzy classification according to fuzzy c-means clustering algorithm. The figure is the adapted from Shen et al. (2019a) (Figure 3 and Figure 4, Appendix B.2).

During the entire measurement campaign, I have applied the LAAPTOF and AMS, which can provide complementary chemical information of the aerosol particles. According the mass spectrometer results, I have identified two interesting episode with sodium salts rich and organics rich particles, respectively. In order to track their sources, I have done HYSPLIT back-trajectory analysis for both episodes and found that sodium salts were sea salt particles from the North Atlantic Ocean, while the particles in organic rich episode were from the continental area. With an aim to address the whether the high organic particle concentrations were from local formation, regional transport, or vertical mixing, I applied the COSMO-ART modelling. The corresponding results are in my 3ʳᵈ first author paper Shen et al. (2019b; submitted). During some periods, a high-resolution time-of-flight chemical ionization mass spectrometer (FIGAERO-HR-ToF-CIMS, hereafter, CIMS for short) was deployed to characterize chemical composition of the particles at molecular level. CIMS results show that highly functionalized organonitrates contributed to night-time organic aerosol mass loadings and particle growth. This has been shown in my co-authored publication (Huang et al., 2019a). In the following, my 3ʳᵈ first author publication and this co-authored publication are shown successively, with their titles, authors, journal, authorship statement and abstract, respectively. Two major plots from my first author publication are also shown to illustrate the major findings.

First author publication title: Composition and origin of PM$_{2.5}$ aerosol particles in the upper Rhine valley in summer

Authors: <u>**Xiaoli Shen,**</u> Heike Vogel, Bernhard Vogel, Wei Huang, Claudia Mohr, Ramakrishna Ramisetty, Thomas Leisner, André S. H. Prévôt, and Harald Saathoff

Journal: Atmospheric Chemistry and Physics (submitted)

Authorship statement: This research article was written by me. It is based on the field measurement campaign TRAM01. I operated LAAPTOF and AMS, did alignments and calibration for these two instruments during the field campaign, did all the LAAPTOF data analysis, all the COSMO-ART model runs and all the model output data analysis, HYSPLIT back-trajectory analysis, and produced all figures.

Harald Saathoff organized the campaign, provided trace gas, meteorology, and particle measurements as well as suggestions for the data analysis, interpretation, and discussion. Heike Vogel and Bernhard Vogel provided the input data for COSMO-ART model, provided suggestions for the model simulation, the model data analysis, interpretation, and discussion. Wei Huang operated AMS during the whole campaign and did AMS data analysis. Claudia Mohr helped to operate the instruments, provided suggestions for the data analysis, interpretation, and discussion. Ramakrishna Ramisetty helped to operate LAAPTOF. André Prevot gave comments for interpretation of black carbon data. Thomas Leisner gave general advices and comments for this paper. All authors contributed to the final text.

Abstract: We conducted a six-week measurement campaign in summer 2016 at a rural site about 11 km north of the city of Karlsruhe in southwest Germany in order to study the chemical composition and origin of aerosols in the upper Rhine valley. In particular, we deployed a single particle mass spectrometer (LAAPTOF) and an aerosol mass spectrometer (AMS) to provide complementary chemical information of the aerosol particles smaller than 2.5 µm. For the entire measurement period, the total aerosol particle mass was dominated by sodium salts contributing on average (36 ± 27)% to the total single particles. The total particulate organic compounds, sulfate, nitrate, and ammonium contributed on average (58 ± 12)%, (22 ± 7)%, (10 ± 1)%, and (9 ± 3)% to the total non-refractory particle mass, respectively. The regional transport model

COSMO-ART was applied for source apportionment and to achieve a better understanding of the impact of complex transport pattern on the field observations. Combining field observations and model simulations, we attributed high particle numbers and SO_2 concentrations observed at this rural site to industrial emissions from power plants and a refinery in Karlsruhe. In addition, two characteristic episodes with aerosol particle mass dominated by sodium salts particles compromising $(70 \pm 24)\%$ of the total single particles and organic compounds comprising accounting for $(77 \pm 6)\%$ of total non-refractory species, respectively, were investigated in detail. For the first episode, we identified relatively fresh and aged sea salt particles originating from the Atlantic Ocean more than 800 km away. These particles showed markers like m/z 129 $C_5H_7NO_3^+$ indicating the influence of anthropogenic emissions modifying their composition e.g., from chloride to nitrate salts during the long-range transport. For a 3-day episode including high organic mass concentrations, model simulations show that on average $(74 \pm 7)\%$ of the particulate organics at this site were of biogenic origin. Detailed model analysis allowed us to find out that three subsequent peaks of high organic mass concentrations originated from different sources, including local emissions from the city and industrial area of Karlsruhe, regional transport from the city of Stuttgart (~64 km away), and potential local night-time formation and growths. Biogenic (forest) and anthropogenic (urban) emissions were mixed during transport and contributed to the formation of organic particles. In addition, topography, temperature inversion, and stagnant meteorological conditions also played a role in the build-up of higher organic particle mass concentrations. Furthermore, the model was evaluated using the field observations and corresponding sensitivity tests. The model results show good agreement with trends and concentrations observed for several trace gases (e.g., O_3, NO_2, and SO_2) and aerosol particle compounds (e.g., ammonium and nitrate). However, the model underestimates the number of particles by an order of magnitude and underestimates the mass of organic particles by a factor of 2.3. The discrepancy was expected for particle number since the model does not include all nucleation processes. The missing organic mass indicates either an underestimated regional background, missing sources, and/or mechanisms in the model like night-time chemistry. This study demonstrates the potential of combining comprehensive field observations with dedicated transport modelling to understand the chemical composition and complex origin of aerosols.

Major plots: The following plots show the overall agreement between field measurements and model calculations, sensitivity tests to understand the discrepancy of the measured and calculated, as well as the model calculation that verified industrial contributions to the particles measured at this rural site and downward transport and mixing of the aerosols.
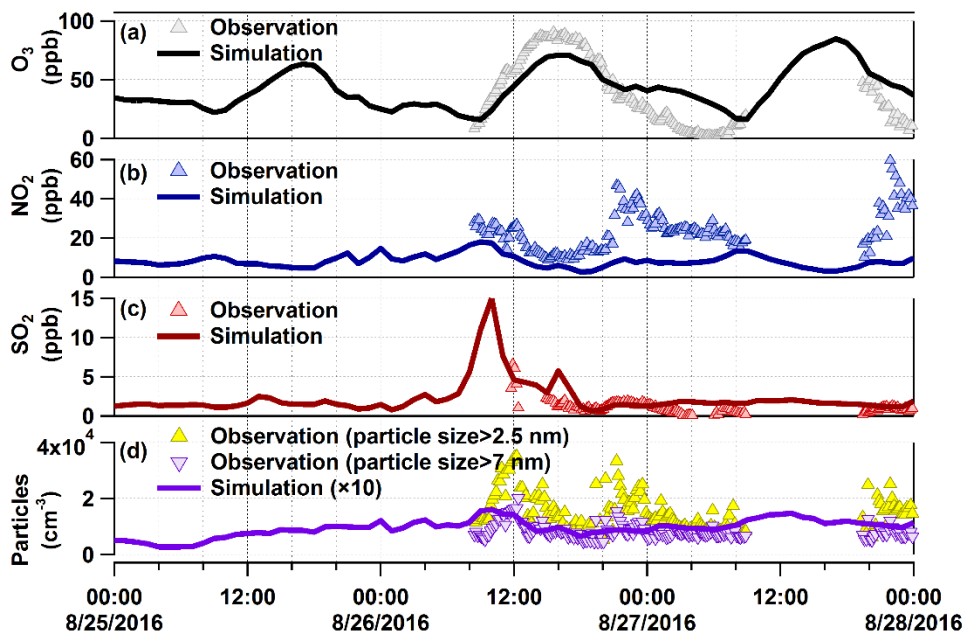
Figure 14: Comparison between observations and model results for O_3, NO_2, SO_2, and particle number in organic-rich episode. The modelled particles do not represent the ultrafine particles to their full extend, especially for the particles in the nucleation mode. Reproduced from Shen et al. (2019b; submitted) (Figure 4, Appendix B.3).
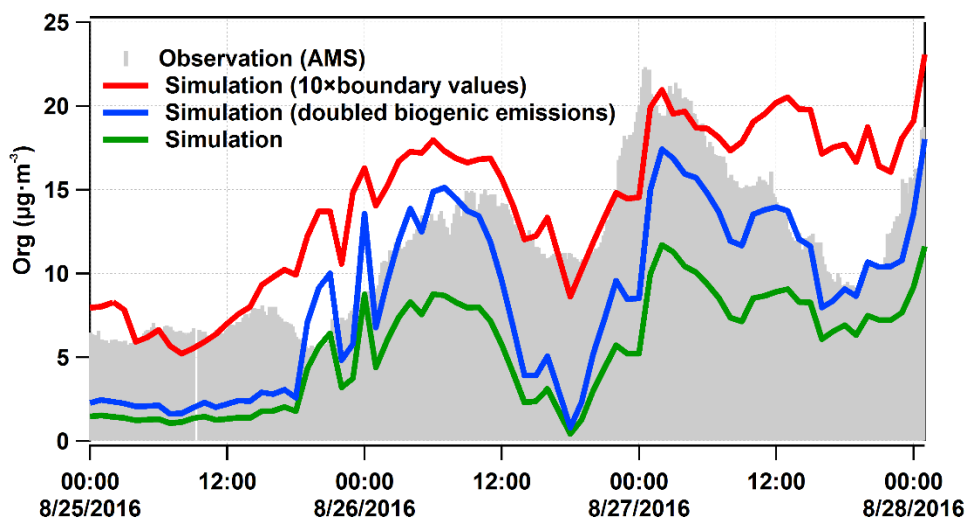
Figure 15: Modelled organic mass concentrations (lines) compared to measured values (grey area). The green line is the modelled organics with basic model settings, the red line was calculated for a tenfold-enhanced regional background in organics, and the blue was calculated for doubles biogenic emissions in COSMO-ART. Reproduced from Shen et al. (2019b; submitted) (Figure 9, Appendix B.3).
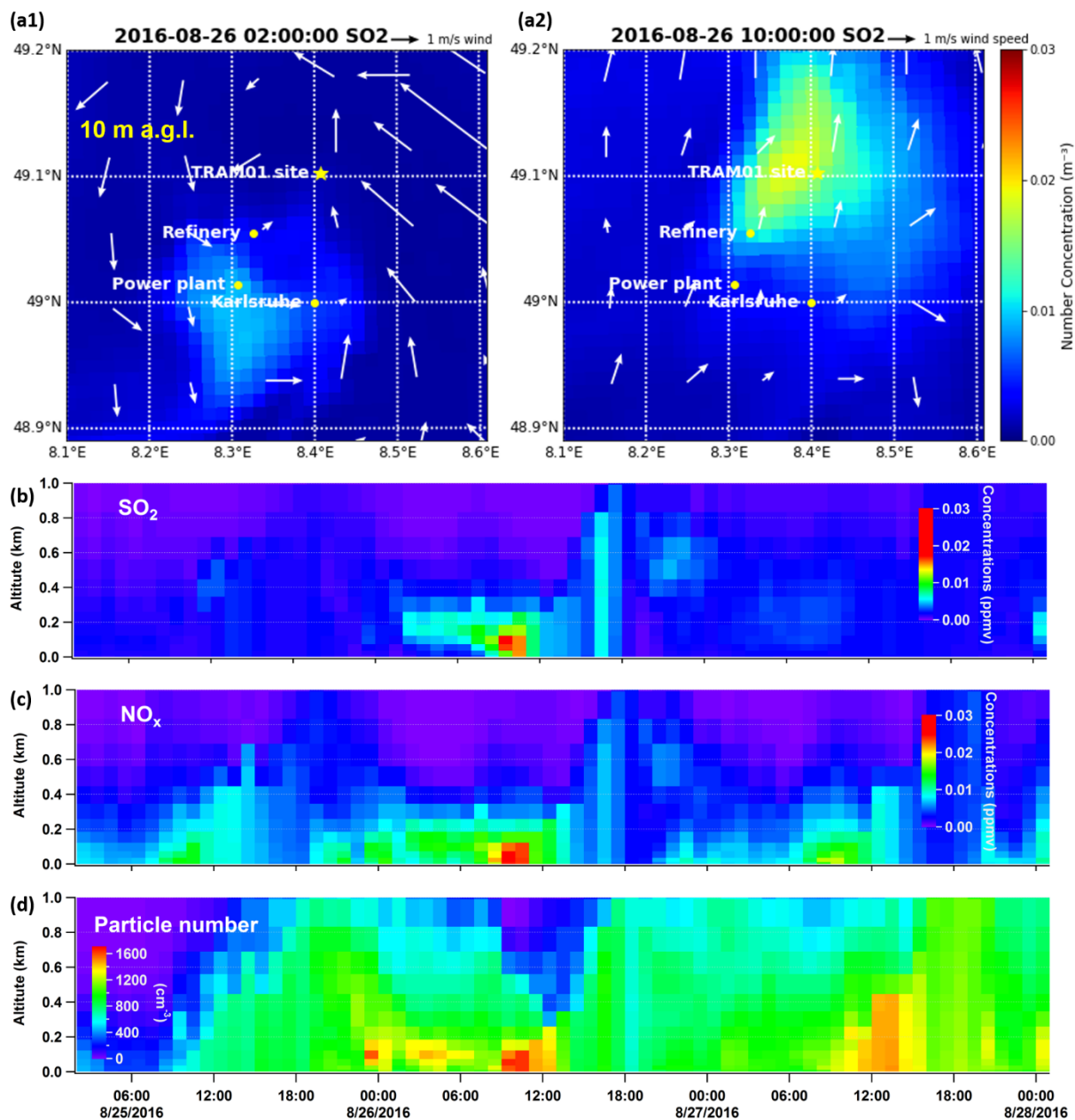
Figure 16: Modelled SO₂ concentrations at 2:00 (a1) and 10:00 (a2) on August 26th at 10 m a.g.l.. Panels (b) to (d) are time series of vertical profiles above the measurement site for simulated SO₂, NOₓ and total particle number. Reproduced from Shen et al. (2019b; submitted) (Figure 5, Appendix B.3).

The full article is reprinted in Appendix B.3. © Shen et al., (2019b; submitted)

Co-authored publication title: Chemical characterization of highly functionalized organonitrates contributing to night-time organic aerosol mass loadings and particle growth

Authors: Wei Huang, Harald Saathoff, **<u>Xiaoli Shen,</u>** Ramakrishna Ramisetty, Thomas Leisner, and Claudia Mohr

Authorship statement: This peer-reviewed scientific journal article is based on the field measurement TRAM01. I operated the AMS, did alignments and calibrations and I contributed to scientific discussions on the analysis and interpretation of the results.

Abstract: Reactions of volatile organic compounds (VOC) with NO3 radicals and of reactive intermediates of oxidized VOC with NOx can lead to the formation of highly functionalized organonitrates (ON). We present quantitative and chemical information on ON contributing to high nighttime organic aerosol (OA) mass concentrations measured during July−August 2016 in a rural area in southwest Germany. A filter inlet for gases and aerosols coupled to a high-resolution time-of-flight chemical ionization mass spectrometer (FIGAERO-HR-ToF-CIMS) was used to analyze the molecular composition of ON in both the gas and particle phase. We find larger contributions of ON to OA mass during the night. Identified ON are highly functionalized, with 4 to 12 oxygen atoms. The diel patterns of ON compounds with 5, 7, 10, or 15 carbon atoms per molecule vary, indicating a corresponding behavior of their potential precursor VOC. The temporal behavior of ON after sunset correlates with that of the number concentration of ultrafine particles, indicating a potential role of ON in night-time new particle formation (NPF) regularly observed at this location. We estimate an ON contribution of 18−25% to the mass increase of newly formed particles after sunset. Our study provides insights into the chemical composition of highly functionalized ON in the rural atmosphere and the role of anthropogenic emissions for night-time SOA formation in an area where biogenic VOC emissions dominate.

2.3.3 Urban background site in downtown Stuttgart

During the Stuttgart01 campaign in summer 2017, the LAAPTOF has identified six major particle classes from 265759 single particles. Preliminary analysis suggests that the representative spectra of these classes are similar as those (except for organosulfate containing class) identified in the aforementioned summer campaign TRAM01 at a rural site in the upper Rhine valley, which is ~64 km Northwest of Stuttgart. As shown in Figure 17, 31% of the total particles can be classified as potassium (K)–organic–sulfate–nitrate particles (assigned to aged biomass burning particles). Sodium salts rich particles (assigned to aged sea salt)dominate the larger particle size ($d_{va} > 1$ µm). For the submicron size range (< 1µm d_{va}): aged soot dominates the smallest particles (< 400 nm d_{va}), secondary inorganics particles are in the middle size range ($d_{va} = 400$ to 1 µm), and aged biomass burning particles have two modes, covering broader size range. These particle types and size ranges are similar as those found for the corresponding particles measured at the Jungfraujoch and the upper Rhine valley.
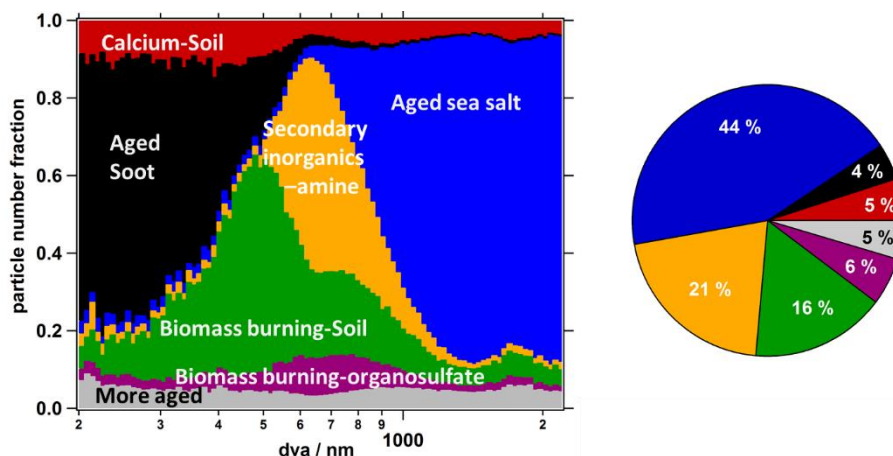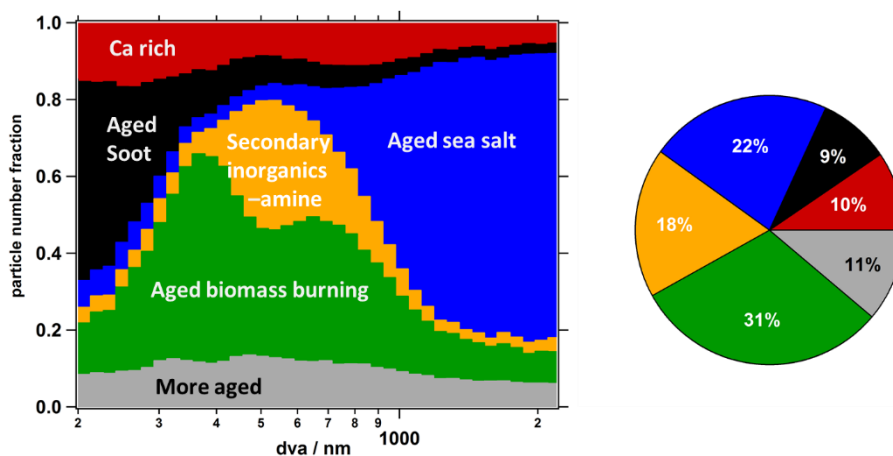

Figure 17: Size resolved number fraction for seven particle classes measured during the field campaign Stuttgart 01 from July 5th to August 17th 2017, based on fuzzy classification according to fuzzy c-means clustering algorithm. Particle size shown here is vacuum aerodynamic diameter (d_{va}).

As mentioned before, I also operated LAATOF and AMS in the Stuttgart02 campaign in February 2018. The corresponding LAAPTOF data analysis is still ongoing. The general comparison between summer and winter is listed in Table 2. In winter, the averaged trigger rate was seven times higher than that in summer. The highest trigger rate was up to ten particles per second. The pair of empty negative spectrum and unique 30 NO^+ in positive spectrum were showing most often, might attributed to the pure ammonium sulfate particles.

In these campaigns, I also collected filter samples for the CIMS measurements. The CIMS results have shown seasonal characteristics of organic aerosol chemical composition and volatility in this urban area. This has been shown in my co-authored publication Huang et al. (2019b; in review). In the following, this co-authored publication is shown with its title, authors, journal, authorship statement and abstract.

Co-authored publication title: Seasonal characteristics of organic aerosol chemical composition and volatility in Stuttgart, Germany

Authors: Wei Huang, Harald Saathoff, **<u>Xiaoli Shen,</u>** Ramakrishna Ramisetty, Thomas Leisner, and Claudia Mohr

Authorship statement: This research article is based on the field measurement campaigns Stuttgart 01 (summer 2017) and 02 (winter 2018). I collected filter samples for CIMS measurements, operated the AMS, and did alignments and calibration for the AMS. I also contributed to the scientific discussions on the interpretation of the results.

Abstract: Chemical composition and volatility of organic aerosol (OA) particles were investigated during July–15 August 2017 and February–March 2018 in the city of Stuttgart, one of the most polluted cities in Germany. Total non-refractory particle mass was measured with a high-resolution time-of-flight aerosol mass spectrometer (HR-ToF-AMS; hereafter AMS). Aerosol particles were collected on filters and analyzed in the laboratory with a filter inlet for gases and aerosols coupled to a high-resolution time-of-flight chemical ionization mass spectrometer (FIGAERO-HR-ToF-CIMS; hereafter CIMS), yielding the molecular composition of oxygenated OA (OOA) compounds. While the average organic mass loadings are lower in the summer period (5.1 ± 3.2 μg m^{-3}) than in the winter period (8.4 ± 5.6 μg m^{-3}), we find relatively larger mass contributions of organics measured by AMS in summer ($68.8 \pm 13.4\%$) compared to winter ($34.8 \pm 9.5\%$). CIMS mass spectra show OOA compounds in summer have O:C ratios of 0.82 ± 0.02 and are more influenced by biogenic emissions, while OOA compounds in winter have O:C ratios of 0.89 ± 0.06 and are more influenced by biomass burning emissions. Volatility parametrization analysis shows that OOA in winter is less volatile with higher contributions of low volatile organic compounds

(LVOC) and extremely low volatile organic compounds (ELVOC). We partially explain this by the higher contributions of compounds with shorter carbon chain lengths and higher number of oxygen atoms, i.e. higher O:C ratios in winter. Organic compounds desorbing from the particles deposited on the filter samples also exhibit a shift of signal to higher desorption temperatures (i.e. lower apparent volatility) in winter. This is consistent with the relatively higher O:C ratios in winter, but may also be related to higher particle viscosity due to the higher contributions of larger molecular-weight LVOC and ELVOC, interactions between different species and/or particles (particle matrix), and/or thermal decomposition of larger molecules. The results suggest that whereas lower temperature in winter may lead to increased partitioning of semi-volatile organic compounds (SVOC) into the particle phase, this does not result in a higher overall volatility of OOA in winter, and that the difference in sources and/or chemistry between the seasons plays a more important role. Our study provides insights into the seasonal variation of molecular composition and volatility of ambient OA particles, and into their potential sources.

The full article is reprinted in Appendix C.3. © Huang et al. (2019b; in review)

2.4 Composition, formation, and aging of secondary organic aerosols

The chamber studies on secondary organic aerosol (SOA) provide laboratory evidence for its formation and chemical aging, which is useful for the interpretation of field measurements. During SOA related AIDA campaigns, I used the LAAPTOF and AMS to characterize different types of SOA. The reference spectra for SOA measured by the LAAPTOF have been made publicly available (https://data.eurochamp.org/) and are shown in my first author paper (Figure 4; Shen et al., 2018). Some other results regarding SOA molecular composition and corresponding particle volatility were published in a co-authored paper (Huang et al., 2018). In the following, this co-authored publication is shown with its title, authors, journal, authorship statement and abstract as well as the organonitrate markers identified by two different single particle mass spectrometers (LAAPTOF & PALMS) during chamber experiments s at KIT and MIT, respectively.

Co-authored publication title: α-Pinene secondary organic aerosol at low temperature: Chemical composition and implications for particle viscosity

Authors: Wei Huang, Harald Saathoff, Pajunoja, A., **Xiaoli Shen,** Karl-Heinz Naumann, Robert Wagner, Virtanen, Annele, Thomas Leisner, and Claudia Mohr

Journal: Atmospheric Chemistry and Physics, 18, 2883–2898, 2018

Authorship statement: This peer-reviewed scientific journal article is based on the AIDA chamber campaign (SOA15), focusing on formation, aging and ice nucleation ability of secondary organic aerosol (SOA). I helped operated AMS, did alignments and calibration for the AMS, as well as the corresponding data analysis. I also participated in scientific discussions on the interpretation of the results.

Abstract: Chemical composition, size distributions, and degree of oligomerization of secondary organic aerosol (SOA) from α-pinene ($C_{10}H_{16}$) ozonolysis were investigated for low-temperature conditions (223 K). Two types of experiments were performed using two simulation chambers at the Karlsruhe Institute of Technology: the Aerosol Preparation and Characterization (APC) chamber, and the Aerosol Interaction and Dynamics in the Atmosphere (AIDA) chamber. Experiment type 1 simulated SOA formation at upper tropospheric conditions: SOA was generated

in the AIDA chamber directly at 223 K at 61% relative humidity (RH; experiment termed "cold humid", CH) and for comparison at 6% RH (experiment termed "cold dry", CD) conditions. Experiment type 2 simulated SOA uplifting: SOA was formed in the APC chamber at room temperature (296 K) and < 1% RH (experiment termed "warm dry", WD) or 21% RH (experiment termed "warm humid", WH) conditions, and then partially transferred to the AIDA chamber kept at 223 K, and 61% RH (WDtoCH) or 30% RH (WHtoCH), respectively. Precursor concentrations varied between 0.7 and 2.2 ppm α-pinene, and between 2.3 and 1.8 ppm ozone for type 1 and type 2 experiments, respectively. Among other instrumentation, a chemical ionization mass spectrometer (CIMS) coupled to a filter inlet for gases and aerosols (FIGAERO), deploying I⁻ as reagent ion, was used for SOA chemical composition analysis.

For type 1 experiments with lower α-pinene concentrations and cold SOA formation temperature (223 K), smaller particles of 100–300 nm vacuum aerodynamic diameter (d_{va}/and higher mass fractions (> 40%) of adducts (molecules with more than 10 carbon atoms) of α-pinene oxidation products were observed. For type 2 experiments with higher α-pinene concentrations and warm SOA formation temperature (296 K), larger particles (~500 nm d_{va}) with smaller mass fractions of adducts (< 35%) were produced. We also observed differences (up to 20 °C) in maximum desorption temperature (T_{max}) of individual compounds desorbing from the particles deposited on the FIGAERO Teflon filter for different experiments, indicating that T_{max} is not purely a function of a compound's vapor pressure or volatility, but is also influenced by diffusion limitations within the particles (particle viscosity), interactions between particles deposited on the filter (particle matrix), and/or particle mass on the filter. Highest T_{max} were observed for SOA under dry conditions and with higher adduct mass fraction; lowest T_{max} were observed for SOA under humid conditions and with lower adduct mass fraction. The observations indicate that particle viscosity may be influenced by intra- and inter-molecular hydrogen bonding between oligomers, and particle water uptake, even under such low-temperature conditions.

Our results suggest that particle physicochemical properties such as viscosity and oligomer content mutually influence each other, and that variation in T_{max} of particle desorptions may have implications for particle viscosity and particle matrix effects. The differences in particle physicochemical properties observed between our different experiments demonstrate the

importance of taking experimental conditions into consideration when interpreting data from laboratory studies or using them as input in climate models.

The full article is reprinted in Appendix C.4. © Huang et al. (2018)

During the SOA17 campaign at the AIDA chamber, I performed experiments with α-pinene and/or toluene OH oxidation on sodium nitrate (NaNO$_3$) seed particles in presence/absence of NO$_x$. The corresponding single particle mass spectra measured by the LAAPTOF are shown in Figure 18. I found an organonitrate signature, m/z 129 C$_5$H$_7$NO$_3^+$, in the spectra of the SOA particles under NO$_x$ conditions, especially in the toluene system. For the α-pinene system, m/z 129+ is quite weak even in the presence of NO$_x$ (panel b), but it is becoming stronger after toluene is added (panel c). For the toluene system (panel d to f), m/z 129+ is present when toluene derived SOA coated NaNO$_3$ seeds without NO$_x$. This might due to the complex laser desorption and ionization mechanisms, which might allows recombination of ion fragments from toluene and nitrate. When extra OH is added to this system, m/z 129+ is more obvious, likely due to the more aged toluene SOA. When NO$_x$ is added to toluene system (panel e), m/z 129+ becomes much stronger, likely due to the organonitrate formation. Hence, we can conclude that m/z 129$^+$ is more related to anthropogenic precursor toluene rather than biogenic α-pinene. Therefore, in the LAAPTOF spectra, m/z 129 C$_5$H$_7$NO$_3^+$ could be taken as a signature peak for anthropogenic sources in the ambient. This has been used for interpretation of the field observation results in my 3rd first author paper Shen et al. (2019b; submitted): For aged sea salt particles that contain m/z 129 C$_5$H$_7$NO$_3^+$, this indicates interaction of anthropogenic emissions with the sea salt particles.
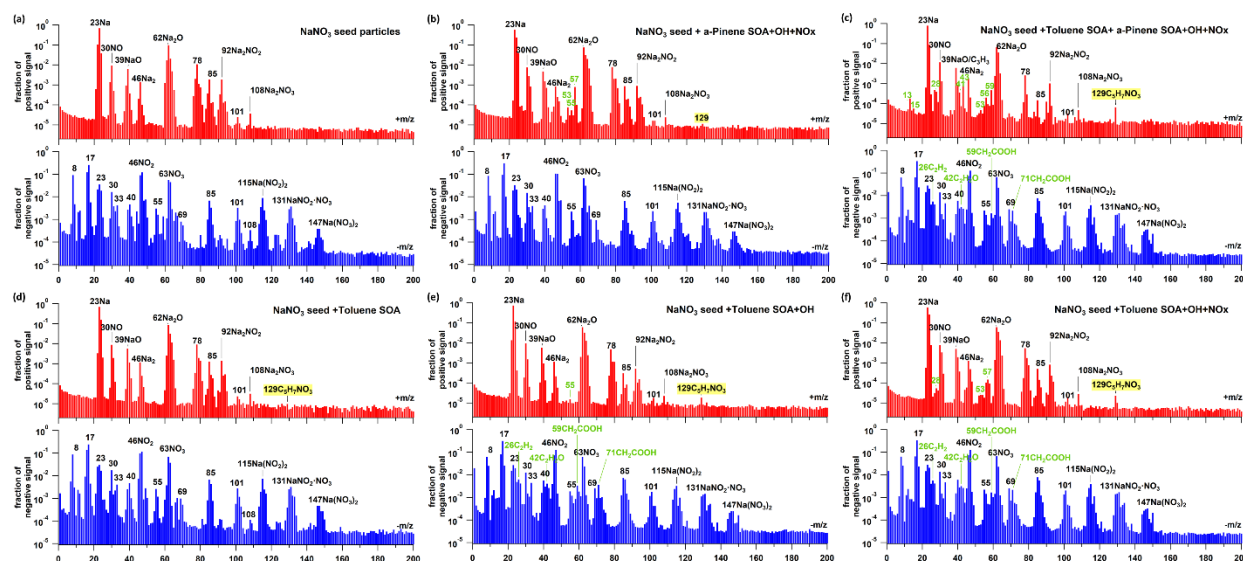
Figure 18: Laboratory evidence for anthropogenic organonitrate (LAAPTOF signature m/z 129 C$_5$H$_7$NO$_3^+$). (a) to (f) are the averaged spectra from several thousand single particles, respectively. Y-axis is the normalized ion intensity (each ion peak intensity is normalized to the sum of all ion signals; positive and negative ions were analysed separately). Reproduced from Shen et al. (2019b; submitted) (Figure S9, Appendix B.3).

In another aerosol chamber study at MIT, I employed another single particle mass spectrometer PALMS to characterise different types of SOA, including α-pinene SOA, toluene SOA, β-caryophyllene SOA and isoprene SOA. I have done the PALMS data analysis and found interesting results regarding isoprene derived SOA system. For this system, we used IEPOX (2,3-epoxy-2-methyl-1,4-butanediol, $C_5H_{10}O_3$), a gas-phase epoxydiol generated at high yield from isoprene oxidation, to react with ammonium bisulfate to mimic isoprene SOA, namely IEPOX-derived SOA. IEPOX sulfate ester, , with the marker peak at m/z 215 $C_5H_{11}O_3SO_4^-$ was observed, as well as some other organosulfate signature peaks, such as m/z 139 $C_3H_7SO_4^-$ and 153 $C_4H_9SO_4^-$ (Figure 19). These organosuflate peaks have been observed in the free troposphere with PALMS (Froyd et al., 2010). As the reaction between IEPOX and ammonium bisulfate started, sulfate patterns (64 SO_2^-, 80 SO_3^-, 97 HSO_4^-, 177 $SO_3HSO_4^-$, 195 $HSO_4H_2SO_4^-$, and 196 $H_2SO_4H_2SO_4^-$) in PALMS spectra was becoming more intensive, especially the small marker peaks at higher mass, while the AMS-sulfate mass concentration was decreasing.
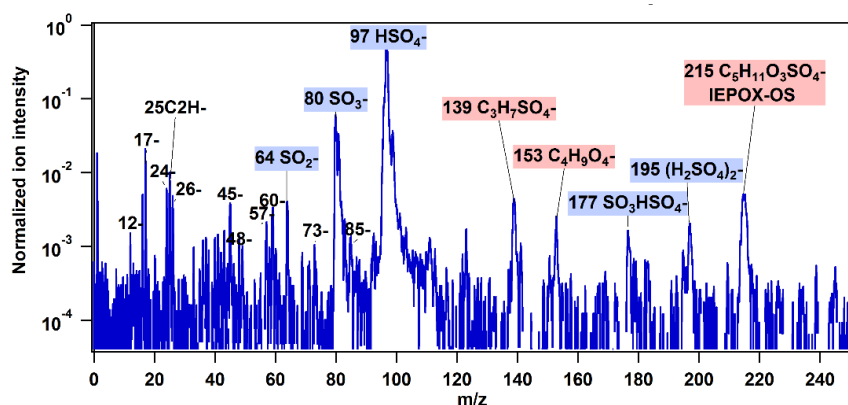
Figure 19: Representative single particle mass spectrum of IEPOX-derived SOA. Sulfate signature peaks are labelled in blue. Organosulfate signature peaks are labelled in red.

During the field campaign TRAM01, I also observed similar organosulfte signature peaks in the LAAPTOF spectra and identified an episode rich in biomass burning-organosulfate particles at the beginning of the measurement campaign (refer to Figure 9 in section 2.2), but our AMS cannot identify organosulfate as well. Given the PALMS, LAAPTOF, and AMS measurements, I conclude that single particle mass spectrometry is a useful tool to identify organosulfates while AMS is not. This is most likely due to the variety of different organosulfate types and their complex yet unclear fragmentation pattern in AMS.

48

2.5 Impact of particle composition on its ice nucleation ability

During my PhD study, I contributed to several ice nucleation studies. In this section, I will focus on results from the studies on secondary organic aerosol and soil dust particles.

In the literature on ice nucleation research, there is still a debate on the ice nucleation ability of SOA. Depending on the organic precursors and their mixtures quite different properties were observed. Therefore, further data from laboratory experiments are needed to advance our understanding. AIDA chamber studies have shown that the unprocessed α-pinene SOA and toluene SOA were poor ice nucleating particles (INP$_s$) at cirrus temperatures (~ -80°C to -37°C). This could be substantiated in my ice nucleation study at MIT, while β-caryophyllene SOA and the aforementioned IEPOX-derived SOA (section 2.4) were found to be better INP$_s$ (Figure 20) under the similar temperature and pressure conditions. The corresponding paper with me as co-author is in preparation (Zhang et al., 2019; in preparation).
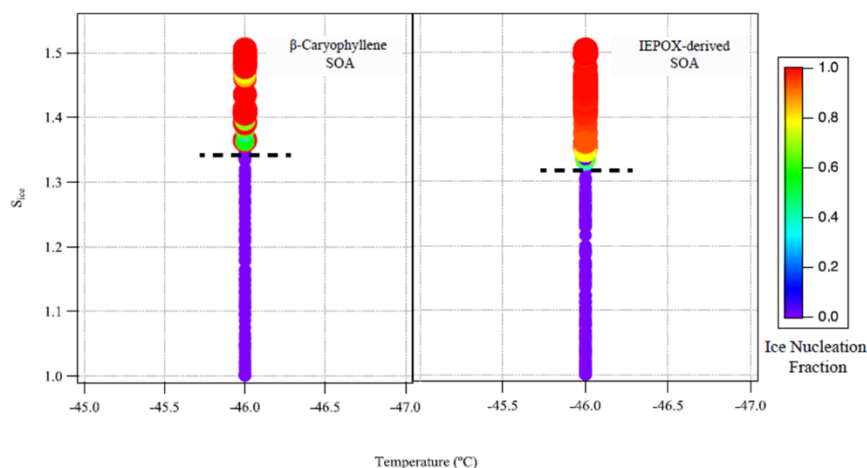
Figure 20: Ice nucleation onsets of β-caryophyllene SOA (left) and IEPOX-derived SOA (right) in a chamber study at the MIT (Zhang et al., 2019; in preparation). S$_{ice}$ stands for ice saturation ratio. Homogeneous ice nucleation generally requires high supersaturations in aqueous aerosol droplets, occurring at ice saturation ratios of S$_{ice}$> 1.4 (this is the case for α-pinene SOA and Toluene SOA), while heterogeneous ice nucleation occurs with lower S$_{ice}$ (e.g., < 1.35 for β-caryophyllene SOA and IEPOX-derived SOA). The latter one corresponds to better ice nucleation ability.

Please note, when the morphology of SOA particles changed to be highly porous, SOA can be well activated to form ice, namely becoming good INP$_s$. This has been published in my co-authored paper (Wagner et al., 2017). In the following, this co-authored publication is shown with its title, authors, journal, authorship statement and abstract.

Co-authored publication title: Heterogeneous ice nucleation of α-pinene SOA particles before and after ice cloud processing.

Authors: Wagner, R., Höhler, K., Huang, W., Kiselev, A., Möhler, O., Mohr, C., Pajunoja, A., Saathoff, H., Schiebel, T., **Shen, X. L.,** and Virtanen, A.

Authorship statement: This peer-reviewed scientific journal article is based on the AIDA chamber campaign (SOA15), focusing on formation, aging and ice nucleation ability of SOA. I helped operated AMS, did alignments and calibration for the AMS, as well as the corresponding data analysis. I also participated in scientific discussions on the interpretation of the results.

Abstract: The ice nucleation ability of α-pinene secondary organic aerosol (SOA) particles was investigated at temperatures between 253 and 205 K in the Aerosol Interaction and Dynamics in the Atmosphere cloud simulation chamber. Pristine SOA particles were nucleated and grown from pure gas precursors and then subjected to repeated expansion cooling cycles to compare their intrinsic ice nucleation ability during the first nucleation event with that observed after ice cloud processing. The unprocessed α-pinene SOA particles were found to be inefficient ice-nucleating particles at cirrus temperatures, with nucleation onsets (for an activated fraction of 0.1%) as high as for the homogeneous freezing of aqueous solution droplets. Ice cloud processing at temperatures below 235 K only marginally improved the particles' ice nucleation ability and did not significantly alter their morphology. In contrast, the particles' morphology and ice nucleation ability was substantially modified upon ice cloud processing in a simulated convective cloud system, where the α-pinene SOA particles were first activated to supercooled cloud droplets and then froze homogeneously at about 235 K. As evidenced by electron microscopy, the α-pinene SOA particles adopted a highly porous morphology during such a freeze-drying cycle. When probing the freeze-dried particles in succeeding expansion cooling runs in the mixed-phase cloud regime up to 253 K, the increase in relative humidity led to a collapse of the porous structure. Heterogeneous ice formation was observed after the droplet activation of the collapsed, freeze-dried SOA particles, presumably caused by ice remnants in the highly viscous material or the larger surface area of the particles.

Soil dust particles are the second largest atmospheric primary particle source globally (Silva et al., 2000). Mineral and organic species of such particles may play a yet unclear but potentially crucial role in atmospheric ice nucleation (Hill et al., 2016; O'Sullivan et al., 2014; Tobo et al., 2014). Large knowledge gaps still exist related to the chemical composition of different components, their mutual interaction, and especially the influence of the organics on the propensity of soil dust particles to act as INP_s. In AIDA chamber campaign SOIL02, four different soil dusts sampled at two sites from Germany (SDGe01 and SDPA01), Argentina (SDAr08), and Wyoming in USA (SDWY01) were studied with and without heat treatment (2 hours at 300°C in air), and before and after cloud expansion. The characteristics of the size dependent chemical composition of the differently treated soil dust particles before and after cloud expansion experiments are: 1) the mass spectral peak patterns are similar for all soil dust particle types studied and are dominated by mineral components (Shen et al., 2018). 2) As shown in Figure 21, more elemental carbon (EC) was found in the heated samples than in the untreated ones, especially for smaller particles. 3) Compared to the untreated samples, the peaks related to nitrogen-containing organic compounds (m/z 26 CN⁻) and EC are much more pronounced for heat treated samples, while the peaks indicative of organic acids (m/z 45 COOH⁻) are substantially reduced. The experiments show that heated particles are less ice-active than untreated ones. This implies that organic acids in soil dust particles seem to play a significant role for ice nucleation.
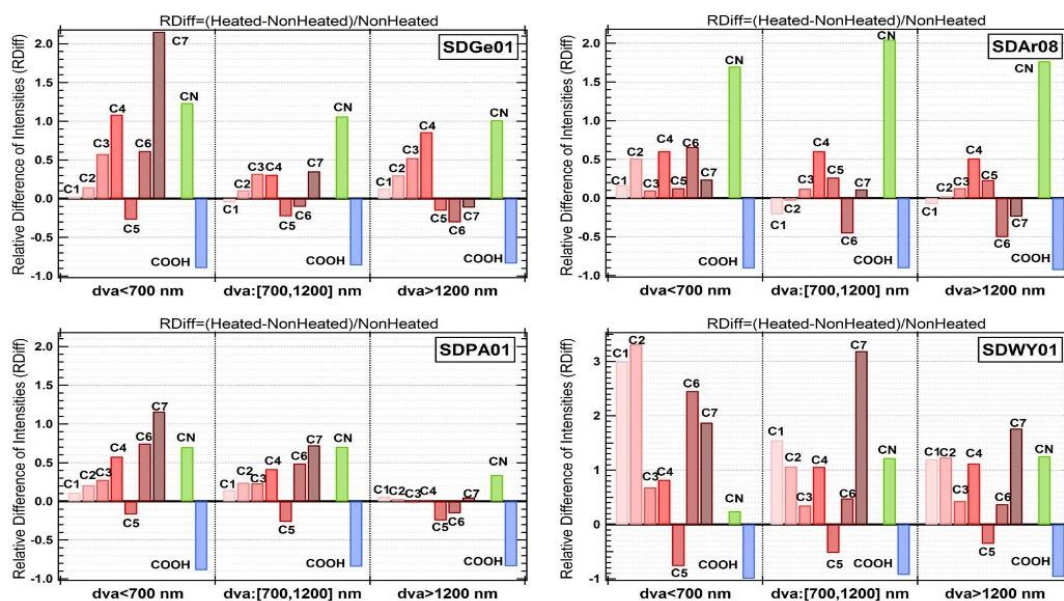
Figure 21: Relative difference of the characteristic mass peak intensities due to the heat treatment. The differences are shown in three different size ranges of the aerosol particles. C1 to C7 stand for EC with carbon number from 1 to 7.

3 Conclusions and outlook

3.1 Conclusions and implications

Atmospheric aerosols play an essential role in visibility and air quality, human and ecosystem health, weather and climate change. The impact of particles' composition on their optical, toxic, hygroscopic properties, and ice nucleation ability, especially on single particle basis, is the key to assess their effects on the aforementioned societal and environmental issues. However, the diversity of particle types, the complex internal mixing state of individual particles, and the variable aerosol transport pattern make it necessary to combine most advanced analytical tools with state of the art transport models to achieve a scientific understanding of the atmospheric aerosol dynamics, sufficient to allow a reliable prediction, e.g., of suitable abatement strategies.

Real-time single particle mass spectrometry (SPMS) measures size and chemical composition of individual particles, and thus hints information of particle internal mixing state. The commonly used strong laser desorption and ionization (LDI) method in SPMS allows for analysis of almost all the particulate components from volatile to refractory. However, the LDI mechanism is quite complex and the laser cannot interact with the entire particle, posing long lasting challenging issues regarding particle identification and quantification.

In this dissertation, I have shown well-characterized performance data and reference spectra from the newly commercially available single-particle mass spectrometer LAAPTOF. The main characteristic of the instrument, its overall detection efficiency (ODE), was determined to range from ~0.01% to ~5% for different particle types (e.g., ammonium nitrate, sodium chloride, soil dust, sea salt, and organic particles) in the size range of 200 nm to 2.5 µm d_{va} (vacuum aerodynamic diameter). The maximum ODE values correspond to the size range between 400 nm to 1 µm. For evaluation of the LAAPTOF performance, particle matrix effects (from e.g. size, morphology, and optical property) and certain instrument influences (from e.g. aerodynamic lens and detection system), as well as particle-instrument interactions must be considered. Moreover, I determined reference spectra of 32 well-defined particle types relevant for atmospheric aerosols. It turns out that internally mixed aerosol particles can result in spectra with new clusters of ions, rather than simply a combination of the spectra from the single components. This underscores the importance of reference spectra for interpretation of complex ambient data. Given the laboratory-based

reference spectra with known mass spectral patterns, the interpretation of spectra from unknown particle types in ambient aerosols is significantly improved. Furthermore, the reference spectra are useful for target-oriented particle classification, which allows identifying particles with low number fraction in the ambient, e.g., lead-containing particles. This implies the usefulness for targeting particles bearing e.g., toxic species that affect human and ecosystem health.

Combining the laboratory-based reference spectra, marker peaks, typical peak ratios, and fuzzy classification, I improved the single particle identification significantly. In a field measurement at a rural site in the upper Rhine valley, I identified seven major particle classes among $\sim 3.7 \times 10^5$ single particles. With the precise particle identification and the laboratory-derived and chemically resolved ODE for the LAAPTOF, I have developed a new method to transfer particle similarity into corrected number and mass fractions without a need of a reference instrument in the field. As a result, more realistic fractions of the major particle types can be determined, e.g., biomass burning-soil dominated the particle number and mass (~45% and ~32%, respectively), and sodium salts contributed little to number but much to particle mass (~3% and ~30%, respectively). This demonstrates the importance of a reliable quantification of particle number and mass using single particle mass spectrometry, especially since the corresponding fractions are key for environmental strategies against air pollution.

Based on the LAAPTOF and the AMS measurements at the rural site in the upper Rhine valley, I have identified two characteristic episodes with aerosol particles rich in sodium salts and organics, respectively. HYSPLIT back trajectory analysis indicated that the sodium salts were relatively fresh and sometimes more aged sea salt particles originating from the Atlantic Ocean more than ~800 km away. The anthropogenic signature peak m/z 129 $C_5H_7NO_3^+$, which I identified in AIDA chamber measurements on oxidation and aging of secondary organic aerosol (SOA), was present in the LAAPTOF mass spectra of ambient sea salt particles. This indicates interactions of natural sea salt particles with anthropogenic emissions, not only of NO_x but also of VOC, during their long-range transport. For the episode rich in organics, I applied the regional transport model COSMO-ART for investigation of the complex transformation processes during transport of atmospheric aerosols. Combining field observations and model simulations, I attributed SO_2 concentrations observed at this rural site to industrial emissions from power plants and a refinery in Karlsruhe, and further verified that downward transport and mixing of the aerosols originating

from industry contributed to the high particle numbers measured at this site. Figure 22 shows the overall agreement between field measurements and model calculations, regarding the particulate species. Detailed model analysis suggested that the successive high organic peaks measured were originating from different sources, including local emissions from the industrial and urban area of Karlsruhe, regional transport from Stuttgart (~64 km away; illustrated in Figure 23), and potential local night-time formation and growths. Model simulations also showed that biogenic (forest) and anthropogenic (urban) emissions were mixed during the transport. Both sources contributed to the formation of organics with the biogenic contributing 74% (± 7%) to the particle mass. Besides, topography and stagnant meteorological conditions also play a role in the build-up of high organic mass concentrations.
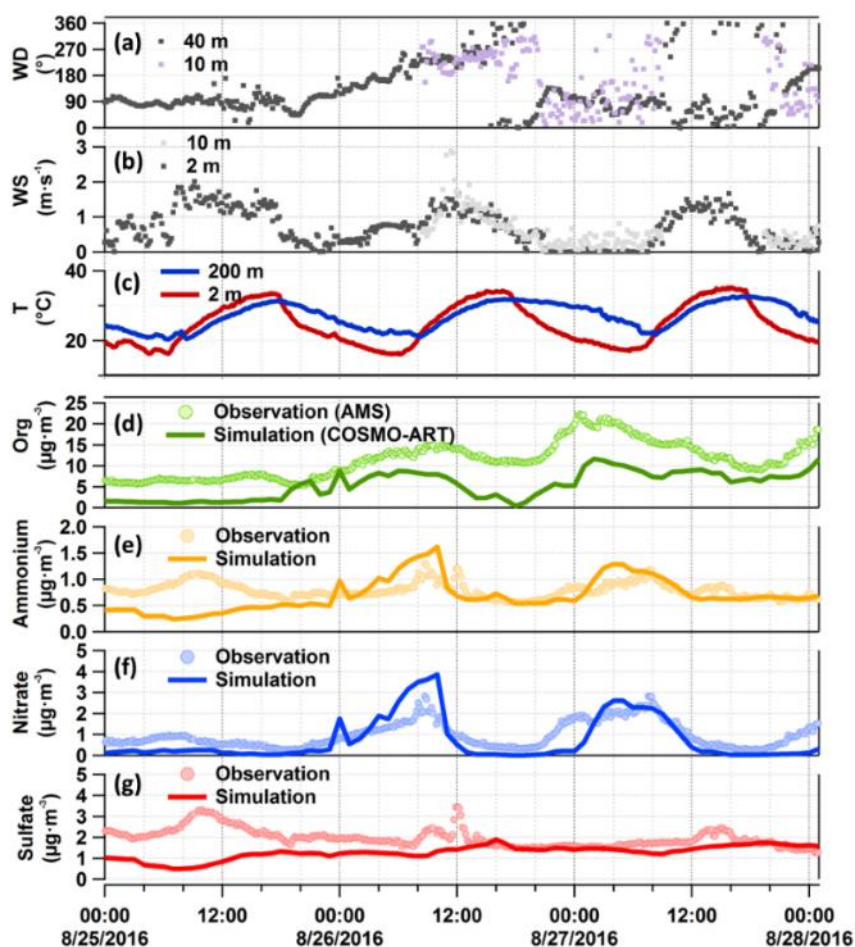
Figure 22: Comparison between observations and model simulations for organic-rich episode. Panel (a) and (b) are wind conditions measured 10 m a.g.l. at our measurement site (purple and light grey dots for wind direction and speed, respectively), as well as the complementary KIT-tower data (dark grey dots). Panel (c) is the temperature data from the KIT-tower. Panel (d) to (g) are the particulate organic compounds, ammonium, nitrate, and sulfate measured by AMS and simulated by COSMO-ART. The simulation results are at the lowest atmospheric level in the model, namely 10 m a.g.l. Reproduced from Shen et al. (2019b; submitted) (Figure 7, Appendix B.3).
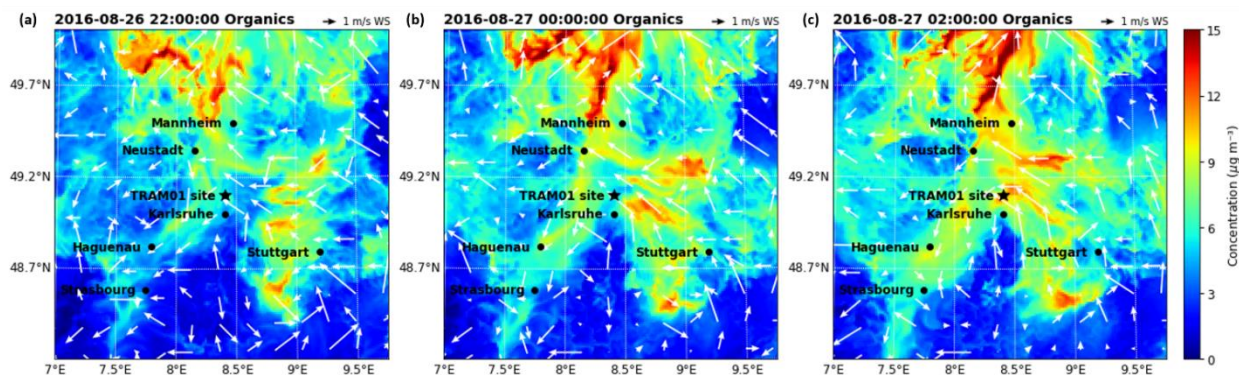
Figure 23: Particulate organics concentrations calculated by COSMO-ART for three different time points (a) to (c) during the night from August 26th to 27th for 10 m a.g.l.. Reproduced from Shen et al. (2019b; submitted) (Figure 8, Appendix B.3).

These results show how close physical and chemical nature of aerosols is related to emission sources, transformation processes, and complex transport pattern. Consequently, model systems suitable for a reasonable environmental policy should be validated by comprehensive field studies combining state of the art aerosol analytics but also meteorological parameters. One example for this kind of scientific approach is the project "Three-dimensional Observation of Atmospheric Processes in Cities (3DO)" (http://uc2-3do.org/en) in which I participated during measurements in the city of Stuttgart.

In addition to the rural site in the upper Rhine valley in Germany, I have also characterised particles in the other locations of central Europe, i.e., a remote mountain site (Jungfraujoch in Switzerland), as well as an urban background site in downtown (Unterer Schlossgarten) Stuttgart in Germany. The corresponding fuzzy clustering analysis of the aerosol particles measured by LAAPTOF shows that similar particle types are present at different locations (Figure 24). These types are aged soot, biomass burning, secondary inorganics rich, and aged sea salt particles, dominating size ranges of < 400 nm, 300 to 500 nm, 400 nm to 1 μm, and > 1 μm d_{va}, respectively. These common features are potentially useful for investigating their common properties and transformations in the lab and assessing their effect on the societal and environmental issues in regional scale modelling.

Apart from that, at the remote mountain, I identified nine characteristic single particle types, which are more than I observed at rural or urban locations. Besides common particle types, dust and phosphate containing particles were also identified at this location. This may be explained by particles originating from a variety of sources and long-range transport in the free troposphere, but most likely also by a partial influence of boundary layer air during the measurements at the

Jungfraujoch. Comparing the chemical composition of the total particles with the ice crystal residual particles allows to determine the impact of chemical composition on the ice nucleation ability of the ambient particles collected in clouds. Furthermore, these chemical composition related ice nucleation properties can be substantiated by aerosol and cloud chamber experiments.
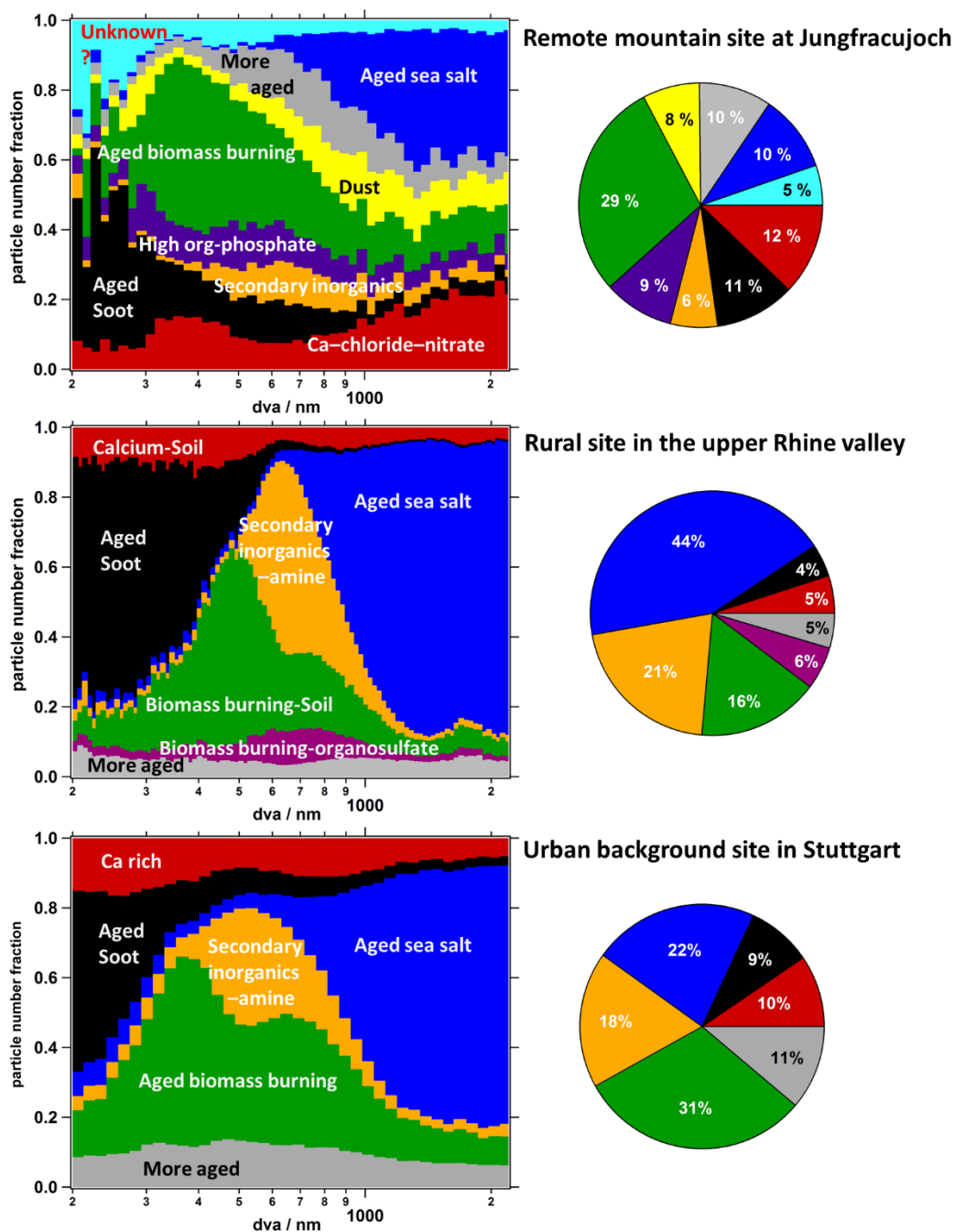
Figure 24: Size resolved number fraction for particle classes measured by single particle mass spectrometer LAAPTOF in remote, rural, and urban locations of central Europe, based on fuzzy classification according to fuzzy c-means clustering algorithm. Particle size shown here is vacuum aerodynamic diameter (d$_{va}$).

56

I have also investigated the impact of particle composition on its ice nucleation abilities in AIDA chamber campaigns at KIT and a campaign at the MIT. It turns out that unprocessed α-pinene SOA and Toluene SOA were inefficient ice nucleating particles (INP$_s$), while under the similar temperature and pressure conditions isoprene SOA and β-caryophyllene SOA could be better INP$_s$. For soil dust, I have found that organic acids in these particles are related to their ice nucleation ability. These findings imply the important role of particle composition in their ice nucleation process. The aforementioned field measurements and laboratory experiments on ice nucleation will help to improve the understanding of aerosol-cloud interaction, and to reduce the uncertainty regarding aerosol indirect effects on climate change.

Taken together, I demonstrate the strength of combining laboratory, field, and model studies as a solid "three-legged stool" (Figure 25) for investigating atmospheric aerosols. This work supports the hypothesis that the complexity of chemical composition and mixing state, the variability of emission sources and transport pattern of atmospheric aerosols requires all three legs for a sustainable advancement of our understanding of the atmospheric aerosol.
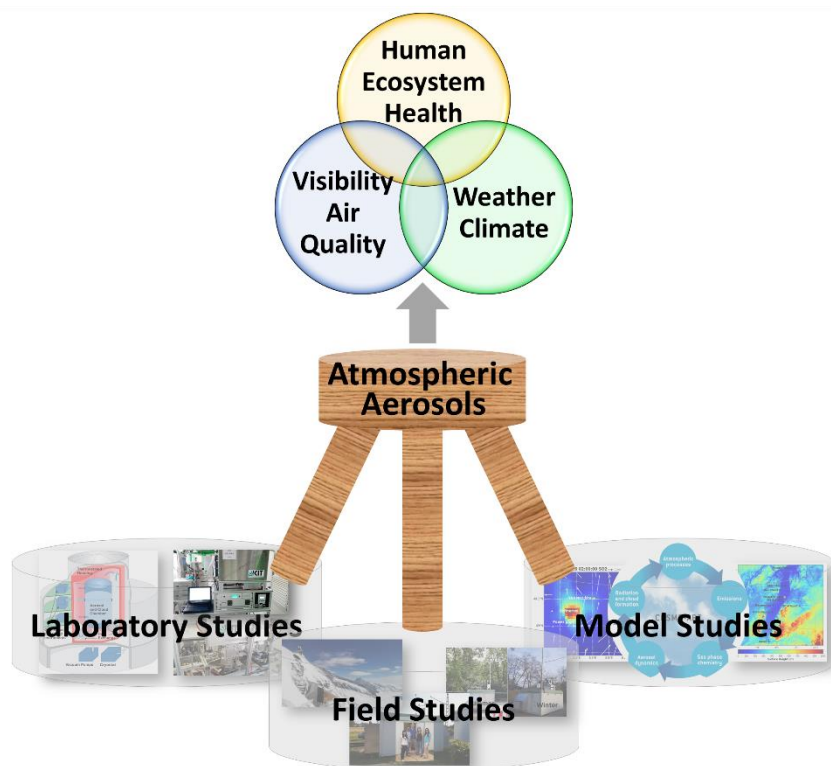
Figure 25: Three-legged stool to advance atmospheric aerosol science.

3.2 Outlook

It would be desirable to continue my work on the following topics:

- Improve the LAAPTOF with delayed extraction and better software with implementation of mass calibration for each spectrum, in order to overcome the peak shifting (jitter) issue.

- Improve the sensitivity of the LAAPTOF to some particle types such as pure ammonium sulfate and organic-rich particles, which are "missing" in the ambient measurements. Develop a new method to estimate the number and mass of these "missing" particles.

- Link the particle types at Jungfraujoch to the ice nucleation ability of the particles, which have impact on the cloud properties and precipitation. Therefore, it is of special interest to investigate this relationship as soon as ice nucleation data becomes available. These data could then be compared also the ice nucleation properties of those particles which I studied in aerosol chamber experiments.

- Based on the Jungfraujoch results from the two single particle mass spectrometers LAAPTOF and ALABAMA should be compared and validated including the analysis and quantification methods I developed.

- Compare the Jungfraujoch data with transport model data to understand the long-range transport of aerosol, potential cloud condensation nuclei (CCN), and ice nucleating particles. For this purpose the global transport model ICON-ART, successor of COSMO-ART would be most suitable.

- Make a more detailed comparison of the aerosol properties observed for Stuttgart in summer and winter and compare it with transport model results of either COSMO-ART or the street canyon resolving model PALMS-4U.

- Make a more detailed comparison of single particle data from different measurement sites, i.e., remote mountain site at Jungfraujoch station, rural site in the upper Rhine valley, and urban background site in downtown Stuttgart to develop a more general understanding of aerosol aging and transport pattern for central Europe.

References

Ahern, A. T., Subramanian, R., Saliba, G., Lipsky, E. M., Donahue, N. M., and Sullivan, R. C.: Effect of secondary organic aerosol coating thickness on the real-time detection and characterization of biomass-burning soot by two particle mass spectrometers, Atmos Meas Tech, 9, 6117–6137, 2016.

Allen, J. O., Bhave, P. V., Whiteaker, J. R., and Prather, K. A.: Instrument busy time and mass measurement using aerosol time-of-flight mass spectrometry, Aerosol Sci Tech, 40, 615–626, 2006.

Allen, J. O., Fergenson, D. P., Gard, E. E., Hughes, L. S., Morrical, B. D., Kleeman, M. J., Gross, D. S., Galli, M. E., Prather, K. A., and Cass, G. R.: Particle detection efficiencies of aerosol time of flight mass spectrometers under ambient sampling conditions, Environ Sci Technol, 34, 211–217, 2000.

Backes, A., Aulinger, A., Bieser, J., Matthias, V., and Quante, M.: Ammonia emissions in Europe, part I: Development of a dynamical ammonia emission inventory, Atmos Environ, 131, 55–66, 2016.

Bahreini, R., Keywood, M. D., Ng, N. L., Varutbangkul, V., Gao, S., Flagan, R. C., Seinfeld, J. H., Worsnop, D. R., and Jimenez, J. L.: Measurements of secondary organic aerosol from oxidation of cycloalkenes, terpenes, and m-xylene using an Aerodyne aerosol mass spectrometer, Environ Sci Technol, 39, 5674–5688, 2005.

Baldauf, M., Seifert, A., Forstner, J., Majewski, D., Raschendorfer, M., and Reinhardt, T.: Operational Convective-Scale Numerical Weather Prediction with the COSMO Model: Description and Sensitivities, Mon Weather Rev, 139, 3887–3905, 2011.

Bein, K. J., Zhao, Y. J., Pekney, N. J., Davidson, C. I., Johnston, M. V., and Wexler, A. S.: Identification of sources of atmospheric PM at the Pittsburgh Supersite - Part II: Quantitative comparisons of single particle, particle number, and particle mass measurements, Atmos Environ, 40, S424–S444, 2006.

Bieser, J., Aulinger, A., Matthias, V., Quante, M., and Builtjes, P.: SMOKE for Europe - adaptation, modification and evaluation of a comprehensive emission model for Europe, Geosci Model Dev, 4, 47–68, 2011.

Burkholder, J. B., Abbate, J. P. D., Barnes, I., Roberts, J. M., Melamed, M. L., Ammann, M., Bertram, A. K., Cappa, C. D., Carlton, A. G., Carpenter, L. J., Crowley, J. N., Dubowski, Y., Georges, C., Heard, D. E., Herrmann, H., Keutsch, F. N., Kroll, J. H., McNeill, V. F., Ng, N. L., Nizkorodov, S. A., Orlando, J. J., Percival, C. J., Picquet-Varrault, B., Rudich, Y., Seakins, P. W., Surratt, J. D., Tanimoto, H., Thornton, J. A., Tong, Z., Tyndall, G. S., Wahner, A., Weschler, C. J., Wilson, K. R., and Ziemann, P. J.: The Essential Role for Laboratory Studies in Atmospheric Chemistry, Environ Sci Technol, 51, 2519–2528, 2017.

Bytnerowicz, A. and Fenn, M. E.: Nitrogen deposition in California forests: A review, Environ Pollut, 92, 127–146, 1996.

Canagaratna, M. R., Jayne, J. T., Jimenez, J. L., Allan, J. D., Alfarra, M. R., Zhang, Q., Onasch, T. B., Drewnick, F., Coe, H., Middlebrook, A., Delia, A., Williams, L. R., Trimborn, A. M., Northway, M. J., DeCarlo, P. F., Kolb, C. E., Davidovits, P., and Worsnop, D. R.:

Chemical and microphysical characterization of ambient aerosols with the aerodyne aerosol mass spectrometer, Mass Spectrom Rev, 26, 185–222, 2007.

Canonaco, F., Crippa, M., Slowik, J. G., Baltensperger, U., and Prevot, A. S. H.: SoFi, an IGOR-based interface for the efficient use of the generalized multilinear engine (ME-2) for the source apportionment: ME-2 application to aerosol mass spectrometer data, Atmos Meas Tech, 6, 3649–3661, 2013.

Canonaco, F., Slowik, J. G., Baltensperger, U., and Prevot, A. S. H.: Seasonal differences in oxygenated organic aerosol composition: implications for emissions sources and factor analysis, Atmos Chem Phys, 15, 6993–7002, 2015.

Christopoulos, C. D., Garimella, S., Zawadowicz, M. A., Mohler, O., and Cziczo, D. J.: A machine learning approach to aerosol classification for single-particle mass spectrometry, Atmos Meas Tech, 11, 5687–5699, 2018.

Crippa, M., Canonaco, F., Lanz, V. A., Aijala, M., Allan, J. D., Carbone, S., Capes, G., Ceburnis, D., Dall'Osto, M., Day, D. A., DeCarlo, P. F., Ehn, M., Eriksson, A., Freney, E., Hildebrandt Ruiz, L., Hillamo, R., Jimenez, J. L., Junninen, H., Kiendler-Scharr, A., Kortelainen, A. M., Kulmala, M., Laaksonen, A., Mensah, A., Mohr, C., Nemitz, E., O'Dowd, C., Ovadnevaite, J., Pandis, S. N., Petaja, T., Poulain, L., Saarikoski, S., Sellegri, K., Swietlicki, E., Tiitta, P., Worsnop, D. R., Baltensperger, U., and Prevot, A. S. H.: Organic aerosol components derived from 25 AMS data sets across Europe using a consistent ME-2 based source apportionment approach, Atmos Chem Phys, 14, 6159–6176, 2014.

Cziczo, D. J., Froyd, K. D., Gallavardin, S. J., Moehler, O., Benz, S., Saathoff, H., and Murphy, D. M.: Deactivation of ice nuclei due to atmospherically relevant surface coatings, Environ Res Lett, 4, 2009.

DeCarlo, P. F., Kimmel, J. R., Trimborn, A., Northway, M. J., Jayne, J. T., Aiken, A. C., Gonin, M., Fuhrer, K., Horvath, T., Docherty, K. S., Worsnop, D. R., and Jimenez, J. L.: Field-deployable, high-resolution, time-of-flight aerosol mass spectrometer, Anal Chem, 78, 8281–8289, 2006.

DeMott, P. J., Mohler, O., Cziczo, D. J., Hiranuma, N., Petters, M. D., Petters, S. S., Belosi, F., Bingemer, H. G., Brooks, S. D., Budke, C., Burkert-Kohn, M., Collier, K. N., Danielczok, A., Eppers, O., Felgitsch, L., Garimella, S., Grothe, H., Herenz, P., Hill, T. C. J., Hohler, K., Kanji, Z. A., Kiselev, A., Koop, T., Kristensen, T. B., Kruger, K., Kulkarni, G., Levin, E. J. T., Murray, B. J., Nicosia, A., O'Sullivan, D., Peckhaus, A., Polen, M. J., Price, H. C., Reicher, N., Rothenberg, D. A., Rudich, Y., Santachiara, G., Schiebel, T., Schrod, J., Seifried, T. M., Stratmann, F., Sullivan, R. C., Suski, K. J., Szakall, M., Taylor, H. P., Ullrich, R., Vergara-Temprado, J., Wagner, R., Whale, T. F., Weber, D., Welti, A., Wilson, T. W., Wolf, M. J., and Zenker, J.: The Fifth International Workshop on Ice Nucleation phase 2 (FIN-02): laboratory intercomparison of ice nucleation measurements, Atmos Meas Tech, 11, 6231–6257, 2018.

DeMott, P. J., Mohler, O., Stetzer, O., Vali, G., Levin, Z., Petters, M. D., Murakami, M., Leisner, T., Bundke, U., Klein, H., Kanji, Z. A., Cotton, R., Jones, H., Benz, S., Brinkmann, M., Rzesanke, D., Saathoff, H., Nicolet, M., Saito, A., Nillius, B., Bingemer, H., Abbatt, J., Ardon, K., Ganor, E., Georgakopoulos, D. G., and Saunders, C.: Resurgence in Ice Nuclei Measurement Research, B Am Meteorol Soc, 92, 1623–1635, 2011.

Dockery, D. W., Pope, C. A., Xu, X. P., Spengler, J. D., Ware, J. H., Fay, M. E., Ferris, B. G., and Speizer, F. E.: An Association between Air-Pollution and Mortality in 6 United-States Cities, New Engl J Med, 329, 1753–1759, 1993.

Dominici, F., Peng, R. D., Bell, M. L., Pham, L., McDermott, A., Zeger, S. L., and Samet, J. M.: Fine particulate air pollution and hospital admission for cardiovascular and respiratory diseases, Jama-J Am Med Assoc, 295, 1127–1134, 2006.

Donahue, N. M., Henry, K. M., Mentel, T. F., Kiendler-Scharr, A., Spindler, C., Bohn, B., Brauers, T., Dorn, H. P., Fuchs, H., Tillmann, R., Wahner, A., Saathoff, H., Naumann, K. H., Mohler, O., Leisner, T., Muller, L., Reinnig, M. C., Hoffmann, T., Salo, K., Hallquist, M., Frosch, M., Bilde, M., Tritscher, T., Barmet, P., Praplan, A. P., DeCarlo, P. F., Dommen, J., Prevot, A. S. H., and Baltensperger, U.: Aging of biogenic secondary organic aerosol via gas-phase OH radical reactions, P Natl Acad Sci USA, 109, 13503–13508, 2012.

Fahey, D. W., Gao, R. S., Mohler, O., Saathoff, H., Schiller, C., Ebert, V., Kramer, M., Peter, T., Amarouche, N., Avallone, L. M., Bauer, R., Bozoki, Z., Christensen, L. E., Davis, S. M., Durry, G., Dyroff, C., Herman, R. L., Hunsmann, S., Khaykin, S. M., Mackrodt, P., Meyer, J., Smith, J. B., Spelten, N., Troy, R. F., Vomel, H., Wagner, S., and Wienhold, F. G.: The AquaVIT-1 intercomparison of atmospheric water vapor measurement techniques, Atmos Meas Tech, 7, 3177–3213, 2014.

Fergenson, D. P., Song, X. H., Ramadan, Z., Allen, J. O., Hughes, L. S., Cass, G. R., Hopke, P. K., and Prather, K. A.: Quantification of ATOFMS data by multivariate methods, Anal Chem, 73, 3535–3541, 2001.

Froyd, K. D., Murphy, S. M., Murphy, D. M., de Gouw, J. A., Eddingsaas, N. C., and Wennberg, P. O.: Contribution of isoprene-derived organosulfates to free tropospheric aerosol mass, P Natl Acad Sci USA, 107, 21360–21365, 2010.

Fuzzi, S., Baltensperger, U., Carslaw, K., Decesari, S., van Der Gon, H. D., Facchini, M. C., Fowler, D., Koren, I., Langford, B., Lohmann, U., Nemitz, E., Pandis, S., Riipinen, I., Rudich, Y., Schaap, M., Slowik, J. G., Spracklen, D. V., Vignati, E., Wild, M., Williams, M., and Gilardoni, S.: Particulate matter, air quality and climate: lessons learned and future needs, Atmos Chem Phys, 15, 8217–8299, 2015.

Gallavardin, S., Lohmann, U., and Cziczo, D.: Analysis and differentiation of mineral dust by single particle laser mass spectrometry, Int J Mass Spectrom, 274, 56–63, 2008.

Garimella, S., Kristensen, T. B., Ignatius, K., Welti, A., Voigtlander, J., Kulkarni, G. R., Sagan, F., Kok, G. L., Dorsey, J., Nichman, L., Rothenberg, D. A., Rosch, M., Kirchgassner, A. C. R., Ladkin, R., Wex, H., Wilson, T. W., Ladino, L. A., Abbatt, J. P. D., Stetzer, O., Lohmann, U., Stratmann, F., and Cziczo, D. J.: The SPectrometer for Ice Nuclei (SPIN): an instrument to investigate ice nucleation, Atmos Meas Tech, 9, 2781–2795, 2016.

Gemayel, R., Hellebust, S., Temime-Roussel, B., Hayeck, N., Van Elteren, J. T., Wortham, H., and Gligorovski, S.: The performance and the characterization of laser ablation aerosol particle time-of-flight mass spectrometry (LAAP-ToF-MS), Atmos Meas Tech, 9, 1947–1959, 2016.

Gemayel, R., Temime-Roussel, B., Hayeck, N., Gandolfo, A., Hellebust, S., Gligorovski, S., and Wortham, H.: Development of an analytical methodology for obtaining quantitative mass concentrations from LAAP-ToF-MS measurements, Talanta, 174, 715–724, 2017.

Gross, D. S., Gälli, M. E., Silva, P. J., and Prather, K. A.: Relative sensitivity factors for alkali metal and ammonium cations in single particle aerosol time-of-flight mass spectra, Anal Chem, 72, 416–422, 2000.

Gunsch, M. J., May, N. W., Wen, M., Bottenus, C. L. H., Gardner, D. J., VanReken, T. M., Bertman, S. B., Hopke, P. K., Ault, A. P., and Pratt, K. A.: Ubiquitous influence of wildfire emissions and secondary organic aerosol on summertime atmospheric aerosol in the forested Great Lakes region, Atmos Chem Phys, 18, 3701–3715, 2018.

Hagemann, R., Corsmeier, U., Kottmeier, C., Rinke, R., Wieser, A., and Vogel, B.: Spatial variability of particle number concentrations and NOx in the Karlsruhe (Germany) area obtained with the. mobile laboratory 'AERO-TRAM', Atmos Environ, 94, 341–352, 2014.

Healy, R. M., Sciare, J., Poulain, L., Crippa, M., Wiedensohler, A., Prevot, A. S. H., Baltensperger, U., Sarda-Esteve, R., McGuire, M. L., Jeong, C. H., McGillicuddy, E., O'Connor, I. P., Sodeau, J. R., Evans, G. J., and Wenger, J. C.: Quantitative determination of carbonaceous particle mixing state in Paris using single-particle mass spectrometer and aerosol mass spectrometer measurements, Atmos Chem Phys, 13, 9479–9496, 2013.

Hill, T. C. J., DeMott, P. J., Tobo, Y., Froehlich-Nowoisky, J., Moffett, B. F., Franc, G. D., and Kreidenweis, S. M.: Sources of organic ice nucleating particles in soils, Atmos Chem Phys, 16, 7195–7211, 2016.

Huang, W., Saathoff, H., Pajunoja, A., Shen, X. L., Naumann, K. H., Wagner, R., Virtanen, A., Leisner, T., and Mohr, C.: alpha-Pinene secondary organic aerosol at low temperature: chemical composition and implications for particle viscosity, Atmos Chem Phys, 18, 2883–2898, 2018.

Huang, W., Saathoff, H., Shen, X. L., Ramakrishna, R., Leisner, T., and Mohr, C.: Chemical characterization of highly functionalized organonitrates contributing to high night-time organic aerosol mass loadings and particle growth, Environ Sci Technol, 53, 1165–1174, 2019a.

Huang, W., Saathoff, H., Shen, X. L., Ramakrishna, R., Leisner, T., and Mohr, C.: Seasonal characteristics of organic aerosol chemical composition and volatility in Stuttgart, Germany, Atmos Chem Phys Discuss, 2019b. https://doi.org/10.5194/acp-2019-5364, 2019b.

IPCC: Climate Change 2013: The Physical Science Basis. Contribution of Working Group I to the Fifth Assessment Report of the Intergovernmental Panel on Climate Change. Cambridge Univ. Press.

Jeong, C. H., McGuire, M. L., Godri, K. J., Slowik, J. G., Rehbein, P. J. G., and Evans, G. J.: Quantification of aerosol chemical composition using continuous single particle measurements, Atmos Chem Phys, 11, 7027–7044, 2011.

Jimenez, J. L., Canagaratna, M. R., Donahue, N. M., Prevot, A. S. H., Zhang, Q., Kroll, J. H., DeCarlo, P. F., Allan, J. D., Coe, H., Ng, N. L., Aiken, A. C., Docherty, K. S., Ulbrich, I. M., Grieshop, A. P., Robinson, A. L., Duplissy, J., Smith, J. D., Wilson, K. R., Lanz, V. A., Hueglin, C., Sun, Y. L., Tian, J., Laaksonen, A., Raatikainen, T., Rautiainen, J., Vaattovaara, P., Ehn, M., Kulmala, M., Tomlinson, J. M., Collins, D. R., Cubison, M. J., Dunlea, E. J., Huffman, J. A., Onasch, T. B., Alfarra, M. R., Williams, P. I., Bower, K., Kondo, Y., Schneider, J., Drewnick, F., Borrmann, S., Weimer, S., Demerjian, K., Salcedo, D., Cottrell, L., Griffin, R., Takami, A., Miyoshi, T., Hatakeyama, S., Shimono, A., Sun,

J. Y., Zhang, Y. M., Dzepina, K., Kimmel, J. R., Sueper, D., Jayne, J. T., Herndon, S. C., Trimborn, A. M., Williams, L. R., Wood, E. C., Middlebrook, A. M., Kolb, C. E., Baltensperger, U., and Worsnop, D. R.: Evolution of organic aerosols in the atmosphere, Science, 326, 1525–1529, 2009.

Köllner, F., Schneider, J., Willis, M. D., Klimach, T., Helleis, F., Bozem, H., Kunkel, D., Hoor, P., Burkart, J., Leaitch, W. R., Aliabadi, A. A., Abbatt, J. P. D., Herber, A. B., and Borrmann, S.: Particulate trimethylamine in the summertime Canadian high Arctic lower troposphere, Atmos Chem Phys, 17, 13747–13766, 2017.

Laborde, M., Schnaiter, M., Linke, C., Saathoff, H., Naumann, K. H., Mohler, O., Berlenz, S., Wagner, U., Taylor, J. W., Liu, D., Flynn, M., Allan, J. D., Coe, H., Heimerl, K., Dahlkotter, F., Weinzierl, B., Wollny, A. G., Zanatta, M., Cozic, J., Laj, P., Hitzenberger, R., Schwarz, J. P., and Gysel, M.: Single Particle Soot Photometer intercomparison at the AIDA chamber, Atmos Meas Tech, 5, 3077–3097, 2012.

Lu, D. W., Liu, Q., Yu, M., Yang, X. Z., Fu, Q., Zhang, X. S., Mu, Y. J., and Jiang, G. B.: Natural silicon isotopic signatures reveal the sources of airborne fine particulate matter, Environ Sci Technol, 52, 1088–1095, 2018.

Marsden, N. A., Flynn, M. J., Allan, J. D., and Coe, H.: Online dfferentiation of mineral phase in aerosol particles by ion formation mechanism using a LAAP-TOF single-particle mass spectrometer, Atmos Meas Tech, 11, 195–213, 2018.

Marsden, N. A., Flynn, M. J., Taylor, J. W., Allan, J. D., and Coe, H.: Evaluating the influence of laser wavelength and detection stage geometry on optical detection efficiency in a single-particle mass spectrometer, Atmos Meas Tech, 9, 6051–6068, 2016.

Marsden, N. A., Ullrich, R., Möhler, O., Hammer, S. E., Kandler, K., Cui, Z., Williams, P. I., Flynn, M. J., Liu, D., Allan, J. D., and Coe, H.: Mineralogy and mixing state of north African mineral dust by online single-particle mass spectrometry, Atmos Chem Phys, 19, 2259–2281, 2019.

May, N. W., Gunsch, M. J., Olson, N. E., Bondy, A. L., Kirpes, R. M., Bertman, S. B., China, S., Laskin, A., Hopke, P. K., Ault, A. P., and Pratt, K. A.: Unexpected contributions of sea spray and lake spray aerosol to inland particulate matter, Environ Sci Tech Let, 5, 405–412, 2018.

Middlebrook, A. M., Bahreini, R., Jimenez, J. L., and Canagaratna, M. R.: Evaluation of composition-dependent collection efficiencies for the aerodyne aerosol mass spectrometer using field data, Aerosol Sci Tech, 46, 258–271, 2012.

Mohler, O., Buttner, S., Linke, C., Schnaiter, M., Saathoff, H., Stetzer, O., Wagner, R., Kramer, M., Mangold, A., Ebert, V., and Schurath, U.: Effect of sulfuric acid coating on heterogeneous ice nucleation by soot aerosol particles, J Geophys Res-Atmos, 110, 2005.

Mohler, O., Field, P. R., Connolly, P., Benz, S., Saathoff, H., Schnaiter, M., Wagner, R., Cotton, R., Kramer, M., Mangold, A., and Heymsfield, A. J.: Efficiency of the deposition mode ice nucleation on mineral dust particles, Atmos Chem Phys, 6, 3007–3021, 2006.

Murphy, D. M.: The design of single particle laser mass spectrometers, Mass Spectrom Rev, 26, 150–165, 2007.

Murphy, D. M., Cziczo, D. J., Froyd, K. D., Hudson, P. K., Matthew, B. M., Middlebrook, A. M., Peltier, R. E., Sullivan, A., Thomson, D. S., and Weber, R. J.: Single-particle mass

spectrometry of tropospheric aerosol particles, J Geophys Res-Atmos, 111, D23S32, doi: 10.1029/2006jd007340, 2006.

Nash, D. G., Baer, T., and Johnston, M. V.: Aerosol mass spectrometry: An introductory review, Int J Mass Spectrom, 258, 2–12, 2006.

Noble, C. A. and Prather, K. A.: Real-time single particle mass spectrometry: a historical review of a quarter century of the chemical analysis of aerosols, Mass Spectrom Rev, 19, 248–274, 2000.

O'Sullivan, D., Murray, B. J., Malkin, T. L., Whale, T. F., Umo, N. S., Atkinson, J. D., Price, H. C., Baustian, K. J., Browse, J., and Webb, M. E.: Ice nucleation by fertile soil dusts: relative importance of mineral and biogenic components, Atmos Chem Phys, 14, 1853–1867, 2014.

Pope, C. A., Burnett, R. T., Thun, M. J., Calle, E. E., Krewski, D., Ito, K., and Thurston, G. D.: Lung cancer, cardiopulmonary mortality, and long-term exposure to fine particulate air pollution, Jama-J Am Med Assoc, 287, 1132–1141, 2002.

Pöschl, U.: Atmospheric aerosols: Composition, transformation, climate and health effects, Angew Chem Int Edit, 44, 7520–7540, 2005.

Pratt, K. A. and Prather, K. A.: Mass spectrometry of atmospheric aerosols-Recent developments and applications. Part II: On-line mass spectrometry techniques, Mass Spectrom Rev, 31, 17–48, 2012.

Qin, X. Y., Bhave, P. V., and Prather, K. A.: Comparison of two methods for obtaining quantitative mass concentrations from aerosol time-of-flight mass spectrometry measurements, Anal Chem, 78, 6169–6178, 2006.

Ramisetty, R., Abdelmonem, A., Shen, X. L., Saathoff, H., Leisner, T., and Mohr, C.: Exploring femtosecond laser ablation in single-particle aerosol mass spectrometry, Atmos Meas Tech, 11, 4345–4360, 2018.

Reilly, P. T. A., Lazar, A. C., Gieray, R. A., Whitten, W. B., and Ramsey, J. M.: The elucidation of charge-transfer-induced matrix effects in environmental aerosols via real-time aerosol mass spectral analysis of individual airborne particles, Aerosol Sci Tech, 33, 135–152, 2000.

Reinard, M. S. and Johnston, M. V.: Ion formation mechanism in laser desorption ionization of individual nanoparticles, J Am Soc Mass Spectr, 19, 389–399, 2008.

Reitz, P., Zorn, S. R., Trimborn, S. H., and Trimborn, A. M.: A new, powerful technique to analyze single particle aerosol mass spectra using a combination of OPTICS and the fuzzy c-means algorithm, J Aerosol Sci, 98, 1–14, 2016.

Rieger, D., Bangert, M., Bischoff-Gauss, I., Forstner, J., Lundgren, K., Reinert, D., Schröter, J., Vogel, H., Zängl, G., Ruhnke, R., and Vogel, B.: ICON-ART 1.0-a new online-coupled model system from the global to regional scale, Geosci Model Dev, 8, 1659–1676, 2015.

Saathoff, H., Naumann, K. H., Mohler, O., Jonsson, A. M., Hallquist, M., Kiendler-Scharr, A., Mentel, T. F., Tillmann, R., and Schurath, U.: Temperature dependence of yields of secondary organic aerosols from the ozonolysis of alpha-pinene and limonene, Atmos Chem Phys, 9, 1551–1577, 2009.

Schill, G. P. and Tolbert, M. A.: Heterogeneous ice nucleation on phase-separated organic-sulfate particles: effect of liquid vs. glassy coatings, Atmos Chem Phys, 13, 4681–4695, 2013.

Seinfeld, J. H. and Pandis, S. N.: Atmospheric chemistry and physics: From air pollution to climate change, Wiley, J & Sons, Inc., Hoboken, New Jersey, 2006.

Shen, X. L., Ramisetty, R., Mohr, C., Huang, W., Leisner, T., and Saathoff, H.: Laser ablation aerosol particle time-of-flight mass spectrometer (LAAPTOF): performance, reference spectra and classification of atmospheric samples, Atmos Meas Tech, 11, 2325–2343, 2018.

Shen, X. L., Saathoff, H., Huang, W., Mohr, C., Ramisetty, R., and Leisner, T.: Understanding of atmospheric aerosol particles with improved particle identification and quantification by single particle mass spectrometry, Atmos Meas Tech, 12, 2219–2240, 2019a.

Shen, X. L., Vogel, H., Vogel, B., Huang, W., Mohr, C., Ramisetty, R., Leisner, T., Prevot, A. S. H., and Saathoff, H.: Chemical composition and origin of aerosol particles (PM 2.5) in the upper Rhine valley in summer, Atmos Chem Phys Discuss, 12, submitted, 2019b.

Silva, P. J., Carlin, R. A., and Prather, K. A.: Single particle analysis of suspended soil dust from Southern California, Atmos Environ, 34, 1811–1820, 2000.

Stein, A. F., Draxler, R. R., Rolph, G. D., Stunder, B. J. B., Cohen, M. D., and Ngan, F.: Noaa's Hysplit Atmospheric Transport and Dispersion Modeling System, B Am Meteorol Soc, 96, 2059–2077, 2015.

Sullivan, R. C. and Prather, K. A.: Recent advances in our understanding of atmospheric chemistry and climate made possible by on-line aerosol analysis instrumentation, Anal Chem, 77, 3861–3885, 2005.

Thomson, D. S., Middlebrook, A. M., and Murphy, D. M.: Thresholds for laser-induced ion formation from aerosols in a vacuum using ultraviolet and vacuum-ultraviolet laser wavelengths, Aerosol Sci Tech, 26, 544–559, 1997.

Tobo, Y., DeMott, P. J., Hill, T. C. J., Prenni, A. J., Swoboda-Colberg, N. G., Franc, G. D., and Kreidenweis, S. M.: Organic matter matters for ice nuclei of agricultural soil origin, Atmos Chem Phys, 14, 8521–8531, 2014.

Tsigaridis, K., Krol, M., Dentener, F. J., Balkanski, Y., Lathière, J., Metzger, S., Hauglustaine, D. A., and Kanakidou, M.: Change in global aerosol composition since preindustrial times, Atmos Chem Phys, 6, 5143–5162, 2006.

Usher, C. R., Michel, A. E., and Grassian, V. H.: Reactions on mineral dust, Chem Rev, 103, 4883–4939, 2003.

Vogel, B., Fiedler, F., and Vogel, H.: Influence of Topography and Biogenic Volatile Organic-Compounds Emission in the State of Baden-Wurttemberg on Ozone Concentrations during Episodes of High Air Temperatures, J Geophys Res-Atmos, 100, 22907–22928, 1995.

Vogel, B., Vogel, H., Baumer, D., Bangert, M., Lundgren, K., Rinke, R., and Stanelle, T.: The comprehensive model system COSMO-ART - Radiative impact of aerosol on the state of the atmosphere on the regional scale, Atmos Chem Phys, 9, 8661–8680, 2009.

Wagner, R., Hohler, K., Huang, W., Kiselev, A., Mohler, O., Mohr, C., Pajunoja, A., Saathoff, H., Schiebel, T., Shen, X. L., and Virtanen, A.: Heterogeneous ice nucleation of α-pinene SOA particles before and after ice cloud processing, J Geophys Res-Atmos, 122, 4924-4943, 2017.

Wagner, R., Linke, C., Naumann, K. H., Schnaiter, M., Vragel, M., Gangl, M., and Horvath, H.: A review of optical measurements at the aerosol and cloud chamber AIDA, J Quant Spectrosc Ra, 110, 930–949, 2009.

Watson, J. G.: Visibility: Science and regulation, J Air Waste Manage, 52, 628–713, 2002.

Weimer, M., Schröter, J., Eckstein, J., Deetz, K., Neumaier, M., Fischbeck, G., Hu, L., Millet, D. B., Rieger, D., Vogel, H., Vogel, B., Reddmann, T., Kirner, O., Ruhnke, R., and Braesicke, P.: An emission module for ICON-ART 2.0: implementation and simulations of acetone, Geosci Model Dev, 10, 2471–2494, 2017.

Wenzel, R. J., Liu, D. Y., Edgerton, E. S., and Prather, K. A.: Aerosol time-of-flight mass spectrometry during the Atlanta Supersite Experiment: 2. Scaling procedures, J Geophys Res-Atmos, 108, 2003.

Zawadowicz, M. A., Froyd, K. D., Murphy, D., and Cziczo, D. J.: Improved identification of primary biological aerosol particles using single particle mass spectrometry, Atmos Chem Phys, 17, 7193–7212, 2017.

Zenobi, R. and Knochenmuss, R.: Ion formation in MALDI mass spectrometry, Mass Spectrom Rev, 17, 337–366, 1998.

Zhang, Q., Jimenez, J. L., Canagaratna, M. R., Allan, J. D., Coe, H., Ulbrich, I., Alfarra, M. R., Takami, A., Middlebrook, A. M., Sun, Y. L., Dzepina, K., Dunlea, E., Docherty, K., DeCarlo, P. F., Salcedo, D., Onasch, T., Jayne, J. T., Miyoshi, T., Shimono, A., Hatakeyama, S., Takegawa, N., Kondo, Y., Schneider, J., Drewnick, F., Borrmann, S., Weimer, S., Demerjian, K., Williams, P., Bower, K., Bahreini, R., Cottrell, L., Griffin, R. J., Rautiainen, J., Sun, J. Y., Zhang, Y. M., and Worsnop, D. R.: Ubiquity and dominance of oxygenated species in organic aerosols in anthropogenically-influenced Northern Hemisphere midlatitudes, Geophys Res Lett, 34, L13801, doi: 13810.11029/12007gl029979, 2007.

Zhang, R. Y., Wang, G. H., Guo, S., Zarnora, M. L., Ying, Q., Lin, Y., Wang, W. G., Hu, M., and Wang, Y.: Formation of Urban Fine Particulate Matter, Chem Rev, 115, 3803–3855, 2015.

Zhou, Y., Huang, X. H. H., Griffith, S. M., Li, M., Li, L., Zhou, Z., Wu, C., Meng, J. W., Chan, C. K., Louie, P. K. K., and Yu, J. Z.: A field measurement based scaling approach for quantification of major ions, organic carbon, and elemental carbon using a single particle aerosol mass spectrometer, Atmos Environ, 143, 300–312, 2016.

Zhang, Y., Wolf, M. J., Koss, A. R., Shen, X. L., Nichamn, L., Zhang, Z., Gold, A., Davidivots, P., Jayne, J. T., Worsnop, D. R., Onasch, T. B., Surratt, J. D., Kroll, J. H., and Cziczo, D. J.: Enhancement of the heterogeneous ice nucleation by the phase state change of organic aerosols, Environ Sci Technol, in preparation, 2019.

Appendix A-List of publications during my PhD study

1. Zhang, Y., Wolf, M. J., Koss, A. R., **Shen, X. L.,** Nichamn, L., Zhang, Z., Gold, A., Davidivots, P., Jayne, J. T., Worsnop, D. R., Onasch, T. B., Surratt, J. D., Kroll, J. H., and Cziczo, D. J.: Enhancement of the heterogeneous ice nucleation by the phase state change of organic aerosols. *Environ. Sci. Technol., in preparation, 2019.*

2. **Shen, X. L.,** Vogel, H., Vogel, B., Huang, W., Mohr, C., Ramisetty R., Leisner, T., Prevot, A., and Saathoff, H. Composition and origin of $PM_{2.5}$ aerosol particles in the upper Rhine valley in summer. *Atmos. Chem. Phys., submitted, 2019.*

3. Huang, W., Saathoff, H., **Shen, X. L.,** Ramisetty R., Leisner, T., and Mohr, C. Seasonal characteristics of organic aerosol chemical composition and volatility in Stuttgart, Germany. *Atmos. Chem. Phys. Discuss., https://doi.org/10.5194/acp-2019-364, in review, 2019.*

4. **Shen, X. L.,** Saathoff, H., Huang, W., Mohr C., Ramisetty R., and Leisner, T. Understanding of *atmospheric aerosol particles with improved particle identification and quantification* by single particle mass spectrometry. *Atmos. Meas. Tech. 12, 2219–2240, 2019.*

5. Huang, W., Saathoff, H., **Shen, X. L.,** Ramisetty R., Leisner, T., and Mohr, C. Chemical characterization of highly functionalized organonitrates contributing to high night-time organic aerosol mass loadings and particle growth. *Environ. Sci. Technol. 53, 1165–1174, 2019.*

6. Ramisetty, R., Abdelmonem, A., **Shen, X. L.,** Saathoff, H., Leisner, T., and Mohr, C. Exploring femtosecond laser ablation in single particle aerosol mass spectrometry. *Atmos. Meas. Tech. 11, 4345–4360, 2018.*

7. **Shen, X. L.,** Ramisetty R., Mohr C., Huang, W., Leisner, T., and Saathoff, H. Laser ablation aerosol particle time-of-flight mass spectrometer (LAAPTOF): Performance, reference spectra and classification of atmospheric samples. *Atmos. Meas. Tech. 11, 2325–2343, 2018.*

8. Huang, W., Saathoff, H., Pajunoja, A., **Shen, X. L.,** Naumann, K., Wagner, R., Virtanen, A., Leisner, T., and Mohr, C. α-pinene secondary organic aerosol at low temperature: Chemical composition and implications for particle viscosity. *Atmos. Chem. Phys. 18, 2883–2898, 2018.*

9. Wagner, R., Höhler, K., Huang, W., Kiselev, A., Möhler, O., Mohr, C., Pajunoja, A., Saathoff, H., Schiebel, T., **Shen, X. L.,** and Virtanen, A. Heterogeneous ice nucleation of α-pinene SOA particles before and after ice cloud processing. *J. Geophys. Res. Atmos. 122, 4924–4943, 2017.*

Appendix B-Full articles of scientific publications as first author

Appendix B.1 Laser ablation aerosol particle time-of-flight mass spectrometer (LAAPTOF): Performance, reference spectra and classification of atmospheric samples

Atmospheric
Measurement
Techniques

Laser ablation aerosol particle time-of-flight mass spectrometer (LAAPTOF): performance, reference spectra and classification of atmospheric samples

Xiaoli Shen[1,2], **Ramakrishna Ramisetty**[1], **Claudia Mohr**[1,a], **Wei Huang**[1,2], **Thomas Leisner**[1], and **Harald Saathoff**[1]

[1]Institute of Meteorology and Climate Research (IMK-AAF), Karlsruhe Institute of Technology (KIT),
Hermann-von-Helmholtz-Platz 1, 76344 Eggenstein-Leopoldshafen, Germany
[2]Institute of Geography and Geoecology (IfGG), Karlsruhe Institute of Technology (KIT), Kaiserstr. 12,
76131 Karlsruhe, Germany
[a]now at: Department of Environmental Science and Analytical Chemistry, Stockholm University,
Stockholm, 11418, Sweden

Correspondence: Harald Saathoff (harald.saathoff@kit.edu)

Abstract. The laser ablation aerosol particle time-of-flight mass spectrometer (LAAPTOF, AeroMegt GmbH) is able to identify the chemical composition and mixing state of individual aerosol particles, and thus is a tool for elucidating their impacts on human health, visibility, ecosystem, and climate. The overall detection efficiency (ODE) of the instrument we use was determined to range from $\sim (0.01 \pm 0.01)$ to $\sim (4.23 \pm 2.36)\%$ for polystyrene latex (PSL) in the size range of 200 to 2000 nm, $\sim (0.44 \pm 0.19)$ to $\sim (6.57 \pm 2.38)\%$ for ammonium nitrate (NH_4NO_3), and $\sim (0.14 \pm 0.02)$ to $\sim (1.46 \pm 0.08)\%$ for sodium chloride (NaCl) particles in the size range of 300 to 1000 nm. Reference mass spectra of 32 different particle types relevant for atmospheric aerosol (e.g. pure compounds NH_4NO_3, K_2SO_4, NaCl, oxalic acid, pinic acid, and pinonic acid; internal mixtures of e.g. salts, secondary organic aerosol, and metallic core–organic shell particles; more complex particles such as soot and dust particles) were determined. Our results show that internally mixed aerosol particles can result in spectra with new clusters of ions, rather than simply a combination of the spectra from the single components. An exemplary 1-day ambient data set was analysed by both classical fuzzy clustering and a reference-spectra-based classification method. Resulting identified particle types were generally well correlated. We show how a combination of both methods can greatly improve the interpretation of single-particle data in field measurements.

1 Introduction

Atmospheric aerosol particles impact visibility, interact with trace gases, can act as cloud condensation and ice nuclei, and influence the Earth's radiation budget (Seinfeld and Pandis, 2006). Especially the continuously evolving chemical composition of aerosol particles is of scientific interest, as it influences all aerosol effects (Burkholder et al., 2017; Pöschl, 2005). However, large knowledge gaps still exist related to the chemical composition of the organic and inorganic components and their mutual interaction (Jimenez et al., 2009; Murphy et al., 2006; Schill and Tolbert, 2013; Zhang et al., 2007).

Aerosol particles can contain various components, ranging from volatile to refractory species (Pratt and Prather, 2012). The global aerosol mass burden was estimated to consist of 73.6 % dust, 16.7 % sea salt, 2.8 % biogenic secondary organic aerosols (SOA), 2.3 % primary organic aerosols (POA), 1.3 % sulfate, 1.3 % ammonium, 1.2 % nitrate, 0.4 % black carbon (soot), 0.2 % anthropogenic SOA, and 0.2 % methane sulfonic acid (Tsigaridis et al., 2006). During the ambient aerosols' lifetime, ranging from hours to a few weeks (Pöschl, 2005), the complexity of their chemical composition usually increases by coagulation, cloud processing, and chemical reactions (Seinfeld and Pandis, 2006; Usher et al., 2003). This modifies the particles' mixing state, with both internal (individual particles consisting of mixed

compounds, e.g. coating structures) and external mixtures, e.g. mixture of particles consisting of different compounds (Li et al., 2016). The aforementioned findings underscore the importance of measuring aerosol chemical composition and its changes on short timescales and on a single-particle basis, which can be realized by online mass spectrometry.

Online mass spectrometry includes bulk and single-particle measurements (Pratt and Prather, 2012). Single-particle mass spectrometry, which can be dated back to the 1970s, aims at in situ and real-time identification of the chemical composition of individual aerosol particles, hereby elucidating a particle's external and internal mixing properties (Noble and Prather, 2000). Online single-particle mass spectrometers (SPMSs) commonly use pulsed lasers for particle desorption and ionization (LDI), with the advantage of ionizing nearly all atmospheric particle components, including both non-refractory and refractory materials (Kulkarni et al., 2011). To the best of our knowledge, so far there is no quantitative analysis of particle composition by SPMS, since the ablation/ionization laser cannot interact with the entire particle and the generated ion fragments/clusters are susceptible to matrix effects (Ramisetty et al., 2017). In addition, ionization mechanisms are not fully understood (Murphy, 2007). SPMSs have identified many different ambient particle types in different regions of the atmosphere, such as elemental carbon and organic carbon (ECOC), organic sulfate, aged sea salt, biological, soil dust, and different metal dominated types (Dall'Osto et al., 2016; Moffet et al., 2008; Murphy et al., 2006; Schmidt et al., 2017). These measurements all confirmed the complexity of individual particles' mixing state and demonstrated the usefulness of single-particle mass spectra for apportionment of individual particle sources, including e.g. fossil fuel and biomass burning combustion, cooking, marine, and shipping sources (Arndt et al., 2017; Schmidt et al., 2017).

Currently, there are only two commercially available SPMSs, i.e. the single-particle aerosol mass spectrometer (SPAMS, Hexin Analytical Instrument Co., Ltd., China; Li et al., 2011; Lin et al., 2017) and the laser ablation aerosol particle time-of-flight mass spectrometer (LAAPTOF, AeroMegt GmbH, Germany). LAAPTOF uses two laser diodes (405 nm wavelength, ~ 40 mW, ~ 50 μm beam spot diameter; Marsden et al., 2016; Zawadowicz et al., 2017) for optical counting and size recording by light scattering, and one excimer laser (ArF, 193 nm, ~ 4 mJ) for one-step ablation/ionization. The overall detection efficiency (ODE) of this instrument, defined as the number of single-particle mass spectra obtained from the total number of aerosol particles in the sampled air, was determined to range from ~ 0.15 to $\sim 2.2\%$ for polystyrene latex (PSL) particles with geometric diameters (d_p) between 350 nm and 800 nm (Gemayel et al., 2016; Marsden et al., 2016). The instrument used by Gemayel et al. (2016) exhibited a maximum ODE of $\sim 2.2\%$ for PSL particle diameters of 450 nm, while $\sim 1\%$ at 600 nm was the peak ODE reported by Marsden et al. (2016) be-

fore the instrument modification. Neither the response of the LAAPTOF to spherical PSL particles smaller than 350 nm and bigger than 800 nm nor the response to other particle types with different shapes has been investigated systematically. The scattering efficiency (SE), defined as the number fraction of particles detected by light scattering compared to the number of particles in the sampled air in front of the aerodynamic inlet lens (ADL) of the instrument (refer to Fig. 1), is determined by the laser diodes, the detection optics, and the photomultiplier tubes (PMT), and it has a strong influence on the ODE of the instrument. Therefore, several groups have tried to improve this part of the instrument. Marsden et al. (2016) modified the detection stage geometry by replacing the detection laser with a fibre-coupled 532 nm, 1 W Nd:YAG solid-state laser system with a collimated laser beam, accomplishing an order-of-magnitude improvement in light detection sensitivity to PSL particles with 500–800 nm diameter. Zawadowicz et al. (2017) modified the optical path of the laser diodes with a better laser beam of < 1 mrad full-angle divergence and 100 μm detection beam spot size, and applied light guides to enhance the scattered-light collection. This resulted in improvement of 2–3 orders of magnitude in optical counting efficiency of incident PSL particles with 500–2000 nm vacuum aerodynamic diameter (d_{va}). There are only very few studies so far that discuss mass spectral patterns of different particle types measured by LAAPTOF. Gemayel et al. (2016) presented spectra from ambient particles collected in the city centre of Marseille, France; spectra (positive only) from pure soot and SOA-coated soot particles were shown by Ahern et al. (2016); spectra from potassium rich feldspar, soot, Argentinian soil dust, and Snomax (commercial ice nuclei) were shown by Zawadowicz et al. (2017); PSL and potassium rich feldspar spectra were measured by Marsden et al. (2018); and radiolytically formed particles spectra were measured by Wonaschuetz et al. (2017). Reitz et al. (2016) presented peak assignments for pure ammonium nitrate and sulfate particles, as well as for ambient particles measured at a suburban site of Düsseldorf, Germany, but did not show any spectra. Marker ions generated from SPMS are likely instrument specific, as pointed out by Schmidt et al. (2017). Therefore, there is a need for publicly available spectral information of this relatively new instrument.

There exists several techniques to group the large number of individual particle types and spectra resulting from SMPS measurements – such as k-means, c-means, and hierarchical clustering algorithms; neural-network-based methods such as ART2-A; and the most recent algorithm of ordering points to identify the clustering structure (OPTICS) – to help analyse the data (Hinz et al., 1999; Murphy et al., 2003; Reitz et al., 2016; Zelenyuk et al., 2006b; Zhao et al., 2008). There also exist target (reference spectra/predefined clusters)-oriented methods (Hinz et al., 1999; Gleanta GmbH; LAAPTOF AnalysisPro, AeroMegt GmbH).

In this paper we have characterized our LAAPTOF instrument with respect to its ODE for PSL, NH_4NO_3, and
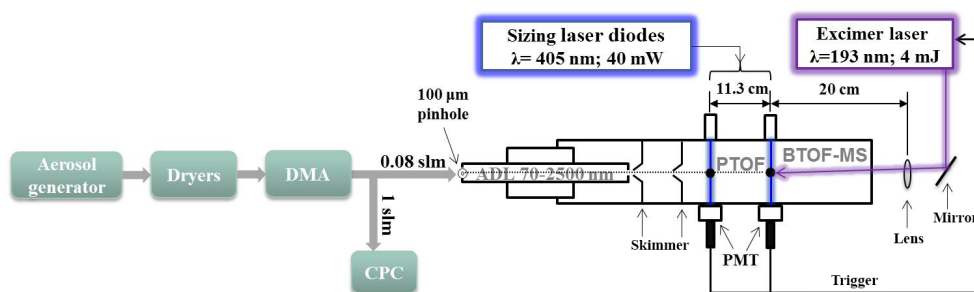
Figure 1. Schematic of the LAAPTOF instrument and the experimental setup for measuring standard samples (method A), e.g. PSL, NH_4NO_3, and K_2SO_4 particles, which were generated from a nebulizer, passed through two dryers, were size-selected by a differential mobility analyser (DMA), and were then measured by LAAPTOF.

sodium chloride (NaCl) particles for a wide size range (d_m: 200–2000 nm PSL; 300–1000 nm NH_4NO_3 and NaCl). We present laboratory-based reference spectra for aerosol particles containing atmospherically relevant components, which were grouped into three categories: (1) particles consisting of pure compounds, e.g. NH_4NO_3, K_2SO_4, and organic acids; (2) particles consisting of well-defined mixtures of pure salts and mixtures of organic compounds, e.g. α-pinene SOA, and PSL internally mixed with K_2SO_4, as well as other core–shell type of particles; and (3) particles consisting of complex mixtures, e.g. soot and dust particles. These reference spectra may also provide other users comprehensive references for comparison purposes and thus help better interpret ambient data. An example of field data analysis based on reference spectra as well as fuzzy c-means clustering will be given in Sect. 3.3.

2 Methods

2.1 The LAAPTOF instrument

The LAAPTOF has been described in several recent publications (Ahern et al., 2016; Gemayel et al., 2016; Marsden et al., 2016, 2018; Reitz et al., 2016; Wonaschuetz et al., 2017; Zawadowicz et al., 2017). Therefore, here we only briefly review the general operation steps that yield size and composition information of individual aerosol particles. The LAAPTOF instrument used in this study was delivered in April 2015 and may differ in a few technical aspects from earlier or later versions. A schematic of the main LAAPTOF components is given in Fig. 1. Particles with a vacuum aerodynamic diameter (d_{va}) between ~ 70 nm and 2.5 µm are sampled with a sampling flow rate of ~ 80 standard cubic centimetres per minute (SCCM); focused and accelerated by an ADL (LPL-2.5, AeroMegt GmbH) with close to 100 % transmission efficiency for particles with d_{va} 100 nm to 2 µm (http://www.aeromegt.com/#products?LPL-2.5_details, last access: 16 April 2018); and then pass through the particle time-of-flight (PTOF) chamber

in which the individual particle can be detected by two sizing laser beams (405 nm continuous wave, 40 mW) separated by 11.3 cm. Based on the particle time of flight between the two laser beams, its d_{va} can be determined and recorded. After detection by the second sizing laser, a nanosecond excimer laser pulse (wavelength: 193 nm; pulse duration: 4 to 8 ns; maximum pulse energy: ~ 8 mJ; beam diameter: ~ 300 µm when it hits the particle (Ramisetty et al., 2017); power density: $\sim 10^9$ W cm^{-2}; ATLEX-S, ATL Lasertechnik GmbH) can be triggered to desorb and ionize particle compounds. A laser pulse energy of 4 mJ was used for all the measurements in this study. More details about the ionization region geometry are given by Ramisetty et al. (2017). The resulting ions are analysed by a bipolar time-of-flight mass spectrometer (BTOF-MS; TOFWERK AG; mass resolution of $m/\Delta m \sim 600$ to 800 at 184 Th, mass range $m/q = 1$ up to ~ 2000 Th). The cations and anions are detected by corresponding microchannel plate arrays (MCPs), producing a pair of positive and negative spectra for each single particle.

2.2 Aerosol particle generation and experimental setup in the laboratory

The laboratory-based aerosol particles measured in this study (summarized in Table 1) were generated in four different ways (A, B1, B2, and S).

Method A: samples for pure particles and homogeneous and heterogeneous mixtures were dissolved/suspended in purified water and nebulized (ATM 221, Topas GmbH) with dry synthetic air, passed through two diffusion dryers (cylinder filled with Silica gel, Topas GmbH), and then size-selected by a differential mobility analyser (DMA 3080, TSI GmbH) before being sampled by LAAPTOF.

Method B1: particles were sampled from the 84.5 m^3 simulation chamber AIDA (Aerosol Interactions and Dynamics in the Atmosphere) of KIT (Saathoff et al., 2003). SOA particles were formed in the 3.7 m^3 stainless-steel Aerosol Preparation and Characterization (APC) chamber via ozonolysis (~ 6 ppm ozone) of α-pinene (~ 2.2 ppm) and then transferred into AIDA. Soil dust samples were dispersed by a ro-

Table 1. Overview of laboratory-generated aerosol particles for reference mass spectra.

Aerosol particle types	Size (nm)		Morphology	Source	Generation method	No. of spectra
	d_{va}	Width[a]				
1. Particles consisting of pure compounds						
Ammonium nitrate, NH_4NO_3	1160	101	aspherical	$\geq 99.5\%$, Fluka	A	497
Ammonium sulfate[b], $(NH_4)_2SO_4$	611	79	aspherical	$\geq 99.5\%$, Merck	A	537
Potassium sulfate, K_2SO_4	1465	232	aspherical	$\geq 99\%$, Merck	A	300
Sodium chloride, NaCl	1202	133	cubic	$\geq 99.5\%$, Merck	A	250
Silica, SiO_2 (Glass beads)	2097	44	spherical	Palas GmbH	S	347
Oxalic acid, $C_2H_4O_2$	1081	322	spherical	Merck	A	736
Pinic acid, $C_9H_{14}O_4$	902	94	spherical	University of Mainz	A	683
Cis-pinonic acid, $C_{10}H_{16}O_3$	702	88	spherical	98 %, ACROS ORGANICS	A	600
Humic acid	1221	126	spherical	100 %, Alfa Aesar	A	773
Polystyrene latex (PSL)	818	3	spherical	Thermo scientific	A	235
2. Particles consisting of well-defined mixtures						
Ammonium nitrate & ammonium sulfate (mass ratio = 1 : 1)	1102	165	aspherical	Single-component samples are from the same source	A	454
Potassium sulfate & sodium chloride (mass ratio = 1 : 1)	1375	197	aspherical	as the corresponding pure compounds		259
Ammonium nitrate & potassium sulfate (mass ratio = 2 : 1)	854	112	aspherical			576
Hematite	1091	817	spherical	Karlsruhe Institute of Technology (KIT)	S	320
Pure sea salt	1205	218	cubic	Sigma Aldrich	B1	422
α−Pinene secondary organic aerosols (SOA)	505	84	spherical	$(1S) - (-) - \alpha$-pinene (99 %) from Aldrich	B1[c]	1938
Potassium-sulfate-coated PSL	805	58	partially coated	Merck & Thermo scientific	A	609
Poly(allylamine hydrochloride)-coated gold	400[d]		300 nm core– 50 nm shell	Nanopartz Inc.	Nebulized without sizing	417
3. Particles consisting of complex mixtures						
Soot 1 with low organic carbon	386[e]	275	agglomerates	incomplete combustion of propane, C / O = 0.29	B2	617
Soot 1 with high organic carbon	120[e]	58	agglomerates	incomplete combustion of propane, C / O = 0.54	B2	347
Soot 2, diesel particles	624 ± 980[f]		agglomerates	NIST (2975)	S	533
Soot 3, lignocellulosic char	828	766	agglomerates	lignocellulosic char from chestnut wood; University of Zurich, Switzerland	S	390
Arizona test dust	1169	874	aspherical	Powder Technology Inc.	S	261
Saharan dust 1 (Morocco)	890	1230	aspherical	Konrad Kandler, TU Darmstadt	S	338
Saharan dust 2 (Cairo)	1334 ± 1454[f]		aspherical	Khaled Megahed, KIT	S	396
Arable soil dust SDGe01 (Gottesgabe, Germany)	912	392	aspherical	Roger Funk[g]	B1[h]	583
Arable soil dust SDPA01 (Paulinenaue, Germany)	787	334	aspherical	Roger Funk[g]	B1[h]	385
Arable soil dust SDAr08 (Argentina)	910	407	aspherical	Roger Funk[g]	B1[h]	592
Arable soil dust SDWY01 (Wyoming, USA)	864	430	aspherical	Tom Hill[i]	B1[h]	623
Agricultural soil dust (northern Germany)	561	249	aspherical	Roger Funk[g]	B1[h]	286
Urban dust	1329	1266	aspherical	NIST(1649a)	S	375
Illite_NX	825	260	sheet	Arginotec	S	807
Sea salt with *Skeletonema marinoi*[j]	1212	338	cubic	Matt Salter[j]	B1	526

Note that for aerosol generation methods, "A" represents the method of using a nebulizer and a DMA (refer to the setup in Fig. 1) for sizing d_m =800 nm; "B1" and "B2" represent the methods in which particles were sampled from AIDA and a stainless-steel cylinder, respectively; "S" corresponds to particles mobilized by shaking in a reservoir. For particles size information, d_{va} values represent the expected values from Gaussian fitting to the particle sizes measured by LAAPTOF. Spectra number is the number of averaged spectra. [a] These values represent the standard deviation from Gaussian fitting to the measured particle sizes (d_{va}). [b] There is only one weak but reproducible peak m/z 30 NO^+ in the positive spectra. Therefore we do not give the reference spectra in this paper. [c] SOA particles were formed in the Aerosol Preparation and Characterization (APC) chamber and then transferred into the AIDA chamber. [d] The nominal geometric size given by the manufacture Nanopartz Inc. [e] Electrical mobility equivalent diameter, d_m, measured by a scanning mobility particle sizer (SMPS). [f] The sizes (d_{va}) of Diesel particles and Saharan dust 2 are average values with their standard deviation. [g] Institute of Soil Landscape Research, Leibniz Centre for Agricultural Landscape Research, Germany. [h] Soil dust samples were dispersed by a rotating brush generator and injected via cyclones into the AIDA chamber. [i] Department of Atmospheric Science, Colorado State University, Fort Collins, Colorado, USA. [j] Samples, provided by Elena Gorokhova and Matt Salter at Stockholm University, that were prepared by diluting a pure *Skeletonema marinoi* culture with artificial seawater (sigma sea salt) to conditions representative of a bloom in the ocean.

tating brush generator (RBG1000, PALAS) and injected via cyclones into the AIDA chamber. Sea salt particles were generated and injected into AIDA by ultrasonically nebulizing artificial seawater (Sigma Aldrich) and highly concentrated *Skeletonema marinoi* culture (in artificial seawater), respectively, via a droplet separator and two diffusion dryers (Wagner et al., 2018).

Method B2 was used only for soot particles, which were generated with a propane burner (RSG miniCAST; Jing Ltd.) and injected into and sampled from a stainless-steel cylinder of $0.2\,m^3$ volume.

Method S: silica, hematite, illite NX, Arizona test dust, desert and urban dust, black carbon from chestnut wood (University of Zurich, Switzerland), and diesel soot reference particles from NIST were suspended in their reservoir bottles by shaking them and sampled directly from the headspace (upper part) of these reservoirs through a tube connecting it with the LAAPTOF.

For all the measurements, except measuring the particles generated by method S, a condensation particle counter (CPC 3010, TSI GmbH) was used to record the particle number concentration in parallel with the LAAPTOF inlet. The setup in Fig. 1 was specific for particles generated from method A.

2.3 Field measurement

Unusually high particle number concentrations, similar to downtown Karlsruhe (a city in southwest Germany), were observed frequently northeast of Karlsruhe by particle counters on board a tram wagon (www.aero-tram.kit.edu, last access: 16 April 2018) intersecting the city (Hagemann et al., 2014). To study the nature and to identify possible sources of these particles, their number, size, chemical composition, associated trace gases, and meteorological conditions were measured from 15 July to 1 September 2016 at a rural location ($49°6'10.54''$ N, $8°24'26.07''$ E), next to the tram line north of the village of Leopoldshafen, Germany. Ambient aerosol particles were sampled through a $PM_{2.5}$ inlet (SH 2.5–16, Comde-Derenda GmbH) with $1\,m^3\,h^{-1}$, a fraction of which was guided into the LAAPTOF, which was deployed for ~ 5 weeks from 26 July to 31 August. LAAPTOF measurements provided information on size and mass spectral patterns for individual particles. In this paper we use data from 1 day as an example of the potential interpretation of LAAPTOF spectral data using reference spectra.

2.4 Efficiency calculations

In the literature, two definitions of detection efficiency (DE) of SPMS are used: one is equal to the scattering efficiency (SE) of the detection lasers (Brands et al., 2011; Gaie-Levrel et al., 2012; Su et al., 2004; Zelenyuk and Imre, 2005; Zelenyuk et al., 2009), which is the fraction of particles detected by the scattering optics in the detection region of the instrument; the other one is the product of SE and hit rate (HR)

of the ablation/ionization laser (Su et al., 2004; Gemayel et al., 2016; Marsden et al., 2016). The hit rate is the fraction of particles detected actually leading to a useful mass spectrum. In this paper we use ODE, defined by the following equations:

$$ODE = SE \times HR \times 100\% \tag{1}$$
$$SE = N_d/N_0 \times 100\% \;\; \text{(transmission efficiency}$$
$$\text{of ADL is included)}, \tag{2}$$
$$HR = N_s/N_d \times 100\% \;\; \text{(ionization efficiency}$$
$$\text{is included)}, \tag{3}$$
$$N_0 = C_n \times \text{flow rate} \times \text{time}, \tag{4}$$

where N_d is the number of particles detected by light scattering, N_0 is the number of particles in front of the ADL, N_s is the number of bipolar spectra, C_n is the particle number concentration (cm^{-3}) measured by a CPC in front of the ADL, and the flow rate is the LAAPTOF sample flow rate.

2.5 Spectral and size data analysis

For each type of laboratory-generated aerosol particles, we measured at least 300 mass spectra. Data analysis is done via the Igor LAAPTOF data analysis software (version 1.0.2, AeroMegt GmbH). There are five main steps for the basic analysis procedure: (a) removal of the excimer laser ringing signal from the raw mass spectra; (b) determination of the signal baseline; (c) filtering for empty spectra; (d) mass calibration; and (e) stick integration, that is, the integration of nominal masses for peaks. It should be noted that spectrum-to-spectrum differences in peak positions for the same ion fragments/clusters complicate the mass calibrations. This may be caused by differences in kinetic energy of the ions produced; however this effect is typically compensated in the TOFs with reflectron (Kulkarni et al., 2011). Spectrum-to-spectrum peak shifts, especially in the positive spectra in our study, are mainly because of variance in the position of particle–laser interaction, which cannot be corrected with the existing AeroMegt software or the LAAPTOF instrument (Ramisetty et al., 2017). Details can be found in "Procedure 1" in the Supplement. Spectra presented in this paper were typically normalized to the sum of ion signal before further aggregation.

For ambient data analysis, we used two different classification methods. The first one is fuzzy c-means clustering algorithm embedded in the Igor LAAPTOF data analysis software, commonly used to do classification based on the similarities of the individual spectra. The number of the classes is chosen manually; afterwards the particle spectra with a minimum distance between their data vectors and a cluster centre are grouped into a specific class (Hinz et al., 1999; Reitz et al., 2016). Since each spectrum can belong to multiple classes (Reitz et al., 2016), the resulting fraction/percentage for each class represents the information about the degree of

similarity between aerosol particles in one particular class, not a number percentage. The second method developed in this study is based on the correlation between each ambient spectrum and our reference spectra. The resulting Pearson's correlation coefficient (r) is used as the criterion to group particles into different types (here we use "types" instead of "classes" in order to differentiate these two classification methods). When r is higher than a threshold value of 0.6, the ambient spectrum is considered to have high correlation with the corresponding reference spectrum. For simplification we chose 10 positive and 7 negative reference spectra. For example, we only use German soil dust as the reference for arable soil dust, rather than using four arable soil dust samples from different places. More details about the procedure for this method as well as the corresponding equations and uncertainties estimation can be found in "Procedure 2" in the Supplement.

In addition, particle size (d_{va}) was recorded for individual particles. The corresponding size distribution can be plotted as d_{va} histogram, a Gaussian fit of which yields number mean d_{va} values and the standard deviation (width).

3 Results and discussion

3.1 LAAPTOF performance

3.1.1 Hit rate, scattering efficiency, and overall detection efficiency for standard samples

HR, SE, and ODE for spherical PSL particles as a function of electrical mobility equivalent diameter d_m are plotted in Fig. 2. It should be noted that the LAAPTOF detection behaviour may vary depending on the alignment of the ADL and the optical components (especially the detection laser diodes), which is difficult to reproduce. We therefore show results for PSL particles based on two repeated experiments after three alignments each and thus a total of six experiments for each data point. The uncertainty intervals in Fig. 2 are the difference between the maximum/minimum and the average values obtained from these six experiments. As shown in panel a of Fig. 2, for particle diameters from 200 to 400 nm, HR_{PSL} exhibits an increase from 69 to 94 %, decreases to 83 % for 700 nm particles, and then becomes stable at ~ 85 % for particles with diameters up to 2 μm. The average HR_{PSL} ($\overline{HR_{PSL}}$) is ~ 84 %. SE_{PSL} and ODE_{PSL} show an M-like shape with two peaks, at 500 nm (SE_{PSL} 3.0 %, ODE_{PSL} 2.7 %) and at 1000 nm (SE_{PSL} 4.8 %, ODE_{PSL} 4.2 %) (see panels b and c of Fig. 2). We attribute this behaviour to a combined effect of the spherical shape of PSL particles and the optical system of this instrument, e.g. Mie resonances related to particle size and laser wavelength (see Sect. 3.1.2 for details). As shown in panel c of Fig. 2, values and trends of ODE_{PSL} in the size range of 300–800 nm of our instrument are similar to those reported by Gemayel et al. (2016) and

Marsden et al. (2016) for their LAAPTOF instruments. A recent LAAPTOF study by Zawadowicz et al. (2017) shows comparable results for PSL particles with $d_p \leq 500$ nm and an M-like shape of ODE in the size range of 200–2000 nm (after instrument modification).

We also measured mass spectra of non-spherical NH_4NO_3 ($\chi = 0.8$; Williams et al., 2013) and NaCl particles (cubic, $\chi = 1.06$ to 1.17; Zelenyuk et al., 2006a). Similar to PSL particles, NH_4NO_3 and NaCl particles show relatively high and stable HR with average values of 80 and 66 % (see panel d in Fig. 2); thus SE and ODE have a similar trend. No M-like shape of ODE as a function of particle size is observed due to the different light scattering properties of the non-spherical salt particles (Bohren and Huffman, 2007; see panels e and f in Fig. 2). Comparable results were shown for $(NH_4)_2SO_4$ particles ($\chi = 1.03$ to 1.07; Zelenyuk et al., 2006a) by Zawadowicz et al. (2017). As shown in Fig. 2e–f, SE and ODE decrease with increasing shape factor for salt particles of the same size. We will discuss this in more detail in the following section.

3.1.2 Factors influencing overall detection efficiency

There are various factors that can influence the ODE of LAAPTOF. One of these is particle size. For particles with diameters below 200 nm, the scattered light becomes too weak to be detected due to the strong dependence of the scattering intensity on particle size (Bohren and Huffman, 2007). For particles with diameters larger than 2 μm, focusing by the ADL is much less efficient, resulting in a higher divergence of the particle beam (Schreiner et al., 1999). This lowers the probability of larger particles being detected by the detection/scattering laser and/or being hit by the ionization laser. In addition, light scattering of spherical particles like PSL changes from Rayleigh to Mie to geometric scattering as the size parameter $\alpha = \pi d_p/\lambda$ increases from $\ll 1$ to ~ 1 to $\gg 1$ (Seinfeld and Pandis, 2006). The scattering efficiencies of PSL particles, based on Mie calculation at the particle sizes and detection laser wavelength relevant to our LAAPTOF measurement, validate the M-like shape of SE_{PSL} (refer to Fig. S1 in the Supplement). As long as the particle diameter (d_p) is smaller than the wavelength of the detection laser light, here 405 nm, the scattered-radiation intensity (proportional to d_p^6) will rapidly decrease with decreasing particle sizes, resulting in low ODE. ODE is e.g. 0.01 % for 200 nm PSL particles. For non-spherical particles like salts, their SE and ODE are also size dependent (panel f in Fig. 2), due to size-dependent light scattering ability and particle beam divergence. However, in the size range of 300 to 1000 nm studied here, they do not exhibit Mie resonance and thus do not show an M-like shape in their scattering efficiency.

Optical properties of the particles have a strong impact on how light is scattered and absorbed, and thus it should be noted that the optical properties influence not only scattering efficiency but also absorption and ionization efficiency (or hit
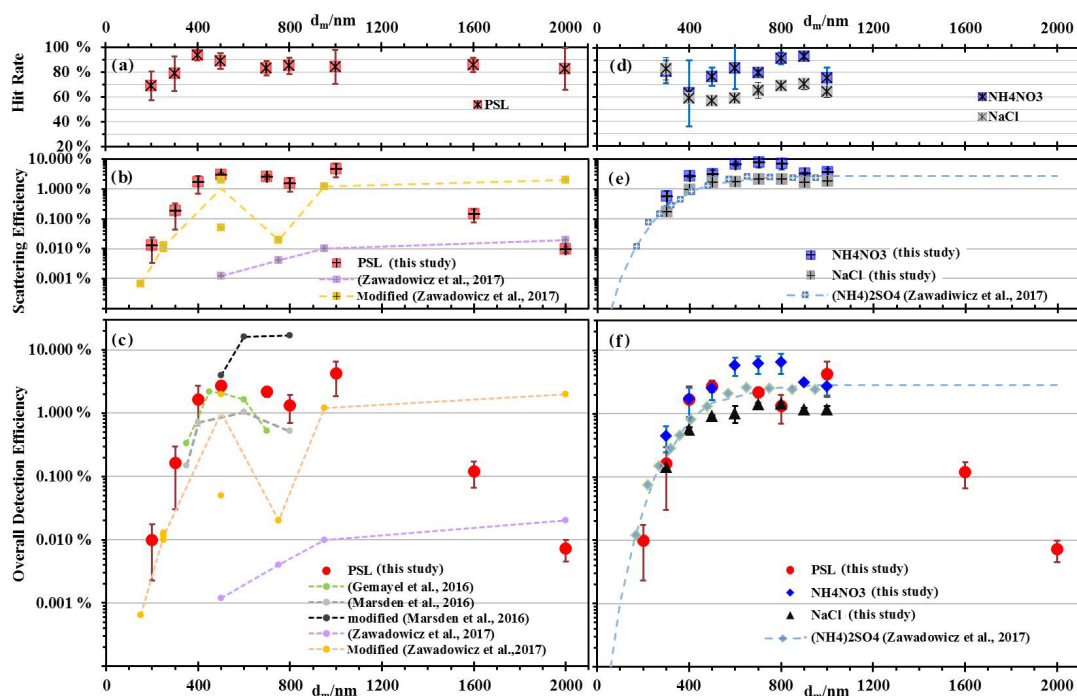
Figure 2. Hit rate (HR, **a** and **d**), scattering efficiency (SE, **b** and **e**), and overall detection efficiency (ODE, **c** and **f**) for PSL, ammonium nitrate (NH_4NO_3), and sodium chloride (NaCl) salt particles as a function of mobility diameter, d_m. Aerosol particles in this study were generated from a nebulizer and size-selected by DMA. In (**b**) and (**e**), OCEs for PSL and ammonium sulfate (($NH_4)_2SO_4$) at the detection beam from the study by Zawadowlcz et al. (2017), corresponding to the SE defined in this study, are plotted for comparison. In (**c**) and (**f**), ODE for PSL and salt particles from other studies (Gemayel et al., 2016; Marsden et al., 2016; Zawadowicz et al., 2017) are plotted for comparison. In this figure, dashed lines are used only to guide the eyes.

rate). As shown in Fig. 2f, ODE for NH_4NO_3 is higher than that for NaCl at any size we studied. This is mainly caused by differences in their optical properties of scattering. Fresh soot particles scatter only little light due to their black colour and the small size (typically ~ 20 nm) of the primary particles forming their agglomerates, and are thus hardly detected by the detection laser. However they are good light absorbers and thus relatively easy to ablate and ionize. The reference spectra of pure NH_4NO_3 and $(NH_4)_2SO_4$ particles showed intensive prominent peaks for pure NH_4NO_3 particles (refer to Fig. 3a) but only one weak peak of m/z 30 NO^+ for pure $(NH_4)_2SO_4$ particles. This indicates that NH_4NO_3 is a better absorber than $(NH_4)_2SO_4$ and thus easier to ablate and ionize. For homogeneous mixtures of these two ammonium salts, the sulfate species are ablated and ionized much more easily (refer to Sect. 3.2.2), due to increased UV light absorption by the nitrate component. Some small organic compounds with weak absorption properties are hard to ablate and ionize, e.g. oxalic acid ($C_2H_2O_4$), pinic acid, and cis-pinonic acid. They exhibited much weaker signals ($\sim 80\%$ lower) than macromolecular organic compounds in PSL or humic acid particles.

Particle morphology is another important factor. The scattering efficiency for non-spherical NH_4NO_3 is higher than for spherical PSL particles in the size range of 300–800 nm (Fig. 2b–e) (Ackerman et al., 2015). For larger particle sizes ($d_m > 800$ nm), beam divergence offsets the shape effect (Murphy, 2007). Apart from that, the increase of surface roughness and inhomogeneity can promote the scattering capability of particles (Ackerman et al., 2015).

The incident intensity of radiation, which is another parameter that influences the light scattered by particles (as well as background signal caused by stray light), is related to power and beam dimensions of the detection laser. Corresponding instrument modifications were done by Marsden et al. (2016) and Zawadowicz et al. (2017) (refer to Sect. 1). In addition, alignment of the excimer laser focus in the x, y, and z position influences optimum hit rates (Ramisetty et al., 2017).

There are further instrumental aspects that affect the detection efficiency. High number concentrations of the incoming particles influence the ODE, since there can be more than one particle present between the two detection lasers. The transmission efficiency of the ADL is included in the scattering efficiency and thus directly influences it. The size
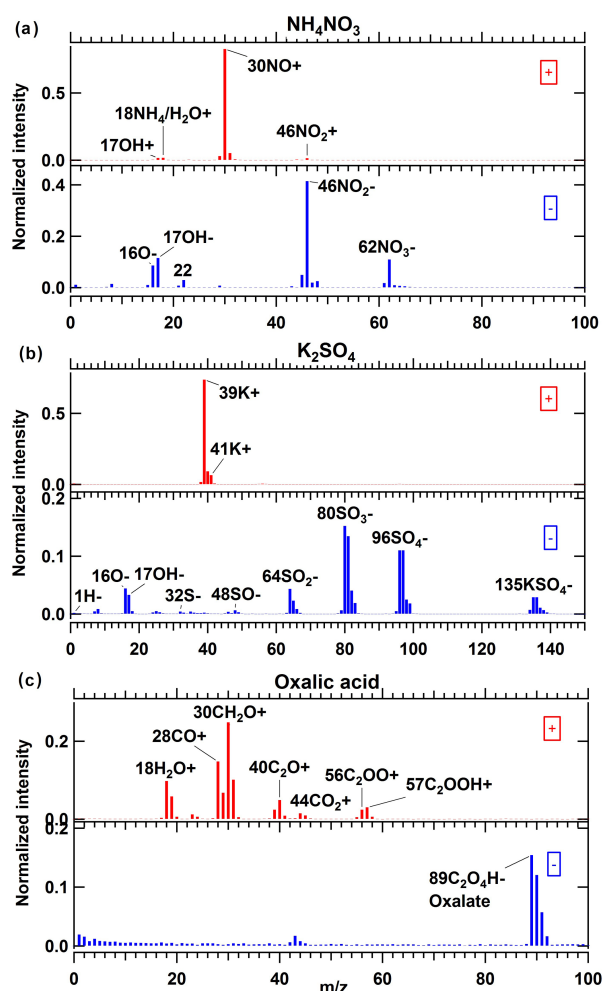
Figure 3. Average mass spectra for pure compound aerosol particles: **(a)** NH_4NO_3 ($d_{va} = 1160$ nm), 497 single spectra averaged; **(b)** K_2SO_4 ($d_{va} = 1465$ nm), 300 single spectra averaged; and **(c)** oxalic acid particles ($d_{va} = 1081$ nm), 736 single spectra averaged.

range of particles focused by the lens and the particle beam width strongly depend on the configuration of the ADL (Canagaratna et al., 2007; Johnston, 2000). Liu lenses and Schreiner lenses can focus the particles in the size range of 80–800 and 300–3000 nm, respectively (Kamphus et al., 2008; Liu et al., 1995; Schreiner et al., 1999). The ADL transmission efficiency of our instrument, as determined by the manufacturer (AeroMegt GmbH), is close to 100 % for particles with d_{va} 100–2000 nm.

3.2 LAAPTOF reference spectra of laboratory-generated particle types

Particles for which reference spectra are presented here are listed in Table 1. For each type of these aerosol particles, we present averaged spectra for typically 300 to 500 single particles. The relative standard deviations (RSDs, SD normalized to signal) for the characteristic peaks are in the range of 15–186 %, with a median value of 77 %.

Despite the lack of full quantitativeness of the LAAPTOF, mass spectral signal amplitudes show an increase with particle size (refer to Fig. S2). However, no systematic changes in the mass spectral signatures were observed for different particle sizes. Therefore, for the samples passing through the DMA, particles in the optimum size range of the LAAPTOF ($d_m = 800$ nm) and with good signal-to-noise ratio were chosen to generate reference spectra. For polydisperse particles generated in the AIDA chamber, the corresponding average spectra include particles of broader size distributions than those preselected by the DMA. Information on particle generation or source as well as the sizes is listed in Table 1.

A qualitative comparison between the relative peak intensity ratios within a single-particle spectrum and those in another spectrum can yield relative quantitation information, as suggested by Gross et al. (2000). We add information on typical peak ratios to some of our reference spectra to help identify specific species.

3.2.1 Pure compound particles

Although particles consisting of one single species only are rarely sampled in the atmosphere, interpretation of mass spectra of ambient samples is supported by the knowledge about the mass spectra of pure compounds. In the following, mass spectra for a few typical ambient aerosol constituents are discussed.

Figure 3 shows average spectra for pure compound aerosol particles. For NH_4NO_3 particles (panel a), we observed the positive ions m/z 18 NH_4^+ and m/z 30 NO^+, and the negative ions m/z 46 NO_2^- and m/z 62 NO_3^-, similar to Reitz et al. (2016). The LAAPTOF is much less sensitive to ammonium than nitrate fragments, leading to a weak NH_4^+ signal and prominent NO^+, NO_2^- and NO_3^- peaks. The ratio of NO^+ to NH_4^+ is ~ 48, and the ratio of NO_2^- to NO_3^- is ~ 4. The prominent peak of NO^+ arises not only from nitrate (majority), but also from ammonium (Murphy et al., 2006). In our ammonium nitrate spectra, there are weaker signatures of m/z 46 NO_2^+ and m/z 125 $HNO_3 \cdot NO_3^-$ (not shown here, but visible and reproducible), which were also observed in PALMS mass spectra (Zawadowicz et al., 2015). For K_2SO_4 particles, we observed the potassium signals at m/z 39 K^+ and m/z 41 K^+, and a sulfate signature with ion clusters grouped around m/z 32 S^-, m/z 64 SO_2^-, m/z 80 SO_3^-, and m/z 96 SO_4^-. Note that the extra peak at m/z 40$^+$ besides m/z 39 K^+ in Fig. 3b is likely due to the incorrect mass as-

Atmos. Meas. Tech., 11, 2325–2343, 2018   www.atmos-meas-tech.net/11/2325/2018/

76

signments as a result of peak shifts (refer to Sect. 2.5 and "Procedure 1" in the Supplement). For high-intensity peaks such as sodium chloride NaCl, extra peaks next to the main peak (Fig. S3) may have an additional cause: "ringing" due to partial saturation of the data acquisition system or signal reflections within the data acquisition circuitry (Gross et al., 2000). The real intensities of m/z 35 Cl^- should include its corresponding side ringing peak. The ratio of m/z 39 K^+ to m/z 41 K^+ is ~ 13.2, close to the natural isotopic ratio of ~ 13.9 for $^{39}K / ^{41}K$. For pure NaCl particles, the ratio of m/z 35 Cl^- to m/z 37 Cl^- is ~ 3.2, similar to the natural isotopic ratio of ~ 3.1 for $^{35}Cl / ^{37}Cl$. Therefore, these two isotopic ratios can be used as markers to identify K and Cl measured by LAAPTOF. Another inorganic compound measured here is silica (Fig. S4), and its typical peak ratio of (m/z 76 $SiO_3^- + m/z$ 77 $HSiO_3^-$) to m/z 60 SiO_2^- is ~ 1.0. The corresponding histograms of such ratios for different particle samples can be found in Fig. S5.

High signal intensities in oxalic acid spectra are observed at m/z 18 H_2O^+, 28 CO^+, and 30 CH_2O^+, as well as some weaker peaks at m/z 40^+, 44^+, 56^+, and 57^+. M/z 89 $C_2O_4H^-$ is used as a signature ion for oxalic acid in other SPMS studies (Roth et al., 2016). In our study, a distinct signal at around m/z 89^- is observed as well, indicating oxalate fragment formation after laser ablation.

In order to identify humic-like substances in the ambient particles, we measured humic acid particles (Fig. S6) and found hydrocarbon and elemental carbon fragments, with very prominent peaks at m/z 24^-, 25^-, and 26^- suggested to be organic ions (Silva et al., 2000), as well as peaks at m/z 25^-, 26^-, 49^-, and 73^- for unsaturated organic compounds.

3.2.2 Particles consisting of well-defined internal mixtures

Figure 4 shows average spectra from homogeneously internally mixed particles. The spectrum from the mixture of NH_4NO_3 and $(NH_4)_2SO_4$ (panel a) contains the signature from pure NH_4NO_3 particles, but with lower relative intensities (each peak intensity is normalized to the sum of ion signal) for NO_2^- and NO_3^-, due to the formation of anion clusters at $\sim m/z = 80$ SO_3^- and 97 HSO_4^-. Compared to the pure NH_4NO_3 particles, the ratio of NO^+ to NH_4^+ (~ 34) is $\sim 30\%$ lower in the spectrum for the mixture, due to its lower molar ratio of nitrate to ammonium, whereas the ratio of NO_2^- to NO_3^- (~ 7) is 80 % higher. In addition, as already discussed in Sect. 3.1.2, the better UV light absorber NH_4NO_3 assists in light absorbing for mixed particles, resulting in a sulfate signature that could not be observed for pure $(NH_4)_2SO_4$. This exemplifies potential effects of individual particle chemical composition on mass spectral performance of the LAAPTOF. For the mixture of K_2SO_4 and NaCl (panel b), similar signatures to those of the pure particles were observed. Compared to the pure NaCl particle

spectra, the signal intensity of Na^+ is decreased. This can be explained by more cations formed from the mixed particles, including from potassium, which has a higher ionization potential and lower lattice energy than NaCl. For the mixed particles, expected clusters such as 113/115 K_2Cl^+, 109 KCl_2^-, and 119 $NaSO_4^-$ and a minor fragment 97 $KNaCl^+$ were observed, but not 81/83 Na_2Cl^+ as found in pure NaCl particles. These results show that, compared to pure compounds, mass spectra from aerosol particles consisting of mixtures can feature new ions, while some marker ions for the pure compounds may disappear. These spectra are thus not simply a combination of the spectra from single-component particles. Another example of an inorganic mixture of NH_4NO_3 and K_2SO_4 is provided in Fig. S7. The α-pinene SOA spectrum is shown in panel c of Fig. 4. Ablation of α-pinene SOA particles forms different types of organic fragments: (1) hydrocarbon and oxygenated organic fragments $C_xH_yO_z$ ($x = 1$–6, $y = 0$–9, $z = 0$–3; details about the peak assignments can be found in Table S1) – except for m/z 59^+, 83^+, 85^+, and 95^+ – are comparable to the combination mass spectral patterns for cis-pinonic and pinic acids (refer to Fig. S8), which are oxidation products from α-pinene ozonolysis (Saathoff et al., 2009; Yu et al., 1999); (2) carbon clusters 12 C^+, 24 C_2^+, 36 C_3^+, and 60 C_5^+, with the most prominent peak in 12 C^+, assigned to both soot and organic matter fragments in another LAAPTOF study (Ahern et al., 2016); and (3) carboxylic acid groups in the negative spectra, e.g. 45 $COOH^-$, 59 CH_2COOH^-, 73 $C_2H_4COOH^-$, 85 $C_3H_4COOH^-$, and 99 $C_4H_6COOH^-$.

Figure 5a shows the spectrum for heterogeneously internally mixed K_2SO_4 and PSL particles (PSL core, K_2SO_4 shell). All signatures for PSL particles – i.e. hydrocarbon fragments in positive spectra; intensive organic signature m/z 24^-, 25^-, and 26^-; carbon clusters $C_n^{+/-}$; and m/z 49^- and 73^- fragments arising from unsaturated structures such as aromatic structures – are retained in this spectra (grey labels), and the corresponding peak intensities are similar to the pure PSL particles (Fig. S9). However, the intensities of most of the K_2SO_4 fragments are weaker than pure K_2SO_4 particles, likely due to the quite thin or only partial coating layer of K_2SO_4 on the PSL core (the nominal geometric size of the PSL particles mixed with the aqueous solution of K_2SO_4 was 800 nm, which is the same size that was selected by the DMA prior to sampling by the mass spectrometer.). The most prominent peak at m/z 39^+ with a normalized intensity of ~ 0.46, containing both K^+ and $C_3H_3^+$ fragments, is mainly attributed to K^+ (intensity ~ 0.73 for pure K_2SO_4), since the intensity of $C_3H_3^+$ (~ 0.06) for pure PSL is much lower (refer to Fig. S9). The still intensive signal from 39 K^+, despite the weaker sulfate peaks, corresponds to the high sensitivity of the instrument to potassium. Figure 5b shows the average spectrum for poly(allylamine hydrochloride)-coated gold particles. Prominent signatures of nitrogen-containing compounds (NOCs) are observed at m/z 58 C_2H_5–NH–CH_2^+, 15 NH^+, 26 CN^-, and 42 CNO^-,

www.atmos-meas-net/11/2325/2018/   Atmos. Meas. Tech., 11, 2325–2343, 2018

77
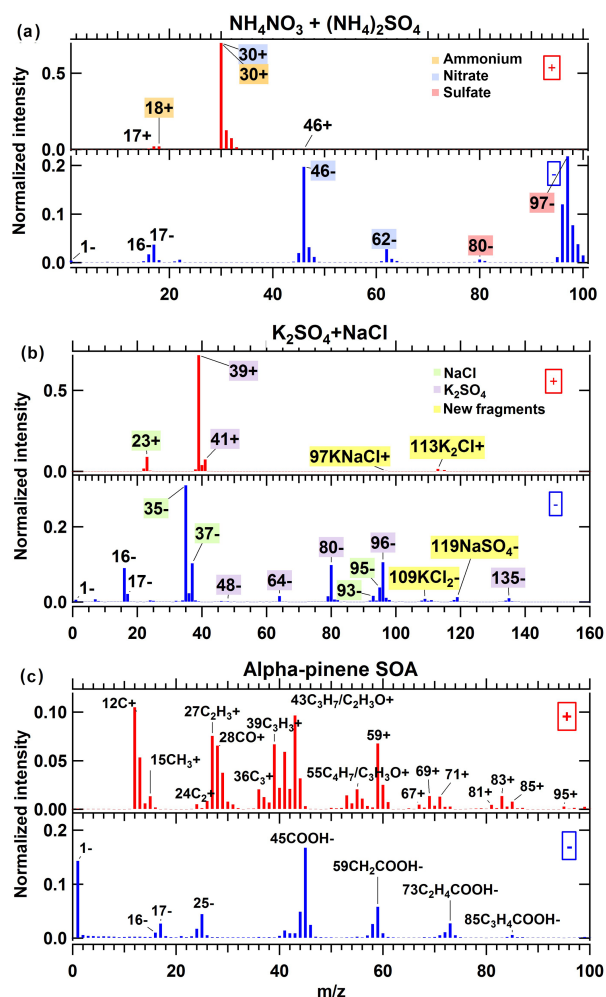
Figure 4. Average mass spectra for particles of internal mixtures of **(a)** NH_4NO_3 and $(NH_4)_2SO_4$ ($d_{va} = 1102$ nm), 454 single spectra averaged, and **(b)** NaCl and K_2SO_4 ($d_{va} = 1375$ nm), 259 single spectra averaged, as well as **(c)** secondary organic aerosol (SOA) particles from α-pinene ozonolysis, which was performed in the APC chamber, and then the resulting particles were transferred into the AIDA chamber at 263 K and 95 % RH, $d_{va} = 505$ nm, 1938 single spectra averaged. In **(a)**, red, blue, and orange label shadings represent fragments of sulfate, nitrate, and ammonium, respectively. In **(b)**, green and purple label shadings represent fragments from NaCl and K_2SO_4 components (see Sect. 3.2.1) in the mixed particles, respectively; yellow label shadings represent the fragments only in the internal mixture of NaCl and K_2SO_4.

Figure 5. Average mass spectra for core–shell particles of **(a)** PSL coated with K_2SO_4, $d_{va} = 805$ nm, 609 single spectra averaged, and **(b)** poly(allylamine hydrochloride)-coated gold (Au) particles with geometric 300 nm gold core and 50 nm thick organic shell, 417 single spectra averaged. In **(a)**, grey and purple label shadings represent the fragments arising from pure PSL and pure K_2SO_4 components, respectively; box labels represent the fragments with contributions from core and shell compounds. In **(b)** orange and blue label shadings represent the fragments arising from nitrogen-containing and unsaturated organic compounds, respectively, and yellow label shadings represent gold.

Mass spectra for other well-defined compounds, i.e. synthetic hematite and pure sea salt particles, are also provided in the Supplement (Figs. S10 and S11).

3.2.3 Particles consisting of complex mixtures

Figure 6 shows the average spectra for different types of soot particles. All of them show characteristic patterns for elemental carbon (EC) $Cn^{+/-}$. For soot 1 with high organic carbon (OC) content from propane combustion in the laboratory (panel b), prominent peaks were observed at m/z 28 CO^+ and 27 $C_2H_3^+$, as well as some other organic carbon signatures at m/z 39^+, 40^+, 44^+, and 56^+. All the organic signatures in soot 1 with high OC were also observed for soot 3, lignocellulosic char from chestnut wood (panel d), indicating that biomass burning soot contains a significant fraction of OC. It should be noted that biomass burning will also form potassium; thus m/z 39^+ contains both K^+ and $C_3H_3^+$ frag-

as well as the signatures for unsaturated organic compounds at m/z 25^-, 26^-, 49^-, and 73^-. Strong intensities for m/z (35^- plus 36^-) and 37^- with a ratio of ~ 3.1 can be assigned to Cl isotopes derived from the hydrochloride. We also observed small gold peaks at m/z $197^{+/-}$ both in positive and negative spectra.

Atmos. Meas. Tech., 11, 2325–2343, 2018   www.atmos-meas-tech.net/11/2325/2018/

78
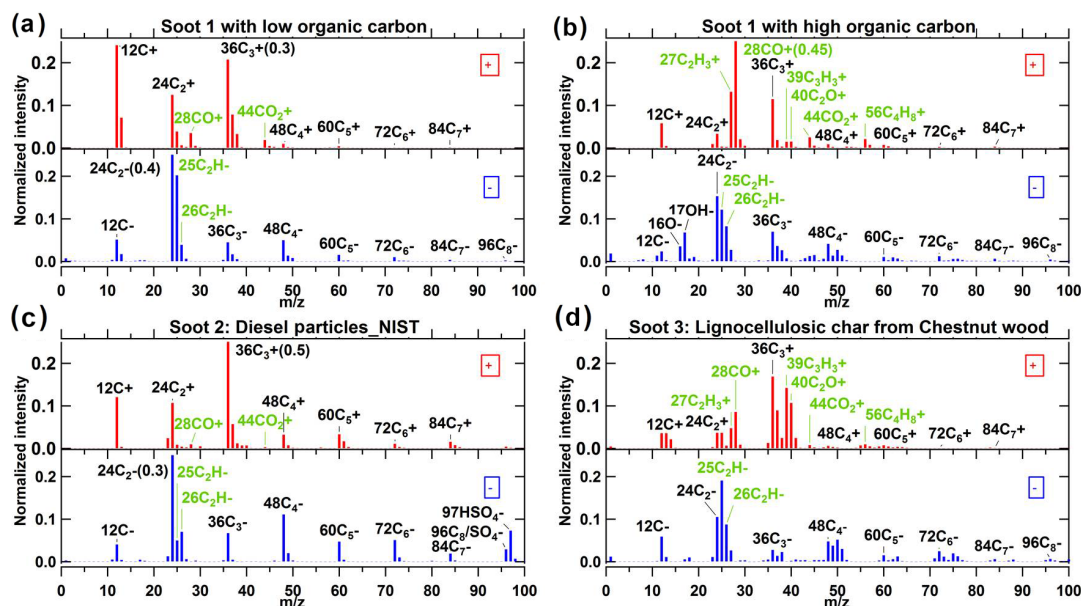
Figure 6. Average mass spectra for soot particles with **(a)** high elemental carbon (EC) and low organic carbon (OC) content, and **(b)** low EC and high OC from combustion of propane in a soot generator and transferred to a stainless-steel cylinder of $\sim 0.2\,\text{m}^3$ volume, as well as soot particles of **(c)** diesel particles (NIST) and **(d)** lignocellulosic char from chestnut wood. In **(a)** and **(c)**, the numbers in brackets beside peak 36^+ and 24^- are the exact intensity values for them. The OC signatures are labelled in green. The numbers of spectra averaged for each spectrum are 617 **(a)**, 347 **(b)**, 533 **(c)** and 390 **(d)**.

ments. $M/z\ 24^-$, 25^-, and 26^- can be observed in all the soot types, but with slightly different patterns: (1) soot with high EC content shows very high $m/z\ 24^-$ (~ 2 to 3 times that of $m/z\ 25^-$), while (2) soot with high OC shows comparable or even higher $m/z\ 25^-$ to/than $m/z\ 24^-$. These patterns might help to distinguish EC and OC contributions in the spectra from ambient particles.

Figure 7 shows spectra for Arizona test dust (milled desert dust) (panel a), arable soil SDGe01 sampled from Gottesgabe in Germany (panel b), and agricultural soil dust collected from harvesting machines after rye and wheat harvest (panel c). For Arizona test dust, we observed high mineral signatures of aluminium- and silicon-containing clusters, namely $27\ \text{Al}^+$, $28\ \text{Si}^+$, $44\ \text{SiO}^+$, $43\ \text{AlO}^-$, $59\ \text{AlO}_2^-$, $60\ \text{SiO}_2^-$, $76\ \text{SiO}_3^-$, $119\ \text{AlSiO}_4^-$, $179\ \text{AlSiO}_4.\text{SiO}_2^-$, and $136\ (\text{SiO}_2)_2\text{O}^-$. It should be noted that high $16\ \text{O}^-$ and $17\ \text{OH}^-$ accompany the intensive mineral signatures, attributed to the adsorbed water on the active surface of mineral particles. In panel a, we also observed the following peaks: other mineral related metal clusters (e.g. $7\ \text{Li}^+$, $23\ \text{Na}^+$, $24\ \text{Mg}^+$, $40\ \text{Ca}^+$, $39/41\ \text{K}^+$, $55\ \text{Mn}^+$, $56\ \text{Fe}^+$, $58\ \text{Ni}^+$, and $64\ \text{Zn}^+$); metal oxides and hydroxides (e.g. $56\ \text{CaO}^+$, $57\ \text{CaOH}^+$, $96\ \text{Ca}_2\text{O}^+$, and $112\ (\text{CaO})_2^+$, and $88\ \text{FeO}_2^-$); and weak anion clusters of organic signature ($m/z\ 24\ \text{C}_2^-$, $25\ \text{C}_2\text{H}^-$, $26\ \text{C}_2\text{H}_2^-$, and $42\ \text{C}_2\text{H}_2\text{O}^-$), NOCs ($m/z\ 26\ \text{CN}^-$ and $42\ \text{CNO}^-$), chloride ($m/z\ 35^-$ and 37^-), sulfate ($m/z\ 32^-$, 48^-, 64^-, 80^-, and 97^-), phosphate ($63\ \text{PO}_2^-$ and $79\ \text{PO}_3^-$), diacids (oxalate 89

$(\text{CO})_2\text{OOH}^-$ and $117(\text{CO})_3\text{OOH}^-$), and an unknown fragment $m/z\ 148^-$. $M/z\ 26^+$ in panels b and c is much higher than $m/z\ 24^-$ and 25^-, due to the contribution of CN fragments from NOCs. Similar signatures can also be observed in the spectra for Saharan dust (Fig. S12).

Most of the mineral and organic fragments of soil dust are similar to those of desert dust; however with different intensities – e.g. $m/z\ 24^-$, 25^-, 26^-, and 42^- (labelled in green) – they are more intensive than those in desert dust, indicating higher organic compound content. Some peak ratios of fragments are similar across the different dust types; e.g. $40\ \text{Ca}^+$ to $56\ \text{CaO}^+$ is 2.2, 1.1, and 2 for desert dust, arable soil dust and agricultural soil dust, respectively. Compared with desert dust, there are different fragments from soil dust particles, e.g. EC patterns (labelled in grey), organic acids signatures (blue), ammonium signatures (orange), unsaturated organic fragments ($m/z\ 49^-$ and 73^-), and some other unknown fragments (red). For arable soil dust particles, we also measured samples from Paulinenaue in Germany (SDPA01), Argentina (SDAr08), and Wyoming in the USA (SDWY01) (refer to Fig. S13). Dominant mass spectral peak patterns are similar across all soil dust samples. They are located at around $m/z\ 27^+$, 39^+, and 56^+ in the positive spectra, and 26^-, 42^-, 60^-, and 76^- in negative spectra. Less prominent but reproducibly detected are carboxylic acid groups (e.g. COOH^-) and EC patterns. The German soil dust, however, contains more organic species than soil dust

www.atmos-meas-tech.net/11/2325/2018/   Atmos. Meas. Tech., 11, 2325–2343, 2018

79

Table 2. Summary of mass spectral patterns.

Species	Signature peaks in positive spectra	Signature peaks in negative spectra	Typical peak ratios histogram x_0 (width)*
potassium	$39\ K^+$, $41\ K^+$		$I39 : I41 = \sim 13.5\ (0.9)$
calcium	$40\ Ca^+$, $56\ CaO^+$		
aluminium	$27\ Al^+$	$43\ AlO^-$, $59\ AlO_2^-$	
silicon	$28\ Si^+$, $44\ SiO^+$	$60\ SiO_2^-$, $76\ SiO_3^-$, $77\ HSiO_3^-$	$(I76 + I77) : I60 = \sim 1.0\ (0.33)$
silicon & aluminium	$27\ Al^+$, $28\ Si^+$, $44\ SiO^+$	$43\ AlO^-$, $59\ AlO_2^-$, $60\ SiO_2^-$, $76\ SiO_3^-$,	
	$77\ HSiO_3^-$, $119\ AlSiO_4^-$, $179\ AlSiO_4.SiO_2^-$		
ammonium	$18\ NH_4^+ / H_2O^+$, $30\ NO^+$		
nitrate	$30\ NO^+$	$46\ NO_2^-$, $62\ NO_3^-$	
sulfate		$32\ S^-$, $48\ SO^-$, $64\ SO_2^-$, $80\ SO_3^-$, $81HSO_3^-$, $96\ SO_4^-$, $97\ HSO_4^-$,	
chloride		$35\ Cl^-$, $37\ Cl^-$	$(I35 + I36) : I37 = \sim 3.1\ (0.5)$
elemental carbon	$12_n\ C_n^+$	$12_n C_n^-$	
organics		$24\ C_2^-$, $25\ C_2H^-$, $26\ C_2H_2 / CN^-$ $26\ C_2H_2 / CN^-$	
organic acids		$45\ COOH^-$, $59\ CH_2COOH^-$, $71\ CCH_2COOH^-$, $73\ C_2H_4COOH^-$, $85\ C_3H_4COOH^-$, $99\ C_4H_6COOH^-$, $117\ (CO)_3OOH^-$	
nitrogen-containing organics		$26\ CN^-$, $42\ CNO^-$	
unsaturated organics		$25\ C_2H^-$, $26\ C_2H_2^-$, unknown fragments 49- and 73-	
aromatic compounds	$77\ C_6H_5^+$, $91C_7H_7^+$, $103\ C_8H_7^+ /$ $105\ C_8H_9^+$, $115\ C_9H_7^+$	$25\ C_2H^-$, $26\ C_2H_2^-$, unknown fragments 49- and 73-	

* We have made histograms for each of the three typical peak ratios (ref. Fig. S5). Histogram x_0 is the expected value that indicates the position of the peak resulting from Gaussian fit, and the width is the corresponding standard deviation. I is short for the intensity of the corresponding peak in LAAPTOF spectra; typical peak ratios for potassium and chloride are based on pure and mixed salt containing K and Cl; typical peak ratios for silicon are based on pure SiO_2.

from Argentina and the USA, reflected in higher intensities at $m/z\ 24^-$, 25^-, and 26^-. Argentinian soil dust contains far fewer mineral species, expressed in much lower intensities of mineral signatures, e.g. $m/z\ 27^+$, 28^+, 40^+, 44^+, and 56^+. The ratios of $m/z\ 39\ K^+$ and $41\ K^+$ (3.6, 3.8, 3.5, and 5.3 for SDGe01, SDPA01, SDAr08, and SDWY01, respectively) are much lower than the typical peak ratio (~ 13.5) for potassium (Table 2), indicating that they are likely contributed to by both potassium isotopes and hydrocarbon fragments.

For agricultural soil dust particles, obviously ammonium ($m/z\ 18\ NH_4^+$ and $30\ NO^+$), phosphate ($m/z\ 63\ PO_2^-$, $79\ PO_3^-$, and $95\ PO_5^-$), and potassium signatures ($m/z\ 39\ K^+$ and $41\ K^+$) can be found in the spectra, attributed to fertilization. Apart from that, typical biological signatures were observed: (1) the strong $m/z\ 26^-$, 42^-, and 39^+ pattern is similar to the potassium organo-nitrogen particle type observed by an ATOFMS at an urban site in Barcelona (Dall'Osto et al., 2016), which was assigned to carbohydrates arising from

biogenic species (Schmidt et al., 2017; Silva et al., 2000). (2) 26^- and 42^- could also be contributed by CN^- and CNO^- derived from NOCs, i.e. amines, as well as $m/z\ 30$ CH_3NH^+, $58\ C_2H_5NHCH_2^+$, and $59\ (CH_3)_3N^+$. These biological signatures have also been observed by ALABAMA in the field (Schmidt et al., 2017). (3) Some weak but reproducibly detected fragment pattern at around $m/z\ 77\ C_6H_5^+$, $91\ C_7H_7^+$, $103\ C_8H_7^+$, $105\ C_8H_9^+$, and $115\ C_9H_7^+$ might originate from aromatic compounds. Similar patterns can also be found for PSL particles.

Other examples for complex mixtures, i.e. illite and sea salt particles with biological components, are provided in the Supplement (Figs. S14 and S11).

All the peak assignments and mass spectral patterns, like signature peaks, as well as some stable peak ratios mentioned above have been summarized in Table S1 in the Supplement and Table 2, respectively. We consider these laboratory-based reference spectra as useful for the analysis of data obtained
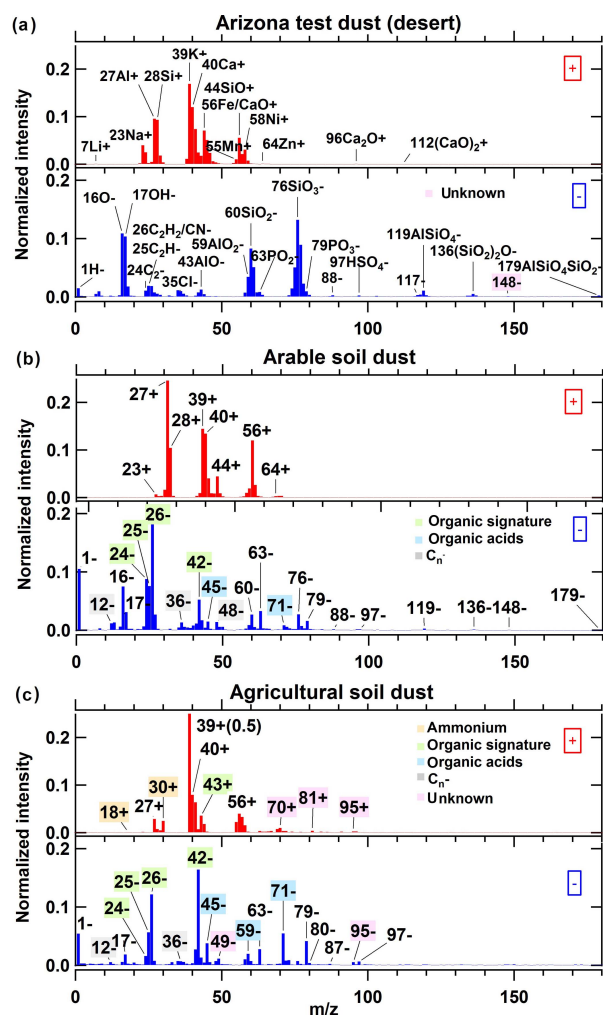
Figure 7. Average mass spectra for particles of complex mixtures: **(a)** Arizona test dust (desert dust), directly sampled into the LAAPTOF from a shaked bottle **(b)** arable soil dust, collected from Gottesgabe in Germany, was dispersed by a rotating brush generator and injected via cyclones into the AIDA chamber at 256 K and 80 % RH, and **(c)** agricultural soil dust, collected from harvesting machines after rye and wheat harvest, were generated by using the same method as **(b)**. For **(b)** and **(c)**, fragments labelled in green represent more intensive organic signatures in soil dust particles; grey labels represent EC patterns; blue labels represent organic acids; orange labels represent ammonium salts; red labels represent unknown fragments. The numbers of spectra averaged for each spectrum are 261 **(a)**, 583 **(b)**, and 286 **(c)**.

also by other LAAPTOF versions and to some extent even for other single-particle mass spectrometers. Similar mass spectra are to be expected as long as they use similar ablation and ionization laser pulses (4 mJ, 193 nm), inlet regions for the mass spectrometer, and mass spectrometer types. In the near future, we plan to make these laboratory-based reference spectra publicly available via the EUROCHAMP-2020 database (www.eurochamp.org, last access: 16 April 2018).

3.3 Interpretation of field data

Figure 8 shows an example of bipolar mass spectra for six different particle classes measured in the field campaign at a rural site near Leopoldshafen in southwest Germany. On 29 July 2016 within 24 h, 7314 particles were detected and successfully ablated, and mass spectra were generated by LAAPTOF. The 7314 pairs of spectra were then clustered by the fuzzy c-means algorithm, resulting in six classes. The resulting number of classes with clearly different features depends on the experience of the operating scientist to identify them (please refer to the details of fuzzy clustering in Procedure 1 in the Supplement). The fuzzy results are compared with the laboratory-based reference spectra by calculating their correlation coefficients (Fig. 9). All classes exhibit a sulfate signature with m/z 97 HSO_4^- and m/z 80 SO_3^-; a nitrate signature with m/z 46 NO_2^- and 62 NO_3^-; an organic compound signature with m/z 24 C_2^-, 25 C_2H^-, and 26 C_2H_2/CN^-; and a NOC signature with m/z 26 CN^- and 42 CNO^- in the negative spectra. More characteristic signatures for each particle class can be observed in the positive spectra. All particles measured on this day show a 35 % similarity to class 5 with obvious signatures for potassium (K) and sulfate, with significant correlation with the reference particles containing potassium and sulfate (Fig. 9). Additionally, class 5 has a significant correlation with some other cations arising from ammonium, organic compounds, and dust. The ratio of m/z ($39^+ + 40^+$) to 41^+ is ~ 11, close to the value for pure K_2SO_4 particles (~ 13.5); thus we assigned them to K^+ rather than organic fragments. Further, there is a 15 % similarity to class 4 with prominent ammonium signatures at m/z 18 NH_4^+ and 30 NO^+, sulfate signatures, and a relatively weaker but reproducible nitrate signature. The corresponding spectrum is similar to the spectrum for the homogeneous mixtures of NH_4NO_3 and $(NH_4)_2SO_4$ (panel a in Fig. 4). This class also has strong correlation with both positive and negative reference spectra for the mixture of ammonium nitrate and ammonium sulfate particles. Ammonium, nitrate, and sulfate are the major secondary inorganic species in atmospheric aerosol particles (Seinfeld and Pandis, 2006); thus we name this class "secondary inorganic". It should be noted that this class has a significant correlation with ammonium and cations arising from oxalic acid; however class 4 has a weak correlation with the signature anion, i.e. m/z 89 $C_2O_4H^-$ (oxalate), of oxalic acid. Therefore, we can rule out a significant contribution of oxalic acid. There is also a 15 % similarity to class 2 (sodium rich), with a characteristic pattern of a strong signal at m/z 23 Na^+ accompanied by two weaker peaks at m/z 39 K^+ (with typical potassium peak ratio of ~ 12) and 63^+ (might contain both Cu^+ and $C_5H_3^+$ fragments). Class 2 has a significant correlation with the cations (i.e. Na and K) arising from sea salt
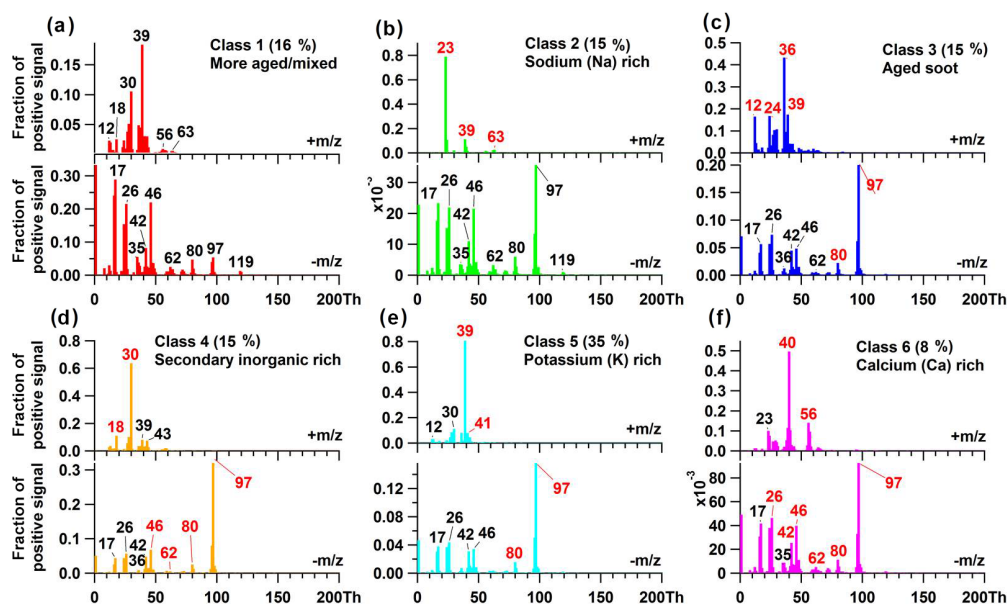
Figure 8. Mass spectra for six classes of particles measured on 29 July 2016 during the field campaign TRAM01, based on classification according to the fuzzy c-means algorithm. The percentage in each pair of spectra (**a** to **f**) gives us information about the similarity of the total aerosols to different classes. The red tags represent the signatures for each typical class, but there is no red tag in (**b**), since this class consists of more aged particles containing signatures for different classes. Mean particle size: d_{va} (676 ± 165) nm.

but a weak correlation with its anions, such as $m/z\,35^-$ and 37^- chloride isotopes. A sea salt contribution can thus be ruled out. Its negative spectrum significantly correlates with nitrate, sulfate, and dust particles. Besides sodium-rich dust, aged sea salt may be an appropriate classification. Class 3 is named "aged soot", since it has a significant correlation with soot particles, especially diesel soot, and a prominent sulfate signal. This class has an EC pattern with $m/z\,12n\,C_n^+$, similar to those in the reference spectra for soot particles (Fig. 6) as well as the reference spectra for PSL particles (Fig. S9). The patterns at $m/z\,27\,C_2H_3^+$ and 28 CO^+; $m/z\,36\,C_3^+$ and 39 $C_3H_3^+$; and the $m/z\,24^-$, 25^-, and 26^- with higher $m/z\,26^-$ indicate an OC contribution. This is supported by the correlations, especially with PSL particles, as well as several other organic compounds, suggesting that this class of particles contains organic species. Class 6 is dominated by calcium (Ca) and sulfate with characteristic calcium signature peaks at $m/z\,40\,Ca^+$ and 56 CaO^-, also found in the spectra for dust particles (Figs. 7, S12, and S13). $M/z\,40^+$ and 56^+ may also contain 40 C_2O^+ and 56 $Fe/C_4H_8^+$ fragments, respectively. Class 1 contains almost all fragments observed in other classes and is thus named "more aged/mixed particles". As shown in Fig. 9, class 6 is consequently correlated with almost all of the reference spectra (both positive and negative ones).

In order to further interpret the field data, we also classified the ambient mass spectra only based on correlation with 17 selected laboratory-based reference spectra (10 positive

+7 negative spectra) listed in Table S2. This approach resulted in 13 particle types, 7 more than were distinguished by fuzzy clustering. It should be mentioned that at the beginning we were able to identify all but the Ca-rich particle class resulting from fuzzy clustering, since initially we did not have a reference for this type. We therefore used class 6 as an additional reference spectrum for this type of particles, which is among one of the 13 types (here we use "types" instead of "classes" in order to differentiate these two classification methods). Their corresponding spectra are shown in Fig. 10. All the types above the dashed line (panels a to i) exhibit more prominent secondary inorganic signatures ($m/z\,97\,HSO_4^-$) and higher number fractions than the ones below the dashed line. Although particle types A to I all exhibit a more prominent sulfate pattern with $m/z\,80$ and 97 than nitrate pattern with $m/z\,46$ and 62, they are more highly correlated with the mixture of nitrate and sulfate than either of them. Therefore, we assign the corresponding types to nitrate and sulfate. All the types in the lower panels (j to m) have significant correlation with arable soil dust in the negative spectra, which have organic signatures (e.g. $m/z\,24^-$, 25^-, and 26^-) as well as some mineral signatures like $m/z\,119^-$. Compared with the negative spectra, the positive spectra are more characteristic, which was also observed in the fuzzy results. Type A, B, C, D, and E are comparable with fuzzy class 5, 4, 2, 6, and 3, respectively (the correlation coefficients are 0.89 for type A and class 5, 0.95 for type B and class 4, 0.84 for type C and class 2, 0.76 for type D and
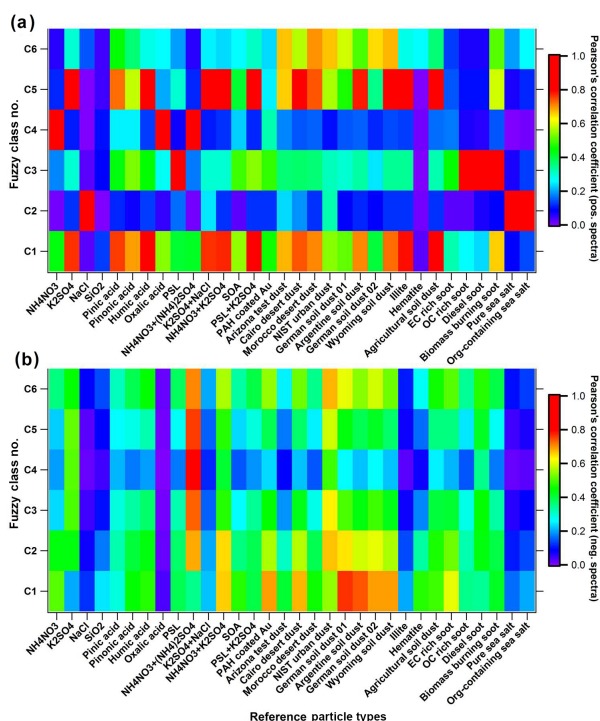
Figure 9. Correlation between fuzzy classification results (6 classes, C1 to C6) and laboratory-based reference spectra. **(a)** and **(b)** are the correlation results for the positive and negative spectra, respectively. PAH is short for poly(allylamine hydrochloride); biomass burning soot is the lignocellulosic char from chestnut wood.

class 6, and 0.81 for type E and class 3). Types F to I are more similar to aged/mixed particles, with more fragments than types A to E. Type H is comparable with fuzzy class 1. About 10 % of the particles cannot be grouped into any type. This is most likely because of an incorrect mass assignment for the stick spectra, resulting from too-large spectrum-to-spectrum peak shifts for the same ion fragments/clusters which cannot be corrected on a single-particle basis with the existing software (Ramisetty et al., 2017). As shown in the spectra in both Figs. 8 and 10, all organic species were internally mixed with inorganic species.

This reference-spectra-based classification can also be used for identification of particles with low number fractions among the huge amount of ambient data, and for selection of particles containing particular species, e.g. ones to which the instrument has a lower sensitivity. This can be achieved by e.g. excluding peaks with high signal, such as m/z 39 $K/C_3H_3^+$, or by selecting a certain particle size range or mass range. As an example, 55 lead-containing particles (Pb, with isotopes at m/z 206, 207, and 208) (details are given in the Procedure 3 in the Supplement) were identified among the 7314 ambient aerosol particles. The resulting spectra of particle classes/types in one field study can also be used as a

reference for other studies. More applications of these procedures for field data interpretation will be presented in an upcoming paper.

In short, fuzzy and reference-spectra-based classifications have some comparable results with high correlations (r: 0.76–0.95) and also have different advantages: fuzzy classification can identify special ambient particle types without any existing reference if they have a significant abundance and signal strength, while reference-spectra-based methods can identify target particle types even with little abundance. They are complementary to some extent, and thus their combination has the potential to improve interpretation of field data.

4 Conclusions

In this study, the overall detection efficiency (ODE) of LAAPTOF was determined to range from $\sim (0.01 \pm 0.01)$ to $\sim (4.23 \pm 2.36)$ % for polystyrene latex (PSL), with the size of 200 to 2000 nm, $\sim (0.44 \pm 0.19)$ to $\sim (6.57 \pm 2.38)$ % for ammonium nitrate (NH_4NO_3) and $\sim (0.14 \pm 0.02)$ to $\sim (1.46 \pm 0.08)$ % for sodium chloride (NaCl) particles in the size range of 300 to 1000 nm. This is a relative good detection efficiency compared to earlier versions of the instruments, especially when considering the good reproducibility and stability even during field measurements. A comparison to other single-particle mass spectrometers is the subject of another study and will be discussed in a separate publication. Matrix effects from aerosol particles (e.g. size, morphology, and optical property) and certain instrument influences (e.g. aerodynamic lens, detection system) and their interaction must be taken into account to evaluate the LAAPTOF performance.

In order to facilitate the interpretation of single-particle mass spectra from field measurements, we have measured various well-defined atmospherically relevant aerosol particles in the laboratory and provide here laboratory-based reference spectra for aerosol particles of different complexity with comprehensive spectral information about the components (such as organic compounds, elemental carbon, sulfate, nitrate, ammonium, chloride, mineral compounds, and metals, as commonly observed in atmospheric aerosol particles). Our results show that the interpretation of spectra from unknown particle types is significantly supported by using known mass spectral patterns like signature peaks for ammonium, nitrate, sulfate, and organic compounds as well as typical peak ratios for e.g. potassium, silicon, and chlorides. Spectra for internally mixed particles may show new clusters of ions, rather than simply a combination of the ions from single-component particles. This may be a complication for data interpretation which can be overcome if suitable reference spectra for correspondingly mixed particles are available. Organic compounds generally have some ions in common but exhibit variations depending on the com-

www.atmos-meas-tech.net/11/2325/2018/   Atmos. Meas. Tech., 11, 2325–2343, 2018

83
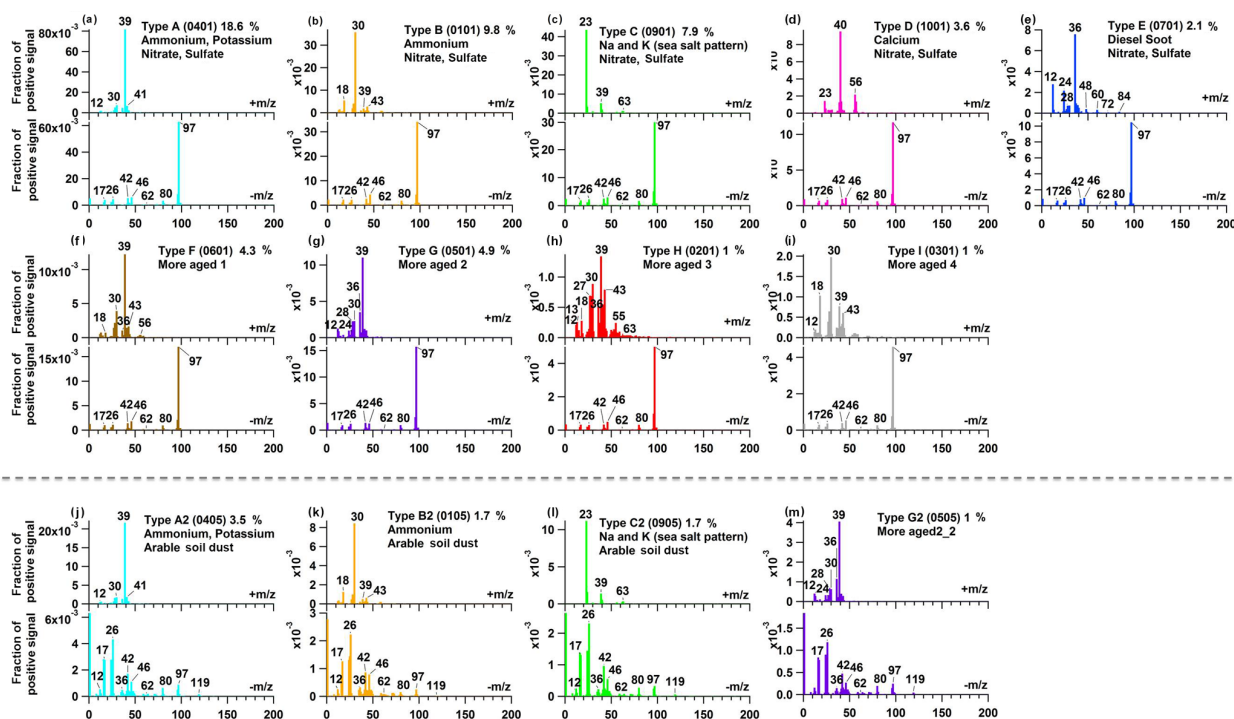
Figure 10. Mass spectra for 13 different types of particles measured on 29 July 2016 during the field campaign TRAM01, based on the classification according to laboratory-based reference spectra. The four-digit codes in the brackets represent particle types (refer to Table S2). The percent values are the particle number fractions. For **(a)** to **(e)** and **(j)** to **(l)**, there are two lines for the names; the first and second lines correspond to the highly correlated positive and negative references, respectively.

pound. Several peaks can originate from different fragments: for example, $m/z\,26^-$ and 42^- could be CN^- and CNO^- and/or $C_2H_2^-$ and $C_2H_2O^-$, $m/z\,39^+$ and 41^+ could originate from K^+ isotopes and/or organic fragments, and organic matter can also be ionized to form the typical elemental carbon pattern with $C_n^{+/-}$ ions. Hence the interpretation is not always unambiguously possible for such particles but may require additional information (e.g. size, additional marker peaks, or even higher-resolution spectra) or comparison to data from other instruments like online aerosol mass spectrometers (e.g. AMS) or chemical ionization mass spectrometers (e.g. FIGAERO-CIMS).

A set of 7314 mass spectra obtained during 1 day of field measurements was used for particle type classification by both fuzzy clustering and reference spectra. Fuzzy clustering yielded six different classes, which could then be identified with the help of reference spectra. Classification of the mass spectra based on comparison with 17 reference spectra resulted in 13 different particle types, 6 of which exhibited high correlation with the fuzzy clusters (r: 0.76–0.95). Compared with the reference spectra, we found that each particle class/type has a sulfate signature at $m/z\,80\,SO_3^-$ and 97 HSO_4^-; a nitrate signature at $m/z\,46\,NO_2^-$ and 62 NO_3^-; an organic compound signature at $m/z\,24\,C_2^-$, 25 C_2H^-, and

26 C_2H_2/CN^-; and a nitrogen-containing organic signature at $m/z\,26\,CN^-$ and 42 CNO^-. Furthermore, we performed a target-oriented classification by using selected reference spectra, allowing for the identification of particles with low number fraction in the ambient aerosol, e.g. lead-containing particles. Based on our results, we advise using a combination of both methods for the analysis of SPMS field data.

We conclude that the reference spectra presented in this paper are useful for interpretation of field measurements and for understanding the impact of mixing on typical mass spectral signatures. Furthermore, the reference spectra should be useful for interpretation of data obtained by other LAAPTOF versions or other single-particle mass spectrometers using a similar ionization method and comparable mass spectrometers. For future experiments using the LAAPTOF, systematic studies are still required on its sensitivity to different species, distinguishing the organic and inorganic contribution to the same peak in the spectra, and investigating peak ratios.

Atmos. Meas. Tech., 11, 2325–2343, 2018   www.atmos-meas-tech.net/11/2325/2018/

84

The Supplement related to this article is available online at https://doi.org/10.5194/amt-11-2325-2018-supplement.

Edited by: Joachim Curtius
Reviewed by: two anonymous referees

References

Ackerman, A. A., Adam, J. A., Cairns, B., Cho, H., Gritsevich, M., Jethva, H., Kacenelenbogen, M., Kandler, K., Knobelspiesse, K., Lanconelli, C., Lupi, A., Mazzola, M., Nousiainen, T., Peltoniemi, J. I., Platnick, S., Puttonen, E., Savenkov, S. N., Segal-Rosenheimer, M., Sharma, S., Tomasi, C., Torres, O., and Zhang, Z.: Light scattering reviews 9: Light scattering and radiative transfer, Springer-Praxis, 2015.

Ahern, A. T., Subramanian, R., Saliba, G., Lipsky, E. M., Donahue, N. M., and Sullivan, R. C.: Effect of secondary organic aerosol coating thickness on the real-time detection and characterization of biomass-burning soot by two particle mass spectrometers, Atmos. Meas. Tech., 9, 6117–6137, https://doi.org/10.5194/amt-9-6117-2016, 2016.

Arndt, J., Sciare, J., Mallet, M., Roberts, G. C., Marchand, N., Sartelet, K., Sellegri, K., Dulac, F., Healy, R. M., and Wenger, J. C.: Sources and mixing state of summertime background aerosol in the north-western Mediterranean basin, Atmos. Chem. Phys., 17, 6975–7001, https://doi.org/10.5194/acp-17-6975-2017, 2017.

Bohren, C. F. and Huffman, R. D.: Absorption and scattering of light by small particles, WILEY-VCH Verlag GmbH & Co. KGaA, 2007.

Brands, M., Kamphus, M., Böttger, T., Schneider, J., Drewnick, F., Roth, A., Curtius, J., Voigt, C., Borbon, A., Beekmann, M., Bourdon, A., Perrin, T., and Borrmann, S.: Characterization of a newly developed aircraft-based laser ablation aerosol mass spectrometer (ALABAMA) and first field deployment in urban pollution plumes over Paris during MEGAPOLI 2009, Aerosol Sci. Tech., 45, 46–64, 2011.

Burkholder, J. B., Abbatt, J. P. D., Barnes, I., Roberts, J. M., Melamed, M. L., Ammann, M., Bertram, A. K., Cappa, C. D., Carlton, A. G., Carpenter, L. J., Crowley, J. N., Dubowski, Y., George, C., Heard, D. E., Herrmann, H., Keutsch, F. N., Kroll, J. H., McNeill, V. F., Ng, N. L., Nizkorodov, S. A., Orlando, J. J., Percival, C. J., Picquet-Varrault, B., Rudich, Y., Seakins, P. W., Surratt, J. D., Tanimoto, H., Thornton, J. A., Tong, Z., S., T. G., Wahner, A., Weschler, C. J., Wilson, K. R., and Ziemann, P. J.: The essential role for laboratory studies in atmospheric chemistry, Environ. Sci. Technol., 51, 2519–2528, 2017.

Canagaratna, M. R., Jayne, J. T., Jimenez, J. L., Allan, J. D., Alfarra, M. R., Zhang, Q., Onasch, T. B., Drewnick, F., Coe, H., Middlebrook, A., Delia, A., Williams, L. R., Trimborn, A. M., Northway, M. J., DeCarlo, P. F., Kolb, C. E., Davidovits, P., and Worsnop, D. R.: Chemical and microphysical characterization of ambient aerosols with the aerodyne aerosol mass spectrometer, Mass Spectrom. Rev., 26, 185–222, 2007.

Dall'Osto, M., Beddows, D. C. S., McGillicuddy, E. J., Esser-Gietl, J. K., Harrison, R. M., and Wenger, J. C.: On the simultaneous deployment of two single-particle mass spectrometers at an urban background and a roadside site during SAPUSS, Atmos. Chem. Phys., 16, 9693–9710, https://doi.org/10.5194/acp-16-9693-2016, 2016.

EUROCHAMP: EUROCHAMP DATA CENTER – Library of Analytical Resources of the EU project EUROCHAMP-2020, available at: https://data.eurochamp.org/, last access: 16 April 2018.

Gaie-Levrel, F., Perrier, S., Perraudin, E., Stoll, C., Grand, N., and Schwell, M.: Development and characterization of a single particle laser ablation mass spectrometer (SPLAM) for organic aerosol studies, Atmos. Meas. Tech., 5, 225–241, https://doi.org/10.5194/amt-5-225-2012, 2012.

Gemayel, R., Hellebust, S., Temime-Roussel, B., Hayeck, N., Van Elteren, J. T., Wortham, H., and Gligorovski, S.: The performance and the characterization of laser ablation aerosol particle time-of-flight mass spectrometry (LAAP-ToF-MS), Atmos. Meas. Tech., 9, 1947–1959, https://doi.org/10.5194/amt-9-1947-2016, 2016.

Gross, D. S., Gälli, M. E., Silva, P. J., and Prather, K. A.: Relative sensitivity factors for alkali metal and ammonium cations in single particle aerosol time-of-flight mass spectra, Anal. Chem., 72, 416–422, 2000.

Hagemann, R., Corsmeier, U., Kottmeier, C., Rinke, R., Wieser, A., and Vogel, B.: Spatial variability of particle number concentra-

www.atmos-meas-tech.net/11/2325/2018/   Atmos. Meas. Tech., 11, 2325–2343, 2018

85

tions and NOx in the Karlsruhe (Germany) area obtained with the mobile laboratory "AERO-TRAM", Atmos. Environ., 94, 341–352, 2014.

Hinz, K. P., Greweling, M., Drews, F., and Spengler, B.: Data processing in on-line laser mass spectrometry of inorganic, organic, or biological airborne particles, J. Am. Soc. Mass Spectr., 10, 648–660, 1999.

Jimenez, J. L., Canagaratna, M. R., Donahue, N. M., Prevot, A. S. H., Zhang, Q., Kroll, J. H., DeCarlo, P. F., Allan, J. D., Coe, H., Ng, N. L., Aiken, A. C., Docherty, K. S., Ulbrich, I. M., Grieshop, A. P., Robinson, A. L., Duplissy, J., Smith, J. D., Wilson, K. R., Lanz, V. A., Hueglin, C., Sun, Y. L., Tian, J., Laaksonen, A., Raatikainen, T., Rautiainen, J., Vaattovaara, P., Ehn, M., Kulmala, M., Tomlinson, J. M., Collins, D. R., Cubison, M. J., Dunlea, E. J., Huffman, J. A., Onasch, T. B., Alfarra, M. R., Williams, P. I., Bower, K., Kondo, Y., Schneider, J., Drewnick, F., Borrmann, S., Weimer, S., Demerjian, K., Salcedo, D., Cottrell, L., Griffin, R., Takami, A., Miyoshi, T., Hatakeyama, S., Shimono, A., Sun, J. Y., Zhang, Y. M., Dzepina, K., Kimmel, J. R., Sueper, D., Jayne, J. T., Herndon, S. C., Trimborn, A. M., Williams, L. R., Wood, E. C., Middlebrook, A. M., Kolb, C. E., Baltensperger, U., and Worsnop, D. R.: Evolution of organic aerosols in the atmosphere, Science, 326, 1525–1529, 2009.

Johnston, M. V.: Sampling and analysis of individual particles by aerosol mass spectrometry, J. Mass Spectrom., 35, 585–595, 2000.

Kamphus, M., Ettner-Mahl, M., Brands, M., Curtius, J., Drewnick, F., and Borrmann, S.: Comparison of two aerodynamic lenses as an inlet for a single particle laser ablation mass spectrometer, Aerosol Sci. Tech., 42, 970–980, 2008.

Kulkarni, P., Baron, P. A., and Willeke, K.: Aerosol measurement: Principles,techniques, and applications, Wiley, J & Sons, Inc., 2011.

Li, L., Huang, Z. X., Dong, J. G., Li, M., Gao, W., Nian, H. Q., Fu, Z., Zhang, G. H., Bi, X. H., Cheng, P., and Zhou, Z.: Real time bipolar time-of-flight mass spectrometer for analyzing single aerosol particles, Int. J. Mass Spectrom., 303, 118–124, 2011.

Li, W., Sun, J., Xu, l., Shi, Z., Riemer, N., Sun, Y., Fu, P., Zhang, J., Lin, Y., Wang, X., Shao, L., Chen, J., Zhang, X., Wang, Z., and Wang, W.: A conceptual framework for mixing structures in individual aerosol particles, J. Geophys. Res.-Atmos., 121, 13784–13798, 2016.

Lin, Q., Zhang, G., Peng, L., Bi, X., Wang, X., Brechtel, F. J., Li, M., Chen, D., Peng, P., Sheng, G., and Zhou, Z.: In situ chemical composition measurement of individual cloud residue particles at a mountain site, southern China, Atmos. Chem. Phys., 17, 8473–8488, https://doi.org/10.5194/acp-17-8473-2017, 2017.

Liu, P., Ziemann, P. J., Kittelson, D. B., and McMurry, P. H.: Generating particle beams of controlled dimensions and divergence: II. Experimental evaluation of particle motion in aerodynamic lenses and nozzle expansions, Aerosol Sci. Tech., 22, 314–324, 1995.

Marsden, N., Flynn, M. J., Taylor, J. W., Allan, J. D., and Coe, H.: Evaluating the influence of laser wavelength and detection stage geometry on optical detection efficiency in a single-particle mass spectrometer, Atmos. Meas. Tech., 9, 6051–6068, https://doi.org/10.5194/amt-9-6051-2016, 2016.

Marsden, N. A., Flynn, M. J., Allan, J. D., and Coe, H.: Online differentiation of mineral phase in aerosol particles

by ion formation mechanism using a LAAP-TOF single-particle mass spectrometer, Atmos. Meas. Tech., 11, 195–213, https://doi.org/10.5194/amt-11-195-2018, 2018.

Moffet, R. C., de Foy, B., Molina, L. T., Molina, M. J., and Prather, K. A.: Measurement of ambient aerosols in northern Mexico City by single particle mass spectrometry, Atmos. Chem. Phys., 8, 4499–4516, https://doi.org/10.5194/acp-8-4499-2008, 2008.

Murphy, D. M.: The design of single particle laser mass spectrometers, Mass Spectrom. Rev., 26, 150–165, 2007.

Murphy, D. M., Middlebrook, A. M., and Warshawsky, M.: Cluster analysis of data from the Particle Analysis by Laser Mass Spectrometry (PALMS) instrument, Aerosol Sci. Tech., 37, 382–391, 2003.

Murphy, D. M., Cziczo, D. J., Froyd, K. D., Hudson, P. K., Matthew, B. M., Middlebrook, A. M., Peltier, R. E., Sullivan, A., Thomson, D. S., and Weber, R. J.: Single-particle mass spectrometry of tropospheric aerosol particles, J. Geophys. Res.-Atmos., 111, D23S32, https://doi.org/10.1029/2006JD007340, 2006.

Noble, C. A. and Prather, K. A.: Real-time single particle mass spectrometry: a historical review of a quarter century of the chemical analysis of aerosols, Mass Spectrom. Rev., 19, 248–274, 2000.

Pöschl, U.: Atmospheric aerosols: Composition, transformation, climate and health effects, Angew. Chem. Int. Edit., 44, 7520–7540, 2005.

Pratt, K. A. and Prather, K. A.: Mass spectrometry of atmospheric aerosols-Recent developments and applications. Part II: On-line mass spectrometry techniques, Mass Spectrom. Rev., 31, 17–48, 2012.

Ramisetty, R., Abdelmonem, A., Shen, X., Saathoff, H., Leisner, T., and Mohr, C.: Exploring femtosecond laser ablation in single particle aerosol mass spectrometry, Atmos. Meas. Tech. Discuss., https://doi.org/10.5194/amt-2017-357, in review, 2017.

Reitz, P., Zorn, S. R., Trimborn, S. H., and Trimborn, A. M.: A new, powerful technique to analyze single particle aerosol mass spectra using a combination of OPTICS and the fuzzy c-means algorithm, J. Aerosol Sci., 98, 1–14, 2016.

Roth, A., Schneider, J., Klimach, T., Mertes, S., van Pinxteren, D., Herrmann, H., and Borrmann, S.: Aerosol properties, source identification, and cloud processing in orographic clouds measured by single particle mass spectrometry on a central European mountain site during HCCT-2010, Atmos. Chem. Phys., 16, 505–524, https://doi.org/10.5194/acp-16-505-2016, 2016.

Saathoff, H., Möhler, O., Schurath, U., Kamm, S., Dippel, B., and Mihelcic, D.: The AIDA soot aerosol characterisation campaign 1999, J. Aerosol Sci., 34, 1277–1296, 2003.

Saathoff, H., Naumann, K.-H., Möhler, O., Jonsson, Å. M., Hallquist, M., Kiendler-Scharr, A., Mentel, Th. F., Tillmann, R., and Schurath, U.: Temperature dependence of yields of secondary organic aerosols from the ozonolysis of α-pinene and limonene, Atmos. Chem. Phys., 9, 1551–1577, https://doi.org/10.5194/acp-9-1551-2009, 2009.

Schill, G. P. and Tolbert, M. A.: Heterogeneous ice nucleation on phase-separated organic-sulfate particles: effect of liquid vs. glassy coatings, Atmos. Chem. Phys., 13, 4681–4695, https://doi.org/10.5194/acp-13-4681-2013, 2013.

Schmidt, S., Schneider, J., Klimach, T., Mertes, S., Schenk, L. P., Kupiszewski, P., Curtius, J., and Borrmann, S.: Online single particle analysis of ice particle residuals from mountain-top mixed-

phase clouds using laboratory derived particle type assignment, Atmos. Chem. Phys., 17, 575–594, https://doi.org/10.5194/acp-17-575-2017, 2017.

Schreiner, J., Schild, U., Voigt, C., and Mauersberger, K.: Focusing of aerosols into a particle beam at pressures from 10 to 150 Torr, Aerosol Sci. Tech., 31, 373–382, 1999.

Seinfeld, J. H. and Pandis, S. N.: Atmospheric chemistry and physics: From air pollution to climate change, Wiley, J & Sons, Inc., Hoboken, New Jersey, 2006.

Silva, P. J., Carlin, R. A., and Prather, K. A.: Single particle analysis of suspended soil dust from Southern California, Atmos. Environ., 34, 1811–1820, 2000.

Su, Y. X., Sipin, M. F., Furutani, H., and Prather, K. A.: Development and characterization of an aerosol time-of-flight mass spectrometer with increased detection efficiency, Anal. Chem., 76, 712–719, 2004.

Tsigaridis, K., Krol, M., Dentener, F. J., Balkanski, Y., Lathière, J., Metzger, S., Hauglustaine, D. A., and Kanakidou, M.: Change in global aerosol composition since preindustrial times, Atmos. Chem. Phys., 6, 5143–5162, https://doi.org/10.5194/acp-6-5143-2006, 2006.

Usher, C. R., Michel, A. E., and Grassian, V. H.: Reactions on mineral dust, Chem. Rev., 103, 4883–4939, 2003.

Wagner, R., Kaufmann, J., Möhler, O., Saathoff, H., Schnaiter, M., Ullrich, R., and Leisner, T.: Heterogeneous ice nucleation ability of NaCl and sea salt aerosol particles at cirrus temperatures, J. Geophys. Res., 123, 2841–2860, https://doi.org/10.1002/2017JD027864, 2018.

Williams, L. R., Gonzalez, L. A., Peck, J., Trimborn, D., McInnis, J., Farrar, M. R., Moore, K. D., Jayne, J. T., Robinson, W. A., Lewis, D. K., Onasch, T. B., Canagaratna, M. R., Trimborn, A., Timko, M. T., Magoon, G., Deng, R., Tang, D., de la Rosa Blanco, E., Prévôt, A. S. H., Smith, K. A., and Worsnop, D. R.: Characterization of an aerodynamic lens for transmitting particles greater than 1 micrometer in diameter into the Aerodyne aerosol mass spectrometer, Atmos. Meas. Tech., 6, 3271–3280, https://doi.org/10.5194/amt-6-3271-2013, 2013.

Wonaschuetz, A., Kallinger, P., Szymanski, W., and Hitzenberger, R.: Chemical composition of radiolytically formed particles using single-particle mass spectrometry, J. Aerosol Sci., 113, 242–249, 2017.

Yu, J. Z., Cocker, D. R., Griffin, R. J., Flagan, R. C., and Seinfeld, J. H.: Gas-phase ozone oxidation of monoterpenes: Gaseous and particulate products, J. Atmos. Chem., 34, 207–258, 1999.

Zawadowicz, M. A., Abdelmonem, A., Mohr, C., Saathoff, H., Froyd, K. D., Murphy, D. M., LeisnerI, T., and Cziczo, D. J.: Single-particle time-of-flight mass spectrometry utilizing a femtosecond desorption and ionization laser, Anal. Chem., 87, 12221–12229, 2015.

Zawadowicz, M. A., Lance, S., Jayne, J. T., Croteau, P., Worsnop, D. R., Mahrt, F., Leisner, T., and Cziczo, D. J.: Quantifying and improving the performance of the Laser Ablation Aerosol Particle Time of Flight Mass Spectrometer (LAAPToF) instrument, Atmos. Meas. Tech. Discuss., https://doi.org/10.5194/amt-2017-1, 2017.

Zelenyuk, A. and Imre, D.: Single particle laser ablation time-of-flight mass spectrometer: An introduction to SPLAT, Aerosol Sci. Tech., 39, 554–568, 2005.

Zelenyuk, A., Cai, Y., and Imre, D.: From agglomerates of spheres to irregularly shaped particles: Determination of dynamic shape factors from measurements of mobility and vacuum aerodynamic diameters, Aerosol Sci. Tech., 40, 197–217, 2006a.

Zelenyuk, A., Imre, D., Cai, Y., Mueller, K., Han, Y. P., and Imrich, P.: SpectraMiner, an interactive data mining and visualization software for single particle mass spectroscopy: A laboratory test case, Int. J. Mass Spectrom., 258, 58–73, 2006b.

Zelenyuk, A., Yang, J., Choi, E., and Imre, D.: SPLAT II: An aircraft compatible, ultra-sensitive, high precision instrument for in-situ characterization of the size and composition of fine and ultrafine particles, Aerosol Sci. Tech., 43, 411–424, 2009.

Zhang, Q., Jimenez, J. L., Canagaratna, M. R., Allan, J. D., Coe, H., Ulbrich, I., Alfarra, M. R., Takami, A., Middlebrook, A. M., Sun, Y. L., Dzepina, K., Dunlea, E., Docherty, K., DeCarlo, P. F., Salcedo, D., Onasch, T., Jayne, J. T., Miyoshi, T., Shimono, A., Hatakeyama, S., Takegawa, N., Kondo, Y., Schneider, J., Drewnick, F., Borrmann, S., Weimer, S., Demerjian, K., Williams, P., Bower, K., Bahreini, R., Cottrell, L., Griffin, R. J., Rautiainen, J., Sun, J. Y., Zhang, Y. M., and Worsnop, D. R.: Ubiquity and dominance of oxygenated species in organic aerosols in anthropogenically-influenced Northern Hemisphere midlatitudes, Geophys. Res. Lett., 34, L13801, https://doi.org/10.1029/2007GL029979, 2007.

Zhao, W. X., Hopke, P. K., and Prather, K. A.: Comparison of two cluster analysis methods using single particle mass spectra, Atmos. Environ., 42, 881–892, 2008.

www.atmos-meas-tech.net/11/2325/2018/   Atmos. Meas. Tech., 11, 2325–2343, 2018

87

Atmospheric
Measurement
Techniques
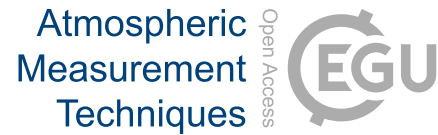
Supplement of

Laser ablation aerosol particle time-of-flight mass spectrometer (LAAPTOF): performance, reference spectra and classification of atmospheric samples

Xiaoli Shen et al.

Correspondence to: Harald Saathoff (harald.saathoff@kit.edu)

Appendix B

1 In the supporting information, the contents are organised as 1) tables, 2) figures, and 3) description of some procedures for

2 LAAPTOF data analysis as well as the corresponding equations and uncertainties.

3

4 **Table S1: Summary of peak assignments**

	Cations				Anions		
m/z	carbon	inorganic	organic	m/z	carbon	inorganic	organic
7+		Li^+		1-		H^-	
12+	C^+			8-		O^{2-}	
13+			CH^+	12-	C^-		
15+			CH_3^+/NH^+	16-		O^-	
17+		OH^+		17-		OH^-	
18+		NH_4^+/H_2O^+		24-	C_2^-		
23+		Na^+		25-			C_2H^-
24+	C_2^+	Mg^+		26-			$CN/C_2H_2^-$
27+		Al^+	$C_2H_3^+$	32-		S^-	
28+		Si^+	CO^+	36-	C_3^-		
29+			$C_2H_5^+/CHO^+$	35-		Cl^-	
30+		NO^+	CH_3NH^+/CH_2O^+	37-		Cl^-	
36+	C_3^+			42-			$CNO/C_2H_2O^-$
39+		K^+	$C_3H_3^+$	43-		AlO^-	
40+		Ca^+	C_2O^+	45-			$COOH^-$
41+		K^+	$C_3H_5^+$	46-		NO_2^-	
43+			$C_3H_7^+/C_2H_3O^+$	48-	C_4^-	SO^-	
44+		SiO^+	CO_2^+	59-		AlO_2^-	CH_2COOH^-
46+		NO_2^+		60-	C_5^-	SiO_2^-	
48+	C_4^+			62-		NO_3^-	
51+			$C_4H_3^+$	63-		PO_2^-	
53+			$C_4H_5^+$	64-		SO_2^-	
54+		Fe^+		70-		$^{35}Cl_2^-$	
55+		Mn^+	$C_4H_7^+/C_3H_3O^+$	71-			CCH_2COOH^-
56+		$Fe/CaO/Si_2^+$	$C_4H_8^+$	72-	C_6^-	FeO^-	
57+		$CaOH^+$	$C_4H_9^+/C_2OOH^+$	73-			$C_2H_4COOH^-$
58+		Ni^+	$C_2H_5-NH-CH_2^+$	76-		SiO_3^-	
59+			$(CH_3)_3N^+$	77-		$HSiO_3^-$	
60+	C_5^+			79-		PO_3^-	
63+		Cu^+	$C_5H_3^+$	80-		SO_3^-	
64+		Zn^+		81-		HSO_3^-	
65+		Cu^+		84-	C_7^-		
66+		Zn^+		85-			$C_3H_4COOH^-$
69+			$C_5H_9^+$	86-		FeO_2^-	
71+			$C_4H_7O^+$	88-		$Si_2O_2^-/FeO_2^-$	
72+	C_6^+			89-			$(CO)_2OOH^-$
77+			$C_6H_5^+$	93-		$NaCl_2^-$	
81+		Na_2Cl^+	$C_6H_9^+$	95-		$NaCl_2^-/PO_4^-$	
83+		Na_2Cl^+	$C_5H_7O^+$	96-	C_8^-	SO_4^-	
84+	C_7^+			97-		HSO_4^-	
85+			$C_7H_5^+/C_3HO_3^+$	99-			$C_4H_6COOH^-$
88+		FeO_2^+		103-		$(AlO)SiO_2^-$	
91+			$C_7H_7^+$	108-	C_9^-		
95+			$C_7H_{11}^+$	109-		KCl_2^-	
96+	C_8^+	Ca_2O^+		117-			$(CO)_3OOH^-$
97+		$KNaCl^+$	$C_4HO_3^+$	119-		$AlSiO_4^-/NaSO_4^-$	
103+			$C_8H_7^+$	130-		$NaCl_3^-$	
105+			$C_8H_9^+$	135-		KSO_4^-	
108+	C_9^+			136-		$(SiO_2)_2O^-/KHSO_4^-$	
112+		$(CaO)_2^+$		148-		$(SiO_2)_2Si^-$	
113+		K_2Cl^+		151-		$Na_2Cl_3^-$	
115+		K_2Cl^+	$C_9H_7^+$	153-		$Na_2Cl_3^-$	
120+	C_{10}			179-		$AlSiO_4.SiO_2^-$	
132+	C_{11}^+						
206–208+		Pb^+					

5

1

6   **Table S2: Codes for reference particle types used for classification by using the reference spectra based classification**

positive code	reference particle	negative code	reference particle
01	Ammonium Nitrate	01	Ammonium Nitrate and Sulfate
02	Pinonic Acid	02	Ammonium Nitrate and Potassium Sulfate
03	Oxalic Acid	03	Desert Dust (Morroco)
04	Ammonium Nitrate and Potassium Sulfate	04	Urban Dust
05	Potassium Sulfate Coated PSL	05	Arable Soil Dust (German) (SDGe01)
06	Agricultural Soil Dust	06	Diesel Soot
07	Diesel Soot	07	Biomass Burning Soot
08	Biomass Burning Soot		
09	Sea salt (pure)		
10	Fuzzy Class 6_Calcium rich		

7

8   Note: In order to minimize the complexity, the reference number was reduced by observing the histogram of particle types based on the

9   correlation between each ambient spectrum (7314 in total) and our 32 laboratory based reference spectra relevant for atmospheric aerosol

10   (refer to the details of reference spectra based classification in Procedures 2 in the supplementary information).

2

11
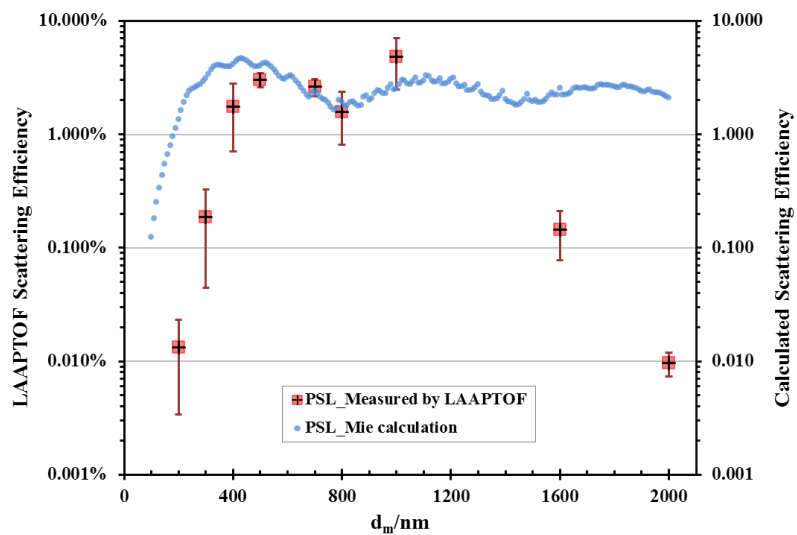
Figure S1: Comparison of scattering efficiencies for PSL particles measured by LAAPTOF and values from Mie calculation at the particle sizes relevant to measurement. The input parameters for Mie calculation are refractive index of 1.62 and wavelength of 405 nm.

3
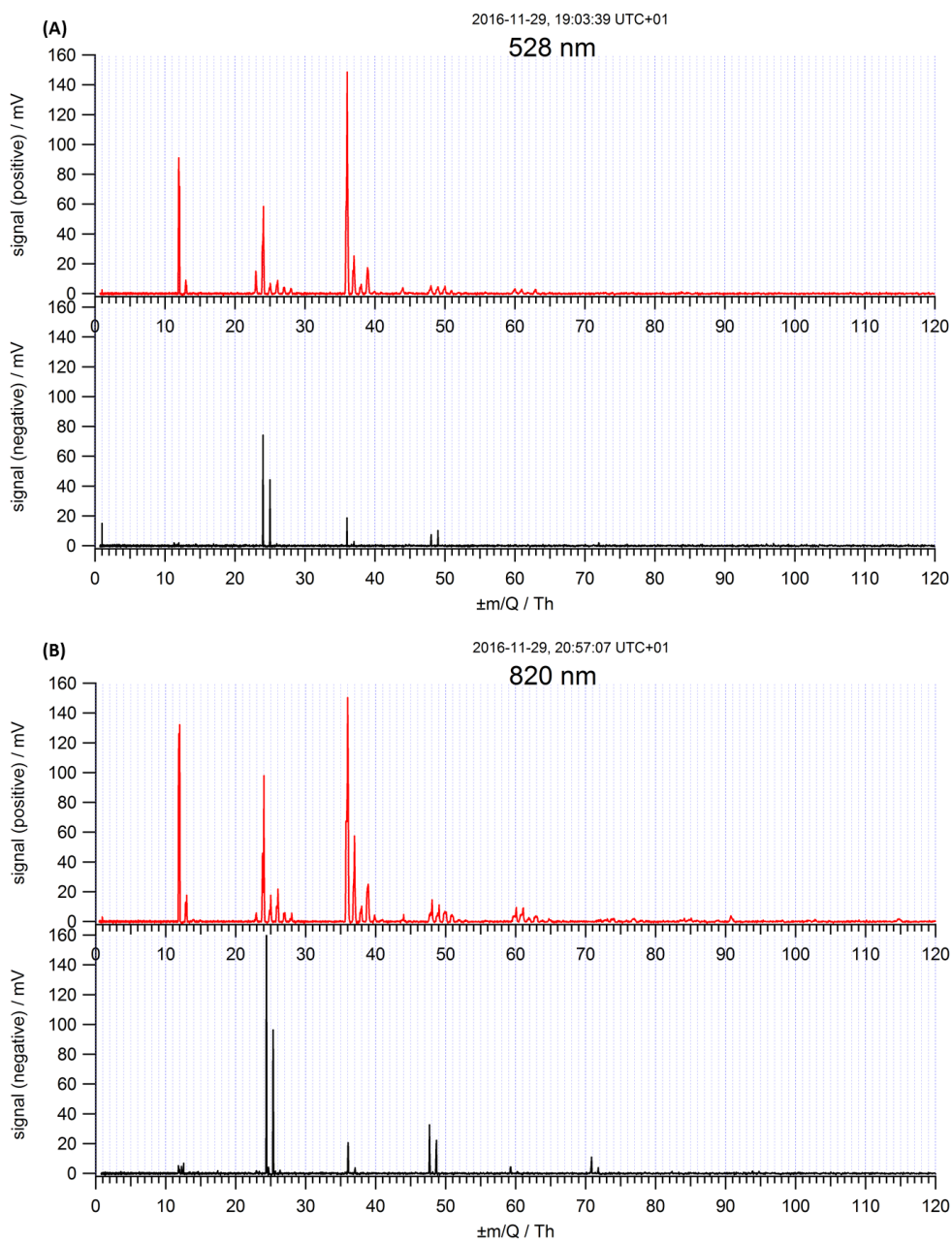
Figure S2: Typical spectra with raw signal for individual PSL particles of dva 528 nm (panel A) and 820 nm (panel B), respectively.

4
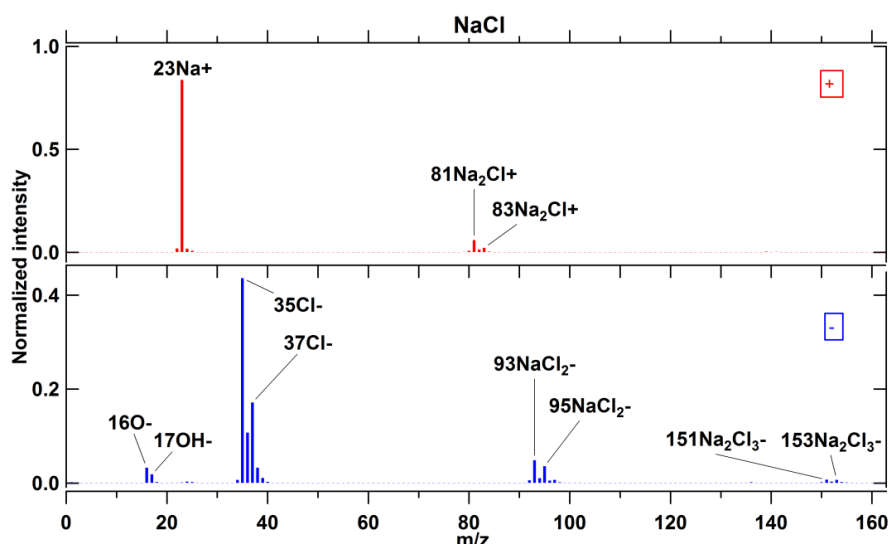
18

19 **Figure S3: Average mass spectrum for 1170 nm (d_{va}) pure NaCl particles. The ratio of m/z 35 Cl$^-$ to m/z 37 Cl$^-$ is ~3.2, similar as**
20 **the natural isotopic ratio of ~3.1 for ^{35}Cl/^{37}Cl. 250 single particle mass spectra were averaged for this spectrum.**

21
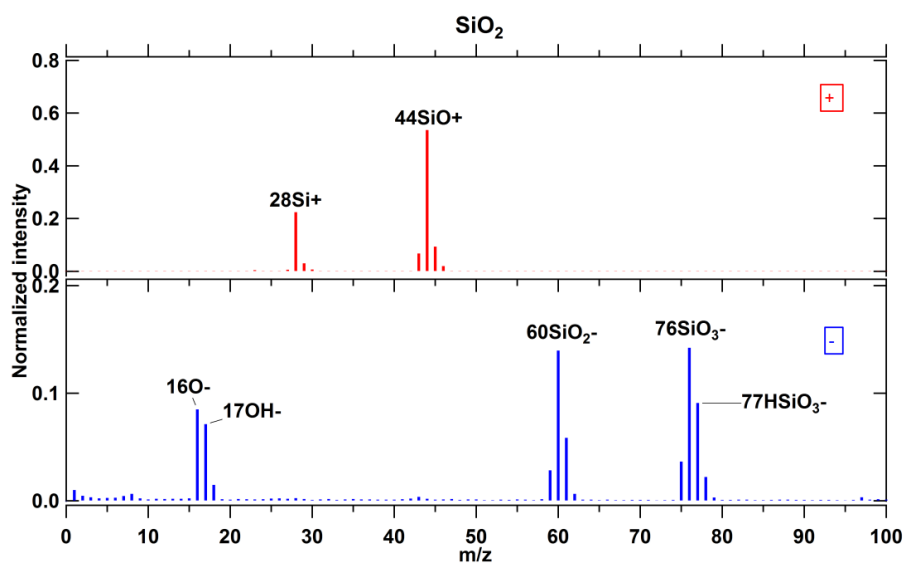
22

23 **Figure S4: Average mass spectrum for 2097 nm (d_{va}) SiO$_2$ particles (glass beads). The ratio of m/z 44 SiO$^+$ to m/z 28 Si$^+$ is ~2.4;**
24 **(m/z 76 SiO$_3^-$ + m/z 77 HSiO$_3^-$) to m/z 60 SiO$_2^-$ is ~1. Such peak ratios are typical for SiO$_2$ particles. 347 single particle mass**
25 **spectra were averaged for this spectrum.**

5

26

27
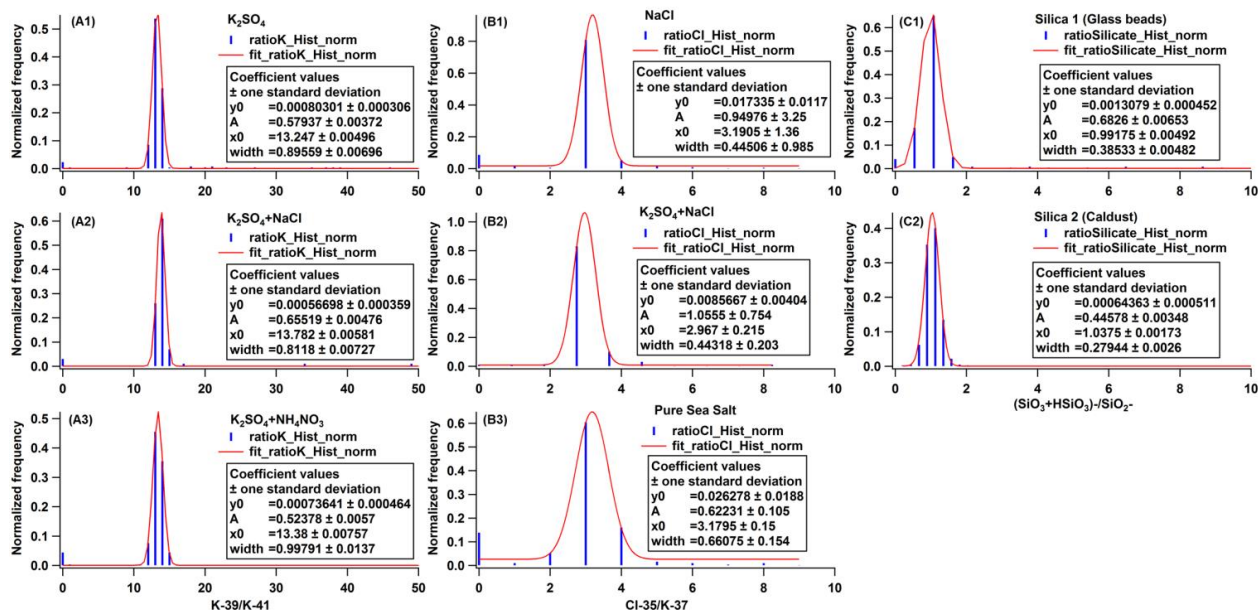
Figure S5: Histogram of peak ratios for different particle samples: panel A1 to A3 are for the isotopic ratio of K-39/K-41 arising from K containing samples; panel B1 to B3 are for the isotopic ratio of Cl-35/Cl-37 arising from Cl containing samples; panel C1 and C2 are for the peak ratio of $(SiO_3^- + HSiO_3^-)/SiO_2^-$ arising from silicate containing samples.
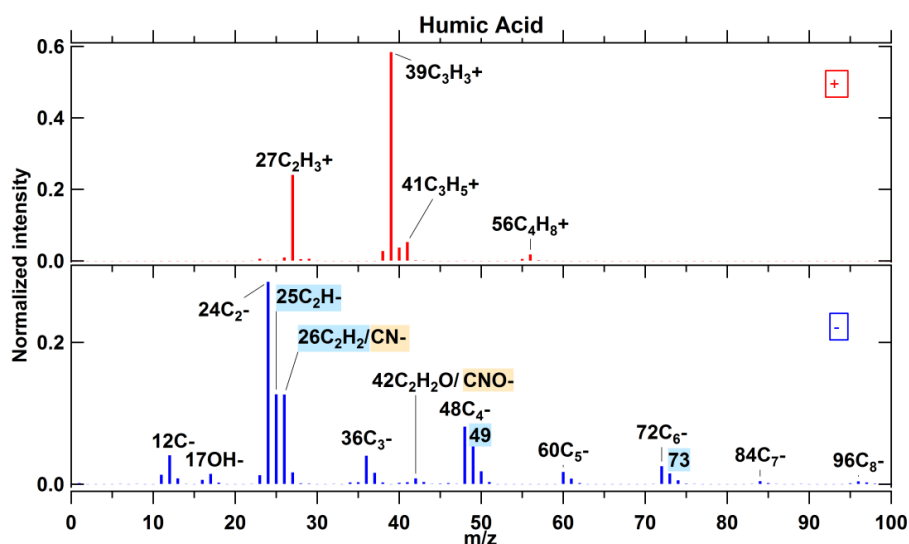
Figure S6: Average mass spectrum for 1221 nm (d_va) humic acid particles. Fragments labelled in blue are typical for unsaturated organic compounds; fragments labelled in orange are from nitrogen-containing organic compounds. 773 single particle mass spectra were averaged for this spectrum.
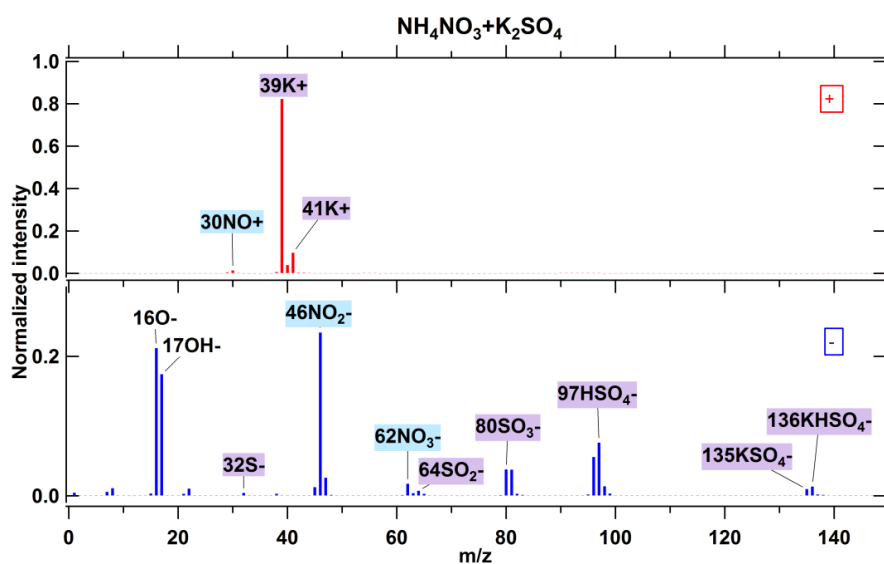
Figure S7: Average mass spectrum for 854 nm (d_va) particles of homogeneous internal mixtures of inorganic compounds, NH₄NO₃ and K₂SO₄, 576 single spectra averaged. The blue and purple labels represent the fragments arising from pure NH₄NO₃ and pure K₂SO₄ components, respectively.

7
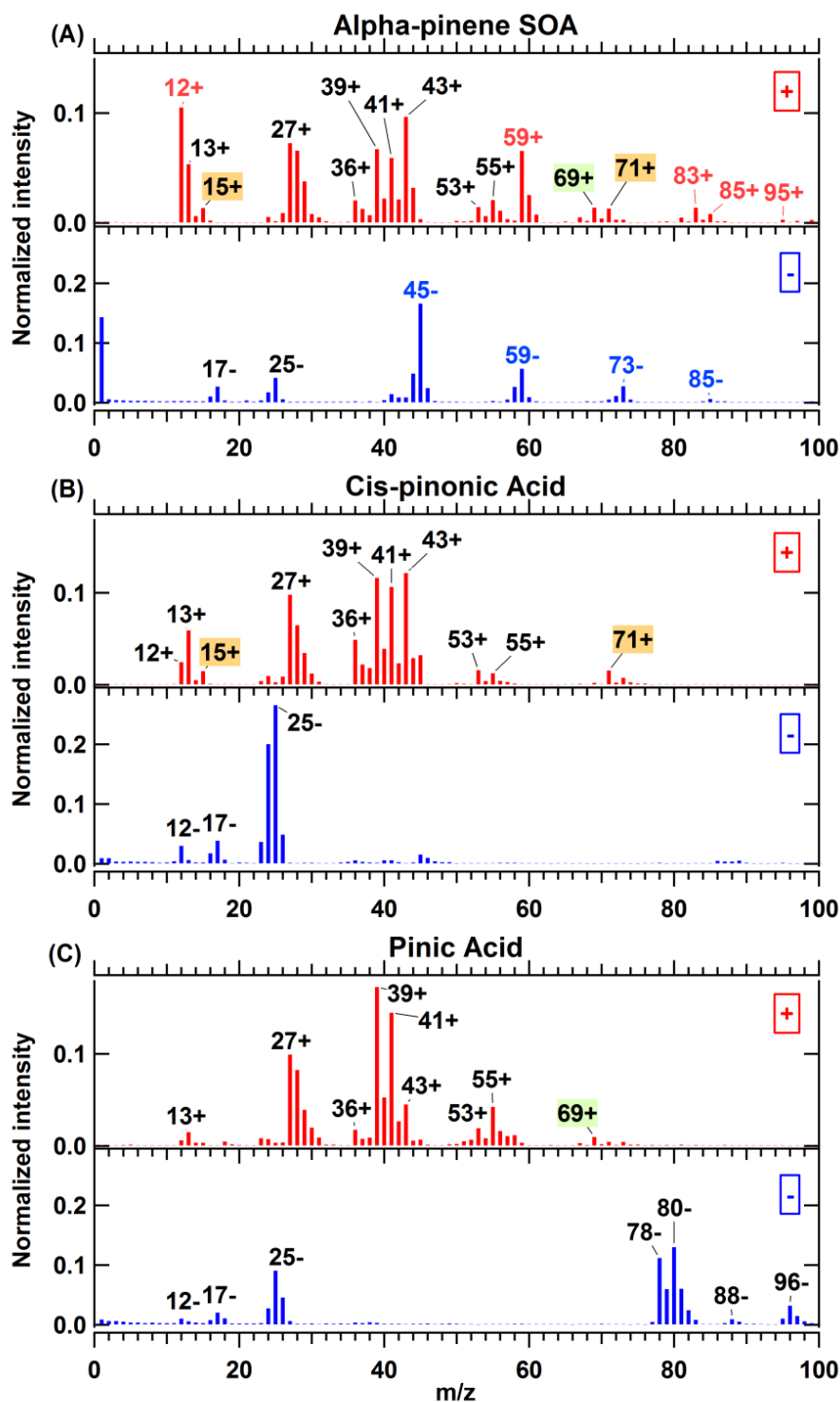
Figure S8: Average mass spectra for particles of homogeneous internal mixtures of (A) secondary organic aerosol (SOA) particles from α-pinene ozonolysis, which was performed in the APC chamber then the resulting particles were transferred into AIDA chamber at 263 K and 95% RH, d_{va}= 505 nm, 1938 single spectra averaged, as well as pure aerosol particles consisting of (B) cis-pinonic acid, d_{va}= 702 nm, 600 single spectra averaged and (C) pinic acid, d_{va}= 902 nm, 683 single spectra averaged. In panel (A), m/z 15+ and 71+ labelled in orange are arising from cis-pinonic acid, while m/z 69+ labelled in green is arising from pinic acid.
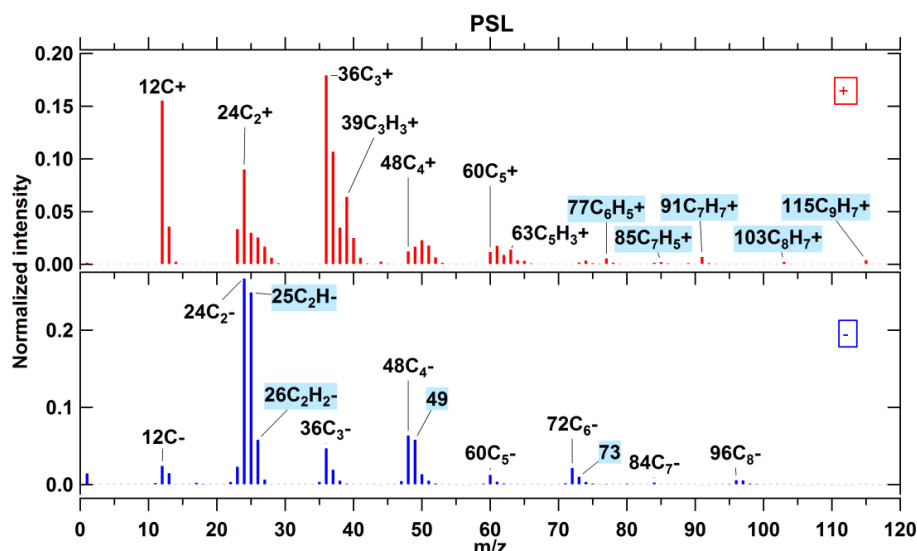
8

Figure S9: Average mass spectra for 818 nm (d_{va}) pure PSL. Fragments labelled in blue are typical patterns for aromatic compounds. 235 single particle mass spectra were averaged for this spectrum.
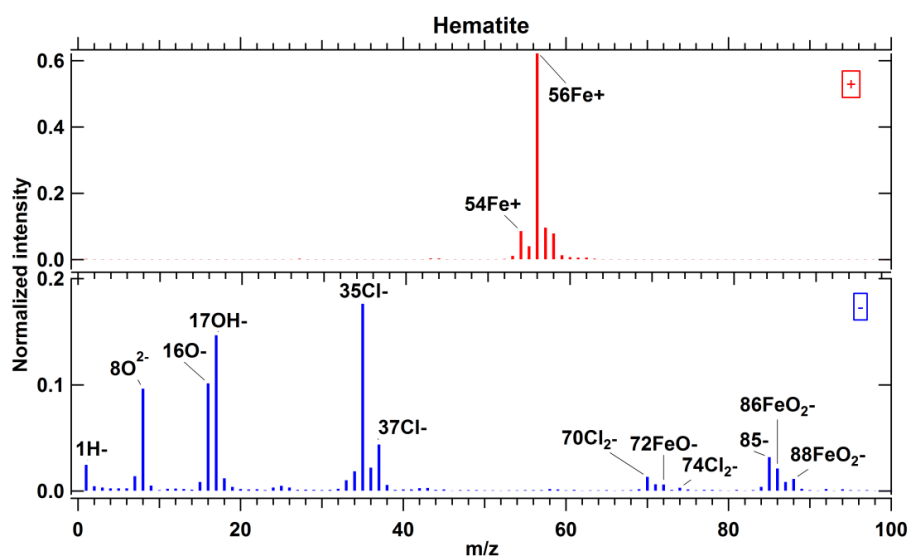
Figure S10: Average mass spectrum for 800 nm (geometric size) hematite particles, 320 single spectra averaged.

Hematite with signatures for iron (intensive m/z 56 Fe^+ and the other iron isotopes m/z 54, 57, and 58), oxides of iron (m/z 72 FeO^-, 86 FeO_2^-, and 88 FeO_2^-), and chlorides (m/z 35 Cl^-, 37 Cl^-, 70 Cl_2^-, and 74 Cl_2^-). Chloride ions observed originate from the hematite synthesis process. This is comparable to the hematite spectra measured by PALMS (Gallavardin et al., 2008).

9

58
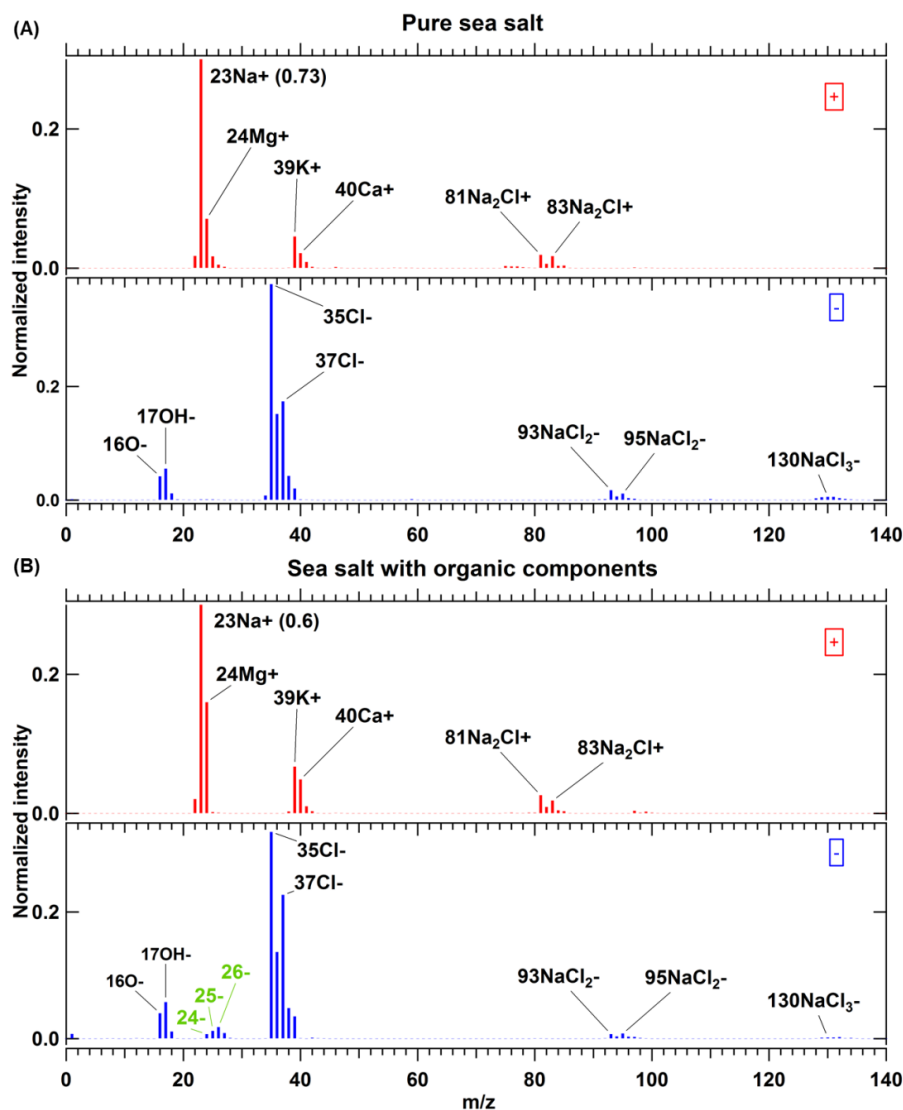
Figure S11: Average mass spectra for (A) pure sea salt, 422 single spectra averaged, and (B) sea salt particles with skeletonema marinoi (organic components), 526 single spectra averaged. These aerosol particles were sampled from the AIDA chamber at 246 K and 75% RH, d_{va}= ~1200 nm. The numbers in brackets beside peaks 23$^+$ are the exact intensity values for them. In panel (B) obvious organic signatures m/z 24$^-$, 25$^-$, and 26$^-$ labelled in green can be observed.

Pure sea salt particles have signatures for NaCl (m/z 23$^+$, 81$^+$, 83$^+$, 35$^-$, 37$^-$, 93$^-$, and 95$^-$), and other metals (m/z 24 Mg$^+$, 39 K$^+$, and 40 Ca$^+$). Sea salt particles containing biological components have the signatures for pure sea salt as well as the signatures for organic compounds (m/z 24$^-$, 25$^-$, and 26$^-$).

10
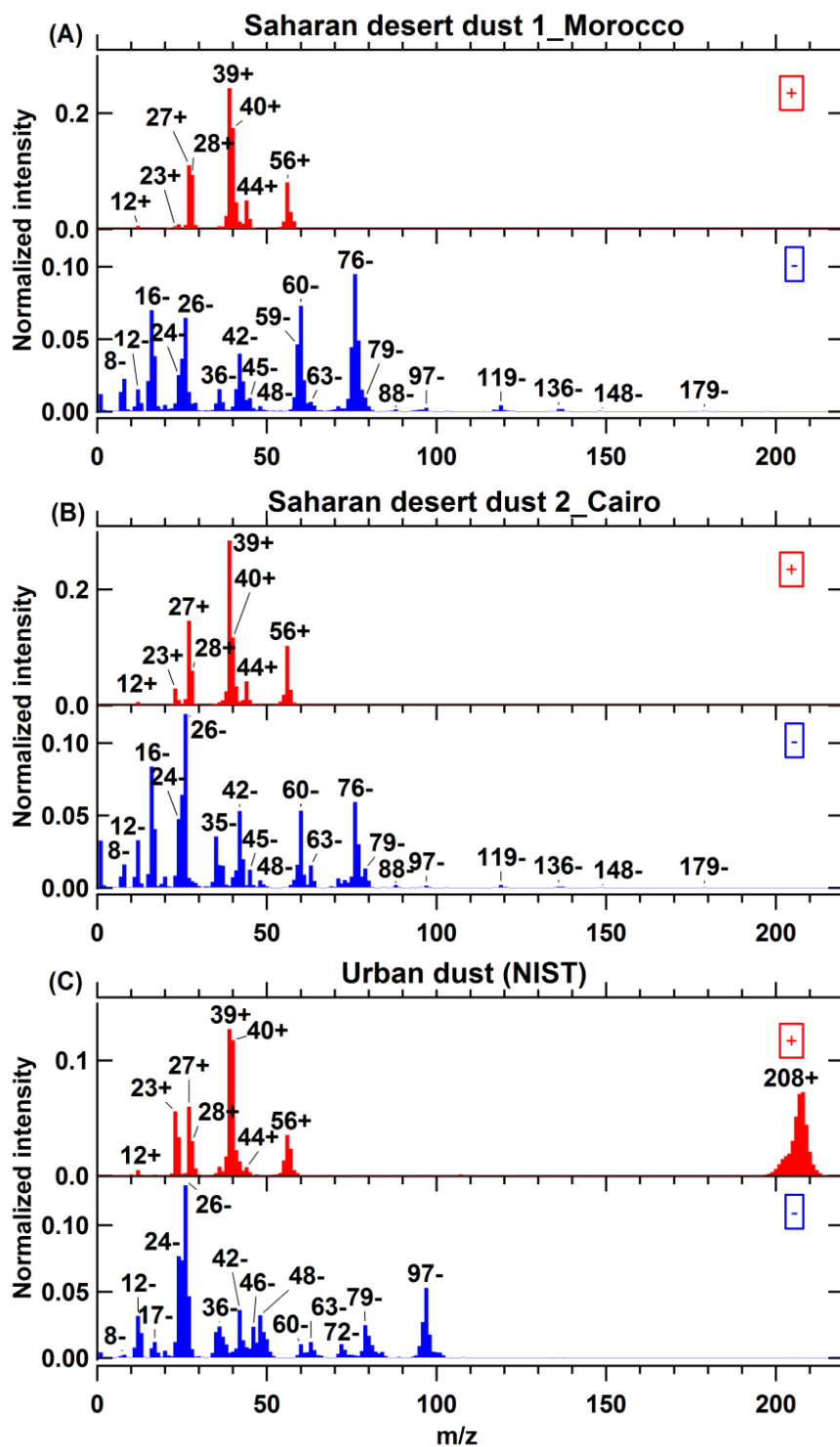
Figure S12: Average mass spectra for Saharan desert dust from (A) Morocco, 338 single spectra averaged and (B) Cairo city, 396 single spectra averaged, and (C) urban dust (standard material from NIST), 375 single spectra averaged.

11
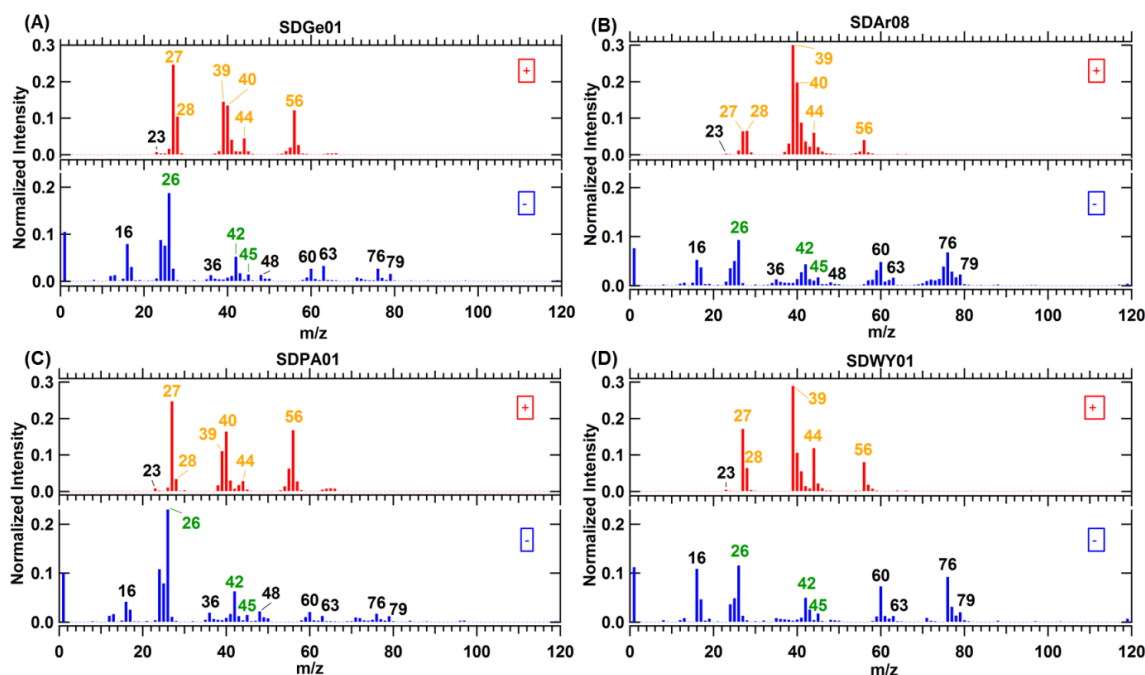
Figure S13: Average mass spectra for four different arable soil dusts sampled at two sites from Germany (SDGe01 is from Gottesgabe and SDPA01 is from Paulinenaue), Argentina (SDAr08), and Wyoming in USA (SDWY01). The corresponding aerosol particles were dispersed by a rotating brush generator and injected via cyclones into the AIDA chamber at 256 K and 80% RH. Black tags represent inorganic fragments; green tags represent organic fragments; orange tags represent fragments originating from inorganic and organic species. The numbers of spectra for each average spectrum are 583 (A), 592 (B), 385 (C) and 623 (D).
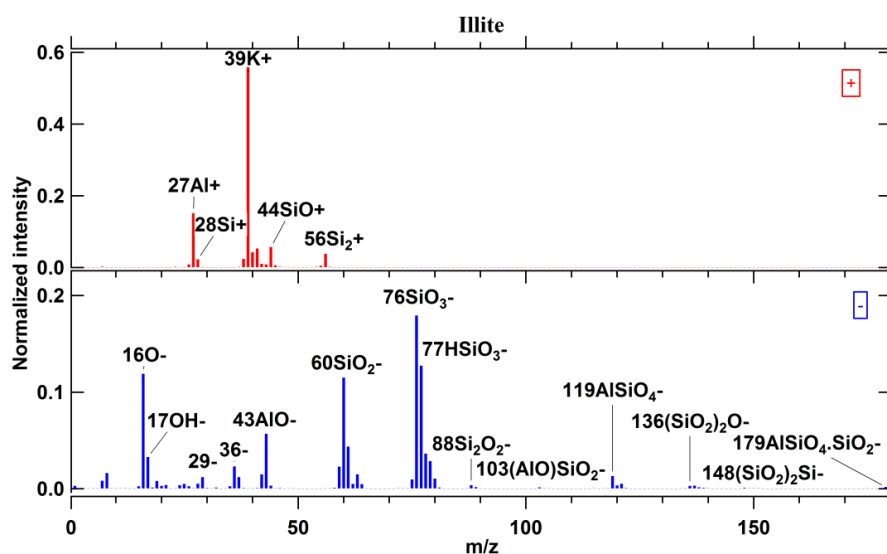
Figure S14: Average mass spectra for illite particles, 807 single spectra averaged

Illite particles, mainly containing aluminosilicates, showed signatures for potassium (m/z 39 K^+ and 41 K^+), alumina (m/z 27 Al^+, 43 AlO^-, and 59 AlO_2^-), silica (m/z 28 Si^+, 44 SiO^+, 56 Si_2^+, 60 SiO_2^-, 76 SiO_3^-, 77 $HSiO_3^-$, 136 $(SiO_2)_2O^-$, and 148 $(SiO_2)_2Si^-$), and oxides of aluminium and silicon (m/z 119 $AlSiO_4^-$, and 179 $AlSiO_4.SiO_2^-$). The K/Si ratio is ~25, which is comparable to this ratio observed in Illite spectra measured by PALMS (Zawadowicz et al., 2017).

12

100
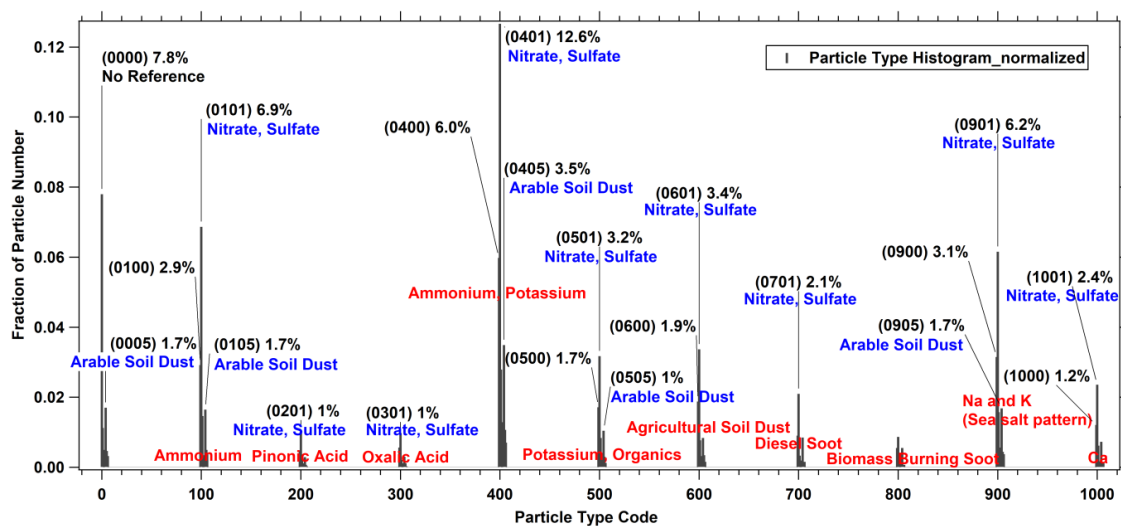
Figure S15: Particle type histogram based on the classification of field data (on July 29th, 2016 during TRAM01 campaign) according to laboratory-based reference spectra. The numbers in the brackets are the combination of positive (the front two digits) and negative codes (the rear two digits) for reference particles, which are listed in Table S2. There are 11 clusters in this plot with 10 positive references labelled in red texts, while the corresponding negative references are labelled in blue texts beneath the corresponding codes.

13

90 **Procedure 1: LAAPTOF data analysis with emphasize on mass calibration**

91 1. Open two Igor experiments, using the same raw data (One is for comparison, another is for further analysis)

92 2. In one Igor experiment: go through the raw spectra (e.g. from the negative spectra, m/z 1, 16 and 17, 24, 25 and 26 are
93   easier to be recognized), to find out the possible fragments, with the help of peak assignments in Table 1 as well as the
94   laboratory based reference spectra.

95 3. In another Igor experiment

96   • Setting the First-tof, base line, and remove the empty spectra

97   • Start mass calibration

98   Step1: Choose 3 masses with relative bigger distance for positive and negative spectra for basic calibration, respectively.
99   (Tips: it is better to choose the corresponding positions for such masses in the spectrum # -1 after pressing the tab
100   "Display spectrum", which give us the stack spectra showing the shift, thus help us better locate the mass; double
101   check the mass values referring to the other Igor experiment with only raw data)

102   Step2: Exact calibration, by using more masses.
103   (Tips: use only values which are certain)

104   Step3: Generate and check the average spectra, then adjust mass calibration by experience and comparing with the
105   individual spectrum.
106   (Tips: If we have done good mass calibration, the resulting average spectra will be representative, which can help
107   to find more fragments including reasonable patterns like m/z 24$^-$, 25$^-$, and 26$^-$ as well as some expected small
108   fragments like m/z 119$^-$ in mineral dust, thus can modify the exact calibration table. Otherwise, we should redo
109   mass calibration from step 1)

110   Step4: Plot ptof vs masses for mass calibration, then use power fit to see whether the value is around 0.5, if yes, then the
111   mass calibration is ok.

112   Step5: If the data is poly dispersed, we can also use fuzzy classification to double check the mass calibration.
113   (Tips: If we have good mass calibration, the fuzzy results will be good, namely the real number of output classes
114   can finally (almost) equal to the input class number)

115 4. Generate average spectra that are normalized to the sum of ion intensities

116 5. Fuzzy Clustering

117   For poly-dispersed particles, we can use Fuzzy classification method. The most important input parameter is the number
118   of classes. We can start from the bigger value (e.g. 20) to the smaller one, until the reasonable number and
119   corresponding classes are found. In this study 6 classes have been found by using this method.

120   (Tips: similar classes would be observed if the input number of classes is too big, and the good situation is that the
121 resulting number of classes we found is equal to the input number, which is 6 in this study. In addition, the resulting number
122 of classes with clearly different features strongly depends on the experience of the operating scientist to identify them.

123   It should be noted that there are spectra-to-spectra peak shifts (~100 ns) due to variance in the position of the interaction
124 of the individual particles with the excimer laser beam, complicating mass calibration. This cannot be corrected with the
125 existing Aeromegt software or the LAAPTOF instrument. It could be avoided by adding/implementing a pulsed extraction,
126 which would store the ions for a certain time and then extract them into the TOF region. Peak shifting is less problematic for
127 the negative spectra than for the positive spectra. This cannot be completely solved even after aforementioned serious mass
128 calibration. Such peak shifting is less problematic in the negative spectra than the positive ones.

129   **Procedure 2: Reference spectra based classification**

130   Step 1: Normalize (to sum) stick spectra from the field data and reference spectra.

131   Step 2: Correlate each ambient spectrum with each reference spectrum (positive spectra 01 to 32 and negative spectra 01

132   to 32). Positive and negative spectra are treated separately due to differences in peak intensities for the two polarities, biasing

133   coefficients r (refer to equation S1); namely high intensive peaks dominating the value of r. However, this can be reduced by

134   selecting specific mass ranges for the correlation.

135   Step 3: Define particle type. Only correlations with a Pearson's correlation coefficient r $\geqslant$ 0.6 are used. Particles are

136   categorized using a 4-digit code: The first 2 digits identify the positive reference spectrum (01 – 32) with which a particle's

137   spectrum exhibits maximum r; the third and fourth digits the negative reference spectrum (01 – 32) with which the particle's

138   negative spectrum exhibits maximum r.

139   Step 4: Reduce the number of references. A histogram with the number of particles per particle type is used to identify

140   the main particle types. For positive spectra, particle types with number fractions $\geqslant$ 1% were chosen. For the negative

141   spectra, no numerical criteria could be used in the first iteration, but spectra were examined individually (we found e.g. that

142   four arable soil dust samples had similar negative spectra and only used SDGe01). For our dataset the number of reference

143   spectra or particle types was reduced to 10 positive and 7 negative spectra (Table S2).

144   Step 5: Repeat step 1 to 3 using the reduced set of reference spectra.

145   Step 6: Identify the main particle types. Categorized particles are again plotted in a histogram, and main particle types

146   are identified based on number fractions $\geqslant$ 1%. Only particles with correlations in both polarities are included here. In our

147   study, 13 main types were found.

148   **The equation (S1) for calculating Pearson's correlation coefficients between two waves A and B (e.g. ambient and**

149   **reference spectrum)**

$$r = \frac{\sum_{i=0}^{n-1}(waveA[i]-A)(waveB[i]-B)}{\sqrt{\sum_{i=0}^{n-1}(waveA[i]-A)^2 \sum_{i=0}^{n-1}(waveB[i]-B)^2}}$$

150   (S1)

151   Here A is the average of the elements in wave A, B is the average of the elements of wave B and the sum is over all

152   wave elements. Although we mainly discuss the main peaks with higher intensities, in this paper, it is should be mentioned

153   that the bias by the peak intensity in calculating r are inevitable, namely high intensive peaks dominate the value of r. Of

154   course this intensity bias can be reduced by selecting specific mass ranges for the correlation.

155

15

156   **Uncertainties for reference-oriented method for grouping mass spectra**

157   In order to estimate the uncertainty for reference-oriented method, we have calculated the relative difference between the

158   highest and the second highest Pearson's correlation coefficients (r1 and r2) for each particle, according to equation (S2):

159     $$\text{Relative Difference} = \frac{r1-r2}{r1} = \frac{r1_{pos} \times r1_{neg} - r2_{pos} \times r2_{neg}}{r1_{pos} \times r1_{neg}} \qquad (S2)$$
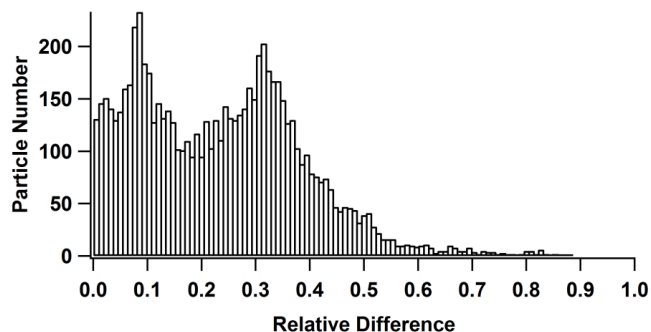
160

161 **Figure S16: Histogram of relative difference between the highest and the second highest Pearson's correlation coefficient values**

162 **for each particle measured in the field (on July 29th, 2016 during TRAM01 campaign).**

163   The corresponding statistic calculation results for such relative difference data are listed as follows:

164   V_npnts= 7314; V_numNaNs= 0; V_numINFs= 0; V_avg= 0.234484;

165   V_Sum= 1715.02; V_sdev= 0.152986; V_sem= 0.00178885;

166   V_rms= 0.279972; V_adev= 0.126782; V_skew= 0.595888;

167   V_kurt= 0.244212; V_minloc= 2005; V_maxloc= 5211;

168   V_min= 4.35069e-05; V_max= 0.882732; V_minRowLoc= 2005;

169   V_maxRowLoc= 5211; V_startRow= 0; V_endRow= 7313;

170   The relative difference mentioned above provides information about the uncertainties for using the reference-spectra

171   oriented method, namely, the bigger the difference is, the smaller the uncertainty will be. It turns out that 77% of the 7314

172   particles we measured have more than 10% relative difference between r1 and r2, therefore such classification method is

173   reasonable to be used.

174   There are some factors that could have impact on the uncertainties: 1) the most important one is selection of reference

175   spectra, since two similar references such German soil dust SDGe01 and SDPA01 will lead to similar r that cause little

176   relative difference between r1 and r2 corresponds to higher uncertainty. 2) Peak intensities and mass ranges selected will

177   influence the r values. Bias by peak intensities leads to higher uncertainties whereas well selected mass ranges can also

178   reduce the uncertainties.

16

179 **Procedure 3: Seeking lead (Pb) containing particles using the reference spectra**

180 In order to pick out the lead-containing particles, we firstly check the fuzzy results by correlating them to all the reference

181 spectra in the size range of 200 to 220. As shown in Fig. S17, all the classes except class 5 have significant correlation with

182 the lead-containg urban dust particles (NIST), which can also be seen in Fig. S18 where the corresponding spectra are

183 stacked, showing clear comparable data points in the m/z range of 200 to 220. For Class 5, there are some points offset,

184 leading to lower r, although it also shows similar shape in such m/z range. In the future we will modify our procedure to do

185 better mass calibrarion and avoid the offset/error data points to solve such problem. Anther problematic issure, which cannot

186 completely solved at present, is the peak shifting mentioned before, expecially for the fragments with bigger mass, such as

187 lead. This will make data interpretation more difficult. In the next step, we correlate each spectrum with the urban dust

188 particles in the m/z range of 200 to 220, and the Pb-containing particles can be selected based on the criteria of r>=0.6. As a

189 result, 55 Pb-containing particles have been found among 7314 particles in the ambient data. Of course also other specific

190 particles can be found using suitable reference spectra.
191
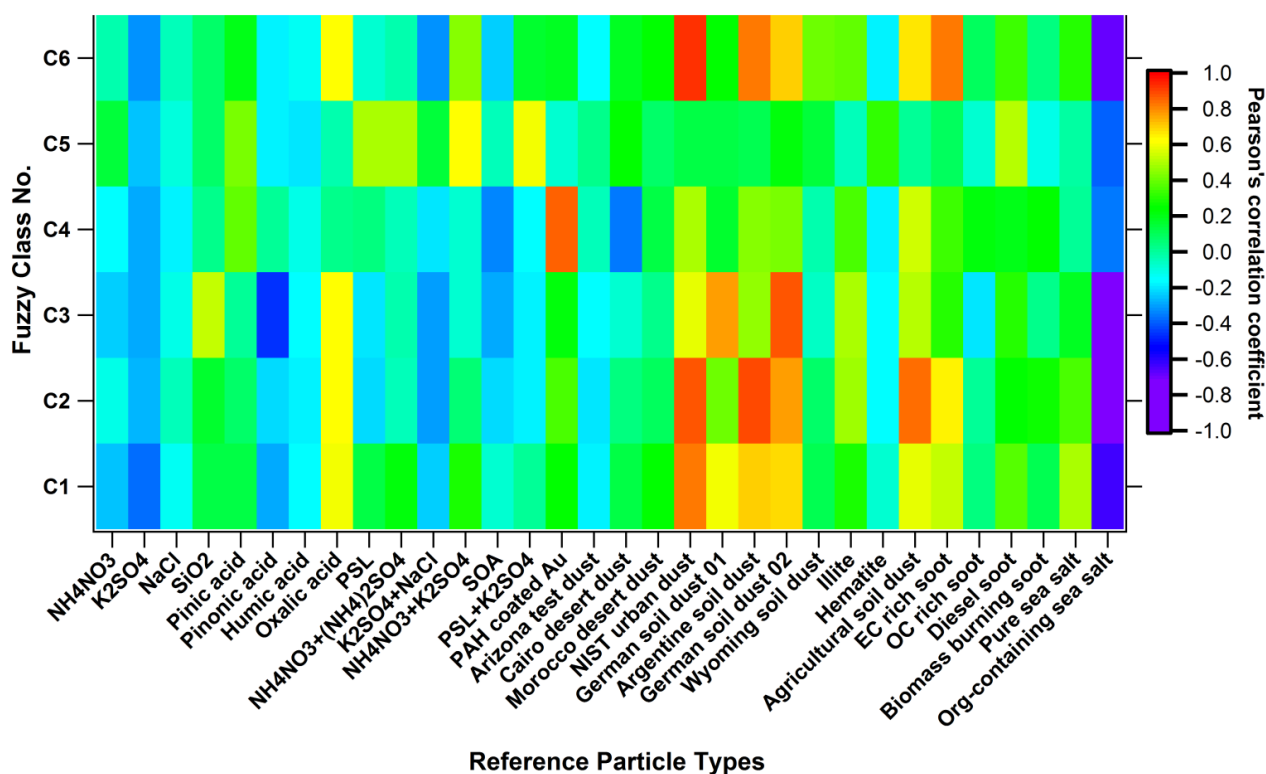
192
193 **Figure S17: Correlation between fuzzy classification results (6 classes, C1 to C6) and laboratory-based reference spectra only in**
194 **the m/z range of 200 to 220 for the positive spectra. PAH is short for poly(allylamine hydrochloride), biomass burning soot is the**
195 **lignocellulosic char from chestnut wood.**
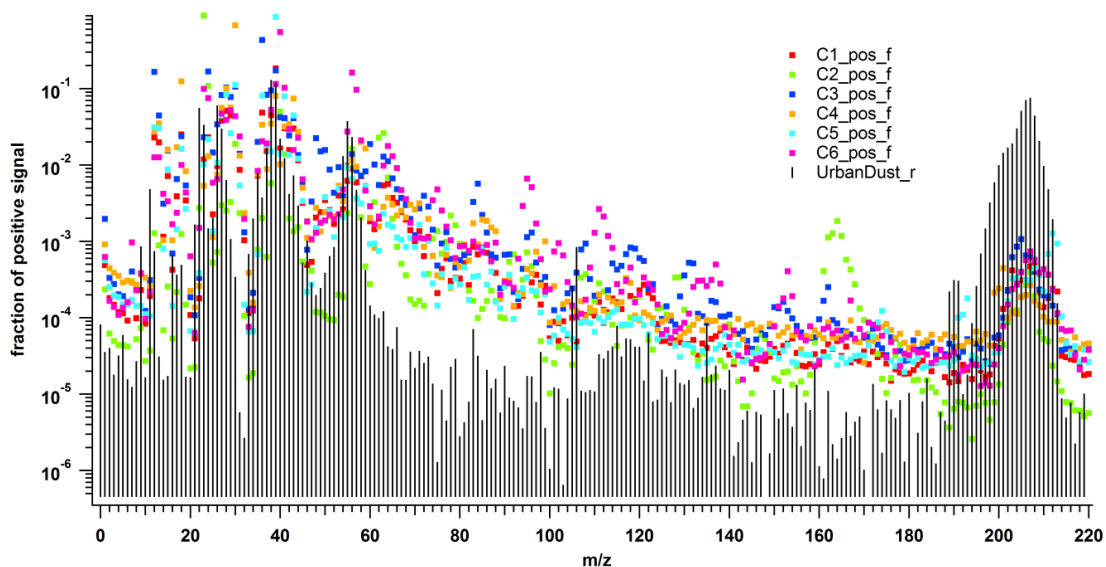
Figure S18: Stacked mass spectra for urban dust particles (NIST) and 5 classes of particles measured on July 29th, 2016 during the field campaign TRAM01.

References

Gallavardin, S., Lohmann, U., and Cziczo, D.: Analysis and differentiation of mineral dust by single particle laser mass spectrometry, Int J Mass Spectrom, 274, 56–63, 2008.

Zawadowicz, M. A., Froyd, K. D., Murphy, D., and Cziczo, D. J.: Improved identification of primary biological aerosol particles using single particle mass spectrometry, Atmos Chem Phys, 17, 7193–7212, 2017.

18

Appendix B.2 Understanding of atmospheric aerosol particles with improved particle identification and quantification by single particle mass spectrometry

Atmospheric
Measurement
Techniques

Understanding atmospheric aerosol particles with improved particle identification and quantification by single-particle mass spectrometry

Xiaoli Shen[1,2], **Harald Saathoff**[1], **Wei Huang**[1,2], **Claudia Mohr**[1,3], **Ramakrishna Ramisetty**[1,a], **and Thomas Leisner**[1,4]

[1]Institute of Meteorology and Climate Research, Karlsruhe Institute of Technology, Hermann-von-Helmholtz-Platz 1, 76344 Eggenstein-Leopoldshafen, Germany
[2]Institute of Geography and Geoecology, Working Group for Environmental Mineralogy and Environmental System Analysis, Karlsruhe Institute of Technology, Kaiserstr.12, 76131 Karlsruhe, Germany
[3]Department of Environmental Science and Analytical Chemistry, Stockholm University, Stockholm, 11418, Sweden
[4]Institute of Environmental Physics, University of Heidelberg, In Neuenheimer Feld 229, 69120 Heidelberg, Germany
[a]now at: TSI Instruments India Private Limited, Bangalore, 560102, India

Correspondence: Harald Saathoff (harald.saathoff@kit.edu)

Abstract. Single-particle mass spectrometry (SPMS) is a widely used tool to determine chemical composition and mixing state of aerosol particles in the atmosphere. During a 6-week field campaign in summer 2016 at a rural site in the upper Rhine valley, near the city of Karlsruhe in southwest Germany, $\sim 3.7 \times 10^5$ single particles were analysed using a laser ablation aerosol particle time-of-flight mass spectrometer (LAAPTOF). Combining fuzzy classification, marker peaks, typical peak ratios, and laboratory-based reference spectra, seven major particle classes were identified. With the precise particle identification and well-characterized laboratory-derived overall detection efficiency (ODE) for this instrument, particle similarity can be transferred into corrected number and mass fractions without the need of a reference instrument in the field. Considering the entire measurement period, aged-biomass-burning and soil-dust-like particles dominated the particle number (45.0 % number fraction) and mass (31.8 % mass fraction); sodium-salt-like particles were the second lowest in number (3.4 %) but the second dominating class in terms of particle mass (30.1 %). This difference demonstrates the crucial role of particle number counts' correction for mass quantification using SPMS data. Using corrections for size-resolved and chemically resolved ODE, the total mass of the particles measured by LAAPTOF accounts for 23 %–68 % of the total mass measured by an aerosol mass spectrometer (AMS) depending on the measurement periods. These two mass spectrometers show a good correlation (Pearson's correlation coefficient $\gamma > 0.6$) regarding total mass for more than 85 % of the measurement time, indicating non-refractory species measured by AMS may originate from particles consisting of internally mixed non-refractory and refractory components. In addition, specific relationships of LAAPTOF ion intensities and AMS mass concentrations for non-refractory compounds were found for specific measurement periods, especially for the fraction of org / (org + nitrate). Furthermore, our approach allows the non-refractory compounds measured by AMS to be assigned to different particle classes. Overall AMS nitrate mainly arose from sodium-salt-like particles, while aged-biomass-burning particles were dominant during events with high organic aerosol particle concentrations.

1 Introduction

Lifetimes of ambient aerosol particles range from hours to several days, except for newly formed particles (~ 3 to 5 nm), which have a lifetime on the order of seconds (Pöschl, 2005). The atmospheric evolution of aerosol particles can alter their internal and external mixing states, as well as their chemical and physical properties on timescales of several hours; e.g.

Published by Copernicus Publications on behalf of the European Geosciences Union.

108

they can acquire coatings of secondary inorganic (e.g. sulfates, nitrates, and ammonium) and secondary organic compounds (Fuzzi et al., 2015). Hence, most aerosol particles are relatively complex mixtures; they are not easy to distinguish and trace to their primary source and/or secondary formation pathway. Single-particle mass spectrometry (SPMS) has the capability of measuring most components of the particles in real time; thus it has been a widely used technique to investigate mixing state and aging of aerosol particles for many years (Murphy, 2007; Noble and Prather, 2000; Pratt and Prather, 2012). However, there are still challenging issues related to large amounts of SPMS data analysis.

Particle type identification, i.e. the assignment of every detected particle to one out of a set of particle types, which are either predefined or deduced from the experimental data, is perhaps one of the most critical issues. Different data classification methods, e.g. fuzzy k-means clustering algorithm, fuzzy c-means (modification of k-means), ART-2a neural network, hierarchical clustering algorithms, and machine learning algorithms, are applied to reduce the complexity and highlight the core information of mass spectrometric data (Reitz et al., 2016; Christopoulos et al., 2018). Reitz et al. (2016) reviewed commonly used data classification methods in SPMS studies and pointed out the advantage of the fuzzy c-means clustering approach, which allows individual particles to belong to different particle classes according to spectral similarities. One recent classification approach applied machine learning algorithms and successfully distinguished SOA, mineral dust, and soil dust, as well as biological aerosols based on a known a priori data set (Christopoulos et al., 2018). In this study we used the fuzzy c-means clustering approach which is embedded in the data analysis Igor software for our laser ablation aerosol particle time-of-flight mass spectrometer (LAAPTOF; AeroMegt GmbH). Based on the data classification, averaged or representative mass spectra of different particle classes can be obtained.

Due to the relatively complex laser desorption and ionization (LDI) mechanisms, including charge and proton transfer, as well as ion-molecule reactions that may occur in the plume with many collisions (Murphy, 2007; Reilly et al., 2000; Reinard and Johnston, 2008; Zenobi and Knochenmuss, 1998), some mass spectroscopic signature peaks do not necessarily reflect the primary composition of the particles. Gallavardin et al. (2008) used a pair of peak area ratios, such as Ca_2O^+/Ca^+ vs. CaO^+/Ca^+ and SiO^-/SiO_2^- vs. SiO_3^-/SiO_2^-, to differentiate calcium-/silicon-containing mineral dust. Normalized histograms of PO_3^-/PO_2^- and CN^-/CNO^- ratios were used to identify primary biological aerosol particles (Zawadowicz et al., 2017). Setting thresholds for marker peak signals can also help to classify and further identify specific particles (Köllner et al., 2017). Lu et al. (2018) used natural silicon isotopic signatures to study the sources of airborne fine particulate matter ($PM_{2.5}$), which shows how useful isotopic signatures can be for particle identification. A combination of peak area and peak shift ratio,

based on subtle changes in ion arrival times in the mass spectrometer, was introduced by Marsden et al. (2018) for the differentiation of mineral phases in silicates. Ternary subcomposition systems, such as $(Al + Si)^+-K^+-Na^+$ and $Cl^--(CN + CNO)^--SO_4^-$, were used to identify mineralogy and internal mixing state of ambient particles (Marsden et al., 2019). In our previous study (Shen et al., 2018), laboratory-based reference spectra were suggested to be a useful tool for particle identification. These methods guide the way for improving the techniques to identify particle type and further identify individual aerosol particles.

An even more challenging issue is the quantitative analysis of individual particles' mass and chemical composition, which cannot be directly provided by SPMS measurements because laser ablation only allows an a priori unknown fraction (neutral species) of the single particle to be vaporized/desorbed and then ionized (Murphy, 2007; Reinard and Johnston, 2008). In addition, matrix effects may obscure the particle composition (Gemayel et al., 2017; Gross et al., 2000; Hatch et al., 2014). Our previous laboratory SPMS study also verified the difficulty of particle quantification due to incomplete ionization, which could not be improved significantly by replacing the originally used nanosecond excimer laser with a femtosecond laser with higher laser power density and shorter laser pulse length (Ramisetty et al., 2018). In the last two decades, great effort has been put into solving such quantification issues by using specific scaling or normalization methods. Allen et al. (2006) developed an explicit scaling method to quantify SPMS data, based on comparison with co-located more quantitative particle measurement. This approach has been widely used to obtain continuous aerosol mass concentrations as a function of particle size (Allen et al., 2006; Bein et al., 2006; Fergenson et al., 2001) and has been improved by a hit rate correction (Qin et al., 2006; Wenzel et al., 2003). Recently, composition-dependent density corrections were applied to such scaling approaches to obtain chemically resolved mass concentrations (Gunsch et al., 2018; May et al., 2018; Qin et al., 2006, 2012). In these studies, the scaled SPMS data showed good agreement with the results from reference instruments, e.g. a micro-orifice uniform deposition impactor (MOUDI), a scanning mobility particle sizer (SMPS), an aerodynamic particle sizer (APS), and other independent quantitative aerosol particle measurements, e.g. by a high-resolution time-of-flight aerosol mass spectrometer (HR-ToF-AMS). With respect to particulate chemical compounds, Gross et al. (2000) reported relative sensitivity factors (RSFs) for ammonium and alkali metal cations in a single-particle mass spectrometer to corresponding bulk concentrations and accurately determined the relative amounts of Na^+ and K^+ in sea salt particles. Jeong et al. (2011) developed a method to quantify ambient particulate species from scaled single-particle analysis. Healy et al. (2013) quantitatively determined the mass contribution of different carbonaceous particle classes to total mass and estimated the mass fractions of different chemical species, i.e.

sulfate, nitrate, ammonium, organic carbon (OC), elemental carbon (EC), and potassium determined for each particle class, by using RSFs. The resulting SPMS-derived mass concentrations of these particulate species were comparable with the reference bulk data. Similar methodologies have been used in other SPMS studies (Gemayel et al., 2017; Zhou et al., 2016). It should be noted that these field-based scaling approaches (field-based overall detection efficiency, ODE) rely on the availability of a reference instrument, and their corrections are mainly class-independent.

Many previous studies have also compared single-particle classes and bulk species (Dall'Osto et al., 2009, 2012, 2013, 2016; Dall'Osto and Harrison, 2012; Decesari et al., 2011, 2014; Drewnick et al., 2008; Gunsch et al., 2018; Pratt et al., 2010, 2011; Pratt and Prather, 2012). Some studies compared ion intensities from single-particle data (Bhave et al., 2002) or specific ion ratios, such as nitrate / sulfate (Middlebrook et al., 2003), OC/EC (Spencer and Prather, 2006), and EC/(EC + OC) (Ferge et al., 2006), carbonaceous / (carbonaceous + sulfate) (Murphy et al., 2006) with the other bulk data. Hatch et al. (2014) used m/z 36 C_3^+ as a pseudo-internal standard to normalize the secondary inorganic and organic peak areas in organic-rich particles, resulting in good correlation with the independent AMS measurements. Similarly, Ahern et al. (2016) used the peak area ratio of organic matter marker at m/z 28 CO^+ to EC markers ($C_2 - {}_5^+$) to account for laser shot-to-shot variability and demonstrated a linear relationship between normalized organic intensity and secondary organic aerosol (SOA) coating thickness on soot particles. A normalized or relative peak area (RPA) method was suggested by Hatch et al. (2014) to account for shot-to-shot variability of laser intensities. Although the LDI matrix effects cannot be completely overcome by the aforementioned method, some examples for good comparisons between single-particle and bulk measurements were shown.

In this study we aim to quantify mass contributions of different particle classes based on single-particle measurements only by employing overall detection efficiencies determined in systematic laboratory studies. As a test case ambient aerosol particles were analysed in summer 2016 at a rural site in the upper Rhine valley of Germany, using a LAAPTOF and a HR-ToF-AMS. Seven major particle classes were identified by a fuzzy c-means analysis among a total of $\sim 3.7 \times 10^5$ measured single particles. Based on laboratory-determined size-dependent overall detection efficiencies (ODEs) of LAAPTOF for different reference particle types, mass contributions for individual aerosol particles could be estimated. Aerosol particle mass concentrations determined independently by LAAPTOF and AMS are compared, and potentially useful relationships of specific ion intensity ratios of LAAPTOF and AMS are discussed.

2 Methods

2.1 Measurement location and instrumentation

The measurements were made as part of the TRAM01 campaign at a rural site in the upper Rhine valley from 15 July to 1 September 2016 next to the tram line north of the village of Leopoldshafen, Germany (49°6′10.54″ N, 8°24′26.07″ E). This location is about 12 km north of the city of Karlsruhe, with 300 000 inhabitants and significant industry including a power plant and refineries (Hagemann et al., 2014). Ambient particles were sampled for mass spectroscopic analysis with a flow rate of $1\,m^3\,h^{-1}$ through a $PM_{2.5}$ inlet (SH 2.5 − 16, Comde-Derenda GmbH) and vertical stainless steel tubes. A total suspended particulate (TSP) inlet (Comde-Derenda GmbH) was used for instruments for particle physical characterization. Trace gases were sampled via an 8 mm PFA sampling tube. All sampling inlets were positioned 1.5 m above a measurement container and 3.7 m a.g.l. To study the nature and to identify possible sources of the particles in this area, their number, size, chemical composition, and associated trace gases, as well as meteorological conditions, were measured using the following instruments: condensation particle counters (CPC3022A, CPC3772, TSI Inc.), an optical particle counter (FIDAS, PALAS GmbH), an aethalometer (AE33-7, Magee Scientific), an ozone monitor (O341M, Environment SA), a SO_2 monitor (AF22M Environment SA), a NO_2 monitor (AS32M, Environment SA), a CO_2 monitor (NGA2000, Rosemont Inc.), and meteorology sensors (WS700 & WS300, Lufft GmbH). From 26 July to 31 August, the following mass spectrometers were in operation: a high-resolution time-of-flight aerosol mass spectrometer (HR-ToF-AMS; Aerodyne Inc.) and a laser ablation aerosol particle time-of-flight mass spectrometer (LAAPTOF; AeroMegt GmbH), providing real-time information on size and mass spectral patterns for bulk samples and individual particles, respectively.

The HR-ToF-AMS yields quantitative information (mass concentration) on size-resolved particle bulk chemical composition with high time resolution and high sensitivity (DeCarlo et al., 2006). Briefly, aerosols are sampled with a flow rate of $\sim 84\,cm^3\,min^{-1}$ via an aerodynamic lens, which focuses particles with sizes of 70 to 2500 nm (vacuum aerodynamic diameter, d_{va}) into a narrow beam. The particle beam passes through a sizing chamber where the particles' size is determined. Afterwards, particles encounter a 600 °C heater that vaporizes the non-refractory species. The vapours are ionized by electron impact (electron energy: 70 eV). The generated positive ions are analysed by a time-of-flight mass spectrometer. Particles can bounce off the heater/vaporizer, leading to an underestimation of ambient mass concentrations measured by AMS. Collection efficiencies (CEs) are used to correct for this (CE is the product of net particle transmission and detection efficiency) (Canagaratna et al., 2007). It is important to note that the CE can vary depending on

composition and phase of the particles (Bahreini et al., 2005). In this study, we applied a CE value of 0.5. This is in agreement with previous studies (Canagaratna et al., 2007; Middlebrook et al., 2012) and close to a composition-dependent CE calculated for this measurement campaign by Huang et al. (2019).

The LAAPTOF is a commercially available SPMS and has been described elsewhere (Ahern et al., 2016; Gemayel et al., 2016; Marsden et al., 2016; Ramisetty et al., 2018; Reitz et al., 2016; Shen et al., 2018; Wonaschuetz et al., 2017). In brief, aerosols are sampled with a flow rate of $\sim 80\,\mathrm{cm^3\,min^{-1}}$ via an aerodynamic lens, focusing and accelerating particles in a size range between 70 and 2500 nm d_{va}. Afterwards, they pass through the detection chamber with two diode laser beams ($\lambda = 405$ nm). Particles smaller than 200 nm and larger than 2 μm are difficult to detect, due to weak light scattering by the smaller particles and due to a larger particle beam divergence for the larger particles. Once a single particle is detected successively by both of the detection lasers, its aerodynamic size is determined and recorded based on its time of flight, and an excimer laser pulse ($\lambda = 193$ nm) is fired for a one-step desorption/ionization of the refractory and non-refractory species of the particle. The resulting cations and anions are analysed by a bipolar time-of-flight mass spectrometer, resulting in mass spectra with unit mass resolution. Thus, for each individual particle, its size and a pair of positive and negative mass spectra are measured.

2.2 Single-particle identification and quantification methods for LAAPTOF data

The general data analysis procedures for particle spectral and size information were described in full detail in our previous study (Shen et al., 2018). In brief, spectral data are classified by a fuzzy c-means clustering algorithm embedded in the LAAPTOF data analysis Igor software (Version 1.0.2, AeroMegt GmbH) to find the major particle classes. Afterwards, we can obtain particle-class-resolved size (d_{va}) distribution and the representative spectra, which will be correlated with laboratory-based reference spectra. The resulting correlations together with marker peaks (characteristic peaks arising from the corresponding species) and some typical peak ratios, e.g. isotopic ratio of potassium, are used to identify the particle classes. Here, we extend this approach to quantify particle class mass contributions using a large ambient sample as test case.

The fuzzy c-means clustering approach has the advantage of allowing particles to belong to multiple classes based on the similarity of the mass spectra (Reitz et al., 2016), namely attributing one spectrum (particle) to multiple clusters (particle classes). The similarity metric is Euclidian distance between the spectral data vectors and a cluster centre (Hinz et al., 1999; Reitz et al., 2016). In our study, the fuzzy-clustering-derived fraction for each particle class is the de-

gree of similarity between aerosol particles in one particular class, rather than a number percentage. Thus, we can obtain similarity information for the whole data set rather than a single particle (Hinz et al., 1999; Reitz et al., 2016). One drawback is that the individual particles are not directly assigned to individual particle classes, which hinders a direct class-dependent quantification of particle mass. In order to quantify particle mass, we first need to assign a particle class to every individual particle, which is achieved by correlating the individual bipolar mass spectra with the representative fuzzy class spectra using Pearson's correlation coefficient (γ). Since the positive LAAPTOF spectra are more characteristic than the negative ones (Shen et al., 2018), the threshold value for the positive spectra correlation was set to $\gamma_{\mathrm{pos}} \geq 0.6$, while for the negative spectra, γ_{neg} was tuned with values ranging from 0.3 to 0.8 (refer to Table S1). Individual particles are assigned to the class for which the corresponding correlation coefficients for both spectra exceed the threshold values. All corresponding correlation coefficients (γ_{pos} and γ_{neg}) are listed in Table S1. This way, we can obtain time series of particle counts, which have good ($\gamma > 0.6$) or strong correlation ($\gamma > 0.8$) with the fuzzy results. The corresponding correlation coefficients are also listed in Table S1, and typical examples are shown in Fig. S1. With this method, we were able to successfully classify 96 % of the measured particles. Once the class information for individual particles has been determined, we are able to calculate single-particle geometric size, volume, and mass as described in the following.

For simplicity, we assume the particles are spherical with a shape factor (χ) of 1; thus particle geometric diameter (d_{p}), volume (V_{p}), and mass (m_{p}) can be obtained from the following equations:

$$d_{\mathrm{p}} = d_{\mathrm{m}} = \frac{d_{\mathrm{va}}}{\rho_{\mathrm{eff}}} \times \rho_0 \left(\chi = 1; \rho_{\mathrm{p}} = \rho_{\mathrm{eff}} \right)$$

$$\text{(DeCarlo et al., 2004)} \tag{1}$$

$$V_{\mathrm{p}} = \frac{1}{6} \times \pi \times d_{\mathrm{p}}^{\,3} \tag{2}$$

$$m_{\mathrm{p}} = V_{\mathrm{p}} \times \rho_{\mathrm{eff}}, \tag{3}$$

where d_{m} is the electrical mobility diameter, d_{va} is the vacuum aerodynamic diameter measured by LAAPTOF, ρ_0 is the standard density ($1\,\mathrm{g\,cm^{-3}}$), ρ_{p} is the particle density, and ρ_{eff} is the effective density. It should be noted that in some previous studies, the particle shapes were also assumed to be spherical, and uniform particle densities ranging from ~ 1.2 to $1.9\,\mathrm{g\,cm^{-3}}$ were applied for total aerosol particle mass quantification (Allen et al., 2000, 2006; Ault et al., 2009; Gemayel et al., 2017; Healy et al., 2012, 2013; Jeong et al., 2011; Wenzel et al., 2003; Zhou et al., 2016). In our study, we have determined an average density of $1.5 \pm 0.3\,\mathrm{g\,cm^{-3}}$ for all ambient particles, based on a comparison between d_{va} measured by AMS and d_{m} measured by SMPS. However, the density for different types of ambient particles varies,

especially for fresh ones (Qin et al., 2006). Particle densities varied during the campaign (Fig. S2), and the representative mass spectra of different particle classes indicate chemical inhomogeneity. In order to reduce the uncertainty induced by the assumption of a uniform density, we assigned specific effective densities (derived from d_{va}/d_m) from literature data to each particle class. A density of $2.2\,\mathrm{g\,cm^{-3}}$ was used for calcium-nitrate-rich particles (Zelenyuk et al., 2005), $1.25\,\mathrm{g\,cm^{-3}}$ for aged soot rich in ECOC and sulfate (Moffet et al., 2008b; Spencer et al., 2007), $2.1\,\mathrm{g\,cm^{-3}}$ for sodium salts (Moffet et al., 2008b; Zelenyuk et al., 2005), $1.7\,\mathrm{g\,cm^{-3}}$ for secondary-inorganic-rich particles (Zelenyuk et al., 2005, 2008), $2.0\,\mathrm{g\,cm^{-3}}$ for aged-biomass-burning particles (Moffet et al., 2008b), and $2.6\,\mathrm{g\,cm^{-3}}$ for dust-like particles (Bergametti and Forêt, 2014; Hill et al., 2016). These densities were used for the individual particles of each class without size dependence. Similar chemically resolved densities have also been used in some previous studies (Gunsch et al., 2018; May et al., 2018; Qin et al., 2006, 2012).

Furthermore, the single-particle identification allows for correcting the particle number counts by using the overall detection efficiency (ODE), which depends strongly on particle size and type (Allen et al., 2000; Dall'Osto et al., 2006; Qin et al., 2006; Shen et al., 2018). In a previous publication, we defined ODE as the number of bipolar mass spectra obtained from the total number of particles in the sampled air, described how to generate the laboratory-derived ODE, and discussed the factors influencing ODE in detail (Shen et al., 2018). Our ODE accounts for both physical and chemical factors (e.g. particle size and types shown in Fig. 1). However, we did not determine relative sensitivity factors for individual chemical compounds. As shown in Fig. 1, we have determined ODEs for several particle types, from particles consisting of pure compounds to the more realistic ones including major ambient particles (refer to Fig. 1). For simplicity and in order to account for different types of ambient particles, we averaged the ODE determined for ammonium nitrate, sodium chloride, PSL particles, and some other particles, e.g. agricultural soil dust, sea salt, and organic acids, as well as secondary organic aerosol particles measured in the lab. The mean ODEs with uncertainties as a function of particle size (d_m) are shown in Fig. 1. However, using a mean ODE will obviously lead to some bias. For example, if we apply ODE mean values to all the ambient particles, the number of ammonium-nitrate-rich particles will be overestimated due to the higher ODE of ammonium nitrate, while the ammonium-sulfate-rich, sea salt particles, and some organic-rich particles will be underestimated. Therefore, we used reference particle ODE values to estimate the size-dependent ODE values for the particle classes observed in the field as follows. ODE values for ammonium nitrate and sodium chloride were used to fit ODE curves for secondary-inorganic-rich and sodium-salt-like particles, respectively. The mean ODE values from all reference particles were used for the class of aged soot particles since they showed best agreement

with the reference soot particles (refer to Fig. 1). For the same reason, the minimum ODE curve from all reference particles was used for all dust-like particle classes. It should be noted that dust-like particles were often mixed with other species such as organics (e.g. biomass burning–soil particles; refer to Sect. 3.1) and that they likely have dust-core-shell structures (Goschnick et al., 1994). We assume that their detection is dominated by the dust core as it significantly influences the light scattering (size) and the particle beam divergence (shape).

The chemically resolved ODE could also bring some bias due to the complex particle matrix. For instance, if ammonium sulfate is internally mixed with ammonium nitrate, LAAPTOF can detect both of them with good efficiency. This has been verified in our laboratory, and the matrix effect has been discussed in our previous study (Shen et al., 2018). As shown in Fig. 1, ODEs for ammonium nitrate are at a higher level, while ODEs for sodium chloride are relatively low. This could lead to an underestimation and overestimation of secondary-inorganic-rich and sodium salt particles, respectively. ODEs from reference particles with low detection efficiency were applied to dust-like particles. This may lead to an overestimation of their concentration if they are mixed with better detectable species. Mean ODE values were applied to soot particles which may lead to an overestimation if they were, e.g. coated. This is because even non-absorbing species, e.g. organics, can refract light towards the absorbing black carbon core, increasing light absorption (Ackerman and Toon, 1981). Since most of the particle classes consist of mixtures of the poorly detectable types with better detectable types, this seems to partially compensate for the limitation of LAAPTOF to detect certain particle types as evident by comparison with the AMS mass concentrations (refer to Sect. 3.2).

As shown Fig. 1, we determined ODE values for mobility equivalent particle sizes (d_m) ranging from 300 to 1 μm. The ODE decreases significantly for larger particles because of increasing particle beam divergence. We assume ODEs for supermicron particles to follow the decreasing trend illustrated in Fig. 1. Please note that LAAPTOF cannot measure particles larger than a d_{va} of 2.5 μm, which corresponds to a d_m of 1.0 to 1.5 μm, assuming effective particle densities of 1.7 to $2.6\,\mathrm{g\,cm^{-3}}$ for different ambient particle classes, respectively. Hence, a large fraction of the ambient particles measured by LAAPTOF could be number-corrected by using our laboratory-derived ODEs.
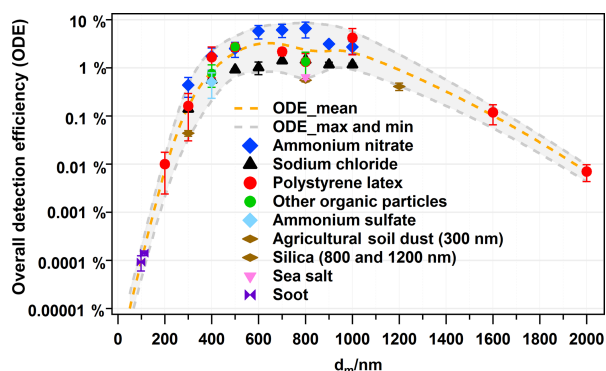
Figure 1. Overall detection efficiency of LAAPTOF for different types of particles as a function of the mobility diameter (d_m), adapted from Shen et al. (2018) and extended. Dashed lines are fitting curves for maximum, mean, and minimum values of ODE. For other organic particles (green), ODE at 400 nm is the data from secondary organic aerosol (SOA) particles from α-pinene ozonolysis, ODE at 500 nm is the data from humic acid, and ODE at 800 nm is the data from humic acid ($1.9 \pm 0.3\,\%$), oxalic acid ($0.3 \pm 0.1\,\%$), pinic acid ($1.6 \pm 0.1\,\%$), and cis-pinonic acid ($1.9 \pm 0.7\,\%$). SOA particles were formed in the Aerosol Preparation and Characterization (APC) chamber and then transferred into the AIDA chamber. Agricultural soil dust (brown symbol) was dispersed by a rotating brush generator and injected via cyclones into the AIDA chamber. Sea salt particles (purple) were also sampled from the AIDA chamber. Soot particles from incomplete combustion of propane were generated with a propane burner (RSG miniCAST; Jing Ltd.) and then injected into and sampled from a stainless steel cylinder of $\sim 0.2\,m^3$ volume. SiO_2 particles were directly sampled from the headspace of their reservoirs. The other aerosol particles shown in this figure were generated from a nebulizer and were size-selected by a DMA. Note that there is uncertainty with respect to particle size due to the particle generation method. The nebulized and DMA-sized samples have relative smaller standard deviation (SD) from Gaussian fitting to the measured particle sizes. PSL size has the smallest size SD (averaged value is 20 nm), and the corresponding relative SD (RSD = SD divided by the corresponding size) is $\sim 6\,\%$, since the original samples are with certain sizes. The other nebulized samples have standard deviations ranging from 70 to 120 nm SD and 3 % to 23 % RSD. Particles sampled from the AIDA chamber have a much bigger size SD: ~ 70 nm for SOA (17 % RSD), ~ 100 nm for agricultural soil dust ($\sim 83\,\%$ RSD), and ~ 180 nm for sea salt particles ($\sim 34\,\%$ RSD). Considering this uncertainty, we have chosen a size segment of 100 nm (± 50 nm) for correction; e.g. particles with sizes of 450 to 550 nm will use the ODE at 500 nm particle number correction.

The equations for correction and calculation of mass concentration are as follows:

$$\text{counts}_{\text{corrected}} = 1/\text{ODE}_{\text{size-resolved and chemically resolved}} \quad (4)$$

$$\text{mass}_{\text{corrected}} = \text{counts}_{\text{corrected}} \times m_p \quad (5)$$

mass concentration =

$$\text{total mass}/(\text{sample flow rate} \times \text{time}), \quad (6)$$

where ODE_{d_m} is the mean ODE that depends on d_m, $\text{counts}_{\text{corrected}}$ and $\text{mass}_{\text{corrected}}$ are the corrected particle

number counts and mass at each time point, and the sample flow rate is $\sim 80\,cm^{-3}\,min^{-1}$. Using Eqs. (4) to (6) we can calculate the corrected number and mass fractions.

The aforementioned assumptions and the related uncertainties in particle mass are summarized as follows: (1) ambient particles are spherical with a shape factor $\chi = 1$. However, several ambient particle types are non-spherical with a shape factor χ not equal to 1, e.g. $\chi_{\text{NaCl}} = 1.02$–$1.26$ (Wang et al., 2010) and $\chi_{\text{NH}_4\text{NO}_3} = 0.8$ (Williams et al., 2013). This can cause uncertainties of 26 % and 20 % for the particle diameter and 100 % and 50 % for the particle mass of sodium-chloride-like and ammonium-nitrate-like particles, respectively. For soot-like particles, the shape-caused uncertainty could be even larger, due to their aggregate structures. Such an uncertainty is difficult to reduce, since we do not have particle shape information for individual particles. However, using effective densities may at least partially compensate for some of the particle-shape-related uncertainties. (2) Particles in the same class have the same density, which is likely to vary and lead to an uncertainty hard to estimate. (3) The variability of the ODE values (refer to Fig. 1) depends on particle size and type. It reaches values ranging from $\pm 100\,\%$ for 200 nm particles to $\pm 170\,\%$ for 800 nm size particles.

Hence, the overall uncertainty in particle mass according to the assumptions is $\sim 300\,\%$, with the ODE-caused uncertainty being dominant. This is because (1) the aforementioned particle matrix effects may cause higher or lower ODEs than their surrogates generated in the laboratory. In addition, the more complex morphology and various optical properties of ambient particles can have a strong impact on their ODE (Shen et al., 2018). (2) Instrumental aspects such as alignment and variance in particle-laser interaction lead to uncertainty in ODE. They are included in the uncertainties given in Fig. 1, for which repeated measurements after various alignments were used. The fluctuations of particle-laser interactions can be reduced by using a homogeneous laser desorption and ionization beam (Wenzel and Prather, 2004) or delayed ion extraction (Li et al., 2018; Vera et al., 2005; Wiley and Mclaren, 1955). Note that we used the same sizing laser and desorption/ionization laser pulse energy (4 mJ) in the field as those used for generating ODE and aligned the instrument in the field with the similar procedures as we did in the lab. During our field measurements we did calibrations of the LAAPTOF with PSL particles of 400, 500, 700, and 800 nm d_m, resulting in ODE values with no significant difference compared to the ODE values determined in the laboratory. This finding reflects the good stability of the LAAPTOF performance in the temperature-controlled container. Actually, once the LAAPTOF adjustments were optimized after transport, no further adjustments were necessary during the 6 weeks of the campaign. Moreover, it is important to note that the ODE curve applied herein should not be extrapolated to other LAAPTOF or SPMS instruments without a standard check against, e.g. PSL particles. In order to evaluate our quantification approach, we will compare the particle

mass estimated based on single-particle measurements with AMS total mass in Sect. 3.2.

It is noteworthy that the major difference between our quantification method and previous SPMS studies is that our ODE is based on elaborate laboratory work, while previous studies typically used field-based scaling approaches (field-derived ODE).

3 Results and discussion

3.1 Identification of particle classes and the internal mixing

During the 6-week measurement campaign, we obtained $\sim 3.7 \times 10^5$ bipolar LAAPTOF spectra for single particles. Seven major particle classes were found using fuzzy c-means classification. The corresponding representative spectra with marker peaks' assignment are shown in Fig. 2. Considering some weak but characteristic peaks, we show the spectra with a logarithmic scale. The linearly scaled spectra (refer to Fig. S3 in the Supplement) are provided for comparison in the supporting information. Furthermore, Fig. 3 shows the size-resolved number fraction for the seven particle classes measured during the field campaign TRAM01, based on fuzzy classification according to the fuzzy c-means clustering algorithm as well as the overall size distribution for all particles measured by LAAPTOF during the campaign. Signatures for organic and secondary inorganic compounds can be observed in each class, i.e. for organics m/z 24 C_2^-, 25 C_2H^-, 26 C_2H_2/CN^-, and 42 C_2H_2O/CNO^-, for sulfate 32 S^-, 64 SO_2^-, 80 SO_3^-, 81 HSO_3^-, 97 HSO_4^-, 177 $SO_3HSO_4^-$, and 195 $HSO_4H_2SO_4^-$, for nitrate 30 NO^+, 46 NO_2^-, and 62 NO_3^-, and for ammonium 18 NH_4^+ and 30 NO^+. Similar species were previously identified offline in the same region (Faude and Goschnick, 1997; Goschnick et al., 1994). Note that 30 NO^+ can not only originate from nitrate (majority), but also from ammonium (Murphy et al., 2006; Shen et al., 2018). Besides, m/z 24 C_2^- could also be related to elemental carbon (EC). In this case, m/z 24$^-$ should actually show a higher intensity than m/z 26$^-$, and further EC markers ($C_n^\pm$) should show up as well. Although different particle classes have similar fragments, they show characteristic patterns with several intensive marker peaks in the corresponding spectra, which can also be identified using reference spectra (Shen et al., 2018).

After fuzzy classification each particle was tested for its similarity to the different particle classes. Although a similarity is not equal to the number fraction, they are related. A higher similarity of the total aerosol particles to one class indicates that a bigger number fraction of this class may be expected once the individual particles are assigned to it. As shown in Fig. 4a, the highest similarity (43.5 % of all particles) is found to class 3, which is named sodium salts due to its strong correlation ($\gamma \geq 0.8$) with Na salts (refer

to Fig. 5). The spectra of this class in our study feature marker peaks arising from $NaNO_3$ (m/z 115 $Na(NO_2)_2^-$, 131 $NaNO_2NO_3^-$, and 147 $Na(NO_3)_2^-$), Na_2SO_4 (m/z 165 $Na_3SO_4^+$), and NaCl (m/z 81/83 Na_2Cl^+, 139/141 $Na_3Cl_2^+$, 35/37 Cl^-, and 93/95 $NaCl_2^-$) (refer to Fig. 2). These signature peaks were also observed for Na-related particle types such as aged sea salt, Na-containing dust, and Na/K-sulfate-rich particles in the other SPMS studies (Gard et al., 1998; Gaston et al., 2011; Jeong et al., 2011; May et al., 2018; Middlebrook et al., 2003; Schmidt et al., 2017). In the positive spectra of class 3, there is a nitrogen-containing organic compound marker at m/z 129 $C_5H_7NO^+$, which could originate from the OH oxidation of volatile organic compounds (VOCs) in the presence of NO_x on the seed particles, since the same peak was observed during simulation chamber studies with OH radicals reacting with α-pinene and/or toluene in the presence of NO_x. Besides, peaks at m/z 149 $C_4H_7O_2NO_3^+$ and 181 $C_4H_7O_4NO_3^+$ are associated with organonitrates that can form from the oxidation of VOCs in the presence of NO_x (Perring et al., 2013) and are expected to increase the light absorbing capability of the particles (Canagaratna et al., 2007). Huang et al. (2019) showed that organonitrates contributed to particle growth during night-time at this location. This class accounts for the largest fraction in the size range from 1000 to 2500 nm d_{va} (refer to Fig. 3). The size distribution of class 3 particles was dominated by two modes centred at about 1400 and 2000 nm d_{va}, indicating two sub-particle populations in this class. Goschnick et al. (1994) did offline depth-resolved analysis of the aerosol particles collected north of Karlsruhe in the upper Rhine valley and observed sodium chloride in both fine and coarse particles, while sodium nitrate was mainly enriched in the coarse mode. This hints at possible sub-class assignments, which are likely to be fresh and aged sea salts. However, the measurement site is relatively far away from the sea (e.g. the North Atlantic Ocean is ~ 800 km away). Therefore, we need more evidence, such as back trajectory analysis or other transport modelling, to prove that this class is really fresh and/or aged sea salt. This will be discussed in a separate study.

A total of 20.8 % of the total particle population belongs to class 4 (secondary inorganics–amine). This class has the most prominent secondary inorganic signature and strongest correlation with the reference spectra for homogeneous mixtures of NH_4NO_3 and $(NH_4)_2SO_4$. In addition, it features marker peaks for amines at m/z 58 $C_2H_5NHCH_2^+$, 59 $(CH_3)_3N^+$, 86 $(C_2H_5)_2NCH_2^+$, 88 $(C_2H_5)_2NO/C_3H_6NO_2^+$, and 118 $(C_2H_5)_2NCH_2^+$, which were also identified by SPMS in the other field and lab studies (Angelino et al., 2001; Dall'Osto et al., 2016; Healy et al., 2013; Jeong et al., 2011; Köllner et al., 2017; Lin et al., 2017; Pratt et al., 2009; Roth et al., 2016; Schmidt et al., 2017). Among all the representative mass spectra for the seven particle classes, class 4 is relatively "clean" with the fewest peaks (refer to Figs. 2 and S3), indicating that these particles did not have had the time
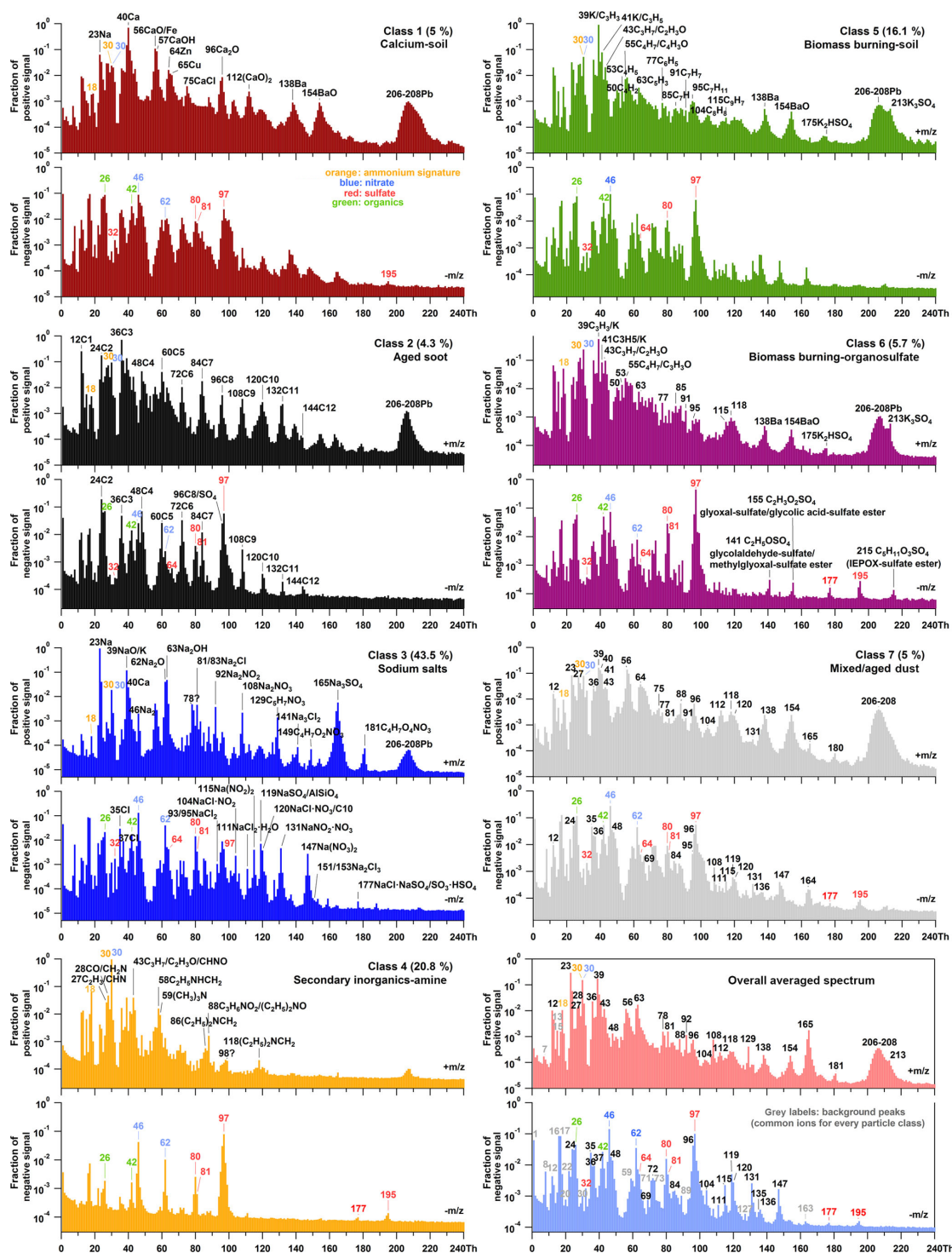
Figure 2. Representative mass spectra of seven particle classes measured during the field campaign TRAM01, based on fuzzy classification according to the fuzzy c-means clustering algorithm, and averaged spectrum of a total of $\sim 3.7 \times 10^5$ single particles measured. The percentage in each pair of spectra gives us information about the similarity of the total aerosol particles to different classes. Black labels represent the ions characteristic for different classes. The red, blue, and orange labels represent the signatures for sulfate (32 S^-, 64 SO_2^-, 80 SO_3^-, 81 HSO_3^-, 97 HSO_4^-, 177 $SO_3HSO_4^-$, and 195 $HSO_4H_2SO_4^-$), nitrate (30 NO^+, 46 NO_2^-, and 62 NO_3^-), and ammonium (18 NH_4^+ and 30 NO^+). The green labels represent the organic compounds (26 C_2H_2/CN^- and 42 C_2H_2O/CNO^-). In the overall averaged spectrum, grey labels represent the background fragments (common ions) that exist for every particle class.

Atmos. Meas. Tech., 12, 2219–2240, 2019   **www.atmos-meas-tech.net/12/2219/2019/**

115

Figure 3. (a) Size-resolved number fraction for seven particle classes measured during the field campaign TRAM01, based on fuzzy classification according to the fuzzy *c*-means clustering algorithm. **(b)** Overall size distribution for the particles measured by LAAPTOF during the whole campaign.

to uptake other components. Hence, most likely they were formed not very long ago by conversion of their precursors. The secondary inorganic–amine particles have a rather narrow size distribution in the range between 500 and 1000 nm d_{va} (refer to Fig. 3).

Aged-biomass-burning and soil-dust-like particles (class 5: biomass burning–soil) comprise 16.1 % of all particles according to the similarity of the mass spectra. It has the most prominent peak at m/z 39 $K/C_3H_3^+$ and aromatic marker peaks at 50 $C_4H_2^+$, 63 $C_5H_3^+$, 77 $C_6H_5^+$, 85 C_7H^+, 91 $C_7H_7^+$, 95 $C_7H_{11}^+$, 104 $C_8H_8^+$, and 115 $C_9H_7^+$. The ratio of m/z 39 $^+/41^+$ is ~ 11.6, which is similar to the value of (13.5 ± 0.9) measured for pure potassium-containing inorganic particles (e.g. K_2SO_4) by our LAAPTOF in the laboratory. The contribution of organic fragments is likely the reason for the slightly lower value, as this ratio was determined to be ~ 8 for humic acid and ~ 1.1 for α-pinene SOA (Shen et al., 2018). Hence, we assign the signal at m/z 39$^+$ mainly to potassium. The aromatic signature was observed by the other SPMS (Dall'Osto and Harrison, 2012; Schmidt et al., 2017; Silva and Prather, 2000). As suggested by previous studies, such potassium-rich particles can originate from biomass burning and are often mixed with sulfate and/or nitrate (Gaston et al., 2013; Lin et al., 2017; Middlebrook et al., 2003; Moffet et al., 2008a; Pratt et al., 2010; Qin et al., 2012; Roth et al., 2016; Schmidt et al., 2017). This is also the case for class 5 particles that exhibit a characteristic peak at m/z 213 $K_3SO_4^+$. Note that we also denoted this class as soil-dust-like particles based on the correlation diagram (Fig. 5), although there are no obvious marker ions visible. It is correlated well ($\gamma \geq 0.6$) with reference spectra of dust particles, especially

agricultural soil dust. The weak spectral signal might be due to the core-shell structure of the particles (Pratt and Prather, 2009). In fact, previous studies identified soil dust as the particle type dominating the coarse particles sampled in the same region (Faude and Goschnick, 1997; Goschnick et al., 1994). Goschnick et al. (1994) found a core-shell structure in both submicron and coarse particles collected north of the city of Karlsruhe in the upper Rhine valley. This supports our hypothesis. In addition, similar to class 3, class 5 also has two modes in its size distribution centred at about 500 and 800 nm d_{va}. Such potential sub-classes will be further analysed in the future.

Particle class 6 contains 5.7 % of all particles, and they have sizes ranging from 400 to 1000 nm d_{va}. This class is named biomass burning–organosulfate, short for aged-biomass-burning and organosulfate-containing particles. It also shows biomass burning markers such as m/z 213 $K_3SO_4^+$ and features organosulfates at m/z 141 $C_2H_5OSO_4^-$, 155 $C_2H_3O_2SO_4^-$, and 215 $C_5H_{11}OSO_4^-$, which are consistent with signals from sulfate esters of glycolaldehyde/methylglyoxal, glyoxal/glycolic acid, and isoprene epoxydiols (IEPOX), respectively, observed by other SPMS in field measurements (Froyd et al., 2010; Hatch et al., 2011a, b). Unfortunately, we do not have laboratory-based reference spectra for organosulfate particles. Such reference values could be very useful for a further analysis. The ratio of m/z 39$^+/41^+$ of ~ 6.7 is closer to organics rather than to potassium. However, we cannot rule out a significant potassium contribution. In addition, this class features a specific pattern of m/z 39$^+$, 41$^+$, and 43$^+$ (which have much higher intensities than their interstitial peaks at m/z 40$^+$ and 42$^+$) and hydrocarbon and oxygenated organic fragments at m/z 53$^+$, 55$^+$, 63$^+$, 65$^+$, 67$^+$, 69$^+$, 71$^+$, 73$^+$, 81$^+$, 83$^+$, 85$^+$, 95$^+$, 97$^+$, and 99$^+$, likely from organic acids and biogenic SOA (Shen et al., 2018).

Class 1 (5.0 % of all particles) is identified as calcium–soil, short for calcium-rich and soil-dust-like particles. It contains calcium-related signatures at m/z 40 Ca^+, 56 CaO^+/Fe^+, 57 $CaOH^+$, 75 $CaCl^+$, 96 Ca_2O^+, and 112 $(CaO)_2^+$, as well as some other metal-related signatures including m/z 23 Na^+, 64/66 Zn^+, 65 Cu^+, 138 Ba^+, 154 BaO^+, and 206–208 Pb^+. Most of the signature peaks for calcium-related particles, such as Ca-rich soil dust, engine exhaust, and lake spray aerosols, were also identified by other SPMS studies (Dall'Osto et al., 2016; May et al., 2018; Roth et al., 2016). This class shows a strong correlation with nitrate and correlates well with all reference spectra of dust samples, especially soil dust (refer to Fig. 5). Class 2 (4.3 % of all particles), aged soot, is predominantly located in the small size range (200 to 600 nm d_{va}) and exhibits prominent EC patterns in mass spectra (characteristic $C_n^\pm$ progressions with up to $n = 12$) and is mixed with sulfate and nitrate. Such soot signatures are normally found in SMPS studies (Ault et al., 2010; Dall'Osto et al., 2016; Gaston et al., 2013; Middlebrook et al., 2003; Spencer and Prather, 2006). These mass
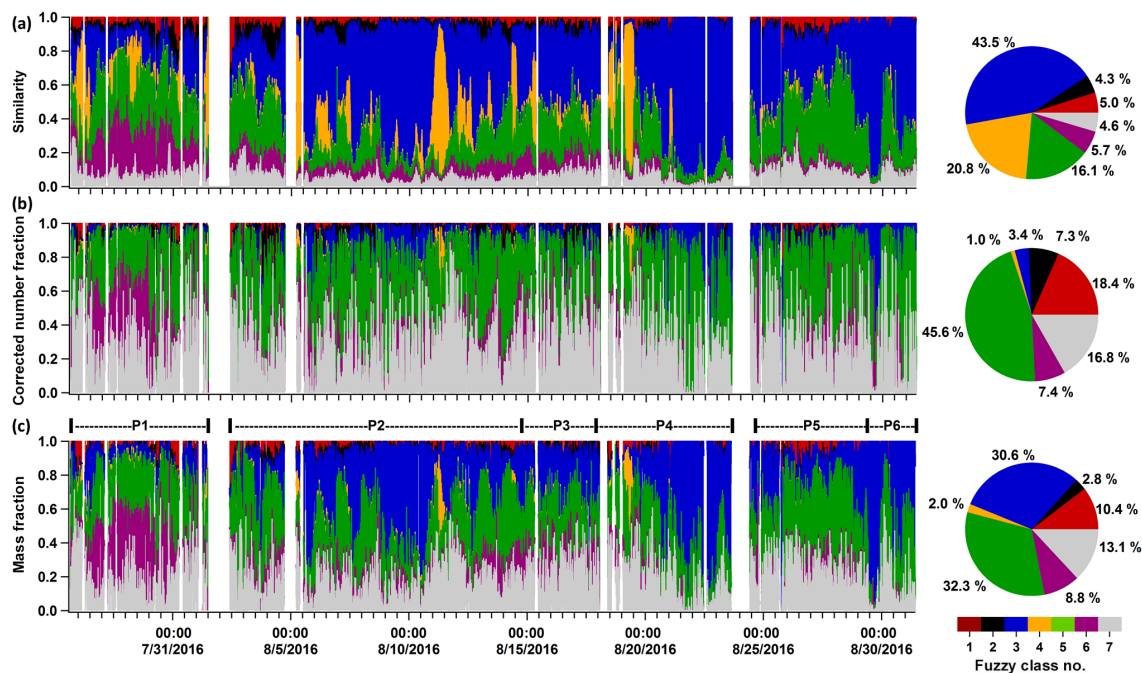
Figure 4. Time series of the similarity, corrected number fraction, and mass fraction of seven major particle classes and the corresponding pie charts for total fractions. Note that the correction shown here is based on a chemically resolved or particle-class-resolved ODE. The seven classes are class 1: calcium–soil; class 2: aged soot; class 3: sodium salts; class 4: secondary inorganics–amine; class 5: biomass burning–soil, class 6: biomass burning–organosulfate; and class 7: mixed/aged dust. In panel (c), six periods have been marked: P1 is Period 1 from 26 July 2016 16:23 to 1 August 2016 11:43, P2 from 2 August 2016 09:43 to 14 August 2016 17:53, P3 from 14 August 2016 18:03 to 17 August 2016 21:03, P4 from 17 August 2016 21:13 to 23 August 2016 15:33, P5 from 24 August 2016 15:03 to 29 August 2016 08:33, and P6 from 29 August 2016 08:43 to 31 August 2016 09:13.

spectra show a strong correlation to the reference spectra of soot particles, especially diesel soot ($\gamma = \sim 1$). Class 7 (4.6 % of all particles) is identified as mixed/aged dust, which contains no obvious characteristic features and is correlated with most of the reference spectra. It has a relatively even and broad size distribution covering the whole size range that LAAPTOF is able to measure.

We observe intensive signals at m/z 138 Ba$^+$ and 154 BaO$^+$ in class 1, 5, 6, and 7, indicating a similar source of these particle types, which all have a good correlation with mineral and soil dust particles (Fig. 5). Prominent lead markers at m/z 206$^+$ to 208$^+$ can be found in each class, except class 4, which is further evidence for these particles being relatively young. The marker peaks for lead appear broader because at higher m/z, we observe larger peak shifts that cannot be completely corrected with the existing LAAPTOF software. Note that even though we did not obtain spectra for pure ammonium sulfate or pure biogenic SOA particles in ambient air, it is still possible for such particles to be present. However, laboratory measurements show a very low sensitivity of the LAAPTOF to these types of particles, potentially due to their low absorbance at 193 nm. Due to this low instrument sensitivity for these types of particles, it is very dif-

ficult to achieve reasonable quantitative estimates about their abundance based on LAAPTOF measurements alone.

The aforementioned full and short names for seven classes, as well as their signature ion peaks, are listed in Table 1. We emphasize here that the expression "rich" as used in this study only indicates a strong signal in the mass spectra rather than a large fraction in mass, since there is no well-defined relationship between LAAPTOF spectral signal and the corresponding quantity. The sensitivities of this instrument to different species have to be established in the future.

All the laboratory-based reference spectra used in this study are publicly available via the EUROCHAMP-2020 database (https://www.eurochamp.org/default.aspx, last access: 28 March 2019). Information on newly added reference spectra is given in Table S2.

3.2 Quantification of single-particle mass and the external mixing

In this section, we estimate mass concentrations of the particle classes observed in the field. This is based on the particle identification discussed above as well as the assignment of appropriate ODE values of surrogate reference particles and on several assumptions on particle density and shape (refer to

Atmos. Meas. Tech., 12, 2219–2240, 2019   www.atmos-meas-tech.net/12/2219/2019/

117
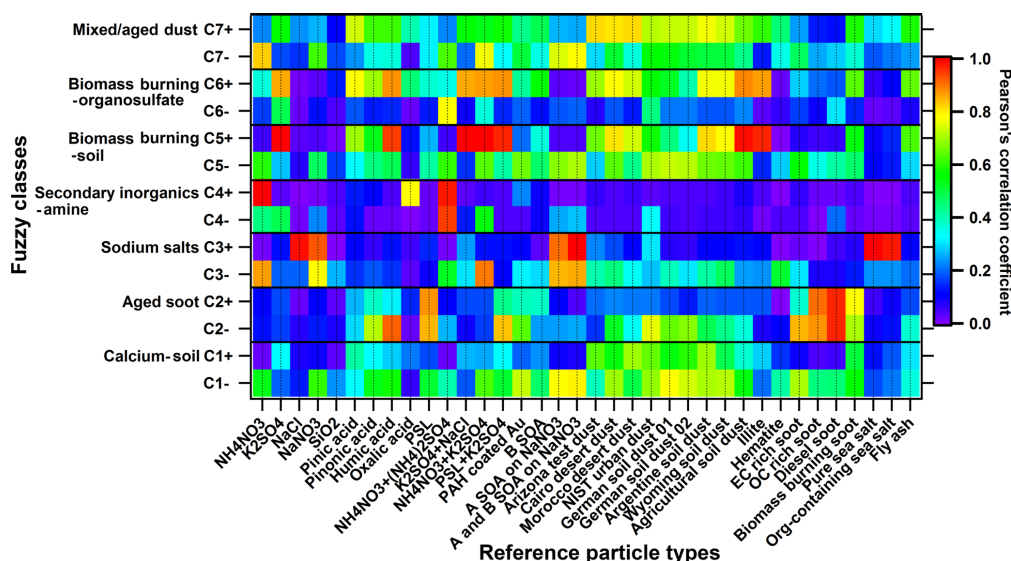
Figure 5. Correlation diagram of fuzzy classification results (seven classes, C1 to C7) and 36 laboratory-based reference spectra. Correlation results for the positive and negative spectra (e.g. for C1) are in the separated rows (e.g. C1+ and C1−). PAH is short for poly(allylamine) hydrochloride), B SOA is short for biogenic SOA (α-pinene SOA in this study), A SOA is short for anthropogenic SOA (toluene SOA in this study), and biomass burning soot is the lignocellulosic char from chestnut wood. Note that the strong and good correlations mentioned in the paper stand for Pearson's correlation coefficient $\gamma \geq 0.8$ and $\gamma \geq 0.6$, respectively. The seven classes are class 1: calcium–soil; class 2: aged soot; class 3: sodium salts; class 4: secondary inorganics–amine; class 5: biomass burning–soil; class 6: biomass burning–organosulfate; and class 7: mixed/aged dust.

Sect. 2.2). Please note that both AMS and LAAPTOF cannot measure particles larger than 2.5 μm, which can be analysed by FIDAS. FIDAS data showed that $PM_{2.5}$ accounted for majority mass of the total aerosol particles sampled through the TSP inlet ($PM_{2.5} = 73\%$ of PM_{10} and 64 % of PM_{total}, respectively). In this study, we only focus on $PM_{2.5}$ particles. The fuzzy-classification-derived similarity (Fig. 4a) can be transferred into corrected number fractions using size-resolved and chemically resolved ODE (Fig. 4b) and further transferred into mass fractions (Fig. 4c) of the seven particle classes. The corresponding time series of chemically resolved number and mass concentrations can be found in Fig. S4. Please note that the aged soot particles (class 2), which dominate the number fraction for particles below 400 nm in the fuzzy c-means analysis, comprise only a minor fraction of the total number counts in Fig. 4 because the total particle number is dominated by particles larger than 500 nm (refer to Fig. 3b). Significant changes can be observed between the similarity number fraction, the corrected number fraction, and the resulting mass fractions (cf. Fig. 4a to b to c). Compared to the similarity fraction, the number fractions of class 3, sodium salts, and class 4, secondary inorganics–amine, decrease dramatically; sodium salt particles changed from 43.5 % (similarity) to 3.4 % (corrected number fraction), and secondary inorganics–amine dramatically decreased from 20.8 % to 2.4 %, while those of the other classes increase. This is because classes 3 and 4 com-

prise mainly larger particles (class 3: d_{va} peaks at ∼ 1400 and 2000 nm corresponding to d_p ∼ 700 and 1000 nm; class 4 peaks at ∼ 680 nm d_{va} and 400 nm d_p), which have the highest ODE values. In contrast the other classes comprise mainly smaller particles ($d_{va} < 500$ nm; $d_p < 300$ nm) (refer to Fig. 3), which have a lower ODE (refer to Fig. 1). Class 5, biomass burning–soil, accounts for the second highest number fraction of the smaller particles and has a relatively high effective density. After correction, the number fraction of particles attributed to this class increased from 16.1 % to 45.0 %, corresponding to 31.8 % mass fraction, and it becomes the dominating class with respect to particle number and mass. Sodium salts are another dominating class with respect to mass (30.1 % mass fraction) due to their relatively large size. These observations demonstrate the crucial role of the corrections applied for particle mass quantification in SPMS data. Note that we can obtain similarly corrected number and mass fractions by using minimum, mean, and maximum ODE, respectively (Table S3). The observed external mixing of aerosol particles varied significantly with time, e.g. class 6, biomass burning-organosulfate, dominated both particle number and mass at the beginning of the measurements until 1 August, while class 3 dominated the mass for 5–10, 21–24, and 29–30 August, and class 4 particles peaked twice on 11–19 August (refer to Fig. 4).

As discussed above, raw LAAPTOF data overestimate the particles with higher ODE, while the ones with lower

Single Particle Characterisation of Atmospheric Aerosol Particles in Central Europe
Appendix B

Table 1. Particle class numbers, names, labels, and corresponding signature ion peaks.

Class number: name (label)	Signature ion peaks (anions are marked in italic)
Class 1: calcium-rich and soil-dust-like particles (calcium–soil)	23 Na^+, 40 Ca^+, 56 CaO/Fe^+, 57 $CaOH^+$, 64/66 Zn^+, 65 Cu^+, 75 $CaCl^+$, 96 Ca_2O^+, 112 $(CaO)_2^+$, 138 Ba^+, 154 BaO^+, 206–208 Pb^+
Class 2: aged-soot-like particles (aged soot)	$12n$ Cn^+, 206–208 Pb^+; *$12n$ Cn^-, sulfate (32 S^-, 64 SO_2^-, 80 SO_3^-, 81 HSO_3^-, 97 HSO_4^-, 177 $SO_3HSO_4^-$, 195 $HSO_4H_2SO_4^-$)*
Class 3: sodium-salt-like particles (sodium salts)	23 Na^+, 39 NaO/K^+, 40 Ca^+, 46 Na_2^+, 62 Na_2O^+, 63 Na_2OH^+, 81/83 Na_2Cl^+, 92 $Na_2NO_2^+$, 108 $Na_2NO_3^+$, 129 $C_5H_7NO_3^+$, 141 $Na_3Cl_2^+$, 149 $C_4H_7O_2NO_3^+$, 165 $Na_3SO_4^+$, 181 $C_4H_7O_4NO_3^+$, 206–208 Pb^+; *35/37 Cl^-, 93/95 $NaCl_2^-$, 104 $NaClNO_2^-$, 111 $NaCl_2H_2O^-$, 115 $Na(NO_2)_2^-$, 119 $NaSO_4/AlSiO_4^-$, 120 $NaClNO_3^-$, 131 $NaNO_2NO_3^-$, 147 $Na(NO_3)_2^-$, 151/153 $Na_2Cl_3^-$, 177 $NaClNaSO_4^-/SO_3HSO_4^-$*
Class 4: secondary- inorganics-rich and amine-containing particles (secondary inorganics–amine)	ammonium and amine (18 NH_4^+, 27 C_2H_3/CHN^+, 28 CO/CH_2N^+, 30 NO^+, 43 $C_3H_7/C_2H_3O/CHNO^+$, 58 $C_2H_5NHCH_2^+$, Amine 59 $(CH_3)_3N^+$, 86 $(C_2H_5)_2NCH_2^+$, 88 $(C_2H_5)_2NO/C_3H_6NO_2^+$, 118 $(C_2H_5)_2NCH_2^+$); *nitrate (46 NO_2^-, 62 NO_3^-), sulfate*
Class 5: aged-biomass-burning and soil-dust-like particles (biomass burning–soil)	39 $K/C_3H_3^+$, 41 $K/C_3H_5^+$, 43 $C_3H_7/C_2H_3O^+$, 50 $C_4H_2^+$, 53 $C_4H_5^+$, 55 $C_4H_4/C_3H_3O^+$, 63 $C_5H_3^+$, 77 $C_6H_5^+$, 85 C_7H^+, 91 $C_7H_7^+$, 95 $C_7H_{11}^+$, 104 $C_8H_8^+$, 115 $C_9H_7^+$, 138 Ba^+, 154 BaO^+, 175 $K_2HSO_4^+$, 206–208 Pb^+, 213 $K_3SO_4^+$; *sulfate*
Class 6: aged-biomass-burning and organosulfate-containing particles (biomass burning– organosulfate)	positive signature peaks feature biomass burning very similar to those given for class 5 *organosulfate (141 $C_2H_5OSO_4^-$, 155 $C_2H_3O_2SO_4^-$, 215 $C_5H_{11}O_3SO_4^-$)*
Class 7: mixed/aged and dust-like particles (mixed/aged dust)	contains almost all the signature peaks from the other classes

Note that "rich" used in the names stands for the strong spectral signal rather than the real mass fraction.

ODE will be underestimated. After correction of the number counts and estimation of the mass concentrations, we can compare the LAAPTOF result with the quantitative instruments such as AMS in the overlapping size range of 200 to 2500 nm d_{va}. A correction for the particles in the size range between 70 and 200 nm considering mass concentrations may be negligible since they typically contribute only a minor mass fraction. It turns out that the total mass of the particles measured by LAAPTOF is $7 \pm 3\%$ (with maximum ODE), $16 \pm 6\%$ (mean ODE), $60 \pm 24\%$ (minimum ODE), and $45 \pm 16\%$ (23 %–68 % with chemically resolved ODE) of the total AMS mass depending on the measurement periods. Two criteria were used to select characteristic time periods: a period should have a stable correlation between LAAPTOF and AMS total mass; and a period should contain special events or dominating particle classes observed by LAAPTOF and/or AMS (refer to Figs. 4c and 6). Despite the relatively large differences in the average mass con-

centrations of LAAPTOF and AMS, they show much better agreement in total mass and also good correlations during specific periods (P), such as P1, 2, 4, and 5 (refer to Figs. 6 and S5), covering ∼ 85 % of the measurement time. Hence, the large differences in the average mass concentrations are caused by larger deviations during some relatively short periods or events. Considering the fact that AMS can only measure non-refractory compounds, the good correlation between AMS and LAAPTOF gives us a hint that the species measured by AMS may mainly originate from the particles of complex mixtures of both refractory and non-refractory species. It is worth noting that the weakest correlation ($\gamma = -0.1$) is observed in P6 when LAAPTOF measured the highest fraction of sodium salt particles (especially sodium chloride) on 29 August, while AMS is unable to measure refractory species such as sodium chloride. Specifically, from 09:00 to 23:53 on 29 August, LAAPTOF and AMS tended to be slightly anti-correlated ($\gamma = -0.3$).

119
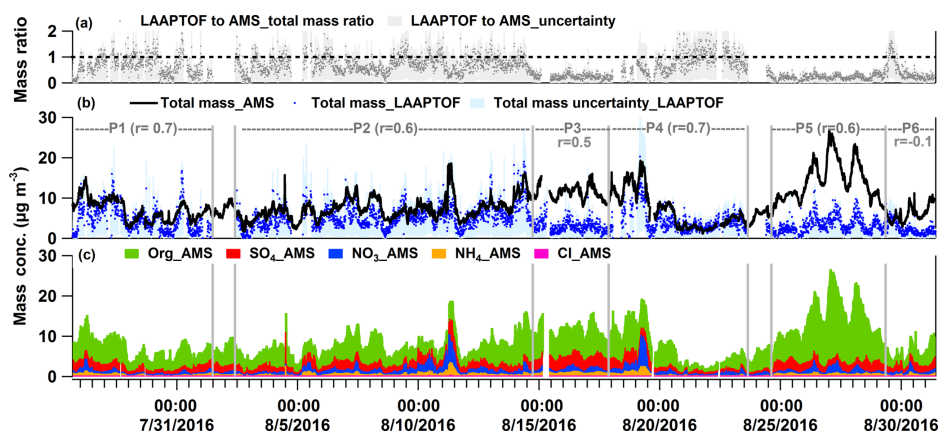
Figure 6. Time series of **(a)** total mass ratio of LAAPTOF to AMS data, **(b)** LAAPTOF total mass and AMS total mass, and **(c)** mass concentrations of organic, sulfate, nitrate, and ammonium compounds measured by AMS. In **(b)** r is Pearson's correlation coefficient between LAAPTOF and AMS results. P1 is Period 1 from 26 July 2016 16:23 to 1 August 2016 11:43, P2 from 2 August 2016 09:43 to 14 August 2016 17:53, P3 from 14 August 2016 18:03 to 17 August 2016 21:03, P4 from 17 August 2016 21:13 to 23 August 2016 15:33, P5 from 24 August 2016 15:03 to 29 August 2016 08:33, and P6 from 29 August 2016 08:43 to 31 August 2016 09:13. Close-up figures for P1, 2, 4, and 5 can be found in Fig. S5, as well as the corresponding scatter plots for LAAPTOF and AMS data comparison.
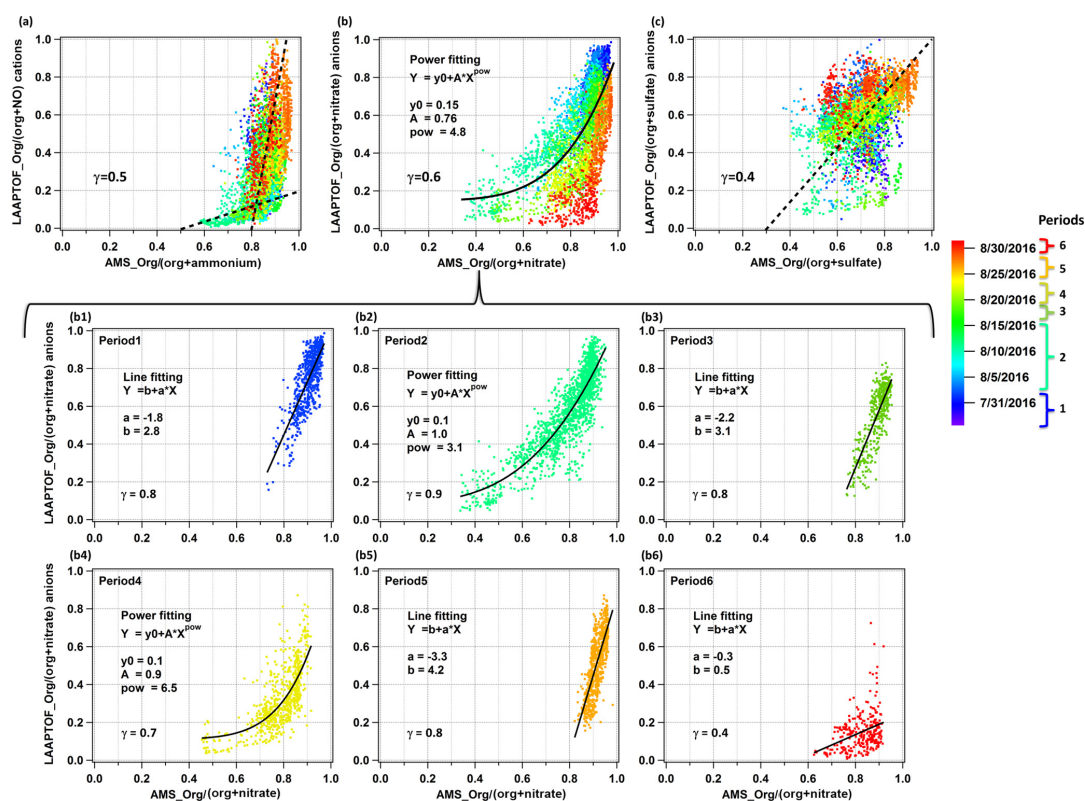
Figure 7. Comparison of non-refractory compounds measured by LAAPTOF and AMS: **(a)** LAAPTOF organic cations and NO^+ fractions org/(org + NO), **(b)** organic anions and nitrate fractions org / (org + nitrate), and **(c)** organic anions and sulfate fractions org / (org + sulfate) to the corresponding AMS mass fractions. Each point is 10 min averaged data, and there are 4483 points in each scatter plot. Dashed lines in **(a)** and **(c)** are used to guide the eyes, while the curve in **(b)** is from the fitting result. The colour scale is related to the timeline, including periods 1 to 6, the same as the ones in Fig. 6. Further comparison of org / (org + nitrate) during six periods are in the scatter plots (b1) to (b6).

As shown in Fig. 6a, the mass ratio of LAAPTOF to AMS has its lower values in P3 and P5 when the AMS organic mass concentration is higher than in most of the other periods. Although LAAPTOF data show a good correlation with the AMS data, e.g. for period P5, they obviously miss a large mass fraction of most likely smaller organic particles. The corresponding chemically resolved size distributions of particles measured by AMS are given in Fig. S6. This may be due to an insufficient representation of this kind of organic-rich particles in the particles classes identified initially. Even using reference spectra of organic particles, it was not possible to identify a number of those particles sufficient to close this gap. In addition, during the whole campaign the sulfate mass fraction measured by AMS is largest in P3 (refer to Fig. 6c). However, the LAAPTOF is not sensitive to some sulfate salts, e.g. pure ammonium sulfate (Shen et al., 2018); thus it is likely that such particles were dominating in P3, which resulted in a weaker correlation between these two instruments. Relatively pure ammonium sulfate was also suggested to be a "missing" particle type in the other SPMS field studies (Erisman et al., 2001; Stolzenburg and Hering, 2000; Wenzel et al., 2003), and Thomson et al. (1997) showed in a laboratory study that pure ammonium sulfate particles were difficult to measure using LDI at various wavelengths.

3.3   Correlation of AMS and LAAPTOF results for non-refractory compounds

Considering the different capabilities of LAAPTOF and AMS, we did not apply the relative sensitivity factor (RSF) method (Healy et al., 2013; Jeong et al., 2011). We analysed our LAAPTOF and AMS data independently and compared them thereafter. For LAAPTOF data, we used relative ion intensities (each ion peak intensity is normalized to the sum of all or selected ion signals; positive and negative ions were analysed separately), similar to the relative peak area (RPA) method suggested by Hatch et al. (2014). As shown in Fig. S7a, m/z 30 NO^+ measured by LAAPTOF has a good correlation ($\gamma = 0.6$) with ammonium measured by AMS, but LAAPTOF m/z 18 NH_4^+ does not show this ($\gamma = 0.3$, not shown in the figure). This was also found by Murphy et al. (2006) for another single-particle mass spectrometer, PALMS, which also uses an excimer laser with the same wavelength for ionization as that in the LAAPTOF. For nitrate (panel b: sum of the marker peaks at m/z 46 NO_2^- and 62 NO_3^-), sulfate (panel c: sum of m/z 32 S^-, 64 SO^-, 80 SO_3^-, 81 HSO_3^-, 96 SO_4^-, 97 HSO_4^-, 177 $SO_3HSO_4^-$, and 195 $H_2SO_4HSO_4^-$), and organics (cations in panel d: sum of m/z 43 $C_3H_7/C_2H_3O/CHNO^+$, 58 $C_2H_5NHCH_2^+$, 59 $(CH_3)_3N^+$, 88 $(C_2H_5)_2NO/C_3H_6NO_2^+$, 95 $C_7H_{11}^+$, 104 $C_8H_8^+$, 115 $C_9H_7^+$, and 129 $C_5H_7NO^+$; and anions in panel e: sum of m/z 24 C_2^-, 25 C_2H^-, 26 C_2H_2/CN^-, 42 C_2H_2O/CNO^-, 45 $COOH^-$, 59 CH_2COOH^-, 71 CCH_2COOH^-, 73 $C_2H_4COOH^-$, 85 $C_3H_4COO^-$, and 89 $(CO)_2OOH^-$), there is a poor corre-

lation ($\gamma \leq 0.4$) between these two instruments if we consider the entire measurement period. However, the fraction of LAAPTOF organic cations to the sum of ammonium and organic cations, org / (org + ammonium), anion fraction of org / (org + sulfate), and org / (org + nitrate), shows better correlations between these two instruments (Fig. 7), especially for org / (org + nitrate). As shown in Fig. 7b, a scatter plot of org / (org + nitrate) measured by LAAPTOF and AMS shows an exponential trend. A similar trend for the ratio carbonaceous / (carbonaceous + sulfate) was observed by PALMS compared to AMS results for free tropospheric aerosol particles measured by Murphy et al. (2006).

Note that the aforementioned comparisons in this section are for the entire measurement period and demonstrate general correlations between these two instruments. Considering different time periods, the correlations vary (Fig. 7). All corresponding Pearson's correlation coefficient (γ) values for the comparisons of compounds measured by LAAPTOF and AMS are summarized in Table S4. During period 4, most of the γ values are above 0.6, suggesting good correlation, which is comparable with the mass comparison results discussed in Sect. 3.2.2. In particular, for the comparison of the org / (org + nitrate) ratio, LAAPTOF and AMS show good or strong correlations for almost the complete measurement time. The corresponding scatter plots are shown in Fig. 7b1–b6. Periods 2 and 4, covering more than 50 % of the measurement time, show similar exponential trends to the general fit in Fig. 7b, while periods 1, 3, and 5 show a linear correlation (especially in periods 3 and 5). This implies different dominant particle types. Consistent with the observations shown in Fig. 4c, period 2 and 4 are dominated by sodium salts, and there are two secondary inorganics–amine burst events, while period 3 and 5 are dominated by biomass burning–soil particles containing more organics, which can also be validated by AMS results as shown in Fig. 6. Therefore, we conclude that the relationship between LAAPTOF-org / (org + nitrate) and AMS-org / (org + nitrate) varies due to changing particle types.

Taken together, the correlations shown in Figs. 7 and S7 may be used to estimate the mass concentrations of non-refractory compounds for LAAPTOF measurements without AMS in rural locations: ammonium mass concentrations can be estimated from Fig. S7a, afterwards organic mass concentrations can be estimated by using Fig. 7a, and then nitrate can be estimated from Fig. 7b and/or Fig. 7b1–b6 once the dominating particle types are determined, and finally the sulfate mass can be estimated from Fig. 7c.

3.4   Particle sources of non-refractory components

The AMS can quantify the bulk particle mass of non-refractory species such as ammonium, nitrate, sulfate, and organics. LAAPTOF measurements suggest that ambient aerosol particles at this location are often internal mixtures of ammonium, nitrate, sulfate, organics, and other character-

Atmos. Meas. Tech., 12, 2219–2240, 2019   www.atmos-meas-tech.net/12/2219/2019/

121
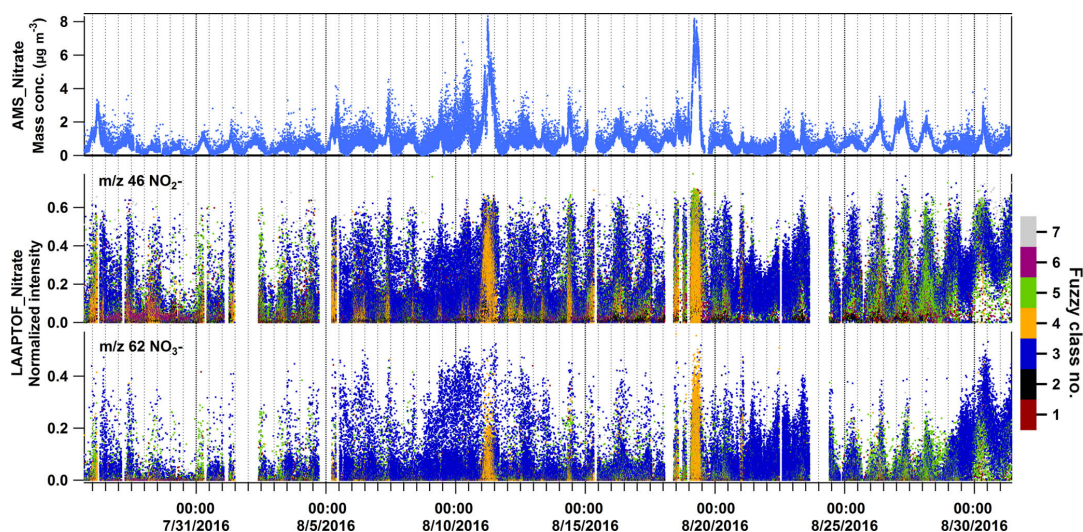
Figure 8. Time series of nitrates measured by AMS in mass concentration and LAAPTOF in normalized ion intensities, respectively. Normalized intensity refers to the fragment intensity divided by the sum of all the ion intensities. Marker peaks for nitrates are at m/z 46 NO_2^- and 62 NO_3^- in LAAPTOF spectra. The seven fuzzy classes are class 1: calcium–soil; class 2: aged soot; class 3: sodium salts; class 4: secondary inorganics–amine; class 5: biomass burning–soil; class 6: biomass burning–organosulfate; and class 7: mixed/aged dust.

istic species such as metals. In order to find out the dominant particle class/classes contributing to/donating a certain non-refractory compound measured by AMS (namely compound-donor particle class/classes), we also need the class information of the single particles, which can be achieved using the single-particle identification method described in Sect. 2.2, and assume that LAAPTOF has a similar sensitivity to the same components of different particle classes. For nitrate measured by AMS, the dominating nitrate-donor particles with marker peaks at m/z 46 NO_2^- and 62 NO_3^- in LAAPTOF varied in different periods (Fig. 8): sodium salts was the dominating class for the whole measurement campaign, but secondary inorganics–amine was dominant in its burst events (11 and 19 August), while biomass burning–soil was dominant from 25–29 August. For ammonium measured by AMS, we have observed a similar trend as for secondary inorganic–amine particles, indicating that the ammonium AMS measured mainly originated from this class. This can be reinforced by comparing marker peaks for ammonium and amine at m/z 18 NH_4^+, 30 NO^+, 58 $C_2H_5NHCH_2^+$, 59 $(CH_3)_3N^+$, and 88 $(C_2H_5)_2NO/C_3H_6NO_2^+$ with the time series of LAAPTOF (Fig. S8). For sulfate measured by AMS, we cannot infer the dominating donor class, since there is no comparable LAAPTOF class and fragments. This indicates again that this instrument has a low sensitivity to some sulfate-containing particles, such as pure ammonium sulfate. For organic compounds measured by AMS, it is also hard to find the comparable class and marker peaks in LAAPTOF data, probably due to two reasons: one is the same as that for sulfate-containing particles, and another one is that compared with AMS there are more fragments (cations and an-

ions) arising from organics in LAAPTOF mass spectra. Nevertheless, we have found that peaks at m/z 129 $C_5H_7NO_3^+$ (arising from organonitrates) and 73 $C_2H_4COO^-$ (from organic acids) have a similar trend as the organics measured by AMS (Fig. 9b and c). At the beginning of the LAAPTOF measurements, the dominating organic-donor class is class 6, biomass burning–organosulfate (mainly contributing organic acids to be measured by AMS), while at the end of the measurement period this changed to sodium-salt-rich particles and biomass burning–soil (mainly contributing organonitrate and organic acids, respectively). Apart from that, aromatic compounds mainly in biomass burning–soil could also contribute to the organic mass fraction measured by AMS, especially for the strongest organic burst event towards the end of the measurement period (refer to Fig. 9d and e).

Although the LDI matrix effects cannot be completely overcome by using relative ion intensities, the time series of the corresponding maker peaks (Figs. 8, 9, and S8) can still be used for preliminary assignments of the bulk species to different particle types.

4   Conclusions and atmospheric implications

In this study, we used a combination of representative spectra obtained by fuzzy classification, laboratory-based reference spectra, marker peaks, and typical peak ratios for the improved single aerosol particle identification at a rural site in the upper Rhine valley near the city of Karlsruhe, Germany. Seven major particle classes were identified among a total of $\sim 3.7 \times 10^5$ single particles: calcium–soil, aged soot,
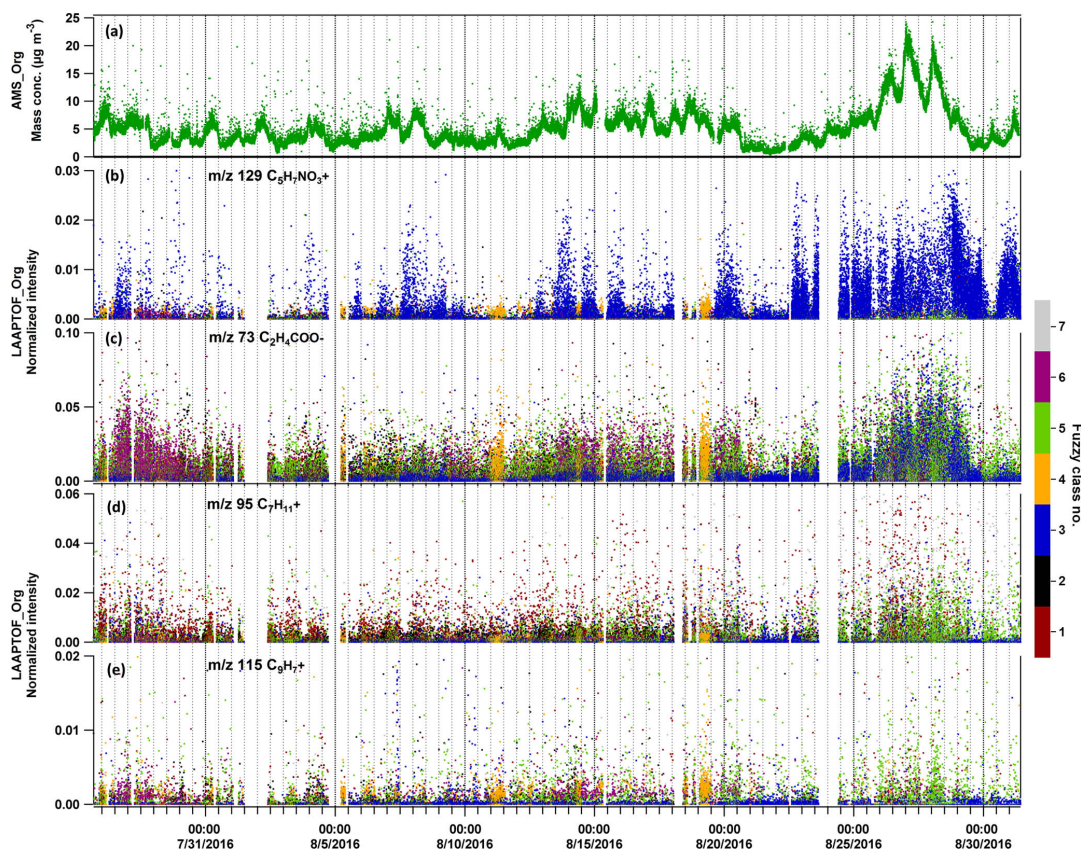
Figure 9. Time series of organic species measured by AMS in mass concentration and LAAPTOF in normalized ion intensities, respectively. Normalized intensity refers to the fragment intensity divided by the sum of all the ion intensities. In LAAPTOF spectra, the peak at m/z 129 $C_5H_7NO_3^+$ is arising from organonitrates, m/z 73 $C_2H_4COO^-$ from organic acids, and m/z 95 $C_7H_{11}^+$ as well as m/z 115 $C_9H_7^+$ from aromatic compounds. The seven classes are class 1: calcium–soil; class 2: aged soot; class 3: sodium salts; class 4: secondary inorganics–amine; class 5: biomass burning–soil; class 6: biomass burning–organosulfate; and class 7: mixed/aged dust.

sodium salts, secondary inorganics–amine, biomass burning–soil, biomass burning–organosulfate, and mixed/aged dust. All particles were internally mixed with organic and secondary inorganic compounds, i.e. ammonium, sulfate, and nitrate. According to our observations, these particles are expected to show a significant hygroscopicity due to their secondary inorganic contents (Fuzzi et al., 2015), as well as the presence of organosulfates (Thalman et al., 2017). The light absorption of soot particles is expected to be enhanced by mixing with non-absorbing species such as organic compounds (Bond et al., 2013). Organonitrate signatures found on sodium salt particles are also expected to increase their light absorbing capability (Canagaratna et al., 2007) and to assist nocturnal particle growth (Huang et al., 2019). The good correlation of most of the particle classes and dust signatures suggests that condensation processes and heterogeneous chemistry have modified the dust particles during their transportation. For example, organosulfate-coated dust could form from heterogeneous reactions of volatile organic compounds (VOCs), such as glyoxal, on mineral dust particles aged by reaction with, e.g. SO_2 (Shen et al., 2016). Since organosulfates can form by heterogeneous reactions of IEPOX on acidic particles at low NO_x level (Froyd et al., 2010; Surratt et al., 2010), it is likely that they form also on acidified dust particles under similar conditions. Our general observation of dominating aged and mixed aerosol particles is expected at a location about 2 h downwind of nearest major emission sources (12 km distance to Karlsruhe at an average daytime wind speed of $1.7 \, \text{m s}^{-1}$).

Based on the precise identification for particle classes and individual particles, we applied a quantification method for single particles, employing size- and particle-class-resolved/chemically resolved overall detection efficiency (ODE) for this instrument. In contrast to methods used in previous SPMS studies, our approach is laboratory-based and does not rely on the availability of a reference instrument in the field. The corresponding "corrections" to the standard similarity classification result in substantial changes in

Atmos. Meas. Tech., 12, 2219–2240, 2019   **www.atmos-meas-tech.net/12/2219/2019/**

123

the particle class abundances: sodium salt particles changed from 43.5 % (similarity) to 3.4 % (corrected number fraction), corresponding to a mass fraction of 30.1 %, becoming the second dominating class in mass; secondary inorganics–amine dramatically decreased from 20.8 % to 2.4 %, corresponding to a mass fraction of 3.6 %, becoming the second least abundant class; biomass burning–soil changed from 16.1 % to 45.0 %, corresponding to a mass fraction of 31.8 %, becoming the dominating class in number and mass. The big difference between number-based and mass-based SPMS results has reinforced the importance of particle mass quantification. It is noteworthy that our quantification approach requires several assumptions mainly regarding particle shape and density, which results in potential uncertainties of up to ~ 300 %, with the dominant source still being the ODE values. Despite this large uncertainty, the resulting total particle mass shows good agreement with the total mass of non-refractory compounds measured by AMS in different periods, covering ~ 85 % of the measurement time. However, some discrepancies still remain, most likely due to the low sensitivity of LAAPTOF for small particles as well as ammonium sulfate and organic-rich particles. Furthermore, we have found specific relationships of LAAPTOF ion intensity ratios and AMS mass concentration results for non-refractory compounds, especially for the fraction of org / (org + nitrate). This will be applied for source apportionment in an upcoming publication. The corresponding scatter plots may be used to estimate mass concentrations in future SPMS studies as well.

We have shown how particle size, density, morphology (shape), and chemical composition have impacted the ODE of the LAAPTOF. Therefore, these factors need to be taken into account for a reasonable quantitative interpretation of SPMS data. Considering reduced quantification uncertainties, systematic measurements on different types of standard samples, as well as real ambient samples (size-selected) under controlled environmental conditions (temperature and relative humidity), are still needed to obtain more comprehensive sensitivities for LAAPTOF.

Employing particle class information for individual particles and specific marker peaks with relative ion intensities, this study is able to assign non-refractory compounds measured by AMS to different classes of particles measured by SPMS. It turns out that nitrate measured by AMS was mainly from sodium-salt-like particles. Ammonium measured by AMS mainly arose from secondary inorganic–amine particles. However, the dominating donor particle classes varied in different time periods during the measurements. Organic compounds measured by AMS were from organic acids (mainly on aged-biomass-burning particles), organonitrates (from sodium salts), and aromatic compounds (from aged-biomass-burning particles). During the entire measurement campaign, the dominating particle classes changed with respect to particle number and mass, and the donor classes

for non-refractory compounds also varied substantially, indicating changes of particles sources.

In spite of significant uncertainties stemming from several assumptions and instrumental aspects, our study provides a good example for the identification and quantitative interpretation of single-particle data. Together with the complimentary results from bulk measurements by AMS, we have shown how a better understanding of the internal and external mixing state of ambient aerosol particles can be achieved.

References

Ackerman, T. P. and Toon, O. B.: Absorption of visible radiation in atmosphere containing mixtures of absorbing and non-absorbing particles, Appl. Opt., 20, 3661–3668, 1981.

Ahern, A. T., Subramanian, R., Saliba, G., Lipsky, E. M., Donahue, N. M., and Sullivan, R. C.: Effect of secondary organic aerosol coating thickness on the real-time detection and characterization of biomass-burning soot by two particle mass spectrometers, Atmos. Meas. Tech., 9, 6117–6137, https://doi.org/10.5194/amt-9-6117-2016, 2016.

Allen, J. O., Fergenson, D. P., Gard, E. E., Hughes, L. S., Morrical, B. D., Kleeman, M. J., Gross, D. S., Galli, M. E., Prather, K. A., and Cass, G. R.: Particle detection efficiencies of aerosol time of flight mass spectrometers under ambient sampling conditions, Environ. Sci. Technol., 34, 211–217, 2000.

Allen, J. O., Bhave, P. V., Whiteaker, J. R., and Prather, K. A.: Instrument busy time and mass measurement using aerosol time-of-flight mass spectrometry, Aerosol Sci. Tech., 40, 615–626, 2006.

Angelino, S., Suess, D. T., and Prather, K. A.: Formation of aerosol particles from reactions of secondary and tertiary alkylamines: Characterization by aerosol time-of-flight mass spectrometry, Environ. Sci. Technol., 35, 3130–3138, 2001.

Ault, A. P., Moore, M. J., Furutani, H., and Prather, K. A.: Impact of emissions from the Los Angeles port region on San Diego air quality during regional transport events, Environ. Sci. Technol., 43, 3500–3506, 2009.

Ault, A. P., Gaston, C. J., Wang, Y., Dominguez, G., Thiemens, M. H., and Prather, K. A.: Characterization of the single particle mixing state of individual ship plume events measured at the port of Los Angeles, Environ. Sci. Technol., 44, 1954–1961, 2010.

Bahreini, R., Keywood, M. D., Ng, N. L., Varutbangkul, V., Gao, S., Flagan, R. C., Seinfeld, J. H., Worsnop, D. R., and Jimenez, J. L.: Measurements of secondary organic aerosol from oxidation of cycloalkenes, terpenes, and m-xylene using an Aerodyne aerosol mass spectrometer, Environ. Sci. Technol., 39, 5674–5688, 2005.

Bein, K. J., Zhao, Y. J., Pekney, N. J., Davidson, C. I., Johnston, M. V., and Wexler, A. S.: Identification of sources of atmospheric PM at the Pittsburgh Supersite – Part II: Quantitative comparisons of single particle, particle number, and particle mass measurements, Atmos. Environ., 40, 424–444, 2006.

Bergametti, G. and Forêt, G.: Mineral Dust: a key player in the earth system, Chapter 8, 183 pp., Springer, Dordrecht, 2014.

Bhave, P. V., Allen, J. O., Morrical, B. D., Fergenson, D. P., Cass, G. R., and Prather, K. A.: A field-based approach for determining ATOFMS instrument sensitivities to ammonium and nitrate, Environ. Sci. Technol., 36, 4868–4879, 2002.

Bond, T. C., Doherty, S. J., Fahey, D. W., Forster, P. M., Berntsen, T., DeAngelo, B. J., Flanner, M. G., Ghan, S., Karcher, B., Koch, D., Kinne, S., Kondo, Y., Quinn, P. K., Sarofim, M. C., Schultz, M. G., Schulz, M., Venkataraman, C., Zhang, H., Zhang, S., Bellouin, N., Guttikunda, S. K., Hopke, P. K., Jacobson, M. Z., Kaiser, J. W., Klimont, Z., Lohmann, U., Schwarz, J. P., Shindell, D., Storelvmo, T., Warren, S. G., and Zender, C. S.: Bounding the role of black carbon in the climate system: A scientific assessment, J. Geophys. Res.-Atmos., 118, 5380–5552, 2013.

Canagaratna, M. R., Jayne, J. T., Jimenez, J. L., Allan, J. D., Alfarra, M. R., Zhang, Q., Onasch, T. B., Drewnick, F., Coe, H., Middlebrook, A., Delia, A., Williams, L. R., Trimborn, A. M.,

Northway, M. J., DeCarlo, P. F., Kolb, C. E., Davidovits, P., and Worsnop, D. R.: Chemical and microphysical characterization of ambient aerosols with the aerodyne aerosol mass spectrometer, Mass Spectrom. Rev., 26, 185–222, 2007.

Christopoulos, C. D., Garimella, S., Zawadowicz, M. A., Möhler, O., and Cziczo, D. J.: A machine learning approach to aerosol classification for single-particle mass spectrometry, Atmos. Meas. Tech., 11, 5687–5699, https://doi.org/10.5194/amt-11-5687-2018, 2018.

Dall'Osto, M. and Harrison, R. M.: Urban organic aerosols measured by single particle mass spectrometry in the megacity of London, Atmos. Chem. Phys., 12, 4127–4142, https://doi.org/10.5194/acp-12-4127-2012, 2012.

Dall'Osto, M., Harrison, R. M., Beddows, D. C. S., Freney, E. J., Heal, M. R., and Donovan, R. J.: Single-particle detection efficiencies of aerosol time-of-flight mass spectrometry during the North Atlantic marine boundary layer experiment, Environ. Sci. Technol., 40, 5029–5035, 2006.

Dall'Osto, M., Harrison, R. M., Coe, H., and Williams, P.: Real-time secondary aerosol formation during a fog event in London, Atmos. Chem. Phys., 9, 2459–2469, https://doi.org/10.5194/acp-9-2459-2009, 2009.

Dall'Osto, M., Ceburnis, D., Monahan, C., Worsnop, D. R., Bialek, J., Kulmala, M., Kurten, T., Ehn, M., Wenger, J., Sodeau, J., Healy, R., and O'Dowd, C.: Nitrogenated and aliphatic organic vapors as possible drivers for marine secondary organic aerosol growth, J. Geophys. Res.-Atmos., 117, D12311, https://doi.org/10.1029/2012JD017522, 2012.

Dall'Osto, M., Querol, X., Alastuey, A., Minguillon, M. C., Alier, M., Amato, F., Brines, M., Cusack, M., Grimalt, J. O., Karanasiou, A., Moreno, T., Pandolfi, M., Pey, J., Reche, C., Ripoll, A., Tauler, R., Van Drooge, B. L., Viana, M., Harrison, R. M., Gietl, J., Beddows, D., Bloss, W., O'Dowd, C., Ceburnis, D., Martucci, G., Ng, N. L., Worsnop, D., Wenger, J., Mc Gillicuddy, E., Sodeau, J., Healy, R., Lucarelli, F., Nava, S., Jimenez, J. L., Gomez Moreno, F., Artinano, B., Prévôt, A. S. H., Pfaffenberger, L., Frey, S., Wilsenack, F., Casabona, D., Jiménez-Guerrero, P., Gross, D., and Cots, N.: Presenting SAPUSS: Solving Aerosol Problem by Using Synergistic Strategies in Barcelona, Spain, Atmos. Chem. Phys., 13, 8991–9019, https://doi.org/10.5194/acp-13-8991-2013, 2013.

Dall'Osto, M., Beddows, D. C. S., McGillicuddy, E. J., Esser-Gietl, J. K., Harrison, R. M., and Wenger, J. C.: On the simultaneous deployment of two single-particle mass spectrometers at an urban background and a roadside site during SAPUSS, Atmos. Chem. Phys., 16, 9693–9710, https://doi.org/10.5194/acp-16-9693-2016, 2016.

DeCarlo, P. F., Kimmel, J. R., Trimborn, A., Northway, M. J., Jayne, J. T., Aiken, A. C., Gonin, M., Fuhrer, K., Horvath, T., Docherty, K. S., Worsnop, D. R., and Jimenez, J. L.: Field-deployable, high-resolution, time-of-flight aerosol mass spectrometer, Anal. Chem., 78, 8281–8289, 2006.

DeCarlo, P. F., Slowik, J. G., Worsnop, D. R., Davidovits, P., and Jimenez, J. L.: Particle morphology and density characterization by combined mobility and aerodynamic diameter measurements, Part 1: Theory, Aerosol Sci. Tech., 38, 1185–1205, 2004.

Decesari, S., Finessi, E., Rinaldi, M., Paglione, M., Fuzzi, S., Stephanou, E. G., Tziaras, T., Spyros, A., Ceburnis, D., O'Dowd, C., Dall'Osto, M., Harrison, R. M., Allan, J., Coe,

125

H., and Facchini, M. C.: Primary and secondary marine organic aerosols over the North Atlantic Ocean during the MAP experiment, J. Geophys. Res.-Atmos., 116, D22210, https://doi.org/10.1029/2011jd016204, 2011.

Decesari, S., Allan, J., Plass-Duelmer, C., Williams, B. J., Paglione, M., Facchini, M. C., O'Dowd, C., Harrison, R. M., Gietl, J. K., Coe, H., Giulianelli, L., Gobbi, G. P., Lanconelli, C., Carbone, C., Worsnop, D., Lambe, A. T., Ahern, A. T., Moretti, F., Tagliavini, E., Elste, T., Gilge, S., Zhang, Y., and Dall'Osto, M.: Measurements of the aerosol chemical composition and mixing state in the Po Valley using multiple spectroscopic techniques, Atmos. Chem. Phys., 14, 12109–12132, https://doi.org/10.5194/acp-14-12109-2014, 2014.

Drewnick, F., Dall'Osto, M., and Harrison, R. M.: Characterization of aerosol particles from grass mowing by joint deployment of ToF-AMS and ATOFMS instruments, Atmos. Environ., 42, 3006–3017, 2008.

Erisman, J. W., Otjes, R., Hensen, A., Jongejan, P., van den Bulk, P., Khlystov, A., Mols, H., and Slanina, S.: Instrument development and application in studies and monitoring of ambient ammonia, Atmos. Environ., 35, 1913–1922, 2001.

Faude, F. and Goschnick, J.: XPS, SIMS and SNMS applied to a combined analysis of aerosol particles from a region of considerable air pollution in the upper Rhine valley, Fresen. J. Anal. Chem., 358, 67–72, 1997.

Ferge, T., Karg, E., Schroppel, A., Coffee, K. R., Tobias, H. J., Frank, M., Gard, E. E., and Zimmermann, R.: Fast determination of the relative elemental and organic carbon content of aerosol samples by on-line single-particle aerosol time-of-flight mass spectrometry, Environ. Sci. Technol., 40, 3327–3335, 2006.

Fergenson, D. P., Song, X. H., Ramadan, Z., Allen, J. O., Hughes, L. S., Cass, G. R., Hopke, P. K., and Prather, K. A.: Quantification of ATOFMS data by multivariate methods, Anal. Chem., 73, 3535–3541, 2001.

Froyd, K. D., Murphy, S. M., Murphy, D. M., de Gouw, J. A., Eddingsaas, N. C., and Wennberg, P. O.: Contribution of isoprene-derived organosulfates to free tropospheric aerosol mass, P. Natl. Acad. Sci. USA, 107, 21360–21365, 2010.

Fuzzi, S., Baltensperger, U., Carslaw, K., Decesari, S., Denier van der Gon, H., Facchini, M. C., Fowler, D., Koren, I., Langford, B., Lohmann, U., Nemitz, E., Pandis, S., Riipinen, I., Rudich, Y., Schaap, M., Slowik, J. G., Spracklen, D. V., Vignati, E., Wild, M., Williams, M., and Gilardoni, S.: Particulate matter, air quality and climate: lessons learned and future needs, Atmos. Chem. Phys., 15, 8217–8299, https://doi.org/10.5194/acp-15-8217-2015, 2015.

Gallavardin, S., Lohmann, U., and Cziczo, D.: Analysis and differentiation of mineral dust by single particle laser mass spectrometry, Int. J. Mass Spectrom., 274, 56–63, 2008.

Gard, E. E., Kleeman, M. J., Gross, D. S., Hughes, L. S., Allen, J. O., Morrical, B. D., Fergenson, D. P., Dienes, T., Galli, M. E., Johnson, R. J., Cass, G. R., and Prather, K. A.: Direct observation of heterogeneous chemistry in the atmosphere, Science, 279, 1184–1187, 1998.

Gaston, C. J., Furutani, H., Guazzotti, S. A., Coffee, K. R., Bates, T. S., Quinn, P. K., Aluwihare, L. I., Mitchell, B. G., and Prather, K. A.: Unique ocean-derived particles serve as a proxy for changes in ocean chemistry, J. Geophys. Res.-Atmos., 116, D18310, https://doi.org/10.1029/2010JD015289, 2011.

Gaston, C. J., Quinn, P. K., Bates, T. S., Gilman, J. B., Bon, D. M., Kuster, W. C., and Prather, K. A.: The impact of shipping, agricultural, and urban emissions on single particle chemistry observed aboard the R/V *Atlantis* during CalNex, J. Geophys. Res.-Atmos., 118, 5003–5017, 2013.

Gemayel, R., Hellebust, S., Temime-Roussel, B., Hayeck, N., Van Elteren, J. T., Wortham, H., and Gligorovski, S.: The performance and the characterization of laser ablation aerosol particle time-of-flight mass spectrometry (LAAP-ToF-MS), Atmos. Meas. Tech., 9, 1947–1959, https://doi.org/10.5194/amt-9-1947-2016, 2016.

Gemayel, R., Temime-Roussel, B., Hayeck, N., Gandolfo, A., Hellebust, S., Gligorovski, S., and Wortham, H.: Development of an analytical methodology for obtaining quantitative mass concentrations from LAAP-ToF-MS measurements, Talanta, 174, 715–724, 2017.

Goschnick, J., Schuricht, J., and Ache, H. J.: Depth-structure of airborne microparticles sampled downwind from the city of Karlsruhe in the river Rhine Valley, Fresen. J. Anal. Chem., 350, 426–430, 1994.

Gross, D. S., Gälli, M. E., Silva, P. J., and Prather, K. A.: Relative sensitivity factors for alkali metal and ammonium cations in single particle aerosol time-of-flight mass spectra, Anal. Chem., 72, 416–422, 2000.

Gunsch, M. J., May, N. W., Wen, M., Bottenus, C. L. H., Gardner, D. J., VanReken, T. M., Bertman, S. B., Hopke, P. K., Ault, A. P., and Pratt, K. A.: Ubiquitous influence of wildfire emissions and secondary organic aerosol on summertime atmospheric aerosol in the forested Great Lakes region, Atmos. Chem. Phys., 18, 3701–3715, https://doi.org/10.5194/acp-18-3701-2018, 2018.

Hagemann, R., Corsmeier, U., Kottmeier, C., Rinke, R., Wieser, A., and Vogel, B.: Spatial variability of particle number concentrations and NO_x in the Karlsruhe (Germany) area obtained with the mobile laboratory 'AERO-TRAM', Atmos Environ, 94, 341–352, 2014.

Hatch, L. E., Creamean, J. M., Ault, A. P., Surratt, J. D., Chan, M. N., Seinfeld, J. H., Edgerton, E. S., Su, Y. X., and Prather, K. A.: Measurements of isoprene-derived organosulfates in ambient aerosols by aerosol time-of-flight mass spectrometry – Part 2: temporal variability and formation mechanisms, Environ. Sci. Technol., 45, 8648–8655, 2011a.

Hatch, L. E., Creamean, J. M., Ault, A. P., Surratt, J. D., Chan, M. N., Seinfeld, J. H., Edgerton, E. S., Su, Y. X., and Prather, K. A.: Measurements of isoprene-derived organosulfates in ambient aerosols by aerosol time-of-flight mass spectrometry – Part 1: single particle atmospheric observations in Atlanta, Environ. Sci. Technol., 45, 5105–5111, 2011b.

Hatch, L. E., Pratt, K. A., Huffman, J. A., Jimenez, J. L., and Prather, K. A.: Impacts of aerosol aging on laser desorption/ionization in single-particle mass spectrometers, Aerosol Sci. Tech., 48, 1050–1058, 2014.

Healy, R. M., Sciare, J., Poulain, L., Kamili, K., Merkel, M., Müller, T., Wiedensohler, A., Eckhardt, S., Stohl, A., Sarda-Estève, R., McGillicuddy, E., O'Connor, I. P., Sodeau, J. R., and Wenger, J. C.: Sources and mixing state of size-resolved elemental carbon particles in a European megacity: Paris, Atmos. Chem. Phys., 12, 1681–1700, https://doi.org/10.5194/acp-12-1681-2012, 2012.

Healy, R. M., Sciare, J., Poulain, L., Crippa, M., Wiedensohler, A., Prévôt, A. S. H., Baltensperger, U., Sarda-Estève, R., McGuire,

126

M. L., Jeong, C.-H., McGillicuddy, E., O'Connor, I. P., Sodeau, J. R., Evans, G. J., and Wenger, J. C.: Quantitative determination of carbonaceous particle mixing state in Paris using single-particle mass spectrometer and aerosol mass spectrometer measurements, Atmos. Chem. Phys., 13, 9479–9496, https://doi.org/10.5194/acp-13-9479-2013, 2013.

Hill, T. C. J., DeMott, P. J., Tobo, Y., Fröhlich-Nowoisky, J., Moffett, B. F., Franc, G. D., and Kreidenweis, S. M.: Sources of organic ice nucleating particles in soils, Atmos. Chem. Phys., 16, 7195–7211, https://doi.org/10.5194/acp-16-7195-2016, 2016.

Hinz, K. P., Greweling, M., Drews, F., and Spengler, B.: Data processing in on-line laser mass spectrometry of inorganic, organic, or biological airborne particles, J. Am. Soc. Mass Spectr., 10, 648–660, 1999.

Huang, W., Saathoff, H., Shen, X. L., Ramakrishna, R., Leisner, T., and Mohr, C.: Chemical characterization of highly functionalized organonitrates contributing to high night-time organic aerosol mass loadings and particle growth, Environ. Sci. Technol., 53, 1165–1174, 2019.

Jeong, C.-H., McGuire, M. L., Godri, K. J., Slowik, J. G., Rehbein, P. J. G., and Evans, G. J.: Quantification of aerosol chemical composition using continuous single particle measurements, Atmos. Chem. Phys., 11, 7027–7044, https://doi.org/10.5194/acp-11-7027-2011, 2011.

Köllner, F., Schneider, J., Willis, M. D., Klimach, T., Helleis, F., Bozem, H., Kunkel, D., Hoor, P., Burkart, J., Leaitch, W. R., Aliabadi, A. A., Abbatt, J. P. D., Herber, A. B., and Borrmann, S.: Particulate trimethylamine in the summertime Canadian high Arctic lower troposphere, Atmos. Chem. Phys., 17, 13747–13766, https://doi.org/10.5194/acp-17-13747-2017, 2017.

Li, L., Liu, L., Xu, L., Li, M., Li, X., Gao, W., Huang, Z. X., and Cheng, P.: Improvement in the Mass Resolution of Single Particle Mass Spectrometry Using Delayed Ion Extraction, J. Am. Soc. Mass Spectr., 29, 2105–2109, 2018.

Lin, Q., Zhang, G., Peng, L., Bi, X., Wang, X., Brechtel, F. J., Li, M., Chen, D., Peng, P., Sheng, G., and Zhou, Z.: In situ chemical composition measurement of individual cloud residue particles at a mountain site, southern China, Atmos. Chem. Phys., 17, 8473–8488, https://doi.org/10.5194/acp-17-8473-2017, 2017.

Lu, D. W., Liu, Q., Yu, M., Yang, X. Z., Fu, Q., Zhang, X. S., Mu, Y. J., and Jiang, G. B.: Natural silicon isotopic signatures reveal the sources of airborne fine particulate matter, Environ. Sci. Technol., 52, 1088–1095, 2018.

Marsden, N. A., Flynn, M. J., Taylor, J. W., Allan, J. D., and Coe, H.: Evaluating the influence of laser wavelength and detection stage geometry on optical detection efficiency in a single-particle mass spectrometer, Atmos. Meas. Tech., 9, 6051–6068, https://doi.org/10.5194/amt-9-6051-2016, 2016.

Marsden, N. A., Flynn, M. J., Allan, J. D., and Coe, H.: Online differentiation of mineral phase in aerosol particles by ion formation mechanism using a LAAP-TOF single-particle mass spectrometer, Atmos. Meas. Tech., 11, 195–213, https://doi.org/10.5194/amt-11-195-2018, 2018.

Marsden, N. A., Ullrich, R., Möhler, O., Eriksen Hammer, S., Kandler, K., Cui, Z., Williams, P. I., Flynn, M. J., Liu, D., Allan, J. D., and Coe, H.: Mineralogy and mixing state of north African mineral dust by online single-particle mass spectrometry, Atmos. Chem. Phys., 19, 2259–2281, https://doi.org/10.5194/acp-19-2259-2019, 2019.

May, N. W., Gunsch, M. J., Olson, N. E., Bondy, A. L., Kirpes, R. M., Bertman, S. B., China, S., Laskin, A., Hopke, P. K., Ault, A. P., and Pratt, K. A.: Unexpected contributions of sea spray and lake spray aerosol to inland particulate matter, Environ. Sc. Tech. Lett., 5, 405–412, 2018.

Middlebrook, A. M., Murphy, D. M., Lee, S. H., Thomson, D. S., Prather, K. A., Wenzel, R. J., Liu, D. Y., Phares, D. J., Rhoads, K. P., Wexler, A. S., Johnston, M. V., Jimenez, J. L., Jayne, J. T., Worsnop, D. R., Yourshaw, I., Seinfeld, J. H., and Flagan, R. C.: A comparison of particle mass spectrometers during the 1999 Atlanta Supersite Project, J. Geophys. Res.-Atmos., 108, 8424, https://doi.org/10.1029/2001jd000660, 2003.

Middlebrook, A. M., Bahreini, R., Jimenez, J. L., and Canagaratna, M. R.: Evaluation of composition-dependent collection efficiencies for the aerodyne aerosol mass spectrometer using field data, Aerosol Sci. Tech., 46, 258–271, 2012.

Moffet, R. C., de Foy, B., Molina, L. T., Molina, M. J., and Prather, K. A.: Measurement of ambient aerosols in northern Mexico City by single particle mass spectrometry, Atmos. Chem. Phys., 8, 4499–4516, https://doi.org/10.5194/acp-8-4499-2008, 2008a.

Moffet, R. C., Qin, X. Y., Rebotier, T., Furutani, H., and Prather, K. A.: Chemically segregated optical and microphysical properties of ambient aerosols measured in a single-particle mass spectrometer, J. Geophys. Res.-Atmos., 113, D12213, https://doi.org/10.1029/2007jd009393, 2008b.

Murphy, D. M.: The design of single particle laser mass spectrometers, Mass Spectrom. Rev., 26, 150–165, 2007.

Murphy, D. M., Cziczo, D. J., Froyd, K. D., Hudson, P. K., Matthew, B. M., Middlebrook, A. M., Peltier, R. E., Sullivan, A., Thomson, D. S., and Weber, R. J.: Single-particle mass spectrometry of tropospheric aerosol particles, J. Geophys. Res.-Atmos., 111, D23S32, https://doi.org/10.1029/2006jd007340, 2006.

Noble, C. A. and Prather, K. A.: Real-time single particle mass spectrometry: a historical review of a quarter century of the chemical analysis of aerosols, Mass Spectrom. Rev., 19, 248–274, 2000.

Perring, A. E., Pusede, S. E., and Cohen, R. C.: An observational perspective on the atmospheric impacts of alkyl and multifunctional nitrates on ozone and secondary organic aerosol, Chem. Rev., 113, 5848–5870, 2013.

Pöschl, U.: Atmospheric aerosols: Composition, transformation, climate and health effects, Angew. Chem. Int. Edit, 44, 7520–7540, 2005.

Pratt, K. A., Hatch, L. E., and Prather, K. A.: Seasonal Volatility Dependence of Ambient Particle Phase Amines, Environ. Sci. Technol., 43, 5276–5281, 2009.

Pratt, K. A., Heymsfield, A. J., Twohy, C. H., Murphy, S. M., DeMott, P. J., Hudson, J. G., Subramanian, R., Wang, Z. E., Seinfeld, J. H., and Prather, K. A.: In situ chemical characterization of aged biomass-burning aerosols impacting cold wave clouds, J. Atmos. Sci., 67, 2451–2468, 2010.

Pratt, K. A., Murphy, S. M., Subramanian, R., DeMott, P. J., Kok, G. L., Campos, T., Rogers, D. C., Prenni, A. J., Heymsfield, A. J., Seinfeld, J. H., and Prather, K. A.: Flight-based chemical characterization of biomass burning aerosols within two prescribed burn smoke plumes, Atmos. Chem. Phys., 11, 12549–12565, https://doi.org/10.5194/acp-11-12549-2011, 2011.

Atmos. Meas. Tech., 12, 2219–2240, 2019   **www.atmos-meas-tech.net/12/2219/2019/**

127

Pratt, K. A. and Prather, K. A.: Real-time, single-particle volatility, size, and chemical composition measurements of aged urban aerosols, Environ. Sci. Technol., 43, 8276–8282, 2009.

Pratt, K. A. and Prather, K. A.: Mass spectrometry of atmospheric aerosols-Recent developments and applications, Part II: Online mass spectrometry techniques, Mass Spectrom. Rev., 31, 17–48, 2012.

Qin, X. Y., Bhave, P. V., and Prather, K. A.: Comparison of two methods for obtaining quantitative mass concentrations from aerosol time-of-flight mass spectrometry measurements, Anal. Chem., 78, 6169–6178, 2006.

Qin, X. Y., Pratt, K. A., Shields, L. G., Toner, S. M., and Prather, K. A.: Seasonal comparisons of single-particle chemical mixing state in Riverside, CA, Atmos. Environ., 59, 587–596, 2012.

Ramisetty, R., Abdelmonem, A., Shen, X., Saathoff, H., Leisner, T., and Mohr, C.: Exploring femtosecond laser ablation in single-particle aerosol mass spectrometry, Atmos. Meas. Tech., 11, 4345–4360, https://doi.org/10.5194/amt-11-4345-2018, 2018.

Reilly, P. T. A., Lazar, A. C., Gieray, R. A., Whitten, W. B., and Ramsey, J. M.: The elucidation of charge-transfer-induced matrix effects in environmental aerosols via real-time aerosol mass spectral analysis of individual airborne particles, Aerosol Sci. Tech., 33, 135–152, 2000.

Reinard, M. S. and Johnston, M. V.: Ion formation mechanism in laser desorption ionization of individual nanoparticles, J. Am. Soc. Mass Spectr., 19, 389–399, 2008.

Reitz, P., Zorn, S. R., Trimborn, S. H., and Trimborn, A. M.: A new, powerful technique to analyze single particle aerosol mass spectra using a combination of OPTICS and the fuzzy c-means algorithm, J. Aerosol Sci., 98, 1–14, 2016.

Roth, A., Schneider, J., Klimach, T., Mertes, S., van Pinxteren, D., Herrmann, H., and Borrmann, S.: Aerosol properties, source identification, and cloud processing in orographic clouds measured by single particle mass spectrometry on a central European mountain site during HCCT-2010, Atmos. Chem. Phys., 16, 505–524, https://doi.org/10.5194/acp-16-505-2016, 2016.

Schmidt, S., Schneider, J., Klimach, T., Mertes, S., Schenk, L. P., Kupiszewski, P., Curtius, J., and Borrmann, S.: Online single particle analysis of ice particle residuals from mountain-top mixed-phase clouds using laboratory derived particle type assignment, Atmos. Chem. Phys., 17, 575–594, https://doi.org/10.5194/acp-17-575-2017, 2017.

Shen, X., Ramisetty, R., Mohr, C., Huang, W., Leisner, T., and Saathoff, H.: Laser ablation aerosol particle time-of-flight mass spectrometer (LAAPTOF): performance, reference spectra and classification of atmospheric samples, Atmos. Meas. Tech., 11, 2325–2343, https://doi.org/10.5194/amt-11-2325-2018, 2018.

Shen, X. L., Wu, H. H., Zhao, Y., Huang, D., Huang, L. B., and Chen, Z. M.: Heterogeneous reactions of glyoxal on mineral particles: A new avenue for oligomers and organosulfate formation, Atmos. Environ., 131, 133–140, 2016.

Silva, P. J. and Prather, K. A.: Interpretation of mass spectra from organic compounds in aerosol time-of-flight mass spectrometry, Anal. Chem., 72, 3553–3562, 2000.

Spencer, M. T. and Prather, K. A.: Using ATOFMS to determine OC/EC mass fractions in particles, Aerosol Sci. Tech., 40, 585–594, 2006.

Spencer, M. T., Shields, L. G., and Prather, K. A.: Simultaneous measurement of the effective density and chemical composition

of ambient aerosol particles, Environ. Sci. Technol., 41, 1303–1309, 2007.

Stolzenburg, M. R. and Hering, S. V.: Method for the automated measurement of fine particle nitrate in the atmosphere, Environ. Sci. Technol., 34, 907–914, 2000.

Surratt, J. D., Chan, A. W. H., Eddingsaas, N. C., Chan, M. N., Loza, C. L., Kwan, A. J., Hersey, S. P., Flagan, R. C., Wennberg, P. O., and Seinfeld, J. H.: Reactive intermediates revealed in secondary organic aerosol formation from isoprene, P. Natl. Acad. Sci. USA, 107, 6640–6645, 2010.

Thalman, R., de Sá, S. S., Palm, B. B., Barbosa, H. M. J., Pöhlker, M. L., Alexander, M. L., Brito, J., Carbone, S., Castillo, P., Day, D. A., Kuang, C., Manzi, A., Ng, N. L., Sedlacek III, A. J., Souza, R., Springston, S., Watson, T., Pöhlker, C., Pöschl, U., Andreae, M. O., Artaxo, P., Jimenez, J. L., Martin, S. T., and Wang, J.: CCN activity and organic hygroscopicity of aerosols downwind of an urban region in central Amazonia: seasonal and diel variations and impact of anthropogenic emissions, Atmos. Chem. Phys., 17, 11779–11801, https://doi.org/10.5194/acp-17-11779-2017, 2017.

Thomson, D. S., Middlebrook, A. M., and Murphy, D. M.: Thresholds for laser-induced ion formation from aerosols in a vacuum using ultraviolet and vacuum-ultraviolet laser wavelengths, Aerosol Sci. Tech., 26, 544–559, 1997.

Vera, C. C., Trimborn, A., Hinz, K. P., and Spengler, B.: Initial velocity distributions of ions generated by in-flight laser desorption/ionization of individual polystyrene latex microparticles as studied by the delayed ion extraction method, Rapid Commun. Mass Sp., 19, 133–146, 2005.

Wang, Z., King, S. M., Freney, E., Rosenoern, T., Smith, M. L., Chen, Q., Kuwata, M., Lewis, E. R., Poschl, U., Wang, W., Buseck, P. R., and Martin, S. T.: The dynamic shapefactor of sodium chloride nanoparticles as regulated by drying rate, Aerosol Sci. Tech., 44, 939–953, 2010.

Wenzel, R. J., Liu, D. Y., Edgerton, E. S., and Prather, K. A.: Aerosol time-of-flight mass spectrometry during the Atlanta Supersite Experiment: 2. Scaling procedures, J. Geophys. Res.-Atmos., 108, 8427, https://doi.org/10.1029/2001jd001563, 2003.

Wenzel, R. J. and Prather, K. A.: Improvements in ion signal reproducibility obtained using a homogeneous laser beam for on-line laser desorption/ionization of single particles, Rapid Commun. Mass Sp., 18, 1525–1533, 2004.

Wiley, W. C. and Mclaren, I. H.: Time-of-Flight Mass Spectrometer with Improved Resolution, Rev. Sci. Instrum., 26, 1150–1157, 1955.

Williams, L. R., Gonzalez, L. A., Peck, J., Trimborn, D., McInnis, J., Farrar, M. R., Moore, K. D., Jayne, J. T., Robinson, W. A., Lewis, D. K., Onasch, T. B., Canagaratna, M. R., Trimborn, A., Timko, M. T., Magoon, G., Deng, R., Tang, D., de la Rosa Blanco, E., Prévôt, A. S. H., Smith, K. A., and Worsnop, D. R.: Characterization of an aerodynamic lens for transmitting particles greater than 1 micrometer in diameter into the Aerodyne aerosol mass spectrometer, Atmos. Meas. Tech., 6, 3271–3280, https://doi.org/10.5194/amt-6-3271-2013, 2013.

Wonaschuetz, A., Kallinger, P., Szymanski, W., and Hitzenberger, R.: Chemical composition of radiolytically formed particles using single-particle mass spectrometry, J. Aerosol Sci., 113, 242–249, 2017.

Zawadowicz, M. A., Froyd, K. D., Murphy, D. M., and Cziczo, D. J.: Improved identification of primary biological aerosol particles using single-particle mass spectrometry, Atmos. Chem. Phys., 17, 7193–7212, https://doi.org/10.5194/acp-17-7193-2017, 2017.

Zelenyuk, A., Cai, Y., Chieffo, L., and Imre, D.: High precision density measurements of single particles: The density of metastable phases, Aerosol Sci. Tech., 39, 972–986, 2005.

Zelenyuk, A., Imre, D., Han, J. H., and Oatis, S.: Simultaneous measurements of individual ambient particle size, composition, effective density, and hygroscopicity, Anal. Chem., 80, 1401–1407, 2008.

Zenobi, R. and Knochenmuss, R.: Ion formation in MALDI mass spectrometry, Mass Spectrom. Rev., 17, 337–366, 1998.

Zhou, Y., Huang, X. H. H., Griffith, S. M., Li, M., Li, L., Zhou, Z., Wu, C., Meng, J. W., Chan, C. K., Louie, P. K. K., and Yu, J. Z.: A field measurement based scaling approach for quantification of major ions, organic carbon, and elemental carbon using a single particle aerosol mass spectrometer, Atmos. Environ., 143, 300–312, 2016.

Atmos. Meas. Tech., 12, 2219–2240, 2019 **www.atmos-meas-tech.net/12/2219/2019/**

129

Atmospheric
Measurement
Techniques

Open Access

EGU

Supplement of

Understanding atmospheric aerosol particles with improved particle identification and quantification by single-particle mass spectrometry

Xiaoli Shen et al.

Correspondence to: Harald Saathoff (harald.saathoff@kit.edu)

Single Particle Characterisation of Atmospheric Aerosol Particles in Central Europe
Appendix B

In summer time of 2016, a six-week field campaign was conducted at a rural site in the upper Rhine valley near Karlsruhe city in southwest Germany. ~3.7×10^5 single particles were analysed by the laser ablation aerosol particle time-of-flight mass spectrometer (LAAPTOF). In the main manuscript we have shown an improved particle identification and quantification, and discussed the internal and external mixing state of the aerosol particles. Here is the supporting information, including tables and figures, as well as some detailed descriptions.

Table S1: Criteria for single particle identification method and the resulting correlation with fuzzy results

	class 1	class 2	class 3	class 4	class 5	class 6	class 7	total
criteria of γ_{pos} for positive spectra	≥ 0.6	≥ 0.6	≥ 0.6	≥ 0.6	≥ 0.6	≥ 0.8	≥ 0.6	—
criteria of γ_{neg} for negative spectra	≥ 0.45	≥ 0.45	≥ 0.5	≥ 0.3	≥ 0.53	≥ 0.8	≥ 0.5	—
correlation (γ) for particle number counts comparison	0.85	0.86	0.98	0.99	0.85	0.87	0.66	0.98

Note that, we have tuned both γ_{pos} and γ_{neg} in order to obtain the comparable time series of particle counts with fuzzy results.

Table S2: Four new laboratory generated aerosol particles for reference mass spectra

	Aerosol particle types	Size/nm		Source	No. of
		d_{va}	width		Spectra
1	Sodium nitrate (NaNO$_3$)	935	230	Merck KGaA	3908
2	Secondary organic aerosol from toluene +OH radicals (A SOA) coated onto NaNO$_3$ seed particles	860	208	Toluene from Merck KGaA	5530
3	Secondary organic aerosol from α-pinene and toluene + OH radicals (A and B SOA) coated onto NaNO$_3$	838	207	(1S)-(-)-α-pinene (99%) from Aldrich	3982
4	Fly ash from coal combustion	0 to 20 μm * (sieved)		One power plant in UK	962

For aerosol generation and sampling methods: 1) Sodium nitrate particles were sampled from the 84.5 m^3 simulation chamber AIDA (Aerosol Interactions and Dynamics in the Atmosphere) of KIT; 2) SOA particles coated NaNO$_3$ particles were formed via OH oxidation of toluene/ toluene and α-pinene SOA with particle seeds in the presence of NO$_x$, and sampled from AIDA chamber; 3) Fly ash particles were suspended in their reservoir bottle by shaking them and sampled directly from the headspace (upper part) of these reservoir through a tube connecting it with the LAAPTOF.

For particles size information, d_{va} values represent the expected values from Gaussian fitting to the particle sizes measured by LAAPTOF. Size width represents the standard deviation from Gaussian fitting to the measured particle sizes (d_{va}).

*For fly ash particles, we give its size which was labelled in the original samples which were sieved with a 20 μm test sieve.

No. of Spectra is the number of averaged spectra.

Table S3: Corrected number fraction and mass fraction of different particle classes with different ODE*

	class 1	class 2	class 3	class 4	class 5	class 6	class 7
Corrected Number Fraction							
ODE_max	14.9%	26.0%	5.1%	4.1%	33.4%	3.5%	12.9%
ODE_mean	14.2%	24.3%	5.9%	5.0%	33.5%	4.5%	12.6%
ODE_min	13.8%	23.1%	5.5%	5.2%	34.2%	5.6%	12.6%
ODE_chemically resolved	18.2%	7.2%	3.4%	2.4%	45.0%	7.3%	16.5%
Particle Mass Fraction							
ODE_max	7.5%	9.6%	40.5%	8.8%	20.4%	3.8%	9.4%
ODE_mean	7.1%	8.0%	42.2%	9.4%	20.4%	4.7%	8.3%
ODE_min	7.6%	9.4%	33.9%	9.6%	23.6%	6.5%	9.5%
ODE_chemically resolved	10.3%	2.7%	30.1%	3.6%	31.8%	8.7%	12.9%

*see Fig. 1 for ODE_max/mean/min.

Table S4: Correlation for the comparison of non-refractory compounds measured by LAAPTOF and AMS

	Overall	Period 1	Period 2	Period 3	Period 4	Period 5	Period 6
Ammonium	**0.63**	0.37	**0.74**	0.46	**0.88**	0.38	**0.65**
Nitrate	0.32	**0.65**	**0.70**	**0.67**	0.47	0.55	0.43
Sulfate	0.10	-0.20	0.26	-0.14	**0.69**	0.07	0.15
Organic Cations	0.43	0.16	0.45	0.28	**0.76**	0.41	0.36
Organic Anions	0.32	-0.23	0.32	0.30	0.40	0.25	0.16
Org/(Org+Ammoinium)	0.52	-0.02	0.52	0.28	0.55	0.01	0.46
Org/(Org+Nitrate)	**0.62**	**0.78**	**0.85**	**0.81**	**0.68**	**0.76**	0.35
Org/(Org+Sulfate)	0.38	-0.02	0.44	0.35	0.32	0.37	0.10

Note: The values in this table are the Pearson's correlation coefficients (γ) for the compounds measured by LAAPTOF in relative ion intensity (normalized to total ions) and AMS in mass concentration. $\gamma > 0.6$ are in bold. Periods 1 to 6 are the same time periods as in Fig. 6 and Fig. S4; LAAPTOF fragments for ammonium, nitrate, sulfate, and organics can refer to Fig. 7 and Fig. S7 captions. These two instruments show good correlations on Org/(Org+nitrate) for almost all the measurement time.
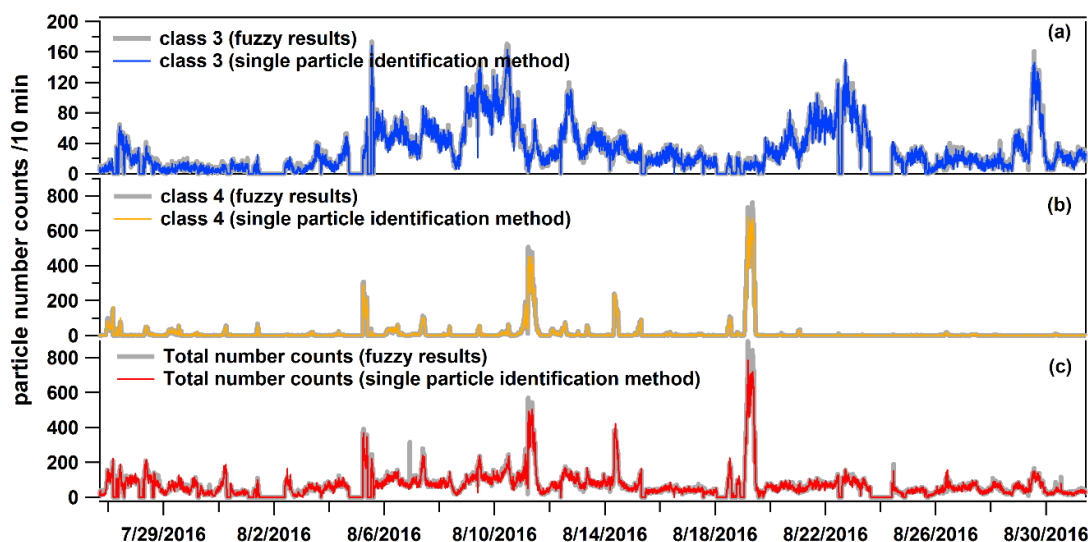
Figure S1: Time series of particle number counts obtained by fuzzy clustering and the single particle identification method using the fuzzy representative spectra as reference.
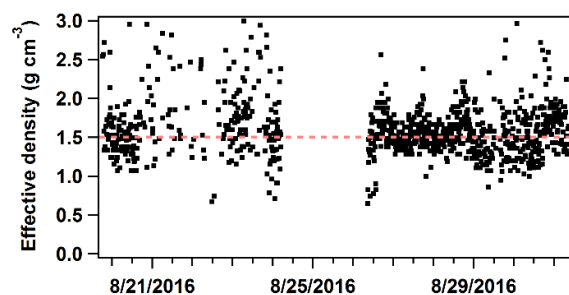
Figure S2. Time series of effective densities derived from comparison between AMS-d_{va} and SMPS-d_m.

2
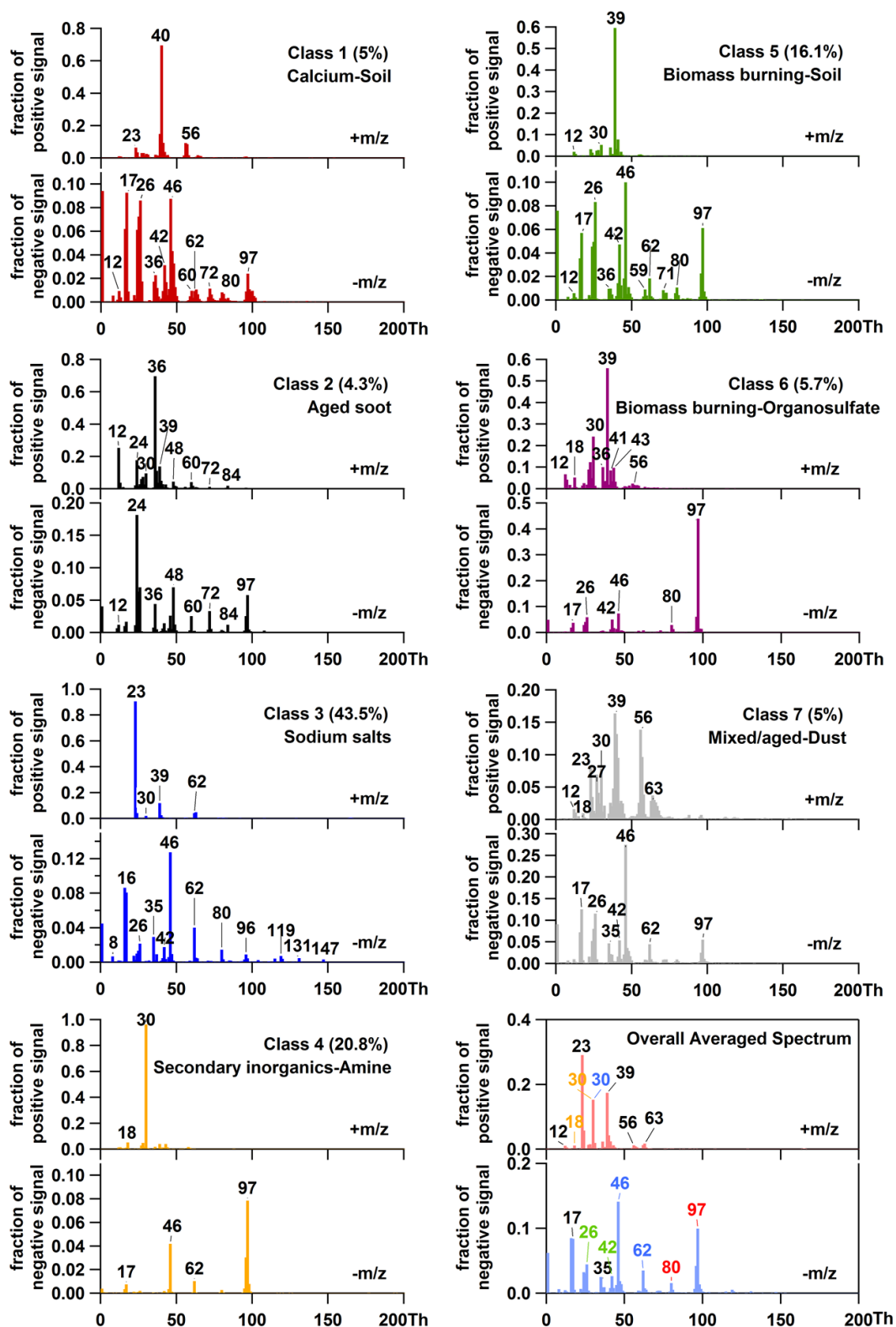
Figure S3: Representative mass spectra of seven particle classes and averaged spectrum of total ~3.7 × 10⁵ single particles measured during the field campaign TRAM01 (same as Fig. 2, except with linear mode).

3
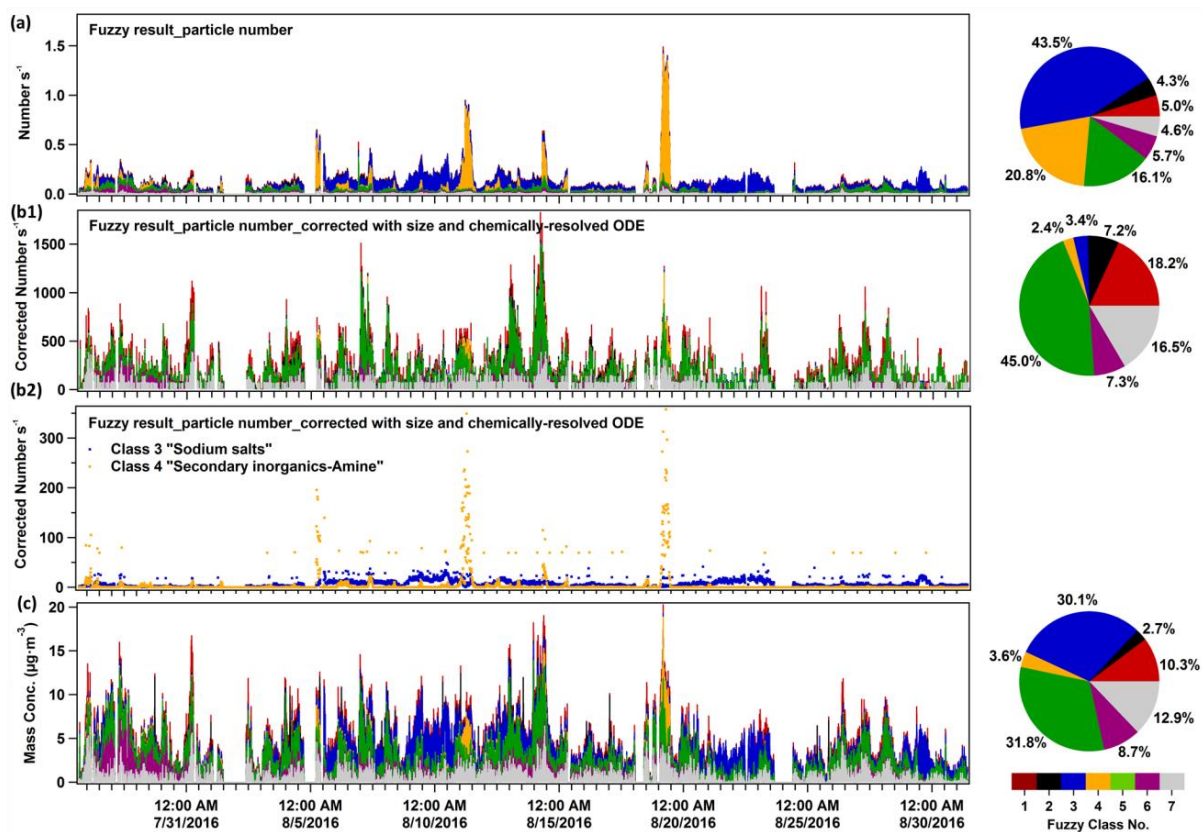
Figure S4: Time series of the particle number, corrected number, and mass concentration of seven major particle classes and the corresponding pie charts for total fractions. 7 fuzzy classes are class 1 "Calcium-Soil"; class 2 "Aged soot"; class3: "Sodium salts"; class 4 "Secondary inorganics-Amine"; class 5 "Biomass-Soil"; class 6 "Biomass-Organosulfate"; and class 7: "Mixed/aged-Dust". This figure is similar as Fig. 4, except with the absolute values. Besides, panel (b2) is added in order to visualize the time series of class 3 and 4, since their number fraction is too small after correction.

4
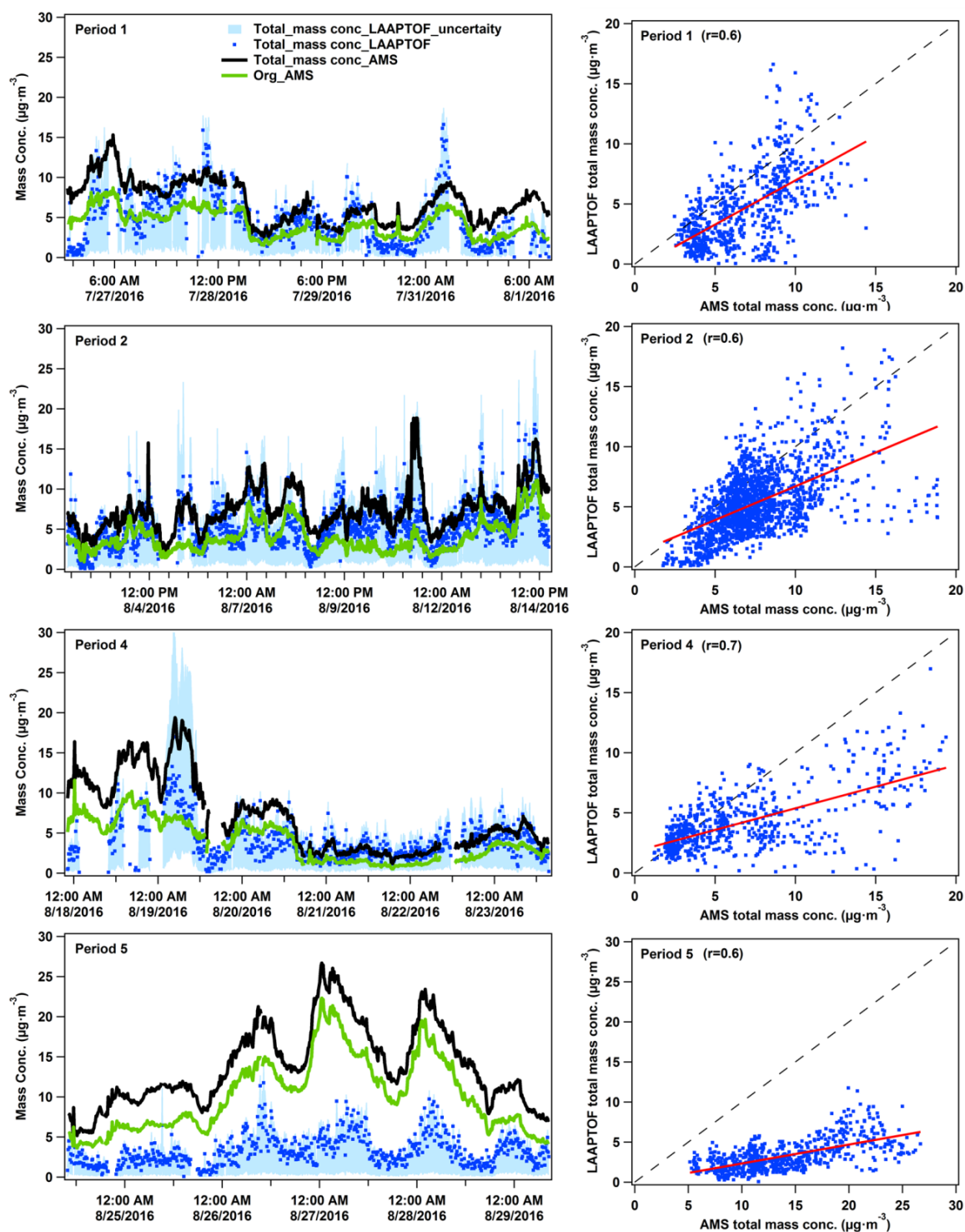
Figure S5: Comparison of mass concentration results between LAAPTOF and AMS in four periods. r represents for Pearson's correlation coefficient. Period 1 is from 7/26/2016 16:23 to 8/1/2016 11:43; P2 from 8/2/2016 09:43 to 8/14/2016 17:53; P4 from 8/17/2016 21:13:00 to 8/23/2016 15:33; P5 from 8/24/2016 15:03 to 8/29/2016 08:33.

5
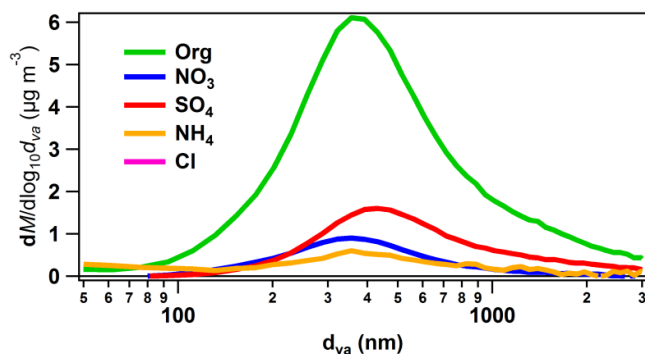
Figure S6: Chemical resolved size distributions for the particles measured by AMS during organics rich period (P5).
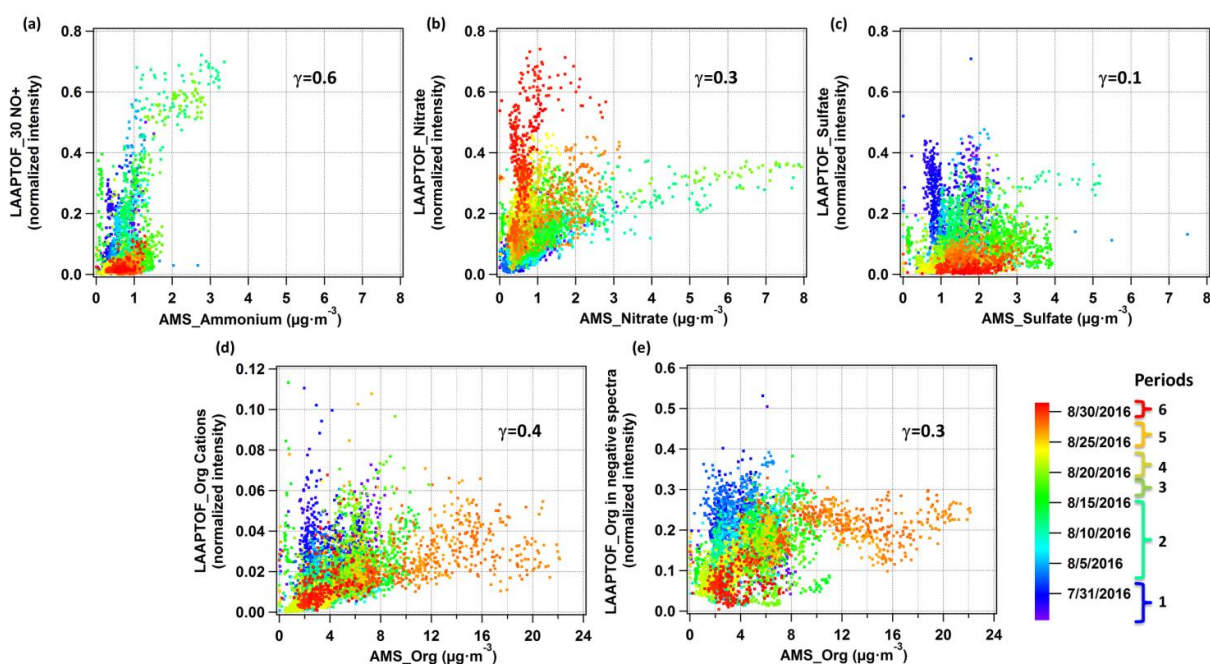
Figure S7: Comparison of non-refractory compounds measured by LAAPTOF and AMS: The normalized intensity of (a) 30 NO⁺;
(b) nitrate (46 NO₂⁻ + 62 NO₃⁻); (c) sulfate (32 S⁻+64 SO⁻ + 80 SO₃⁻ + 81HSO₃⁻ + 96 SO₄⁻ + 97 HSO₄⁻ +177 SO₃HSO₄⁻ +195 H₂SO₄HSO₄⁻
); (d) sum of positive organic markers at m/z 43 C₃H₇/C₂H₃O/CHNO⁺, 58 C₂H₅NHCH₂⁺, 59 (CH₃)₃N⁺, 88 (C₂H₅)₂NO/C₃H₆NO₂⁺, 95
C₇H₁₁⁺, 104 C₈H₈⁺, 115 C₉H₇⁺, and 129 C₅H₇NO⁺and (e) sum of the negative organic markers at m/z 24 C₂⁻, 25 C₂H⁻, 26 C₂H₂/CN⁻,
42 C₂H₂O/CNO⁻, 45 COOH⁻, 59 CH₂COOH⁻, 71 CCH₂COOH⁻, 73 C₂H₄COOH⁻, 85 C₃H₄COOH⁻, and 89 (CO)₂OOH⁻ measured by
LAAPTOF are plotted verses the mass concentration of ammonium, nitrate, sulfate, and organics measured by AMS, respectively.
Each point is 10 min averaged data, and there are 4483 points in each scatter plot. Colour scale is related to the timeline, including
periods 1 to 6.

6
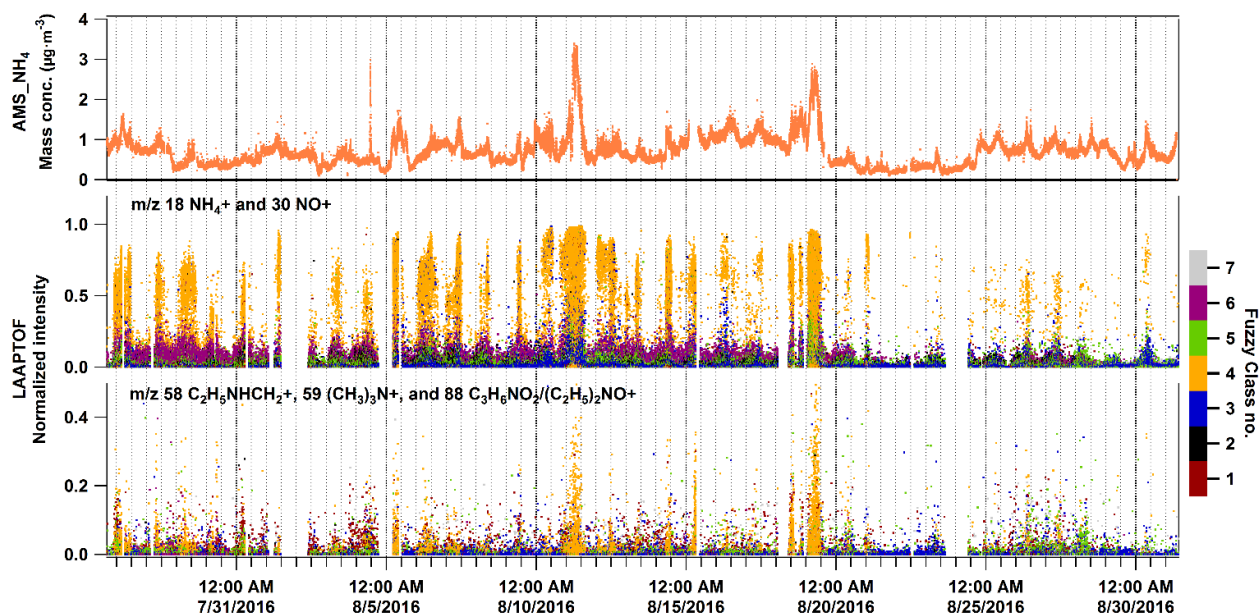
Figure S8: Time series of ammonium measured by in mass concentration and LAAPTOF in ion intensity. Normalized intensity refers to the fragment intensity divided by sum of all the ion intensities. Marker peaks for ammonium are at m/z 18 NH_4^+ and 30 NO^+ in LAAPTOF spectra, thus we use them to represent ammonium. In addition, some amine derived fragments at m/z 58 $C_2H_5NHCH_2^+$, 59 $(CH_3)_3N^+$, and 88 $(C_2H_5)_2NO/C_3H_6NO_2^+$ could also contribute to ammonium ions, therefore we also show them in this figure.

Appendix B.3 Composition and origin of PM$_{2.5}$ aerosol particles in the upper Rhine valley in summer

Composition and origin of PM$_{2.5}$ aerosol particles in the upper Rhine valley in summer

Xiaoli Shen[1,2], Heike Vogel[1], Bernhard Vogel[1], Wei Huang[1,2], Claudia Mohr[3], Ramakrishna Ramisetty[1,4], Thomas Leisner[1,5], André S. H. Prévôt[6], and Harald Saathoff[1,*]

[1]Institute of Meteorology and Climate Research, Karlsruhe Institute of Technology, Hermann-von-Helmholtz-Platz 1, 76344 Eggenstein-Leopoldshafen, Germany
[2]Institute of Geography and Geoecology, Working Group for Environmental Mineralogy and Environmental System Analysis, Karlsruhe Institute of Technology, Kaiserstr.12, 76131 Karlsruhe, Germany
[3]Department of Environmental Science and Analytical Chemistry, Stockholm University, Stockholm, 11418, Sweden
[4]Now at: TSI Instruments India Private Limited, Bangalore, 560102, India
[5]Institute of Environmental Physics, University Heidelberg, In Neuenheimer Feld 229, 69120 Heidelberg, Germany
[6]Laboratory of Atmospheric Chemistry, Paul Scherrer Institute (PSI), 5232 Villigen PSI, Switzerland

Correspondence to: Harald Saathoff (harald.saathoff@kit.edu)

Abstract. We conducted a six-week measurement campaign in summer 2016 at a rural site about 11 km north of the city of Karlsruhe in southwest Germany in order to study the chemical composition and origin of aerosols in the upper Rhine valley. In particular, we deployed a single particle mass spectrometer (LAAPTOF) and an aerosol mass spectrometer (AMS) to provide complementary chemical information of the aerosol particles smaller than 2.5 µm. For the entire measurement period, the total aerosol particle mass was dominated by sodium salts contributing on average (36 ± 27) % to the total single particles. The total particulate organic compounds, sulfate, nitrate, and ammonium contributed on average (58 ± 12) %, (22 ± 7) %, (10 ± 1) %, and (9 ± 3) % to the total non-refractory particle mass, respectively. The regional transport model COSMO-ART was applied for source apportionment and to achieve a better understanding of the impact of complex transport pattern on the field observations. Combining field observations and model simulations, we attributed high particle numbers and SO$_2$ concentrations observed at this rural site to industrial emissions from power plants and a refinery in Karlsruhe. In addition, two characteristic episodes with aerosol particle mass dominated by sodium salts particles compromising (70 ± 24) % of the total single particles and organic compounds comprising accounting for (77 ± 6) % of total non-refractory species, respectively, were investigated in detail. For the first episode, we identified relatively fresh and aged sea salt particles originating from the Atlantic Ocean more than 800 km away. These particles showed markers like m/z 129 C$_5$H$_7$NO$_3$$^+$ indicating the influence of anthropogenic emissions modifying their composition e.g., from chloride to nitrate salts during the long-range transport. For a 3-day episode including high organic mass concentrations, model simulations show that on average (74 ± 7) % of the particulate organics at this site were of biogenic origin. Detailed model analysis allowed us to find out that three subsequent peaks of high organic mass concentrations originated from different sources, including local emissions from the city and industrial area of Karlsruhe, regional transport from the city of Stuttgart (~64 km away), and potential local night-time formation and growths. Biogenic

(forest) and anthropogenic (urban) emissions were mixed during transport and contributed to the formation of organic particles. In addition, topography, temperature inversion, and stagnant meteorological conditions also played a role in the build-up of

35 higher organic particle mass concentrations. Furthermore, the model was evaluated using the field observations and corresponding sensitivity tests. The model results show good agreement with trends and concentrations observed for several trace gases (e.g., O_3, NO_2, and SO_2) and aerosol particle compounds (e.g., ammonium and nitrate). However, the model underestimates the number of particles by an order of magnitude and underestimates the mass of organic particles by a factor of 2.3. The discrepancy was expected for particle number since the model does not include all nucleation processes. The missing

40 organic mass indicates either an underestimated regional background, missing sources, and/or mechanisms in the model like night-time chemistry. This study demonstrates the potential of combining comprehensive field observations with dedicated transport modelling to understand the chemical composition and complex origin of aerosols.

1 Introduction

Aerosols are ubiquitous in the atmosphere and play a crucial role in air quality, human health, ecosystem and climate change.

45 In particular, aerosol particles modify atmospheric radiative fluxes and can serve as cloud condensation nuclei (CCN) and/or be activated as ice nuclei (IN), which influences the cloud formation, properties (albedo) and precipitation, thus has further impact on weather and climate change (Fuzzi et al., 2015; Pöschl, 2005; Seinfeld and Pandis, 2006). Such indirect impacts of aerosols on climate are still related to large uncertainties and low confidence levels (IPCC, 2013). There are various types of atmospheric aerosol particles, such as mineral dust, sea salt, soot, and organic aerosol particles, originating from biogenic and/or

50 anthropogenic emission sources, as well as secondary formation from precursors within the atmosphere (Tsigaridis et al., 2006). Aerosol particles are not typically purely inorganic or organic; instead, they are often composed of different inorganic and organic species. The diverse origins and atmospheric aging cause the complexity of the aerosol particle mixtures.

Real-time mass spectrometry is widely used to measure size and chemical composition of aerosol particles with high temporal resolution. Two major instrument types are single particle mass spectrometers (singe-particle MS) and aerosol mass

55 spectrometers (AMS). The single-particle MS is sensitive to both non-refractory and refractory species and to the mixing state of individual particles, and thus identifies particle types (Murphy, 2007), while the AMS can quantify mass concentrations of non-refractory particulate compounds in bulk samples (Canagaratna et al., 2007). Complementary data from single-particle MS and AMS allows quantitative interpretation of the internal and external mixing state of the aerosol (Gemayel et al., 2017; Gunsch et al., 2018; Healy et al., 2013; Jeong et al., 2011; Shen et al., 2019; Zhou et al., 2016). The mixing state of the aerosol particles

60 can reflect their evolution e.g. caused by chemical reactions leading to changing compositions or coatings (Reitz et al., 2016). A good example is the aging of sea salt particles: chloride replacement by nitrate on sea-salt particles can be well identified by single-particle MS (Gard et al., 1998).

Single Particle Characterisation of Atmospheric Aerosol Particles in Central Europe
Appendix B

The large diversity of aerosols, containing hundreds of gaseous and particulate components, makes it difficult to trace their sources. Therefore, several source apportionment methods have been developed with the common aim of reducing the complexity of the aerosol particle mixtures and thus helping to identify the major particle types in the atmosphere. Clustering algorithms have been used commonly for the single-particle MS data analysis (Reitz et al., 2016), while positive matrix factorization (PMF; Paatero, 1997; Paatero and Tapper, 1994) is commonly applied for AMS data analysis (Canonaco et al., 2013; Canonaco et al., 2015; Crippa et al., 2014; Zhang et al., 2011). However, these methods can only provide indirect source information. The application of a transport model gives additional information. It can predict the state of the atmosphere based on detailed meteorology, emission data, as well as conversions of reactive species and thus allows studying the aerosol evolution from the emissions to a site of interest.

There exists a variety of so-called online coupled chemical transport models. A recent review is given by (Baklanov et al., 2014). Such models are important tools to better understand aerosol particles' sources and aging processes, and their impact on particles' climate-relevant properties, such as cloud condensation nuclei (CCN) activity, optical properties, and hygroscopicity (Fierce et al., 2017). Models can be improved with a good process understanding, e.g., emissions, transport and deposition, and corresponding parameterisations obtained from dedicated laboratory studies (Burkholder et al., 2017). They are often used to predict the evolution of the atmospheric composition on different spatial scales, which can be evaluated by comparison with field measurements. Besides, comparisons between model simulations and field observations also help to validate the model or to identify weaknesses like poorly represented chemistry, missing sources or mechanisms.

For comparison with measurements at a single location, regional scale models with small grid sizes (down to a few kilometres) are required. In addition, phenomena such as mountain and valley winds, land-sea breezes or lee waves become important, which requires a non-hydrostatic formulation of the model equations. In this study we use the regional-scale model system COSMO-ART (Consortium for small-scale modelling - aerosols and reactive trace gases; Vogel et al., 2009). The part of the model describing aerosols and reactive trace gases was developed at the Karlsruhe Institute of Technology (http://www.imk-tro.kit.edu/english/3509.php). It extends the operational weather forecast model COSMO of the German Weather Service (DWD), and it allows studying the feedback processes between aerosol particles and the state of the atmosphere covering the continental to the regional scale.

Mobile particle measurements on a tram line intersecting the city of Karlsruhe in southwest Germany and in the upper Rhine valley, showed particle number concentrations in the rural area north of the city almost as high as in downtown (particle size > 4 nm; mean value = 1.2×10^4 cm^{-3}, maximum values 3×10^4 cm^{-3}) (Hagemann et al., 2014). The Rhine valley provides a well-known wind channel of large-scale flow. This results in faster transport of pollutants along the valley axis, e.g., NO_x, SO_2, volatile organic compounds (VOCs) and particles (Gross and Wippermann, 1987; Hagemann et al., 2014; Kalthoff and Vogel, 1992; Vogel et al., 1986).According to data from the local air quality monitoring administration (LUBW, https://www.lubw.baden-wuerttemberg.de/luft) from 2016 to 2018, the annual averaged mass concentrations of NO_2, SO_2, PM_{10}, and soot are 20, 2, 16, and 1.8 $\mu g\ m^{-3}$, respectively, measured at their Eggenstein monitoring station (3.3 km south of the

141

measurement site used in this study and about 9 km north of the city of Karlsruhe). Specifically, NO_2 concentrations are about half of the values measured in downtown Karlsruhe, but they exhibit comparable peak values (around 50–80 μg m^{-3}). SO_2 levels at Eggenstein are the second highest in the state of Baden-Württemberg (from the available data from 2016 to 2018), and maximum hourly values can reach up to~50 μg m^{-3}.

100   In order to understand the sources for high local particle concentrations as well the chemical nature and mass concentrations of aerosol types prevailing in the upper Rhine valley in summer-time we combine comprehensive aerosol information from point measurements with a regional transport model. Besides a better understanding of the origin of the aerosol in that region, we want to validate the capabilities of our transport model to predict characteristic air quality parameters.

2 Methods

2.1 Measurement site and instrumentation

The measurement site (49°6'10.54" N, 8°24'26.07" E) is in the upper Rhine valley 175 m north of the village of Leopoldshafen and 10 m east of the tramline No S1/11 described by Hagemann et al., (2014) (marked with a star in Fig. 1). The Rhine valley often acts as a wind channel leading to wind directions mainly from southwest or northeast. As shown in Fig. 1, the measurement site is located ~11 km north of downtown Karlsruhe and ~5 to 15 km northeast of an industrial area, including a refinery with

110   15.5 Mt/yr capacity, a 1450 MW hard coal fired power plant, as well as a 365 MW gas fired power plant (Hagemann et al., 2014). Therefore, the measurement site is potentially subject to the urban and industrial emissions especially for southerly wind directions. Apart from that, there are several nearby biogenic emission sources, e.g., forests, sunflower fields, as well as other agricultural areas (Hagemann et al., 2014; Huang et al., 2019). Local traffic emissions from the minor road near the measurement site was identified by measurements with high time resolution. Its contributions to the aerosol load are small due to the generally

115   weak traffic.

The instrumentation for this campaign has been described in detail in previous publications (Huang et al., 2019; Shen et al., 2019). Briefly, the data we use here are from the 6-week (26 July to 31 August 2016) deployment of a laser ablation aerosol particles time-of-flight mass spectrometer (LAAPTOF; AeroMegt GmbH) and a high-resolution time-of-flight aerosol mass spectrometer (HR-ToF-AMS; Aerodyne Inc.; hereafter AMS). These instruments were used to provide real time information

120   on size and chemical composition for individual particles and bulk samples, respectively. The LAAPTOF is a commercially available single particle mass spectrometer and has been well described in recent publications (Ahern et al., 2016; Gemayel et al., 2016; Gemayel et al., 2017; Marsden et al., 2018; Marsden et al., 2016; Marsden et al., 2019; Ramisetty et al., 2018; Reitz et al., 2016; Shen et al., 2018; Shen et al., 2019). In brief, aerosol particles with a size range of 70 nm to 2.5 μm vacuum aerodynamic diameter (d_{va}) are sampled with a flowrate of ~80 cm^3 min^{-1}, focused and accelerated via an aerodynamic lens

125   (ADL). Afterwards, the particles of ~200 nm to 2.5 μm d_{va} can be detected with two laser diodes (λ = 405 nm) mounted in the

particle time-of-flight (PTOF) chamber. Once a single particle is detected successively by both of the detection lasers, its d_{va} is calculated from the time of flight and an excimer laser ($\lambda = 193$ nm) is triggered to desorb and ionize the refractory and non-refractory species of the particle. The resulting cations and anions are analysed with a bipolar ToF mass spectrometer. The AMS measures the particle size-resolved bulk chemical composition, e.g., organic compounds, ammonium, nitrate, sulfate, and

130   chloride, in mass concentrations with high time resolution and sensitivity (DeCarlo et al., 2006). Similarly as the LAAPTOF, aerosols are sampled with a flowrate of ~84 cm^3 min^{-1} via a similar ADL in the size range 70 nm to 2.5 µm d_{va} and then pass through a PTOF chamber. At the end of the PTOF chamber, particles encounter a 600 °C heater that vaporises the non-refractory species. The corresponding vapours are ionized by electron impact with high energy of 70 eV, generating positive ions that are analysed with a ToF mass spectrometer. To account for a particle bouncing effect, a collection efficiency (CE, the product of

135   net particle transmission and detection efficiency) is used (Canagaratna et al., 2007). The CE depends on composition and phase of the particles (Bahreini et al., 2005). Therefore, composition dependent CEs were used to correct the AMS data for this measurement campaign.

All sampling inlets (PM_{10}, $PM_{2.5}$, TSP) were positioned at the top of a measurement container (3.7 m above ground level, a.g.l.). Particle number (size>2.5 and >7 nm, CPC3776 and CPC 3022A, TSI Inc.), particle mass (total suspended particulates,

140   PM_{10}, and $PM_{2.5}$; FIDAS, PALAS GmbH), black carbon (AE33-7 Aethalometer, Magee Scientific Co.), and trace gases O_3 (O341M, Environment SA), SO_2 (AF22M, Environment SA), NO_2 (AS32M, Environment SA) CO_2 (NGA2000, Rosemont Inc.) were measured. Meteorological parameters temperature, relative humidity, solar radiation, wind direction and speed (WS700, Lufft GmbH) were measured 10 m a.g.l. and complemented by meteorological data from a 200 m tower located at the KIT campus north, ~2 km east of the measurement site (49°5′43.0″N 8°25′46.0″E).

145   **2.2 Regional transport model COSMO-ART**

The regional transport model COSMO-ART is used in this study to simulate an episode with high mass concentration of organics (up to ~25 µg m^{-3} measured by AMS). Detailed model descriptions can be found in previous studies (Bangert et al., 2011; Knote et al., 2011; Stanelle et al., 2010; Vogel et al., 2009). Therefore, we will only give a brief review here. COSMO-ART is a fully online coupled model system, which uses the same spatial and temporal resolution for all scalars, such as temperature, gas and

150   aerosol particle concentrations. The meteorological module is based on the operational weather forecast model COSMO of the German weather service (Deutscher Wetterdienst, DWD). When atmospheric chemistry and aerosol dynamics are coupled to COSMO, it allows the online calculation of the transport of reactive trace gases and aerosol particles as well as their interaction with the state of the atmosphere. Physical processes, e.g., nucleation, coagulation, condensation and sedimentation are included in the model. The aerosol particles are represented by five interactive log-normal modes representing particles consisting of

155   internally mixed sulfate, ammonium, nitrate and organic compounds, pure soot, as well as internal mixtures of them all. The hourly biogenic emissions are calculated online according to the land use data, the simulated temperatures, and radiative fluxes (Vogel et al., 1995). The anthropogenic emissions, including traffic emissions, large point and area sources such as industrial

and households' areas, were pre-calculated by J. Bieser at Helmholtz Zentrum Geesthacht (Backes et al., 2016; Bieser et al., 2011). In our study, the simulation domain is covered by a 350×330 grid with a horizontal resolution of 1×1 km^2 and 50 vertical

160   atmospheric layers (nonlinear increase up to 22 km a.g.l.). Most of the simulation results shown in this paper correspond to the lowest atmospheric level (10 m a.g.l.) and we indicate if results are from higher levels. The hourly emissions of SO_2, NO_x, CO, NH_3, anthropogenic volatile organic compounds (VOCs), and primary organic aerosols (POA) were pre-calculated. As shown in Fig S1, VOCs, NO_x and POA are mainly emitted at a lower atmospheric level in urban areas, such as the cities of Karlsruhe, Stuttgart, Mannheim, and Strasburg, as well as the corresponding highways. SO_2 hot spots typically correspond to the stack

165   heights of the power plants emitting, such as the one in the western part of Karlsruhe.

3 Results and Discussion

In the first section, we give an overview of the meteorological conditions, the trace gases, and particles measured during the whole measurement campaign and will then give an example for source identification using the transport model. In the following two sections, we discuss two selected episodes in more detail, which are dominated by aged sea salt particles and relatively high

170   organic particle mass concentrations, respectively.

3.1 Overview of the field observation

Table 1 and Fig. S2 give an overview of meteorological conditions, trace gases, and particle concentrations for the entire measurement campaign. In summer 2016, the major wind direction was southwest (174 ± 75°) and an average wind speed was (1.3 ± 0.9) m s^{-1} at the measurement site in the upper Rhine valley. This wind speed allows trace gases and particles to be

175   transported over a distance of 10 km within 2 hours e.g. from the city of Karlsruhe to the measurement site. During the measurement time the sunrise and sunset were at around 06:30 and 20:30, respectively. Temperature and relative humidity (RH) were showing relatively stable anti-correlated diurnal patterns. Given the frequent clear nights, night-time temperature inversions occurred for 32 out of 37 nights during the entire measurement period (Fig. S3). Among the trace gases, CO_2 and O_3 were showing clear diurnal patterns with ozone peaking in the afternoon. NO_2 concentrations were higher in the morning

180   hours and in the late evenings and generally behaved anti-correlated to O_3. NO_2 and particle number were showing spikes at similar times (more frequently during the day-time), mainly due to the local emissions from nearby road traffic. The averaged particle number concentration of (1.2 ± 0.8) × 10^4 cm^{-3} for particles larger than 2.5 nm measured in this study, is comparable with that observed at the same site in previous tram-based measurements (Hagemann et al., 2014). SO_2 concentrations showed peaks with low frequency (up to >10 ppb) but only when the wind was coming from the direction of the industrial area in the

185   southwest. As shown in Fig. S2, these SO_2 peaks correspond to higher particle number concentrations at around noontime, when the wind speed is higher (~1.7 m s^{-1}) and vertical mixing intensified. This is in agreement with downward mixing of stack emissions from industrial sources, which can be validated by model calculations using COSMO-ART (refer to section 3.2).

In the entire measurement period, the total organic compounds, sulfate, nitrate, and ammonium were analysed to contribute on average (58 ± 12) %, (22 ± 7) %, (10 ± 1) %, and (9 ± 3) % to the total non-refractory PM$_{2.5}$ mass measured by AMS, respectively. In a previous publication (Shen et al., 2019), we could identify seven major particle classes at the measurement site among ~3.7×10^5 single particles with sizes between 200 nm and 2.5 µm d_{va}: Calcium-soil (class 1, C1); Aged soot (C2); Sodium salts (C3); Secondary inorganic–amine (C4); Biomass burning–soil (C5); Biomass burning–organosulfate (C6); and Mixed/aged dust (C7). These particle types were not always present in similar fractions but showed distinct periods with one or two types dominating the particle mass (Shen et al., 2019). Here, we will mainly discuss two particle classes that dominated the total particle mass, i.e., sodium salts and biomass burning–soil particles, contributing on average (36 ± 27) % and (30 ± 18) % to the PM$_{2.5}$ mass measured by the LAAPTOF, respectively. We will also discuss one characteristic particle class, i.e., secondary inorganic–amine particles, which showed relatively intensive and distinct peaks three times during this campaign (Fig. S2) as well as several weaker peaks.

As shown in Fig. 2 (a), total particle mass concentrations have clear diurnal pattern, showing higher night-time values and a peak during the morning rush hour (~9:00 local time). Higher particle mass values mainly correspond to southern wind directions, with one exception of extremely high masses associated with northwesterly winds (Fig. 2c). Specifically, sodium salt containing particles have higher fractions during day-time and correspond to southwesterly wind directions (Fig. 2b). Such wind was observed mainly during day-time and with higher wind speeds than at night. Biomass burning–soil particles enrich during night-time and mainly correspond to southeast wind (Fig. 2d). Secondary inorganic–amine particles typically rise in the morning and correspond to south and southwest wind directions (Fig. 2). When we compare weekdays (Monday to Friday) and weekends (Saturday and Sunday) in Fig. S4, the sodium salt particles were always correlated with southwest wind directions. Obvious differences can be found for secondary inorganic–amine and biomass burning–soil, respectively. For secondary inorganic–amine type particles, they were mainly advected by south and southwest wind during weekdays. However, they were much less abundant during weekends and did not show a clear relationship with wind directions (only a small peak for northwest). For biomass burning–soil particles the observations are a bit more complex.

The biomass burning–soil particles measured during weekdays were correlated with south and southwest wind as well, indicating potential sources from the city of Karlsruhe and its industrial area. Please note, that the representative spectra of these particles show aromatic ion peaks which may arise from aromatic compounds such as toluene and xylene due to motor vehicle emissions. Besides, this type of particles contains also some metals such as barium and lead that are related to coal combustion from industry. These features correspond to urban and industrial sources. During the weekends, biomass burning–soil particles had higher mass concentrations than during weekdays and were correlated with wind directions from east, southeast and northwest, where are mainly forests and agricultural areas. Therefore, we can infer that there were various sources for biomass burning–soil particles and these sources differed between weekdays and weekends. This could be e.g., barbeque fires during weekends while the weekdays' source is likely to be associated with that for secondary inorganic–amine particles.

220   In order to refine this type of particles, we compared them with black carbon particles measured by an Aethalometer (AE33-7). The equivalent black carbon concentration was calculated by the mass absorption cross sections value of 11.7 $m^2 g^{-1}$ (Herich et al., 2011). They seem to show a similar trend in the time series with a triplet of peaks from August 25th to 28th (refer to Fig. S2 and Fig. S5). We found that biomass burning-soil and black carbon concentrations are well correlated only for the weekends, with Pearson's correlation coefficients $\gamma \geq 0.6$ (Fig. S5 b), and poorly correlated for weekdays ($\gamma < 0.3$). This points to different

225   major sources for weekdays and weekends. In addition, the black carbon instrument measuring the light absorption at different wavelengths (λ) can be used to determine the absorption Ångström exponent (α) (Drinovec et al., 2015). For the entire campaign, the average α was 0.96 ± 0.24, calculated by using a pair of wavelengths and their corresponding mass absorption cross sections (MAC=11.7 and 23.6 $m^2 g^{-1}$ for λ=950 and 470 nm, respectively, Herich et al., 2011). Herich et al. (2011) and Zotter et al. (2017) have assigned an $\alpha =\sim0.9$ to BC from road traffic emissions, while the α values for wood burning BC were typically higher

230   ~1.68 (Zotter et al., 2017). Our measurements indicate that traffic was the dominating source of BC. Considering the good correlation between BC and biomass burning–soil particles during the weekend, we could infer the corresponding traffic emissions that contributed to biomass burning–soil particles. All observations support the conclusion that this particle class has significant anthropogenic sources, which may vary between weekends and weekdays. However, it still needs some more analysis to identify the different sources contributing to this particle class.

235   As mentioned before, the dominating particle classes varied for different time periods (Shen et al., 2019). In the following we focus on an episode with particles rich in sodium salts, to find out if sea salt particles can significantly influence the aerosol particle composition at this central European location about 800 km inland. Furthermore, we discuss another episode with relatively high organic mass concentrations to find out how these mass loads could form and exist for a relatively long time period. Both episodes are easily recognized from the time series of particles measured by LAAPTOF and organic compounds

240   measured by AMS (Fig. S2 and Fig. 3; see also Fig. 4 in Shen et al, 2019). Apart from the difference of dominating particle classes and particulate organics, the particle acidity, organonitrate fraction and organic carbon oxidation state, as well as meteorological conditions were quite different between these two episodes. For particle acidity, we used an acidity indicator, namely the ratio of NH_4^+ measured/predicted from AMS measurement (Zhang et al., 2007). The predicted NH_4^+ value is the mass concentration required to fully neutralize sulfate, nitrate, and chloride measured by AMS. The averaged value of NH_4^+

245   measured/predicted for the entire campaign is 0.82 ± 0.10. As shown in Fig. 3, this ratio reaches lowest value during sodium salts rich episode, corresponding to the highest acidity, while the value in the organic rich episode is at the averaged level. While the apparent high acidity for the sea salt may partially be due to sea salt sulfate included in the AMS measurement, the correlation between particle acidity and organics concentrations may be related to acid-catalysed organic particle formation. For the fraction of organonitrates, the AMS derived ratio of NO^+/NO_2^+ is commonly used as an indicator (Farmer et al., 2010; Kiendler-Scharr

250   et al., 2016). In the episode rich in sodium salts, particles contain the highest organonitrate fraction while the particles in the organic rich episode contain the lowest fraction (refer to Fig. S6). Both, higher acidity and higher fraction of organonitrates are indicators for a stronger influence of anthropogenic emissions on the sodium rich aerosol. The averaged carbon oxidation state

$(\overline{OS}_C)$ of the organic compounds is a robust metric of its degree of oxidation or processing (Canagaratna et al., 2015; Kroll et al., 2011). It turns out that the organics were more oxidized in the organic rich episode (refer to Fig. S6). In addition, the major

255 wind with higher speeds was from southwest in the episode rich in sodium salt particles, and we will show in section 3.3 that this is related to long-range transport of sea salt particles. For the organic rich episode, the wind speeds were lower for most of the time. The different features of these two episodes are also summarized in Table 2. We will discuss these two episodes in more detail in sections 3.3 and 3.4, but will first demonstrate the usefulness of the transport model to identify an industrial point source.

260 **3.2 Identification of an industrial point source**

As shown in Fig. 4, we have modelled O_3, NO_2, SO_2, and particle number for the organic rich episode with COSMO-ART. Model simulations show comparable results and/or trends with field observations. For SO_2, there is a modelled peak at 10:00 on August 26th. As mentioned above, in the upwind direction of our measurement site is a coal fired power plant, where SO_2 is emitted from a stack at 230 m a.g.l.. Therefore, we compared SO_2 concentrations in an area including the power plant and our

265 measurement site (refer to Fig. 5 a1 and a2), as well as time series of their vertical profile at the measurement site (Fig. 5b). The model results show that SO_2 emissions were starting at 02:00 from the stack of the power plant, continuously transported by southwest wind (from 06:00, not shown here). Around noon, the SO_2 was transported downward due to enhanced vertical mixing. Similar to SO_2, we found corresponding vertical transport of NO_x and primary particles (refer to Fig. 5 c and d), as well as secondary inorganic particles which will be discussed in section 3.3.3. In addition to the power plant emissions, particle

270 emissions from the Karlsruhe refinery (e.g., around 8:00 at 122 m a.g.l.) and downtown Karlsruhe (at 10 m a.g.l.) were observed in the model results, which are visualized via videos of the evolution of particle number at these two altitudes (refer to Data availability). Given these findings, we have verified industrial contributions to the particles measured at this rural site. However, the particle numbers calculated by the model are 10 times lower than the measured values. In this context, it should be noted that, the observations relate to particles larger than 2.5 nm and 7 nm, respectively. The modelled particles include Aitken and

275 accumulation mode particles with median diameter at around 30−80 nm and 300−400 nm, respectively. The model does not represent the ultrafine particles to their full extend, especially e.g., the contribution of organic compounds or ammonia to nucleation.

3.3 Aged sea salt in central Europe

Sodium salt particles accounted on average for (35.6 ± 26.7) % of the particle mass measured by LAAPTOF during the whole

280 campaign, and they dominated several time periods (refer to Fig. S2). However, not all the peak events were the same. We chose a unique episode when sodium chloride signatures, e.g., m/z 81 Na_2Cl^+, were showing the strongest signal, as plotted in Fig. 6 (a). In this episode, the sodium salts accounted for (70 ± 24) % of total mass of the single particles. To study the origin of these particles, we used the Hybrid Single-Particle Lagrangian Integrated Trajectory (HYSPLIT; Stein et al., 2015) on the READY

website (http://www.ready.noaa.gov; Rolph et al., 2017) for back-trajectory analysis. The corresponding result suggests that

285   these particles were coming from the Atlantic Ocean, which is more than 800 km west of our measurement site (refer to Fig. S7 a). Therefore, we can constrain the type of sodium salts particles as sea salts with an age of about 1.5 to 3 days.

    In this episode, sea salt particles retained strong chloride signatures in spite of the long-range transport, due to relatively high wind speeds (e.g., the average wind speed was ~6 m s^{-1} from the ocean to our measurement site at noontime on August 21st and 22nd, based on 72 h back-trajectory analysis). Therefore, we interpret them as relatively fresh sea salt, which is the 1st

290   sub-class of sodium salts particles identified with the fuzzy clustering analysis of the single particle mass spectra. As shown in Fig. 6 (a), there is an obvious decrease of m/z 81 Na_2Cl^+ at the end of this episode, while the sodium nitrate signature at m/z 108 $Na_2NO_3^+$ increases. Such trends can also be found in similar but much less prominent sodium chloride rich episodes (see the red guiding arrows in Fig. 6a). This indicates the aging process of sea salt particles, namely heterogeneous replacement of chloride by nitrate on sea salt particles (Gard et al., 1998). We assigned the 2nd sub-class of sodium salts to more aged sea salt

295   particles, which are bigger than the relatively young sea salt (Fig. 6b). 72 h back-trajectory analysis suggests that these particles were coming from the Atlantic Ocean and were carried with southwesterly wind of relatively lower speed (~3.5 m s^{-1}) to reach our measurement site on August 23rd, thus they spent more time (~3 days) over the continent and are more aged. The representative spectra of sodium salt particles and the averaged spectra of their sub-classes can be found in Fig. S8. The signal difference between aged and young sea salts spectra (aged - young) is shown in Fig. 6 (c), highlighting their signatures. Similar

300   relationships as for m/z 81 Na_2Cl^+ and 108 $Na_2NO_3^+$ can also be found for the other signature peaks (refer to Fig. S9). It is worth noting that there are also nitrate related peaks in young sea salt, such as m/z 104 $NaClNO_2^-$, verifying that these young sea salts were not fresh. In addition, m/z 92 $Na_2NO_2^+$ and 131 $NaNO_2NO_3^-$ increase earlier than 108 $Na_2NO_3^+$ and 147 Na $(NO_3)_2^-$. Such that, we can infer the aging degree from a series of signature peaks in LAAPTOF spectra: 81 Na_2Cl^+ →104 $NaClNO_2^-$ → 92 $Na_2NO_2^+$ and 131 $NaNO_2NO_3^-$ → 108 $Na_2NO_3^+$ and 147 Na $(NO_3)_2^-$ (from relatively fresh to more aged, corresponding to

305   chloride to nitrite to nitrate salts). However, this requires further systematic studies to be validated.

    For sodium salt particles, a weak but characteristic peak at m/z 129 $C_5H_7NO_3^+$ was assigned to organonitrate in LAAPTOF spectra in our previous study (Shen et al., 2019). As shown in Fig. S9, m/z 129 $C_5H_7NO_3^+$ has a similar trend as m/z 131 $NaNO_2NO_3^-$ and it is more pronounced in the LAAPTOF spectra of aged sea salt. In the sodium chloride rich episode, m/z 129 $C_5H_7NO_3^+$ has a similar trend as organonitrate mass concentrations estimated by AMS results. The method for organonitrate

310   estimation can be referred to Farmer et al. (2010) and the parameters used here are the same as those used by Huang et al. (2019). We have briefly described this method in the supplement after the caption for Fig. S9. AMS derived organonitrate mass concentrations are comparable with the results of molecular analysis using FIGAERO-HR-ToF-CIMS (stands for a filter inlet for gases and aerosols coupled to a high-resolution time-of-flight chemical ionization mass spectrometer) in a companion study by (Huang et al., 2019). Therefore, we can confirm that the m/z 129 $C_5H_7NO_3^+$ signal is due to organonitrates, rather than the

315   recombination of nitrate and organic fragments due to the laser desorption and ionization (LDI) matrix effect in single-particle MS (Murphy, 2007; Reilly et al., 2000; Reinard and Johnston, 2008; Zenobi and Knochenmuss, 1998). In addition, our

simulation chamber studies revealed that m/z 129 $C_5H_7NO_3^+$ in LAAPTOF spectra could be a signature for anthropogenic sources (refer to Fig. S10 and the corresponding detailed description in the supporting information). Therefore, m/z 129 $C_5H_7NO_3^+$ on sea salt particles indicates interactions between the natural sea salt and anthropogenic emissions. It is worth noting that another weak but characteristic peak was observed at m/z 165 $Na_3SO_4^+$. This signature peak for sea salt sulfate can be found with stronger signal in young sea salt than in aged sea salt (Gard et al., 1998).

3.4 Origin of the aerosol particles during the organics rich episode

At the end of the measurement period, we observed three subsequent organic peaks (see Fig. 3, Fig. S2, or Fig. S5): one peak during Friday August 26th day-time and two peaks during following two nights. Organics measured in this episode exhibited the highest mass concentrations of (12.9 ± 3.9) µg m^{-3}, which accounted for (77 ± 6) % of the total non-refractory particle mass and is almost 3 times more than organic masses measured in other periods of the entire AMS measurement period. Please note, some secondary inorganic components were also measured in this episode, showing some peaks at similar times as the high organic peaks. As for the sodium chloride rich episode, we have also done a HYSPLIT back-trajectory analysis for the organic rich episode. Fig. S7 (b) shows these results: the air mass was coming from the continent during this episode. In order to better interpret the measurements and to understand the impact of transport processes for the particles measured in the organics rich episode, we have done COSMO-ART simulations covering the time period from August 25th to 28th, 2016. Fig. 7 shows the particulate organic compounds, the secondary inorganics (ammonium, nitrate, and sulfate) measured by AMS, and the result calculated using COSMO-ART (panels d to g). The corresponding meteorological conditions measured are shown in panels (a) to (c) of Figure 7. In general, the trends and also the amplitudes of the model results compare quite well with the observations. In the following, we will combine field observation and transport model simulation results to address these questions: 1) were the organic rich aerosols due to local formation, regional transport, or vertical mixing; 2) were all three organic peaks caused by the same reasons; 3) were the secondary inorganics originating from the same sources as the organics. We will start the discussion with the inorganics, will then go to the organics, and will end up with a typical particle type in this episode.

3.4.1 Secondary inorganic compounds

As shown in Fig. 7 (e) to (g), observations and model results for secondary inorganic compounds show comparable diurnal cycles and even the concentration levels match quite well. While ammonium and nitrate have a similar trend for most of the time, the trend for sulfate seems to be somewhat different. The major peaks of ammonium and nitrate appear at similar times as the high organic peaks. As will be shown in the following section, these compounds originated from anthropogenic sources in the urban and industrial area of Karlsruhe and from the city of Stuttgart. There is only one instant when all the measured secondary inorganics are showing peaks together: the inorganics are peaking at ~10:00 on August 26th, when also high SO_2 concentrations were observed (c.f. Fig. 4) which were due to the emissions from a power plant located in upwind direction. To verify this, we can refer to the time series of vertical profiles for the simulated secondary inorganics (Fig. S11 b to d). Despite

similar spatial distributions of nitrate, ammonium, NO_2, and SO_2 from 02:00 to 12:00 (c.f. Fig. 5) the measured sulfate peak for that time is missing in the model output. The reason for this is still unclear. It should be noted that, compared to the sulfate peak observed, the companion ammonium and nitrate peaks are much broader, attributed to additional anthropogenic sources from the city and refineries rather than only the power plant.

Some of the differences between model result and observation, such as that on August 25th or e.g., for sharper peaks, may be explained by to missing (point) sources in the emission data and/or the limited spatial resolution. The general agreement is however quite well and also for some point sources like the largest power plant in Karlsruhe. Some of the differences in the trends of nitrate and sulfate may be caused by the different nature of the sources of their precursor gases SO_2 and NO_x. While SO_2 is emitted in this area mainly from a few point sources, NO_x is emitted from various sources over a larger area.

3.4.2 Organic compounds

For the organic compounds, the general temporal development is represented well by the model, showing similar trends as measured by AMS, but underestimates the mass concentrations by a factor of ~2.3; averaged model result is (5.5 ± 3.3) µg m^{-3}, while observed were (12.9 ± 3.9) µg m^{-3}. Potential reasons for this discrepancy will be discussed in the light of sensitivity tests at the end of this section.

As mentioned above, the organic particle fraction shows a peak on Friday August 26th during day-time (peak 1) and two more during the following nights of the weekend (peak 2 and 3) in the organics rich episode. Model result cover peak 1 and 2, as well as of the first part of peak 3. Analysis of the model results shows that the three peaks were caused by different reasons including meteorological conditions, regional transport, and local or in-situ new particle formation and growths (such as night-time new particle formation; Huang et al., 2019). As shown in Fig. 7a and d, peak 1 corresponds to south and southwest wind, indicating that the air masses came from the urban and industrial area of Karlsruhe. This is illustrated very well in a video showing the transmission of particulate organics leading to peak 1 (refer to Data availability). The most intensive peak in organic particle mass (peak 2), starts from August 26th 20:30 (Fig. 3 and Fig. S2) when the wind direction shifts from northwest to east (northeast, straight east, and southeast), the wind speed decreases to < 0.5 m s^{-1}, and the night-time temperature inversion starts. Such stagnant conditions limit aerosol mixing and support build up aerosols and their growth. During the entire campaign, the strongest temperature inversion was observed during this night from August 26th to 27th (peak inversion at 02:40 on August 27; Fig. S3). In spite of the stagnant conditions and rather low wind speeds, regional transport still plays an important role. The model results for this time show transport of organic aerosol particles from the city of Stuttgart (southeast to the measurement site) over forested areas into the Rhine valley. This is clearly visible in a corresponding video of the model results for particulate organics and wind directions (refer to Data availability). Furthermore, we investigate the relative contribution of biogenic and anthropogenic emissions and their interactions for this episode by comparing the model results with and without biogenic emissions. It turns out that the corresponding air masses originating from anthropogenic emissions in the Stuttgart area were transported to the measurement site by south-easterly winds via forested hills. During this transport, the organic particle mass

380 concentrations increased while being mixed with biogenic emissions from the forest. The resulting air mass finally reaching the measurement site consisted therefore of anthropogenic and biogenic organics. For peak 3, we can also find impact of transport as illustrated in another video of particulate organic mass evolution (refer to data availability). However, the origin of this peak is more complex and is most likely more influenced by local particle formation and growths. After the night-time peak 2, from 12:00 on August 27 the air mass were doing back and forth movements in west-east directions, showing a strong concentration

385 gradient (west-east). Such a conditions lead to a high uncertainty of the model results for one point. Hence, although we observed quite similar particle compositions in these three subsequent peaks with high organic mass concentrations for similar meteorological conditions with low wind speeds, all three peaks were caused by air masses of different origin.

As mentioned above, the model underestimates the organic aerosol mass on average by a factor of 2.3. In order to better understand this discrepancy, we have done three sensitivity tests: with/without biogenic emissions (test 01), one with doubled

390 biogenic emissions (test 02) and one with boundary values or regional background values (outside the model domain) of particulate organic compounds increased by a factor of 10 (test 03). The results of test 01 suggest that (80 ± 4) % of the organic mass calculated was resulting from biogenic sources for the peak 1 time period, corresponding to the air masses coming from Karlsruhe. Regarding the time period of peak 2, there was a sharp drop of the biogenic contribution from the 88% to 68% corresponding to August 26th 23:00 to August 27th 2:00 when the air mass was coming from direction of Stuttgart (see Fig. 8).

395 Hence, we can infer that the anthropogenic contribution to the air mass that originated from Stuttgart was somewhat larger than that originated from Karlsruhe. Over the entire organic rich episode, on average (74 ± 7) % of the organics mass was contributed by biogenic sources. To test if missing emissions of biogenic precursors can explain the underestimated organic particulate masses we doubled this major (biogenic) source for organics (test 02). As shown in Fig. 9, doubling biogenic emissions makes some of the peaks of organic mass fit the observations better but the concentrations before and in between the peak values are

400 still underestimated. Another potential reason for the discrepancy could be to low boundary values (regional background); therefore, we increased them by a factor of 10 (test 03). This elevates the overall simulated concentration levels, leading to an overestimation especially of the first peak. These tests demonstrate the potential role of precursor emissions and regional transport of organic aerosol particles on the model results. There seems to be evidence that the model underestimates the regional background of organic aerosol particles. However, we cannot rule out that also underestimated sources of VOC or weaknesses

405 in the SOA formation mechanism may contribute to the underestimation of the organic aerosol particle mass. For example, night-time new particle formations mechanisms are not included in the current model version.

4 Conclusions and atmospheric implication

High particle number concentrations have been observed at a rural site in the upper Rhine valley by measurements on a tramline (Hagemann et al., 2014). In order to study the nature of the aerosols in the same region, we conducted a 6-week stationary field

410 measurement campaign at a rural site next to the tramline in summer 2016, and applied a regional transport model COSMO-

ART to analyse the origin of the aerosols. Comparing the field observations and model calculations, we have verified that industrial emissions contribute to the high particle number concentrations at this rural site.

For the whole measurement period, the particles that dominate the mass are sodium salts, which contributed (36 ± 27) % to the $PM_{2.5}$ mass measured by the LAAPTOF. According to the AMS measurements, organics, sulfate, nitrate, and ammonium

415   contributed (58 ± 12) %, (22 ± 7) %, (10 ± 1) %, and (9 ± 3) % to the total non-refractory $PM_{2.5}$ mass, respectively. Furthermore, we have investigated two episodes, which were dominated by aged sea salt and organics, which show characteristic features such as higher particle acidities and carbon oxidation states, respectively. Both episodes selected, were dominated by particles formed from the interaction of natural/biogenic and anthropogenic emissions.

For the sodium chloride rich episode, sodium salt particles accounted for (70 ± 24) % of total mass of the single particles.

420   We could show that the dominating particles were originally sea salt, from the Atlantic Ocean (~800 km away from the measurement site). These particles consisted of two classes with different aging stages. After $1.5-3$ days of transport, the original sea salt particles retained strong chloride signatures while after $3.5-4$ days of transport over the continent aged sea salt with stronger nitrate signatures and larger size arrived at the measurement location. In addition, the organonitrate signature peaks at m/z 129 $C_5H_7NO_3^+$ were stronger for the aged sea salt particles. According to chamber experiments on OH oxidation of α-

425   pinene and/ or toluene in the presence of NO_x on sodium nitrate seed particles, we have evidence that m/z 129 $C_5H_7NO_3^+$ is a signature peak for anthropogenic organics in single particle mass spectra. Hence, the m/z 129 $C_5H_7NO_3^+$ observed on sea salt particles in this study is another indicator for the interaction of anthropogenic emissions with the sea salt particles. Besides, the observed signature peak at m/z 165 $Na_3SO_4^+$ for sea salt sulfate may indirectly explain apparently higher particle acidity in this episode. Some other signature peaks such as 81 Na_2Cl^+, 92 $Na_2NO_2^+$, 108 $Na_2NO_3^+$, 104 $NaClNO_2^-$, 131 $NaNO_2NO_3^-$, and 147

430    $Na(NO_3)_2^-$ have the potential to indicate degree of aging of sea salt particles.

For the organics rich episode, the particulate organic compounds accounted for (77 ± 6) % of total non-refractory particle mass. We identified potential sources of the elevated organic particle concentrations and of secondary inorganic compounds. Transport model results suggest that (74 ± 7) % of the particulate organic mass calculated was related to biogenic emissions. With the combination of mass spectrometry and COSMO-ART modelling, we can confirm that during Friday, August 26th , air

435   masses came from an industrial area and the city of Karlsruhe, leading to high particle numbers (including all the particles with size >2.5 nm), high particulate organics and secondary inorganics, as well as high fractions of aged-biomass-burning and soil-dust like particles. During night-time on August 26th, south-easterly winds transported air masses from Stuttgart via forested areas to the measurement site, resulting in particles formed by the interaction of anthropogenic and biogenic precursors. Such air masses flowed into the Rhine valley and contributed also to the high organic aerosol mass concentrations during the night

440   from August 27th to 28th. In addition, low wind speeds and temperature inversion limited mixing and supported new particle formation and growth, partially contributing to higher organic particle masses.

Comparing comprehensive field observations with the COSMO-ART model results showed quite good agreement for trends and most concentration levels for several aerosol particle compounds and trace gases even if not all details could be reproduced

445 by the model. However, the simulated particle numbers are 10 times less than the observed values. This is mainly due to the fact that not all new particle formation processes (nucleation mode) are included in the model (e.g. night time chemistry as well as the role of organics or ammonia). Furthermore, the model underestimates particulate organics by a factor of 2.3. This discrepancy may be partly explained by an underestimated regional background, missing sources, or incomplete SOA formation and growths mechanisms, in the current model version.

450 As discussed above, we can conclude that factors related to topography, metrological conditions, local emissions, in-situ formation and growths, regional transport, as well as the interaction of biogenic and anthropogenic compounds need to be considered for a comprehensive understanding of aerosol composition and processing in this region. This study provides a good insight into the chemical nature and complex origin of aerosols in the upper Rhine valley, achieved by combining complimentary mass spectrometry and transport modelling.

Data availability

455 Video data will be available at KIT open data (https://publikationen.bibliothek.kit.edu/1000094401).

Author contributions

X.S. operated LAAPTOF and AMS during the whole field campaign, did the LAAPTOF data analysis, did COSMO-ART model runs and model output data analysis, did HYSPLIT back-trajectory analysis, produced all figures, and wrote the manuscript. H.S. organized the campaign, provided trace gas, meteorology, and particle measurements as well as suggestions 460 for the data analysis, interpretation, and discussion. H.V. and B.V. provided the input data for COSMO-ART model, provided suggestions for the model simulation, the model data analysis, interpretation, and discussion. W.H. operated AMS during the whole campaign and did AMS data analysis. C.M. helped to operate the instruments, did black carbon data analysis, and provided suggestions for the data analysis, interpretation, and discussion. R.R. helped to operate LAAPTOF. A.S.H.P. gave comments for interpretation of black carbon data. T.L. gave general advices and comments for this paper. All authors contributed 465 to the final text.

Competing interests

The authors declare no conflict of interest.

Acknowledgements

153

References

475   Ahern, A. T., Subramanian, R., Saliba, G., Lipsky, E. M., Donahue, N. M., and Sullivan, R. C.: Effect of secondary organic aerosol coating thickness on the real-time detection and characterization of biomass-burning soot by two particle mass spectrometers, Atmos Meas Tech, 9, 6117–6137, 2016.

Backes, A., Aulinger, A., Bieser, J., Matthias, V., and Quante, M.: Ammonia emissions in Europe, part I: Development of a dynamical ammonia emission inventory, Atmos Environ, 131, 55–66, 2016.

480   Bahreini, R., Keywood, M. D., Ng, N. L., Varutbangkul, V., Gao, S., Flagan, R. C., Seinfeld, J. H., Worsnop, D. R., and Jimenez, J. L.: Measurements of secondary organic aerosol from oxidation of cycloalkenes, terpenes, and m-xylene using an Aerodyne aerosol mass spectrometer, Environ Sci Technol, 39, 5674–5688, 2005.

Baklanov, A., Schlunzen, K., Suppan, P., Baldasano, J., Brunner, D., Aksoyoglu, S., Carmichael, G., Douros, J., Flemming, J., Forkel, R., Galmarini, S., Gauss, M., Grell, G., Hirtl, M., Joffre, S., Jorba, O., Kaas, E., Kaasik, M., Kallos, G., Kong,
485   X., Korsholm, U., Kurganskiy, A., Kushta, J., Lohmann, U., Mahura, A., Manders-Groot, A., Maurizi, A., Moussiopoulos, N., Rao, S. T., Savage, N., Seigneur, C., Sokhi, R. S., Solazzo, E., Solomos, S., Sorensen, B., Tsegas, G., Vignati, E., Vogel, B., and Zhang, Y.: Online coupled regional meteorology chemistry models in Europe: current status and prospects, Atmos Chem Phys, 14, 317–398, 2014.

Bangert, M., Kottmeier, C., Vogel, B., and Vogel, H.: Regional scale effects of the aerosol cloud interaction simulated with an
490   online coupled comprehensive chemistry model, Atmos Chem Phys, 11, 4411–4423, 2011.

Bieser, J., Aulinger, A., Matthias, V., Quante, M., and Builtjes, P.: SMOKE for Europe - adaptation, modification and evaluation of a comprehensive emission model for Europe, Geosci Model Dev, 4, 47–68, 2011.

Burkholder, J. B., Abbate, J. P. D., Barnes, I., Roberts, J. M., Melamed, M. L., Ammann, M., Bertram, A. K., Cappa, C. D., Carlton, A. G., Carpenter, L. J., Crowley, J. N., Dubowski, Y., Georges, C., Heard, D. E., Herrmann, H., Keutsch, F.
495   N., Kroll, J. H., McNeill, V. F., Ng, N. L., Nizkorodov, S. A., Orlando, J. J., Percival, C. J., Picquet-Varrault, B., Rudich, Y., Seakins, P. W., Surratt, J. D., Tanimoto, H., Thornton, J. A., Tong, Z., Tyndall, G. S., Wahner, A., Weschler,

C. J., Wilson, K. R., and Ziemann, P. J.: The Essential Role for Laboratory Studies in Atmospheric Chemistry, Environ Sci Technol, 51, 2519–2528, 2017.

Canagaratna, M. R., Jayne, J. T., Jimenez, J. L., Allan, J. D., Alfarra, M. R., Zhang, Q., Onasch, T. B., Drewnick, F., Coe, H., Middlebrook, A., Delia, A., Williams, L. R., Trimborn, A. M., Northway, M. J., DeCarlo, P. F., Kolb, C. E., Davidovits, P., and Worsnop, D. R.: Chemical and microphysical characterization of ambient aerosols with the aerodyne aerosol mass spectrometer, Mass Spectrom Rev, 26, 185–222, 2007.

Canagaratna, M. R., Jimenez, J. L., Kroll, J. H., Chen, Q., Kessler, S. H., Massoli, P., Hildebrandt Ruiz, L., Fortner, E., Williams, L. R., Wilson, K. R., Surratt, J. D., Donahue, N. M., Jayne, J. T., and Worsnop, D. R.: Elemental ratio measurements of organic compounds using aerosol mass spectrometry: characterization, improved calibration, and implications, Atmos Chem Phys, 15, 253–272, 2015.

Canonaco, F., Crippa, M., Slowik, J. G., Baltensperger, U., and Prevot, A. S. H.: SoFi, an IGOR-based interface for the efficient use of the generalized multilinear engine (ME-2) for the source apportionment: ME-2 application to aerosol mass spectrometer data, Atmos Meas Tech, 6, 3649–3661, 2013.

Canonaco, F., Slowik, J. G., Baltensperger, U., and Prevot, A. S. H.: Seasonal differences in oxygenated organic aerosol composition: implications for emissions sources and factor analysis, Atmos Chem Phys, 15, 6993–7002, 2015.

Crippa, M., Canonaco, F., Lanz, V. A., Aijala, M., Allan, J. D., Carbone, S., Capes, G., Ceburnis, D., Dall'Osto, M., Day, D. A., DeCarlo, P. F., Ehn, M., Eriksson, A., Freney, E., Hildebrandt Ruiz, L., Hillamo, R., Jimenez, J. L., Junninen, H., Kiendler-Scharr, A., Kortelainen, A. M., Kulmala, M., Laaksonen, A., Mensah, A., Mohr, C., Nemitz, E., O'Dowd, C., Ovadnevaite, J., Pandis, S. N., Petaja, T., Poulain, L., Saarikoski, S., Sellegri, K., Swietlicki, E., Tiitta, P., Worsnop, D. R., Baltensperger, U., and Prevot, A. S. H.: Organic aerosol components derived from 25 AMS data sets across Europe using a consistent ME-2 based source apportionment approach, Atmos Chem Phys, 14, 6159–6176, 2014.

DeCarlo, P. F., Kimmel, J. R., Trimborn, A., Northway, M. J., Jayne, J. T., Aiken, A. C., Gonin, M., Fuhrer, K., Horvath, T., Docherty, K. S., Worsnop, D. R., and Jimenez, J. L.: Field-deployable, high-resolution, time-of-flight aerosol mass spectrometer, Anal Chem, 78, 8281–8289, 2006.

Drinovec, L., Mocnik, G., Zotter, P., Prevot, A. S. H., Ruckstuhl, C., Coz, E., Rupakheti, M., Sciare, J., Muller, T., Wiedensohler, A., and Hansen, A. D. A.: The "dual-spot" Aethalometer: an improved measurement of aerosol black carbon with real-time loading compensation, Atmos Meas Tech, 8, 1965–1979, 2015.

Farmer, D. K., Matsunaga, A., Docherty, K. S., Surratt, J. D., Seinfeld, J. H., Ziemann, P. J., and Jimenez, J. L.: Response of an aerosol mass spectrometer to organonitrates and organosulfates and implications for atmospheric chemistry, P Natl Acad Sci USA, 107, 6670–6675, 2010.

Fierce, L., Riemer, N., and Bond, T. C.: Toward reduced representation of mixing state for simulating aerosol effects on climate, B Am Meteorol Soc, 98, 971–980, 2017.

530 Fuzzi, S., Baltensperger, U., Carslaw, K., Decesari, S., van Der Gon, H. D., Facchini, M. C., Fowler, D., Koren, I., Langford, B., Lohmann, U., Nemitz, E., Pandis, S., Riipinen, I., Rudich, Y., Schaap, M., Slowik, J. G., Spracklen, D. V., Vignati, E., Wild, M., Williams, M., and Gilardoni, S.: Particulate matter, air quality and climate: lessons learned and future needs, Atmos Chem Phys, 15, 8217–8299, 2015.

Gard, E. E., Kleeman, M. J., Gross, D. S., Hughes, L. S., Allen, J. O., Morrical, B. D., Fergenson, D. P., Dienes, T., Galli, M. E., Johnson, R. J., Cass, G. R., and Prather, K. A.: Direct observation of heterogeneous chemistry in the atmosphere, 535 Science, 279, 1184–1187, 1998.

Gemayel, R., Hellebust, S., Temime-Roussel, B., Hayeck, N., Van Elteren, J. T., Wortham, H., and Gligorovski, S.: The performance and the characterization of laser ablation aerosol particle time-of-flight mass spectrometry (LAAP-ToF-MS), Atmos Meas Tech, 9, 1947–1959, 2016.

Gemayel, R., Temime-Roussel, B., Hayeck, N., Gandolfo, A., Hellebust, S., Gligorovski, S., and Wortham, H.: Development 540 of an analytical methodology for obtaining quantitative mass concentrations from LAAP-ToF-MS measurements, Talanta, 174, 715–724, 2017.

Gross, G. and Wippermann, F.: Channeling and Countercurrent in the Upper Rhine Valley - Numerical Simulations, J Clim Appl Meteorol, 26, 1293–1304, 1987.

Gunsch, M. J., May, N. W., Wen, M., Bottenus, C. L. H., Gardner, D. J., VanReken, T. M., Bertman, S. B., Hopke, P. K., Ault, 545 A. P., and Pratt, K. A.: Ubiquitous influence of wildfire emissions and secondary organic aerosol on summertime atmospheric aerosol in the forested Great Lakes region, Atmos Chem Phys, 18, 3701–3715, 2018.

Hagemann, R., Corsmeier, U., Kottmeier, C., Rinke, R., Wieser, A., and Vogel, B.: Spatial variability of particle number concentrations and NOx in the Karlsruhe (Germany) area obtained with the. mobile laboratory 'AERO-TRAM', Atmos Environ, 94, 341–352, 2014.

550 Healy, R. M., Sciare, J., Poulain, L., Crippa, M., Wiedensohler, A., Prevot, A. S. H., Baltensperger, U., Sarda-Esteve, R., McGuire, M. L., Jeong, C. H., McGillicuddy, E., O'Connor, I. P., Sodeau, J. R., Evans, G. J., and Wenger, J. C.: Quantitative determination of carbonaceous particle mixing state in Paris using single-particle mass spectrometer and aerosol mass spectrometer measurements, Atmos Chem Phys, 13, 9479–9496, 2013.

Herich, H., Hueglin, C., and Buchmann, B.: A 2.5 year's source apportionment study of black carbon from wood burning and 555 fossil fuel combustion at urban and rural sites in Switzerland, Atmos Meas Tech, 4, 1409–1420, 2011.

Huang, W., Saathoff, H., Shen, X. L., Ramakrishna, R., Leisner, T., and Mohr, C.: Chemical characterization of highly functionalized organonitrates contributing to high night-time organic aerosol mass loadings and particle growth, Environ Sci Technol, 53, 1165–1174, 2019.

IPCC: Climate Change 2013: The Physical Science Basis. Contribution of Working Group I to the Fifth Assessment Report of
560   the Intergovernmental Panel on Climate Change. Cambridge Univ. Press.

Jeong, C. H., McGuire, M. L., Godri, K. J., Slowik, J. G., Rehbein, P. J. G., and Evans, G. J.: Quantification of aerosol chemical composition using continuous single particle measurements, Atmos Chem Phys, 11, 7027–7044, 2011.

Kalthoff, N. and Vogel, B.: Countercurrent and Channeling Effect under Stable Stratification in the Area of Karlsruhe, Theor Appl Climatol, 45, 113–126, 1992.

565   Kiendler-Scharr, A., Mensah, A. A., Friese, E., Topping, D., Nemitz, E., Prevot, A. S. H., Aijala, M., Allan, J., Canonaco, F., Canagaratna, M., Carbone, S., Crippa, M., Dall Osto, M., Day, D. A., De Carlo, P., Di Marco, C. F., Elbern, H., Eriksson, A., Freney, E., Hao, L., Herrmann, H., Hildebrandt, L., Hillamo, R., Jimenez, J. L., Laaksonen, A., McFiggans, G., Mohr, C., O'Dowd, C., Otjes, R., Ovadnevaite, J., Pandis, S. N., Poulain, L., Schlag, P., Sellegri, K., Swietlicki, E., Tiitta, P., Vermeulen, A., Wahner, A., Worsnop, D., and Wu, H. C.: Ubiquity of organic nitrates from
570   nighttime chemistry in the European submicron aerosol, Geophys Res Lett, 43, 7735–7744, 2016.

Knote, C., Brunner, D., Vogel, H., Allan, J., Asmi, A., Aijala, M., Carbone, S., van der Gon, H. D., Jimenez, J. L., Kiendler-Scharr, A., Mohr, C., Poulain, L., Prevot, A. S. H., Swietlicki, E., and Vogel, B.: Towards an online-coupled chemistry-climate model: evaluation of trace gases and aerosols in COSMO-ART, Geosci Model Dev, 4, 1077–1102, 2011.

Kroll, J. H., Donahue, N. M., Jimenez, J. L., Kessler, S. H., Canagaratna, M. R., Wilson, K. R., Altieri, K. E., Mazzoleni, L. R.,
575   Wozniak, A. S., Bluhm, H., Mysak, E. R., Smith, J. D., Kolb, C. E., and Worsnop, D. R.: Carbon oxidation state as a metric for describing the chemistry of atmospheric organic aerosol, Nat Chem, 3, 133–139, 2011.

Marsden, N. A., Flynn, M. J., Allan, J. D., and Coe, H.: Online dfferentiation of mineral phase in aerosol particles by ion formation mechanism using a LAAP-TOF single-particle mass spectrometer, Atmospheric Measurement Techniques Discussions, 11, 195–213, 2018.

580   Marsden, N. A., Flynn, M. J., Taylor, J. W., Allan, J. D., and Coe, H.: Evaluating the influence of laser wavelength and detection stage geometry on optical detection efficiency in a single-particle mass spectrometer, Atmos Meas Tech, 9, 6051–6068, 2016.

Marsden, N. A., Ullrich, R., Möhler, O., Hammer, S. E., Kandler, K., Cui, Z., Williams, P. I., Flynn, M. J., Liu, D., Allan, J. D., and Coe, H.: Mineralogy and mixing state of north African mineral dust by online single-particle mass spectrometry,
585   Atmos Chem Phys, 19, 2259–2281, 2019.

Murphy, D. M.: The design of single particle laser mass spectrometers, Mass Spectrom Rev, 26, 150–165, 2007.

Paatero, P.: Least squares formulation of robust non-negative factor analysis, Chemometr Intell Lab, 37, 23–35, 1997.

Paatero, P. and Tapper, U.: Positive Matrix Factorization - a Nonnegative Factor Model with Optimal Utilization of Error-Estimates of Data Values, Environmetrics, 5, 111–126, 1994.

590   Pöschl, U.: Atmospheric aerosols: Composition, transformation, climate and health effects, Angew Chem Int Edit, 44, 7520–7540, 2005.

Ramisetty, R., Abdelmonem, A., Shen, X. L., Saathoff, H., Leisner, T., and Mohr, C.: Exploring femtosecond laser ablation in single-particle aerosol mass spectrometry, Atmos Meas Tech, 11, 4345–4360, 2018.

Reitz, P., Zorn, S. R., Trimborn, S. H., and Trimborn, A. M.: A new, powerful technique to analyze single particle aerosol mass
595   spectra using a combination of OPTICS and the fuzzy c-means algorithm, J Aerosol Sci, 98, 1–14, 2016.

Rolph, G., Stein, A., and Stunder, B.: Real-time Environmental Applications and Display sYstem: READY, Environ Modell Softw, 95, 210–228, 2017.

Seinfeld, J. H. and Pandis, S. N.: Atmospheric chemistry and physics: From air pollution to climate change, Wiley, J & Sons, Inc., Hoboken, New Jersey, 2006.

600   Shen, X. L., Ramisetty, R., Mohr, C., Huang, W., Leisner, T., and Saathoff, H.: Laser ablation aerosol particle time-of-flight mass spectrometer (LAAPTOF): performance, reference spectra and classification of atmospheric samples, Atmos Meas Tech, 11, 2325–2343, 2018.

Shen, X. L., Saathoff, H., Huang, W., Mohr, C., Ramisetty, R., and Leisner, T.: Understanding of atmospheric aerosol particles with improved particle identification and quantification by single particle mass spectrometry, Atmos. Meas. Tech. , 12,
605   2219–2240, 2019.

Stanelle, T., Vogel, B., Vogel, H., Baumer, D., and Kottmeier, C.: Feedback between dust particles and atmospheric processes over West Africa during dust episodes in March 2006 and June 2007, Atmos Chem Phys, 10, 10771–10788, 2010.

Stein, A. F., Draxler, R. R., Rolph, G. D., Stunder, B. J. B., Cohen, M. D., and Ngan, F.: Noaa's Hysplit Atmospheric Transport and Dispersion Modeling System, B Am Meteorol Soc, 96, 2059–2077, 2015.

610   Tsigaridis, K., Krol, M., Dentener, F. J., Balkanski, Y., Lathière, J., Metzger, S., Hauglustaine, D. A., and Kanakidou, M.: Change in global aerosol composition since preindustrial times, Atmos Chem Phys, 6, 5143–5162, 2006.

Vogel, B., Fiedler, F., and Vogel, H.: Influence of Topography and Biogenic Volatile Organic-Compounds Emission in the State of Baden-Wurttemberg on Ozone Concentrations during Episodes of High Air Temperatures, J Geophys Res-Atmos, 100, 22907–22928, 1995.

615   Vogel, B., Gross, B., and Wippermann, F.: Mesoklip (1st Special Observation Period) - Observations and Numerical-Simulation - a Comparison, Bound-Lay Meteorol, 35, 83–102, 1986.

Vogel, B., Vogel, H., Baumer, D., Bangert, M., Lundgren, K., Rinke, R., and Stanelle, T.: The comprehensive model system COSMO-ART - Radiative impact of aerosol on the state of the atmosphere on the regional scale, Atmos Chem Phys, 9, 8661–8680, 2009.

620   Zhang, Q., Jimenez, J. L., Canagaratna, M. R., Ulbrich, I. M., Ng, N. L., Worsnop, D. R., and Sun, Y. L.: Understanding atmospheric organic aerosols via factor analysis of aerosol mass spectrometry: a review, Anal Bioanal Chem, 401, 3045–3067, 2011.

Zhang, Q., Jimenez, J. L., Worsnop, D. R., and Canagaratna, M.: A case study of urban particle acidity and its influence on secondary organic aerosol, Environ Sci Technol, 41, 3213–3219, 2007.

625   Zhou, Y., Huang, X. H. H., Griffith, S. M., Li, M., Li, L., Zhou, Z., Wu, C., Meng, J. W., Chan, C. K., Louie, P. K. K., and Yu, J. Z.: A field measurement based scaling approach for quantification of major ions, organic carbon, and elemental carbon using a single particle aerosol mass spectrometer, Atmos Environ, 143, 300–312, 2016.

Zotter, P., Herich, H., Gysel, M., El-Haddad, I., Zhang, Y. L., Mocnik, G., Huglin, C., Baltensperger, U., Szidat, S., and Prevot, A. H.: Evaluation of the absorption angstrom ngstrom exponents for traffic and wood burning in the Aethalometer-
630   based source apportionment using radiocarbon measurements of ambient aerosol, Atmos Chem Phys, 17, 4229–4249, 2017.

Single Particle Characterisation of Atmospheric Aerosol Particles in Central Europe
Appendix B

Table 1: Mean values (±sdev) of characteristic parameters for the entire measurement period.

Parameter	Mean value ± sdev	Parameter	Mean value ± sdev
Wind Direction (°)	174.0 ± 75.0	**Particulate compounds measured by AMS**	
Wind Speed (m s^{-1})	1.3 ± 0.9	Organics (µg m^{-3})	5.1 ± 3.3
Temperature (K)	294.4 ± 4.5	Ammonium (µg m^{-3})	0.7 ± 0.4
Relative Humidity (%)	70.0 ± 17.0	Nitrate (µg m^{-3})	0.8 ± 0.8
O$_3$ (ppb)	26.5 ± 15.8	Sulfate (µg m^{-3})	1.7 ± 0.8
NO$_2$ (ppb)	11.4 ± 6.9	**Seven particle classes measured by LAAPTOF**	
SO$_2$ (ppb)	1.2 ± 2.7	C1: Calcium-soil (µg m^{-3})	0.4 ± 0.5
CO$_2$ (ppm)	446.0 ± 32.0	C2: Aged soot (µg m^{-3})	0.1 ± 0.4
Particle Number (10^4 cm^{-3}) (size >2.5 nm)	1.2 ± 0.8	C3: Sodium salts (µg m^{-3})	1.2 ± 1.2
Particle Number (10^3 cm^{-3}) (size: 2.5 to7 nm)	4.7 ± 4.9	C4: Secondary inorganics-amine (µg m^{-3})	0.1 ± 0.6
BC (µg m^{-3})	0.8 ± 0.7	C5: Biomass burning–soil (µg m^{-3})	1.2 ± 1.3
PM$_{2.5}$ (µg m^{-3})	6.3 ± 3.2	C6: Biomass burning–organosulfate (µg m^{-3})	0.4 ± 0.6
PM$_{10}$ (µg m^{-3})	8.6 ± 4.2	C7: Mixed/aged dust (µg m^{-3})	0.5 ± 0.7

635 Note that the full names of seven particle classes are C1: calcium-rich and soil-dust-like particles; C2: aged-soot-like particles; C3: sodium-salt-like particles; C4: secondary- inorganics-rich and amine containing particles; C5: aged-biomass-burning and soil-dust like particles; C6: aged-biomass-burning and organosulfate-containing particles; C7: mixed/aged and dust-like particles

Table 2: Features and mean values (±sdev) of characteristic parameters for the two selected episodes

	Sodium chloride rich episode	Organics rich episode	Instrument
Date and time	0820 noon to 0823 noon	0825 midnight to 0828 midnight	
Sodium salts (µg m^{-3})	2.2 ± 1.0 Higher	0.6 ± 0.4 Lower	LAAPTOF
Biomass burning–soil (µg m^{-3})	0.7 ± 0.7 Lower	1.7 ± 1.1 Higher	LAAPTOF
Organics (µg m^{-3})	2.0 ± 1.2 Lowest	12.9 ± 3.9 Highest	HR-Tof-AMS
Particle acidity indicator NH$_4^+$ measured/predicted	0.67 ± 0.10 Highest acidity	0.83 ± 0.06 Average acidity Anti-correlated with org	HR-Tof-AMS
Organonitrate fraction indicator NO$^+$/NO$_2^+$	11.0 ± 6.1 Highest	6.1 ± 0.9 Lowest	HR-Tof-AMS
Oxidation state (Osc) (Anti-correlated with org)	-0.24 ± 0.34 Less oxidized Strongest variability	-0.10 ± 0.20 More oxidized Least variability	HR-Tof-AMS
Wind Direction (°)	Southwest	Varying	Meteorology sensor (WS700, Lufft GmbH)
Wind Speed (m s^{-1})	1.6 ± 1.0	1.2 ± 1.0	

640
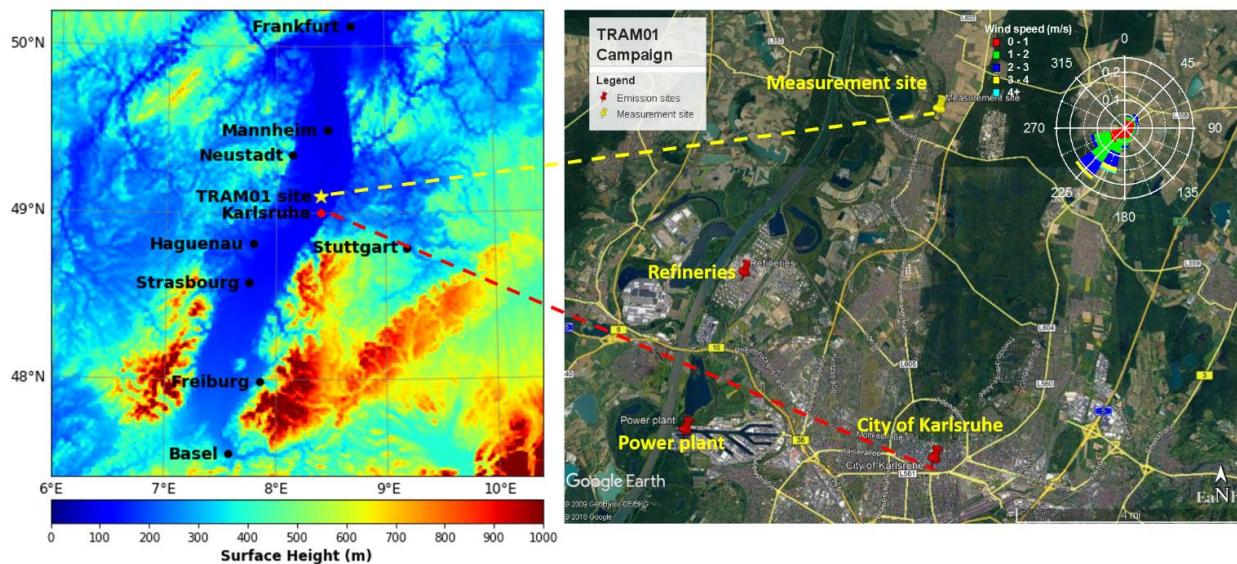
Figure 1: Measurement location and topography (left), nearby peak emission sites and wind rose for the complete measurement campaign in summer 2016 (right).

645
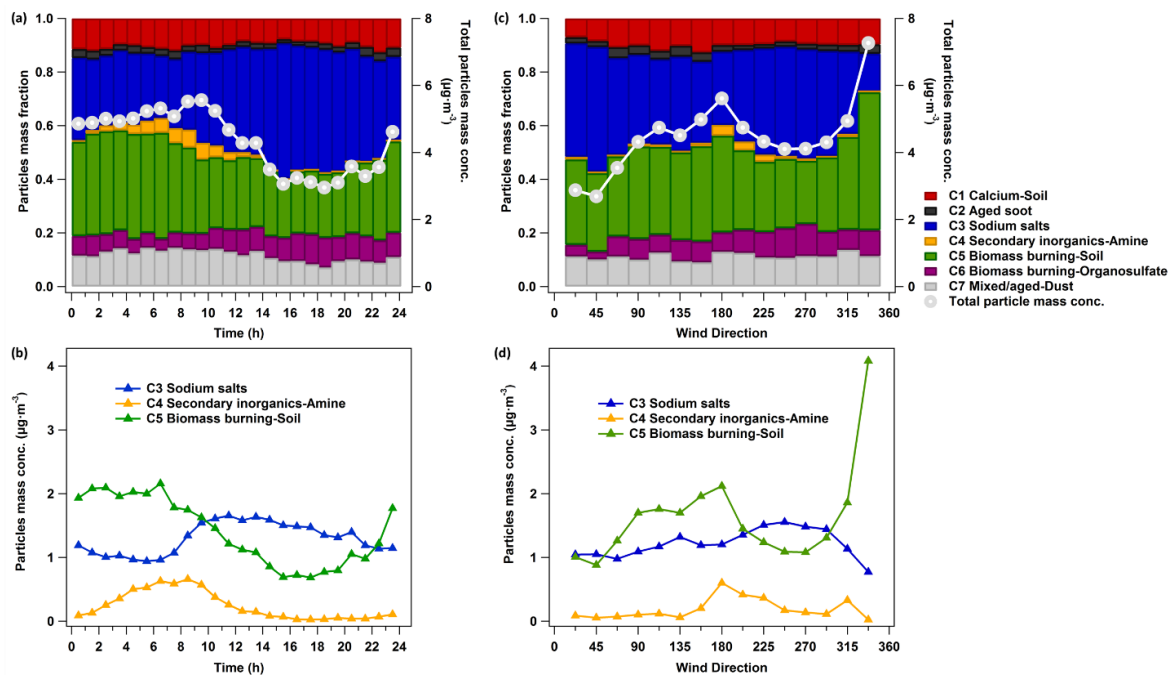
Figure 2: Diurnal pattern (a and b) and wind direction resolved particle class masses (c and d) measured by LAAPTOF. Please note that the uncertainties of the particle class mass concentrations are relatively large (Shen et al., 2019).
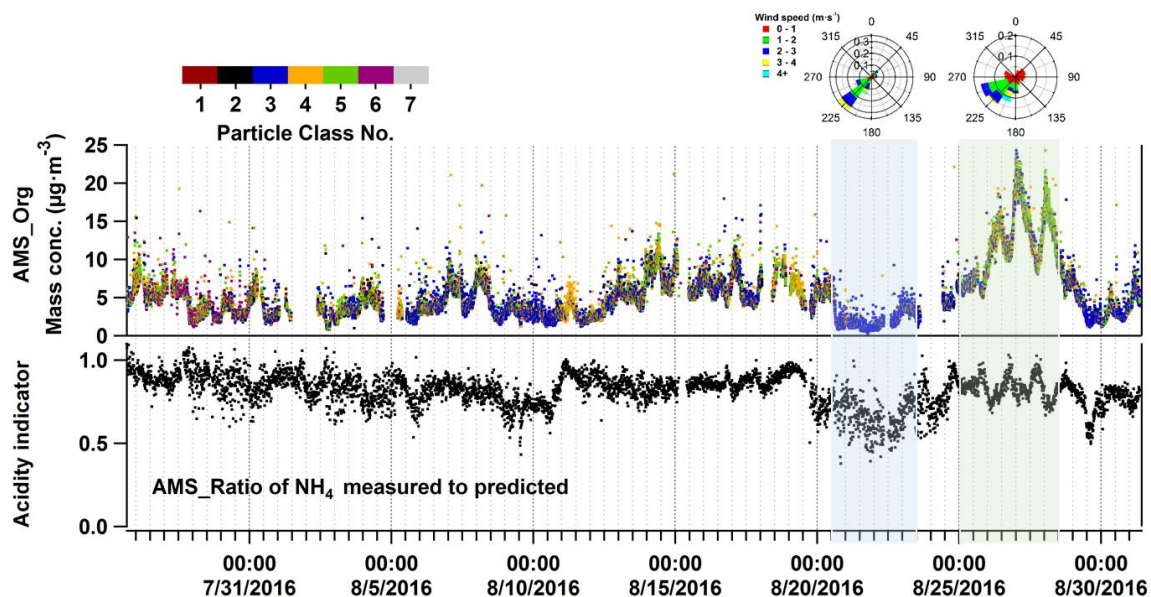
Figure 3: Time series of particulate organic mass measured by the AMS (AMS org in the upper panel), the particle acidity indicator (the lower the value the more acidic, lower panel), and the particle class number classified by LAAPTOF (colour code, upper panel). The seven classes are class 1: calcium-Soil; class 2: aged soot; class3: sodium salts; class 4: secondary inorganics-amine; class 5: biomass burning-soil; class 6: biomass burning-organosulfate; and class 7: mixed/aged-dust. The first (blue) and second (green) shaded areas mark the sodium chloride rich and organic rich episodes, respectively.

163
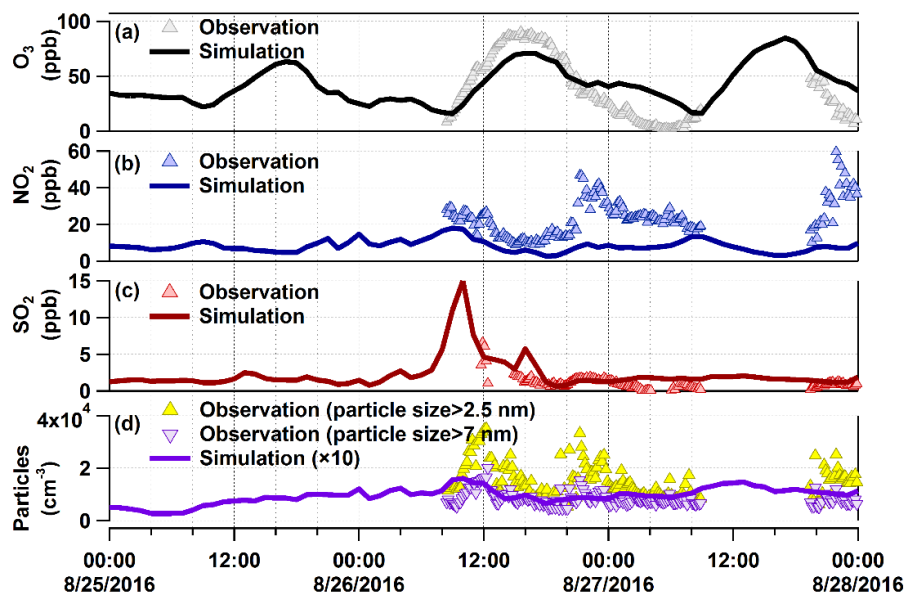
Figure 4: Comparison between observations and model results for O₃, NO₂, SO₂, and particle number in organic-rich episode. The modelled particles do not represent the ultrafine particles to their full extend, especially for the particles in the nucleation mode.

660
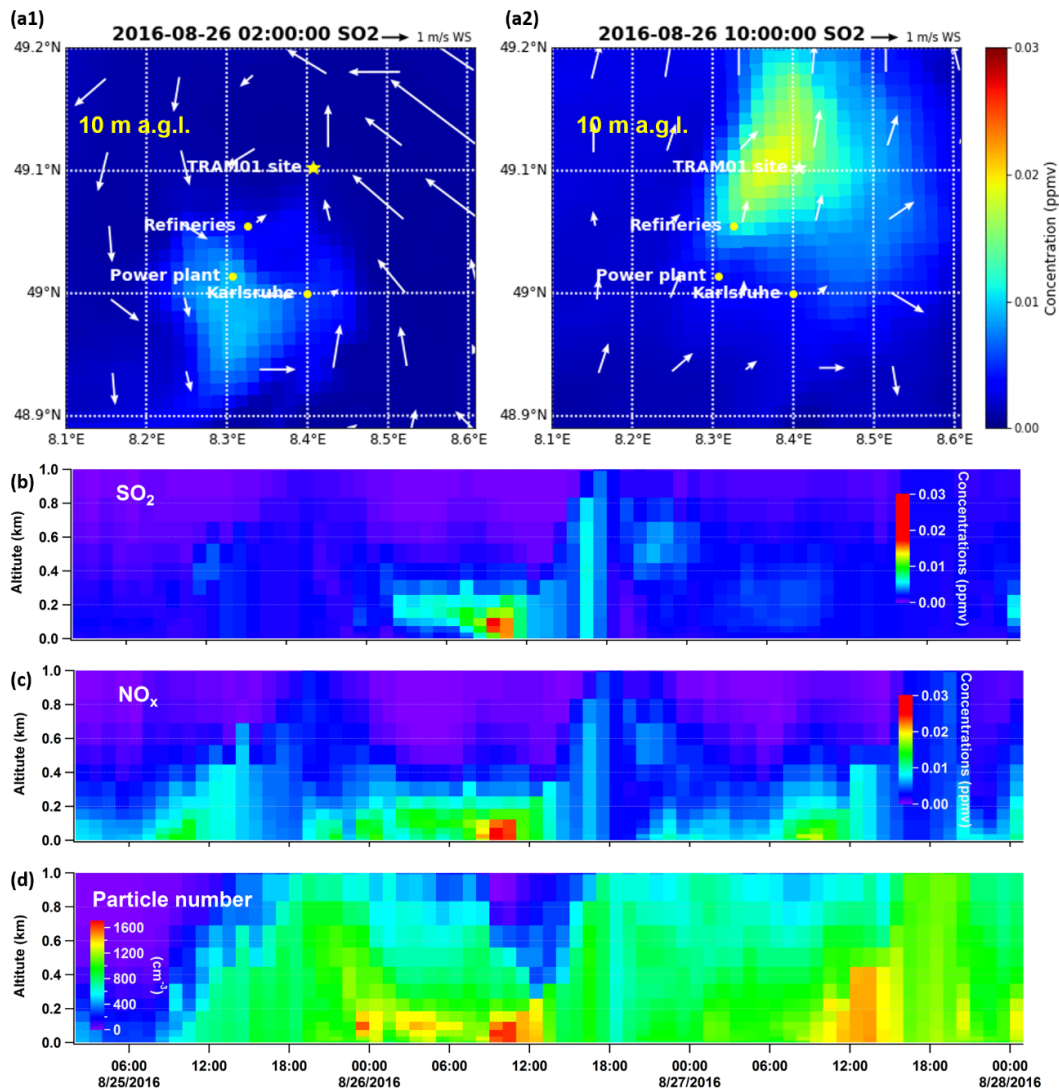
Figure 5: Modelled SO₂ concentrations at 2:00 (a1) and 10:00 (a2) on August 26th at 10 m a.g.l.. Panels (b) to (d) are time series of vertical profiles above the measurement site for simulated SO₂, NOₓ and total particle number.
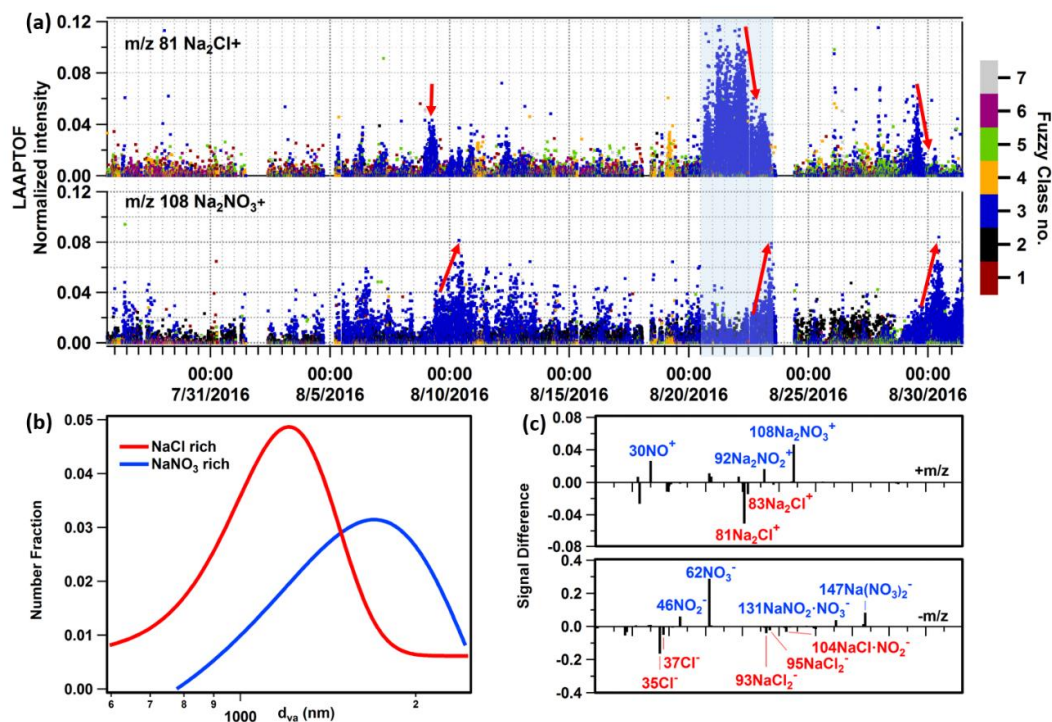
665 **Figure 6: (a) Time series of sodium chloride and nitrate signatures in seven particle classes. Y-axis is the normalized ion intensity (each ion peak intensity is normalized to the sum of all ion signals; positive and negative ions were analysed separately). The seven classes are class 1: calcium-Soil; class 2: aged soot; class3: sodium salts; class 4: secondary inorganics-amine; class 5: biomass burning-soil; class 6: biomass burning-organosulfate; and class 7: mixed/aged-dust. Obvious sodium chloride and nitrate signatures are mainly found in class 3 labelled in blue colour. (b) Size distributions of NaCl rich (young sea salt) and NaNO₃ rich (aged sea salt) particles.**
670 **Gaussian fit NaCl dva (±σ) = 1211(±352) nm; NaNO₃ 1697(±946) nm. (c) Spectra difference between aged and young sea salt particles (aged-young). The blue band marks the sodium chloride rich episode.**
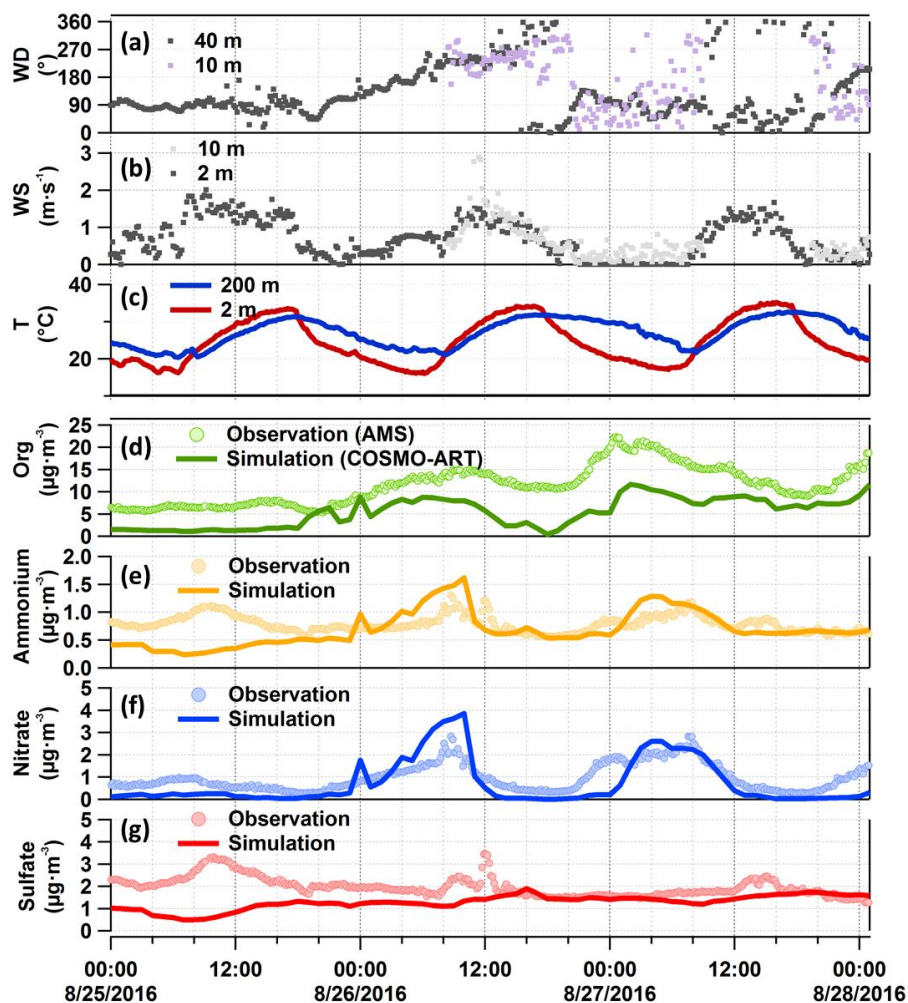
Figure 7: Comparison between observations and model simulations for organic-rich episode. Panel (a) and (b) are wind conditions measured 10 m a.g.l. at our measurement site (purple and light grey dots for wind direction and speed, respectively), as well as the complementary KIT-tower data (dark grey dots). Panel (c) is the temperature data from the KIT-tower. Panel (d) to (g) are the particulate organic compounds, ammonium, nitrate, and sulfate measured by AMS and simulated by COSMO-ART. The simulation results are at the lowest atmospheric level in the model, namely 10 m a.g.l.

680
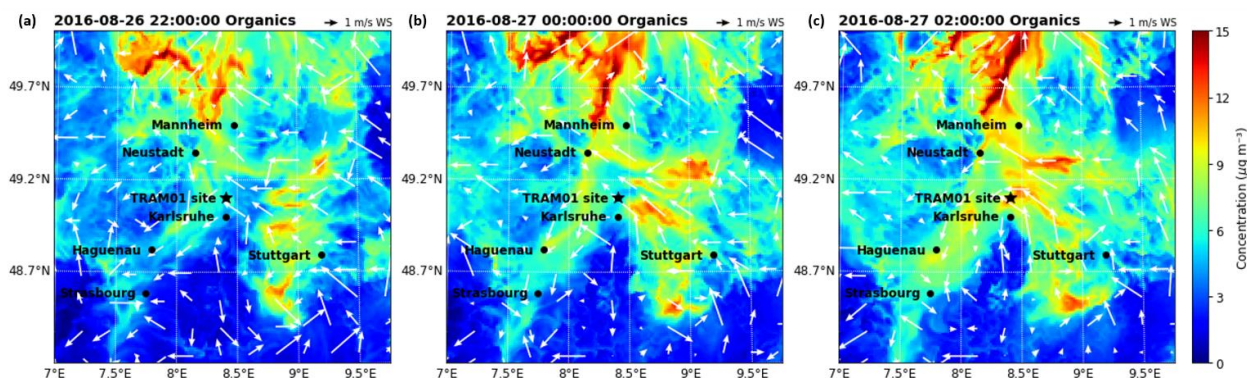
Figure 8: Particulate organics concentrations calculated by COSMO-ART for three different time points (a) to (c) during the night from August 26th to 27th for 10 m a.g.l..

685
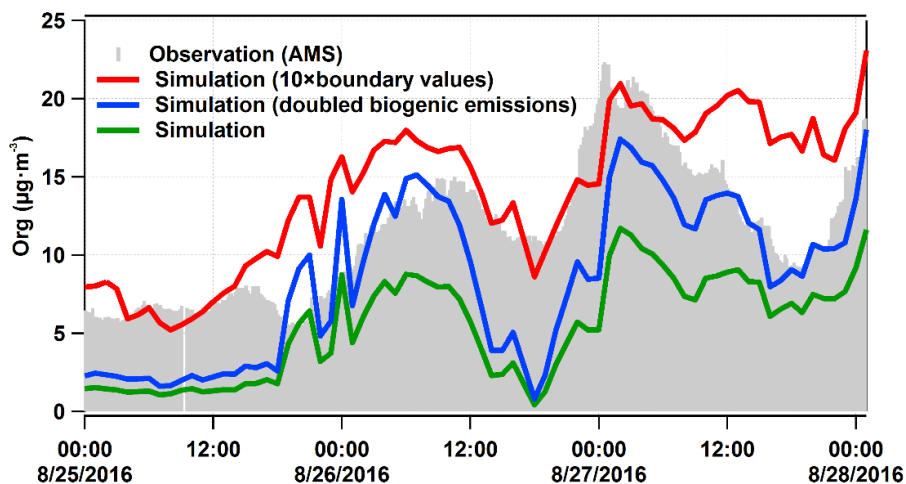
Figure 9: Modelled organic mass concentrations (lines) compared to measured values (grey area). The green line is the same as in Figure 7, the red line was calculated for a tenfold-enhanced regional background in organics, and the blue was calculated for doubles biogenic emissions in COSMO-ART.

690

In order to study the nature and origin of aerosols at a rural site in the upper Rhine valley, we conducted a stationary measurement campaign (TRAM01) in summer 2016, and applied a transport model COSMO-ART to help source apportionment and to achieve a better understanding of the impact of complex transport pattern on the field observations. In the main manuscript, we have mainly discussed two selected episodes, one is rich in sodium chloride and another is rich in organics. Here is the supporting information, including figures, as well as some detailed descriptions.
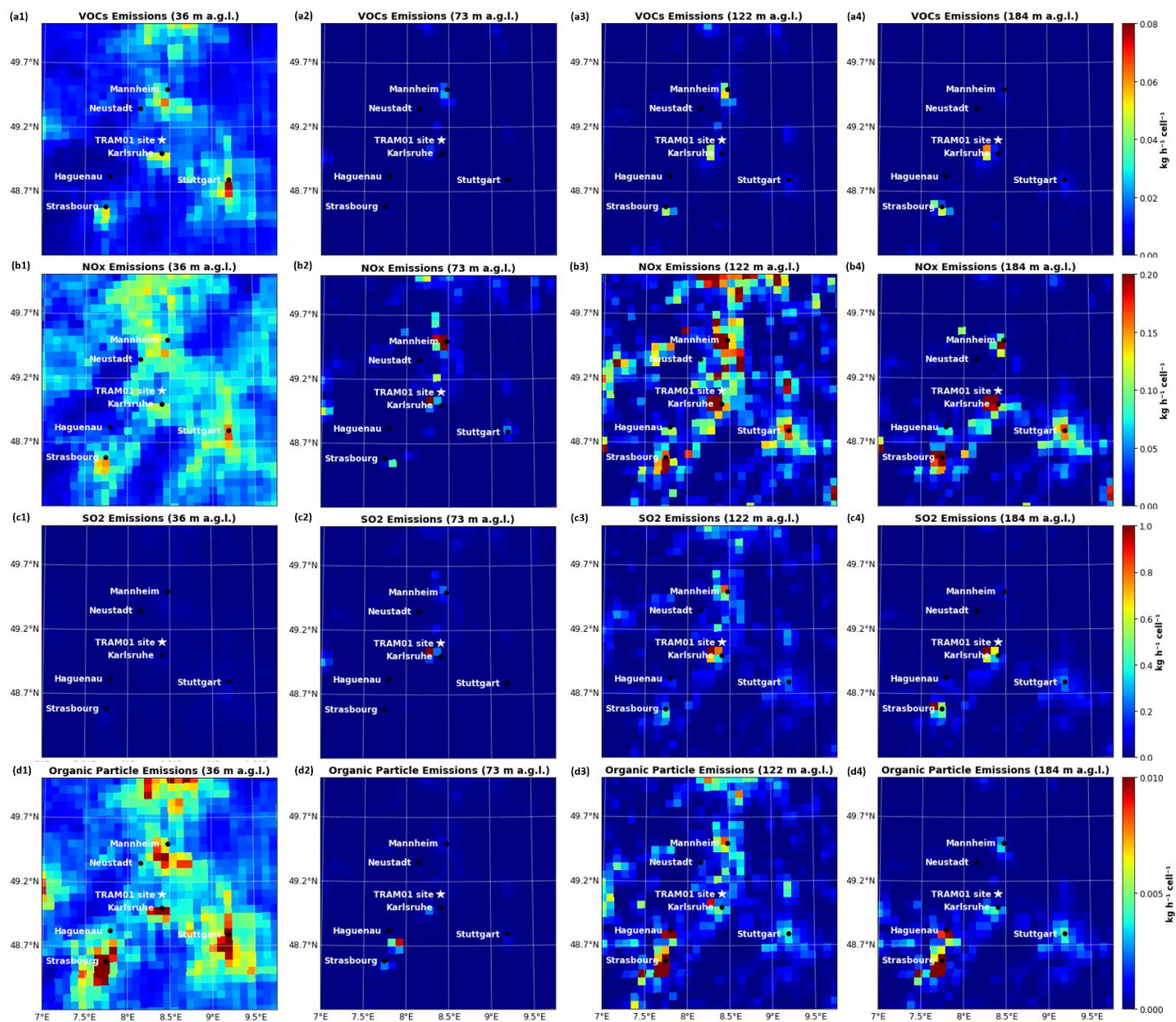
Figure S1: Emission maps of VOCs (a1 to a4), NOx (b1 to b4), SO₂ (c1 to c4), and primary organic particles (d1 to d4) at different altitudes, i.e., 36, 74, 122, and 184 m (from left to right) above ground level (a.g.l.).
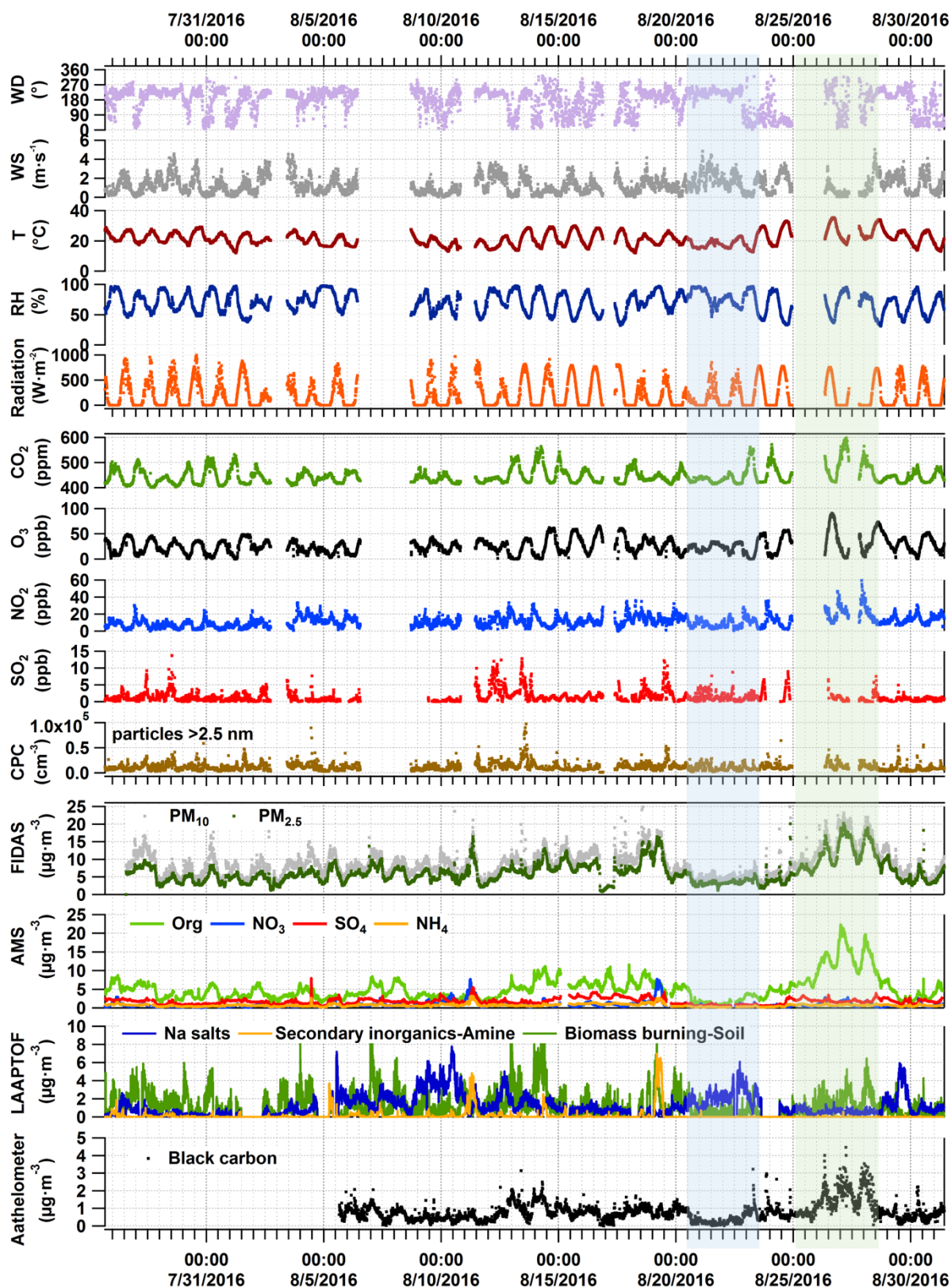
Figure S2: Overview of the whole measurement campaign including meteorology parameters, trace gases, and aerosol particle mass and composition. The first (blue) and second (green) shaded areas mark the sodium chloride rich and the organic rich episodes, respectively.
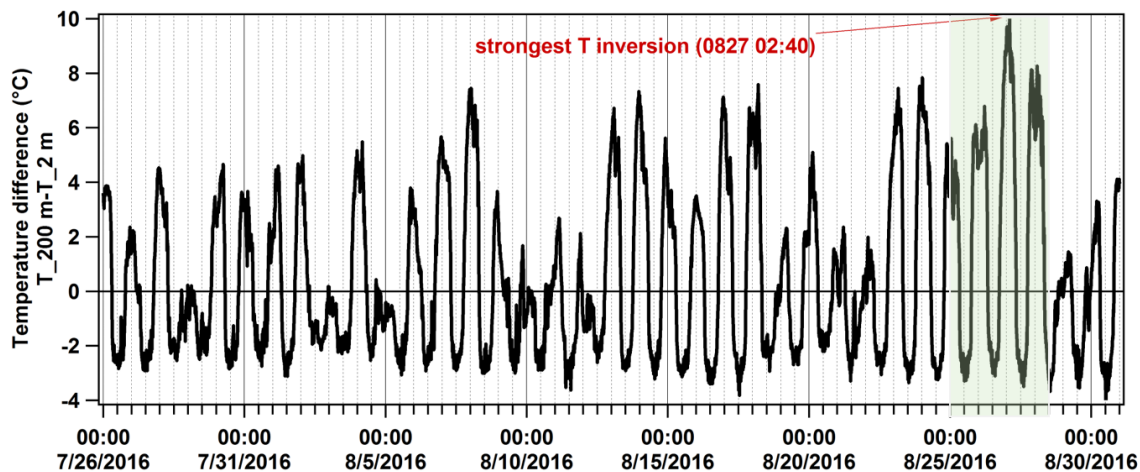
Figure S3: Time series of temperature difference between 200 m and 2 m above ground level (a.g.l.), measured at the KIT-tower. The bigger difference denotes the stronger temperature inversion. Temperature inversions are stronger during the organics rich episode marked with a shaded background. The strongest temperature inversion was measured at 02:40 on August 27.

5
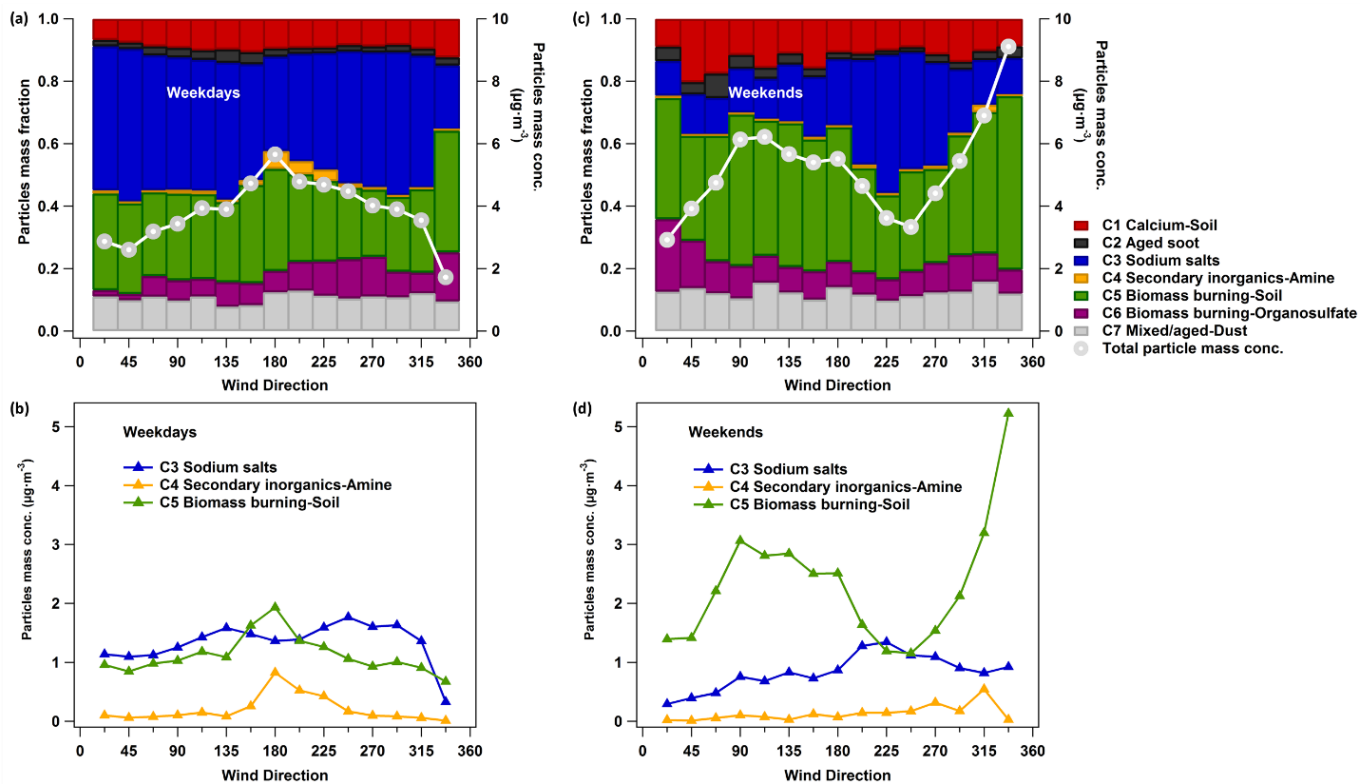
Figure S4: Comparison of particle classes measured by LAAPTOF as a function of wind direction for weekdays (left) and weekends (right).
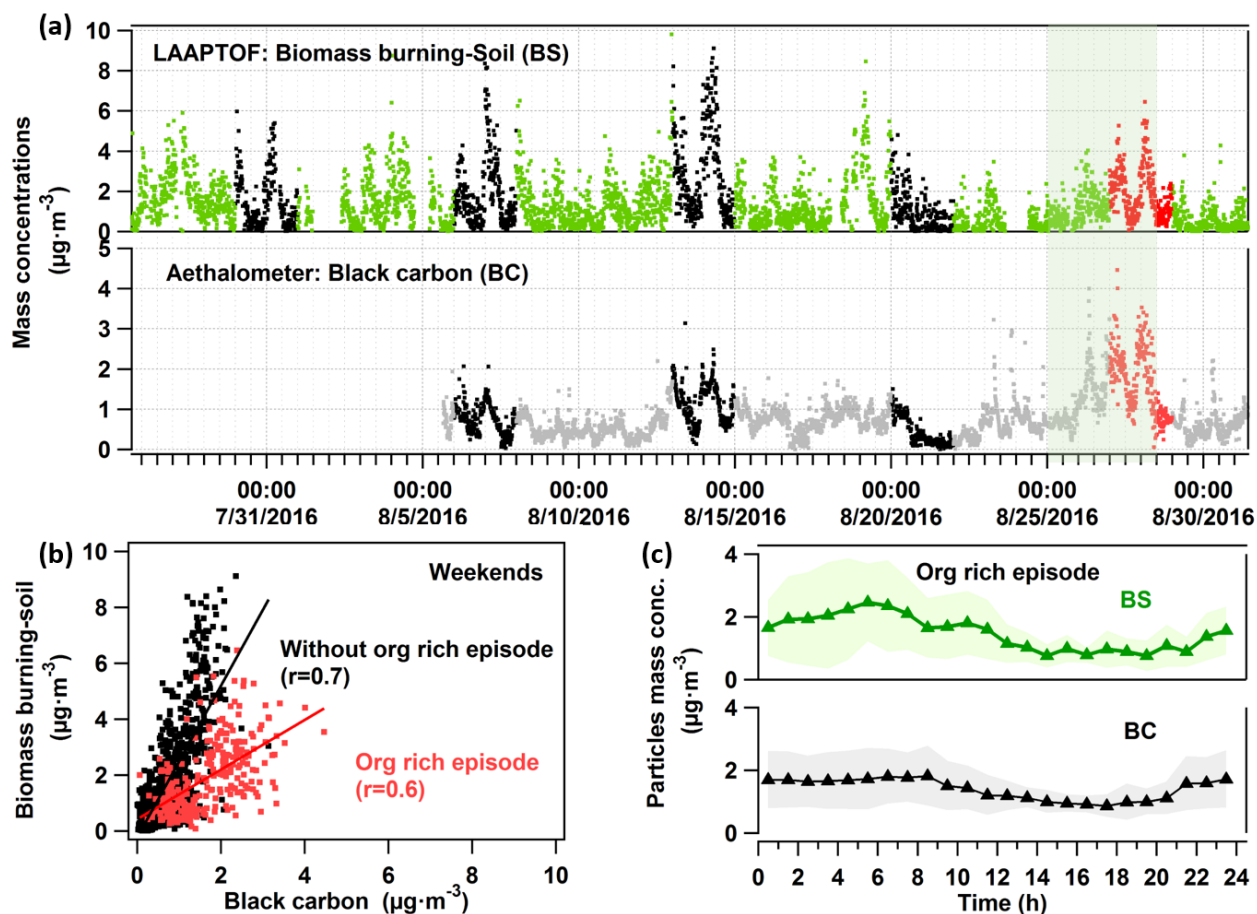
Figure S5: (a) Time series of aged-biomass-burning and soil-dust like particles and black carbon (black and red dots are weekend data); red dots are in organics rich episode. The shaded area marks the organics rich episode. (b) Comparison of mass concentration between biomass burning-soil and black carbon measured during the weekends. Black and red dots are the data without and with organic rich episode, respectively. (c) Diurnal pattern of particle mass concentration of biomass burning-soil (BS) and black carbon (BC) during organics rich episode, respectively.
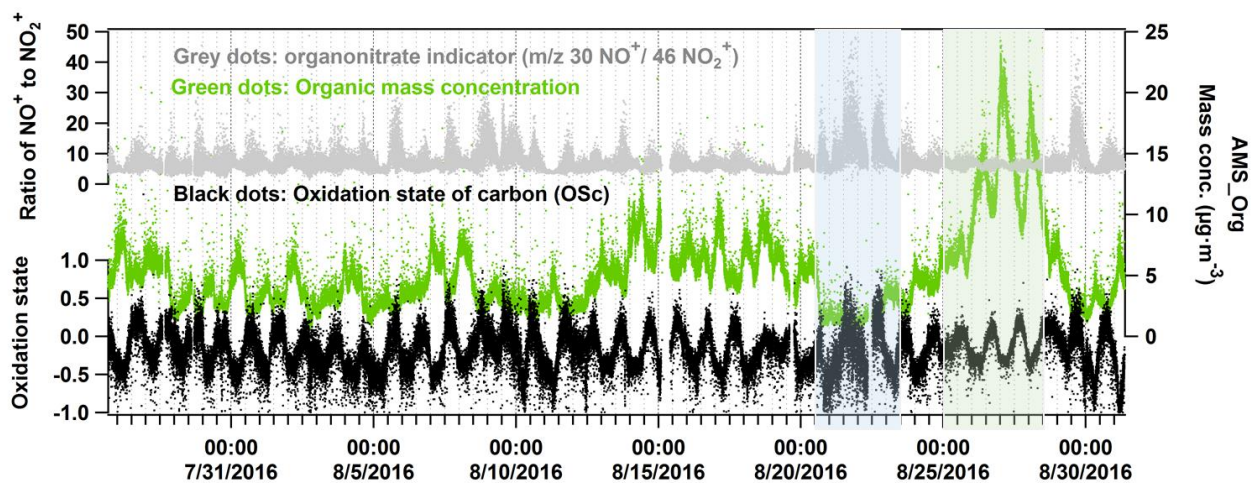
Figure S6: Time series of organonitrate indicator (grey dots) and oxidation state (black dots). The first (blue) and second (green) shaded areas mark the sodium chloride rich and organic rich episodes, respectively.
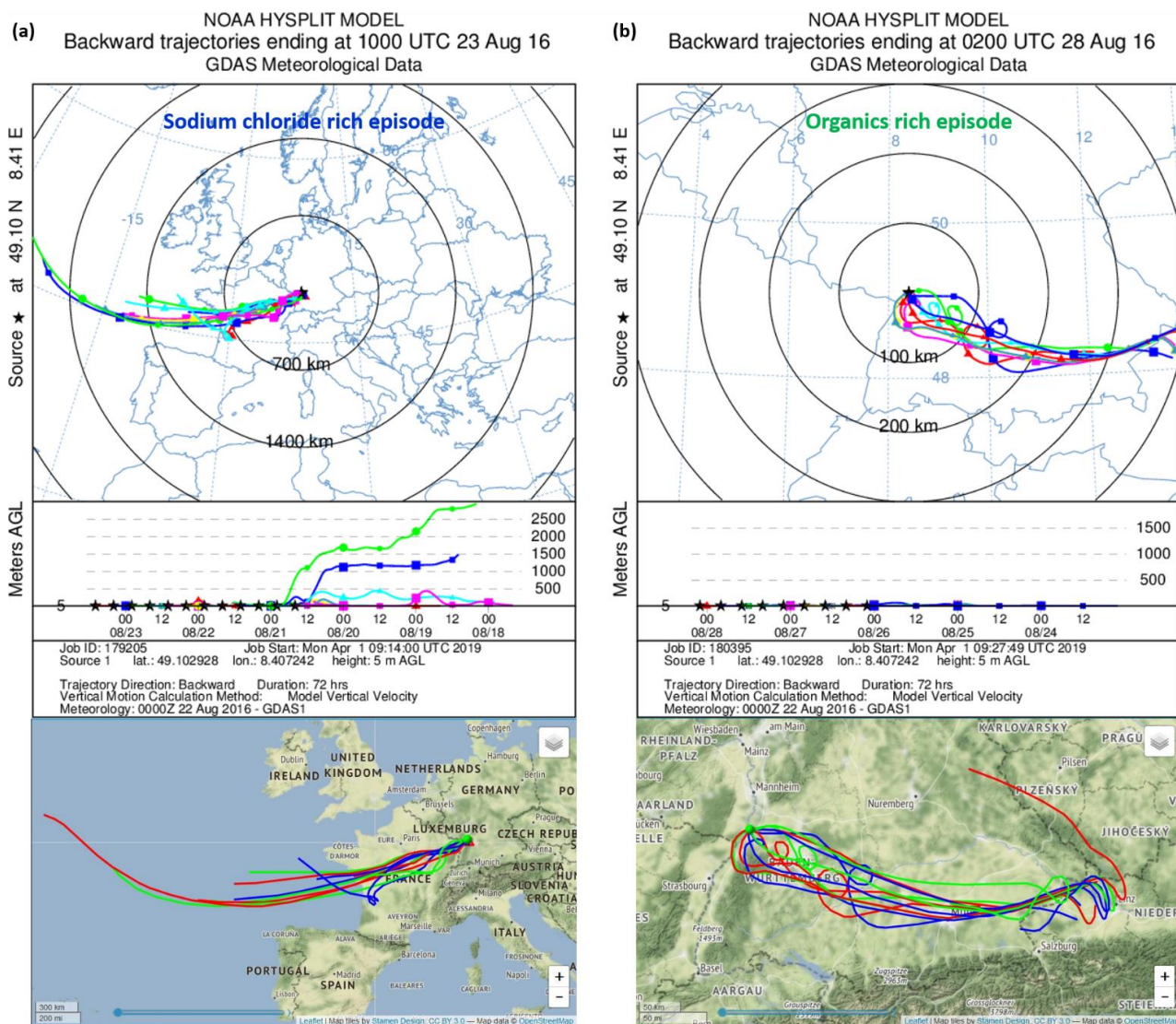
Figure S7: Hybrid Single-Particle Lagrangian Integrated Trajectory (HYSPLIT) back-trajectory analysis for 72 hours for sodium chloride rich (a) and organics rich (b) episodes, respectively.
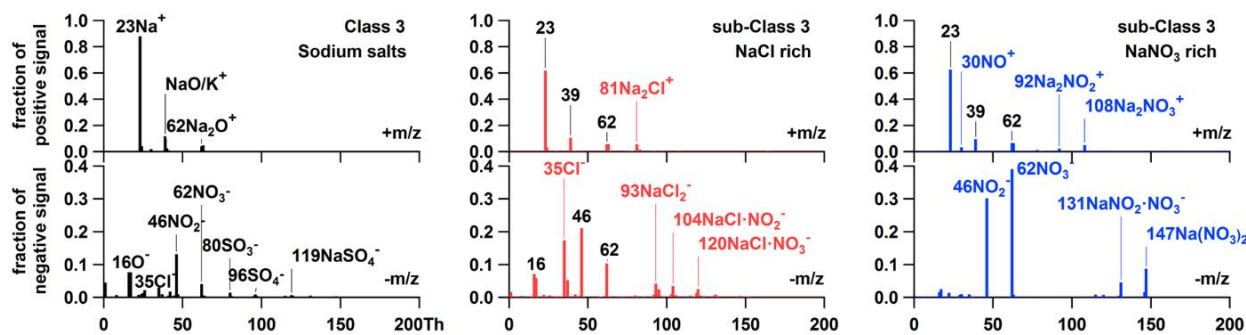
Figure S8: Spectra of the sodium salts class (Shen et al., 2019) and its sub-classes: NaCl rich (averaged from 1487 particles) and NaNO₃ rich (averaged from 300 particles).
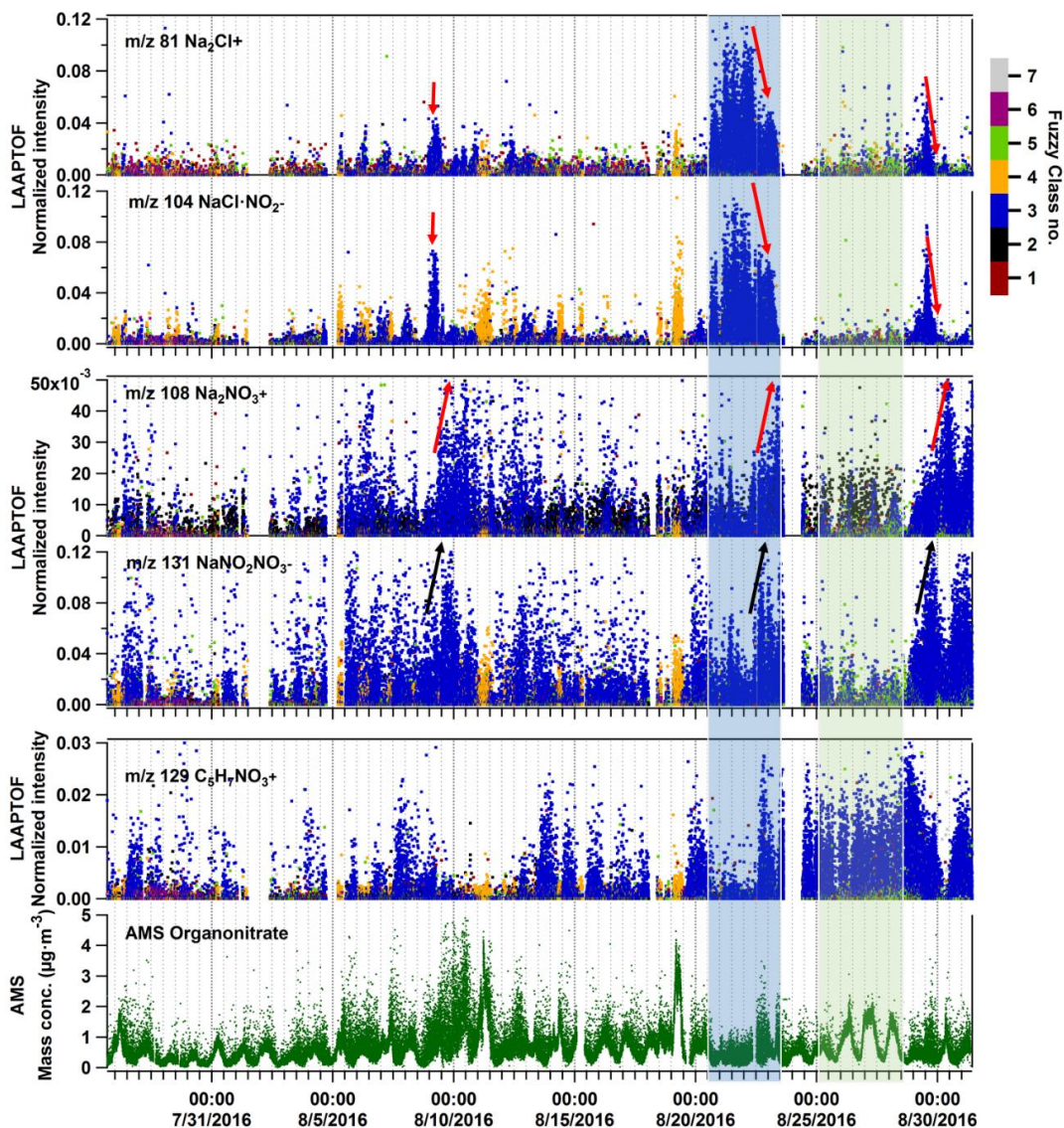
Figure S9: Time series of sodium chloride, nitrate, and organonitrate. Y-axis is the normalized ion intensity (each ion peak intensity is normalized to the sum of all ion signals; positive and negative ions were analysed separately). The seven classes are class 1: calcium-Soil; class 2: aged soot; class3: sodium salts; class 4: secondary inorganics-amine; class 5: biomass burning-soil; class 6: biomass burning-organosulfate; and class 7: mixed/aged-dust. Obvious sodium chloride and nitrate signatures are mainly found in class 3 labelled in blue colour. The first (blue) and second (green) bands mark the sodium chloride rich and organic rich episodes, respectively.

The method to estimate organonitrate based on AMS measurement can be referred to Farmer et al. (2010) and the parameters used here are the same as that used by Huang et al. (2019). The result in Fig. S8 is based on our AMS measurements and the corresponding equation suggested by Farmer et al. (2010), as follows:

y=[(Robs-Ran)(1+Ron)]/[(Ron-Ran)(1+Robs)], where y is the estimated organonitrate mass concentration (µg m⁻³), Robs is the observed ambient ratio of NO_2^+/NO^+; Ran and Ron are the NO_2^+/NO^+ ratio for ammonium nitrate and organonitrate, respectively. In our study Ran=0.43 based on the measurement and Ron=0.1 based on literature data. More details can be found by Huang et al. (2019).
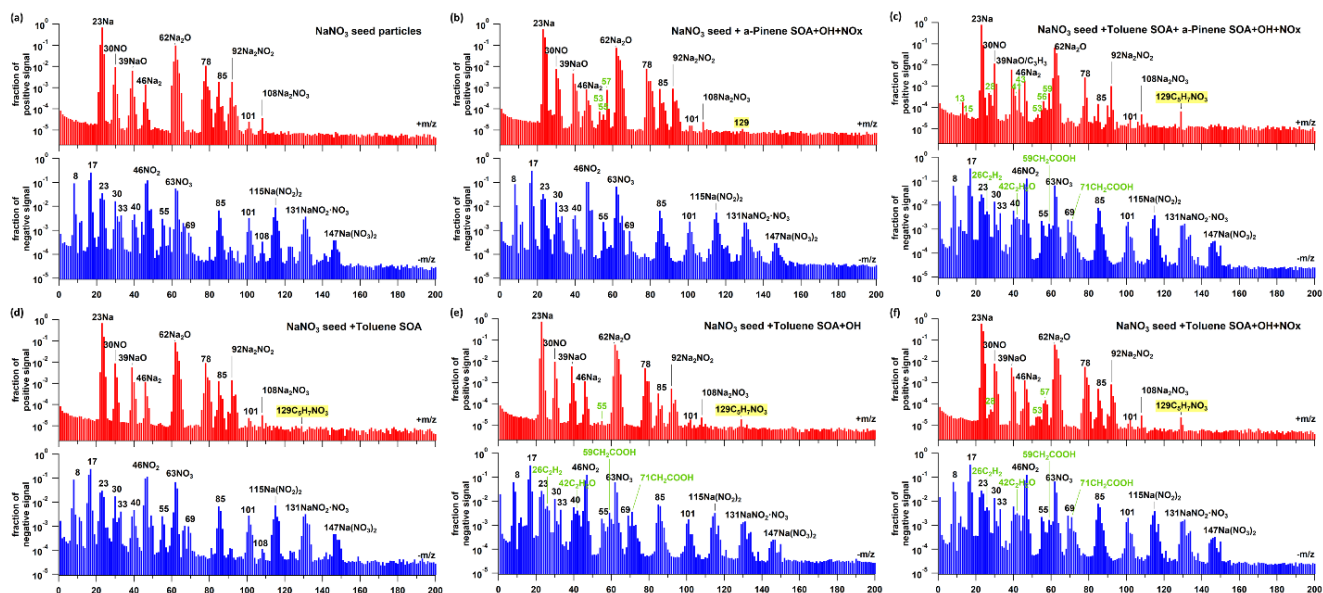
Figure S10: Laboratory evidence for anthropogenic organonitrate (LAAPTOF signature m/z 129 $C_5H_7NO_3^+$). (a) to (f) are the averaged spectra from several thousand single particles, respectively. Y-axis is the normalized ion intensity (each ion peak intensity is normalized to the sum of all ion signals; positive and negative ions were analysed separately).

5 Regarding organonitrate, we have found some laboratory evidence for its potential origin. AIDA (aerosol interaction and dynamics in the atmosphere) simulation chamber studies have been done with α-pinene and/or toluene OH oxidations on $NaNO_3$ seeds in the presence/absence of NO_x. The corresponding single particle mass spectra are shown in Fig. S9. It turns out that m/z 129+ is quite weak in α-pinene system even with NO_x (panel b), but it is much stronger after toluene is added (panel c). In the toluene system (refer to panel d to f), m/z 129+ is already present when $NaNO_3$ seeds are coated with toluene derived secondary organic

10 aerosol (SOA) (panel d), likely due to the recombined fragments from toluene and nitrate. After adding extra OH, m/z 129+ is becoming stronger, likely due to the more aged toluene SOA. When NOx is added to toluene system, m/z 129+ becomes much stronger (panel e), likely due to the organonitrate formation. Hence, we can conclude that m/z 129 $C_5H_7NO_3^+$ is more related to toluene rather than α-pinene, namely m/z 129 $C_5H_7NO_3^+$ could be a signature peak for anthropogenic sources in LAAPTOF spectra.
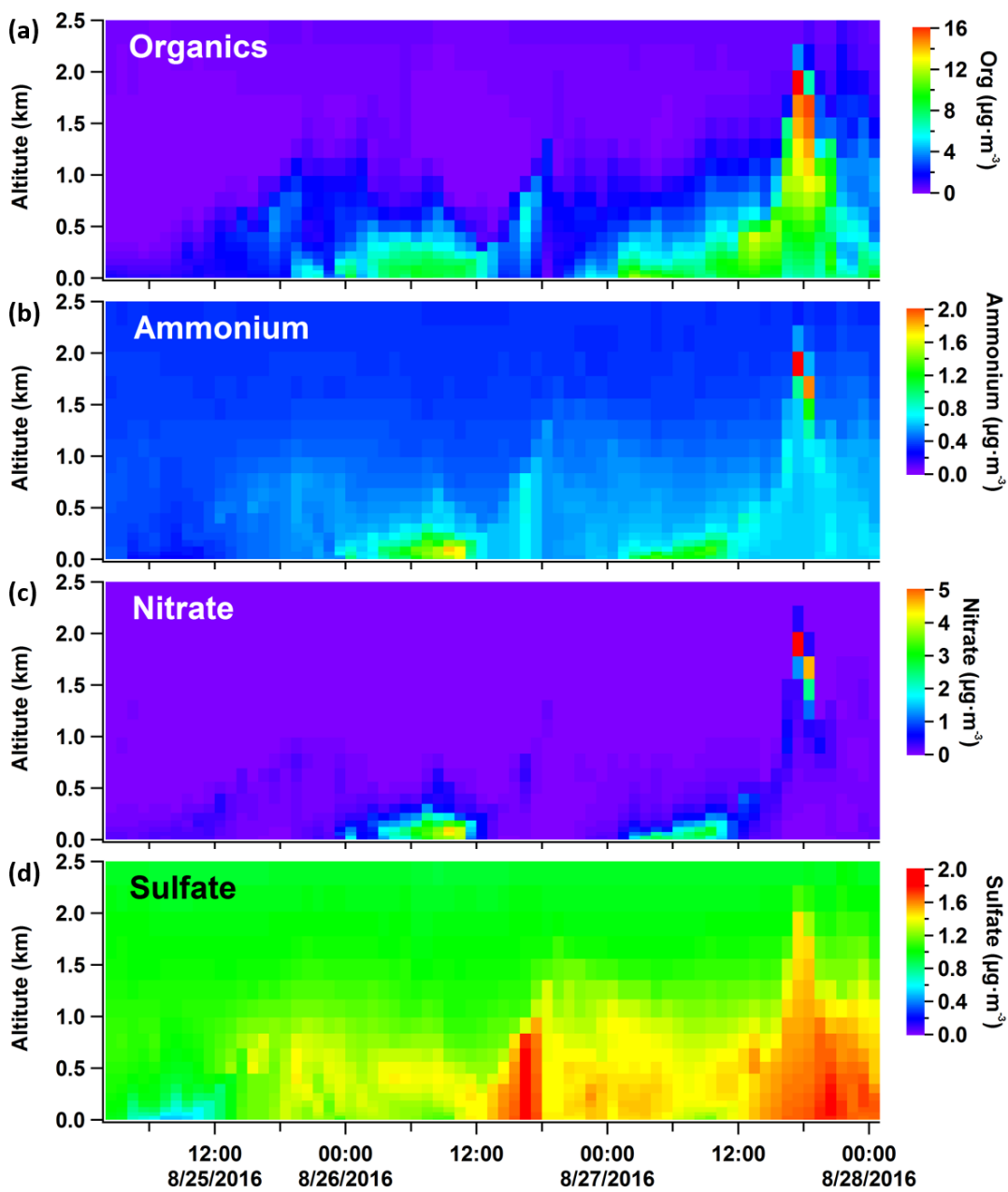
Figure S11: Time series of vertical profiles for organics, ammonium, nitrate, and sulfate as calculated by COSMO-ART.

References

Farmer, D. K., Matsunaga, A., Docherty, K. S., Surratt, J. D., Seinfeld, J. H., Ziemann, P. J., and Jimenez, J. L.: Response of an aerosol mass spectrometer to organonitrates and organosulfates and implications for atmospheric chemistry, P Natl Acad Sci USA, 107, 6670–6675, 2010.

5   Huang, W., Saathoff, H., Shen, X. L., Ramakrishna, R., Leisner, T., and Mohr, C.: Chemical characterization of highly functionalized organonitrates contributing to high night-time organic aerosol mass loadings and particle growth, Environ Sci Technol, 53, 1165–1174, 2019.

10

Five supporting videos (.gif files) will be available at KIT open data (https://publikationen.bibliothek.kit.edu/1000094401)

1. **SI_PN_10m.gif**

15   Particle number concentrations and wind field calculated by COSMO-ART during high SO_2 period (from 20160826 0:00 to 13:00 (local time) for 10 m a.g.l.

2. **SI_PN_122m.gif**

Particle number concentrations and wind field calculated by COSMO-ART during high SO_2 period from 20160826 0:00 to 13:00 (local time) for 122 m a.g.l.

20   3. **SI_Org1_10m.gif**

Particulate organic mass concentrations and wind field calculated by COSMO-ART from 20160826 18:00 to 20160827 12:00 (local time) for 10 m a.g.l.

4. **SI_Org2_10m.gif**

Particulate organic mass concentrations and wind field calculated by COSMO-ART from 20160825 17:00 to 20160826 18:00
25   (local time) for 10 m a.g.l.

5. **SI_Org3_10m.gif**

Particulate organic mass concentrations and wind field calculated by COSMO-ART from 20160827 12:00 to 20160828 01:00 (local time) for 10 m a.g.l.

Appendix C-Full articles of scientific publications as co-author

Appendix C.1 Exploring femtosecond laser ablation in single particle aerosol mass spectrometry

Atmospheric
Measurement
Techniques

Exploring femtosecond laser ablation in single-particle aerosol mass spectrometry

Ramakrishna Ramisetty[1], **Ahmed Abdelmonem**[1], **Xiaoli Shen**[1], **Harald Saathoff**[1], **Thomas Leisner**[1], **and Claudia Mohr**[1,2]

[1]Institute of Meteorology and Climate Research, Karlsruhe Institute of Technology, Karlsruhe, Germany
[2]Department of Environmental Science and Analytical Chemistry, Stockholm University, Stockholm, Sweden

Correspondence: Claudia Mohr (claudia.mohr@aces.su.se)

Abstract. Size, composition, and mixing state of individual aerosol particles can be analysed in real time using single-particle mass spectrometry (SPMS). In SPMS, laser ablation is the most widely used method for desorption and ionization of particle components, often realizing both in one single step. Excimer lasers are well suited for this task due to their relatively high power density (10^7–10^{10} W cm^{-2}) in nanosecond (ns) pulses at ultraviolet (UV) wavelengths and short triggering times. However, varying particle optical properties and matrix effects make a quantitative interpretation of this analytical approach challenging. In atmospheric SPMS applications, this influences both the mass fraction of an individual particle that is ablated, as well as the resulting mass spectral fragmentation pattern of the ablated material. The present study explores the use of shorter (femtosecond, fs) laser pulses for atmospheric SPMS. Its objective is to assess whether the higher laser power density of the fs laser leads to a more complete ionization of the entire particle and higher ion signal and thus improvement in the quantitative abilities of SPMS. We systematically investigate the influence of power density and pulse duration on airborne particle (polystyrene latex, SiO_2, NH_4NO_3, NaCl, and custom-made core-shell particles) ablation and reproducibility of mass spectral signatures. We used a laser ablation aerosol time-of-flight single-particle mass spectrometer (LAAPTOF, AeroMegt GmbH), originally equipped with an excimer laser (wavelength 193 nm, pulse width 8 ns, pulse energy 4 mJ), and coupled it to an fs laser (Spectra Physics Solstice-100F ultrafast laser) with similar pulse energy but longer wavelengths (266 nm with 100 fs and 0.2 mJ, 800 nm with 100 fs and 3.2 mJ). We successfully coupled the free-firing fs laser with the single-particle mass spectrometer employing the fs laser light scattered by the particle to trigger mass spectra acquisition. Generally, mass spectra exhibit an increase in ion intensities (factor 1 to 5) with increasing laser power density ($\sim 10^9$ to $\sim 10^{13}$ W cm^{-2}) from ns to fs laser. At the same time, fs-laser ablation produces spectra with larger ion fragments and ion clusters as well as clusters with oxygen, which does not render spectra interpretation more simple compared to ns-laser ablation. The idea that the higher power density of the fs laser leads to a more complete particle ablation and ionization could not be substantiated in this study. Quantification of ablated material remains difficult due to incomplete ionization of the particle. Furthermore, the fs-laser application still suffers from limitations in triggering it in a useful time frame. Further studies are needed to test potential advantages of fs- over ns-laser ablation in SPMS.

1 Introduction

Atmospheric aerosols are known to have large impacts on climate change, air quality and human health, and these effects are strongly related to the chemical composition of individual aerosol particles (Fuzzi et al., 2015). Atmospheric aerosols are highly heterogeneous in composition due to the vast number of natural and anthropogenic sources, as well as transformation and mixing processes during their residence time in the atmosphere (Kulkarni et al., 2011). Most analyses of aerosol chemical composition focus on the bulk, not least due to the very small mass and number of molecules present in an average atmospheric particle, making single-

particle studies challenging. However, the mixing state and composition of individual particles are crucial pieces of information for the assessment of particle interaction with light or water vapour and thus their contribution to climate change (Charles, 2012; IPCC, 2007; Jacobson, 2005; John, 2016; Laskin et al., 2018).

Single-particle mass spectrometry (SPMS) is a powerful tool for the investigation of the size-resolved chemical composition of individual atmospheric aerosol particles in real time (Brands et al., 2011; Gaie-Levrel et al., 2012; Murphy, 2007; Murphy et al., 2006; Pratt et al., 2009; Pratt and Prather, 2012; Zelenyuk et al., 2010). Although a two-step approach separating laser ablation and laser ionization bears several advantages for identifying specific molecules (Passig et al., 2017) many instruments currently still use single-step laser desorption and ionization. Single-particle mass spectrometers currently in use by different groups worldwide have very similar designs (Gaie-Levrel et al., 2012; Johnston, 2000; Murphy and Thomson, 1995; Zelenyuk et al., 2009). They usually consist of one or two scattering lasers that detect the particle size by particle time-of-flight, an ionization laser, commonly a nanosecond (ns) excimer laser for particle desorption and ionization in one single step, and the mass analyser (Murphy, 2007).

Quantitative analysis of single aerosol particles via laser ablation remains challenging, although several studies achieved advancements (Bhave et al., 2001; Fergenson et al., 2001; Gross et al., 2005; Healy et al., 2013), e.g. by detailed characterization of instrument sensitivity for individual chemical species and by optimizing ionization laser parameters to reduce fragmentation. However, so far no single-particle mass spectrometer is available for quantitative online analysis of particle mixtures. Single-step laser desorption and ionization with excimer lasers is highly non-linear (Zelenyuk and Imre, 2005). Usually, particles are not completely ablated (Ge et al., 1996; Murphy, 2007), and the ablation process leads to irreproducible spectra. The dominant yield of species with low ionization potential further limits the quantitative ability of ns-laser SPMS (Reilly et al., 2000). The absorption of photons depends on the optical properties of the chemical components of the particle, with important implications for core-shell or multi-component particles (Cahill et al., 2015). Reported approaches to improve the quantitative abilities of SPMS include two-step vaporization–ionization, where a CO_2 laser was used prior to excimer laser ionization for the evaporation of the particles (Cabalo et al., 2000; Morrical et al., 1998; Smith et al., 2002; Whiteaker and Prather, 2003; Woods et al., 2002), or the use of a high power density Nd:YAG laser of 5 ns pulse duration with 100 mJ pulse energy ($> 10^{10}$ W m^{-2}) (Lee et al., 2005; Mahadevan et al., 2002; Zhou et al., 2007). Lee and Mahadevan found that the kinetic energy of ions produced from ns-laser pulses is proportional to the particle size with a power law relationship, which influences ion detection efficiency in traditional time-of-flight mass spectrometer optics. The power density is much higher for femtosecond (fs) laser pulses compared to nanosecond laser pulses. The interaction of a high-intensity laser beam with a solid particle leads to the generation of a plasma that increases its energy content, its average charge state, and its charge density during the pulse duration. Zhou et al. (2007) used a one-dimensional hydrodynamic model and experimental observations to explain ns-laser pulse interactions with particles and observed that the laser energy absorption efficiency and thus ionization efficiency increase with shorter pulse width (from 10 ns to 10 picoseconds, ps). Molecular dynamic model simulations by Schoolcraft et al. (2001, 2000) explained the process of laser desorption and ionization of submicron particles for amorphous and crystalline particles with and without inclusions as a function of the nature of the material.

Fs lasers are widely used in the fields of micromachining and nanoparticle ablation (Chichkov et al., 1996; Gattass and Mazur, 2008; Malvezzi, 2014; Richard et al., 2013; Tsuji et al., 2003). Fs-laser ablation mechanisms include Coulomb explosion (soft ablation) and phase explosion followed by thermal ablation (strong ablation), depending on fs-laser intensities (Amoruso et al., 1999; Leitz et al., 2011; Roeterdink et al., 2003; Zhou et al., 2007). Coulomb explosion and/or phase explosion happen in multi-photon ionization, depending on pulse energy. Because of the very short interaction time in the femtosecond laser ablation and ionization, it is considered to be almost instantaneous, with the resulting kinetic energy of the electrons high enough to immediately escape the target. Therefore, no space charge shielding of the sample should occur. Consequently, the target is left behind with a corresponding density of localised positive holes. Once a sufficient density of holes is achieved, the target surface becomes electrostatically unstable, resulting in a Coulomb explosion of ions, the Coulomb explosion takes place in the initial phase and/or phase explosion occurs at a higher stage of multi-photon ionization (Roeterdink et al., 2003). Various mechanisms of the fs-laser ablation (excitation, melting, ablation) were compared to the nanosecond laser ablation (Harilal et al., 2014; Malvezzi, 2014) at different timescales. Substantial atomization and strong cluster formation are the major effects due to the phase and/or Coulomb explosion in the fs-laser ablation (Malvezzi, 2014; Roeterdink et al., 2003; Xu et al., 2000; Zaidi et al., 2010). The fs-laser ablation generates more atomic ions than in the nanosecond laser ablation due to rapid energy transfer and also leads to the formation of more ion clusters because of the explosions. A brief comparison between nanosecond and femtosecond laser ablation mechanisms for different timescales is given in the Supplement (Fig. S1). Most of the processes discussed above are based on studies with solid substrates in material science in which laser ablation is widely used. Only a few studies have been done with single particles so far (Murphy and Thomson, 1995; Zhou et al., 2007). The ablation and ionization of airborne particles may be different from ablation of solid substrates, e.g. with

respect to energy dissipation within the substrate. However, the basic principle of laser–matter interaction should be similar in both cases, especially within the first nanoseconds.

Potential differences in the ablation mechanism and resulting single-particle mass spectra as a function of pulse duration were also a focus of our studies. Compared to ns-laser ablation, the pulse duration of ultrashort (ps and fs) laser pulses is less than the typical ps time range of thermal diffusion effects. During ns-laser ablation thermal diffusion may reach deeper into the particles and the laser radiation may interact with the forming plume of ablated material. In contrast, for fs-laser ablation the plasma that formed near the particle surface without deeper thermal diffusion generates a plume by Coulomb and/or phase explosion which does not interact with the laser light (Fig. S1). The multi-photon ionization generates ions during the ablation phase, which may undergo association reactions in the expanding plume. The Coulomb explosions can also lead to ions with high kinetic energy which can lead to broader peaks in the mass spectra (Henyk et al., 2000a, b). In the case of fs-laser ablation, the higher photon density may favour multi-photon ionization, which may lead to the formation of new species during Coulomb or phase explosion. However, the ion formation mechanism is not well understood. Also, for the widely used ns lasers in SPMS, the ion formation mechanism is not completely understood (Murphy, 2007). Note that the ablated particle components move up to $\sim 5\,\mu m$ during a 5 ns pulse or $\sim 0.1\,nm$ during a 100 fs pulse and in both cases they remain well within the typical laser beam width. This estimate is based on an average ion speed of $1000\,m\,s^{-1}$ (Marine et al., 1992; Walsh and Deutsch, 1991).

Ultimately, the resulting mass spectral pattern in SPMS will depend on the energy transferred to the particle via the ionization laser, which is related to pulse width, laser power, and wavelength. Shorter pulses exhibit higher power densities than longer pulses at the same laser energy. Higher power densities usually lead to higher ionization efficiencies, e.g. in multi-photon interactions, where the total ion intensity is proportional to the power density of the ionization laser (Malvezzi, 2014). High-energy, short-wavelength and short-pulse-duration ionization lasers may thus be a valid choice in single-particle ionization.

In this study we explore the potential of high power density fs-laser pulses for improved quantitative abilities of SPMS. We compare mass spectra of atmospherically relevant airborne particles and dedicated test particles from ns- and fs-laser ablation using a commercially available laser ablation aerosol time-of-flight mass spectrometer (LAAPTOF, AeroMegt GmbH). The results presented here are an extension of the work by Zawadowicz et al. (2015), who coupled a particle analysis by laser mass spectrometry (PALMS) with an fs laser (Spectra Physics Solstice-100F ultrafast laser) to investigate mass spectral patterns of NaCl, NH_4NO_3, and lead-doped NH_4NO_3 particles. Overall, they observed similar mass spectra in both ns- and fs-laser ablation but also

showed that ions with high ionization energy such as Cl^+ are more easily generated by the fs laser due to its higher power density. At the same time, their fs PALMS exhibited lower sensitivity to lead than the PALMS employing the ns laser.

To achieve a better understanding of fs-laser ablation in SPMS, we systematically obtained mass spectra of particles of different size, morphology (core-shell), and chemical composition for both ns- and fs-laser ionization. Please note that for this work the geometry of ablation–ionization laser beam particle interaction was not orthogonal as for the experiments described by Zawadowicz et al. (2015) but almost collinear, as this was favoured by the design of the LAAPTOF. Furthermore, we varied the power density of the ionization lasers by varying the laser energy and laser wavelength in the case of the fs laser (800 and 266 nm) and by changing the focus positions of the lasers. We describe qualitative and quantitative differences of the mass spectra obtained and discuss implications of our results for the quantitative abilities of the LAAPTOF, and SPMS in general.

2 Methodology

2.1 LAAPTOF

The LAAPTOF has already been described in several other publications (Gemayel et al., 2016; Marsden et al., 2016; Shen et al., 2018) and therefore here we will especially focus on those aspects related to its operation with the fs laser. The LAAPTOF consists of four major modules: an aerodynamic lens focusing incoming particles into a narrow beam, the sizing section with two ultraviolet (UV) 405 nm continuous-wave detection laser diodes (DL1, DL2) set 11.3 cm apart from each other, the laser ablation/particle ionization region, and a bipolar time-of-flight mass spectrometer (Fig. 1). In the sizing region, the time delay between the detection of the scattered laser light of DL1 and DL2 by photomultiplier tubes (PMT, Thorn EMI, UK, type 9781R) is used to calculate the size of particles in the range of 200–2500 nm. The particle size detection methods and detection efficiencies for the LAAPTOF have been described in several publications (Gemayel et al., 2016; Marsden et al., 2016; Shen et al., 2018). Shen et al. (2018) show a comparison of the performance of the instrument we used in this study with other (some of them modified) LAAPTOF instruments. The scattering signal from DL2 produces a 10 V transistor–transistor logic (TTL) electronic signal that triggers the 193 nm ns excimer laser (ArF, pulse width of 5–8 ns, adjustable pulse energy from 0 to 10 mJ, ATLEX-S, ATL Lasertechnik GmbH). The excimer laser shoots at the particle and at the same time triggers the data acquisition system with a 5 V TTL electronic signal. We varied the laser focus to the left–right and up–down, and determined the diameter of the particle beam to 1–2 mm, depending on particle type. The ns-laser beam is slightly defocused at the position F1, increasing the
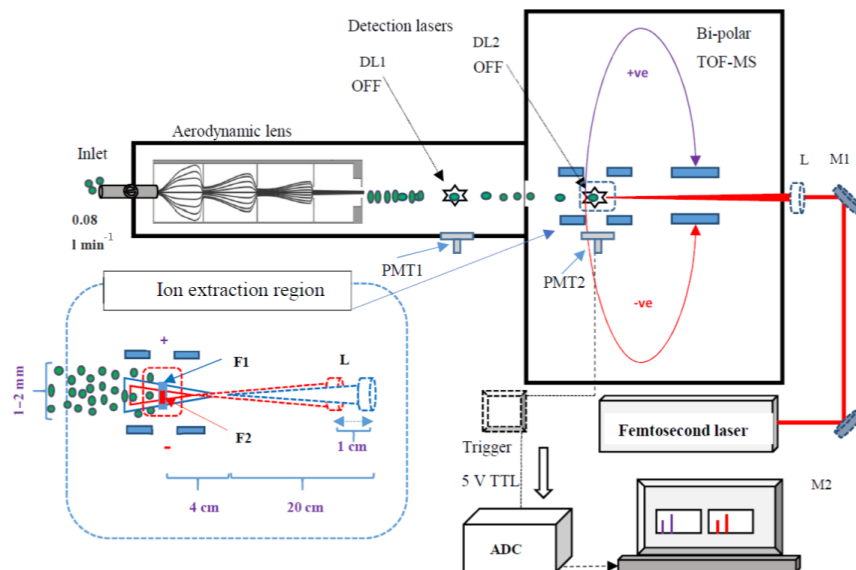
Figure 1. Schematic diagram of the LAAPTOF coupled with the fs laser. The detection lasers DL1 and DL2 are turned off, as well as the first set of PMT (PMT1). PMT2 collects the scattered light from the interaction of the fs laser with the particle. The PMT2 signal is connected to the trigger box and produces a trigger with a 5 V TTL signal for the ADC data acquisition. M1 and M2 are mirrors, and the aerosol particles are shown as green dots. The corresponding spectra of each ablated particle are recorded and stored in the computer. The inset picture shows the centre of ion extraction region (dashed red square) and the variation in laser beam diameters for the two different lens or focus positions (F1 blue and F2 red). The laser focus is 3–4 cm before the ion extraction region. The counter-propagating particle beam (green dots) has a diameter of 1–2 mm depending on the particle type. Moving the lens 1 cm towards the ion extraction region (F2) reduces the beam diameter and increases the power density at the centre of the extraction region. Picture is not to the exact scale.

particle–laser interaction area, and the defocused beam diameter is 99 ± 31 μm where it encounters the aerosol particle (F1, Fig. 1). The focus position of the excimer laser is 20 cm from the lens, and ionization happens 3–4 cm after the focus position for F2 and F1. This is the distance from the focus point to the centre of the ion extraction region from where the ions are extracted into the mass analyser. The movable lens can be used to shift the focus position from F1 to F2 where the defocused beam diameter is 81 ± 7 μm, resulting in higher power densities acting on the particles. Please note that the position of the ionization region is quite well defined in this case, close to the centre of the ion extraction zone, due to the scattering signal of the second detection laser, whereas for the experiments with the fs laser we had to apply a different procedure to define this (see Sects. 2.2 and 3.1). Variation in the focus position allows the power density to be varied by a factor of ~ 1.5 for otherwise similar conditions, for F1 and F2. The laser beam produces both positive and negative ions, which are deflected into the corresponding time-of-flight regions of the bipolar mass spectrometer. Typically, each particle hit by the excimer laser generates a positive and negative mass spectrum.

2.2 Fs-laser-coupled LAAPTOF

The fs laser (Spectra Physics Solstice-100F ultrafast laser) we coupled to the LAAPTOF is a Ti : Sapphire source, emitting pulses of 800 nm radiation with 1 kHz. Pulse duration is ~ 100 fs. The laser beam profile is close to Gaussian with a beam quality factor $M^2 < 1.3$ ($M^2 = 1$ for an ideal Gaussian beam). The maximum pulse energy is ~ 3.5 mJ. We also used a third harmonic generation module (Spectra Physics, TP-THG-F) to generate 266 nm pulses of 0.2 mJ and 100 fs duration. However, the resulting pulse energy of the laser was 1 order of magnitude smaller compared to the default 800 nm wavelength and led to a reduced light-scattering signal, and thus ineffective triggering of mass spectra recording, reduced particle detection, and lower ion signal. We therefore focus our analysis in this paper on fs-laser spectra at 800 nm wavelength. In this work, the peak power density (calculated as the power per beam area at focal point) is varied by changing the pulse energies. Excimer (ns-) and fs-laser beam parameters as well as pulse energies and corresponding peak power densities at focus points F1 and F2 are listed in Tables 1 and 2.

For the coupling of the fs laser with the LAAPTOF, a few technical changes were necessary. Figure 1 also includes a schematic of the modified LAAPTOF. Since it was not possible to trigger the fs laser, it was running in free-firing mode with a frequency of 1 kHz. To only record spectra from when

Table 1. Parameters of the ns and fs lasers: λ is wavelength, E is energy per pulse, and τ is pulse duration. Beam diameters before focusing lens and at the two interaction positions F1 and F2.

Parameter	λ (nm)	E (mJ)	t (ns)	f (Hz)	Laser beam diameter	Laser beam diameter (µm)	
					incident	At F1	At F2
Excimer – ns laser (ArF)	193	0.4–8	$\sim$5–8	Max 300	24 mm	99 ± 31	81 ± 7
Fs laser Ti : sapphire	800	$\sim$0.3–3.5	$\sim$0.10	1000	7 mm	487 ± 77	246 ± 36
Fs laser Ti : sapphire	266	$\sim$0.2	$\sim$0.10	1000	7 mm	270 ± 32	182 ± 32

Table 2. Excimer ns-laser and fs-laser pulse energies and corresponding power densities at positions F1 and F2. The corresponding beam diameters are given in Table S4.

	Laser type							
	Excimer ns-UV laser (193 nm)			fs UV (266 nm)	fs IR (800 nm)			
Energy (mJ)	0.8	4.0	8.0	0.2	0.3	1.7	3.2	3.5
Peak power density at F1 (W cm^{-2})	2.06×10^9	1.03×10^{10}	2.06×10^{10}	3.49×10^{12}	1.61×10^{12}	9.12×10^{12}	1.72×10^{13}	1.88×10^{13}
Peak power density at F2 (W cm^{-2})	3.11×10^9	1.55×10^{10}	3.11×10^{10}	7.69×10^{12}	6.32×10^{12}	3.58×10^{13}	6.74×10^{13}	7.37×10^{13}

a particle was hit by the fs laser, the scattered light from the fs-laser interaction with the particle detected by the second set of PMT was used to trigger the data acquisition. This and the fact that scattered light of the high-power fs laser could be detected by the PMT (yielding false particle size information) meant that both detection lasers were futile and thus switched off. This led to an absence of size information. To avoid loss of spectral signal due to the delay of $\sim$10 µs between triggering and the start of the data acquisition, the data acquisition was run in pre-trigger mode (Fig. 2). To define the ionization region for this case also close to the centre of the ion extraction region, a procedure selecting those mass spectra with more than 90 % of the maximum total ion intensities was applied (see Sect. 3.1).

A movable focusing lens set-up was used for multiple focusing positions between F1 and F2 further towards the inlet to better understand the effect of power density on mass spectral patterns (insert in Fig. 1). The laser beam diameters are calculated for all three wavelengths and for two different focus positions (Table S4). For the wavelength of 800 nm the laser beam diameters are 487 ± 77 and 246 ± 36 µm at the positions F1 and F2, respectively. The focal positions were varied to study the effect of power density on the mass spectra. The power densities at F2 are $\sim$3.5 times higher than at F1.

2.3 Particle types and experiments

For comparison of mass spectral patterns and signal intensities of fs- and ns-laser ablation in the LAAPTOF, we chose

the following particle samples: monodisperse polystyrene latex (PSL) particles, core-shell particles with a gold core and shells of silver (Ag), silica (SiO_2), and poly(allylamine hydrochloride) (PAH), salts (NaCl, NH_4NO_3), and spherical silica (SiO_2) particles. The sample details are tabulated in Table S3. All samples were dissolved or diluted in nano-pure water (18 MΩ), nebulized (Topas ATM 221, Topas AG), and then dried with silica dryers (Topas AG). The dried aerosol particles were size-selected with a differential mobility analyser (DMA 3080, TSI) and sent to the LAAPTOF.

All samples were measured with different laser power densities corresponding to different energies for both ns and fs lasers (Table 2). Per sample and laser type and setting, we tried to record spectra from at least 500 particles (see Tables S1 and S2). Empty spectra were excluded in the data analysis.

3 Results and discussion

3.1 Qualitative differences between ns- and fs-laser spectra

In the following, the qualitative differences between ns- and fs-laser positive and negative mass spectra are compared for typical pulse energies (4 mJ in the ns laser and 3.2 mJ in the fs laser). The mass spectra that are discussed in this section were selected to be representative of each particle type in the following manner. From the typically 200–600 useful single-particle mass spectra measured for each particle type,
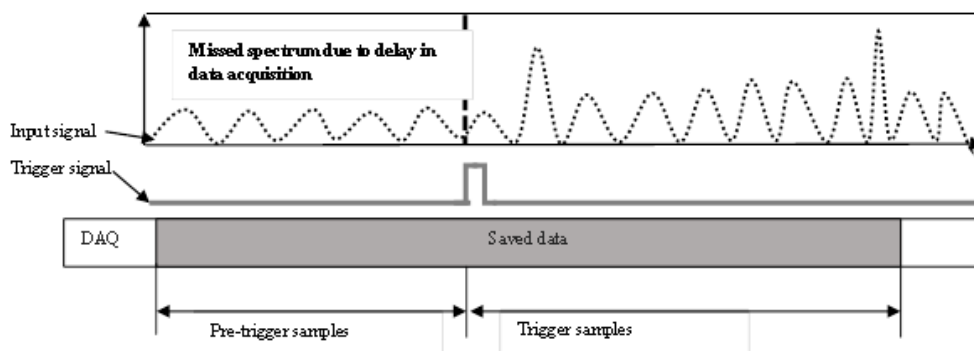
Figure 2. Pre-trigger sampling mechanism of the data acquisition system. The data (input signal, the dotted wavy line) arriving before the trigger event (pre-trigger samples) are saved in the temporary memory of the data acquisition card and then combined with the trigger samples.
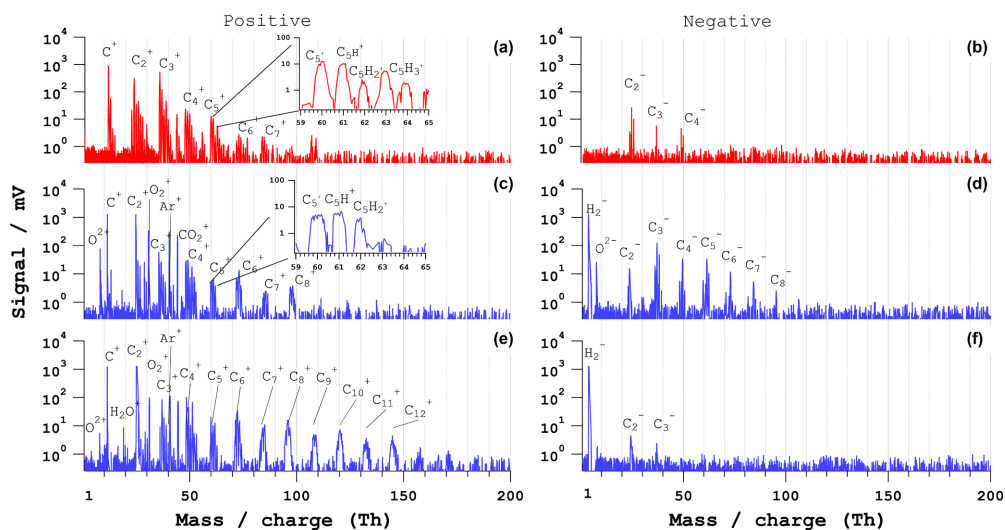
Figure 3. Bipolar mass spectra of single PSL particles of $d_p = 500\,\text{nm}$. **(a, b)** Typical ns-laser spectra, **(c, d)** fs-laser ($\lambda = 800\,\text{nm}$) spectra for 54 % of particles (type 1), and **(e, f)** fs-laser ($\lambda = 800\,\text{nm}$) spectra for 42 % of particles (type 2). The pulse energy is 4 mJ for the ns laser and 3.2 mJ for the fs laser.

only those 30–40 % (60–240 spectra) with at least 90 % of the maximum total ion intensities were selected to ensure optimal hit of the particles by the ablation and ionization laser. These remaining spectra were classified using the fuzzy c-mean algorithm available in the LAAPTOF data analysis software. This typically resulted in two classes of mass spectra per particle type. For each class of mass spectra we manually selected 10 spectra representing all main characteristics and applied an additional mass axis calibration for each spectrum. These 10 spectra showed correlation coefficients of $r = 0.7$–0.9. An example demonstrating the reproducibility and representativeness of this selection process is given in the Supplement (Figs. S2–S5). Analysis of mass spectra for both polarities from this work resulted in mass resolutions at full width half maxima for masses 16, 24 and 48 of 458,

530, and 593. At this resolution we can distinguish peak differences on a single mass unit basis. Please note that most difficulties in peak assignment do not originate from mass resolution but from the jitter of the mass axis from spectrum to spectrum or particle to particle.

3.1.1 PSL particles

A comparison of typical mass spectra of individual PSL particles with a geometric diameter (d_p) of 500 nm for ns and fs LAAPTOF is shown in Fig. 3. The positive ns-laser spectrum consists of series of carbon clusters C_n^+ ($n = 1$–7) and hydrogenated carbon clusters $C_nH_m^+$ ($n = 1$–7, $m = 1$–3) with different intensities (± 10 %) for different single particles. The insert in Fig. 3a shows the clusters with five carbon atoms. All other carbon clusters have similar numbers of hydrogen

atoms. The negative ns spectrum exhibits generally lower signal intensity and consists only of three major C_n^- ($n = 1$–3) and $C_nH_m^-$ ($m = 1$–2) peaks.

With the fs laser (800 nm, similar results for 266 nm, not shown), a total of ~ 500 particle spectra were recorded. Of these, 54 % are of type 1 (Fig. 3c–d) and 42 % are of type 2 (Fig. 3e–f). Type 1 consists of series of positive and negative C_n^+, $C_nH_m^+$ ($n = 1$–8, $m = 1$–2), C_n^- and $C_nH_m^-$ ($n = 2$–8, $m = 1$–2) ions. The positive spectrum also exhibits signals at m/z 18 and 16, which we assign to H_2O^+ and O^+, potentially from residual water. The insert in Fig. 3c shows the clusters with five carbon atoms ($C_5H_m^+$, $m = 0$–2). The ion patterns are similar for positive ion clusters with different carbon atom numbers. The type 2 spectra consist of a longer series of carbon-containing clusters C_n^+ and $C_nH_m^+$ ($n = 1$–15, $m = 1$–2) in positive mode. Signal intensity is lower in negative mode, with shorter carbon cluster series C_n^- ($n = 2$–3). The type 1 spectra show more negative ion clusters than the type 2 spectra, whereas type 2 shows more positive ion clusters. One explanation for this observation could be that the type 2 spectra are generated from particles that are ionized closer to the positive ion extraction region, whereas the type 1 spectra may arise from particles ionized closer to the negative ion extraction region or in the middle of the ion extraction region of the mass spectrometer. Since the particle beam at the ionization region has a width of 1–2 mm and the laser beam a width between 487 ± 77 μm (F1) and 246 ± 36 μm (F2) it is possible that some particles are ionized closer to either one of the electrodes leading to these two types of mass spectra.

In both laser ablation methods we observe the formation of carbon clusters and hydrogenated carbon cluster ions from PSL particles. For fs-laser ablation, larger carbon clusters (> 7 carbon atoms) with (in positive mode) fewer hydrogen atoms (< 3 hydrogen atoms) are observed. In both laser ablation methods we observe the formation of carbon clusters and hydrogenated carbon cluster ions from PSL particles. For fs-laser ablation, larger carbon clusters (> 7 carbon atoms) with (in positive mode) fewer hydrogen atoms (< 3 hydrogen atoms) are observed. Such large clusters in the fs-laser spectra can potentially form during the Coulomb or phase explosion of the fs-laser ablation process but some studies claim that reactions of the primary ion species with the source plume can also generate larger clusters (Zaidi et al., 2015, 2010). For both laser pulse durations, the number of larger clusters increased with increasing laser pulse energy for the PSL spectra as has also been reported for ns-laser pulses by Weiss et al. (1997).

3.1.2 NaCl particles

Bipolar mass spectra of NaCl particles of an electrical mobility diameter (d_m) of 400 nm for ns and fs laser are shown in Fig. 4. The positive ns-laser spectrum consists of atomic sodium and molecular ions (Na^+, Na_2^+), and Na_2Cl^+ and

$Na_3Cl_2^+$ ions. The negative ion spectrum consists of chlorine ions (Cl^-, Cl_2^-), and sodium chloride cluster ions ($NaCl_2^-$, $Na_3Cl_2^-$). The bipolar spectrum is representative of 55 % of a total of 600 spectra. The remaining spectra are empty or contain no features of NaCl.

From the fs-LAAPTOF measurements (800 nm, similar results for 266 nm, not shown) ~ 80 single-particle spectra were considered for analysis. This low hit rate for the fs laser compared to the ns laser may be related to both the particle shape widening the particle beam and the reduced absorption at 800 nm compared to 193 nm. A representative single-particle bipolar spectrum is shown in Fig. 4c–d. The positive spectrum consists of Na^+, Na_2^+, Cl^+, Na_2Cl^+, $NaCl_2^+$, $Na_3Cl_2^+$, NaO_2^+ ions, and H^+, O_2^+ ions, most likely from residual water. The negative spectrum consists of Na^-, Na_2^-, Cl^-, Cl_2^-, Na_2Cl^-, $Na_2Cl_3^-$, and $Na_4Cl_4^-$ ions. Around 20 % of particles exhibited less intense signals of $Na^{+/-}$ and $Na_2^{+/-}$ by ~ 10 %, while the signals of the other ions were similar across the spectra.

The qualitative difference between ns- and fs-LAAPTOF spectra is the presence of Cl^+ and Na_2^+ ions in positive fs spectra, and Na_2^- and Cl_2^- ions in negative fs spectra, which are not commonly observed in ns spectra. In addition, NaO_2^+ and NaO_2^{2+} ions (O likely from residual water) are present in the positive spectrum of the fs LAAPTOF. Zawadowicz et al. (2015) reported ions with similar combinations of Na and Cl in their fs-PALMS single-particle spectra but no NaO clusters. The dissociation energy of the NaCl molecule is 4.26 eV, which is smaller than the ionization energy of Na^+ (5.13 eV) and Cl^+ (12.96 eV). The electron affinities of Na^- and Cl^- are 0.52 and 2.35 eV, respectively (Sansonetti and Martin, 2005). In the case of ns-laser ablation with lower power density, NaCl can easily dissociate and form Na^+ and Cl^- ions. For Cl^+ ion formation, twice as much energy (12.96 eV) is required, which is available during the fs-laser ablation process. Ionization energies are even higher for molecular Na and Cl, as well as for doubly charged Na and Cl ions. We also observed more cluster ions in the fs-laser spectra (Na_2Cl^+, $NaCl_2^+$, Na_2Cl^-, $Na_2Cl_3^-$ and $Na_4Cl_4^-$) compared to the ns-laser spectra, which again indicates a more complex ionization mechanism during fs-laser ablation. Several studies on fs-laser ablation of NaCl have observed the formation of cluster ions at higher power densities due to Coulomb or phase explosion, depending on excitation energy (Hada et al., 2014; Henyk et al., 2000a, b; Reif et al., 2004).

3.1.3 NH$_4$NO$_3$ particles

The positive and negative mass spectra of NH_4NO_3 particles with $d_m = 400$ nm for ns and fs LAAPTOF are shown in Fig. 5. The ns-laser spectrum is representative of 500 particles. The positive spectrum consists of NH_2^+ / O^+, OH^+, NH_4^+, NO_2^{2+}, NO^+, NO_2^+, and NO_3^+ ion signatures, while
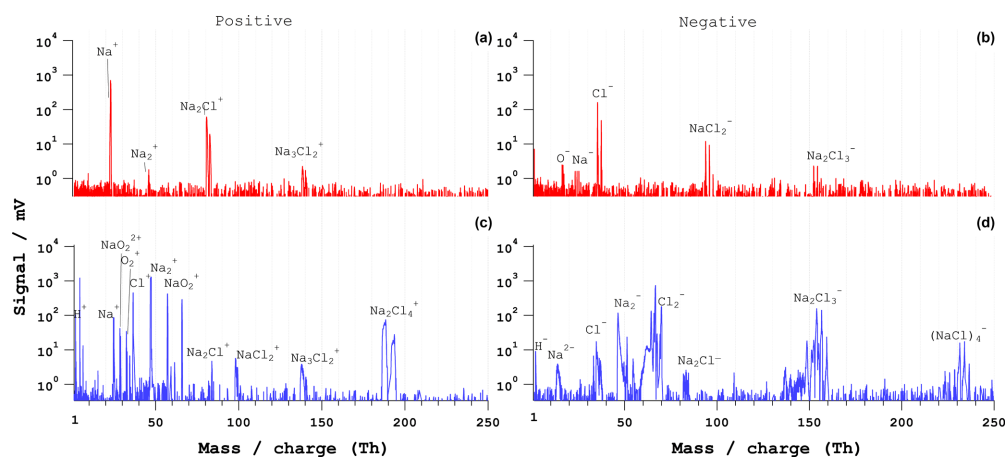
Figure 4. Bipolar mass spectra of NaCl single particles of $d_m = 400\,\mathrm{nm}$. **(a, b)** Typical ns-laser spectra and **(c, d)** fs-laser ($\lambda = 800\,\mathrm{nm}$) spectra. The pulse energy is 4 mJ for the ns laser and 3.2 mJ for the fs laser.
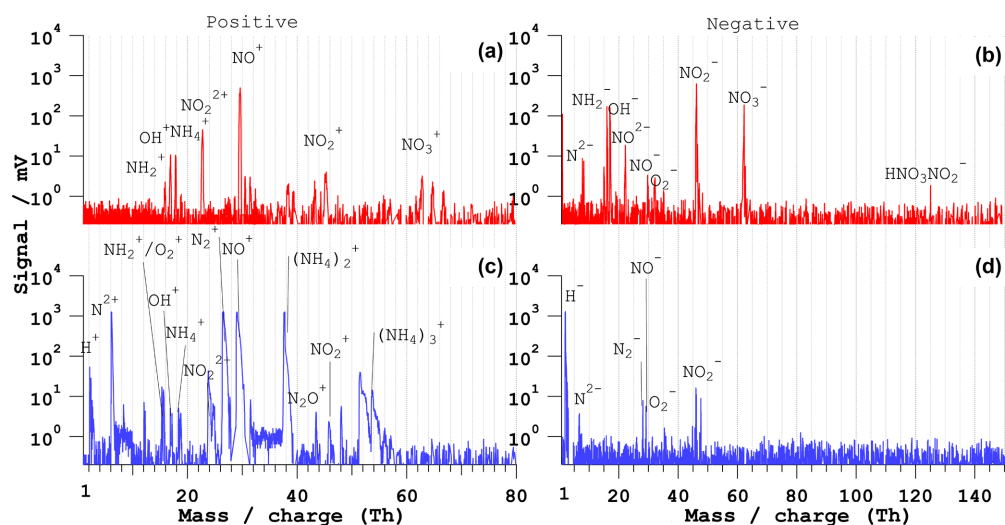
Figure 5. Bipolar mass spectra of NH_4NO_3 particles of $d_p = 400\,\mathrm{nm}$. **(a, b)** Typical ns-LAAPTOF spectra and **(c, d)** fs-LAAPTOF ($\lambda = 800\,\mathrm{nm}$) spectra. The pulse energy is 4 mJ for the ns laser and 3.2 mJ for the fs laser.

the negative spectrum contains N^{2-}, NH_2^- / O^-, OH^-, NH_4^-, NO_2^{2-}, NO^-, O_2^-, NO_2^-, NO_3^-, and $HNO_3NO_2^-$ ions.

The fs-LAAPTOF (800 nm) bipolar spectrum represents only 10 % of a total of 500 spectra. The majority of the particles were poorly hit and/or ionized. The positive spectrum contains H^+, N_2^+, $(NH_4)_2^+$, and $(NH_4)_3^+$ ions in addition to the ions observed in the ns-LAAPTOF positive spectrum; however there is no NO_3^+ signature. There is a much lower (2 orders of magnitude) signal intensity in the negative spectrum compared to the positive spectrum. Only $\sim 1\,\%$ of negative fs-laser spectra exhibit significant signals (panel d), with peaks from N^{2-}, N_2^-, NO^-, O_2^-, and NO_2^- ions, albeit with lower sensitivity.

The ns-LAAPTOF bipolar spectrum is comparable to the ammonium nitrate single-particle spectrum obtained by the PALMS (Zawadowicz et al., 2015). NH_4NO_3 predominantly leads to positive ions (NH_2^+ / O^+, OH^+, NH_4^+, NO_2^{2+}, NO^+, and NO_2^+ are the most intense peaks). A clear signal was observed with the ns LAAPTOF for the $HNO_3NO_2^-$ ion in accordance with observations with an online laser desorption–ionization (LDI) mass spectrometer with excimer laser wavelength 193 nm (Neubauer et al., 1998), but in contradiction to observations with the PALMS (Zawadowicz et al., 2015) or the real-time single-particle mass spectrometer (RSMS) with excimer laser wavelength 193 nm (Reinard and Johnston, 2008). The fs-LAAPTOF positive spectrum consists of $N_xO_y^+$ ($x = 0$–2, $y = 0$–2), $(NH_4)_x^+$ (where $x = 1$–3), H^+,

Atmos. Meas. Tech., 11, 4345–4360, 2018   www.atmos-meas-tech.net/11/4345/2018/

188
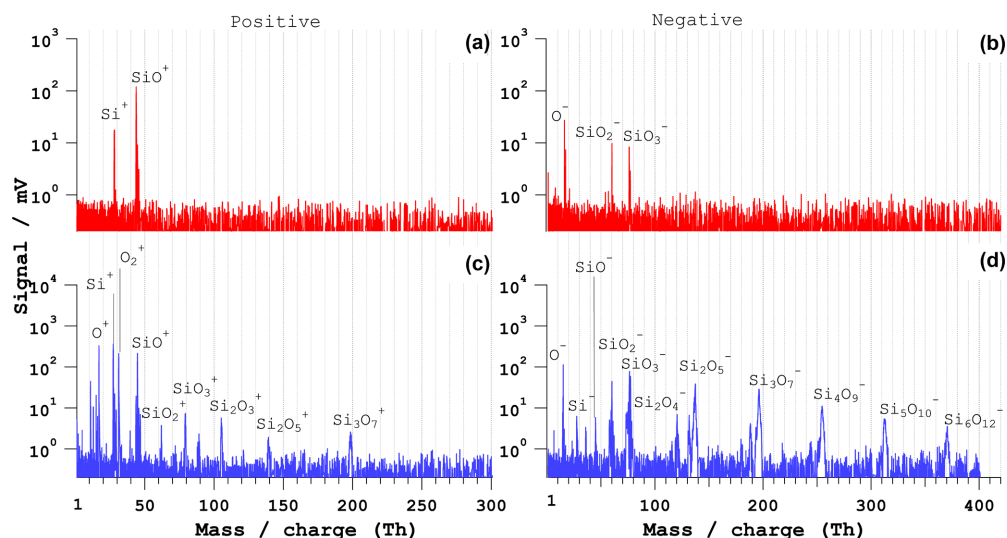
Figure 6. Bipolar mass spectra of SiO_2 single particles of $d_p = 1100$ nm. **(a, b)** Typical ns-laser spectra and **(c, d)** fs-LAAPTOF ($\lambda = 800$ nm) spectra. The pulse energy is 4 mJ for the ns laser and 3.2 mJ for the fs laser.

and N_2^+ ions. The ionization energies of $(NH_4)_x^+$ (for $x > 1$) cluster ions are very high (Dunlap and Doyle, 1996), which may be the reason for the absence of these ions in the ns spectra.

3.1.4 SiO₂ particles

Mass spectra of individual SiO_2 particles of $d_p = 1000$ nm measured by ns and fs LAAPTOF are shown in Fig. 6. A bipolar spectrum of SiO_2 particles, representative of about 80 % of 860 spectra from ns LAAPTOF obtained with 4 mJ pulse energy is presented in panels (a) and (b). The positive spectrum consists of Si^+ and SiO^+ ions. The negative spectrum contains O^-, SiO_2^-, and SiO_3^- ions. The other 20 % of spectra have three more $Si_xO_y^-$ clusters ($x = 2$–3, $y = 4$–5).

Recent studies with a LAAPTOF by Marsden et al. (2016) of silicate (SiO_4)-rich ambient dust particles featured similar mass spectral peaks, namely from Si^+, SiO^+, O^-, SiO^-, and SiO_2^- ions. Single-particle characterization studies of SiO_2-rich particles by Cahill et al. (2015) with an aerosol time-of-flight mass spectrometer (ATOFMS) using a 266 nm Nd : YAG ionization laser also produced O^-, SiO_2^-, and SiO_3^- ions. Both studies presented similar spectra to the ones shown in Fig. 6a–b. Another ambient single-particle study with a PALMS powered with an excimer laser (193 nm, $\sim$4 mJ pulse energy) by Gallavardin et al. (2008) showed Si_xO_y negative ion clusters ($x = 1$–2, $y = 1$–4), similar to the peaks in 20 % of spectra from our LAAPTOF (not shown here). Another experimental study of silica clusters with a 308 nm XeCl excimer-laser-coupled time-of-flight mass spectrometer observed clusters of silica $(SiO_2)_n^-$ units ($n = 1$–6) (Xu et al., 2000).

The fs-LAAPTOF bipolar spectra for silica are shown in Fig. 6c–d, which is representative of $\sim$80 % of 530 particles. The positive spectrum consists of O^+, Si^+, O_2^+, $Si_xO_y^+$ ($x = 1$–3, $y = 2x+1$), and $Si_xO_y^+$ ($x = 1$–2, $y = x+1$) ions. The negative spectrum of O^-, Si^-, O_2^-, $Si_xO_y^-$ ($x = 1$–6, $y = 2x + 1$), and $Si_xO_y^-$ ($x = 1$–2, $y = x+1$) ions. To our knowledge there are no studies on the fs-laser ablation of individual silica particles; we thus cannot compare our spectra with other single-particle spectra. Kato et al. (2007) investigated fs- and ns-laser ablation of silica substrates, and silicon-rich solutions. They observed positive silicon clusters, Si_x^+ ($x = 1$–6), and claimed that ns-laser ablation leads to more fragmentation, whereas fs-laser ablation leads to better atomization with elemental ionization. With fs-laser ablation of silicon substrate, clusters of Si_n^+ ($n =$ up to 10) have been observed (Bulgakov et al., 2004).

The major difference between the positive ns-LAAPTOF and fs-LAAPTOF spectra is the existence of elemental oxygen (O^+, O_2^+), and silica clusters (SiO_2^+, $Si_2O_3^+$, $Si_2O_5^+$, and $Si_3O_7^+$) in the fs-laser spectra. In the negative fs-laser spectra, O^- and Si^- elemental ions as well as $Si_xO_y^-$ ($x = 1$–6, $y = 2x + 1$) and $Si_xO_y^-$ ($x = 1$–2, $y = x + 1$) cluster ions are observed. Only O^-, SiO_2^-, and SiO_3^- ions are also common in ns-laser negative spectra. Another major difference is the high signal intensity in the fs-LAAPTOF spectra. Overall, fs-laser ablation yields more elemental information (positive silicon and positive oxygen) but also leads to higher-order clusters than ns-laser ablation. The increasing abundance of larger clusters with increasing laser pulse energy is shown in Fig. S6 for SiO_2 particles.

Since the SiO_2 is bonded covalently in nature, a high amount of energy is required to break it. Consequently, we
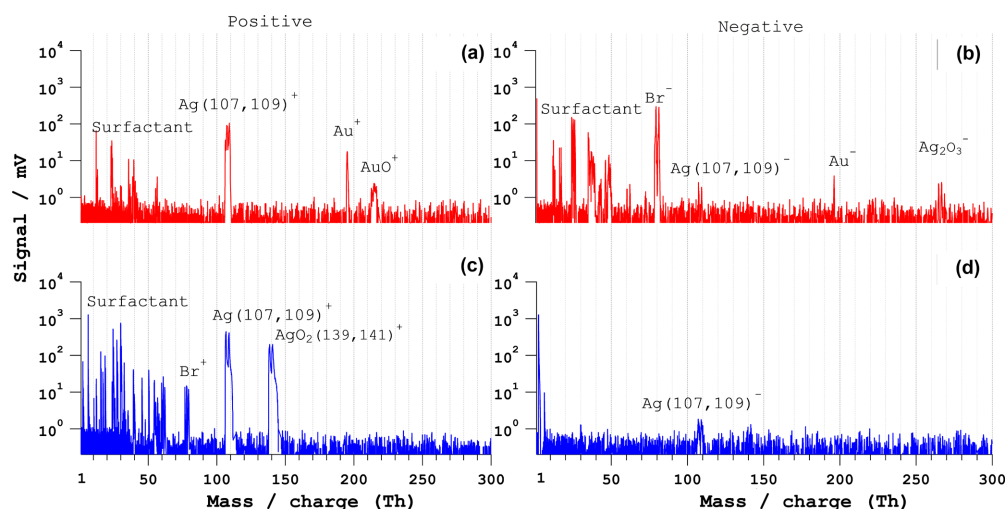
Figure 7. Bipolar mass spectra of gold–silver core-shell particles of $d_p = 600$ nm. **(a, b)** Typical ns-LAAPTOF spectra and **(c, d)** fs-LAAPTOF ($\lambda = 800$ nm) spectra. The pulse energy is 4 mJ for the ns laser and 3.2 mJ for the fs laser.

observe both cations and anions of SiO_2 constituents in the fs spectra. The 266 nm UV fs-LAAPTOF spectra of SiO_2 particles contain similar spectral features (Fig. S10) but less intense signals than the 800 nm fs-laser spectra.

3.1.5 Gold–silver core-shell particles

A bipolar single-particle mass spectrum of gold–silver core-shell particles from ns LAAPTOF is shown in panels (a) and (b) of Fig. 7. This bipolar spectrum represents 27 % of a total of 850 particles or spectra. The peaks below 100 Th are fragments from the surfactant Cetyl-trimethylammonium bromide (CTAB), $C_{19}H_{42}BrN$, which was used to stabilize the gold–silver particles in the suspension. The positive spectrum consists of signals from the two silver isotopes $Ag^{(107,109)+}$, of Au^+, and AuO^+. The negative spectrum contains signals from $Ag^{(107,109)-}$, Au^-, silver oxide isotopes $AgO_2^{(139,141)-}$, and also silver dioxide $(AgO_2)^-$. About 43 % of the 850 spectra contain only signals from elemental silver and silver oxides, and no gold peaks. The remaining 30 % of single-particle spectra consist only of a signal from CTAB.

The respective fs-LAAPTOF bipolar spectrum is shown in Fig. 7c–d, which is representative of 19 % of ~ 1500 particles. The positive spectrum consists of signals from the surfactant CTAB, elemental silver isotopes $Ag^{(107,109)+}$, and silver oxide isotopes $Ag^{(139,141)+}$. The negative spectrum is almost empty, with very small peaks of silver and silver oxide, and none of the fs-LAAPTOF spectra contains a gold signal. 8 % of the negative fs-LAAPTOF spectra have a clear signal from the surfactant and very small silver peaks.

The gold–silver particles contain a 300 nm gold core (nearly 67 % of total the weight percentage with a mass of 2.18 pg), and a 150 nm thick shell of silver (about 33 %

of the total mass percentage with a mass of 1.08 pg). The ns-LAAPTOF mass spectral signatures, however, feature a higher signal for silver than for gold. More signals from both core and shell are observed when there is less surfactant signal in the ns spectra. The major difference between ns-LAAPTOF and fs-LAAPTOF spectra is the absence of gold peaks in the fs spectra. At the wavelength of the excimer ns laser (193 nm), the reflectance of both gold and silver are nearly 35 % (Kah et al., 2015). At the wavelength of the fs laser (800 nm), the reflectance is more than 95 % for both gold and silver. The high reflectance of gold and silver in the IR likely contributes to the reduced ablation of the core. Although the reflectance of these particles is much lower at 266 nm these fs-laser pulses were also not capable of generating a significant signal from the core for the reduced pulse energy of 0.2 mJ.

The existence of gold and silver oxides in both ns- and fs-laser spectra may be explained by oxygen-containing coatings on the particles, e.g. water or surfactants. However, we cannot fully exclude interactions of the ablated plume with background ions or residual water like in the study by Neubauer et al. (1998).

3.1.6 Gold-poly(allylamine hydrochloride) core-shell particles

The second type of core-shell particles we tested for mass spectral comparison between ns and fs laser is made of a gold core ($d_p = 300$ nm) and an organic polymer (poly(allylamine hydrochloride), PAH) shell (coating thickness = 50 nm). Ns- and fs-LAAPTOF spectra are shown in Fig. 8.

The ns-LAAPTOF bipolar spectrum (panels a and b) is representative of 44 % of a total of 450 particles. It features signals from the organic PAH shell (elemental carbon

Atmos. Meas. Tech., 11, 4345–4360, 2018   www.atmos-meas-tech.net/11/4345/2018/

190
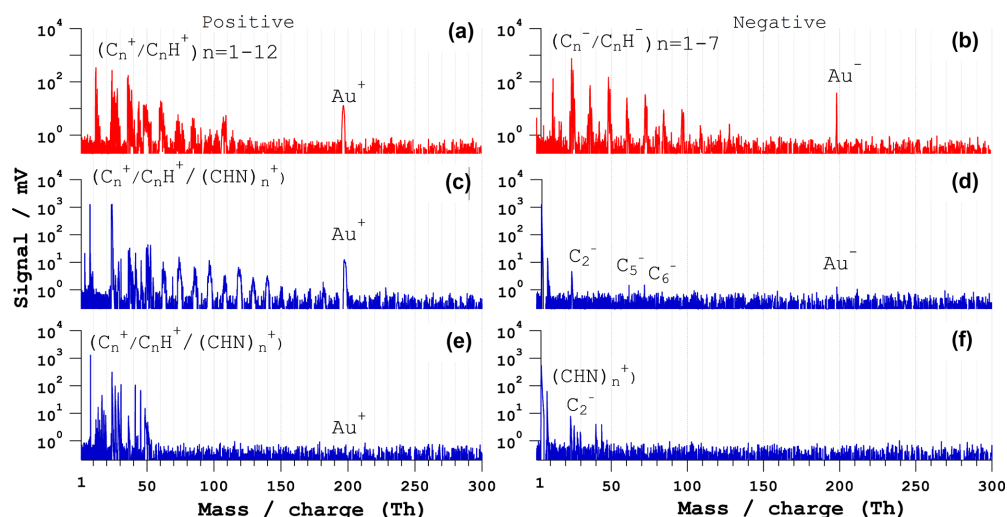
Figure 8. Bipolar mass spectra of Au-PAH core-shell particles. **(a, b)** Typical ns-LAAPTOF spectra and **(c, d)** fs-LAAPTOF ($\lambda = 800$ nm) spectrum that contains both gold and PAH signals, **(e, f)** fs-LAAPTOF ($\lambda = 800$ nm) spectrum without gold signal. The pulse energy is 4 mJ for the ns laser and 3.2 mJ for the fs laser.

$C_n^{+/-}$, and hydrocarbons $C_n H^{+/-}$), as well as elemental gold ($Au^{+/-}$) ions. The remaining 56 % of spectra mainly consist of signals from the PAH shell and exhibit no or almost no signals from the gold core.

Two types of fs-LAAPTOF spectra are shown in panels (c)–(f). The spectra are representative of 10 and 15 % of the total number of spectra (1000). Spectra that do not contain gold or PAH signals are excluded, as are spectra that contain only background signal peaks (Ar^+, CO_2^+). Figure 8c–d is representative of a spectrum that contains a distinctive signal from the gold core, and C_n^+ ions as well as $C_n H_n^+$ cluster ions. The second type (panels e–f) does not exhibit any signal from the gold core and also less signal from the carbon clusters. The spectra with both an organic shell and gold core signature are most likely produced from particles that were hit very close to the centre of the laser beam. The spectra without the gold signature are most likely produced from particles interacting only with part of the laser beam. Please note that the particle beam has a diameter ranging between 1 and 2 mm, while the laser beam diameter ranges between 246 and 487 µm (see Table S4).

The comparison between ns- and fs-LAAPTOF spectra of gold-PAH core-shell particles reveals more signal from carbon clusters, which are similar to the peaks from PSL particles, in the fs spectra. The signal from the gold core was only observed in one of a total of 1000 particles, again due to the low absorption of gold in the IR (Manca et al., 2007; Pereira et al., 2015). The spectra of gold-PAH particles from the 266 nm fs LAAPTOF (not shown) also did not exhibit signal from the gold core, and only low signal intensity from the PAH shell.

The third type of core-shell particles, Au-SiO$_2$, produced mass spectra and no signal from the gold core at both fs-laser wavelengths (Fig. S2). Signal from the gold core was again observed in the ns-laser spectra. They contained Si, SiO, SiO$_2$ positive ions, as well as hydrocarbon ions from the surfactant, and negative hydrocarbon, elemental carbon, and oxygen signals from the SiO$_2$ shell.

3.1.7 Fs-laser ablation with a wavelength of 266 nm

The mass spectra obtained for fs-laser pulses of 266 nm wavelength and 0.2 mJ energy/pulse show very similar features for all the samples measured as obtained for the other fs-laser wavelength of 800 nm. Please note that about 80 % of the spectra collected for 266 nm was empty due to the reduced light-scattering signal and corresponding ineffective triggering of mass spectra recording. Furthermore, the mass spectra containing information have lower average intensity of 3 to 5 times for all particle types compared to those obtained for fs-laser pulses of 800 nm, with a similar energy of 0.3 mJ per pulse. A discussion on single-particle mass spectra for 266 nm (fs laser) in comparison with those obtained using 193 nm (ns laser) and 800 nm (fs laser) is presented in the Supplement (Figs. S7–S13).

3.2 Signal intensity as a function of laser power density and particle size

3.2.1 Signal intensity variation with laser power density

We investigated the relationship between ion signal intensity and laser power density for all particle samples. The in-
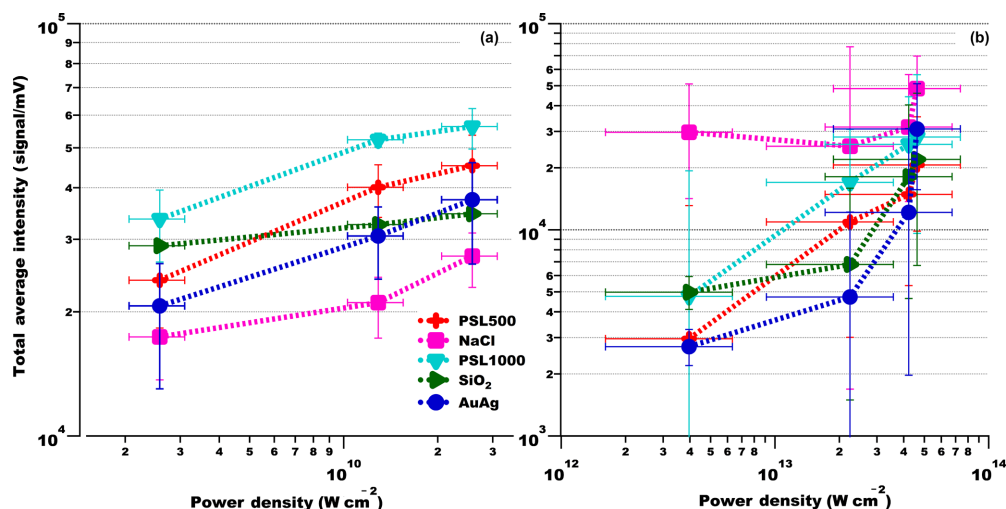
Figure 9. Average ion intensity versus laser power density for different particle types. **(a)** Excimer laser and **(b)** fs laser. Error bars of the average ion signal intensity correspond to ±1 standard deviation, error bars of the power density to the value of power density of the laser beam at the corresponding possible maximum and minimum position of particle–laser interaction.

crease in power density from the lowest (0.8 mJ) to the highest (8 mJ) excimer laser pulse energy corresponds to 1 order of magnitude (2.06×10^9–2.06×10^{10} W cm^{-2}). For the fs laser, the energy was varied from 0.3 to 3.5 mJ, corresponding to more than 1 order of magnitude difference in power density. Due to the large spectrum-to-spectrum variance, average signal intensities per power density settings were calculated for 20 mass spectra that are representative of the typical spectra discussed in Sect. 3.1 (Fig. S2).

The mass spectra generated with the fs laser have on average a factor of 5 higher total ion intensity compared to those generated with the ns laser. Average signal intensity versus power density for both ns and fs lasers is shown in Fig. 9. All samples exhibit an increase in average signal intensity (by a factor of up to 5, depending on particle type) with increasing ns- or fs-laser (800 nm) power. The exception is NaCl, which seems to be more efficiently ionized (compare Sect. 3.1.2) at the higher power densities of the fs laser compared to the ns laser, albeit with a saturation effect. Based on our limited data and the available literature one can only speculate about potential reasons. The observed slight saturation effect of signal intensity at higher power densities for both lasers and most particle types may be due the Coulomb repulsion among the ions during multi-photon ionization, observed by L'Huillier et al. (1987). Furthermore, penetration of the plasma into the particles with increasing power density may be limited due to absorption of part of the additional power by the plasma near the surface.

Figure S14 shows the same data as Fig. 1 but separated for focus positions F1 and F2. Note that for the fs laser, due its free-firing mode, the ionization position and corresponding power density are highly uncertain and represent a best esti-

mate. Consequently, we cannot rule out an overlap between possible power densities corresponding to F1 and F2.

3.2.2 Ion signal intensity variation with particle size

To explore the quantitative abilities of the fs and ns laser we also investigated the average ion signal intensity variation as a function of laser power density with respect to particle size (Fig. 10a, b) using PSL particles of 500 and 1000 nm diameter. Similar subplots (Fig. 10c–d) are shown for focus position F1 with lower power density. The average signal intensity for the 1000 nm size particles as a function of the excimer laser power density is 2–4 times higher compared to the signal intensity for 500 nm particles for both focus positions. The femtosecond laser produced average ion signals only 1.5–2 times larger for 1000 nm particles compared to 500 nm particles. However, this difference between ns- and fs-laser ion intensities for these different particle sizes is within the uncertainties and also has to be verified for different types of particles. The mass ratio of the two particle sizes is 8; hence much larger than the relative differences in the total ion intensities. The ratio of the surface area of the 1000 nm PSL and 500 nm PSL particles is 4, which is comparable to the maximum intensity difference observed. This could be an indication that the ionization scales with the particle surface area. The increase in ion signal thus does not scale linearly with the difference in mass of the two particles sizes and of the total material that is potentially ablated. Similar effects were observed for $RbNO_3$ and $(NH_4)_2SO_4$ particles (Reents et al., 1994). This demonstrates the quantitative limitations of both ns- and fs-laser ablation.
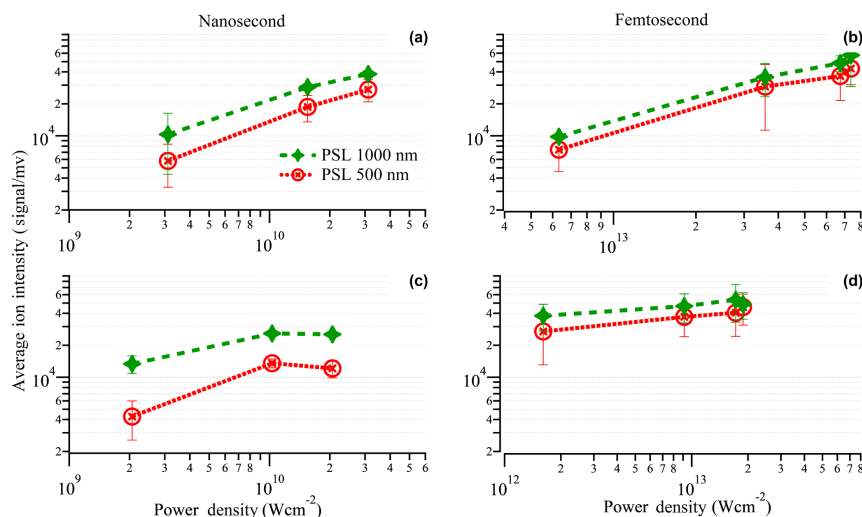
Figure 10. Variation in average total ion intensity with respect to the size of PSL particles. The total ion intensities were averaged for 10 representative spectra of each particle type. Particle diameters are 500 nm for red circles, and 1000 nm for green triangles). **(a, b)** At the focus position F2 and **(c, d)** at the focus position F1.

4   Conclusions

We coupled the commercially available single-particle mass spectrometer LAAPTOF, originally equipped with an ns ex-cimer laser, with a free-firing fs laser to investigate mass spectral patterns and signal intensity for a variety of atmo-spherically relevant aerosol particles and dedicated test par-ticles. We successfully employed the fs laser light scattered by the particles to trigger mass spectra acquisition with a certain pre-trigger. Particle types sampled (and their diam-eter) include PSL particles (500, 1000 nm), NaCl (400 nm), NH_4NO_3 (400 nm), Silica (1000 nm), and gold–silver, gold-SiO_2, and gold-PAH core-shell particles (600, 400, and 400 nm).

Overall, mass spectral signatures for ns-and fs-laser ab-lation and different particle types are fairly similar. Gener-ally, ns-laser spectra for the same particle type exhibit higher reproducibility of the spectral pattern than fs-laser spectra with the LAAPTOF in counter-propagating geometry. This is most likely because the ns laser can be triggered, which leads to some limitation of the physical extent of the poten-tial interaction region of particle and laser beam, which is not the case for the free-firing fs laser. Please note that between 30 and 40 % of the spectra obtained using the fs laser have the same spectral features, which demonstrates the reproducibil-ity within a single type of measurement and which is a good basis with which to compare results for different measure-ment conditions. Qualitative differences between fs- and ns-laser spectra vary depending on particle type. Larger clusters (C_nH_m clusters with $n > 7$ for PSL particles, or higher or-der SiO_2 clusters) were observed in the higher power density fs-laser spectra. Such larger clusters in the fs-laser spectra

can potentially form during the Coulomb or phase explosion of the fs-laser ablation process. Some studies claim that also reactions of the primary ion species with the source plume may generate the larger clusters (Zaidi et al., 2010). How-ever, these complex processes of fs-laser ionization are be-yond the scope of this paper but require further study. We find that these large clusters in fs-laser spectra do not neces-sarily improve the quantitative abilities of SPMS. For NaCl particles, only in fs-laser spectra were high ionization energy species like Cl^+ or N^+ detected. Fs-laser ablation also led to the formation of oxides, e.g. core-shell particles, silica par-ticles, and silver oxides, for the gold–silver core-shell parti-cles.

Apart from differences in the ionization process, laser wavelength and particle optical properties also play an im-portant role in SPMS, especially for core-shell particles or inhomogeneously mixed particles. However, for fs-laser ab-lation it seems that the rapid plasma formation on the sur-face, e.g. of the core-shell particles, prevents a deeper im-pact and hence ablation and ionization of core material at least for shell thicknesses of 150 nm. The mass spectra avail-able from the fs laser with 266 nm and an energy of 0.2 mJ have shown very similar spectra to the fs laser operating with 800 nm and 0.3 mJ. Despite the relatively small number of usable spectra for 266 nm, we consider it very likely that high power densities and hence multi-photon ionization tak-ing place for both wavelengths lead to the formation of sim-ilar ions, which points to similar ion formation mechanisms. However, a more detailed discussion of possible ion forma-tion mechanisms is not possible based on the data available.

Generally, fs-laser-generated mass spectra show higher to-tal ion intensities compared to those from the ns laser by a

www.atmos-meas-tech.net/11/4345/2018/
Atmos. Meas. Tech., 11, 4345–4360, 2018

193

4358

factor of 1 to 5. Variation in power density does not have a large impact on mass spectral patterns for both laser types but influences ion signal intensity. The average ion signal intensity is increased by a factor of 2–5 with an increase in laser power density of at least 1 order of magnitude for both laser modes. Ion signal intensity also shows a (albeit non-linear) dependency on particle size, as tested for PSL particles with diameters of 500 and 1000 nm. This non-linearity would warrant further investigation for these instruments to improve their quantitative abilities. The smaller impact of particle size on ion signal intensity for the fs laser compared to the ns-laser system observed here indicates that fs lasers might not be the most effective way of improving SPMS quantification. High-energy ($\sim 100\,\mathrm{mJ}$) nanosecond lasers may be a better choice than high power density fs lasers due to the operational ease and cost.

The idea that the higher power density that can be achieved with fs-laser pulses leads to a more complete particle ablation and ionization could not be substantiated in this study. However, the cluster formation nature of fs-laser ablation rewards more studies with aerosol particles to understand and correlate the results for potential improvements in quantification and mixing state analysis. Further tests including, for example, two-step ionization or delayed extraction are needed to investigate potential advantages of fs- over ns-laser ablation in atmospheric SPMS.

The Supplement related to this article is available online at https://doi.org/10.5194/amt-11-4345-2018-supplement.

Author contributions. RR set up the experiment, did the measurements, analysed the data and wrote the manuscript. AA operated the femtosecond laser system and did the optical coupling. XS helped with the set-up. HS, TL, and CM developed the scientific approach, and supported the experimental procedures and data analysis. RR, HS, and CM developed the manuscript. All co-authors participated in scientific discussions on the interpretation of the results.

Edited by: Francis Pope
Reviewed by: Cristian Focsa and two anonymous referees

References

Amoruso, S., Bruzzese, R., Spinelli, N., and Velotta, R.: Characterization of laser-ablation plasmas, J. Phys. B-At. Mol. Opt., 32, R131, https://doi.org/10.1088/0953-4075/32/14/201, 1999.

Bhave, P. V., Allen, J. O., Morrical, B. D., Fergenson, D. P., Cass, G. R., and Prather, K. A.: A Field-Based Approach for Determining ATOFMS Instrument Sensitivities to Ammonium and Nitrate, Environ. Sci. Technol., 36, 4868–4879, 2001.

Brands, M., Kamphus, M., Böttger, T., Schneider, J., Drewnick, F., Roth, A., Curtius, J., Voigt, C., Borbon, A., Beekmann, M., Bourdon, A., Perrin, T., and Borrmann, S.: Characterization of a Newly Developed Aircraft-Based Laser Ablation Aerosol Mass Spectrometer (ALABAMA) and First Field Deployment in Urban Pollution Plumes over Paris During MEGAPOLI 2009, Aerosol Sci. Tech., 45, 46–64, 2011.

Bulgakov, A. V., Ozerov, I., and Marine, W.: Silicon clusters produced by femtosecond laser ablation: non-thermal emission and gas-phase condensation, Appl. Phys. A, 79, 1591–1594, 2004.

Cabalo, J., Zelenyuk, A., Baer, T., and Miller, R. E.: Two-Color Laser Induced Evaporation Dynamics of Liquid Aerosols Probed by Time-of-Flight Mass Spectrometry, Aerosol Sci. Tech., 33, 3-19, 2000.

Cahill, J. F., Fei, H., Cohen, S. M., and Prather, K. A.: Characterization of core-shell MOF particles by depth profiling experiments using on-line single particle mass spectrometry, Analyst, 140, 1510–1515, 2015.

Charles, K.: Chemistry and Composition of Atmospheric Aerosol Particles, Annu. Rev. Phys. Chem., 63, 471–491, 2012.

Chichkov, B. N., Momma, C., Nolte, S., von Alvensleben, F., and Tünnermann, A.: Femtosecond, picosecond and nanosecond laser ablation of solids, Appl. Phys. A, 63, 109–115, 1996.

Dunlap, B. I. and Doyle, R. J.: Ammonium Nitrate Cluster Ions, J. Phys. Chem., 100, 5281–5285, 1996.

Fergenson, D. P., Song, X.-H., Ramadan, Z., Allen, J. O., Hughes, L. S., Cass, G. R., Hopke, P. K., and Prather, K. A.: Quantification of ATOFMS Data by Multivariate Methods, Anal. Chem., 73, 3535–3541, 2001.

Fuzzi, S., Baltensperger, U., Carslaw, K., Decesari, S., Denier van der Gon, H., Facchini, M. C., Fowler, D., Koren, I., Langford, B., Lohmann, U., Nemitz, E., Pandis, S., Riipinen, I., Rudich, Y., Schaap, M., Slowik, J. G., Spracklen, D. V., Vignati, E., Wild, M., Williams, M., and Gilardoni, S.: Particulate matter, air quality and climate: lessons learned and future needs, Atmos. Chem. Phys., 15, 8217–8299, https://doi.org/10.5194/acp-15-8217-2015, 2015.

194

Gaie-Levrel, F., Perrier, S., Perraudin, E., Stoll, C., Grand, N., and Schwell, M.: Development and characterization of a single particle laser ablation mass spectrometer (SPLAM) for organic aerosol studies, Atmos. Meas. Tech., 5, 225–241, https://doi.org/10.5194/amt-5-225-2012, 2012.

Gallavardin, S. J., Froyd, K. D., Lohmann, U., Moehler, O., Murphy, D. M., and Cziczo, D. J.: Single Particle Laser Mass Spectrometry Applied to Differential Ice Nucleation Experiments at the AIDA Chamber, Aerosol Sci. Tech., 42, 773–791, 2008.

Gattass, R. R. and Mazur, E.: Femtosecond laser micromachining in transparent materials, Nat. Photon., 2, 219–225, 2008.

Ge, Z., Wexler, A. S., and Johnston, M. V.: Multicomponent Aerosol Crystallization, J. Colloid Interf. Sci., 183, 68–77, 1996.

Gemayel, R., Hellebust, S., Temime-Roussel, B., Hayeck, N., Van Elteren, J. T., Wortham, H., and Gligorovski, S.: The performance and the characterization of laser ablation aerosol particle time-of-flight mass spectrometry (LAAP-ToF-MS), Atmos. Meas. Tech., 9, 1947–1959, https://doi.org/10.5194/amt-9-1947-2016, 2016.

Gross, D. S., Barron, A. R., Sukovich, E. M., Warren, B. S., Jarvis, J. C., Suess, D. T., and Prather, K. A.: Stability of single particle tracers for differentiating between heavy- and light-duty vehicle emissions, Atmos. Environ., 39, 2889–2901, 2005.

Hada, M., Zhang, D., Pichugin, K., Hirscht, J., Kochman, M. A., Hayes, S. A., Manz, S., Gengler, R. Y. N., Wann, D. A., Seki, T., Moriena, G., Morrison, C. A., Matsuo, J., Sciaini, G., and Miller, R. J. D.: Cold ablation driven by localized forces in alkali halides, Nat. Comm., 5, 3863, https://doi.org/10.1038/ncomms4863, 2014.

Harilal, S. S., Freeman, J. R., Diwakar, P. K., and Hassanein, A.: Femtosecond Laser Ablation: Fundamentals and Applications, in: Laser-Induced Breakdown Spectroscopy: Theory and Applications, edited by: Musazzi, S. and Perini, U., Springer Berlin Heidelberg, Berlin, Heidelberg, 2014.

Healy, R. M., Sciare, J., Poulain, L., Crippa, M., Wiedensohler, A., Prévôt, A. S. H., Baltensperger, U., Sarda-Estève, R., McGuire, M. L., Jeong, C.-H., McGillicuddy, E., O'Connor, I. P., Sodeau, J. R., Evans, G. J., and Wenger, J. C.: Quantitative determination of carbonaceous particle mixing state in Paris using single-particle mass spectrometer and aerosol mass spectrometer measurements, Atmos. Chem. Phys., 13, 9479–9496, https://doi.org/10.5194/acp-13-9479-2013, 2013.

Henyk, M., Wolfframm, D., and Reif, J.: Ultra short laser pulse induced charged particle emission from wide bandgap crystals, Appl. Surf. Sci., 168, 263–266, 2000a.

Henyk, M., Wolfframm, D., and Reif, J.: Ultrafast laser desorption from transparent insulators, Nucl. Instrum. Meth. B, 166–167, 716–721, 2000b.

IPCC: Climate change 2007: The physical science basis, Cambridge University Press, New York, NY, 2007.

Jacobson, M. Z.: Fundamentals of Atmospheric Modeling, Cambridge University Press, Cambridge, 2005.

John, S.: Atmospheric Chemistry and Physics: From Air Pollution to Climate Change, Wiley, 1152 pp., 2016.

Johnston, M. V.: Sampling and analysis of individual particles by aerosol mass spectrometry, J. Mass Spectrom., 35, 585–595, 2000.

Kah, P., Rajan, R., Martikainen, J., and Suoranta, R.: Investigation of weld defects in friction-stir welding and fusion welding of aluminium alloys, Int. J. Mech. Mater. Des., 10, 26, https://doi.org/10.1186/s40712-015-0053-8, 2015.

Kato, T., Kobayashi, T., Matsuo, Y., Kurata-Nishimura, M., Oyama, R., Matsumura, Y., Yamamoto, H., Kawai, J., and Hayashizaki, Y.: Comparison between femtosecond and nanosecond laser ablation of solution samples applied on a substrate, J. Phys. Conf. Ser., 59, 372, https://doi.org/10.1088/1742-6596/59/1/078, 2007.

Kulkarni, P., Baron, P. A., and Willeke, K.: Introduction to Aerosol Characterization, in: Aerosol Measurement, John Wiley & Sons, Inc., 2011.

Laskin, J., Laskin, A., and Nizkorodov, S. A.: Mass Spectrometry Analysis in Atmospheric Chemistry, Anal. Chem., 90, 166–189, 2018.

Lee, D., Park, K., and Zachariah, M. R.: Determination of the Size Distribution of Polydisperse Nanoparticles with Single-Particle Mass Spectrometry: The Role of Ion Kinetic Energy, Aerosol Sci. Tech., 39, 162–169, 2005.

Leitz, K.-H., Redlingshöfer, B., Reg, Y., Otto, A., and Schmidt, M.: Metal Ablation with Short and Ultrashort Laser Pulses, Physics Proc., 12, 230–238, 2011.

L'Huillier, A., Jönsson, L., and Wendin, G.: Multiphoton ionization of many-electron atoms, Int. J. Quantum Chem., 31, 833–840, 1987.

Mahadevan, R., Lee, D., Sakurai, H., and Zachariah, M. R.: Measurement of Condensed-Phase Reaction Kinetics in the Aerosol Phase Using Single Particle Mass Spectrometry, J. Phys. Chem. A, 106, 11083–11092, 2002.

Malvezzi, A. M.: Laser–Matter Interaction in LIBS Experiments, in: Laser-Induced Breakdown Spectroscopy: Theory and Applications, edited by: Musazzi, S. and Perini, U., Springer Berlin Heidelberg, Berlin, Heidelberg, 2014.

Manca, L., Boštjan, J., Danilo, S., and Rok, K.: In situ synthesis of Ag nanoparticles in polyelectrolyte multilayers, Nanotechnology, 18, 325601, https://doi.org/10.1088/0957-4484/18/32/325601, 2007.

Marine, W., Scotto d'Aniello, J. M., and Gerri, M.: Velocity measurement of the ablated particles during picosecond laser ablation, Mater. Sci. Eng. B-Adv., 13, 57–62, 1992.

Marsden, N., Flynn, M. J., Taylor, J. W., Allan, J. D., and Coe, H.: Evaluating the influence of laser wavelength and detection stage geometry on optical detection efficiency in a single-particle mass spectrometer, Atmos. Meas. Tech., 9, 6051–6068, https://doi.org/10.5194/amt-9-6051-2016, 2016.

Morrical, B. D., Fergenson, D. P., and Prather, K. A.: Coupling two-step laser desorption/ ionization with aerosol time-of-flight mass spectrometry for the analysis of individual organic particles, J. Am. Soc. Mass Spectr., 9, 1068–1073, 1998.

Murphy, D. M.: The design of single particle laser mass spectrometers, Mass Spectrom. Rev., 26, 150–165, 2007.

Murphy, D. M. and Thomson, D. S.: Laser Ionization Mass Spectroscopy of Single Aerosol Particles, Aerosol Sci. Tech., 22, 237–249, 1995.

Murphy, D. M., Cziczo, D. J., Froyd, K. D., Hudson, P. K., Matthew, B. M., Middlebrook, A. M., Peltier, R. E., Sullivan, A., Thomson, D. S., and Weber, R. J.: Single-particle mass spectrometry of tropospheric aerosol particles, J. Geophys. Res.-Atmos., 111, D23S32, https://doi.org/10.1029/2006JD007340, 2006.

195

Neubauer, K. R., Johnston, M. V., and Wexler, A. S.: Humidity effects on the mass spectra of single aerosol particles, Atmos. Environ., 32, 2521–2529, 1998.

Passig, J., Schade, J., Oster, M., Fuchs, M., Ehlert, S., Jäger, C., Sklorz, M., and Zimmermann, R.: Aerosol Mass Spectrometer for Simultaneous Detection of Polyaromatic Hydrocarbons and Inorganic Components from Individual Particles, Anal. Chem., 89, 6341–6345, 2017.

Pereira, S. O., Trindade, T., and Barros-Timmons, A.: Biotinylation of optically responsive gold/polyelectrolyte nanostructures, Gold Bull., 48, 3–11, 2015.

Pratt, K. A., Mayer, J. E., Holecek, J. C., Moffet, R. C., Sanchez, R. O., Rebotier, T. P., Furutani, H., Gonin, M., Fuhrer, K., Su, Y., Guazzotti, S., and Prather, K. A.: Development and Characterization of an Aircraft Aerosol Time-of-Flight Mass Spectrometer, Anal. Chem., 81, 1792–1800, 2009.

Pratt, K. A. and Prather, K. A.: Mass spectrometry of atmospheric aerosols – Recent developments and applications, Part II: On-line mass spectrometry techniques, Mass Spectrom. Rev., 31, 17–48, 2012.

Reents, W. D. J., Downey, S. W., Emerson, A. B., Mujsce, A. M., Muller, A. J., Siconolfi, D. J., Sinclair, J. D., and Swanson, A. G.: Real-time compositional analysis of submicrometre particles, Plasma Sources Sci. T., 3, 369, https://doi.org/10.1088/0963-0252/3/3/020, 1994.

Reif, J., Costache, F., Eckert, S., and Henyk, M.: Mechanisms of ultra-short laser pulse ablation from ionic crystals, Appl. Phys. A, 79, 1229–1231, 2004.

Reilly, P. T. A., Lazar, A. C., Gieray, R. A., Whitten, W. B., and Ramsey, J. M.: The Elucidation of Charge-Transfer-Induced Matrix Effects in Environmental Aerosols Via Real-Time Aerosol Mass Spectral Analysis of Individual Airborne Particles, Aerosol Sci. Tech., 33, 135–152, 2000.

Reinard, M. S. and Johnston, M. V.: Ion Formation Mechanism in Laser Desorption Ionization of Individual Nanoparticles, J. Am. Soc. Mass Spectr., 19, 389–399, 2008.

Richard, E. R., Xianglei, M., Jhanis, J. G., and Jong-Hyun, Y.: Femtosecond vs. nanosecond laser pulse duration for laser ablation chemical analysis, Spectroscopy, 28, available at: http://www.spectroscopyonline.com/femtosecond-vs-nanosecond-laser-pulse-duration-laser-ablation-chemical-analysis (last access: 27 June 2018), 2013.

Roeterdink, W. G., Juurlink, L. B. F., Vaughan, O. P. H., Diez, J. D., Bonn, M., and Kleyn, A. W.: Coulomb explosion in femtosecond laser ablation of Si(111), Appl. Phys. Lett., 82, 4190–4192, 2003.

Sansonetti, J. E. and Martin, W. C.: Handbook of Basic Atomic Spectroscopic Data, J. Phys. Chem. Ref. Data, 34, 1559–2259, 2005.

Schoolcraft, T. A., Constable, G. S., Jackson, B., Zhigilei, L. V., and Garrison, B. J.: Molecular dynamics simulations of laser disintegration of amorphous aerosol particles with spatially nonuniform absorption, Nucl. Instrum. Meth. B, 180, 245–250, 2001.

Schoolcraft, T. A., Constable, G. S., Zhigilei, L. V., and Garrison, B. J.: Molecular Dynamics Simulation of the Laser Disintegration of Aerosol Particles, Anal. Chem., 72, 5143–5150, 2000.

Shen, X., Ramisetty, R., Mohr, C., Huang, W., Leisner, T., and Saathoff, H.: Laser ablation aerosol particle time-of-flight mass spectrometer (LAAPTOF): performance, reference spectra and classification of atmospheric samples, Atmos. Meas. Tech., 11, 2325–2343, https://doi.org/10.5194/amt-11-2325-2018, 2018.

Smith, G. D., Woods, E., DeForest, C. L., Baer, T., and Miller, R. E.: Reactive Uptake of Ozone by Oleic Acid Aerosol Particles: Application of Single-Particle Mass Spectrometry to Heterogeneous Reaction Kinetics, J. Phys. Chem. A, 106, 8085–8095, 2002.

Tsuji, T., Kakita, T., and Tsuji, M.: Preparation of nano-size particles of silver with femtosecond laser ablation in water, Appl. Surf. Sci., 206, 314–320, 2003.

Walsh, J. T. and Deutsch, T. F.: Measurement of Er:YAG laser ablation plume dynamics, Appl. Phys. B, 52, 217–224, 1991.

Weiss, M., Verheijen, P. J. T., Marijnissen, J. C. M., and Scarlett, B.: On the performance of an on-line time-of-flight mass spectrometer for aerosols, J. Aerosol Sci., 28, 159–171, 1997.

Whiteaker, J. R. and Prather, K. A.: Detection of Pesticide Residues on Individual Particles, Anal. Chem., 75, 49–56, 2003.

Woods, E., Smith, G. D., Miller, R. E., and Baer, T.: Depth Profiling of Heterogeneously Mixed Aerosol Particles Using Single-Particle Mass Spectrometry, Anal. Chem., 74, 1642–1649, 2002.

Xu, C., Long, Y., Qian, S., and Li, Y.: The generation mechanism of silicon oxide–aluminum oxide compound clusters by laser ablation of siliceous materials, Micropor. Mesopor. Mat., 39, 351–358, 2000.

Zaidi, A. A., Hu, A., Wesolowski, M. J., Fu, X., Sanderson, J. H., Zhou, Y., and Duley, W. W.: Time of flight mass spectrometry of polyyne formation in the irradiation of liquid alkanes with femtosecond laser pulses, Carbon, 48, 2517–2520, 2010.

Zaidi, A. A., Alkhesho, I., Karimi, R., Sanderson, J. H., and Duley, W. W.: Femtosecond laser ablation of solid methane, Int. J. Mass Spectrom., 376, 32–34, 2015.

Zawadowicz, M. A., Abdelmonem, A., Mohr, C., Saathoff, H., Froyd, K. D., Murphy, D. M., Leisner, T., and Cziczo, D. J.: Single-Particle Time-of-Flight Mass Spectrometry Utilizing a Femtosecond Desorption and Ionization Laser, Anal. Chem., 87, 12221–12229, 2015.

Zelenyuk, A. and Imre, D.: Single Particle Laser Ablation Time-of-Flight Mass Spectrometer: An Introduction to SPLAT, Aerosol Sci. Tech., 39, 554–568, 2005.

Zelenyuk, A., Yang, J., Choi, E., and Imre, D.: SPLAT II: An Aircraft Compatible, Ultra-Sensitive, High Precision Instrument for In-Situ Characterization of the Size and Composition of Fine and Ultrafine Particles, Aerosol Sci. Tech., 43, 411–424, 2009.

Zelenyuk, A., Imre, D., Earle, M., Easter, R., Korolev, A., Leaitch, R., Liu, P., Macdonald, A. M., Ovchinnikov, M., and Strapp, W.: In Situ Characterization of Cloud Condensation Nuclei, Interstitial, and Background Particles Using the Single Particle Mass Spectrometer, SPLAT II, Anal. Chem., 82, 7943–7951, 2010.

Zhou, L., Park, K., Milchberg, H. M., and Zachariah, M. R.: Understanding the Interaction of an Intense Laser Pulse with Nanoparticles: Application to the Quantification of Single Particle Mass Spectrometry, Aerosol Sci. Tech., 41, 818–827, 2007.

Appendix C.2 Chemical characterization of highly functionalized organonitrates contributing to high night-time organic aerosol mass loadings and particle growth

Chemical Characterization of Highly Functionalized Organonitrates Contributing to Night-Time Organic Aerosol Mass Loadings and Particle Growth

Wei Huang,[†,‡] Harald Saathoff,[†] Xiaoli Shen,[†,‡] Ramakrishna Ramisetty,[†,○] Thomas Leisner,[†,§] and Claudia Mohr[*,‖]

[†]Institute of Meteorology and Climate Research, Karlsruhe Institute of Technology, Eggenstein-Leopoldshafen, 76344, Germany

[‡]Institute of Geography and Geoecology, Working Group for Environmental Mineralogy and Environmental System Analysis, Karlsruhe Institute of Technology, Karlsruhe, 76131, Germany

[§]Institute of Environmental Physics, Heidelberg University, Heidelberg, 69120, Germany

[‖]Department of Environmental Science and Analytical Chemistry, Stockholm University, Stockholm, 11418, Sweden

S *Supporting Information*

ABSTRACT: Reactions of volatile organic compounds (VOC) with NO_3 radicals and of reactive intermediates of oxidized VOC with NO_x can lead to the formation of highly functionalized organonitrates (ON). We present quantitative and chemical information on ON contributing to high night-time organic aerosol (OA) mass concentrations measured during July−August 2016 in a rural area in southwest Germany. A filter inlet for gases and aerosols coupled to a high-resolution time-of-flight chemical ionization mass spectrometer (FIGAERO-HR-ToF-CIMS) was used to analyze the molecular composition of ON in both the gas and particle phase. We find larger contributions of ON to OA mass during the night. Identified ON are highly functionalized, with 4 to 12 oxygen atoms. The diel patterns of ON compounds with 5, 7, 10, or 15 carbon atoms per molecule vary, indicating a corresponding behavior of their potential precursor VOC. The temporal behavior of ON after sunset correlates with that of the number concentration of ultrafine particles, indicating a potential role of ON in night-time new particle formation (NPF) regularly observed at this location. We estimate an ON contribution of 18−25% to the mass increase of newly formed particles after sunset. Our study provides insights into the chemical composition of highly functionalized ON in the rural atmosphere and the role of anthropogenic emissions for night-time SOA formation in an area where biogenic VOC emissions dominate.

1. INTRODUCTION

Organic aerosols (OA) are ubiquitous in the Earth's atmosphere and have significant impacts on climate,[1] visibility,[2] and health.[3,4] They can be of anthropogenic and/or biogenic origin. OA are either directly emitted into the atmosphere (primary organic aerosol, POA) or formed by gas-phase oxidation of volatile organic compounds (VOC) with hydroxyl radicals (OH), ozone (O_3), or nitrate radicals (NO_3), the products of which can partition into the particle phase either by contributing to forming new particles or by adding mass to pre-existing particles (secondary organic aerosol, SOA).[5−11] OH radicals are the dominant oxidant during the day in the troposphere, while NO_3 radicals are one of the main oxidants during the night in addition to O_3.[12] Ground-level observations have indicated that new particle formation (NPF, the process of atmospheric nucleation and ultrafine particle growth from subnanometers to larger sizes (tens of nanometers)) during the night may be related to organics formed via

biogenic VOC (BVOC, e.g., monoterpenes) oxidation by O_3 or NO_3 radicals in the absence of UV and OH or by OH radicals resulting from ozonolysis of BVOC.[13,14]

NO_3 radicals are formed by reaction of nitrogen oxides (NO_x, including NO and NO_2), predominantly emitted by high temperature combustion processes, with O_3.[12,15] The oxidation of BVOC (e.g., monoterpenes, isoprene) by NO_3 radicals during the night can lead to significant formation of SOA mass[16−18] and therefore "converts" biogenic emissions into an anthropogenic source of SOA. Reported SOA yields from the reaction of different BVOC with NO_3 radicals range from close to 0 (α-pinene) to up to 86% (β-caryophyllene).[19−21] The type of BVOC being oxidized by NO_3 radicals

Single Particle Characterisation of Atmospheric Aerosol Particles in Central Europe
Appendix C

also influences the resulting SOA compounds' behavior during photochemical aging, with α-pinene SOA exhibiting more photolabile properties than β-pinene SOA.[22]

In addition to forming NO$_3$ radicals, NO$_x$ can significantly alter SOA chemistry and influence SOA particle formation, composition, and properties during VOC oxidation.[15,23−25] SOA yields for α-pinene decrease as NO$_x$ levels increase, while SOA yields for isoprene increase at low NO$_x$ conditions and decrease at high NO$_x$ conditions.[26,27] SOA yields for sesquiterpenes (longifolene and aromadendrene) are substantially higher under high NO$_x$ conditions.[24] SOA particles also have lower vapor pressures when formed at high NO$_x$ compared to those formed at low NO$_x$ conditions.[23]

Reactions of VOC with NO$_3$ radicals during the night can lead to the formation of alkyl nitrates and multifunctional nitrates (RONO$_2$), while during the day organic peroxy radicals (RO$_2$) can react with NO or NO$_2$ to form RONO$_2$ or peroxy nitrates (RO$_2$NO$_2$).[28,29] Organonitrates (ON, including RONO$_2$ and RO$_2$NO$_2$) are therefore an important reservoir or sink (temporary or permanent) of NO$_x$, depending on the precursor VOC.[22] RO$_2$NO$_2$ are mostly thermally unstable or photolabile and can decompose back to NO$_x$.[28,30,31] It has been shown across different sites in Europe that ON are an important fraction of the total organic aerosol particle mass measured by aerosol mass spectrometers (AMS).[12] Specified ON measurements showed higher contributions during the night (4−8%) and lower contributions during the day (2−4%).[15,32] A large fraction of the particulate ON is highly functionalized, with dominant contributions from ON possessing 6 to 8 oxygen atoms.[22,32,33] The highly functionalized ON are of low volatility, since the addition of different functional groups including the nitrate group (ONO$_2$) to a hydrocarbon is estimated to lower its saturation vapor pressure by orders of magnitude.[34] ON are thus likely to partition into the particle phase and contribute to SOA particle formation.[24,32] Non-negative matrix factorization (NNMF) and positive matrix factorization (PMF) have been used to separate ON with different diel behaviors (higher contributions during the night, or during the day or early morning hours), indicative of NO$_3$ radical initiated or NO$_x$-driven chemistry.[33,35] Despite this, a coherent understanding of interactions between anthropogenic and biogenic emissions and the role of highly functionalized ON in the atmosphere is still needed.

In this paper, we present organic aerosol concentrations and chemical composition measured during July and August 2016 at a rural site in the upper Rhine Valley in southwest Germany. We investigate the molecular composition of ambient ON contributing to high organic aerosol mass loadings during the night and discuss the relationship between these ON and different precursor VOC as well as their potential role in night-time SOA formation and particle growth.

2. METHODS

2.1. Measurement Site. We performed particle and trace gas measurements from July 8 to September 1, 2016 at a rural area in southwest Germany (49°6′10.54″N, 8°24′26.07″E), located ~12 km north of the city of Karlsruhe with more than 300000 inhabitants. The area lies in the upper Rhine Valley, a region with inhomogeneous land use for industry, agriculture, settlements, and some forests. The measurement site was set up in a field next to a rural road and tramway tracks. At a 200 m distance in the south, there was a sunflower (*Helianthus annuus* L. cv. Giganteus) field (~15 km^2), which can

contribute to sesquiterpene emissions.[36] The Hardtwald forest is ~1 km to the east and the Bienwald forest is ~15 km southwest of the measurement site. Both forests are composed of mainly pine trees. About 40 km away is the Black Forest, a large forested area with mostly pine and oak trees of ~6000 km^2. These forests can contribute to significant amounts of BVOC emissions from monoterpenes,[37] sesquiterpenes,[36] and also isoprene.[38] There are several industrial emission sources southwest of the measurement site, including refineries with 15.5 Mt/year capacity and a 550 MW hard coal fired power plant.[39] High particle number concentrations were found in this rural location during previous measurements on a tram.[39]

2.2. Meteorological Parameters, Particle, and Trace Gas Measurements. All instruments were set up in a temperature-controlled measurement container kept at ~298 K. All sampling inlets were located 3.7 m above ground level and 1.5 m above the container roof. An overview on instruments and parameters measured is given in Table S1 in the Supporting Information.

Temperature, relative humidity (RH), wind direction, wind speed, global radiation, pressure, and precipitation data of this site were measured by a meteorological sensor (WS700, Lufft Inc.; see Table S1). As the winds were channeled by the Rhine Valley,[40] the main wind directions during the campaign were southwest and northeast.

Trace gases (O$_3$, CO$_2$, NO, NO$_2$, SO$_2$) were measured with the corresponding sensors (Table S1). Particle number concentrations were recorded with two condensation particle counters (CPC3022, measuring particles with mobility diameters larger than 7 nm; CPC3776, measuring particles with mobility diameters larger than 2.5 nm, TSI Inc.). Particle size distributions were measured with a scanning mobility particle sizer (SMPS, differential mobility analyzer 3071 connected to a CPC 3776 measuring particles with mobility diameters between 10 and 670 nm, TSI Inc.) and an optical particle counter (OPC FIDAS200, measuring particles with optical diameters between 180 nm and 18 μm, Palas Inc.).

A high-resolution time-of-flight aerosol mass spectrometer (HR-ToF-AMS, Aerodyne Research Inc., hereafter AMS) equipped with a high-pressure lens[41] was deployed to continuously measure total nonrefractory particle mass as a function of size (up to 2.5 μm particle aerodynamic diameter d_{va}) at a time resolution of 0.5 min. The AMS inlet was connected to a PM$_{2.5}$ head (flow rate 1 m^3 h^{-1}) and a stainless steel tube of 3.45 m length (flow rate 0.1 L min^{-1}, residence time 0.9 s). AMS data were analyzed by the AMS data analysis software package SQUIRREL (version 1.60C) and PIKA (version 1.20C). An AMS composition-dependent collection efficiency (CDCE) was used for this data.[42] Individual organic compounds in both the gas and particle phase were measured with a filter inlet for gases and aerosols coupled to a high-resolution time-of-flight chemical ionization mass spectrometer (FIGAERO-HR-ToF-CIMS, Aerodyne Research Inc., hereafter CIMS) deploying iodide (I$^-$) as the reagent ion.[43,44] During the gas-phase measurement, gases were sampled via a fluorinated ethylene propylene (FEP) tube of 3.46 m length (flow rate 8 L min^{-1}, residence time 0.7 s). At the same time, particles were collected on a Teflon (Polytetrafluoroethylene, PTFE) filter via a separate sampling port connected to a PM$_{10}$ head (flow rate 1 m^3 h^{-1}) and a stainless steel tube of 2.65 m length (flow rate 8.6 L min^{-1}, residence time 1.2 s). At regular intervals (30−60 min), the gas-phase measurement was switched off and particles on the filter were desorbed by a

199

Single Particle Characterisation of Atmospheric Aerosol Particles in Central Europe
Appendix C

flow of ultrahigh-purity (UHP, 99.999%) nitrogen heated from room temperature to 200 °C over the course of 35 min. Integration of the signal evolution of an individual compound during desorption yields its total signal in counts per deposition, which was then converted to mass concentration using a sensitivity of 22 counts s^{-1} ppt^{-1} (reported collisional limit).[33,45,46] The sensitivity at collisional limit in our instrument may slightly vary from the reported value due to small differences in voltage settings of the respective mass spectrometers. Comparison of formic acid calibrations between the two instruments show a lower sensitivity in our instrument, indicating also a potentially lower sensitivity at the collisional limit. We therefore emphasize that our mass concentrations based on CIMS data represent a lower limit. The influence of RH on sensitivity is expected to be negligible for both particle phase (particles are desorbed in UHP N_2 and thus always at dry conditions) and gas phase. In gas phase, calculated water vapor pressures in the ion−molecule reaction (IMR) region fall into a range where sensitivity dependencies are weak.[44] Sensitivity uncertainties were taken into account in the calculation of the overall uncertainties of CIMS concentrations (±60%) following the approach by Thompson et al.[47] Gas phase backgrounds were determined by sampling zero air (high purity synthetic air). Particle phase backgrounds were assessed by putting an additional Teflon filter upstream of the particle phase sampling port during the deposition.[33]

3. RESULTS AND DISCUSSION

3.1. Diel Patterns of Organic Particle Mass and Trace Gases.
The average organic mass loading measured by AMS is 5.0 ± 3.3 μg m^{-3} (average ±1 standard deviation) at this site during the measurement period (Figure S1), comparable to other rural/urban sites in Europe (0.9−8.2 μg m^{-3}).[48] Organic aerosol (OA) is the dominant component and makes up 58.3% of total nonrefractory $PM_{2.5}$ mass measured by AMS (Figure S1a).

The average diel pattern of OA for this period reveals higher OA mass loadings during the night (00:00−06:00, 5.8 ± 1.6 μg m^{-3}) compared to day (12:00−17:00, 4.6 ± 1.3 μg m^{-3}; Figure 1a, S1b). Data in Figure 1a were normalized to total $PM_{2.5}$ measured by AMS to remove the effect of changes in boundary layer height. The shape of the OA diel evolution thus indicates night-time chemistry contributing to OA formation. High night-time OA mass loadings have also been observed at other European locations and US sites.[15,25,49,50] It is suggested that most night-time SOA formation is due to the oxidation of precursor VOC by NO_3 radicals, which are formed by reactions of O_3 with anthropogenic NO_x emissions.[15]

As generally observed,[15,35] NO_2 concentrations during this campaign also exhibit higher concentrations during the night compared to day (Figure 1b), with a peak after sunset (21:00−22:00) and another peak in the early morning after sunrise (06:00−08:00). The late evening peak could be related to the accumulation of anthropogenic NO_2 from nearby emission sources, decreasing ozone concentrations (Figure 1b) and decreasing boundary layer height, so that more NO_3 radicals can be formed.[15,39,51] Besides increasing emissions, the morning peak of NO_2 may be due to rapid NO_2 formation after sunrise from the photolysis of NO_3 and decomposition of N_2O_5[51] and/or photochemical aging of photolabile ON.[22] The OA mass measured by AMS thus can have contributions from both NO_x-driven and NO_3 radical induced chemistry.
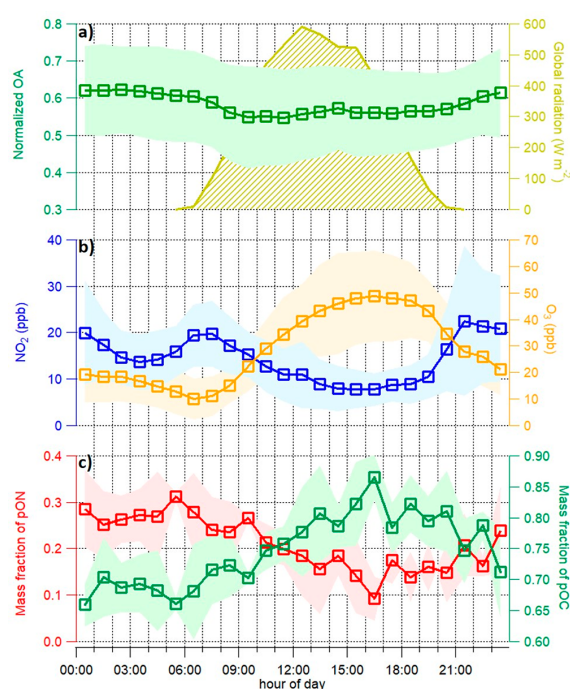
Figure 1. Mean diel patterns of (a) organic aerosol (OA) normalized to the total $PM_{2.5}$ measured by AMS and global radiation, (b) NO_2 and ozone, and (c) of the mass fraction of pON and pOC of total oxygenated hydrocarbons measured by CIMS. The shaded areas represent ±1 standard deviation.

The reaction of NO_2 with O_3 during the night leads to the formation of NO_3 radicals[15,51] which can oxidize VOC and form ON.[28,29] In order to characterize the OA compounds that contribute to the high night-time OA mass loadings measured by AMS, CIMS measurements were used to analyze the molecular composition of OA. The average organic particle size is below 1 μm (Figure S1c), which suggests a minor influence of particle size on total organics measured by AMS and CIMS. The total mass of oxygenated hydrocarbons measured by CIMS (OC-X, 2056 out of a total of 2567 identified compounds, with at least one C atom, one H atom, and one O atom ($C_{x\geq1}H_{y\geq1}O_{z\geq1}X_n$, detected as clustered with I^-)) account for about 31% of OA measured by AMS. Compounds not clustered with I^- (437 compounds) were excluded in this analysis, as their ionization mechanisms and thus sensitivity are highly uncertain. Using the same sensitivity as for the compounds detected as I^--clusters, they only account for 2−4% of particulate OC-X (pOC-X). The differences between CIMS and AMS measurements are likely due to the CIMS measuring only a subset of organics measured by AMS.[44,45,52] Besides, with the maximum sensitivity applied the CIMS concentrations represent a lower limit. Two classes of compounds make up >90% of the mass of OC-X both in gas and particle phase: pure oxygenated hydrocarbons (OC, 61.2−90.8%, 1352 compounds, $C_{x\geq1}H_{y\geq1}O_{z\geq1}$) and nitrogen-containing oxygenated hydrocarbons (ON, 3.6−35.7%, 509 compounds, $C_{x\geq1}H_{y\geq1}O_{z\geq4}N_1$). Oxygenated hydrocarbons with more than one nitrogen atom (e.g., organic dinitrates) were excluded in this analysis. This is in agreement with the study by Lee et al.[33] where dinitrates only represented

200

negligible mass fraction of the total mass measured by CIMS. In addition, their molecular identification is rather uncertain due to overlaps with more abundant non-nitrogen containing compounds.[33] We also determined the mass concentration of the organic bound nitrate fraction ($OrgNO_3$, i.e., organonitrates) from AMS data, assuming an NO_2^+/NO^+ ratio of $OrgNO_3$ of 0.1.[12,53] About 47% of the $OrgNO_3$ calculated in this way can be explained by the highly functionalized particulate ON (pON) measured by CIMS (see Figure S1d), similar to what Lee et al.[32] reported for the southeast US (58%).

Particulate OC (pOC) and pON measured by CIMS exhibit distinct diel patterns, with pOC dominating the particle composition during the day and night and pON accounting for significantly more mass during the night (Figure 1c). On average, pON accounts for 4.6% and 9.7% of total organic particle mass measured by AMS during the day (12:00−17:00) and during the night (00:00−06:00), respectively, consistent with previous studies.[15,32,49] In order to find out if the pON formed during the night originate from NO_3 radical chemistry[15] with different precursor VOC, we investigate the molecular composition of these ON in the next section.

3.2. Chemical Composition of Organonitrates. The average mass-weighted chemical compositions for pON and gaseous ON (gON) observed at our measurement site are $C_{11.4}H_{16.2}O_{8.1}N_1$ and $C_{8.3}H_{12.8}O_{6.5}N_1$, respectively (for comparison: pOC: $C_{9.1}H_{14.5}O_{6.7}$ and gaseous OC (gOC): $C_{7.4}H_{12.0}O_{5.5}$). ON are highly functionalized, containing up to 25 carbon atoms and 4 to 12 oxygen atoms. Figure S2a shows the relative contribution of individual ON to the total ON mass as a function of the number of carbon atoms in the gas and particle phase, respectively. For ON with up to 7 carbon atoms, the relative contributions in the gas phase are higher than those in the particle phase; for larger compounds, the relative contributions in the particle phase become higher. For both phases, C_9N and $C_{10}N$ compounds exhibit the highest contributions to total pON and gON (for comparison: C_xHO compounds are more widely distributed across carbon numbers and exhibit highest contributions of $C_{7−9}HO$ to total OC; see Figure S2b). In order to further investigate the potential relationships between these ON and anthropogenic and biogenic precursor VOC such as isoprene (C_5H_8), toluene (C_7H_8), monoterpenes ($C_{10}H_{16}$), and sesquiterpenes ($C_{15}H_{24}$), we selected the C_5N, C_7N, $C_{10}N$, and $C_{15}N$ compounds for further analysis. Together they contribute 41.0% to total pON and 42.4% to total gON. We stress here that assuming a relationship between the different precursor VOC and resulting ON based on carbon number is simplified, as fragmentation and/or accretion reactions[32] can lead to both negative and positive artifacts in assigned concentrations. Thermal decomposition in the FIGAERO[54] of the four particulate C_xN (pC_xN, x = 5, 7, 10, 15) groups can be neglected based on thermogram shapes (Figure S4).

The mass spectra of the four pC_xN groups are shown in Figure 2a in a similar plot as presented by Lee et al.[32] The mass spectral patterns of pON detected at this central European location are similar to those observed in southeastern US and in northern Europe,[32,33] implying similar chemistry and/or instrument sensitivity. The compounds of the $pC_{10}N$ group exhibit a bell-shaped distribution of the mass contribution of individual compounds to the total pON as a function of the number of oxygen atoms. The mass contributions of the pC_5N and pC_7N compounds drop faster after the maximum, and the
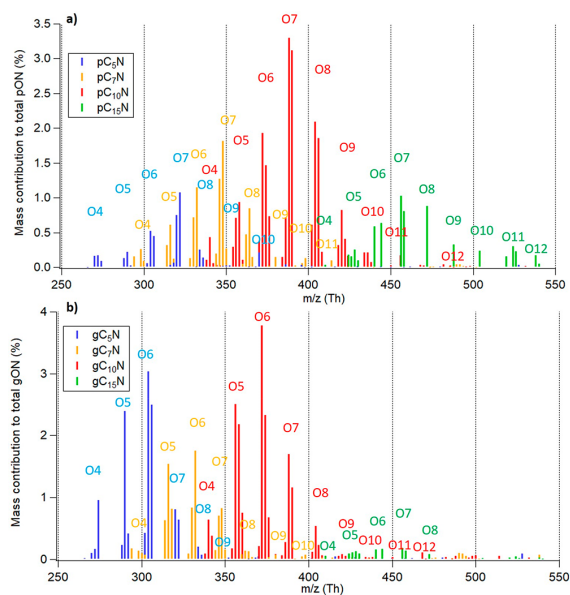
Figure 2. Mass contribution of the compounds of the C_xN (x = 5, 7, 10, 15) groups (a) in the particle phase to total pON and (b) in the gas phase to total gON as a function of m/z (includes mass of I^- ion; m/z 126.9050 Th). The shaded areas represent ±1 standard deviation.

$pC_{15}N$ compounds have a longer tail toward higher elemental oxygen-to-carbon (O:C) ratios, likely related to the length of the carbon backbone influencing the potential number of oxygen atoms that can be added to a molecule. The compounds of the $pC_{10}N$ group in general exhibit the largest contributions with up to 3% of the total pON mass, and significant mass contributions from compounds of the $pC_{15}N$ group are also observed. For all four pON groups, compounds with 6 to 8 oxygen atoms dominate the signal contributions; these pON groups, particularly the $pC_{10}N$ and $pC_{15}N$ groups, have non-negligible contributions from compounds with the number of oxygen atoms up to 10 or even 12, indicating multistep oxidation processes of precursor VOC emissions (e.g., autoxidation).[7] Similar patterns can be found in the mass spectra of the gaseous C_xN (gC_xN, x = 5, 7, 10, 15) compounds (Figure 2b), but here all gC_xN groups have a smaller number of oxygen atoms, with 5 to 7 oxygen atoms dominating the signal contributions. Generally, as expected,[55] the heavier compounds show a stronger tendency to partition into the particle phase (e.g., $C_{15}N$), while the lighter compounds (e.g., C_5N) favor the gas phase. We attribute the compounds in $C_{10}N$ and $C_{15}N$ groups mainly to be nitration products of mono- and sesquiterpenes, as there are important natural (e.g., pine trees in the Hardtwald forest, Bienwald forest, and Black Forest)[36,37] and agricultural (e.g., sunflower plantations)[36] sources of these compounds in the vicinity of the measurement site. Compounds in the C_5N group are assumed to be mainly formed from isoprene, which may originate from oak trees or legume farms present around the site.[38,56] The attribution of the C_7N compounds is more ambiguous, because they may be formed by oxidation of, e.g., toluene,[57] a major compound of anthropogenic emissions related to traffic or industrial activity,[58] but may also stem from the oxidation of monoterpenes, the products of which have

undergone fragmentation of the carbon backbone.[22,32,59] Due to the multitude of oxidation pathways and the resulting molecular compositions of compounds, it is difficult to distinguish the biogenic and anthropogenic contributions to the different C_xN groups, especially to C_7N.

The average diel patterns of the mass contributions of these pC_xN groups to total pON are shown in Figure 3a. The $pC_{10}N$
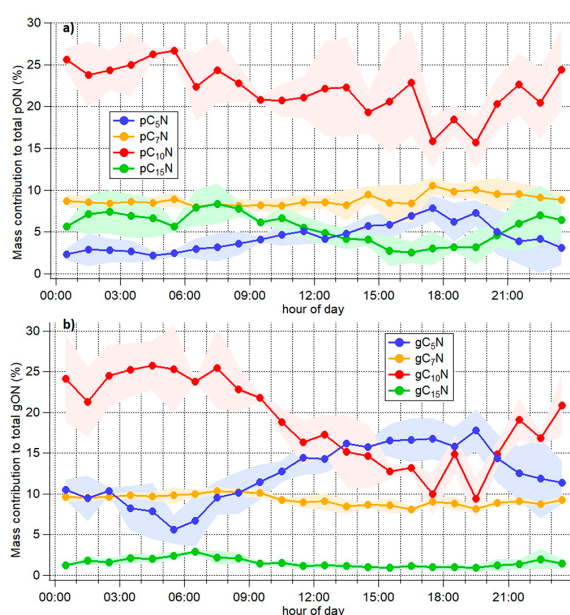
Figure 3. Mean diel patterns of the mass contribution of the C_xN (x = 5, 7, 10, 15) groups (a) in the particle phase to total pON and (b) in the gas phase to total gON. The shaded areas represent ±1 standard deviation.

and $pC_{15}N$ groups, which include compounds with larger molecular weight, account for more pON mass during the night than during the day. On average, the $pC_{10}N$ group accounts for 21.5 ± 2.4% of total pON during the day (12:00−17:00) and 25.3 ± 1.0% of total pON during the night (00:00−06:00). Due to the fact that the compounds of the $pC_{10}N$ group exhibit the largest signal, they also largely influence the diel pattern of the relative contributions of total pON to all compounds measured by CIMS (see Figure 1c). A total of 45 compounds of the $pC_{10}N$ group contribute 0.9% to OA measured by AMS (3.0 ± 1.4% to pOC-X by CIMS) during the day (12:00−17:00) and 2.5% to OA measured by AMS (7.1 ± 0.9% to pOC-X by CIMS) during the night (00:00−06:00), demonstrating the important role of $pC_{10}N$ compounds in night-time OA mass loadings (see Figure 1a). The pC_5N and pC_7N groups, which include compounds with smaller molecular weight, exhibit a distinct diel trend, with higher contributions during the day compared to the night. This may be due to the different diel behaviors of their precursor VOC emissions[32] and/or different oxidation processes favored during the day, e.g., OH radical induced oxidation of aromatic compounds in the presence of NO_x.

In the gas phase, similar to the average diel patterns in the particle phase, the $gC_{10}N$ and $gC_{15}N$ groups account for more mass of the total gON during the night and the gC_5N accounts for more mass during the day (Figure 3b). However, the gC_7N

group exhibits slightly higher contributions to total gON during the night, which is different from its diel behavior in the particle phase. The differences for the C_7N group in particle phase and gas phase may result from the different partitioning behaviors of oxidation products from monoterpenes[32,59] and from toluene with higher anthropogenic contributions during the day.[57,58] In general, the diel evolutions of the gC_xN groups exhibit a more distinct pattern compared to the pC_xN groups, potentially due to the relatively longer lifetimes of particulate compounds smearing out immediate (local) formation effects in time in the particle phase. The more distinct and structured diel patterns of the gC_xN groups may thus better reflect the corresponding precursor VOC emissions. The diel patterns of the mass contributions of the C_xHO (x = 5, 7, 10) groups to total OC all exhibit a peak during the day (Figure S3), indicative of different oxidation processes (e.g., O_3 and/or OH radical induced oxidation).

These results imply different partitioning behaviors of these C_xN groups as well as different oxidation processes of different precursor VOC (e.g., different terpenes, toluene, etc.) which can be induced by NO_3 during the night or by O_3 or OH in the presence of NO_x during the day.[28,32,35]

3.3. Role of Organonitrates in Particle Growth. During the measurement period, night-time NPF was observed for almost all nights, starting after sunset with particle growth lasting well into the morning of the following day (Figure S5a). A two week long measurement series using the same SMPS was also carried out in the same month (August) of 2018 at KIT campus north (49°5′43.0″N 8°25′46.0″E), located ∼2 km east of the measurement site in 2016 (Figure S5b). Night-time NPF was also observed for this measurement period in a different year and a slightly different location, confirming the robustness of the data set as well as the regional nature of this phenomenon. We stress here that since we did not have the instruments to investigate the molecules or ions involved in the very early stages of NPF, i.e., clustering and early growth of particles from subnanometers to a few nanometer sizes, our discussions are focused on the process of particle growth from a few nanometer size ranges to larger sizes (tens of nanometers). NPF during the night has been reported previously,[13,14,60,61] albeit much less often than day-time NPF. It has been suggested that night-time NPF may be induced by organics formed via BVOC (e.g., monoterpenes) oxidation by O_3 or NO_3 radicals in the absence of UV and OH radicals or by OH radicals resulting from BVOC ozonolysis.[13,14] The average O:C ratios are 0.85 for pON and 0.93 for gON, indicating that they could comprise highly oxygenated molecules (HOMs) formed, e.g., by autoxidation processes,[7] which have been shown to play an important role in atmospheric NPF.[8] The mean diel pattern of the number fraction of ultrafine particles (with mobility diameters between 2.5−7 nm) measured with two CPCs (Table S1) also shows a peak after sunset (20:30−00:00, Figure S6), suggesting emission or formation of small particles for this time period. We observe good correlations (Figure S7) between the number concentrations of these ultrafine particles and the above-mentioned four C_xN groups in both gas phase (Pearson's R: 0.53−0.73) and particle phase (Pearson's R: 0.64−0.83) after sunset (20:30−00:00), particularly for the C_7N and $C_{10}N$ groups, indicative of the potentially important role of these ON in the growth of newly formed particles. With night-time anthropogenic activities assumed to be lower and the very low reaction rate of NO_3 radicals with toluene

Single Particle Characterisation of Atmospheric Aerosol Particles in Central Europe
Appendix C

compared to that with α-pinene and isoprene,[62] the C_7N groups may have larger contributions from the fragmentation of oxidation products from monoterpenes[22,32,59] instead of oxidation products from toluene.

In order to investigate the role of NO_x emissions and ON in night-time particle growth and high night-time OA mass loadings, we calculated the production rate of NO_3 radicals ($PNO_3 = k_1[NO_2][O_3]$, $k_1 = 3.5 \times 10^{-17}$ cm^3 molecule^{-1} s^{-1} at 298 K)[63] using the NO_2 and O_3 concentrations measured during the campaign (Figure S8a). N_2O_5 concentrations measured by CIMS are orders of magnitude lower than the NO_2 concentrations. The loss of N_2O_5 (calculated as in Xu et al.,[25] due to homogeneous reaction with water and heterogeneous uptake to aqueous particles)[64−66] is rather slow (lifetime ≥ 1700 s), indicating that the main sink of NO_3 is likely its reaction with BVOC. Besides, good correlations are observed between PNO_3 and the C_xN groups in the particle phase (Pearson's R: 0.60−0.91) and gas phase (Pearson's R: 0.72−0.90) after sunset (20:30−00:00, Figure S9). The number concentrations of the ultrafine particles are also well correlated (Pearson's $R = 0.64$) with PNO_3 (Figure S8a) after sunset (20:30−00:00, Figure S8b). The results together with the good correlation of C_xN and ultrafine particles indicate the potentially important role of NO_3 radicals in night-time VOC oxidation to ON and the resulting growth of newly formed particles. We calculated the particle growth rate (increase rate of count mean diameter) for each night-time NPF (5 events, see Figure S5a) by averaging the diameter difference after sunset until midnight ($\Delta = (\text{diameter}_{midnight} - \text{diameter}_{sunset})/(\text{time}_{midnight} - \text{time}_{sunset})$). The average particle growth rate is 5.3 ± 3.1 nm hr^{-1} (min to max: 2.2−10.3 nm hr^{-1}), which is close to the growth rates for the night-time NPF observed over the Landes forest (9.0−17.5 nm hr^{-1}).[14] We also calculated the mass increase rate of OA measured by AMS, as well as pON, gON and the C_xN groups measured by CIMS for each night-time NPF observed during the CIMS measurement period (2 events, see Figure S1 and S5a) in a similar way ($\Delta = (\text{mass}_{midnight} - \text{mass}_{sunset})/(\text{time}_{midnight} - \text{time}_{sunset})$). The average mass increase rate for these two events is 0.48 ± 0.06 μg m^{-3} hr^{-1} for OA, 0.10 ± 0.04 μg m^{-3} hr^{-1} for pON, and 0.043 ± 0.035 μg m^{-3} hr^{-1} (4.0 $\pm$ 3.6 ppt hr^{-1}) for gON (see Figure 4). This means that 18−25% of the OA mass

increase after sunset can be explained by pON resulting from condensation of gON and/or particle-phase reactions, such as accretion reactions.[67] Within the four C_xN groups in pON and gON, the $C_{10}N$ group shows the largest mass increase (particle phase: 0.029 ± 0.001 μg m^{-3} hr^{-1}, gas phase: 0.024 ± 0.014 μg m^{-3} hr^{-1}), followed by C_7N and $C_{15}N$. The C_5N group has the lowest pON mass increase and decreases a bit in gON, indicating lower emissions of C_5 BVOC (e.g., isoprene) during the night. We rule out a significant influence of the temperature changes between day and night on our observations, as one would expect especially the smaller molecules, of which a larger fraction typically remains in the gas phase, to partition more significantly into the condensed phase. However, we observe the contrary, indicating a smaller influence of temperature-driven partitioning under these conditions. In total, the mass increase rate of these four pC_xN groups accounts for 46.6% of the pON mass increase and 9.7% of the OA mass increase.

Our results indicate that these highly functionalized ON observed after sunset result from NO_3 radical initiated oxidation reactions and that they have potential contributions to SOA formation and particle growth via condensation and/or multiphase chemistry.

Given the location of the measurement station (outside the city and in close proximity to large forested areas) and the season during which the measurements were taken (summer), the majority of the precursor VOC for ON presented here are most likely of biogenic origin (also reflected in the emission inventories of the upper Rhine valley[68]). The abundance of $C_{10}N$ compounds, which are very likely to be the reaction products of the oxidation of monoterpenes by NO_3 radicals,[22,32,35] supports this conclusion. Furthermore, the proximity to the city and the nearby industrial emission sources results in high enough NO_x emissions for NO_3 radical oxidation to be a major pathway for OA particle number and mass formation during the night, especially during the summer months. However, a clear distinction between biogenic and anthropogenic contributions to the different C_xN groups is limited within this data set. This is especially evident for the C_7N group, the compounds of which, based on their number of carbon atoms, are hypothesized to partially result from toluene oxidation[57] but may also result from fragmentation products of monoterpene oxidation.[22,32,59]

Night-time NPF events are also frequently observed at our measurement site, similar to recently reported observations over the Landes forest in southwestern France.[14] Monoterpenes have been shown to play an important role for NPF in boreal regions[69] and were shown to reach maximum concentrations during the night-time NPF events over the Landes forest.[14] Isoprene, emissions of which are controlled by temperature and light,[70] however, was shown to significantly inhibit NPF.[71,72] The good correlation of ultrafine particle number concentrations with $C_{10}N$ compounds, together with calculated particle growth rate and mass increase rate of this group, in our study thus corroborates the important role of night-time VOC oxidation, particularly of monoterpenes, for ON in night-time SOA formation and particle growth. More in-depth and comprehensive studies on ON formation from different anthropogenic and biogenic VOC, and their role in NPF and SOA formation, are needed.

Our study provides insights into the chemical composition of ON, their relationship with different precursor VOC, and

Figure 4. Mass increase rate comparisons of OA, pON and gON (hatched bars). The specified contributions of the different C_xN groups (x = 5, 7, 10, 15) are laid over the hatched areas. The inset shows the enlarged regions of the mass increase rates of the C_xN groups (x = 5, 7, 10, 15) in particle and gas phases; error bars represent ± 1 standard deviation.

Single Particle Characterisation of Atmospheric Aerosol Particles in Central Europe
Appendix C

their role in night-time particle growth in an area where BVOC emissions dominate.

ASSOCIATED CONTENT

Supporting Information

The Supporting Information is available free of charge on the ACS Publications website at DOI: 10.1021/acs.est.8b05826.

Detailed campaign instrumentation overview; results for time series of aerosol composition measured by AMS and CIMS, and average aerosol contribution to total $PM_{2.5}$ measured by AMS, mean diel trend of OA measured by AMS, average size distribution of organics measured by AMS, time series of total OA, NO_3, $OrgNO_3$, and pON, and correlation of $OrgNO_3$ and pON; mass contribution of C_xN groups to total ON and C_xHO groups to total OC as a function of the number of carbon atoms; mean diel patterns of mass contributions of C_xHO (x = 5, 7, 10, 15) groups in the particle phase to total pOC and in the gas phase to total gOC; average thermograms of pC_xN and pC_xHO groups (x = 5, 7, 10, 15); night-time NPF events during the measurement period and during another year (2018) in KIT campus north; mean diel trend of number fraction of ultrafine particles (with mobility diameters between 2.5−7 nm); correlations of C_xN (x = 5, 7, 10, 15) group concentrations in particle and gas phases with ultrafine particle number concentrations; mean calculated production rate of nitrate radicals (PNO_3) during the night, and correlation of ultrafine particle number concentrations with PNO_3; correlations of C_xN (x = 5, 7, 10, 15) group concentrations with PNO_3 (PDF)

AUTHOR INFORMATION

Corresponding Author
*E-mail: claudia.mohr@aces.su.se.

ORCID
Wei Huang: 0000-0002-5049-2117

Present Address
○TSI Instruments India Private Limited, Bangalore, 560102, India.

Notes
The authors declare no competing financial interest.

ACKNOWLEDGMENTS

REFERENCES

(1) IPCC. *Climate change 2013: The physical scientific basis*;Cambridge University Press: Cambridge, England, 2013; p 622−623.

(2) Boers, R.; van Weele, M.; van Meijgaard, E.; Savenije, M.; Siebesma, A. P.; Bosveld, F.; Stammes, P. Observations and projections of visibility and aerosol optical thickness (1956−2100) in the Netherlands: impacts of time-varying aerosol composition and hygroscopicity. *Environ. Res. Lett.* **2015**, *10* (1), 015003.

(3) Nel, A. Air pollution-related illness: Effects of particles. *Science* **2005**, *308* (5723), 804−806.

(4) Rückerl, R.; Schneider, A.; Breitner, S.; Cyrys, J.; Peters, A. Health effects of particulate air pollution: A review of epidemiological evidence. *Inhalation Toxicol.* **2011**, *23* (10), 555−592.

(5) Jimenez, J. L.; Canagaratna, M. R.; Donahue, N. M.; Prevot, A. S. H.; Zhang, Q.; Kroll, J. H.; DeCarlo, P. F.; Allan, J. D.; Coe, H.; Ng, N. L.; Aiken, A. C.; Docherty, K. S.; Ulbrich, I. M.; Grieshop, A. P.; Robinson, A. L.; Duplissy, J.; Smith, J. D.; Wilson, K. R.; Lanz, V. A.; Hueglin, C.; Sun, Y. L.; Tian, J.; Laaksonen, A.; Raatikainen, T.; Rautiainen, J.; Vaattovaara, P.; Ehn, M.; Kulmala, M.; Tomlinson, J. M.; Collins, D. R.; Cubison, M. J.; Dunlea, E. J.; Huffman, J. A.; Onasch, T. B.; Alfarra, M. R.; Williams, P. I.; Bower, K.; Kondo, Y.; Schneider, J.; Drewnick, F.; Borrmann, S.; Weimer, S.; Demerjian, K.; Salcedo, D.; Cottrell, L.; Griffin, R.; Takami, A.; Miyoshi, T.; Hatakeyama, S.; Shimono, A.; Sun, J. Y.; Zhang, Y. M.; Dzepina, K.; Kimmel, J. R.; Sueper, D.; Jayne, J. T.; Herndon, S. C.; Trimborn, A. M.; Williams, L. R.; Wood, E. C.; Middlebrook, A. M.; Kolb, C. E.; Baltensperger, U.; Worsnop, D. R. Evolution of organic aerosols in the atmosphere. *Science* **2009**, *326* (5959), 1525−1529.

(6) Hallquist, M.; Wenger, J. C.; Baltensperger, U.; Rudich, Y.; Simpson, D.; Claeys, M.; Dommen, J.; Donahue, N. M.; George, C.; Goldstein, A. H.; Hamilton, J. F.; Herrmann, H.; Hoffmann, T.; Iinuma, Y.; Jang, M.; Jenkin, M. E.; Jimenez, J. L.; Kiendler-Scharr, A.; Maenhaut, W.; McFiggans, G.; Mentel, T. F.; Monod, A.; Prévôt, A. S. H.; Seinfeld, J. H.; Surratt, J. D.; Szmigielski, R.; Wildt, J. The formation, properties and impact of secondary organic aerosol: current and emerging issues. *Atmos. Chem. Phys.* **2009**, *9* (14), 5155−5236.

(7) Ehn, M.; Thornton, J. A.; Kleist, E.; Sipilä, M.; Junninen, H.; Pullinen, I.; Springer, M.; Rubach, F.; Tillmann, R.; Lee, B.; Lopez-Hilfiker, F.; Andres, S.; Acir, I. H.; Rissanen, M.; Jokinen, T.; Schobesberger, S.; Kangasluoma, J.; Kontkanen, J.; Nieminen, T.; Kurtén, T.; Nielsen, L. B.; Jørgensen, S.; Kjaergaard, H. G.; Canagaratna, M.; Dal Maso, M.; Berndt, T.; Petäjä, T.; Wahner, A.; Kerminen, V. M.; Kulmala, M.; Worsnop, D. R.; Wildt, J.; Mentel, T. F. A large source of low-volatility secondary organic aerosol. *Nature* **2014**, *506* (7489), 476−479.

(8) Bianchi, F.; Tröstl, J.; Junninen, H.; Frege, C.; Henne, S.; Hoyle, C. R.; Molteni, U.; Herrmann, E.; Adamov, A.; Bukowiecki, N.; Chen, X.; Duplissy, J.; Gysel, M.; Hutterli, M.; Kangasluoma, J.; Kontkanen, J.; Kürten, A.; Manninen, H. E.; Münch, S.; Peräkylä, O.; Petäjä, T.; Rondo, L.; Williamson, C.; Weingartner, E.; Curtius, J.; Worsnop, D. R.; Kulmala, M.; Dommen, J.; Baltensperger, U. New particle formation in the free troposphere: A question of chemistry and timing. *Science* **2016**, *352* (6289), 1109−1112.

(9) Tröstl, J.; Chuang, W. K.; Gordon, H.; Heinritzi, M.; Yan, C.; Molteni, U.; Ahlm, L.; Frege, C.; Bianchi, F.; Wagner, R.; Simon, M.; Lehtipalo, K.; Williamson, C.; Craven, J. S.; Duplissy, J.; Adamov, A.; Almeida, J.; Bernhammer, A.-K.; Breitenlechner, M.; Brilke, S.; Dias, A.; Ehrhart, S.; Flagan, R. C.; Franchin, A.; Fuchs, C.; Guida, R.; Gysel, M.; Hansel, A.; Hoyle, C. R.; Jokinen, T.; Junninen, H.; Kangasluoma, J.; Keskinen, H.; Kim, J.; Krapf, M.; Kürten, A.; Laaksonen, A.; Lawler, M.; Leiminger, M.; Mathot, S.; Möhler, O.; Nieminen, T.; Onnela, A.; Petäjä, T.; Piel, F. M.; Miettinen, P.; Rissanen, M. P.; Rondo, L.; Sarnela, N.; Schobesberger, S.; Sengupta, K.; Sipilä, M.; Smith, J. N.; Steiner, G.; Tomè, A.; Virtanen, A.; Wagner, A. C.; Weingartner, E.; Wimmer, D.; Winkler, P. M.; Ye, P. L.; Carslaw, K. S.; Curtius, J.; Dommen, J.; Kirkby, J.; Kulmala, M.; Riipinen, I.; Worsnop, D. R.; Donahue, N. M.; Baltensperger, U. The role of low-volatility organic compounds in initial particle growth in the atmosphere. *Nature* **2016**, *533* (7604), 527−531.

(10) Kirkby, J.; Duplissy, J.; Sengupta, K.; Frege, C.; Gordon, H.; Williamson, C.; Heinritzi, M.; Simon, M.; Yan, C.; Almeida, J.; Tröstl, J.; Nieminen, T.; Ortega, I. K.; Wagner, R.; Adamov, A.; Amorim, A.; Bernhammer, A.-K.; Bianchi, F.; Breitenlechner, M.; Brilke, S.; Chen, X. M.; Craven, J.; Dias, A.; Ehrhart, S.; Flagan, R. C.; Franchin, A.; Fuchs, C.; Guida, R.; Hakala, J.; Hoyle, C. R.; Jokinen, T.; Junninen, H.; Kangasluoma, J.; Kim, J.; Krapf, M.; Kürten, A.; Laaksonen, A.; Lehtipalo, K.; Makhmutov, V.; Mathot, S.; Molteni, U.; Onnela, A.; Peräkylä, O.; Piel, F.; Petäjä, T.; Praplan, A. P.; Pringle, K.; Rap, A.; Richards, N. A. D.; Riipinen, I.; Rissanen, M. P.; Rondo, L.; Sarnela, N.; Schobesberger, S.; Scott, C. E.; Seinfeld, J. H.; Sipilä, M.; Steiner, G.; Stozhkov, Y.; Stratmann, F.; Tomé, A.; Virtanen, A.; Vogel, A. L.;

Single Particle Characterisation of Atmospheric Aerosol Particles in Central Europe
Appendix C

Wagner, A. C.; Wagner, P. E.; Weingartner, E.; Wimmer, D.; Winkler, P. M.; Ye, P. L.; Zhang, X.; Hansel, A.; Dommen, J.; Donahue, N. M.; Worsnop, D. R.; Baltensperger, U.; Kulmala, M.; Carslaw, K. S.; Curtius, J. Ion-induced nucleation of pure biogenic particles. *Nature* **2016**, *533* (7604), 521−526.

(11) Kulmala, M.; Kontkanen, J.; Junninen, H.; Lehtipalo, K.; Manninen, H. E.; Nieminen, T.; Petäjä, T.; Sipilä, M.; Schobesberger, S.; Rantala, P.; Franchin, A.; Jokinen, T.; Järvinen, E.; Äijälä, M.; Kangasluoma, J.; Hakala, J.; Aalto, P. P.; Paasonen, P.; Mikkilä, J.; Vanhanen, J.; Aalto, J.; Hakola, H.; Makkonen, U.; Ruuskanen, T.; Mauldin, R. L., III; Duplissy, J.; Vehkamäki, H.; Bäck, J.; Kortelainen, A.; Riipinen, I.; Kurtén, T.; Johnston, M. V.; Smith, J. N.; Ehn, M.; Mentel, T. F.; Lehtinen, K. E. J.; Laaksonen, A.; Kerminen, V.-M.; Worsnop, D. R. Direct observations of atmospheric aerosol nucleation. *Science* **2013**, *339* (6122), 943−946.

(12) Kiendler-Scharr, A.; Mensah, A. A.; Friese, E.; Topping, D.; Nemitz, E.; Prevot, A. S. H.; Äijälä, M.; Allan, J.; Canonaco, F.; Canagaratna, M.; Carbone, S.; Crippa, M.; Dall Osto, M.; Day, D. A.; De Carlo, P.; Di Marco, C. F.; Elbern, H.; Eriksson, A.; Freney, E.; Hao, L.; Herrmann, H.; Hildebrandt, L.; Hillamo, R.; Jimenez, J. L.; Laaksonen, A.; McFiggans, G.; Mohr, C.; O'Dowd, C.; Otjes, R.; Ovadnevaite, J.; Pandis, S. N.; Poulain, L.; Schlag, P.; Sellegri, K.; Swietlicki, E.; Tiitta, P.; Vermeulen, A.; Wahner, A.; Worsnop, D.; Wu, H.-C. Ubiquity of organic nitrates from nighttime chemistry in the European submicron aerosol. *Geophys. Res. Lett.* **2016**, *43* (14), 7735−7744.

(13) Lee, S.-H.; Young, L.-H.; Benson, D. R.; Suni, T.; Kulmala, M.; Junninen, H.; Campos, T. L.; Rogers, D. C.; Jensen, J. Observations of nighttime new particle formation in the troposphere. *J. Geophys. Res.* **2008**, *113* (D10), D10210.

(14) Kammer, J.; Perraudin, E.; Flaud, P. M.; Lamaud, E.; Bonnefond, J. M.; Villenave, E. Observation of nighttime new particle formation over the French Landes forest. *Sci. Total Environ.* **2018**, *621*, 1084−1092.

(15) Rollins, A. W.; Browne, E. C.; Min, K.-E.; Pusede, S. E.; Wooldridge, P. J.; Gentner, D. R.; Goldstein, A. H.; Liu, S.; Day, D. A.; Russell, L. M.; Cohen, R. C. Evidence for NOx control over nighttime SOA formation. *Science* **2012**, *337* (6099), 1210−1212.

(16) Pye, H. O. T.; Chan, A. W. H.; Barkley, M. P.; Seinfeld, J. H. Global modeling of organic aerosol: the importance of reactive nitrogen (NOx and NO3). *Atmos. Chem. Phys.* **2010**, *10* (22), 11261−11276.

(17) Brown, S. S.; deGouw, J. A.; Warneke, C.; Ryerson, T. B.; Dubé, W. P.; Atlas, E.; Weber, R. J.; Peltier, R. E.; Neuman, J. A.; Roberts, J. M.; Swanson, A.; Flocke, F.; McKeen, S. A.; Brioude, J.; Sommariva, R.; Trainer, M.; Fehsenfeld, F. C.; Ravishankara, A. R. Nocturnal isoprene oxidation over the Northeast United States in summer and its impact on reactive nitrogen partitioning and secondary organic aerosol. *Atmos. Chem. Phys.* **2009**, *9* (9), 3027−3042.

(18) Ayres, B. R.; Allen, H. M.; Draper, D. C.; Brown, S. S.; Wild, R. J.; Jimenez, J. L.; Day, D. A.; Campuzano-Jost, P.; Hu, W.; de Gouw, J.; Koss, A.; Cohen, R. C.; Duffey, K. C.; Romer, P.; Baumann, K.; Edgerton, E.; Takahama, S.; Thornton, J. A.; Lee, B. H.; Lopez-Hilfiker, F. D.; Mohr, C.; Wennberg, P. O.; Nguyen, T. B.; Teng, A.; Goldstein, A. H.; Olson, K.; Fry, J. L. Organic nitrate aerosol formation via NO3 + biogenic volatile organic compounds in the southeastern United States. *Atmos. Chem. Phys.* **2015**, *15* (23), 13377−13392.

(19) Spittler, M.; Barnes, I.; Bejan, I.; Brockmann, K. J.; Benter, T.; Wirtz, K. Reactions of NO3 radicals with limonene and alpha-pinene: Product and SOA formation. *Atmos. Environ.* **2006**, *40*, S116−S127.

(20) Fry, J. L.; Draper, D. C.; Barsanti, K. C.; Smith, J. N.; Ortega, J.; Winkle, P. M.; Lawler, M. J.; Brown, S. S.; Edwards, P. M.; Cohen, R. C.; Lee, L. Secondary organic aerosol formation and organic nitrate yield from NO3 oxidation of biogenic hydrocarbons. *Environ. Sci. Technol.* **2014**, *48* (20), 11944−11953.

(21) Ng, N. L.; Kwan, A. J.; Surratt, J. D.; Chan, A. W. H.; Chhabra, P. S.; Sorooshian, A.; Pye, H. O. T.; Crounse, J. D.; Wennberg, P. O.; Flagan, R. C.; Seinfeld, J. H. Secondary organic aerosol (SOA) formation from reaction of isoprene with nitrate radicals (NO3). *Atmos. Chem. Phys.* **2008**, *8* (14), 4117−4140.

(22) Nah, T.; Sanchez, J.; Boyd, C. M.; Ng, N. L. Photochemical aging of alpha-pinene and beta-pinene secondary organic aerosol formed from nitrate radical oxidation. *Environ. Sci. Technol.* **2016**, *50* (1), 222−231.

(23) D'Ambro, E. L.; Lee, B. H.; Liu, J. M.; Shilling, J. E.; Gaston, C. J.; Lopez-Hilfiker, F. D.; Schobesberger, S.; Zaveri, R. A.; Mohr, C.; Lutz, A.; Zhang, Z. F.; Gold, A.; Surratt, J. D.; Rivera-Rios, J. C.; Keutsch, F. N.; Thornton, J. A. Molecular composition and volatility of isoprene photochemical oxidation secondary organic aerosol under low- and high-NOx conditions. *Atmos. Chem. Phys.* **2017**, *17* (1), 159−174.

(24) Ng, N. L.; Chhabra, P. S.; Chan, A. W. H.; Surratt, J. D.; Kroll, J. H.; Kwan, A. J.; McCabe, D. C.; Wennberg, P. O.; Sorooshian, A.; Murphy, S. M.; Dalleska, N. F.; Flagan, R. C.; Seinfeld, J. H. Effect of NOx level on secondary organic aerosol (SOA) formation from the photooxidation of terpenes. *Atmos. Chem. Phys.* **2007**, *7* (19), 5159−5174.

(25) Xu, L.; Guo, H. Y.; Boyd, C. M.; Klein, M.; Bougiatioti, A.; Cerully, K. M.; Hite, J. R.; Isaacman-VanWertz, G.; Kreisberg, N. M.; Knote, C.; Olson, K.; Koss, A.; Goldstein, A. H.; Hering, S. V.; de Gouw, J.; Baumann, K.; Lee, S.-H.; Nenes, A.; Weber, R. J.; Ng, N. L. Effects of anthropogenic emissions on aerosol formation from isoprene and monoterpenes in the southeastern United States. *Proc. Natl. Acad. Sci. U. S. A.* **2015**, *112* (1), 37−42.

(26) Xu, L.; Kollman, M. S.; Song, C.; Shilling, J. E.; Ng, N. L. Effects of NOx on the volatility of secondary organic aerosol from isoprene photooxidation. *Environ. Sci. Technol.* **2014**, *48* (4), 2253−2262.

(27) Kroll, J. H.; Ng, N. L.; Murphy, S. M.; Flagan, R. C.; Seinfeld, J. H. Secondary organic aerosol formation from isoprene photo-oxidation. *Environ. Sci. Technol.* **2006**, *40* (6), 1869−1877.

(28) Sobanski, N.; Thieser, J.; Schuladen, J.; Sauvage, C.; Song, W.; Williams, J.; Lelieveld, J.; Crowley, J. N. Day and night-time formation of organic nitrates at a forested mountain site in south-west Germany. *Atmos. Chem. Phys.* **2017**, *17* (6), 4115−4130.

(29) Faxon, C.; Hammes, J.; Le Breton, M.; Pathak, R. K.; Hallquist, M. Characterization of organic nitrate constituents of secondary organic aerosol (SOA) from nitrate-radical-initiated oxidation of limonene using high-resolution chemical ionization mass spectrometry. *Atmos. Chem. Phys.* **2018**, *18* (8), 5467−5481.

(30) Fisher, J. A.; Jacob, D. J.; Travis, K. R.; Kim, P. S.; Marais, E. A.; Miller, C. C.; Yu, K. R.; Zhu, L.; Yantosca, R. M.; Sulprizio, M. P.; Mao, J. Q.; Wennberg, P. O.; Crounse, J. D.; Teng, A. P.; Nguyen, T. B.; St Clair, J. M.; Cohen, R. C.; Romer, P.; Nault, B. A.; Wooldridge, P. J.; Jimenez, J. L.; Campuzano-Jost, P.; Day, D. A.; Hu, W. W.; Shepson, P. B.; Xiong, F. L. Z.; Blake, D. R.; Goldstein, A. H.; Misztal, P. K.; Hanisco, T. F.; Wolfe, G. M.; Ryerson, T. B.; Wisthaler, A.; Mikoviny, T. Organic nitrate chemistry and its implications for nitrogen budgets in an isoprene- and monoterpene-rich atmosphere: constraints from aircraft (SEAC4RS) and ground-based (SOAS) observations in the Southeast US. *Atmos. Chem. Phys.* **2016**, *16* (9), 5969−5991.

(31) Singh, H. B.; Hanst, P. L. Peroxyacetyl nitrate (PAN) in the unpolluted atmosphere: An important reservoir for nitrogen oxides. *Geophys. Res. Lett.* **1981**, *8* (8), 941−944.

(32) Lee, B. H.; Mohr, C.; Lopez-Hilfiker, F. D.; Lutz, A.; Hallquist, M.; Lee, L.; Romer, P.; Cohen, R. C.; Iyer, S.; Kurtén, T.; Hu, W. W.; Day, D. A.; Campuzano-Jost, P.; Jimenez, J. L.; Xu, L.; Ng, N. L.; Guo, H. Y.; Weber, R. J.; Wild, R. J.; Brown, S. S.; Koss, A.; de Gouw, J.; Olson, K.; Goldstein, A. H.; Seco, R.; Kim, S.; McAvey, K.; Shepson, P. B.; Starn, T.; Baumann, K.; Edgerton, E. S.; Liu, J. M.; Shilling, J. E.; Miller, D. O.; Brune, W.; Schobesberger, S.; D'Ambro, E. L.; Thornton, J. A. Highly functionalized organic nitrates in the southeast United States: Contribution to secondary organic aerosol and reactive nitrogen budgets. *Proc. Natl. Acad. Sci. U. S. A.* **2016**, *113* (6), 1516−1521.

(33) Lee, B. H.; Lopez-Hilfiker, F. D.; D'Ambro, E. L.; Zhou, P. T.; Boy, M.; Petäjä, T.; Hao, L. Q.; Virtanen, A.; Thornton, J. A. Semivolatile and highly oxygenated gaseous and particulate organic compounds observed above a boreal forest canopy. *Atmos. Chem. Phys.* **2018**, *18* (15), 11547−11562.

(34) Capouet, M.; Müller, J.-F. A group contribution method for estimating the vapour pressures of alpha-pinene oxidation products. *Atmos. Chem. Phys.* **2006**, *6*, 1455−1467.

(35) Massoli, P.; Stark, H.; Canagaratna, M. R.; Krechmer, J. E.; Xu, L.; Ng, N. L.; Mauldin, R. L.; Yan, C.; Kimmel, J.; Misztal, P. K.; Jimenez, J. L.; Jayne, J. T.; Worsnop, D. R. Ambient measurements of highly oxidized gas-phase molecules during the Southern Oxidant and Aerosol Study (SOAS) 2013. *ACS Earth Space Chem.* **2018**, *2*, 653−672.

(36) Duhl, T. R.; Helmig, D.; Guenther, A. Sesquiterpene emissions from vegetation: a review. *Biogeosciences* **2008**, *5* (3), 761−777.

(37) Komenda, M.; Koppmann, R. Monoterpene emissions from Scots pine (Pinus sylvestris): Field studies of emission rate variabilities. *J. Geophys. Res.* **2002**, *107* (D13), ACH1-1−ACH 1-13.

(38) Langford, B.; Cash, J.; Acton, W. J. F.; Valach, A. C.; Hewitt, C. N.; Fares, S.; Goded, I.; Gruening, C.; House, E.; Kalogridis, A.-C.; Gros, V.; Schafers, R.; Thomas, R.; Broadmeadow, M.; Nemitz, E. Isoprene emission potentials from European oak forests derived from canopy flux measurements: an assessment of uncertainties and interalgorithm variability. *Biogeosciences* **2017**, *14* (23), 5571−5594.

(39) Hagemann, R.; Corsmeier, U.; Kottmeier, C.; Rinke, R.; Wieser, A.; Vogel, B. Spatial variability of particle number concentrations and NOx in the Karlsruhe (Germany) area obtained with the mobile laboratory 'AERO-TRAM'. *Atmos. Environ.* **2014**, *94*, 341−352.

(40) Duine, G.-J.; Hedde, T.; Roubin, P.; Durand, P.; Lothon, M.; Lohou, F.; Augustin, P.; Fourmentin, M. Characterization of valley flows within two confluent valleys under stable conditions: observations from the KASCADE field experiment. *Q. J. R. Meteorol. Soc.* **2017**, *143* (705), 1886−1902.

(41) Williams, L. R.; Gonzalez, L. A.; Peck, J.; Trimborn, D.; McInnis, J.; Farrar, M. R.; Moore, K. D.; Jayne, J. T.; Robinson, W. A.; Lewis, D. K.; Onasch, T. B.; Canagaratna, M. R.; Trimborn, A.; Timko, M. T.; Magoon, G.; Deng, R.; Tang, D.; Blanco, E. D. L. R.; Prévôt, A. S. H.; Smith, K. A.; Worsnop, D. R. Characterization of an aerodynamic lens for transmitting particles greater than 1 micrometer in diameter into the Aerodyne aerosol mass spectrometer. *Atmos. Meas. Tech.* **2013**, *6* (11), 3271−3280.

(42) Middlebrook, A. M.; Bahreini, R.; Jimenez, J. L.; Canagaratna, M. R. Evaluation of composition-dependent collection efficiencies for the Aerodyne Aerosol Mass Spectrometer using field data. *Aerosol Sci. Technol.* **2012**, *46* (3), 258−271.

(43) Lopez-Hilfiker, F. D.; Mohr, C.; Ehn, M.; Rubach, F.; Kleist, E.; Wildt, J.; Mentel, T. F.; Lutz, A.; Hallquist, M.; Worsnop, D.; Thornton, J. A. A novel method for online analysis of gas and particle composition: description and evaluation of a Filter Inlet for Gases and AEROsols (FIGAERO). *Atmos. Meas. Tech.* **2014**, *7* (4), 983−1001.

(44) Lee, B. H.; Lopez-Hilfiker, F. D.; Mohr, C.; Kurtén, T.; Worsnop, D. R.; Thornton, J. A. An iodide-adduct high-resolution time-of-flight chemical-ionization mass spectrometer: Application to atmospheric inorganic and organic compounds. *Environ. Sci. Technol.* **2014**, *48* (11), 6309−6317.

(45) Lopez-Hilfiker, F. D.; Iyer, S.; Mohr, C.; Lee, B. H.; D'Ambro, E. L.; Kurtén, T.; Thornton, J. A. Constraining the sensitivity of iodide adduct chemical ionization mass spectrometry to multifunctional organic molecules using the collision limit and thermodynamic stability of iodide ion adducts. *Atmos. Meas. Tech.* **2016**, *9* (4), 1505−1512.

(46) Huang, W.; Saathoff, H.; Pajunoja, A.; Shen, X. L.; Naumann, K.-H.; Wagner, R.; Virtanen, A.; Leisner, T.; Mohr, C. α-Pinene secondary organic aerosol at low temperature: chemical composition and implications for particle viscosity. *Atmos. Chem. Phys.* **2018**, *18* (4), 2883−2898.

(47) Thompson, S. L.; Yatavelli, R. L. N.; Stark, H.; Kimmel, J. R.; Krechmer, J. E.; Day, D. A.; Hu, W. W.; Isaacman-VanWertz, G.; Yee, L.; Goldstein, A. H.; Khan, M. A. H.; Holzinger, R.; Kreisberg, N.; Lopez-Hilfiker, F. D.; Mohr, C.; Thornton, J. A.; Jayne, J. T.; Canagaratna, M.; Worsnop, D. R.; Jimenez, J. L. Field intercomparison of the gas/particle partitioning of oxygenated organics during the Southern Oxidant and Aerosol Study (SOAS) in 2013. *Aerosol Sci. Technol.* **2017**, *51* (1), 30−56.

(48) Crippa, M.; Canonaco, F.; Lanz, V. A.; Äijälä, M.; Allan, J. D.; Carbone, S.; Capes, G.; Ceburnis, D.; Dall'Osto, M.; Day, D. A.; DeCarlo, P. F.; Ehn, M.; Eriksson, A.; Freney, E.; Hildebrandt Ruiz, L.; Hillamo, R.; Jimenez, J. L.; Junninen, H.; Kiendler-Scharr, A.; Kortelainen, A.-M.; Kulmala, M.; Laaksonen, A.; Mensah, A.; Mohr, C.; Nemitz, E.; O'Dowd, C.; Ovadnevaite, J.; Pandis, S. N.; Petäjä, T.; Poulain, L.; Saarikoski, S.; Sellegri, K.; Swietlicki, E.; Tiitta, P.; Worsnop, D. R.; Baltensperger, U.; Prévôt, A. S. H. Organic aerosol components derived from 25 AMS data sets across Europe using a consistent ME-2 based source apportionment approach. *Atmos. Chem. Phys.* **2014**, *14* (12), 6159−6176.

(49) Xu, L.; Suresh, S.; Guo, H.; Weber, R. J.; Ng, N. L. Aerosol characterization over the southeastern United States using high-resolution aerosol mass spectrometry: spatial and seasonal variation of aerosol composition and sources with a focus on organic nitrates. *Atmos. Chem. Phys.* **2015**, *15* (13), 7307−7336.

(50) Fountoukis, C.; Megaritis, A. G.; Skyllakou, K.; Charalampidis, P. E.; Pilinis, C.; van der Gon, H. A. C. D.; Crippa, M.; Canonaco, F.; Mohr, C.; Prévôt, A. S. H.; Allan, J. D.; Poulain, L.; Petäjä, T.; Tiitta, P.; Carbone, S.; Kiendler-Scharr, A.; Nemitz, E.; O'Dowd, C.; Swietlicki, E.; Pandis, S. N. Organic aerosol concentration and composition over Europe: insights from comparison of regional model predictions with aerosol mass spectrometer factor analysis. *Atmos. Chem. Phys.* **2014**, *14* (17), 9061−9076.

(51) Sobanski, N.; Tang, M. J.; Thieser, J.; Schuster, G.; Pöhler, D.; Fischer, H.; Song, W.; Sauvage, C.; Williams, J.; Fachinger, J.; Berkes, F.; Hoor, P.; Platt, U.; Lelieveld, J.; Crowley, J. N. Chemical and meteorological influences on the lifetime of NO3 at a semi-rural mountain site during PARADE. *Atmos. Chem. Phys.* **2016**, *16* (8), 4867−4883.

(52) Mohr, C.; Lopez-Hilfiker, F. D.; Yli-Juuti, T.; Heitto, A.; Lutz, A.; Hallquist, M.; D'Ambro, E. L.; Rissanen, M. P.; Hao, L. Q.; Schobesberger, S.; Kulmala, M.; Mauldin, R. L.; Makkonen, U.; Sipilä, M.; Petäjä, T.; Thornton, J. A. Ambient observations of dimers from terpene oxidation in the gas phase: Implications for new particle formation and growth. *Geophys. Res. Lett.* **2017**, *44* (6), 2958−2966.

(53) Farmer, D. K.; Matsunaga, A.; Docherty, K. S.; Surratt, J. D.; Seinfeld, J. H.; Ziemann, P. J.; Jimenez, J. L. Response of an aerosol mass spectrometer to organonitrates and organosulfates and implications for atmospheric chemistry. *Proc. Natl. Acad. Sci. U. S. A.* **2010**, *107* (15), 6670−6675.

(54) Lopez-Hilfiker, F. D.; Mohr, C.; Ehn, M.; Rubach, F.; Kleist, E.; Wildt, J.; Mentel, T. F.; Carrasquillo, A. J.; Daumit, K. E.; Hunter, J. F.; Kroll, J. H.; Worsnop, D. R.; Thornton, J. A. Phase partitioning and volatility of secondary organic aerosol components formed from α-pinene ozonolysis and OH oxidation: the importance of accretion products and other low volatility compounds. *Atmos. Chem. Phys.* **2015**, *15* (14), 7765−7776.

(55) Donahue, N. M.; Epstein, S. A.; Pandis, S. N.; Robinson, A. L. A two-dimensional volatility basis set: 1. organic-aerosol mixing thermodynamics. *Atmos. Chem. Phys.* **2011**, *11* (7), 3303−3318.

(56) Monson, R. K.; Jones, R. T.; Rosenstiel, T. N.; Schnitzler, J. P. Why only some plants emit isoprene. *Plant, Cell Environ.* **2013**, *36* (3), 503−516.

(57) Stroud, C. A.; Makar, P. A.; Michelangeli, D. V.; Mozurkewich, M.; Hastie, D. R.; Barbu, A.; Humble, J. Simulating organic aerosol formation during the photooxidation of toluene/NOx mixtures: Comparing the equilibrium and kinetic assumption. *Environ. Sci. Technol.* **2004**, *38* (5), 1471−1479.

Article

(58) EPA. Locating and estimating air emissions from sources of toluene, EPA-454/R-93−047; Research Triangle Park: North Carolina, United States, 1994; pp 3−1, 3−4.

(59) Zhang, H. F.; Yee, L. D.; Lee, B. H.; Curtis, M. P.; Worton, D. R.; Isaacman-VanWertz, G.; Offenberg, J. H.; Lewandowski, M.; Kleindienst, T. E.; Beaver, M. R.; Holder, A. L.; Lonneman, W. A.; Docherty, K. S.; Jaoui, M.; Pye, H. O. T.; Hu, W. W.; Day, D. A.; Campuzano-Jost, P.; Jimenez, J. L.; Guo, H. Y.; Weber, R. J.; de Gouw, J.; Koss, A. R.; Edgerton, E. S.; Brune, W.; Mohr, C.; Lopez-Hilfiker, F. D.; Lutz, A.; Kreisberg, N. M.; Spielman, S. R.; Hering, S. V.; Wilson, K. R.; Thornton, J. A.; Goldstein, A. H. Monoterpenes are the largest source of summertime organic aerosol in the southeastern United States. *Proc. Natl. Acad. Sci. U. S. A.* **2018**, *115* (9), 2038−2043.

(60) Salimi, F.; Rahman, M. M.; Clifford, S.; Ristovski, Z.; Morawska, L. Nocturnal new particle formation events in urban environments. *Atmos. Chem. Phys.* **2017**, *17* (1), 521−530.

(61) Wiedensohler, A.; Hansson, H.-C.; Orsini, D.; Wendisch, M.; Wagner, F.; Bower, K. N.; Chourlarton, T. W.; Wells, M.; Parkin, M.; Acker, K.; Wieprecht, W.; Facchini, M. C.; Lind, J. A.; Fuzzi, S.; Arends, B. G.; Kulmala, M. Night-time formation and occurrence of new particles associated with orographic clouds. *Atmos. Environ.* **1997**, *31* (16), 2545−2559.

(62) Atkinson, R.; Aschmann, S. M.; Winer, A. M.; Pitts, J. N., Jr Gas phase reaction of NO2 with alkenes and dialkenes. *Int. J. Chem. Kinet.* **1984**, *16* (6), 697−706.

(63) *International Union of Pure and Applied Chemistry* http://iupac. pole-ether.fr/.

(64) Fry, J. L.; Draper, D. C.; Zarzana, K. J.; Campuzano-Jost, P.; Day, D. A.; Jimenez, J. L.; Brown, S. S.; Cohen, R. C.; Kaser, L.; Hansel, A.; Cappellin, L.; Karl, T.; Roux, A. H.; Turnipseed, A.; Cantrell, C.; Lefer, B. L.; Grossberg, N. Observations of gas- and aerosol-phase organic nitrates at BEACHON-RoMBAS 2011. *Atmos. Chem. Phys.* **2013**, *13* (17), 8585−8605.

(65) Gaston, C. J.; Thornton, J. A.; Ng, N. L. Reactive uptake of N2O5 to internally mixed inorganic and organic particles: the role of organic carbon oxidation state and inferred organic phase separations. *Atmos. Chem. Phys.* **2014**, *14* (11), 5693−5707.

(66) Crowley, J. N.; Thieser, J.; Tang, M. J.; Schuster, G.; Bozem, H.; Beygi, Z. H.; Fischer, H.; Diesch, J.-M.; Drewnick, F.; Borrmann, S.; Song, W.; Yassaa, N.; Williams, J.; Pöhler, D.; Platt, U.; Lelieveld, J. Variable lifetimes and loss mechanisms for NO3 and N2O5 during the DOMINO campaign: contrasts between marine, urban and continental air. *Atmos. Chem. Phys.* **2011**, *11* (21), 10853−10870.

(67) Kroll, J. H.; Seinfeld, J. H. Chemistry of secondary organic aerosol: Formation and evolution of low-volatility organics in the atmosphere. *Atmos. Environ.* **2008**, *42* (16), 3593−3624.

(68) Ponche, J.-L.; Schneider, C. Mirabel, P. Methodology and results of the REKLIP atmospheric emission inventory of the upper Rhine valley transborder region. *Water, Air, Soil Pollut.* **2000**, *124* (1−2), 61−93.

(69) Tunved, P.; Hansson, H.-C.; Kerminen, V.-M.; Ström, J.; Dal Maso, M.; Lihavainen, H.; Viisanen, Y.; Aalto, P. P.; Komppula, M.; Kulmala, M. High natural aerosol loading over boreal forests. *Science* **2006**, *312* (5771), 261−263.

(70) Guenther, A.; Hewitt, C. N.; Erickson, D.; Fall, R.; Geron, C.; Graedel, T.; Harley, P.; Klinger, L.; Lerdau, M.; Mckay, W. A.; Pierce, T.; Scholes, B.; Steinbrecher, R.; Tallamraju, R.; Taylor, J.; Zimmerman, P. A global model of natural volatile organic compound emissions. *J. Geophys. Res.* **1995**, *100* (D5), 8873−8892.

(71) Kiendler-Scharr, A.; Wildt, J.; Dal Maso, M.; Hohaus, T.; Kleist, E.; Mentel, T. F.; Tillmann, R.; Uerlings, R.; Schurr, U.; Wahner, A. New particle formation in forests inhibited by isoprene emissions. *Nature* **2009**, *461* (7262), 381−384.

(72) Lee, S.-H.; Uin, J.; Guenther, A. B.; de Gouw, J. A.; Yu, F. Q.; Nadykto, A. B.; Herb, J.; Ng, N. L.; Koss, A.; Brune, W. H.; Baumann, K.; Kanawade, V. P.; Keutsch, F. N.; Nenes, A.; Olsen, K.; Goldstein, A.; Ouyang, Q. Isoprene suppression of new particle formation: Potential mechanisms and implications. *J. Geophys. Res.* **2016**, *121* (24), 14621−14635.

207

Appendix C.3 Seasonal characteristics of organic aerosol chemical composition and volatility in Stuttgart, Germany

Atmospheric
Chemistry
and Physics
Discussions

Seasonal characteristics of organic aerosol chemical composition and volatility in Stuttgart, Germany

Wei Huang[1,2], Harald Saathoff[1], Xiaoli Shen[1,2], Ramakrishna Ramisetty[1,3], Thomas Leisner[1,4], Claudia Mohr[5,*]

5   [1]Institute of Meteorology and Climate Research, Karlsruhe Institute of Technology, Eggenstein-Leopoldshafen, 76344, Germany

[2]Institute of Geography and Geoecology, Working Group for Environmental Mineralogy and Environmental System Analysis, Karlsruhe Institute of Technology, Karlsruhe, 76131, Germany

[3]Now at: TSI Instruments India Private Limited, Bangalore, 560102, India

10   [4]Institute of Environmental Physics, Heidelberg University, Heidelberg, 69120, Germany

[5]Department of Environmental Science and Analytical Chemistry, Stockholm University, Stockholm, 11418, Sweden

*Correspondence to: claudia.mohr@aces.su.se

Abstract. Chemical composition and volatility of organic aerosol (OA) particles were investigated during July–
15   August 2017 and February–March 2018 in the city of Stuttgart, one of the most polluted cities in Germany. Total non-refractory particle mass was measured with a high-resolution time-of-flight aerosol mass spectrometer (HR-ToF-AMS; hereafter AMS). Aerosol particles were collected on filters and analyzed in the laboratory with a filter inlet for gases and aerosols coupled to a high-resolution time-of-flight chemical ionization mass spectrometer (FIGAERO-HR-ToF-CIMS; hereafter CIMS), yielding the molecular composition of oxygenated OA (OOA)
20   compounds. While the average organic mass loadings are lower in the summer period (5.1 ± 3.2 µg m^{-3}) than in the winter period (8.4 ± 5.6 µg m^{-3}), we find relatively larger mass contributions of organics measured by AMS in summer (68.8 ± 13.4 %) compared to winter (34.8 ± 9.5 %). CIMS mass spectra show OOA compounds in summer have O:C ratios of 0.82 ± 0.02 and are more influenced by biogenic emissions, while OOA compounds in winter have O:C ratios of 0.89 ± 0.06 and are more influenced by biomass burning emissions. Volatility parametrization
25   analysis shows that OOA in winter is less volatile with higher contributions of low volatile organic compounds (LVOC) and extremely low volatile organic compounds (ELVOC). We partially explain this by the higher contributions of compounds with shorter carbon chain lengths and higher number of oxygen atoms, i.e. higher O:C ratios in winter. Organic compounds desorbing from the particles deposited on the filter samples also exhibit a shift of signal to higher desorption temperatures (i.e. lower apparent volatility) in winter. This is consistent with
30   the relatively higher O:C ratios in winter, but may also be related to higher particle viscosity due to the higher contributions of larger molecular-weight LVOC and ELVOC, interactions between different species and/or particles (particle matrix), and/or thermal decomposition of larger molecules. The results suggest that whereas lower temperature in winter may lead to increased partitioning of semi-volatile organic compounds (SVOC) into the particle phase, this does not result in a higher overall volatility of OOA in winter, and that the difference in

1

35   sources and/or chemistry between the seasons plays a more important role. Our study provides insights into the
seasonal variation of molecular composition and volatility of ambient OA particles, and into their potential sources.

1 Introduction

Air pollution has significant impacts on human health (D'Amato et al., 2014), visibility (Majewski et al., 2014),
and also interacts with climate change (Seinfeld and Pandis, 2016). Due to rapid urbanization, industrialization,
40   and growing human population, air quality in urban environments has become a severe issue in more and more
cities all over the world, particularly in densely populated megacities (Guttikunda et al., 2014; Chan and Yao,
2008; Mayer, 1999; Marlier et al., 2016). Air quality in urban environments is influenced by emissions, e.g. from
sources such as industrial processes, automobile traffic, and domestic heating, and also by meteorological
conditions (e.g. solar radiation, wind, temperature, precipitation), atmospheric dispersion, chemical
45   transformation, location, and topography (D'Amato et al., 2014; Baumbach and Vogt, 2003; Kinney, 2018).
Moreover, air pollution is not limited within the boundaries of urban areas, but can be transported over long
distances and contribute to background pollution on the regional to global scale (Baklanov et al., 2016).
    The most abundant air pollutants are nitrogen dioxide (NO_2), ozone (O_3), sulfur dioxide (SO_2), and particulate
matter (PM; D'Amato et al., 2014). Despite its abundance and important impacts on climate and health, PM
50   sources, physicochemical transformation, and fate in the atmosphere still remain to be fully understood in urban
areas. This is especially true for the organic fraction (Hallquist et al., 2009; Fuzzi et al., 2015). Organic aerosol
(OA) often makes up a significant fraction of submicron particulate mass in urban areas (Hallquist et al., 2009;
Jimenez et al., 2009). OA can be directly emitted into the atmosphere from sources such as fossil fuel combustion
and biomass burning (primary organic aerosol, POA), or be formed in the atmosphere from the oxidation of gas-
55   phase precursors (secondary organic aerosol, SOA). POA is dominated by vehicular emissions in urban
environments (Bhattu, 2018). SOA, which dominates the global budget of OA (Shrivastava et al., 2015), can be of
biogenic and/or anthropogenic origin with biogenic sources dominating on a global scale (Heald et al., 2008). SOA
also generally makes up the biggest mass fraction of OA in urban areas, as observed e.g. in Mexico City (Volkamer
et al., 2006; Kleinman et al., 2008), some heavily urbanized areas in the U.S. (de Gouw et al., 2005; Zhang et al.,
60   2005), and during the severe haze pollution events in the big cities in China (Huang et al., 2014). In European
cities, most of the OA mass observed consists of oxygenated compounds (oxygenated organic aerosol, OOA), and
most OOA is of secondary origin and thus SOA (Lanz et al., 2007; Jimenez et al., 2009; Zhang et al., 2007; El
Haddad et al., 2013). Robinson et al. (2007) suggested that semi-volatile and intermediate VOC may play a
dominant role in SOA formation in urban locations. In order to design effective mitigation strategies for urban air
65   pollution, it is therefore of great importance to identify the sources of OA, and especially SOA, in urban areas.
    Source apportionment of OA has been advanced by the application of positive matrix factorization (PMF) to
aerosol mass spectrometer (AMS) or aerosol chemical speciation monitor (ACSM) data (Canonaco et al., 2015;
Crippa et al., 2014; Ulbrich et al., 2009). However, the distinction of OOA sources (biogenic or anthropogenic) by
AMS- or ACSM-PMF remains difficult due to excessive fragmentation and thus loss of molecular information in
70   the AMS or ACSM. The recent advent of new methods provides more insights into the molecular composition of
OA, such as linear trap quadrupole (LTQ) Orbitrap mass spectrometry (Daellenbach et al., 2019), filter inlet for
gases and aerosols coupled to a high-resolution time-of-flight chemical ionization mass spectrometer (FIGAERO-
HR-ToF-CIMS; Huang et al., 2019), and the newly developed extractive electrospray ionization time-of-flight

2

Atmospheric
Chemistry
and Physics
Discussions

mass spectrometer (EESI-ToF; Qi et al., 2019). Whereas AMS-/ACSM-PMF is not directly able to reveal OOA

75   sources, it separates OOA into factors with different degrees of oxygenation and thus presumed volatility, such as semi-volatile oxygenated organic aerosol (SV-OOA) and low-volatile oxygenated organic aerosol (LV-OOA; Ulbrich et al., 2009; Jimenez et al., 2009; Lanz et al., 2007). Abovementioned state-of-the-art instruments (e.g. Orbitrap, FIGAERO-HR-ToF-CIMS, EESI-ToF) enable the link between the molecular composition of OA and its physicochemical properties by use of molecular information in volatility parameterizations to calculate effective

80   saturation mass concentrations (C_{sat}) of different compounds (Li et al., 2016; Donahue et al., 2011). This can be used to define e.g. volatility basis sets (VBS), a framework that has been proposed and widely used for grouping the organic compounds into volatility classes (or bins) based on their C_{sat} values (Donahue et al., 2006; 2011; 2012; Cappa and Jimenez, 2010).

     Volatility determines whether an organic compound partitions into the particle phase and contributes to OA

85   particulate mass. It is thus an important physicochemical property of OA that influences the lifetime of OA and with that air quality. As a consequence of the connection between a compound's molecular composition and structure with its volatility, different types of OA fall into different categories of volatility. For e.g. OA measured in Mexico City, biomass burning OA (BBOA) was found to be the most volatile, followed by hydrocarbon-like OA (HOA), SV-OOA, and LV-OOA (Cappa and Jimenez, 2010). Isoprene epoxydiol (IEPOX) derived SOA was

90   observed to have the highest volatility of the OA measured in the southeastern U.S. (Lopez-Hilfiker et al., 2016). As ambient particles generally consist of a matrix of thousands of different compounds, OA apparent volatility can also be influenced by particle-phase diffusion limitations, e.g. due to amorphous phase state and/or the presence of a high mass fraction of oligomers (Vaden et al., 2011; Roldin et al., 2014; Cappa and Wilson, 2011; Yli-Juuti et al., 2017; Huang et al., 2018). Overall, the relationship between OA molecular composition and its volatility,

95   and how this relationship is influenced by environmental conditions and particle physicochemical properties, are not well characterized, particularly for field data.

     Here we present detailed chemical composition measurements of OA from July–August 2017 and February–March 2018 in the city of Stuttgart, Germany. We investigate the molecular composition and volatility of OA particles, and discuss their seasonal variations as well as their potential sources. Stuttgart, a city located in

100   southwest Germany with a population of more than 600000 in a metropolitan area of 2.6 million inhabitants, is an important industrial center in Germany. It is situated in the steep valley of the Neckar river, in a "bowl" surrounded by a variety of hills, small mountains, and valleys. The complex topography can prevent the dispersion of air pollutants, and the location is characterized by low wind speeds and weak air circulation (Schwartz et al., 1991; Hebbert and Webb, 2012). Air quality has been a long-standing concern in Stuttgart, as it is one of the most polluted

105   cities in Germany (Schwartz et al., 1991; Süddeutsche Zeitung, 2016; Office for Environmental Protection, 2016); however only few detailed studies are available. For the year 2017, the state environmental protection agency, LUBW (Landesanstalt für Umwelt Baden-Württemberg), attributes 58 % of the annual mean PM_{10} at their monitoring station "Am Neckartor" in downtown Stuttgart to road traffic (45 % abrasion, 7 % exhaust, 6 % secondary formation), 8 % to small and middle size combustion sources, and 27 % to regional background (LUBW,

110   2019). Mayer (1999) showed the temporal variability of urban air pollutants (NO, NO_2, O_3, and O_x (sum of NO_2 and O_3)) caused by motor traffic in Stuttgart based on more than 10 years of observations, with higher NO concentrations in winter and higher O_x concentrations in summer. Bari et al. (2011) characterized air pollutants such as polycyclic aromatic hydrocarbons (PAHs) and other wood smoke tracer compounds (levoglucosan, methoxyphenols) from wood-burning in the residential areas of Dettenhausen (about 30 km south of Stuttgart) and

3

Atmospheric
Chemistry
and Physics
Discussions

115   attributed 57% of the ambient PM_{10} pollution to hardwood combustion during wintertime. Our study therefore adds an important piece of information on air quality in Stuttgart by investigating the chemical composition, physicochemical properties, and potential sources of the OA particles in this city.

2 Methodology

2.1 Measurement site

120   We performed particle and trace gas measurements from July 5th to August 17th, 2017 and from February 5th to March 5th, 2018 in the city of Stuttgart, Germany (48°47'55.1"N, 9°12'13.5"E). The measurement site was located near the park "Unterer Schlossgarten" of Stuttgart and can be classified as an urban background site. The only nearby source is a parcel distribution center with delivery trucks passing by with low frequency during daytime. It was set up on a bridge over a train track about 2.2 km northeast of the Stuttgart main station with frequent train
125   traffic (electric). The air quality monitoring station of LUBW, "Am Neckartor", is 1.5 km southwest and one of the busiest roads in Stuttgart, B14 (LUBW, 2019), is about 360 m southwest of the measurement location.

    All instruments were set up in a temperature-controlled measurement container kept at ~298 K. The container has been described elsewhere (Huang et al., 2019; Shen et al., 2018). All sampling inlets were located 3.7 m above ground level and 1.5 m above the container roof. An overview of instruments and parameters measured is given in
130   Table S1 in the Supplement.

2.2 Meteorological, particle and trace gas measurements

    Temperature, relative humidity, wind direction, wind speed, global radiation, pressure, and precipitation data were measured by a meteorological sensor (WS700, Lufft GmbH; see Table S1). The main wind directions during the campaign were southwest during the summer and northeast during the winter. Trace gases (O_3, CO_2, NO_2, SO_2)
135   were measured with the corresponding sensors (Table S1). Particle number concentrations were recorded with two condensation particle counters (a CPC3022, measuring particles with mobility diameters larger than 7 nm, and a CPC3776, measuring particles with mobility diameters larger than 2.5 nm, both TSI Inc.). Particle size distributions were measured with a nanoscan scanning mobility particle sizer (NanoScan SMPS3910, measuring particles with mobility diameters between 10 nm and 420 nm, TSI Inc.). Black carbon (BC) concentrations were measured with
140   an Aethalometer (AE51, Aethlabs Inc.).

    A high-resolution time-of-flight aerosol mass spectrometer (HR-ToF-AMS, Aerodyne Research Inc., hereafter AMS) equipped with an aerodynamic high-pressure lens (Williams et al., 2013) was deployed to continuously measure total non-refractory particle mass as a function of size (up to 2.5 μm particle aerodynamic diameter d_{va}) at a time resolution of 0.5 min. The AMS inlet was connected to a $PM_{2.5}$ head (flow rate 1 m^3 h^{-1}, Comde-Derenda
145   GmbH) and a stainless steel tube of 3.45 m length (flow rate 0.1 L min^{-1}, residence time 0.9 s). AMS data were analyzed with the AMS data analysis software packages SQUIRREL (version 1.60C) and PIKA (version 1.20C). Polytetrafluoroethylene (PTFE) filters (Zefluor PTFE membrane, 2 μm pore size, 25 mm diameter, Pall Corp.), which were prebaked at 200 °C in an oven overnight and stored in clean filter slides, were deposited during daytime (between 10:00 and 16:00) using a stainless steel filter holder connected to a PM_{10} head (flow rate 1 m^3 h^{-1}, Comde-
150   Derenda GmbH) via a stainless steel tube and conductive tubing of 2.85 m length (flow rate 8.7 L min^{-1} (summer) or 10 L min^{-1} (winter), residence time 0.75 s (summer) or 0.72 s (winter)). Deposition times were varied (20–260

4

min) based on ambient organic mass concentrations in order to achieve similar mass concentrations deposited on the filter to avoid mass loading effects (Huang et al., 2018; Wang and Ruiz, 2018). A total of 21 filter samples were collected in the summer and 10 in the winter. After deposition, each filter sample was stored in a filter slide,

155   wrapped in aluminium foil, and then stored in a freezer at −20 °C until analysis in the laboratory by a filter inlet for gases and aerosols coupled to a high-resolution time-of-flight chemical ionization mass spectrometer (FIGAERO-HR-ToF-CIMS, Aerodyne Research Inc., hereafter CIMS) deploying iodide (I⁻) as reagent ion. Particles collected on the filter were thermally desorbed by a flow of ultra-high purity (99.999 %) nitrogen heated to 200 °C over the course of 35 min. The resulting mass spectral desorption signals are termed thermograms

160   (Lopez-Hilfiker et al., 2014). For individual compounds, signals that peak at distinct desorption temperatures (T_{max}) correlate with their saturation vapor pressure (Lopez-Hilfiker et al., 2015; Mohr et al., 2017); however, interference from isomers with different vapor pressures or thermal fragmentation of larger oligomeric molecules can lead to more complex, multimodal thermograms (Lopez-Hilfiker et al., 2015). Integration of thermograms of individual compounds yields their total particle-phase signal. We assume the sensitivity to be the same for all compounds

165   measured by CIMS (Huang et al., 2019) and convert the signal to mass so that the molecular weight of a compound is taken into account. In this study we do not attempt to derive any atmospheric mass concentrations from these filter measurements, since the actual deposited area of aerosol particles on the filter was larger than the area of the desorption flow, and the deposition was not evenly distributed across the filter. We therefore focus on the molecular composition and volatility distributions of OA particles, their seasonal variations, and the interpretation of these

170   observations for potential sources. In order to correct for filter backgrounds, we collected prebaked clean filters from the measurement site without deposition flow for both winter and summer. Field blank samples for winter and summer were analyzed by CIMS in the laboratory and used for background subtraction.

3 Results and discussion

3.1 Particulate OA mass loadings

175   We observe higher total non-refractory $PM_{2.5}$ mass concentrations measured by AMS in winter (27.0 ± 11.9 µg m⁻³, average ± 1 standard deviation) than in summer (7.1 ± 3.3 µg m⁻³) at this measurement site (Figure S1). Similar observations were also made for other central European locations, e.g. Zurich, Switzerland (Jimenez et al., 2009; Zhang et al., 2007). Reasons for this observation are differences in emission sources between the seasons, boundary layer height dynamics, and/or meteorological conditions (Canonaco et al., 2015; Daellenbach et al., 2019;

180   Baumbach and Vogt, 2003). The surface inversion, which develops by radiative cooling of the ground and is dissolved from the bottom up by solar radiation and heating up of the ground (Baumbach and Vogt, 2003), is expected to be stronger in winter due to lower ambient temperature and global radiation (Figure S2), weaker air circulation (i.e. wind speed, Figure S3), and less precipitation. Air pollutants are therefore more likely to be kept beneath this inversion and have longer local residence time in the atmosphere in winter. While the average organic

185   mass loadings measured by AMS are lower in summer (5.1 ± 3.2 µg m⁻³) than in winter (8.4 ± 5.6 µg m⁻³; see Fig. S1), organics contribute relatively more mass to total non-refractory $PM_{2.5}$ measured by AMS in summer (68.8 ± 13.4 %) compared to winter (34.8 ± 9.5 %; see Fig. S1). Contributions of fragments containing only C and H atoms (CH) or also one oxygen atom (CHO₁) or more than one oxygen atoms (CHO$_{gt1}$) to total OA measured by AMS are similar, with slightly higher contributions of CH and CHO₁ in summer (CH: 29.4 ± 3.9 %; CHO₁: 15.7 ± 1.6

5

Atmospheric
Chemistry
and Physics
Discussions

190 %) compared to winter (CH: 27.9 ± 4.6 %; CHO_1: 15.3 ± 1.9 %) and slightly lower contributions of CHO_{gt1} in summer (14.0 ± 2.6 %) compared to winter (15.8 ± 2.8 %). This is also reflected in the higher elemental oxygen-to-carbon (O:C) ratios measured by AMS in winter (0.61 ± 0.12) than in summer (0.55 ± 0.10). The results imply that OA is more oxygenated in winter. Due to fragmentation of organic molecules during the ionization process in the AMS, molecular information of OA is lost. This information is able to retrieve from the filter samples analyzed

195 by CIMS. Due to the fact that the iodide CIMS is selective towards polarizable and thus oxygenated compounds (Lee et al., 2014), the organic compounds measured by CIMS are oxygenated organic aerosol (OOA). In the next section we will discuss the molecular composition of OOA measured by CIMS.

3.2 Molecular composition of OOA

Figure 1a and 1c show a comparison of CIMS mass spectral patterns of all CHOX compounds ($C_{x \geq 1}H_{y \geq 1}O_{z \geq 1}X_{0-n}$

200 detected as clustered with I^-, with X being different atoms like N, S, Cl, or a combination thereof; 1808 out of a total of 2138 identified compounds and accounting for >96 % of total signals), and CHON compounds only for summer and winter (panels b, d). Mass spectra shown were normalized to the sum of the deposited mass of all detected CHOX compounds. Although the absolute CHOX mass concentrations are uncertain, the time series of the sum of the deposited mass of all detected CHOX compounds follows the trend of the OA concentrations

205 measured by AMS quite well. CHO compounds (compounds containing only C, H, and O atoms) are the dominating group and make up 79.4 ± 3.3 % of total CHOX in summer and 74.6 ± 2.2 % of total CHOX in winter, followed by CHON compounds with 20.1 ± 3.4 % of total CHOX in summer and 24.6 ± 2.4 % of total CHOX in winter. CHON compounds contribute relatively more mass in winter (also reflected in the organic bound nitrate fraction ($OrgNO_3$, i.e., organonitrates) from AMS data (summer: 0.3 ± 0.2 µg m^{-3}; winter: 1.7 ± 1.1 µg m^{-3}),

210 determined assuming an NO_2^+/NO^+ ratio of $OrgNO_3$ of 0.1; Farmer et al., 2010; Kiendler-Scharr et al., 2016; see Figure S4 and S5), while CHO compounds contribute relatively more mass in summer. This is possibly due to the higher daytime O_3 concentrations in summer and higher daytime NO_2 concentrations in winter (Figure S6) as well as different emission sources. Contributions of some biogenic marker compounds are higher in summer (Fig. 1a–b), particularly $C_8H_{12}O_5$ (molecular formula corresponding to 2-hydroxyterpenylic acid identified in α-pinene SOA

215 by Claeys et al., 2009; Kahnt et al., 2014) and $C_8H_{11}O_7N$ (identified in the laboratory as α-pinene oxidation product by Lee et al., 2016). We also observe good correlations (Pearson's R: 0.85; Figure S7a) between our summer mass spectra and the summer daytime mass spectra acquired in 2016 near Karlsruhe (a city in southwest Germany, about 70 km northwest of Stuttgart; Huang et al., 2019), indicative of the regional nature of sources and/or chemistry in summer. We therefore conclude that the majority of the precursor VOC for OOA presented here in summer are

220 most likely of biogenic origin, despite the urban location of the measurement site.

Significantly higher contributions of $C_6H_{10}O_5$ (molecular formula corresponding to levoglucosan, a tracer for biomass burning; Saarnio et al., 2010) are observed in winter compared to summer (Fig. 1c). Besides, higher contributions of $C_6H_5O_3N$, $C_7H_7O_3N$, $C_6H_5O_4N$, and $C_7H_7O_4N$ (molecular formulae corresponding to nitrated phenols, tracers for biomass burning identified by Mohr et al., 2013) are also observed in winter (Fig. 1d). Some

225 of these compounds were also observed in the central European city of Zurich, Switzerland in winter (Daellenbach et al., 2019). We cannot completely exclude that these compounds may have contributions from vehicular emissions (Tong et al., 2016). However, significantly higher contributions of levoglucosan and nitrated phenols indicate that biomass burning emissions are a dominant contributor to OOA in Stuttgart in winter. In addition to compounds from biomass burning, we also observe similar patterns of contributions of CHON compounds with

6

Atmospheric
Chemistry
and Physics

Discussions

Open Access

230   m/z between 300–400 Th (also dominated by $C_8H_{11}O_7N$), and high contributions of $C_8H_{12}O_4$ (molecular formula corresponding to terpenylic acid identified in α-pinene SOA by Claeys et al., 2009) and $C_8H_{12}O_6$ (molecular formula corresponding to 3-methyl-1,2,3-butanetricarboxylic acid (MBTCA) in α-pinene SOA identified by Szmigielski et al., 2007; Müller et al., 2012) in winter. After removing the five biomass burning tracer compounds ($C_6H_{10}O_5$, $C_6H_5O_3N$, $C_7H_7O_3N$, $C_6H_5O_4N$, and $C_7H_7O_4N$), good correlations (Pearson's R: 0.70; Figure S7b) are

235   observed between summer mass spectra and winter mass spectra, indicating that biogenic emissions may also contribute significantly to the OOA particulate mass in winter. In addition, in both summer and winter, contributions of $C_7H_8O_5$ (identified in the laboratory as toluene oxidation product by Hinks et al., 2018; Molteni et al., 2018) are also observed, with relatively higher contributions in winter than in summer, indicating anthropogenic influences related to traffic or industrial activities (EPA, 1994).

240   In the following we will have a closer look at the bulk molecular composition for winter and summer daytime OOA measured by CIMS. Consistent with the O:C ratios measured by AMS (winter: 0.61 ± 0.12; summer: 0.55 ± 0.10), higher O:C ratios are also observed by CIMS in winter (0.89 ± 0.06) compared to summer (0.82 ± 0.02), despite lower ambient temperature and weaker global radiation in winter (see Fig. S2). The AMS O:C ratios are expected to be lower than those of the organic compounds measured by iodide CIMS, as the latter is selective

245   towards oxygenated compounds (Lee et al., 2014). Mass contributions of CHO and CHON with different number of oxygen atoms per molecule to total CHOX compounds as a function of the number of carbon atoms are shown in Figure 2. C_8HO compounds exhibit the highest mass contributions in summer, while C_6HO compounds surpass C_8HO compounds in winter due to the large contributions of levoglucosan ($C_6H_{10}O_5$; see Fig. 2a and 2c). The mass distribution of CHO compounds in winter also exhibits higher contributions from compounds with 1–6 carbon

250   atoms and 4, 5 (levoglucosan), 7–9 oxygen atoms, while in summer higher contributions from compounds with 7–10 carbon atoms and 5–7 oxygen atoms are observed. This indicates that the slightly higher oxidation levels (or O:C ratios) in winter are related to both shorter carbon chain lengths and higher number of oxygen atoms of the OOA compounds compared to summer (see also Figure S8). In addition, relatively higher contributions of compounds with larger number of carbon atoms (C16–23) are also observed in winter (Fig. 2). A similar pattern

255   can be found for CHON compounds (Fig. 2b and 2d). $C_{9–10}HON$ compounds exhibit the highest mass contributions in summer, similar to what we observed in 2016 in summer near the city of Karlsruhe, where these compounds were determined to originate from biogenic VOC emissions (Huang et al., 2019). However, the filters in Stuttgart were deposited during daytime, therefore the chemistry involved in the formation of these CHON compounds likely involves the reaction of organic peroxy radicals (RO_2) with NO_x instead of night-time NO_3 radical chemistry.

260   In winter, C_6HON relative contributions exceed those from $C_{9–10}HON$ compounds, similar to the pattern of CHO compounds, indicative of similar sources (biomass burning emissions). Furthermore, in summer CHON compounds are dominated by compounds with 6–9 oxygen atoms, while in winter significantly higher contributions from compounds with 5–7 carbon atoms and 3–4 oxygen atoms are observed, mostly due to nitrated phenols ($C_{6–7}H_{5,7}O_{3–4}N$; see also Fig. 1d).

265   The results imply the importance of non-fossil OA formation from biogenic and/or biomass burning influences in different seasons even in a city with high traffic emissions mainly based on fossil fuel combustion (LUBW, 2019). This is similar to previous studies in other European cities such as Barcelona, Spain (Mohr et al., 2012) and some megacities in China (Ni et al., 2019). In the next section, we investigate the volatility of OOA compounds measured by CIMS, which can influence their lifetime in the atmosphere and thus air quality.

7

Atmospheric
Chemistry
and Physics

Discussions

3.3 Seasonal changes of volatility of OOA

3.3.1 Volatility distribution

Effective saturation mass concentrations (C_{sat}), a measure for volatility of a compound, were parameterized for
each CHO and CHON compound using the approach by Li et al. (2016). The CHO and CHON compounds were
then grouped into a 25-bin volatility basis set (VBS; Donahue et al., 2006) based on their $\log_{10}C_{sat}$ values (Figure
3). Organic compounds with C_{sat} lower than 10^{-5} µg m^{-3}, between 10^{-4}–10^{-2} µg m^{-3}, and higher than 10^{-1} µg m^{-3} are
termed extremely low volatile organic compounds (ELVOC), low volatile organic compounds (LVOC), and semi-
volatile organic compounds (SVOC), respectively. As shown in Fig. 3a, organic compounds with C_{sat} between
10^2–10^3 µg m^{-3} make up the biggest mass contributions during daytime in both summer and winter, suggesting that
SVOC is the dominating group in both seasons (summer: 74.2 ± 3.4 %; winter: 66.7 ± 4.9 %; see Fig. 3b–c). The
dominating compounds in these volatility bins come from the group of $C_{8–12}HO$ compounds in summer and from
the group of $C_{1–7}HO$ compounds with relatively higher O:C ratios in winter (Figure S9a and S9c). Dominant
compounds are 2-hydroxyterpenylic acid ($C_8H_{12}O_5$) and levoglucosan ($C_6H_{10}O_5$) for summer and winter,
respectively (compare also to Fig. 1a and 1c). Non-negligible contributions from $C_{1–7}HON$ compounds are also
observed in these volatility bins in winter (Fig. S9b and S9d), mainly from nitrated phenols ($C_{6–7}H_{5,7}O_{3–4}N$;
compare also to Fig. 1d). In winter we also observe significant contributions of SVOC with C_{sat} between 10^5–10^6
µg m^{-3} in the particle phase. Since winter is much colder compared to summer (Fig. S2), compounds of higher
volatility are expected to be able to condense in winter. However, we may also have contributions from thermal
decomposition products of oligomers to some of these low-molecular weight SVOC (also reflected in the multi-
mode thermograms for CHOX compounds with 1–5 carbon atoms; see Figure S10). But for the larger compounds,
such as dimers and trimers, contributions of thermal decomposition products become negligible (i.e. thermograms
are unimodal; Huang et al., 2018; Wang and Ruiz, 2018). LVOC and ELVOC, which include compounds with
larger molecular weight, exhibit higher mass contributions in winter (LVOC: 26.4 ± 3.1 %; ELVOC: 6.9 ± 1.9 %)
than in summer (LVOC: 21.7 ± 2.5 %; ELVOC: 4.1 ± 1.1 %; see Fig. 3). The average mass-weighted $\log_{10}C_{sat}$
value is 1.05 ± 0.28 µg m^{-3} for summer and 0.63 ± 0.44 µg m^{-3} for winter.

The results indicate that even though the lower ambient temperatures in winter may lead to increased
partitioning of SVOC into the particle phase, the bulk winter OOA is less volatile. Similar results were also
observed in Zurich, Switzerland by Canonaco et al. (2015) based on AMS data. The lower volatility of OOA in
Stuttgart in winter compared to summer can be partially explained by the higher contributions of compounds with
shorter carbon chain lengths and higher number of oxygen atoms in winter (i.e. higher O:C ratios; see Fig. S8),
and the relatively higher contribution of larger molecules (number of carbons atoms >16; see also Fig. 2).
Differences in aging processes (functionalization, fragmentation, and oligomerization; Jimenez et al., 2009)
between the seasons may also play a role, since Keller and Burtscher (2017) found that aging processes reduce the
volatility of OA from biomass burning.

3.3.2 Variation of the maximum desorption temperatures (T_{max})

Thermograms resulting from the thermal desorption of the filter samples were analyzed. T_{max}, the maximum
desorption temperatures at which the signals of a compound peak, were compared for summer and winter. Figure
4a–b shows the campaign-average high resolution two-dimensional (2D) thermogram of CHOX compounds, a

310   framework developed recently to investigate the OOA thermal desorption behavior over the entire m/z and T_{max} range (Wang and Ruiz, 2018). Each thermogram of each individual compound in the 2D space was normalized to its maximum signal. Due to the CHOX compounds containing at least 1 carbon atom, 1 hydrogen atom, and 1 oxygen atom, and being detected as clustered with I$^-$ (m/z 126.9050 Th), the smallest m/z in the 2D thermogram is 168 Th. As shown in Fig. 4a–b, the majority of the OOA compounds exhibit higher T_{max} with a wider spread across different CHOX compounds in winter (114.4 ± 17.1 °C, average ± 1 standard deviation) compared to summer (96.8 ± 18.2 °C; see also Figure S11). For the summer period, T_{max} decreases from 160 °C to 60 °C for m/z 168–

315   280 Th, stays relatively constant at 60–110 °C for m/z 280–550 Th, and increases from 60 °C to 120 °C for m/z >550 Th; for the winter period, T_{max} decreases from 160 °C to 80 °C for m/z 168–280 Th, stays relatively constant at 2 T_{max} regions (one region at 80–100 °C and the other one at 110–130 °C) for m/z 280–550 Th, and increases from 80 °C to 130 °C for m/z >550 Th (see also Fig. S11). The high T_{max} values for m/z <280 Th (SVOC range) result from multi-mode thermograms with thermal decomposition of larger molecules (Lopez-Hilfiker et al., 2015). A

320   similar picture can be seen in the campaign-average thermograms for the sum of the signals of all CHOX, CHO, and CHON compounds detected (normalized to the maximum; Fig. 4c). The pattern of the summer 2D thermogram in Stuttgart, particularly the "zigzag"-like behavior of e.g. m/z 280–380 Th (see Figure S12a), is comparable to that from alkane-Cl SOA at high RH (67 %) and high NO$_x$ conditions observed by Wang and Ruiz (2018), and was explained by increased hydroxyl functionalization over ketone functionalization. The winter 2D thermogram

325   in Stuttgart also has a "zigzag"-like pattern but less pronounced and at higher T_{max} (see Fig. S12b).

The results indicate a generally lower apparent volatility (i.e. higher T_{max}) of bulk OOA in winter, in agreement with the results based on the C_{sat} parametrization (see also Fig. 3). Recent studies show that T_{max} of a compound can be influenced by isomers (Thompson et al., 2017), thermal fragmentation of larger molecules during the heating of the filter (Lopez-Hilfiker et al., 2015), variations in filter mass loading (Huang et al., 2018; Wang and

330   Ruiz, 2018), and/or differences in particles' viscosity (Huang et al., 2018). Since deposited organic mass loadings on the filter samples were similar for summer and winter, we can exclude a mass loading effect on the T_{max} results presented here. However, we also observed by eye that the filter samples in winter were more blackish, possibly due to the higher black carbon (BC) concentrations during daytime (10:00–16:00) in winter (1247 ± 112 ng m^{-3}) compared to summer (1032 ± 311 ng m^{-3}). If (and how) the higher BC concentrations can affect the desorption

335   behaviors of organic compounds (i.e. interactions between organic compounds and BC) is still unknown and requires further laboratory studies. Higher O:C ratios (Buchholz et al., 2019), and/or higher oligomer mass fractions (Huang et al., 2019; compare to LVOC and ELVOC mass contributions in Fig. 3b–c) have been shown to be correlated with higher T_{max}, which is in agreement with our mass spectral observations in winter. Besides, higher inorganic sulfate concentrations in winter (see Fig. S1) might also play a role in the formation of low volatile

340   but thermally unstable organic compounds which can only be detected as their decomposition products with FIGAERO-CIMS (Gaston et al., 2016; Riva et al., 2019). If assuming that the winter thermograms are more influenced by thermal decomposition of oligomers than the summer thermograms, which artificially shifts the molecular formula-based volatility distribution towards higher volatility, the winter OOA are expected to be even less volatile.

345   **4 Conclusions and atmospheric implications**

9

Atmospheric
Chemistry
and Physics
Discussions

In this paper, chemical composition and volatility of OA particles were investigated during July–August 2017 and February–March 2018 in the city of Stuttgart, one of the most polluted cities in Germany. The average organic mass loadings measured by AMS are lower in summer (5.1 ± 3.2 µg m^{-3}) than in winter (8.4 ± 5.6 µg m^{-3}), but the relative contributions of OA to total non-refractory PM$_{2.5}$ mass measured by AMS are higher in summer ($68.8 \pm$ 13.4 %) compared to winter (34.8 ± 9.5 %). This can be explained by the differences in emission sources between the seasons, boundary layer height dynamics, and/or meteorological conditions (Canonaco et al., 2015; Daellenbach et al., 2019; Baumbach and Vogt, 2003). CIMS mass spectra from filter samples collected at the measurement site during daytime (10:00–16:00) show OOA compounds in summer have O:C ratios of 0.82 ± 0.02 and are more influenced by biogenic emissions (as shown by e.g. tracers of α-pinene oxidation products), while OOA compounds in winter have slightly higher O:C ratios (0.89 ± 0.06) and are more influenced by biomass burning emissions (as shown by e.g. signals of levoglucosan and nitrated phenols).

The apparent volatility of the OOA compounds varies between the two seasons. OOA in winter is found to be less volatile, which is reflected in the higher contributions of LVOC and ELVOC in the VBS, as well as in the higher maximum desorption temperatures (T$_{max}$) of the organic compounds desorbing from the particles deposited on the filter samples. Potential possible reason for the lower apparent volatility of winter OOA is the increased residence time of air masses over Stuttgart due to the stronger surface inversion and thus longer atmospheric aging time of the OOA compounds, leading to a reduction in volatility (Keller and Burtscher, 2017; Jimenez et al., 2009). This is also consistent with the higher O:C ratios and the higher mass contributions of larger molecular-weight LVOC and ELVOC in winter. Since the OOA observed in the winter period also shows influence from biogenic emissions, the sources for the LVOC and ELVOC may partly be biogenic. In addition, interactions between different species and/or particles (particle matrix; Huang et al., 2018) due to higher BC, OA and inorganic concentrations, such as the intermolecular interactions between biomass burning compounds and biogenic/anthropogenic organic compounds and/or the interactions between organic compounds, inorganic compounds, and BC, might also play a role in the reduction of volatility of aerosol particles in winter. Overall, the lower apparent volatility of the winter OOA compounds could be caused by higher O:C ratios, but may also be related to the higher particle viscosity due to the higher mass contributions of larger molecular-weight LVOC and ELVOC, interactions between different species and/or particles deposited on the filter (particle matrix; Huang et al., 2018), and/or thermal decomposition of large molecules.

The results suggest that whereas lower temperatures in winter may lead to increased partitioning of SVOC into the particle phase, this does not result in a higher overall volatility of OOA in winter, and that the difference in sources and/or chemistry between the seasons plays a more important role. Our study provides insights into the seasonal variation of molecular composition and volatility of ambient OA particles during daytime, and into their potential sources, which is important for air pollution mitigation in urban locations. Our study shows the important contributions of non-fossil OA from biogenic and biomass burning even in an urban area with high traffic emissions mainly based on fossil fuel combustion (LUBW, 2019). As a consequence, in addition to mitigating traffic emissions, reducing emissions of anthropogenic OOA precursors from e.g. industry and biomass burning may contribute to reducing the environmental and health effects of air pollution.

Data availability

Data are available upon request to the corresponding author.

385 **Author contributions**

WH operated AMS and took the filter samples during the two field campaigns, analyzed the filters by CIMS in the laboratory, did the CIMS and AMS data analysis, produced all figures, and wrote and edited the manuscript; HS organized the campaign, did the trace gas, CPC, and black carbon data analysis, and provided suggestions for the data interpretation and discussion; XS operated AMS and took the filter samples during the field campaigns; RR

390 took the filter samples during the summer campaign; TL gave general advice and comments for this manuscript; CM provided suggestions for the data analysis, interpretation, discussion, and edited the manuscript. All authors contributed to the final text.

Competing interests

The authors declare no conflict of interest.

400 **References**

Baklanov, A., Molina, L. T., and Gauss, M.: Megacities, air quality and climate, Atmos Environ, 126, 235–249, https://doi.org/10.1016/j.atmosenv.2015.11.059, 2016.

Bari, M. A., Baumbach, G., Kuch, B., and Scheffknecht, G.: Air pollution in residential areas from wood-fired heating, Aerosol Air Qual Res, 11, 749–757, https://doi.org/10.4209/aaqr.2010.09.0079, 2011.

405 Baumbach, G., and Vogt, U.: Influence of inversion layers on the distribution of air pollutants in urban areas, Water, Air, & Soil Pollution: Focus, 3, 67–78, https://doi.org/10.1023/A:1026098305581, 2003.

Bhattu, D.: Primary Organic Aerosols. In: Sharma N., Agarwal A., Eastwood P., Gupta T., Singh A. (eds) Air pollution and Control. Energy, Environment, and Sustainability, Springer, Singapore, 109–117 pp., 2018.

Buchholz, A., Lambe, A. T., Ylisirniö, A., Li, Z., Tikkanen, O.-P., Faiola, C., Kari, E., Hao, L. Q., Luoma, O., Huang,

410 W., Mohr, C., Worsnop, D. R., Nizkorodov, S. A., Yli-Juuti, T., Schobesberger, S., and Virtanen, A.: Insights into the O:C dependent mechanisms controlling the evaporation of α-pinene secondary organic aerosol particles, Atmos Chem Phys, 19, 4061–4073, https://doi.org/10.5194/acp-19-4061-2019, 2019.

Canonaco, F., Slowik, J. G., Baltensperger, U., and Prévôt, A. S. H.: Seasonal differences in oxygenated organic aerosol composition: implications for emissions sources and factor analysis, Atmos Chem Phys, 15, 6993–7002,

415 https://doi.org/10.5194/acp-15-6993-2015, 2015.

Cappa, C. D., and Jimenez, J. L.: Quantitative estimates of the volatility of ambient organic aerosol, Atmos Chem Phys, 10, 5409–5424, https://doi.org/10.5194/acp-10-5409-2010, 2010.

11

Cappa, C. D., and Wilson, K. R.: Evolution of organic aerosol mass spectra upon heating: implications for OA phase and partitioning behavior, Atmos Chem Phys, 11, 1895–1911, https://doi.org/10.5194/acp-11-1895-2011, 2011.

420 Chan, C. K., and Yao, X.: Air pollution in mega cities in China, Atmos Environ, 42, 1–42, https://doi.org/10.1016/j.atmosenv.2007.09.003, 2008.

Claeys, M., Iinuma, Y., Szmigielski, R., Surratt, J. D., Blockhuys, F., Van Alsenoy, C., Böge, O., Sierau, B., Gómez-González, Y., Vermeylen, R., Van der Veken, P., Shahgholi, M., Chan, A. W. H., Herrmann, H., Seinfeld, J. H., and Maenhaut, W.: Terpenylic acid and related compounds from the oxidation of α-pinene: Implications for new

425 particle formation and growth above forests, Environ Sci Technol, 43, 6976–6982, https://doi.org/10.1021/es9007596, 2009.

Crippa, M., Canonaco, F., Lanz, V. A., Äijälä, M., Allan, J. D., Carbone, S., Capes, G., Ceburnis, D., Dall'Osto, M., Day, D. A., DeCarlo, P. F., Ehn, M., Eriksson, A., Freney, E., Hildebrandt Ruiz, L., Hillamo, R., Jimenez, J. L., Junninen, H., Kiendler-Scharr, A., Kortelainen, A.-M., Kulmala, M., Laaksonen, A., Mensah, A., Mohr, C., Nemitz,

430 E., O'Dowd, C., Ovadnevaite, J., Pandis, S. N., Petäjä, T., Poulain, L., Saarikoski, S., Sellegri, K., Swietlicki, E., Tiitta, P., Worsnop, D. R., Baltensperger, U., and Prévôt, A. S. H.: Organic aerosol components derived from 25 AMS data sets across Europe using a consistent ME-2 based source apportionment approach, Atmos Chem Phys, 14, 6159–6176, https://doi.org/10.5194/acp-14-6159-2014, 2014.

D'Amato, G., Bergmann, K. C., Cecchi, L., Annesi-Maesano, I., Sanduzzi, A., Liccardi, G., Vitale, C., Stanziola, A.,

435 and D'Amato, M.: Climate change and air pollution: Effects on pollen allergy and other allergic respiratory diseases, Allergo J Int, 23, 17–23, https://doi.org/10.1007/s40629-014-0003-7, 2014.

Daellenbach, K. R., Kourtchev, I., Vogel, A. L., Bruns, E. A., Jiang, J., Petäjä, T., Jaffrezo, J.-L., Aksoyoglu, S., Kalberer, M., Baltensperger, U., El Haddad, I., and Prévôt, A. S. H.: Impact of anthropogenic and biogenic sources on the seasonal variation of the molecular composition of urban organic aerosols: a field and laboratory study using

440 ultra-high resolution mass spectrometry, Atmos Chem Phys Discuss, 1–40, https://doi.org/10.5194/acp-2018-1128, 2019.

de Gouw, J. A., Middlebrook, A. M., Warneke, C., Goldan, P. D., Kuster, W. C., Roberts, J. M., Fehsenfeld, F. C., Worsnop, D. R., Canagaratna, M. R., Pszenny, A. A. P., Keene, W. C., Marchewka, M., Bertman, S. B., and Bates, T. S.: Budget of organic carbon in a polluted atmosphere: Results from the New England Air Quality Study in

445 2002, J Geophys Res-Atmos, 110, D16305, https://doi.org/10.1029/2004JD005623, 2005.

Donahue, N. M., Robinson, A. L., Stanier, C. O., and Pandis, S. N.: Coupled partitioning, dilution, and chemical aging of semivolatile organics, Environ Sci Technol, 40, 2635-2643, https://doi.org/10.1021/es052297c, 2006.

Donahue, N. M., Epstein, S. A., Pandis, S. N., and Robinson, A. L.: A two-dimensional volatility basis set: 1. organic-aerosol mixing thermodynamics, Atmos Chem Phys, 11, 3303–3318, https://doi.org/10.5194/acp-11-3303-2011,

450 2011.

Donahue, N. M., Kroll, J. H., Pandis, S. N., and Robinson, A. L.: A two-dimensional volatility basis set – Part 2: Diagnostics of organic-aerosol evolution, Atmos Chem Phys, 12, 615–634, https://doi.org/10.5194/acp-12-615-2012, 2012.

El Haddad, I., D'Anna, B., Temime-Roussel, B., Nicolas, M., Boreave, A., Favez, O., Voisin, D., Sciare, J., George,

455 C., Jaffrezo, J.-L., Wortham, H., and Marchand, N.: Towards a better understanding of the origins, chemical composition and aging of oxygenated organic aerosols: case study of a Mediterranean industrialized environment, Marseille, Atmos Chem Phys, 13, 7875–7894, https://doi.org/10.5194/acp-13-7875-2013, 2013.

12

Single Particle Characterisation of Atmospheric Aerosol Particles in Central Europe
Appendix C

Atmospheric
Chemistry
and Physics
Discussions

EPA: Locating and estimating air emissions from sources of toluene, EPA-454/R-93-047, in, Research Triangle Park, North Carolina, United States, 3-1, 3-4, 1994.

460 Farmer, D. K., Matsunaga, A., Docherty, K. S., Surratt, J. D., Seinfeld, J. H., Ziemann, P. J., and Jimenez, J. L.: Response of an aerosol mass spectrometer to organonitrates and organosulfates and implications for atmospheric chemistry, P Natl Acad Sci USA, 107, 6670–6675, https://doi.org/10.1073/pnas.0912340107, 2010.

Fuzzi, S., Baltensperger, U., Carslaw, K., Decesari, S., Denier van der Gon, H., Facchini, M. C., Fowler, D., Koren, I., Langford, B., Lohmann, U., Nemitz, E., Pandis, S., Riipinen, I., Rudich, Y., Schaap, M., Slowik, J. G., Spracklen,

465 D. V., Vignati, E., Wild, M., Williams, M., and Gilardoni, S.: Particulate matter, air quality and climate: lessons learned and future needs, Atmos Chem Phys, 15, 8217–8299, http://doi.org/10.5194/acp-15-8217-2015, 2015.

Gaston, C. J., Lopez-Hilfiker, F. D., Whybrew, L. E., Hadley, O., McNair, F., Gao, H. L., Jaffe, D. A., and Thornton, J. A.: Online molecular characterization of fine particulate matter in Port Angeles, WA: Evidence for a major impact from residential wood smoke, Atmos Environ, 138, 99–107,

470 https://doi.org/10.1016/j.atmosenv.2016.05.013, 2016.

Guttikunda, S. K., Goel, R., and Pant, P.: Nature of air pollution, emission sources, and management in the Indian cities, Atmos Environ, 95, 501–510, https://doi.org/10.1016/j.atmosenv.2014.07.006, 2014.

Hallquist, M., Wenger, J. C., Baltensperger, U., Rudich, Y., Simpson, D., Claeys, M., Dommen, J., Donahue, N. M., George, C., Goldstein, A. H., Hamilton, J. F., Herrmann, H., Hoffmann, T., Iinuma, Y., Jang, M., Jenkin, M. E.,

475 Jimenez, J. L., Kiendler-Scharr, A., Maenhaut, W., McFiggans, G., Mentel, T. F., Monod, A., Prévôt, A. S. H., Seinfeld, J. H., Surratt, J. D., Szmigielski, R., and Wildt, J.: The formation, properties and impact of secondary organic aerosol: current and emerging issues, Atmos Chem Phys, 9, 5155−5236, https://doi.org/10.5194/acp-9-5155-2009, 2009.

Heald, C. L., Henze, D. K., Horowitz, L. W., Feddema, J., Lamarque, J.-F., Guenther, A., Hess, P. G., Vitt, F., Seinfeld,

480 J. H., Goldstein, A. H., and Fung, I.: Predicted change in global secondary organic aerosol concentrations in response to future climate, emissions, and land use change, J Geophys Res-Atmos, 113, D05211, https://doi.org/10.1029/2007JD009092, 2008.

Hebbert, M., and Webb, B.: Towards a Liveable Urban Climate: Lessons from Stuttgart, in: C. Gossop and S. Nan (Eds) Liveable Cities: Urbanising World (ISOCARP 07), Routledge, London, 2012.

485 Hinks, M. L., Montoya-Aguilera, J., Ellison, L., Lin, P., Laskin, A., Laskin, J., Shiraiwa, M., Dabdub, D., and Nizkorodov, S. A.: Effect of relative humidity on the composition of secondary organic aerosol from the oxidation of toluene, Atmos Chem Phys, 18, 1643–1652, https://doi.org/10.5194/acp-18-1643-2018, 2018.

Huang, R.-J., Zhang, Y., Bozzetti, C., Ho, K.-F., Cao, J.-J., Han, Y., Daellenbach, K. R., Slowik, J. G., Platt, S. M., Canonaco, F., Zotter, P., Wolf, R., Pieber, S. M., Bruns, E. A., Crippa, M., Ciarelli, G., Piazzalunga, A.,

490 Schwikowski, M., Abbaszade, G., Schnelle-Kreis, J., Zimmermann, R., An, Z., Szidat, S., Baltensperger, U., El Haddad, I., and Prévôt, A. S. H.: High secondary aerosol contribution to particulate pollution during haze events in China, Nature, 514, 218–222, https://doi.org/10.1038/nature13774, 2014.

Huang, W., Saathoff, H., Pajunoja, A., Shen, X. L., Naumann, K.-H., Wagner, R., Virtanen, A., Leisner, T., and Mohr, C.: α-Pinene secondary organic aerosol at low temperature: chemical composition and implications for particle

495 viscosity, Atmos Chem Phys, 18, 2883–2898, https://doi.org/10.5194/acp-18-2883-2018, 2018.

Huang, W., Saathoff, H., Shen, X., Ramisetty, R., Leisner, T., and Mohr, C.: Chemical characterization of highly functionalized organonitrates contributing to night-time organic aerosol mass loadings and particle growth, Environ Sci Technol, 53, 1165–1174, https://doi.org/10.1021/acs.est.8b05826, 2019.

13

Atmospheric
Chemistry
and Physics

Discussions

Open Access

Jimenez, J. L., Canagaratna, M. R., Donahue, N. M., Prevot, A. S. H., Zhang, Q., Kroll, J. H., DeCarlo, P. F., Allan,
500   J. D., Coe, H., Ng, N. L., Aiken, A. C., Docherty, K. S., Ulbrich, I. M., Grieshop, A. P., Robinson, A. L., Duplissy,
        J., Smith, J. D., Wilson, K. R., Lanz, V. A., Hueglin, C., Sun, Y. L., Tian, J., Laaksonen, A., Raatikainen, T.,
        Rautiainen, J., Vaattovaara, P., Ehn, M., Kulmala, M., Tomlinson, J. M., Collins, D. R., Cubison, M. J., Dunlea,
        E. J., Huffman, J. A., Onasch, T. B., Alfarra, M. R., Williams, P. I., Bower, K., Kondo, Y., Schneider, J., Drewnick,
        F., Borrmann, S., Weimer, S., Demerjian, K., Salcedo, D., Cottrell, L., Griffin, R., Takami, A., Miyoshi, T.,
505   Hatakeyama, S., Shimono, A., Sun, J. Y., Zhang, Y. M., Dzepina, K., Kimmel, J. R., Sueper, D., Jayne, J. T.,
        Herndon, S. C., Trimborn, A. M., Williams, L. R., Wood, E. C., Middlebrook, A. M., Kolb, C. E., Baltensperger,
        U., and Worsnop, D. R.: Evolution of organic aerosols in the atmosphere, Science, 326, 1525−1529,
        https://doi.org/10.1126/science.1180353 2009.
Kahnt, A., Iinuma, Y., Mutzel, A., Böge, O., Claeys, M., and Herrmann, H.: Campholenic aldehyde ozonolysis: a
510   mechanism leading to specific biogenic secondary organic aerosol constituents, Atmos Chem Phys, 14, 719–736,
        https://doi.org/10.5194/acp-14-719-2014, 2014.
Keller, A., and Burtscher, H.: Characterizing particulate emissions from wood burning appliances including secondary
        organic aerosol formation potential, J Aerosol Sci, 114, 21–30, https://doi.org/10.1016/j.jaerosci.2017.08.014,
        2017.
515 Kiendler-Scharr, A., Mensah, A. A., Friese, E., Topping, D., Nemitz, E., Prevot, A. S. H., Äijälä, M., Allan, J.,
        Canonaco, F., Canagaratna, M., Carbone, S., Crippa, M., Dall Osto, M., Day, D. A., De Carlo, P., Di Marco, C. F.,
        Elbern, H., Eriksson, A., Freney, E., Hao, L., Herrmann, H., Hildebrandt, L., Hillamo, R., Jimenez, J. L.,
        Laaksonen, A., McFiggans, G., Mohr, C., O'Dowd, C., Otjes, R., Ovadnevaite, J., Pandis, S. N., Poulain, L., Schlag,
        P., Sellegri, K., Swietlicki, E., Tiitta, P., Vermeulen, A., Wahner, A., Worsnop, D., and Wu, H.-C.: Ubiquity of
520   organic nitrates from nighttime chemistry in the European submicron aerosol, Geophys Res Lett, 43, 7735–7744,
        https://doi.org/10.1002/2016GL069239, 2016.
Kinney, P. L.: Interactions of climate change, air pollution, and human health, Curr Environ Health Rep, 5, 179–186,
        https://doi.org/10.1007/s40572-018-0188-x, 2018.
Kleinman, L. I., Springston, S. R., Daum, P. H., Lee, Y.-N., Nunnermacker, L. J., Senum, G. I., Wang, J., Weinstein-
525   Lloyd, J., Alexander, M. L., Hubbe, J., Ortega, J., Canagaratna, M. R., and Jayne, J.: The time evolution of aerosol
        composition over the Mexico City plateau, Atmos Chem Phys, 8, 1559–1575, https://doi.org/10.5194/acp-8-1559-
        2008, 2008.
Lanz, V. A., Alfarra, M. R., Baltensperger, U., Buchmann, B., Hueglin, C., and Prévôt, A. S. H.: Source apportionment
        of submicron organic aerosols at an urban site by factor analytical modelling of aerosol mass spectra, Atmos Chem
530   Phys, 7, 1503–1522, https://doi.org/10.5194/acp-7-1503-2007, 2007.
Lee, B. H., Lopez-Hilfiker, F. D., Mohr, C., Kurtén, T., Worsnop, D. R., and Thornton, J. A.: An iodide-adduct high-
        resolution time-of-flight chemical-ionization mass spectrometer: Application to atmospheric inorganic and organic
        compounds, Environ Sci Technol, 48, 6309−6317, https://doi.org/10.1021/es500362a, 2014.
Lee, B. H., Mohr, C., Lopez-Hilfiker, F. D., Lutz, A., Hallquist, M., Lee, L., Romer, P., Cohen, R. C., Iyer, S., Kurtén,
535   T., Hu, W. W., Day, D. A., Campuzano-Jost, P., Jimenez, J. L., Xu, L., Ng, N. L., Guo, H. Y., Weber, R. J., Wild,
        R. J., Brown, S. S., Koss, A., de Gouw, J., Olson, K., Goldstein, A. H., Seco, R., Kim, S., McAvey, K., Shepson,
        P. B., Starn, T., Baumann, K., Edgerton, E. S., Liu, J. M., Shilling, J. E., Miller, D. O., Brune, W., Schobesberger,
        S., D'Ambro, E. L., and Thornton, J. A.: Highly functionalized organic nitrates in the southeast United States:

14

Single Particle Characterisation of Atmospheric Aerosol Particles in Central Europe
Appendix C

Contribution to secondary organic aerosol and reactive nitrogen budgets, P Natl Acad Sci USA, 113, 1516–1521,
540   https://doi.org/10.1073/pnas.1508108113, 2016.

Li, Y., Pöschl, U., and Shiraiwa, M.: Molecular corridors and parameterizations of volatility in the chemical evolution of organic aerosols, Atmos Chem Phys, 16, 3327–3344, https://doi.org/10.5194/acp-16-3327-2016, 2016.

Lopez-Hilfiker, F. D., Mohr, C., Ehn, M., Rubach, F., Kleist, E., Wildt, J., Mentel, T. F., Lutz, A., Hallquist, M., Worsnop, D., and Thornton, J. A.: A novel method for online analysis of gas and particle composition: description
545   and evaluation of a Filter Inlet for Gases and AEROsols (FIGAERO), Atmos Meas Tech, 7, 983−1001, https://doi.org/10.5194/amt-7-983-2014, 2014.

Lopez-Hilfiker, F. D., Mohr, C., Ehn, M., Rubach, F., Kleist, E., Wildt, J., Mentel, T. F., Carrasquillo, A. J., Daumit, K. E., Hunter, J. F., Kroll, J. H., Worsnop, D. R., and Thornton, J. A.: Phase partitioning and volatility of secondary organic aerosol components formed from α-pinene ozonolysis and OH oxidation: the importance of accretion
550   products and other low volatility compounds, Atmos Chem Phys, 15, 7765−7776, https://doi.org/10.5194/acp-15-7765-2015, 2015.

Lopez-Hilfiker, F. D., Mohr, C., D'Ambro, E. L., Lutz, A., Riedel, T. P., Gaston, C. J., Iyer, S., Zhang, Z., Gold, A., Surratt, J. D., Lee, B. H., Kurten, T., Hu, W. W., Jimenez, J., Hallquist, M., and Thornton, J. A.: Molecular composition and volatility of organic aerosol in the Southeastern U.S.: Implications for IEPOX derived SOA,
555   Environ Sci Technol, 50, 2200–2209, https://doi.org/10.1021/acs.est.5b04769, 2016.

LUBW: Luftreinhaltepläne für Baden-Württemberg (Grundlagenband 2017), in, LUBW State Institute for the Environment Baden-Württemberg, Karlsruhe, Germany, 2019.

Majewski, G., Czechowski, P. O., Badyda, A., and Brandyk, A.: Effect of air pollution on visibility in urban conditions. Warsaw case study, Environ Prot Eng, 40, 47−64, https://doi.org/10.5277/epe140204, 2014.

560   Marlier, M. E., Jina, A. S., Kinney, P. L., and DeFries, R. S.: Extreme air pollution in global megacities, Curr Clim Change Rep, 2, 15−27, https://doi.org/10.1007/s40641-016-0032-z, 2016.

Mayer, H.: Air pollution in cities, Atmos Environ, 33, 4029−4037, https://doi.org/10.1016/S1352-2310(99)00144-2, 1999.

Mohr, C., DeCarlo, P. F., Heringa, M. F., Chirico, R., Slowik, J. G., Richter, R., Reche, C., Alastuey, A., Querol, X.,
565   Seco, R., Peñuelas, J., Jiménez, J. L., Crippa, M., Zimmermann, R., Baltensperger, U., and Prévôt, A. S. H.: Identification and quantification of organic aerosol from cooking and other sources in Barcelona using aerosol mass spectrometer data, Atmos Chem Phys, 12, 1649−1665, https://doi.org/10.5194/acp-12-1649-2012, 2012.

Mohr, C., Lopez-Hilfiker, F. D., Zotter, P., Prévôt, A. S. H., Xu, L., Ng, N. L., Herndon, S. C., Williams, L. R., Franklin, J. P., Zahniser, M. S., Worsnop, D. R., Knighton, W. B., Aiken, A. C., Gorkowski, K. J., Dubey, M. K.,
570   Allan, J. D., and Thornton, J. A.: Contribution of nitrated phenols to wood burning brown carbon light absorption in Detling, United Kingdom during winter time, Environ Sci Technol, 47, 6316−6324, https://doi.org/10.1021/es400683v, 2013.

Mohr, C., Lopez-Hilfiker, F. D., Yli-Juuti, T., Heitto, A., Lutz, A., Hallquist, M., D'Ambro, E. L., Rissanen, M. P., Hao, L. Q., Schobesberger, S., Kulmala, M., Mauldin III, R. L., Makkonen, U., Sipilä, M., Petäjä, T., and Thornton,
575   J. A.: Ambient observations of dimers from terpene oxidation in the gas phase: Implications for new particle formation and growth, Geophys Res Lett, 44, 2958−2966, https://doi.org/10.1002/2017gl072718, 2017.

Molteni, U., Bianchi, F., Klein, F., El Haddad, I., Frege, C., Rossi, M. J., Dommen, J., and Baltensperger, U.: Formation of highly oxygenated organic molecules from aromatic compounds, Atmos Chem Phys, 18, 1909−1921, https://doi.org/10.5194/acp-18-1909-2018, 2018.

580 Müller, L., Reinnig, M.-C., Naumann, K. H., Saathoff, H., Mentel, T. F., Donahue, N. M., and Hoffmann, T.:
Formation of 3-methyl-1,2,3-butanetricarboxylic acid via gas phase oxidation of pinonic acid - a mass
spectrometric study of SOA aging, Atmos Chem Phys, 12, 1483–1496, https://doi.org/10.5194/acp-12-1483-2012,
2012.

Ni, H., Huang, R.-J., Cao, J., Dai, W., Zhou, J., Deng, H., Aerts-Bijma, A., Meijer, H. A. J., and Dusek, U.: High
585 contributions of fossil sources to more volatile organic carbon, Atmos Chem Phys Discuss, 1−34,
https://doi.org/10.5194/acp-2018-1343, 2019.

Office for Environmental Protection. Luft: Erfolgreiche Maßnahmen zur Luftreinhaltung in Stuttgart:
https://www.stuttgart.de/item/show/15638, 2016.

Qi, L., Chen, M., Stefenelli, G., Pospisilova, V., Tong, Y., Bertrand, A., Hueglin, C., Ge, X., Baltensperger, U., Prévôt,
590 A. S. H., and Slowik, J. G.: Organic aerosol source apportionment in Zurich using an extractive electrospray
ionization time-of-flight mass spectrometry (EESI-TOF): Part II, biomass burning influences in winter, Atmos
Chem Phys Discuss, 1−42, https://doi.org/10.5194/acp-2019-64, 2019.

Riva, M., Heikkinen, L., Bell, D. M., Peräkylä, O., Zha, Q., Schallhart, S., Rissanen, M. P., Imre, D., Petäjä, T.,
Thornton, J. A., Zelenyuk, A., and Ehn, M.: Chemical transformations in monoterpene-derived organic aerosol
595 enhanced by inorganic composition, npj Clim Atmos Sci, 2, 1–9, https://doi.org/10.1038/s41612-018-0058-0, 2019.

Robinson, A. L., Donahue, N. M., Shrivastava, M. K., Weitkamp, E. A., Sage, A. M., Grieshop, A. P., Lane, T. E.,
Pierce, J. R., and Pandis, S. N.: Rethinking organic aerosols: Semivolatile emissions and photochemical aging,
Science, 315, 1259−1262, https://doi.org/10.1126/science.1133061, 2007.

Roldin, P., Eriksson, A. C., Nordin, E. Z., Hermansson, E., Mogensen, D., Rusanen, A., Boy, M., Swietlicki, E.,
600 Svenningsson, B., Zelenyuk, A., and Pagels, J.: Modelling non-equilibrium secondary organic aerosol formation
and evaporation with the aerosol dynamics, gas- and particle-phase chemistry kinetic multilayer model ADCHAM,
Atmos Chem Phys, 14, 7953−7993, https://doi.org/10.5194/acp-14-7953-2014, 2014.

Saarnio, K., Aurela, M., Timonen, H., Saarikoski, S., Teinilä, K., Mäkelä, T., Sofiev, M., Koskinen, J., Aalto, P. P.,
Kulmala, M., Kukkonen, J., and Hillamo, R.: Chemical composition of fine particles in fresh smoke plumes from
605 boreal   wild-land   fires   in   Europe,   Sci   Total   Environ,   408,   2527−2542,
https://doi.org/10.1016/j.scitotenv.2010.03.010, 2010.

Schwartz, J., Spix, C., Wichmann, H. E., and Malin, E.: Air pollution and acute respiratory illness in five German
communities, Environ Res, 56, 1−14, https://doi.org/10.1016/S0013-9351(05)80104-5, 1991.

Seinfeld, J. H., and Pandis, S. N.: Atmospheric Chemistry and Physics: From Air Pollution to Climate Change, 3. ed.,
610 John Wiley & Sons, Inc., Hoboken, New Jersey, 2016.

Shen, X., Ramisetty, R., Mohr, C., Huang, W., Leisner, T., and Saathoff, H.: Laser ablation aerosol particle time-of-
flight mass spectrometer (LAAPTOF): performance, reference spectra and classification of atmospheric samples,
Atmos Meas Tech, 11, 2325−2343, https://doi.org/10.5194/amt-11-2325-2018, 2018.

Shrivastava, M., Easter, R. C., Liu, X., Zelenyuk, A., Singh, B., Zhang, K., Ma, P.-L., Chand, D., Ghan, S., Jimenez,
615 J. L., Zhang, Q., Fast, J., Rasch, P. J., and Tiitta, P.: Global transformation and fate of SOA: Implications of low-
volatility SOA and gas-phase fragmentation reactions, J Geophys Res-Atmos, 120, 4169−4195,
https://doi.org/10.1002/2014JD022563, 2015.

Süddeutsche Zeitung. Stuttgart löst als erste Stadt in Deutschland den Feinstaubalarm aus:
http://www.sueddeutsche.de/panorama/luftverschmutzung-stuttgart-loest-als-erste-stadt-in-deutschland-
620 feinstaubalarm-aus-1.2822775, 2016.

Single Particle Characterisation of Atmospheric Aerosol Particles in Central Europe
Appendix C

Atmospheric
Chemistry
and Physics

Discussions

Open Access

EGU

Szmigielski, R., Surratt, J. D., Gómez-González, Y., Van der Veken, P., Kourtchev, I., Vermeylen, R., Blockhuys, F., Jaoui, M., Kleindienst, T. E., Lewandowski, M., Offenberg, J. H., Edney, E. O., Seinfeld, J. H., Maenhaut, W., and Claeys, M.: 3-methyl-1,2,3-butanetricarboxylic acid: An atmospheric tracer for terpene secondary organic aerosol, Geophys Res Lett, 34, L24811, https://doi.org/10.1029/2007GL031338, 2007.

625 Thompson, S. L., Yatavelli, R. L. N., Stark, H., Kimmel, J. R., Krechmer, J. E., Day, D. A., Hu, W. W., Isaacman-VanWertz, G., Yee, L., Goldstein, A. H., Khan, M. A. H., Holzinger, R., Kreisberg, N., Lopez-Hilfiker, F. D., Mohr, C., Thornton, J. A., Jayne, J. T., Canagaratna, M., Worsnop, D. R., and Jimenez, J. L.: Field intercomparison of the gas/particle partitioning of oxygenated organics during the Southern Oxidant and Aerosol Study (SOAS) in 2013, Aerosol Sci Tech, 51, 30–56, https://doi.org/10.1080/02786826.2016.1254719, 2017.

630 Tong, H., Kourtchev, I., Pant, P., Keyte, I. J., O'Connor, I. P., Wenger, J. C., Pope, F. D., Harrison, R. M., and Kalberer, M.: Molecular composition of organic aerosols at urban background and road tunnel sites using ultra-high resolution mass spectrometry, Faraday Discuss, 189, 51–68, https://doi.org/10.1039/c5fd00206k, 2016.

Ulbrich, I. M., Canagaratna, M. R., Zhang, Q., Worsnop, D. R., and Jimenez, J. L.: Interpretation of organic components from positive matrix factorization of aerosol mass spectrometric data, Atmos Chem Phys, 9, 2891–
635 2918, https://doi.org/10.5194/acp-9-2891-2009, 2009.

Vaden, T. D., Imre, D., Beránek, J., Shrivastava, M., and Zelenyuk, A.: Evaporation kinetics and phase of laboratory and ambient secondary organic aerosol, P Natl Acad Sci USA, 108, 2190−2195, https://doi.org/10.1073/pnas.1013391108, 2011.

Volkamer, R., Jimenez, J. L., San Martini, F., Dzepina, K., Zhang, Q., Salcedo, D., Molina, L. T., Worsnop, D. R.,
640 and Molina, M. J.: Secondary organic aerosol formation from anthropogenic air pollution: Rapid and higher than expected, Geophys Res Lett, 33, L17811, https://doi.org/10.1029/2006GL026899, 2006.

Wang, D. S., and Ruiz, L. H.: Chlorine-initiated oxidation of n-alkanes under high-NOx conditions: insights into secondary organic aerosol composition and volatility using a FIGAERO-CIMS, Atmos Chem Phys, 18, 15535−15553, https://doi.org/10.5194/acp-18-15535-2018, 2018.

645 Williams, L. R., Gonzalez, L. A., Peck, J., Trimborn, D., McInnis, J., Farrar, M. R., Moore, K. D., Jayne, J. T., Robinson, W. A., Lewis, D. K., Onasch, T. B., Canagaratna, M. R., Trimborn, A., Timko, M. T., Magoon, G., Deng, R., Tang, D., Blanco, E. D. L. R., Prévôt, A. S. H., Smith, K. A., and Worsnop, D. R.: Characterization of an aerodynamic lens for transmitting particles greater than 1 micrometer in diameter into the Aerodyne aerosol mass spectrometer, Atmos Meas Tech, 6, 3271−3280, https://doi.org/10.5194/amt-6-3271-2013, 2013.

650 Yli-Juuti, T., Pajunoja, A., Tikkanen, O.-P., Buchholz, A., Faiola, C., Väisänen, O., Hao, L., Kari, E., Peräkylä, O., Garmash, O., Shiraiwa, M., Ehn, M., Lehtinen, K., and Virtanen, A.: Factors controlling the evaporation of secondary organic aerosol from α-pinene ozonolysis, Geophys Res Lett, 44, 2562−2570, https://doi.org/10.1002/2016GL072364, 2017.

Zhang, Q., Worsnop, D. R., Canagaratna, M. R., and Jimenez, J. L.: Hydrocarbon-like and oxygenated organic aerosols
655 in Pittsburgh: insights into sources and processes of organic aerosols, Atmos Chem Phys, 5, 3289−3311, https://doi.org/10.5194/acp-5-3289-2005, 2005.

Zhang, Q., Jimenez, J. L., Canagaratna, M. R., Allan, J. D., Coe, H., Ulbrich, I., Alfarra, M. R., Takami, A., Middlebrook, A. M., Sun, Y. L., Dzepina, K., Dunlea, E., Docherty, K., DeCarlo, P. F., Salcedo, D., Onasch, T., Jayne, J. T., Miyoshi, T., Shimono, A., Hatakeyama, S., Takegawa, N., Kondo, Y., Schneider, J., Drewnick, F.,
660 Borrmann, S., Weimer, S., Demerjian, K., Williams, P., Bower, K., Bahreini, R., Cottrell, L., Griffin, R. J., Rautiainen, J., Sun, J. Y., Zhang, Y. M., and Worsnop, D. R.: Ubiquity and dominance of oxygenated species in

17

organic aerosols in anthropogenically-influenced Northern Hemisphere midlatitudes, Geophys Res Lett, 34, L13801, https://doi.org/10.1029/2007GL029979, 2007.

665

Atmospheric
Chemistry
and Physics
Discussions

Figure 1. CIMS mass spectra comparison of CHOX compounds (separated into CHO, CHON and other compounds) (a), and CHON compounds (b) in the summer period, CHOX compounds (c) and CHON compounds (b) in the winter period as a function of *m/z* (includes mass of I⁻ ion; *m/z* 126.9050 Th). Mass contributions of each compound were normalized to the sum of the mass of all detected CHOX compounds.

670

19
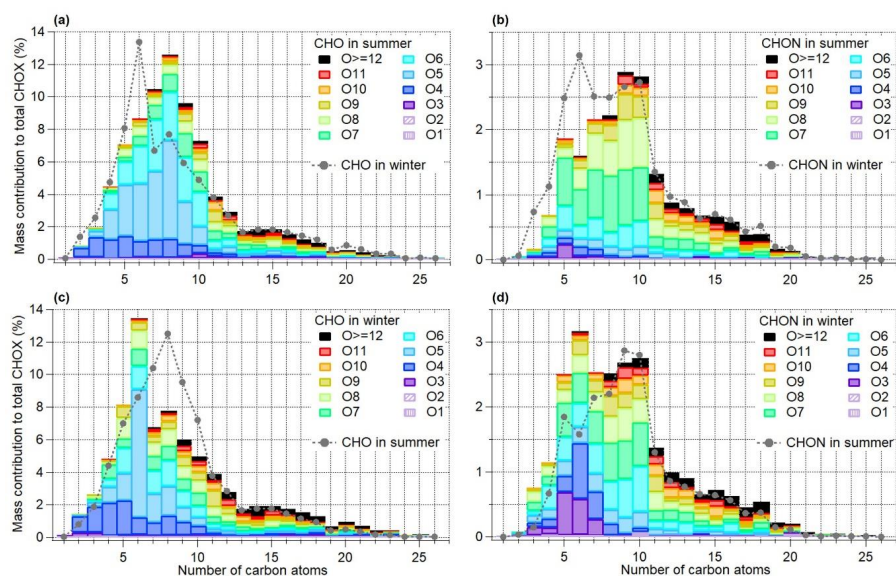
Figure 2. Mass contribution of CHO and CHON compounds with different number of oxygen atoms as a function of the number of carbon atoms to total CHOX compounds for the summer (a, c) and winter (b, d) periods. The corresponding distribution for the other season is plotted as a gray dotted line.

20

Atmospheric
Chemistry
and Physics
Discussions

Open Access

675
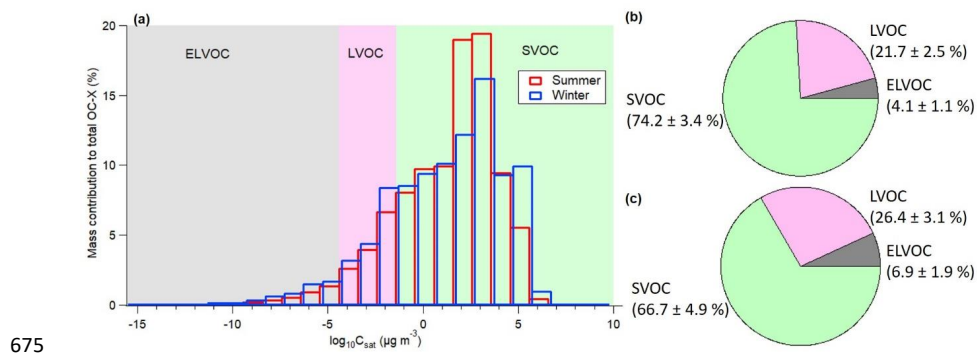
Figure 3. (a) Volatility distribution based on the molecular formula parameterization by Li et al. (2016); resulting pie chart for the mass contributions of SVOC, LVOC, and ELVOC in the summer (b) and winter (c) periods.

21
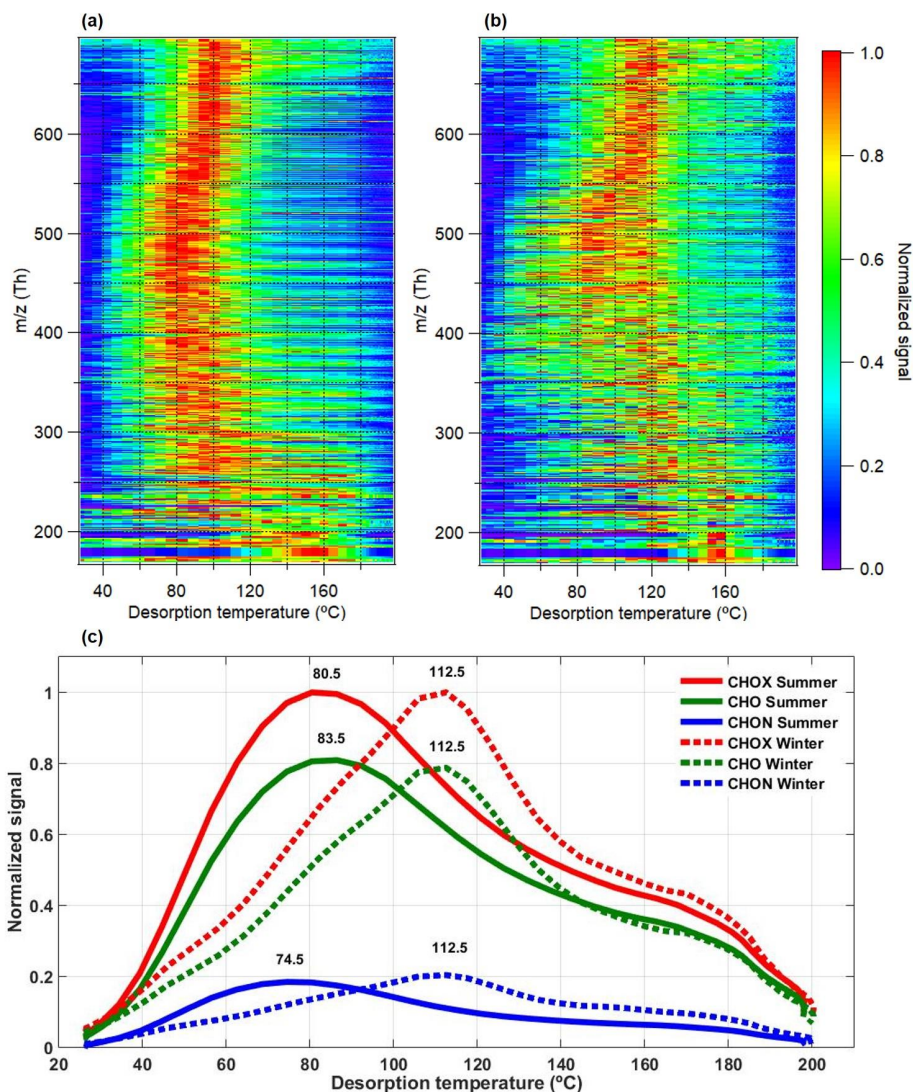
Figure 4. Comparison of campaign-average high resolution two-dimensional (2D) thermograms of CHOX compounds for the summer (a) and winter (b) periods vs m/z (includes mass of I⁻ ion; m/z 126.9050 Th), and the sum thermograms of CHOX, CHO, and CHON compounds (c). The 2D thermograms and sum thermograms were normalized to their maximum values.

680

22

Appendix C.4 α-Pinene secondary organic aerosol at low temperature: Chemical composition and implications for particle viscosity

Atmospheric
Chemistry
and Physics
Open Access

α-Pinene secondary organic aerosol at low temperature: chemical composition and implications for particle viscosity

Wei Huang[1,2], Harald Saathoff[1], Aki Pajunoja[3], Xiaoli Shen[1,2], Karl-Heinz Naumann[1], Robert Wagner[1], Annele Virtanen[3], Thomas Leisner[1], and Claudia Mohr[1,4]

[1]Institute of Meteorology and Climate Research, Karlsruhe Institute of Technology,
76344 Eggenstein-Leopoldshafen, Germany
[2]Institute of Geography and Geoecology, Karlsruhe Institute of Technology,
76131 Karlsruhe, Germany
[3]Department of Applied Physics, University of Eastern Finland, Kuopio, 80101, Finland
[4]Department of Environmental Science and Analytical Chemistry, Stockholm University,
Stockholm, 11418, Sweden

Correspondence: Claudia Mohr (claudia.mohr@aces.su.se)

Abstract. Chemical composition, size distributions, and degree of oligomerization of secondary organic aerosol (SOA) from α-pinene ($C_{10}H_{16}$) ozonolysis were investigated for low-temperature conditions (223 K). Two types of experiments were performed using two simulation chambers at the Karlsruhe Institute of Technology: the Aerosol Preparation and Characterization (APC) chamber, and the Aerosol Interaction and Dynamics in the Atmosphere (AIDA) chamber. Experiment type 1 simulated SOA formation at upper tropospheric conditions: SOA was generated in the AIDA chamber directly at 223 K at 61 % relative humidity (RH; experiment termed "cold humid", CH) and for comparison at 6 % RH (experiment termed "cold dry", CD) conditions. Experiment type 2 simulated SOA uplifting: SOA was formed in the APC chamber at room temperature (296 K) and < 1 % RH (experiment termed "warm dry", WD) or 21 % RH (experiment termed "warm humid", WH) conditions, and then partially transferred to the AIDA chamber kept at 223 K, and 61 % RH (WDtoCH) or 30 % RH (WHtoCH), respectively. Precursor concentrations varied between 0.7 and 2.2 ppm α-pinene, and between 2.3 and 1.8 ppm ozone for type 1 and type 2 experiments, respectively. Among other instrumentation, a chemical ionization mass spectrometer (CIMS) coupled to a filter inlet for gases and aerosols (FIGAERO), deploying I^- as reagent ion, was used for SOA chemical composition analysis.

For type 1 experiments with lower α-pinene concentrations and cold SOA formation temperature (223 K), smaller particles of 100–300 nm vacuum aerodynamic diameter (d_{va}) and higher mass fractions (> 40 %) of adducts (molecules with more than 10 carbon atoms) of α-pinene oxidation products were observed. For type 2 experiments with higher α-pinene concentrations and warm SOA formation temperature (296 K), larger particles (∼ 500 nm d_{va}) with smaller mass fractions of adducts (< 35 %) were produced.

We also observed differences (up to 20 °C) in maximum desorption temperature (T_{max}) of individual compounds desorbing from the particles deposited on the FIGAERO Teflon filter for different experiments, indicating that T_{max} is not purely a function of a compound's vapor pressure or volatility, but is also influenced by diffusion limitations within the particles (particle viscosity), interactions between particles deposited on the filter (particle matrix), and/or particle mass on the filter. Highest T_{max} were observed for SOA under dry conditions and with higher adduct mass fraction; lowest T_{max} were observed for SOA under humid conditions and with lower adduct mass fraction. The observations indicate that particle viscosity may be influenced by intra- and inter-molecular hydrogen bonding between oligomers, and particle water uptake, even under such low-temperature conditions.

Our results suggest that particle physicochemical properties such as viscosity and oligomer content mutually influence each other, and that variation in T_{max} of particle desorptions may have implications for particle viscosity and particle matrix effects. The differences in particle physicochemical properties observed between our different experiments demonstrate the importance of taking experimental conditions into consideration when interpreting data from laboratory studies or using them as input in climate models.

---

1 Introduction

Atmospheric aerosols have adverse impacts on human health (Nel, 2005; Rückerl et al., 2011) and rank among the main drivers of anthropogenic climate change (IPCC, 2013). Organic compounds make up a large fraction (20–90 %) of submicron particulate mass (Zhang et al., 2007; Murphy et al., 2006; Jimenez et al., 2009; Ehn et al., 2014). Organic aerosol (OA) particles can be directly emitted into the atmosphere from sources such as fossil fuel combustion and forest fires (primary organic aerosol, POA), or be formed in the atmosphere from the oxidation of gas-phase precursors (secondary organic aerosol, SOA). Secondary organic aerosol dominates the global budget of OA (Shrivastava et al., 2015), and its gaseous precursors (volatile organic compounds, VOCs) can be of both biogenic and anthropogenic origin. In the atmosphere, VOCs are oxidized by the hydroxyl radical (OH), ozone (O_3), or the nitrate radical (NO_3) into semi-volatile, low-volatility, and/or extremely low-volatility organic compounds (SVOC, LVOC/ELVOC), which can partition into the particle phase and lead to the formation of SOA (Jimenez et al., 2009; Hallquist et al., 2009; Jokinen et al., 2015; Ehn et al., 2014). Due to the wealth of precursors and formation mechanisms in both the gas and particle phase, SOA is very complex and can contain thousands of compounds with a wide range of functionalities, volatilities, and other physicochemical properties (Hallquist et al., 2009; Nozière et al., 2015).

Global estimates indicate that biogenic VOC emissions ($539\,Tg\,C\,a^{-1}$) dominate over anthropogenic VOC emissions ($16\,Tg\,C\,a^{-1}$), and that the global SOA production from biogenic VOCs ($22.9\,Tg\,C\,a^{-1}$) outpaces that from anthropogenic VOCs ($1.4\,Tg\,C\,a^{-1}$) as well (Heald et al., 2008). An important class of biogenic VOCs is monoterpenes ($C_{10}H_{16}$), emitted in substantial amounts ($43\,Tg\,C\,a^{-1}$; Heald et al., 2008) by vegetation (e.g., many coniferous trees, notably pine). One of the most abundant monoterpenes is α-pinene (24.8 % mass contribution to global monoterpenes emissions; Kanakidou et al., 2005). Secondary organic aerosol from monoterpenes is very important in the boreal regions in summertime, and the fraction of total SOA mass from monoterpene oxidation products is estimated to be ~ 15 % globally (Heald et al., 2008).

SOA formation from α-pinene has been studied extensively in smog chambers (e.g., Kristensen et al., 2016; Denjean et al., 2015; McVay et al., 2016), although studies covering a wide temperature range are rare (Saathoff et al., 2009; Donahue et al., 2012). The reactions of α-pinene with O_3 as well as radicals OH and NO_3 lead to a large suite of oxygenated reaction products including aldehydes, oxy-aldehydes, carboxylic acids, oxy-carboxylic acids, hydroxy-carboxylic acids, dicarboxylic acids, organic nitrates, etc. (Winterhalter et al., 2003; Kanakidou et al., 2005). Aerosol yields vary for the different oxidants, and the most important process with regard to aerosol mass formation from the oxidation of α-pinene is the reaction with O_3 (Kanakidou et al., 2005).

The molecular formulae of organic species accounting for ~ 58–72 % of SOA mass from α-pinene ozonolysis have been identified, and can largely be grouped into monomers ($C_{8-10}H_{12-16}O_{3-6}$, oxidation products from one α-pinene molecule) and dimers ($C_{14-19}H_{24-28}O_{5-9}$, oxidation products from two α-pinene molecules; Zhang et al., 2015). Major dimers of the α-pinene SOA system have been structurally elucidated as a *cis*-pinyl-diaterpenyl ester ($C_{17}H_{26}O_8$; MW 358; Yasmeen et al., 2010) and a *cis*-pinyl-hydroxypinonyl ester ($C_{19}H_{28}O_7$; MW 368; Müller et al., 2008). Autoxidation processes can form highly oxidized molecules (HOM; elemental oxygen-to-carbon ratios of 0.7–1.3; Ehn et al., 2012), monomers and dimers, which have been shown to play an important role in atmospheric new particle formation (Ehn et al., 2014). Less oxygenated dimers (e.g., esters and other accretion products), some of which have similarly low volatility as HOM, and for many of which formation mechanisms are still not known, are major products in aerosol particles from α-pinene ozonolysis, and have been proposed to be key components in organic particle growth in field and laboratory (Kristensen et al., 2014, 2016; Tröstl et al., 2016; Zhang et al., 2015; Mohr et al., 2017).

SOA is highly dynamic and continually evolves in the atmosphere, becoming increasingly oxidized, less volatile, and more hygroscopic (Jimenez et al., 2009). As a consequence, SOA residence time in the atmosphere at different temperature (T) and relative humidity (RH) conditions strongly influences the particles' physicochemical properties such as phase state, and thus their effects on air quality and climate (Tsigaridis et al., 2006; Jimenez et al., 2009; Shiraiwa et al., 2017). Biogenic SOA has been shown to exist in phase states ranging from liquid to amorphous (semi-)solid in the atmosphere (Virtanen et al., 2010; Bateman et al., 2016; Shiraiwa et al., 2017). The phase state can affect gas uptake, gas–particle partitioning, diffusion, the particles' ability to act as cloud condensation nuclei (CCN) and/or ice nuclei (IN), and the particles' lifetime in the atmosphere (Shiraiwa et al., 2011; Price et al., 2015; Lienhard et al., 2015). Water diffusion coefficients in the water-soluble fraction of α-pinene SOA were measured for temperatures between 240 and 280 K. The results showed that water diffusion slowed

down as temperature decreased, indicating increasing viscosity of SOA particles (Price et al., 2015). Diffusivity of organic molecules in SOA particles can show similar behavior, leading to large equilibration times under dry conditions (Shiraiwa et al., 2011) and/or cool conditions (Bastelberger et al., 2017). Observations of particle shape transformations (Järvinen et al., 2016), coalescence times (Pajunoja et al., 2014), and the particle bounce factor (BF; Virtanen et al., 2010; Pajunoja et al., 2015) are other parameters used to indicate the phase state and viscosity of particles. At dry conditions and at temperatures close to room temperature, the viscosity of α-pinene SOA is assumed to range from 10^5 to (higher than) 10^8 Pa s (Song et al., 2016; Renbaum-Wolff et al., 2013; Pajunoja et al., 2014), which corresponds to a semisolid state (Shiraiwa et al., 2011), whereas at an RH of about 90 % and room temperature its consistency is comparable to that of honey (~ 10 Pa s: Renbaum-Wolff et al., 2013). Generally, SOA is more viscous in cool and dry conditions (shown, e.g., for α-pinene SOA at temperatures ranging from 235 to 295 K and RH ranging from 35 to 90 %; Song et al., 2016; Järvinen et al., 2016; Shiraiwa et al., 2011; Wang et al., 2015; Kidd et al., 2014).

Differences in α-pinene SOA chemical composition were observed for different SOA formation temperatures and RH conditions, such as lower oligomer content at higher RH (up to 87 %, Kidd et al., 2014) or lower temperature (285 K, Zhang et al., 2015). Given that the differences in physicochemical properties of SOA particles observed as a function of temperature and RH only cover part of the range of atmospheric values, it is of great importance for our understanding of SOA climate effects to expand the investigation of SOA evolution to atmospherically relevant conditions, especially at low temperature. More knowledge on SOA at temperature and RH conditions that are representative of the upper troposphere, where SOA particles can be transported to or formed in situ, is required in order to understand their potential importance for phase state, morphology, chemical composition, and thus ultimately SOA cloud formation potential (Zhang et al., 2015; Virtanen et al., 2010; Lienhard et al., 2015; Frege et al., 2018). However, such studies, particularly of SOA at low temperature, are still scarce.

In the present work, we investigate the chemical composition, size distributions, and degree of oligomerization of α-pinene SOA formed at four different conditions corresponding to temperatures of 223 and 296 K and RH between < 1 and 61 % in order to simulate SOA uplifting to and SOA formation in the upper troposphere. Samples for chemical ionization mass spectrometric analysis were taken from the Aerosol Interaction and Dynamics in the Atmosphere (AIDA) chamber at 223 K and collected on Teflon filters at two different times after starting the experiments. We discuss differences in these mass spectra and corresponding molecular desorption profiles when heating the filters from room temperature to 200 °C as well as possible implications for
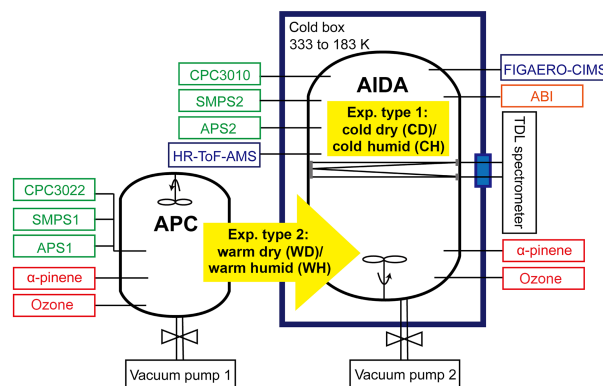
Figure 1. Simple schematic and conditions for the two types of experiments (modified from Wagner et al., 2017). Both chambers at IMK (APC and AIDA) were used in this study. Instruments are annotated in green, blue, and orange, and precursor gases in red. More detailed information on the instruments and precursor gases are explained in the text.

mutual interactions between particle chemical composition and viscosity.

2 Methodology

2.1 Environmental chambers and experimental design

The data for this study were acquired during a 2-month measurement campaign (SOA15) in October and November 2015 at environmental chambers of the Institute of Meteorology and Climate Research (IMK) at the Karlsruhe Institute of Technology (KIT). The measurement campaign investigated yields, physical properties, and chemical composition of SOA from α-pinene ozonolysis as a function of precursor concentration, temperature, RH, and the ice nucleation abilities of the SOA particles (Wagner et al., 2017). The focus on ice cloud formation allowed for the investigation of the particles' physicochemical properties at temperatures as low as 223 K (representative of conditions in the upper troposphere at 8–12 km altitude at the mid-latitudes), a range where detailed characterization is largely missing. Here, we discuss a subset (Table 1) of the large dataset of the SOA15 campaign that is based on experiments investigating the influence and mutual interaction of particle chemical composition and viscosity shortly after SOA formation and after a residence time of ~ 3.5 h. Particles were formed at different temperatures (223–296 K) and RH (< 1–61 %) conditions using both environmental chambers available at IMK (see Fig. 1).

The AIDA (Aerosol Interaction and Dynamics in the Atmosphere) aerosol and cloud chamber is an 84.3 m^3 sized aluminum vessel. It can be operated in the temperature range of 183 to 333 K, pressure range of 1 to 1000 hPa, RH from close to 0 to 200 %, and at different warming and cooling

Table 1. Experimental conditions and precursor concentrations for the four experiments discussed in this study: CH and CD (type 1); WDtoCH and WHtoCH (type 2). Total organic mass (Total org.), CHOI mass concentrations, and elemental oxygen to carbon (O : C) ratios are given for $t0$ and $t1$. RH values (with respect to water) from the APC chamber were measured at room temperature (296 K).

Exp. name	SOA position	T (K)	RH (%)	α-Pinene added (ppm)	O$_3$ added (ppm)	Total org. ($\mu g\,m^{-3}$)	Total CHOI ($\mu g\,m^{-3}$)	O : C
CH	AIDA	223	61.0	0.714	2.3	67.5/319.5	97.8/247.6	0.26/0.30
CD	AIDA	223	6.0	0.714	2.3	260.1/440.1	110.6/160.4	0.28/0.29
WDtoCH	APC → AIDA	296 → 223	<1 → 60.6	2.2	1.8	50.9/48.5	40.7/39.3	0.34/0.34
WHtoCH	APC → AIDA	296 → 223	21 → 30.3	2.2	1.8	64.2/58.4	23.4/23.3	0.36/0.37

rates (Schnaiter et al., 2016; Möhler et al., 2003; Saathoff et al., 2009).

The APC (Aerosol Preparation and Characterization) chamber (Möhler et al., 2008) is a 3.7 m^3 sized stainless steel vessel, situated at a distance of 3 m from AIDA and connected to it with a 7 m stainless steel tube of 24 mm inner diameter. The APC chamber can only be operated at room temperature (296 K) and was used to prepare SOA particles in a reproducible manner (Wagner et al., 2017).

We present two types of chamber experiments (Fig. 1): for the first type, SOA from α-pinene ozonolysis was directly formed at 223 K in the AIDA chamber. For the second type, SOA was first produced in the APC chamber kept at room temperature and then transferred to the AIDA chamber kept at 223 K. The second type of experiment thus represents a simplified simulation of particle formation in the boundary layer and subsequent uplifting of particles to higher altitudes with lower temperature conditions. We stress here that for both types of experiments, the particles were sampled from the cold AIDA chamber for chemical analysis. The detailed conditions for these two types of experiments are listed in Table 1. During the first type of chamber experiment, SOA was formed by reaction of an excess of O$_3$ (initially 2.3 ppm generated by silent discharge in pure oxygen, Semozon 030.2 discharge generator, Sorbios GmbH) with α-pinene (initially 0.714 ppm, 99 %, Aldrich) in the dark AIDA chamber at 223 K at 61 % RH (experiment termed "cold humid", CH) or 6 % RH (experiment termed "cold dry", CD) conditions. For the second type of chamber experiment, SOA was first formed with an excess of O$_3$ (initially 1.8 ppm) and 2.2 ppm α-pinene in the dark APC chamber at room temperature (296 K), <1 % RH (experiment termed "warm dry", WD) or 21 % RH (experiment termed "warm humid", WH) conditions. After a residence time of 1–1.5 h in the APC chamber, its pressure was increased by 5 hPa compared to AIDA, and a fraction of the SOA particles was then transferred to the dark AIDA chamber kept at 223 K at 61 % RH (WDtoCH) or 30 % RH (WHtoCH), respectively, resulting in particle number concentrations ranging between 1500 and 2200 cm^{-3} in the AIDA chamber. No OH scavenger was used during SOA formation, and RH was kept constant in AIDA during the course of the experiments. The time series of total parti-

cle mass for experiment type 1 (particles formed in situ in AIDA, CH) and experiment type 2 (aerosols formed in APC and transferred to AIDA, WDtoCH) are shown in Fig. 2. The times $t0$ (right after SOA formation in CD and CH, or SOA transfer in WDtoCH and WHtoCH) and $t1$ (∼ 3.5 h later) indicate the points in experiment time which were used for the investigation of the physicochemical evolution of α-pinene SOA.

2.2 Temperature and relative humidity measurements

Temperature (T) in the AIDA chamber was measured by in-house thermocouples (NiCrNi) and in-house PT 100 temperature sensors with an accuracy of ±3 %, which are regularly calibrated with reference sensors traceable to standards of the National Institute of Standards and Technology (NIST). Under static conditions, gas temperature in the AIDA chamber deviated by less than 0.3 K in time and in space. Water vapor concentrations in the AIDA chamber were measured by a in-house tunable diode laser (TDL) spectrometer with an accuracy of ±5 % (Fahey et al., 2014; Skrotzki et al., 2013) and by a dew point mirror hygrometer (MBW373LX, MBW Calibration Ltd.) with an accuracy of ±1 % traceable to different national metrology standards including Federal Institution of Physical Technology (PTB), National Physical Laboratory (NPL), Federal Office of Metrology and Surveying (BEV) and NIST. Both instruments agree within ±2 %. RH in the AIDA chamber was calculated using the measured water vapor concentrations and temperature based on the saturation water vapor pressures given by Murphy and Koop (2005), resulting in an accuracy of ±5 %.

2.3 Particle and gas measurements

Number concentrations of SOA particles formed in APC or AIDA were recorded with two condensation particle counters (CPC3022, CPC3010; TSI Inc.) outside the temperature-controlled housing of the chambers via stainless steel tubes extending 35 cm into the AIDA chamber. The absolute uncertainty of the number concentrations is estimated to be ±20 % by comparison of the different CPCs with each other and with an electrometer (3068, TSI Inc.). Particle size distributions were sampled in the same way from both cham-
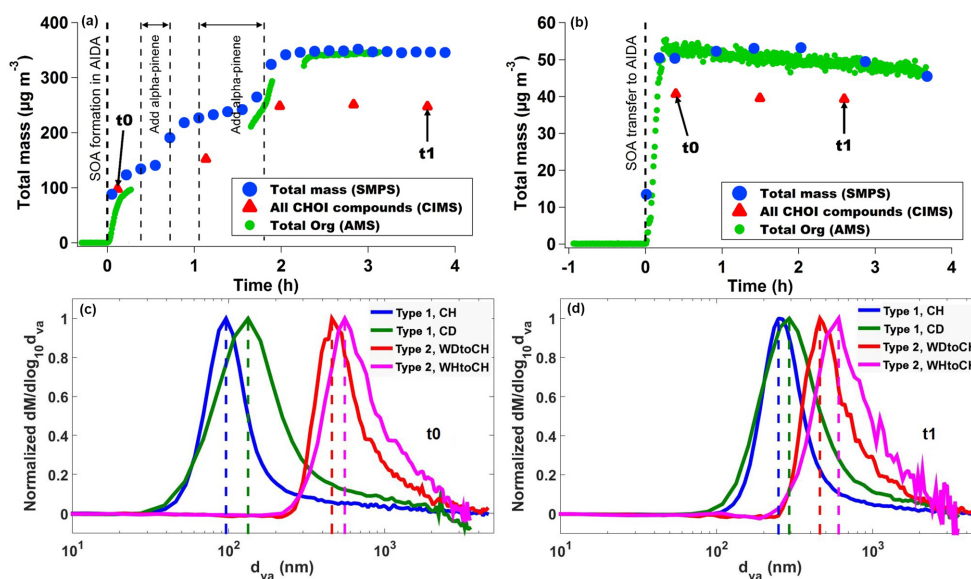
Figure 2. (a) Particle mass concentrations derived from SMPS size distributions (blue circles), CHOI mass concentrations measured by CIMS (red triangles), and organic mass concentrations measured by AMS (green circles) representative of type 1 experiments (here CH), **(b)** representative of type 2 experiments (here WDtoCH). Data were not wall-loss-corrected. $t0$ and $t1$ indicate points in time used for comparisons in this study. Averaged size distributions measured by AMS at $t0$ **(c)** and **(d)** $t1$ for the four experiments.

bers with scanning mobility particle sizers (SMPS; differential mobility analyzer (DMA) 3071 connected to a CPC 3010, TSI Inc.). Mass concentrations were derived from integrated number size distributions and their conversions to mass using their corresponding calculated particle density (1.3–1.5 kg m^{-3}). Particle densities were calculated using the ratio of vacuum aerodynamic diameter (d_{va}) measured by a high-resolution time-of-flight aerosol mass spectrometer (HR-ToF-AMS, hereafter AMS; Aerodyne Research Inc.) and mobility diameter (d_m) measured by the SMPS, assuming particle sphericity (shape factor = 1). O$_3$ concentrations were measured by an O$_3$ monitor (O$_3$ 41M, Environment S.A.). The AMS was connected to the AIDA chamber by a stainless steel tube of 1.35 m length (flow rate 0.1 L min^{-1}, residence time 1.6 s). It was equipped with a high-pressure lens (HPL; Williams et al., 2013) and continuously measured total organic particle mass as a function of size (up to 2.5 μm particle d_{va}) at a time resolution of 0.5 min. Elemental oxygen-to-carbon (O : C) and hydrogen-to-carbon (H : C) ratios were derived using the EALight_1_06 procedure in the AMS data analysis software package SQUIRREL (version 1.57H; Canagaratna et al., 2015). An AMS collection efficiency (CE) of 0.4–0.5 was used, except for the CH experiment where CE was 0.7, likely due to higher particle water content (Middlebrook et al., 2012). AMS mass concentrations compare well with the total mass derived from SMPS (slopes are between 0.87 and 1.04 except for the slope of 2.2 in the CD experiment, possibly due to the lower transmission efficiency in the aerodynamic lens of the AMS

for sub-100 nm particles; Pearson's correlation coefficients are between 0.87 and 0.98 for the experiments presented here). Individual organic compounds in both the gas and particle phase were measured with a Filter Inlet for Gases and AEROsols coupled to a high-resolution time-of-flight chemical ionization mass spectrometer (FIGAERO-HR-ToF-CIMS, Aerodyne Research Inc., hereafter CIMS) deploying iodide ions (I$^-$) as reagent ions (Lopez-Hilfiker et al., 2014; Lee et al., 2014). During the gas-phase measurement, gases were sampled via a fluorinated ethylene propylene (FEP) tube of 0.83 m length, while particles were simultaneously collected on a Teflon (Polytetrafluoroethylene, PTFE) filter via a separate sampling port (stainless steel tube of 0.66 m length, flow rate 5 L min^{-1}, residence time 0.9 s). At regular intervals (5–20 min; see Table S1 in the Supplement), the gas-phase measurement was switched off and particles on the filter were desorbed by a flow of ultra-high-purity (99.999 %) nitrogen heated from room temperature to 200 °C over the course of 35 min. The resulting mass spectral signal evolutions as a function of desorption temperature are termed thermograms (Lopez-Hilfiker et al., 2014). Single-mode thermograms of a compound with signal maxima occurring at distinct desorption temperatures (T_{max}), which correlate with the compound's enthalpy of sublimation, can be used to infer its saturation vapor pressure (Lopez-Hilfiker et al., 2015; Mohr et al., 2017). Multi-mode thermograms indicate contributions from isomers having different vapor pressures, or thermal fragmentation of larger molecules during the heating of the filter (Lopez-Hilfiker et al., 2015). Integration of ther-

mograms of individual compounds yielded their total signal in counts per deposition, which were converted to mass concentrations using a sensitivity of 22 counts s^{-1} ppt^{-1} (collisional limit; Lopez-Hilfiker et al., 2016). For each experiment, backgrounds were determined by sampling from the AIDA chamber before adding any precursor gases. For type 2 experiments, backgrounds were negligible with initial particle number concentrations below 1 cm^{-3}. For type 1 experiments, we observed a small increase in both gas mixing ratio and particle mass (< 0.01 $\mu g\,m^{-3}$) after O_3 addition, which was subtracted from the mass loadings presented here. However, the background and the increase induced by O_3 addition were negligible compared to the increase by the SOA mass (> 1000-fold for particle mass).

All instruments were set up at room temperature, outside the temperature-controlled housing of AIDA. Despite inlet insulation with Armaflex, we calculated a theoretical temperature increase (Fitzer and Fritz, 1989) of ~ 15 K for the particle inlet of the CIMS (the FIGAERO filter was thus presumably at 238 K during deposition), and cannot entirely rule out partial evaporation of water or semivolatile organic compounds, which is taken into account in our interpretation of results.

3   Results and discussion

3.1   Organic particle mass and size distribution

Figure 2a–b show the time series of total particle mass derived from SMPS size distributions, total organic particle mass measured by AMS, and total mass of particulate oxygenated hydrocarbons ($C_{x>1}H_{y>1}O_{z>1}$ detected as clustered with I^-, termed CHOI compounds) measured by CIMS for both types of experiments. Figure 2a depicts the CH experiment, representative of experiment type 1, where particles were directly formed in AIDA. Figure 2b shows experiment type 2, where aerosol was formed in the APC and transferred to AIDA (here the WDtoCH example; see Table 1). Note that the data were not wall-loss-corrected. Gaps in the AMS time series were due to filter measurements. To investigate the evolution of the SOA particles' physicochemical properties with time, we chose two points in time during the experiments, $t0$ and $t1$. $t0$ is the first FIGAERO filter deposition from AIDA after particle formation (experiment type 1) or particle transfer (experiment type 2), while $t1$ is approximately 3.5 h later. Averaged concentrations of total organics and total CHOI compounds, elemental O : C ratios at $t0$ and $t1$, and an overview of the experimental conditions including temperature (T), RH, and added precursor (α-pinene and O_3) concentrations for all experiments discussed here (WDtoCH, WHtoCH, CH, and CD) are listed in Table 1. Particle size distributions measured by AMS for all four experiments at $t0$ and $t1$ are shown in Fig. 2c–d.

For SOA formed in AIDA (type 1 experiments), at $t0$ and $t1$, mean total organic mass concentrations and mean total concentrations of CHOI compounds were in the range of 67.5–440.1 $\mu g\,m^{-3}$ and 97.8–247.6 $\mu g\,m^{-3}$, respectively. When particles were transferred from the APC chamber (type 2 experiments), organic and CHOI mass concentrations in AIDA reached values of 48.5–64.2 $\mu g\,m^{-3}$ and 23.3–40.7 $\mu g\,m^{-3}$, respectively. We stress here that even though particle mass concentrations in AIDA were higher for the experiments of type 1 (particles formed at 223 K directly in AIDA), the α-pinene concentration for the type 2 experiments was higher by a factor of ~ 3 (Fig. 2a–b and Table 1). This also led to larger particle sizes for the type 2 experiments. Due to additional α-pinene addition between $t0$ and $t1$ only for the CH experiment, we observed a step increase of total particle mass for this experiment (Fig. 2a).

The discrepancies between AMS and CIMS concentrations are likely due to the CIMS with I^- as reagent ion being more sensitive to more polar oxygenated organic compounds (Lee et al., 2014), and thus only a potential subset of organic compounds are measured by CIMS. Evaporation losses of particulate compounds during filter deposition in the FIGAERO may play a minor role. In addition, by using the collisional limit for the CIMS data, we apply maximum sensitivity and thus present lower limits of CHOI compounds. The differences between the AMS- and SMPS-derived mass concentrations in Fig. 2a are likely due to the lower transmission of sub-100 nm particles in the aerodynamic lens of the AMS used here. The AMS measured lower concentrations than the SMPS at the beginning of the CH experiment (Fig. 2a), when the newly formed particles were much smaller (see Fig. 2c), compared to later in the experiment when they had grown in size (see Fig. 2d). For the WDtoCH experiment (Fig. 2b) with larger particles transferred from the APC to the AIDA chamber, AMS- and SMPS-derived mass concentrations agree very well. The slightly decreasing trend observed during both experiments was due to wall losses (Donahue et al., 2012).

3.2   Chemical characterization of SOA particles

3.2.1   Elemental oxygen-to-carbon ratios

Elemental O : C ratios were calculated using both AMS and CIMS data. The mean AMS O : C ratios for SOA formed in APC and AIDA were 0.34–0.36 and 0.26–0.30, respectively (Table 1). This is representative of O : C ratios for relatively fresh SOA measured in ambient studies (Mohr et al., 2012; Ge et al., 2012; Canagaratna et al., 2015). For CHOI compounds measured by CIMS, the calculated mean O : C ratios for SOA formed in APC and AIDA were 0.59–0.66 and 0.56–0.61, respectively. The AMS O : C ratio is expected to be lower than that of the CHOI compounds measured by iodide CIMS, as the latter is selective towards polar oxygenated compounds. The potential loss of semivolatiles from the filter

Atmos. Chem. Phys., 18, 2883–2898, 2018   www.atmos-chem-phys.net/18/2883/2018/

237
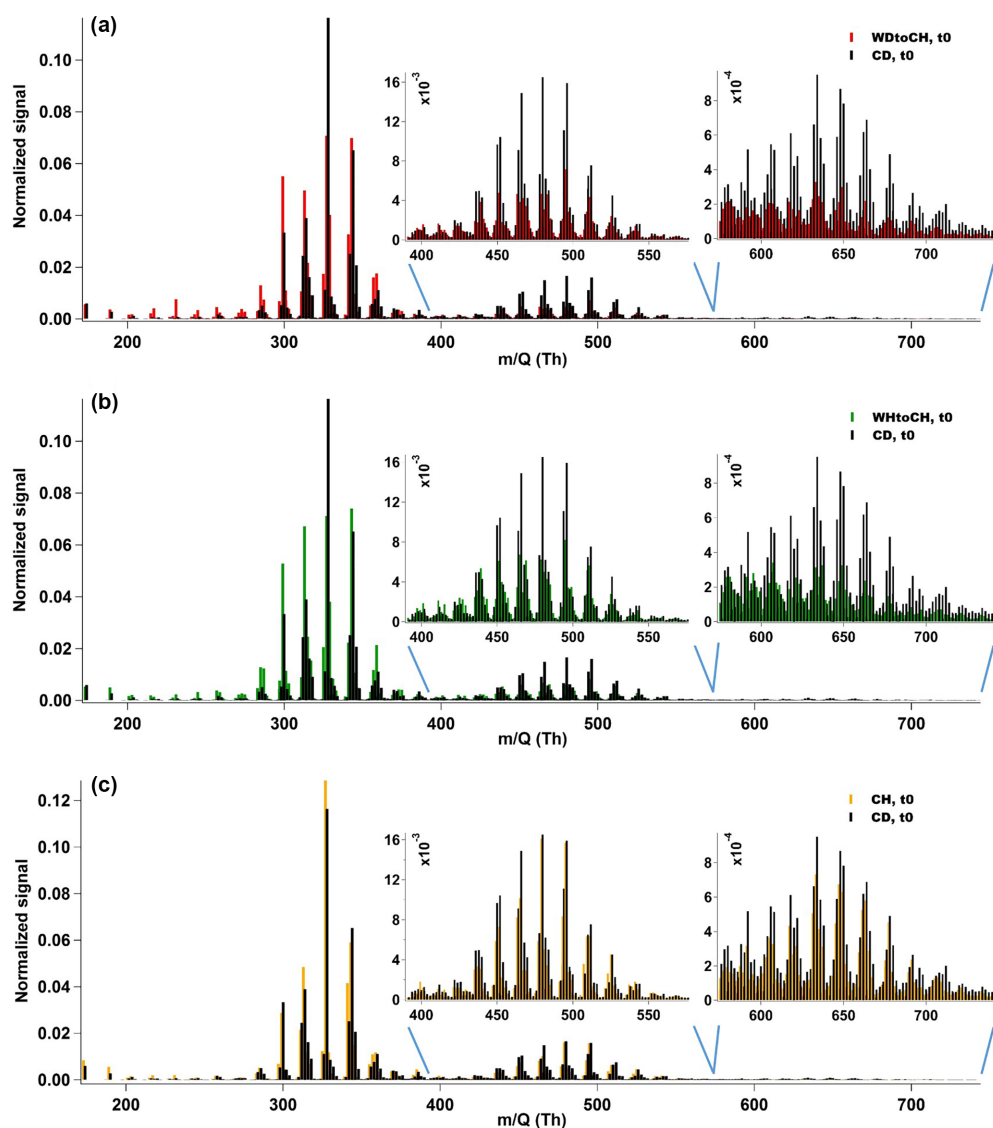
Figure 3. CIMS mass spectra (normalized to the sum of signal of all detected CHOI compounds) of experiments WDtoCH and CD **(a)**, WHtoCH and CD **(b)**, and CH and CD **(c)** at $t0$. Inserts show enlarged regions of dimers (left) and trimers (right).

during FIGAERO deposition may additionally increase the mass-averaged O : C ratio of compounds measured with this instrument. The O : C ratios of SOA formed in the APC were slightly higher than those formed in AIDA, likely a result of the difference in precursor concentrations and temperature and thus partitioning behavior of semivolatile SOA compounds during formation between the particles and chamber walls. We rule out a dilution effect when transferring particles from APC to AIDA since the dilution factor was orders of magnitude smaller than the decrease in saturation vapor pressure due to the temperature reduction from APC (296 K) to AIDA (223 K), and this was confirmed by the absence of

a change in particle size after transfer. For all experiments, O : C ratios remained largely constant from $t0$ to $t1$.

3.2.2 CIMS mass spectra

Mass spectra of integrated desorptions from the CIMS are compared for the four experiments and two points in time, $t0$ and $t1$. Mass spectra shown were normalized to the sum of signal of all detected CHOI compounds. The corresponding mass loadings and sampling times (particle collection on filter) for the four experiments are listed in Table S1. Figure 3a, b, and c show a comparison of mass spectral patterns for the experiments WDtoCH and CD, for WHtoCH and CD, and

238

for CH and CD, respectively, all at $t0$ (the same comparisons for $t1$ are to be found in Fig. S1). Overall, the mass spectral patterns across all experimental conditions and points in time were relatively similar. Monomers ($C_mH_yO_z$ compounds, $m \leq 10$), dimers ($C_nH_yO_z$ compounds, $11 \leq n \leq 20$), and even trimers ($C_pH_yO_z$ compounds, $21 \leq p \leq 30$) clustered with I^- were observed in the mass spectra at $t0$ and $t1$ for all occasions.

Monomers dominated the overall signal of detected compounds, with the largest signal at m/z 327 (mainly $C_{10}H_{16}O_4I_1^-$, likely hydroxy-pinonic acid clustered with I^-). As we can see from Fig. 3, relatively higher contributions of monomers were measured at $t0$ for experiments WDtoCH and WHtoCH compared to CD. The difference in relative monomer contributions for experiments CH and CD was less distinct. At the same time, relatively larger contributions from dimers and trimers (inserts in Fig. 3) were observed for the experiment CD (and to a lesser extent for the CH). This was also the case for $t1$ (Fig. S1).

Figure 4 shows the relative mass contributions of monomers and adducts (this definition includes dimers, trimers, and oligomers in general) for the four experiments at both time points. As already observed in the mass spectral patterns, larger relative mass contributions from monomers were measured for the type 2 experiments (WDtoCH, WHtoCH), and larger relative mass contributions from adducts for the type 1 experiments (CH, CD). There was no significant change for the relative contributions and absolute concentrations of adducts (Fig. S2) between $t0$ and $t1$ for type 2 experiments (WDtoCH, WHtoCH). For type 1 experiments (CH and CD), absolute concentrations of monomers and adducts (Fig. S2) increased from $t0$ to $t1$ due to the addition of α-pinene after $t0$ and hence the continuing production of oxidation products and particle mass (compare to Fig. 2). However, the relative contributions of monomers for type 1 experiments increased from $t0$ to $t1$, which may be partially influenced by smaller FIGAERO sampling time and thus less evaporation losses of semivolatiles at $t1$ (see Table S1 and Supplement), but mostly by increased condensation of semivolatiles or lower-molecular-weight products with increasing particle size (compare Fig. 2c–d).

Figure 5 shows the average mass-weighted number of carbon atoms (numC) and oxygen atoms (numO) for CHOI compounds for the four experiments at $t0$ and $t1$. The corresponding average mass-weighted compounds' formulae for SOA generated in APC and AIDA were $C_{10-12}H_yO_{6-7}$ and $C_{11-13}H_yO_{6-7}$, respectively. Slightly bigger numC were observed for type 1 experiments (CH, CD) than type 2 experiments, with the largest value for experiment CD, followed by CH and WHtoCH. numC was smallest for WDtoCH. There was no obvious trend for numO.

In summary, smaller particles with slightly lower O : C ratios, bigger carbon numbers, and relatively more mass from adducts were observed for type 1 experiments (CH, CD), which had lower α-pinene concentrations and colder for-
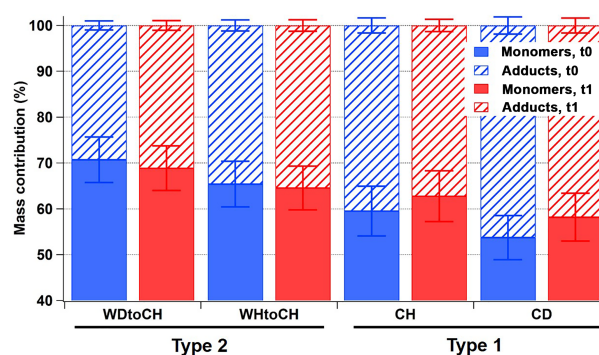
Figure 4. Relative mass contributions of monomers and adducts with error bars at $t0$ (blue) and $t1$ (red).

mation temperature (223 K) compared to the type 2 experiments. For type 2 experiments (WDtoCH, WHtoCH), higher α-pinene concentrations (by a factor of ∼ 3) and warmer formation temperature (296 K) produced larger particles with slightly higher O : C ratios, smaller carbon numbers, and relatively more mass from monomers. The slightly higher O : C ratio in type 2 experiments is thus not due to bigger oxygen numbers, but due to smaller carbon numbers (Fig. 5), indicating that relatively more small oxygenated molecules were formed for type 2 experiments. This is likely due to higher α-pinene concentrations and faster oxidation at 296 K leading to rapid condensation of monomers, providing enough gaseous oxidation products for the equilibrium of semivolatiles to be shifted into the particle phase. Type 1 experiments, on the other hand, were performed with lower α-pinene concentrations, and particles were formed in situ, favoring higher contributions of larger ELVOC/LVOC compounds, especially at the early stages of particle growth (Tröstl et al., 2016). At the same time, the low-temperature conditions may also have shifted equilibrium to the particle phase and led to condensation of compounds with a relatively lower degree of oxygenation (compared to warm temperature conditions). Overall, the differences observed in mass spectral patterns between the two types of experiments are a consequence of both temperature and precursor concentration differences. They underline the importance of experiment conditions when interpreting laboratory data or using them for modeling.

3.3 Thermograms: variation in T_{max} of SOA compounds for different experiments

In addition to information on mass spectral patterns and mass loadings when peaks are integrated, the FIGAERO also provides signal curves as a function of desorption temperature (referred to as thermograms). Although T_{max} can be used to infer the compound's saturation vapor pressure (Lopez-Hilfiker et al., 2015; Mohr et al., 2017), evaporative behavior and inferred volatility of a particle-bound compound are also
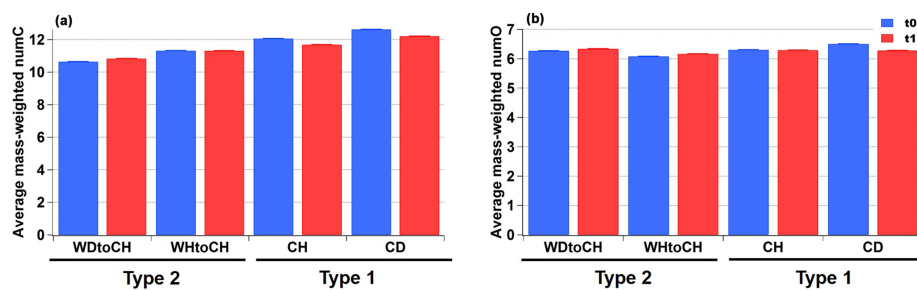
Figure 5. (a) Average mass-weighted number of carbon atoms (numC) and **(b)** oxygen atoms (numO) with error bars at $t0$ (blue) and $t1$ (red).
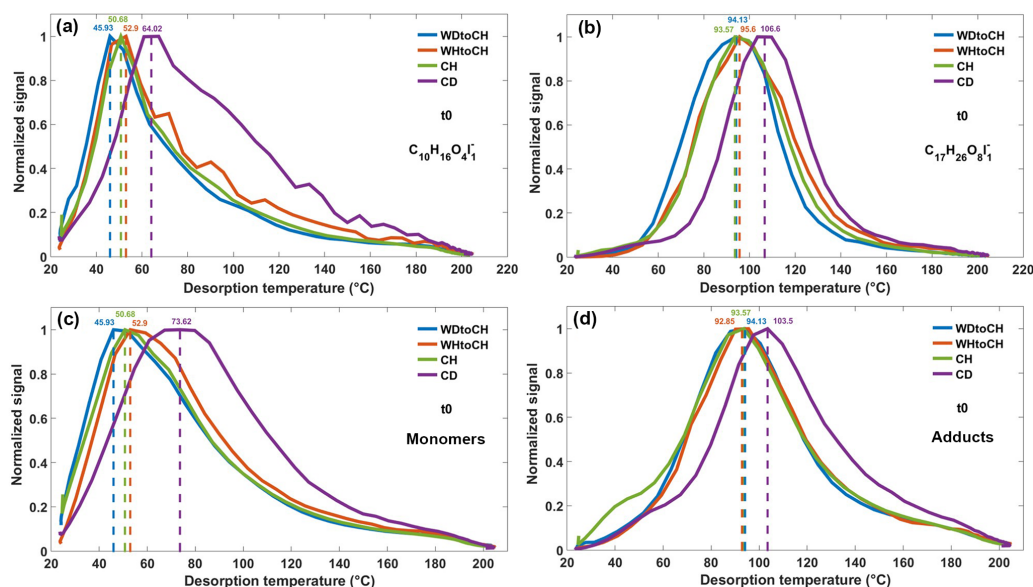
Figure 6. Thermograms of monomer $C_{10}H_{16}O_4$ **(a)** and adduct $C_{17}H_{26}O_8$ **(b)**, both clustered with I$^-$ at $t0$, and sum thermograms of monomers **(c)** and adducts **(d)** at $t0$. Dashed lines refer to the corresponding T_{max}.

influenced by the particles' physical phase state, particle-phase diffusivity, and viscosity (Yli-Juuti et al., 2017). Here we show that thermograms may also be used for qualitative information on particle viscosity.

Thermograms resulting from the thermal desorption of deposited SOA particles from the four experiments CH, CD, WDtoCH, and WHtoCH at both time points $t0$ and $t1$ were analyzed. Examples of the thermograms of a monomer ($C_{10}H_{16}O_4$, molecular formula corresponding to hydroxy-pinonic acid identified by Zhang et al., 2017) and an adduct ($C_{17}H_{26}O_8$, molecular structure identified in SOA from α-pinene ozonolysis as a *cis*-pinyl-diaterpenyl ester by Yasmeen et al., 2010; molecular formula identified in SOA from α-pinene ozonolysis by, e.g., Zhang et al., 2015; Mohr et al., 2017), both clustered with I$^-$ at $t0$ are shown in Fig. 6a–b. Figure 6c shows the sum of thermograms of all monomers, Fig. 6d shows the sum of all adduct thermograms at $t0$. The same plots for $t1$ can be found in Fig. S3. Thermograms

and sums of thermograms were normalized to their maximum values. The corresponding mass loadings and sampling times (particle collection on filter) for the four experiments are listed in Table S1. For experiment CD, the $C_{10}H_{16}O_4I_I^-$ thermograms exhibited a multi-modal shape, indicative of contributions from isomers having different vapor pressures, or thermal decomposition of larger molecules. Different isomeric hydroxypinonic acids were found in α-pinene SOA (Zhang et al., 2017) and the decomposition of *cis*-pinyl-hydroxypinonyl diester could have a residue of *cis*-pinic acid and 7-hydroxypinonic acid (Müller et al., 2008). Based on previous FIGAERO data analyses (Lopez-Hilfiker et al., 2015; D'Ambro et al., 2017; Wang et al., 2016), we can safely presume that the first mode corresponds to the monomer.

Figure 6a–b show that T_{max} of an individual compound varied by up to 20 °C, depending on experimental conditions. It has been shown earlier that thermograms and cor-
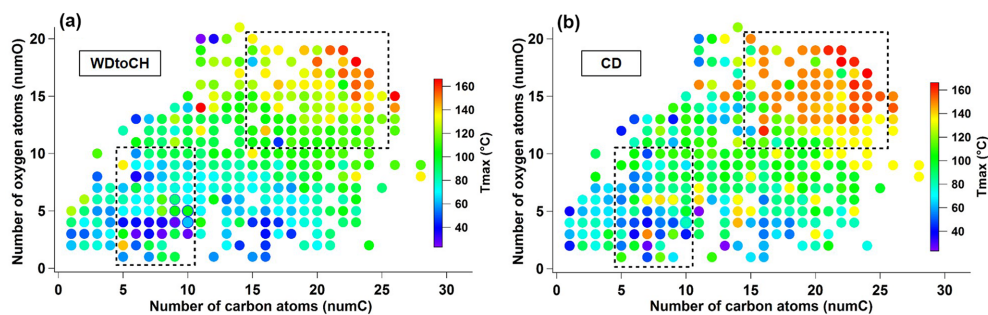
Figure 7. T_{max} distribution for individual CHOI compounds of WDtoCH **(a)** and CD **(b)** experiments at $t0$ according to number of oxygen atoms (numO) vs. number of carbon atoms (numC). Dashed boxes specify the compounds with nominal molecular formulae $C_{5-10}H_yO_{1-10}I^-$ and $C_{15-25}H_yO_{11-20}I^-$ that had bigger T_{max} differences.

responding T_{max} are highly reproducible for stable conditions (Lopez-Hilfiker et al., 2014). In our instrument, T_{max} varied by 2 °C at most for the monomer, $C_{10}H_{16}O_4$, and for another adduct, $C_{16}H_{24}O_6$ (molecular formula identified in SOA from α-pinene ozonolysis by, e.g., Zhang et al., 2015) both clustered with I^-, for six subsequent thermograms under stable conditions (Fig. S4). The variation in T_{max} as a function of experiment types observed here thus indicates that the shape of a thermogram for a given compound and given FIGAERO configuration is not only defined by the compound's enthalpy of evaporation. For both $C_{10}H_{16}O_4I_1^-$ and $C_{17}H_{26}O_8I_1^-$ thermograms, T_{max} was highest for experiment CD, followed by WHtoCH, CH, and WDtoCH. Similar trends were observed for all compounds measured by the CIMS, as shown by the sums of thermograms of all monomer compounds (Fig. 6c), and by the sums of thermograms of all adduct compounds (Fig. 6d). Sum T_{max} of monomers and adducts varied from 46 °C (experiment WDtoCH) to 74 °C (experiment CH) to 93 °C (experiment WHtoCH) to 104 °C (experiment CD).

Variation in T_{max} of the sum of CHOI compounds was larger for monomers (Fig. 6c) than for adducts (Fig. 6d). Monomers are thus the more important contributors to the shifts in T_{max}, likely because at the higher temperatures where adducts desorb, particle matrix effects may become less important. Since the sum of thermograms and its T_{max} is highly influenced by compounds with large signal, we also show a box and whisker diagram of T_{max} for monomers and adducts (Fig. S5). The median T_{max} values showed similar variation as the T_{max} values based on thermogram sums. Examples of the T_{max} distribution of individual CHOI compounds in numO vs. numC space at $t0$ are shown in Fig. 7 for the WDtoCH and CD experiments. Points were color-coded by T_{max}. Compounds with nominal molecular formula $C_{8-10}H_yO_{4-6}I^-$ were the main contributors to mass concentrations (data not shown), and thus also aggregated T_{max} values. Generally, T_{max} for CHOI compounds ranged from 25 to 165 °C, and increased with carbon num-

bers and oxygen numbers of compounds, as is to be expected given the relationship between enthalpy of evaporation and volatility of a compound (Lopez-Hilfiker et al., 2015; Mohr et al., 2017). The comparison between WDtoCH (Fig. 7a) and CD (Fig. 7b) experiments, however, showed differences in T_{max} values for most compounds. T_{max} values, especially of many compounds with nominal molecular formulae $C_{5-10}H_yO_{1-10}I^-$ and $C_{15-25}H_yO_{11-20}I^-$, were higher for the CD experiment. The similar behavior in the variation of T_{max} of most compounds measured by CIMS indicates that T_{max} is not purely a function of a compound's vapor pressure or volatility, but is influenced by diffusion limitations within particles (particle viscosity; Vaden et al., 2011; Yli-Juuti et al., 2017), interactions between particles deposited on the filter (particle matrix), and/or particle mass on the filter. In the following we will discuss these implications in more detail.

Mass transport limitations within SOA particles, often measured or modeled as evaporation rates of specific compounds (Yli-Juuti et al., 2017; Wilson et al., 2015; Roldin et al., 2014), have been related to the particle viscosity (Vaden et al., 2011; Yli-Juuti et al., 2017). Particle viscosity is highly influenced by temperature and RH (Shiraiwa et al., 2017; Kidd et al., 2014), with higher viscosities at cool and/or dry conditions (Shiraiwa et al., 2011). Since the temperature was 223 K in AIDA for all experiments discussed here, the observed differences in T_{max}, and presumed viscosity, cannot be directly explained by differences in temperature. In addition, during desorption of compounds with the FIGAERO, particles are actively heated (with heat transfer assumed to be immediate), and are not evaporating under equilibrium conditions. Presumed variations in particle viscosity based on observed variations in T_{max} must therefore be due to variations in particle chemical composition, and/or RH differences.

The biggest T_{max} difference in Fig. 6 was between WDtoCH and CD experiments, which was in accordance with the largest differences in mass spectra as discussed above (see Figs. 3a and 4). This is indicative of a relationship between

Atmos. Chem. Phys., 18, 2883–2898, 2018   www.atmos-chem-phys.net/18/2883/2018/

241

$T_{\max}$ in the thermograms and particle chemical composition. It has been shown earlier that the chemical properties of particulate compounds influence particle viscosity (Kidd et al., 2014; Hosny et al., 2016). Viscosity is expected to be higher with higher oligomer content, due to inter-component hydrogen bonding, especially at low RH (Kidd et al., 2014). This is in accordance with our results, which showed highest $T_{\max}$ values for the CD experiment, which also had the highest contribution from adducts.

RH is an additional parameter that greatly influences particle viscosity (Kidd et al., 2014; Hosny et al., 2016; Renbaum-Wolff et al., 2013). Despite the fact that the SOA particles might be dried very quickly by the dry heated nitrogen during particle desorption, we suppose that RH might have a "memory effect" and still influence $T_{\max}$. RH conditions during the four experiments presented here ranged from 6 % (CD) to 30 % (WHtoCH) to 61 % (WDtoCH and CH). Note that these were the conditions of the measurement time in the AIDA chamber; for WDtoCH and WHtoCH, the RH conditions during SOA formation in the APC chamber were 1 and 21 %, respectively. We thus need to differentiate between $RH_{formation}$ and $RH_{measurement}$. As shown in Fig. 8, there was no trend between $RH_{formation}$ and $T_{\max}$, indicating that the RH during particle formation did not play an important role in the observed viscosity variation. However, we observed a negative correlation of $RH_{measurement}$ and $T_{\max}$ of all monomer compounds at $t0$, indicating that even under low-temperature conditions of 223 K there is particle water uptake, and an influence of RH on viscosity. Particle water uptake thus seems to influence particle viscosity even at such low temperature and on such short timescales (few hours). To what extent RH and particle water uptake, or chemical properties and adduct content, and their respective influence on water uptake via increased hygroscopicity, contribute to the observed differences in $T_{\max}$ and presumed viscosity, we can only speculate. In the CH and WDtoCH experiments, $RH_{measurement}$ was ~ 60 % for both. The adduct mass fraction was only slightly higher for SOA in the CH experiment, and so was $T_{\max}$ and thus potentially particle viscosity. More controlled studies at low temperature are needed to separate these effects.

We also noticed that different mass loadings on the filter due to different sampling times and/or sample concentrations influenced the shape of thermograms and thus $T_{\max}$. $T_{\max}$ increased as a function of mass loading on the filter, likely due to the increase in heat capacity of the increasing mass of the particle matrix, and potential interactions between the particles. The dependency of $T_{\max}$ on filter mass loading was not linear, and for our FIGAERO, it reached a plateau at mass loadings of 2–4 µg. Our results are therefore not affected by the mass loading effect, but we recommend taking it into account in analyses that involve $T_{\max}$. A detailed discussion can be found in the Supplement.
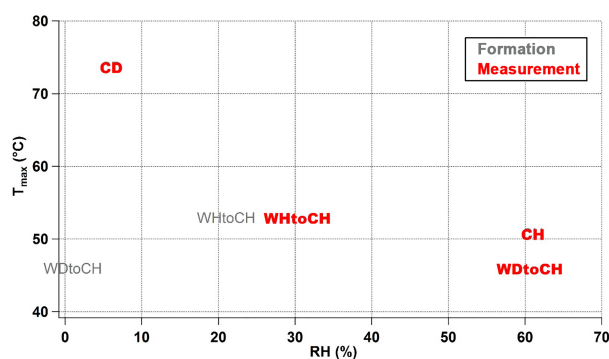
Figure 8. Relationship of $RH_{formation}$ (gray), $RH_{measurement}$ (red), and $T_{\max}$ of all CHOI monomer compounds for four experiments at $t0$.

4 Conclusions and atmospheric implications

In this study, α-pinene SOA physicochemical properties such as chemical composition, size distributions, and degree of oligomerization were investigated at low temperature (223 K) and different relative humidity (RH) using two simulation chambers (APC and AIDA). Two types of experiments were performed: for type 1 experiments, SOA was directly generated in the AIDA chamber kept at 223 K at 61 % RH (experiment termed "cold humid", CH) or 6 % RH (experiment termed "cold dry", CD) conditions. For type 2 experiments, SOA was formed in the APC chamber at room temperature (296 K), < 1 % RH (experiment termed "warm dry", WD) or 21 % RH (experiment termed "warm humid", WH) conditions, and then partially transferred to the AIDA chamber kept at 223 K at 61 % RH (WDtoCH) or 30 % RH (WHtoCH) conditions, respectively, to simulate SOA uplifting.

For type 1 experiments (CH, CD) with lower α-pinene concentrations and cold SOA formation temperature (223 K), smaller particles with relatively more mass from adducts were observed. For type 2 experiments (WDtoCH, WHtoCH) with higher α-pinene concentrations (by a factor of ~ 3) and warm SOA formation temperature (296 K), larger particles with relatively more mass from monomers were produced. The differences observed in mass spectral patterns between the two types of experiments are likely a consequence of both temperature and precursor concentration differences. Higher α-pinene concentrations and faster oxidation at 296 K during SOA formation in the APC chamber shifted the gas–particle equilibrium to the particles, resulting in larger mass fractions of semivolatile and/or monomer compounds. Low-temperature conditions in the AIDA chamber during SOA formation on the other hand may result in condensation of compounds with a relatively lower degree of oxygenation. Our results show that depending on where SOA formation takes place in the atmosphere (e.g., boundary layer or upper troposphere), chemical properties can vary, and with it, reactivity and lifetime.

www.atmos-chem-phys.net/18/2883/2018/ Atmos. Chem. Phys., 18, 2883–2898, 2018

242

In addition to the differences in mass spectral patterns for the different experiments, we also observed differences in the shape of thermograms resulting from the desorption of SOA particles collected on the FIGAERO filter: $T_{\max}$ of an individual compound in the thermograms varied by up to 20 °C depending on experimental conditions, indicating that $T_{\max}$ is not only influenced by a compound's vapor pressure or volatility, but also by diffusion limitations within the particles (particle viscosity). For both $C_{10}H_{16}O_4I_1^-$ and $C_{17}H_{26}O_8I_1^-$ thermograms, $T_{\max}$ was highest for experiment CD, followed by WHtoCH, CH, and WDtoCH. We observed higher $T_{\max}$ for α-pinene SOA particles with higher oligomer mass fractions, indicating the potential role of intra- and inter-molecular hydrogen bonds between these large and highly functionalized molecules for the increase in particle viscosity (Kidd et al., 2014). Furthermore, $T_{\max}$ was negatively correlated with RH in the particle reservoir and particle water content, suggesting that hygroscopic properties and water uptake are important factors even at such low temperature. We also demonstrated an effect of mass deposited on the FIGAERO filter on $T_{\max}$, which needs to be taken into account for further studies relying on $T_{\max}$.

The results suggest that particle physicochemical properties such as viscosity and oligomer content mutually influence each other. More controlled experiments at low temperature are needed to separate the direct effects of RH and particle water uptake as well as chemical properties such as adduct content (i.e., oligomer content), and the indirect effects of chemical properties on water uptake via changes in hygroscopicity on the observed differences in $T_{\max}$ and presumed viscosity. The differences in SOA physicochemical properties observed in our set of experiments as a function of temperature, RH, and precursor conditions demonstrate the importance of ambient and laboratory measurements at a wide range of atmospherically relevant conditions, and of taking experimental conditions into careful consideration when interpreting laboratory studies or using them as input in climate models.

Data availability. Data are available upon request to the corresponding author.

The Supplement related to this article is available online at https://doi.org/10.5194/acp-18-2883-2018-supplement.

Author contributions. WH, HS, AP, XS, KHN, AV, TL, and CM designed research; WH, HS, AP, XS, RW, and CM performed research; WH, HS, AP, XS, and CM analyzed data; and WH and CM wrote the paper.

References

Bastelberger, S., Krieger, U. K., Luo, B., and Peter, T.: Diffusivity measurements of volatile organics in levitated viscous aerosol particles, Atmos. Chem. Phys., 17, 8453–8471, https://doi.org/10.5194/acp-17-8453-2017, 2017.

Bateman, A. P., Gong, Z. H., Liu, P. F., Sato, B., Cirino, G., Zhang, Y., Artaxo, P., Bertram, A. K., Manzi, A. O., Rizzo, L. V., Souza, R. A. F., Zaveri, R. A., and Martin, S. T.: Sub-micrometre particulate matter is primarily in liquid form over Amazon rainforest, Nat. Geosci., 9, 34–37, 2016.

Canagaratna, M. R., Jimenez, J. L., Kroll, J. H., Chen, Q., Kessler, S. H., Massoli, P., Hildebrandt Ruiz, L., Fortner, E., Williams, L. R., Wilson, K. R., Surratt, J. D., Donahue, N. M., Jayne, J. T., and Worsnop, D. R.: Elemental ratio measurements of organic compounds using aerosol mass spectrometry: characterization, improved calibration, and implications, Atmos. Chem. Phys., 15, 253–272, https://doi.org/10.5194/acp-15-253-2015, 2015.

D'Ambro, E. L., Lee, B. H., Liu, J., Shilling, J. E., Gaston, C. J., Lopez-Hilfiker, F. D., Schobesberger, S., Zaveri, R. A., Mohr, C., Lutz, A., Zhang, Z., Gold, A., Surratt, J. D., Rivera-Rios, J. C., Keutsch, F. N., and Thornton, J. A.: Molecular composition and volatility of isoprene photochemical oxidation secondary organic aerosol under low- and high-NO$_x$ conditions, Atmos. Chem. Phys., 17, 159–174, https://doi.org/10.5194/acp-17-159-2017, 2017.

Denjean, C., Formenti, P., Picquet-Varrault, B., Camredon, M., Pangui, E., Zapf, P., Katrib, Y., Giorio, C., Tapparo, A., Temime-Roussel, B., Monod, A., Aumont, B., and Doussin, J. F.: Aging of secondary organic aerosol generated from the ozonolysis of α-pinene: effects of ozone, light and temperature, Atmos. Chem. Phys., 15, 883–897, https://doi.org/10.5194/acp-15-883-2015, 2015.

Donahue, N. M., Henry, K. M., Mentel, T. F., Kiendler-Scharr, A., Spindler, C., Bohn, B., Brauers, T., Dorn, H. P., Fuchs, H., Tillmann, R., Wahner, A., Saathoff, H., Naumann, K. H., Möhler, O., Leisner, T., Müller, L., Reinnig, M. C., Hoffmann, T., Salo, K., Hallquist, M., Frosch, M., Bilde, M., Tritscher, T., Barmet, P., Praplan, A. P., DeCarlo, P. F., Dommen, J., Prévôt, A. S. H., and Baltensperger, U.: Aging of biogenic secondary organic aerosol

via gas-phase OH radical reactions, P. Natl. Acad. Sci. USA, 109, 13503–13508, 2012.

Ehn, M., Kleist, E., Junninen, H., Petäjä, T., Lönn, G., Schobesberger, S., Dal Maso, M., Trimborn, A., Kulmala, M., Worsnop, D. R., Wahner, A., Wildt, J., and Mentel, Th. F.: Gas phase formation of extremely oxidized pinene reaction products in chamber and ambient air, Atmos. Chem. Phys., 12, 5113–5127, https://doi.org/10.5194/acp-12-5113-2012, 2012.

Ehn, M., Thornton, J. A., Kleist, E., Sipilä, M., Junninen, H., Pullinen, I., Springer, M., Rubach, F., Tillmann, R., Lee, B., Lopez-Hilfiker, F., Andres, S., Acir, I. H., Rissanen, M., Jokinen, T., Schobesberger, S., Kangasluoma, J., Kontkanen, J., Nieminen, T., Kurtén, T., Nielsen, L. B., Jørgensen, S., Kjaergaard, H. G., Canagaratna, M., Dal Maso, M., Berndt, T., Petäjä, T., Wahner, A., Kerminen, V. M., Kulmala, M., Worsnop, D. R., Wildt, J., and Mentel, T. F.: A large source of low-volatility secondary organic aerosol, Nature, 506, 476–479, 2014.

Fahey, D. W., Gao, R.-S., Möhler, O., Saathoff, H., Schiller, C., Ebert, V., Krämer, M., Peter, T., Amarouche, N., Avallone, L. M., Bauer, R., Bozóki, Z., Christensen, L. E., Davis, S. M., Durry, G., Dyroff, C., Herman, R. L., Hunsmann, S., Khaykin, S. M., Mackrodt, P., Meyer, J., Smith, J. B., Spelten, N., Troy, R. F., Vömel, H., Wagner, S., and Wienhold, F. G.: The AquaVIT-1 intercomparison of atmospheric water vapor measurement techniques, Atmos. Meas. Tech., 7, 3177–3213, https://doi.org/10.5194/amt-7-3177-2014, 2014.

Fitzer, E. and Fritz, W.: Technische Chemie, 3rd ed., Springer, Berlin, 140 pp., 1989.

Frege, C., Ortega, I. K., Rissanen, M. P., Praplan, A. P., Steiner, G., Heinritzi, M., Ahonen, L., Amorim, A., Bernhammer, A.-K., Bianchi, F., Brilke, S., Breitenlechner, M., Dada, L., Dias, A., Duplissy, J., Ehrhart, S., El-Haddad, I., Fischer, L., Fuchs, C., Garmash, O., Gonin, M., Hansel, A., Hoyle, C. R., Jokinen, T., Junninen, H., Kirkby, J., Kürten, A., Lehtipalo, K., Leiminger, M., Mauldin, R. L., Molteni, U., Nichman, L., Petäjä, T., Sarnela, N., Schobesberger, S., Simon, M., Sipilä, M., Stolzenburg, D., Tomé, A., Vogel, A. L., Wagner, A. C., Wagner, R., Xiao, M., Yan, C., Ye, P., Curtius, J., Donahue, N. M., Flagan, R. C., Kulmala, M., Worsnop, D. R., Winkler, P. M., Dommen, J., and Baltensperger, U.: Influence of temperature on the molecular composition of ions and charged clusters during pure biogenic nucleation, Atmos. Chem. Phys., 18, 65–79, https://doi.org/10.5194/acp-18-65-2018, 2018.

Ge, X. L., Setyan, A., Sun, Y. L., and Zhang, Q.: Primary and secondary organic aerosols in Fresno, California during wintertime: Results from high resolution aerosol mass spectrometry, J. Geophys. Res.-Atmos., 117, D19301, https://doi.org/10.1029/2012jd018026, 2012.

Hallquist, M., Wenger, J. C., Baltensperger, U., Rudich, Y., Simpson, D., Claeys, M., Dommen, J., Donahue, N. M., George, C., Goldstein, A. H., Hamilton, J. F., Herrmann, H., Hoffmann, T., Iinuma, Y., Jang, M., Jenkin, M. E., Jimenez, J. L., Kiendler-Scharr, A., Maenhaut, W., McFiggans, G., Mentel, Th. F., Monod, A., Prévôt, A. S. H., Seinfeld, J. H., Surratt, J. D., Szmigielski, R., and Wildt, J.: The formation, properties and impact of secondary organic aerosol: current and emerging issues, Atmos. Chem. Phys., 9, 5155–5236, https://doi.org/10.5194/acp-9-5155-2009, 2009.

Heald, C. L., Henze, D. K., Horowitz, L. W., Feddema, J., Lamarque, J.-F., Guenther, A., Hess, P. G., Vitt, F., Seinfeld, J. H., Goldstein, A. H., and Fung, I.: Predicted change in global secondary organic aerosol concentrations in response to future climate, emissions, and land use change, J. Geophys. Res.-Atmos., 113, D05211, https://doi.org/10.1029/2007jd009092, 2008.

Hosny, N. A., Fitzgerald, C., Vyšniauskas, A., Athanasiadis, A., Berkemeier, T., Uygur, N., Pöschl, U., Shiraiwa, M., Kalberer, M., Pope, F. D., and Kuimova, M. K.: Direct imaging of changes in aerosol particle viscosity upon hydration and chemical aging, Chem. Sci., 7, 1357–1367, 2016.

IPCC: Climate change 2013: The physical scientific basis, Cambridge University Press, Cambridge, England, 622–623, 2013.

Järvinen, E., Ignatius, K., Nichman, L., Kristensen, T. B., Fuchs, C., Hoyle, C. R., Höppel, N., Corbin, J. C., Craven, J., Duplissy, J., Ehrhart, S., El Haddad, I., Frege, C., Gordon, H., Jokinen, T., Kallinger, P., Kirkby, J., Kiselev, A., Naumann, K.-H., Petäjä, T., Pinterich, T., Prevot, A. S. H., Saathoff, H., Schiebel, T., Sengupta, K., Simon, M., Slowik, J. G., Tröstl, J., Virtanen, A., Vochezer, P., Vogt, S., Wagner, A. C., Wagner, R., Williamson, C., Winkler, P. M., Yan, C., Baltensperger, U., Donahue, N. M., Flagan, R. C., Gallagher, M., Hansel, A., Kulmala, M., Stratmann, F., Worsnop, D. R., Möhler, O., Leisner, T., and Schnaiter, M.: Observation of viscosity transition in α-pinene secondary organic aerosol, Atmos. Chem. Phys., 16, 4423–4438, https://doi.org/10.5194/acp-16-4423-2016, 2016.

Jimenez, J. L., Canagaratna, M. R., Donahue, N. M., Prevot, A. S. H., Zhang, Q., Kroll, J. H., DeCarlo, P. F., Allan, J. D., Coe, H., Ng, N. L., Aiken, A. C., Docherty, K. S., Ulbrich, I. M., Grieshop, A. P., Robinson, A. L., Duplissy, J., Smith, J. D., Wilson, K. R., Lanz, V. A., Hueglin, C., Sun, Y. L., Tian, J., Laaksonen, A., Raatikainen, T., Rautiainen, J., Vaattovaara, P., Ehn, M., Kulmala, M., Tomlinson, J. M., Collins, D. R., Cubison, M. J., Dunlea, E. J., Huffman, J. A., Onasch, T. B., Alfarra, M. R., Williams, P. I., Bower, K., Kondo, Y., Schneider, J., Drewnick, F., Borrmann, S., Weimer, S., Demerjian, K., Salcedo, D., Cottrell, L., Griffin, R., Takami, A., Miyoshi, T., Hatakeyama, S., Shimono, A., Sun, J. Y., Zhang, Y. M., Dzepina, K., Kimmel, J. R., Sueper, D., Jayne, J. T., Herndon, S. C., Trimborn, A. M., Williams, L. R., Wood, E. C., Middlebrook, A. M., Kolb, C. E., Baltensperger, U., and Worsnop, D. R.: Evolution of organic aerosols in the atmosphere, Science, 326, 1525–1529, 2009.

Jokinen, T., Berndt, T., Makkonen, R., Kerminen, V.-M., Junninen, H., Paasonen, P., Stratmann, F., Herrmann, H., Guenther, A. B., Worsnop, D. R., Kulmala, M., Ehn, M., and Sipilä, M.: Production of extremely low volatile organic compounds from biogenic emissions: Measured yields and atmospheric implications, P. Natl. Acad. Sci. USA, 112, 7123–7128, 2015.

Kanakidou, M., Seinfeld, J. H., Pandis, S. N., Barnes, I., Dentener, F. J., Facchini, M. C., Van Dingenen, R., Ervens, B., Nenes, A., Nielsen, C. J., Swietlicki, E., Putaud, J. P., Balkanski, Y., Fuzzi, S., Horth, J., Moortgat, G. K., Winterhalter, R., Myhre, C. E. L., Tsigaridis, K., Vignati, E., Stephanou, E. G., and Wilson, J.: Organic aerosol and global climate modelling: a review, Atmos. Chem. Phys., 5, 1053–1123, https://doi.org/10.5194/acp-5-1053-2005, 2005.

Kidd, C., Perraud, V., Wingen, L. M., and Finlayson-Pitts, B. J.: Integrating phase and composition of secondary organic aerosol

from the ozonolysis of α-pinene, P. Natl. Acad. Sci. USA, 111, 7552–7557, 2014.

Kristensen, K., Cui, T., Zhang, H., Gold, A., Glasius, M., and Surratt, J. D.: Dimers in α-pinene secondary organic aerosol: effect of hydroxyl radical, ozone, relative humidity and aerosol acidity, Atmos. Chem. Phys., 14, 4201–4218, https://doi.org/10.5194/acp-14-4201-2014, 2014.

Kristensen, K., Watne, Å. K., Hammes, J., Lutz, A., Petäjä, T., Hallquist, M., Bilde, M., and Glasius, M.: High-molecular weight dimer esters are major products in aerosols from α-pinene ozonolysis and the boreal forest, Environ. Sci. Tech. Let., 3, 280–285, 2016.

Lee, B. H., Lopez-Hilfiker, F. D., Mohr, C., Kurtén, T., Worsnop, D. R., and Thornton, J. A.: An iodide-adduct high-resolution time-of-flight chemical-ionization mass spectrometer: Application to atmospheric inorganic and organic compounds, Environ. Sci. Technol., 48, 6309–6317, 2014.

Lienhard, D. M., Huisman, A. J., Krieger, U. K., Rudich, Y., Marcolli, C., Luo, B. P., Bones, D. L., Reid, J. P., Lambe, A. T., Canagaratna, M. R., Davidovits, P., Onasch, T. B., Worsnop, D. R., Steimer, S. S., Koop, T., and Peter, T.: Viscous organic aerosol particles in the upper troposphere: diffusivity-controlled water uptake and ice nucleation?, Atmos. Chem. Phys., 15, 13599–13613, https://doi.org/10.5194/acp-15-13599-2015, 2015.

Lopez-Hilfiker, F. D., Mohr, C., Ehn, M., Rubach, F., Kleist, E., Wildt, J., Mentel, Th. F., Lutz, A., Hallquist, M., Worsnop, D., and Thornton, J. A.: A novel method for online analysis of gas and particle composition: description and evaluation of a Filter Inlet for Gases and AEROsols (FIGAERO), Atmos. Meas. Tech., 7, 983–1001, https://doi.org/10.5194/amt-7-983-2014, 2014.

Lopez-Hilfiker, F. D., Mohr, C., Ehn, M., Rubach, F., Kleist, E., Wildt, J., Mentel, Th. F., Carrasquillo, A. J., Daumit, K. E., Hunter, J. F., Kroll, J. H., Worsnop, D. R., and Thornton, J. A.: Phase partitioning and volatility of secondary organic aerosol components formed from a-pinene ozonolysis and OH oxidation: the importance of accretion products and other low volatility compounds, Atmos. Chem. Phys., 15, 7765–7776, https://doi.org/10.5194/acp-15-7765-2015, 2015.

Lopez-Hilfiker, F. D., Iyer, S., Mohr, C., Lee, B. H., D'Ambro, E. L., Kurtén, T., and Thornton, J. A.: Constraining the sensitivity of iodide adduct chemical ionization mass spectrometry to multifunctional organic molecules using the collision limit and thermodynamic stability of iodide ion adducts, Atmos. Meas. Tech., 9, 1505–1512, https://doi.org/10.5194/amt-9-1505-2016, 2016.

McVay, R. C., Zhang, X., Aumont, B., Valorso, R., Camredon, M., La, Y. S., Wennberg, P. O., and Seinfeld, J. H.: SOA formation from the photooxidation of a-pinene: systematic exploration of the simulation of chamber data, Atmos. Chem. Phys., 16, 2785–2802, https://doi.org/10.5194/acp-16-2785-2016, 2016.

Middlebrook, A. M., Bahreini, R., Jimenez, J. L., and Canagaratna, M. R.: Evaluation of composition-dependent collection efficiencies for the Aerodyne Aerosol Mass Spectrometer using field data, Aerosol. Sci. Tech., 46, 258–271, 2012.

Möhler, O., Stetzer, O., Schaefers, S., Linke, C., Schnaiter, M., Tiede, R., Saathoff, H., Krämer, M., Mangold, A., Budz, P., Zink, P., Schreiner, J., Mauersberger, K., Haag, W., Kärcher, B., and Schurath, U.: Experimental investigation of homogeneous freezing of sulphuric acid particles in the aerosol chamber AIDA,

Atmos. Chem. Phys., 3, 211–223, https://doi.org/10.5194/acp-3-211-2003, 2003.

Möhler, O., Benz, S., Saathoff, H., Schnaiter, M., Wagner, R., Schneider, J., Walter, S., Ebert, V., and Wagner, S.: The effect of organic coating on the heterogeneous ice nucleation efficiency of mineral dust aerosols, Environ. Res. Lett., 3, 025007, https://doi.org/10.1088/1748-9326/3/2/025007, 2008.

Mohr, C., DeCarlo, P. F., Heringa, M. F., Chirico, R., Slowik, J. G., Richter, R., Reche, C., Alastuey, A., Querol, X., Seco, R., Peñuelas, J., Jiménez, J. L., Crippa, M., Zimmermann, R., Baltensperger, U., and Prévôt, A. S. H.: Identification and quantification of organic aerosol from cooking and other sources in Barcelona using aerosol mass spectrometer data, Atmos. Chem. Phys., 12, 1649–1665, https://doi.org/10.5194/acp-12-1649-2012, 2012.

Mohr, C., Lopez-Hilfiker, F. D., Yli-Juuti, T., Heitto, A., Lutz, A., Hallquist, M., D'Ambro, E. L., Rissanen, M. P., Hao, L. Q., Schobesberger, S., Kulmala, M., Mauldin, R. L., Makkonen, U., Sipilä, M., Petäjä, T., and Thornton, J. A.: Ambient observations of dimers from terpene oxidation in the gas phase: Implications for new particle formation and growth, Geophys. Res. Lett., 44, 2958–2966, 2017.

Müller, L., Reinnig, M.-C., Warnke, J., and Hoffmann, Th.: Unambiguous identification of esters as oligomers in secondary organic aerosol formed from cyclohexene and cyclohexene/a-pinene ozonolysis, Atmos. Chem. Phys., 8, 1423–1433, https://doi.org/10.5194/acp-8-1423-2008, 2008.

Murphy, D. M. and Koop, T.: Review of the vapour pressures of ice and supercooled water for atmospheric applications, Q. J. Roy. Meteor. Soc., 131, 1539–1565, 2005.

Murphy, D. M., Cziczo, D. J., Froyd, K. D., Hudson, P. K., Matthew, B. M., Middlebrook, A. M., Peltier, R. E., Sullivan, A., Thomson, D. S., and Weber, R. J.: Single-particle mass spectrometry of tropospheric aerosol particles, J. Geophys. Res.-Atmos., 111, D23S32, https://doi.org/10.1029/2006jd007340, 2006.

Nel, A.: Air pollution-related illness: Effects of particles, Science, 308, 804–806, 2005.

Nozière, B., Kaberer, M., Claeys, M., Allan, J., D'Anna, B., Decesari, S., Finessi, E., Glasius, M., Grgić, I., Hamilton, J. F., Hoffmann, T., Iinuma, Y., Jaoui, M., Kahno, A., Kampf, C. J., Kourtchev, I., Maenhaut, W., Marsden, N., Saarikoski, S., Schnelle-Kreis, J., Surratt, J. D., Szidat, S., Szmigielski, R., and Wisthaler, A.: The molecular identification of organic compounds in the atmosphere: State of the art and challenges, Chem. Rev., 115, 3919–3983, 2015.

Pajunoja, A., Malila, J., Hao, L. Q., Joutsensaari, J., Lehtinen, K. E. J., and Virtanen, A.: Estimating the viscosity range of SOA particles based on their coalescence Time, Aerosol. Sci. Tech., 48, i–iv, https://doi.org/10.1080/02786826.2013.870325, 2014.

Pajunoja, A., Lambe, A. T., Hakala, J., Rastak, N., Cummings, M. J., Brogan, J. F., Hao, L. Q., Paramonov, M., Hong, J., Prisle, N. L., Malila, J., Romakkaniemi, S., Lehtinen, K. E. J., Laaksonen, A., Kulmala, M., Massoli, P., Onasch, T. B., Donahue, N. M., Riipinen, I., Davidovits, P., Worsnop, D. R., Petäjä, T., and Virtanen, A.: Adsorptive uptake of water by semisolid secondary organic aerosols, Geophys. Res. Lett., 42, 3063–3068, 2015.

Price, H. C., Mattsson, J., Zhang, Y., Bertram, A. K., Davies, J. F., Grayson, J. W., Martin, S. T., O'Sullivan, D., Reid, J. P., Rickards, A. M. J., and Murray, B. J.: Water diffusion in atmo-

Atmos. Chem. Phys., 18, 2883–2898, 2018   www.atmos-chem-phys.net/18/2883/2018/

245

spherically relevant α-pinene secondary organic material, Chem. Sci., 6, 4876–4883, 2015.

Renbaum-Wolff, L., Grayson, J. W., Bateman, A. P., Kuwata, M., Sellier, M., Murray, B. J., Shilling, J. E., Martin, S. T., and Bertram, A. K.: Viscosity of α-pinene secondary organic material and implications for particle growth and reactivity, P. Natl. Acad. Sci. USA, 110, 8014–8019, 2013.

Roldin, P., Eriksson, A. C., Nordin, E. Z., Hermansson, E., Mogensen, D., Rusanen, A., Boy, M., Swietlicki, E., Svenningsson, B., Zelenyuk, A., and Pagels, J.: Modelling non-equilibrium secondary organic aerosol formation and evaporation with the aerosol dynamics, gas- and particle-phase chemistry kinetic multilayer model ADCHAM, Atmos. Chem. Phys., 14, 7953–7993, https://doi.org/10.5194/acp-14-7953-2014, 2014.

Rückerl, R., Schneider, A., Breitner, S., Cyrys, J., and Peters, A.: Health effects of particulate air pollution: A review of epidemiological evidence, Inhal. Toxicol., 23, 555–592, 2011.

Saathoff, H., Naumann, K.-H., Möhler, O., Jonsson, Å. M., Hallquist, M., Kiendler-Scharr, A., Mentel, Th. F., Tillmann, R., and Schurath, U.: Temperature dependence of yields of secondary organic aerosols from the ozonolysis of a-pinene and limonene, Atmos. Chem. Phys., 9, 1551–1577, https://doi.org/10.5194/acp-9-1551-2009, 2009.

Schnaiter, M., Järvinen, E., Vochezer, P., Abdelmonem, A., Wagner, R., Jourdan, O., Mioche, G., Shcherbakov, V. N., Schmitt, C. G., Tricoli, U., Ulanowski, Z., and Heymsfield, A. J.: Cloud chamber experiments on the origin of ice crystal complexity in cirrus clouds, Atmos. Chem. Phys., 16, 5091–5110, https://doi.org/10.5194/acp-16-5091-2016, 2016.

Shiraiwa, M., Ammann, M., Koop, T., and Pöschl, U.: Gas uptake and chemical aging of semisolid organic aerosol particles, P. Natl. Acad. Sci. USA, 108, 11003–11008, 2011.

Shiraiwa, M., Li, Y., Tsimpidi, A. P., Karydis, V. A., Berkemeier, T., Pandis, S. N., Lelieveld, J., Koop, T., and Pöschl, U.: Global distribution of particle phase state in atmospheric secondary organic aerosols, Nat. Commun., 8, 15002, https://doi.org/10.1038/ncomms15002, 2017.

Shrivastava, M., Easter, R. C., Liu, X. H., Zelenyuk, A., Singh, B., Zhang, K., Ma, P.-L., Chand, D., Ghan, S., Jimenez, J. L., Zhang, Q., Fast, J., Rasch, P. J., and Tiitta, P.: Global transformation and fate of SOA: Implications of low-volatility SOA and gas-phase fragmentation reactions, J. Geophys. Res.-Atmos., 120, 4169–4195, 2015.

Skrotzki, J., Connolly, P., Schnaiter, M., Saathoff, H., Möhler, O., Wagner, R., Niemand, M., Ebert, V., and Leisner, T.: The accommodation coefficient of water molecules on ice – cirrus cloud studies at the AIDA simulation chamber, Atmos. Chem. Phys., 13, 4451–4466, https://doi.org/10.5194/acp-13-4451-2013, 2013.

Song, Y. C., Haddrell, A. E., Bzdek, B. R., Reid, J. P., Barman, T., Topping, D. O., Percival, C., and Cai, C.: Measurements and predictions of binary component aerosol particle viscosity, J. Phys. Chem. A, 120, 8123–8137, 2016.

Tröstl, J., Chuang, W. K., Gordon, H., Heinritzi, M., Yan, C., Molteni, U., Ahlm, L., Frege, C., Bianchi, F., Wagner, R., Simon, M., Lehtipalo, K., Williamson, C., Craven, J. S., Duplissy, J., Adamov, A., Almeida, J., Bernhammer, A.-K., Breitenlechner, M., Brilke, S., Dias, A., Ehrhart, S., Flagan, R. C., Franchin, A., Fuchs, C., Guida, R., Gysel, M., Hansel, A., Hoyle, C. R.,

Jokinen, T., Junninen, H., Kangasluoma, J., Keskinen, H., Kim, J., Krapf, M., Kürten, A., Laaksonen, A., Lawler, M., Leiminger, M., Mathot, S., Möhler, O., Nieminen, T., Onnela, A., Petäjä, T., Piel, F. M., Miettinen, P., Rissanen, M. P., Rondo, L., Sarnela, N., Schobesberger, S., Sengupta, K., Sipilä, M., Smith, J. N., Steiner, G., Tomè, A., Virtanen, A., Wagner, A. C., Weingartner, E., Wimmer, D., Winkler, P. M., Ye, P. L., Carslaw, K. S., Curtius, J., Dommen, J., Kirkby, J., Kulmala, M., Riipinen, I., Worsnop, D. R., Donahue, N. M., and Baltensperger, U.: The role of low-volatility organic compounds in initial particle growth in the atmosphere, Nature, 533, 527–531, 2016.

Tsigaridis, K., Krol, M., Dentener, F. J., Balkanski, Y., Lathière, J., Metzger, S., Hauglustaine, D. A., and Kanakidou, M.: Change in global aerosol composition since preindustrial times, Atmos. Chem. Phys., 6, 5143–5162, https://doi.org/10.5194/acp-6-5143-2006, 2006.

Vaden, T. D., Imre, D., Beránek, J., Shrivastava, M., and Zelenyuk, A.: Evaporation kinetics and phase of laboratory and ambient secondary organic aerosol, P. Natl. Acad. Sci. USA, 108, 2190–2195, 2011.

Virtanen, A., Joutsensaari, J., Koop, T., Kannosto, J., Yli-Pirilä, P., Leskinen, J., Mäkelä, J. M., Holopainen, J. K., Pöschl, U., Kulmala, M., Worsnop, D. R., and Laaksonen, A.: An amorphous solid state of biogenic secondary organic aerosol particles, Nature, 467, 824–827, 2010.

Wagner, R., Höhler, K., Huang, W., Kiselev, A., Möhler, O., Mohr, C., Pajunoja, A., Saathoff, H., Schiebel, T., Shen, X. L., and Virtanen, A.: Heterogeneous ice nucleation of α-pinene SOA particles before and after ice cloud processing, J. Geophys. Res.-Atmos., 122, 4924–4943, 2017.

Wang, B. B., O'Brien, R. E., Kelly, S. T., Shilling, J. E., Moffet, R. C., Gilles, M. K., and Laskin, A.: Reactivity of liquid and semisolid secondary organic carbon with chloride and nitrate in atmospheric aerosols, J. Phys. Chem. A, 119, 4498–4508, 2015.

Wang, M. Y., Yao, L., Zheng, J., Wang, X. K., Chen, J. M., Yang, X., Worsnop, D. R., Donahue, N. M., and Wang, L.: Reactions of atmospheric particulate stabilized Criegee intermediates lead to high-molecular-weight aerosol components, Environ. Sci. Technol., 50, 5702–5710, 2016.

Williams, L. R., Gonzalez, L. A., Peck, J., Trimborn, D., McInnis, J., Farrar, M. R., Moore, K. D., Jayne, J. T., Robinson, W. A., Lewis, D. K., Onasch, T. B., Canagaratna, M. R., Trimborn, A., Timko, M. T., Magoon, G., Deng, R., Tang, D., de la Rosa Blanco, E., Prévôt, A. S. H., Smith, K. A., and Worsnop, D. R.: Characterization of an aerodynamic lens for transmitting particles greater than 1 micrometer in diameter into the Aerodyne aerosol mass spectrometer, Atmos. Meas. Tech., 6, 3271–3280, https://doi.org/10.5194/amt-6-3271-2013, 2013.

Wilson, J., Imre, D., Beránek, J., Shrivastava, M., and Zelenyuk, A.: Evaporation kinetics of laboratory-generated secondary organic aerosols at elevated relative humidity, Environ. Sci. Technol., 49, 243–249, 2015.

Winterhalter, R., Van Dingenen, R., Larsen, B. R., Jensen, N. R., and Hjorth, J.: LC-MS analysis of aerosol particles from the oxidation of α-pinene by ozone and OH-radicals, Atmos. Chem. Phys. Discuss., https://doi.org/10.5194/acpd-3-1-2003, in review, 2003.

Yasmeen, F., Vermeylen, R., Szmigielski, R., Iinuma, Y., Böge, O., Herrmann, H., Maenhaut, W., and Claeys, M.: Terpenylic

acid and related compounds: precursors for dimers in secondary organic aerosol from the ozonolysis of α- and β-pinene, Atmos. Chem. Phys., 10, 9383–9392, https://doi.org/10.5194/acp-10-9383-2010, 2010.

Yli-Juuti, T., Pajunoja, A., Tikkanen, O. P., Buchholz, A., Faiola, C., Väisänen, O., Hao, L. Q., Kari, E., Peräkylä, O., Garmash, O., Shiraiwa, M., Ehn, M., Lehtinen, K., and Virtanen, A.: Factors controlling the evaporation of secondary organic aerosol from α-pinene ozonolysis, Geophys. Res. Lett., 44, 2562–2570, 2017.

Zhang, Q., Jimenez, J. L., Canagaratna, M. R., Allan, J. D., Coe, H., Ulbrich, I., Alfarra, M. R., Takami, A., Middlebrook, A. M., Sun, Y. L., Dzepina, K., Dunlea, E., Docherty, K., De-Carlo, P. F., Salcedo, D., Onasch, T., Jayne, J. T., Miyoshi, T., Shimono, A., Hatakeyama, S., Takegawa, N., Kondo, Y., Schneider, J., Drewnick, F., Borrmann, S., Weimer, S., Demerjian, K., Williams, P., Bower, K., Bahreini, R., Cottrell, L., Griffin, R. J., Rautiainen, J., Sun, J. Y., Zhang, Y. M., and Worsnop, D. R.: Ubiquity and dominance of oxygenated species in organic aerosols in anthropogenically-influenced Northern Hemisphere midlatitudes, Geophys. Res. Lett., 34, L13801, https://doi.org/10.1029/2007gl029979, 2007.

Zhang, X., McVay, R. C., Huang, D. D., Dalleska, N. F., Aumont, B., Flagan, R. C., and Seinfeld, J. H.: Formation and evolution of molecular products in α-pinene secondary organic aerosol, P. Natl. Acad. Sci. USA, 112, 14168–14173, 2015.

Zhang, X., Lambe, A. T., Upshur, M. A., Brooks, W. A., Beì, A. G., Thomson, R. J., Geiger, F. M., Surratt, J. D., Zhang, Z. F., Gold, A., Graf, S., Cubison, M. J., Groessl, M., Jayne, J. T., Worsnop, D. R., and Canagaratna, M. R.: Highly oxygenated multifunctional compounds in α-pinene secondary organic aerosol, Environ. Sci. Technol., 51, 5932–5940, 2017.

Atmos. Chem. Phys., 18, 2883–2898, 2018   **www.atmos-chem-phys.net/18/2883/2018/**

247

Appendix C.5 Heterogeneous ice nucleation of α-pinene SOA particles before and after ice cloud processing

AGUPUBLICATIONS

JGR

Journal of Geophysical Research: Atmospheres

Key Points:
- Pristine α-pinene SOA particles reveal poor heterogeneous ice nucleation ability in the cirrus cloud regime of the upper troposphere
- Ice cloud processing of α-pinene SOA particles in a convective cloud system leads to formation of highly porous particles
- Freeze-dried SOA particles show heterogeneous ice formation in the mixed-phase cloud regime via the CCN-induced ice growth mode

Correspondence to:
R. Wagner,
robert.wagner2@kit.edu

Heterogeneous ice nucleation of α-pinene SOA particles before and after ice cloud processing

Robert Wagner[1] (ID), Kristina Höhler[1], Wei Huang[1], Alexei Kiselev[1] (ID), Ottmar Möhler[1] (ID), Claudia Mohr[1] (ID), Aki Pajunoja[2] (ID), Harald Saathoff[1], Thea Schiebel[1], Xiaoli Shen[1], and Annele Virtanen[2] (ID)

[1]Institute of Meteorology and Climate Research, Karlsruhe Institute of Technology, Karlsruhe, Germany, [2]Department of Applied Physics, University of Eastern Finland, Kuopio, Finland

Abstract The ice nucleation ability of α-pinene secondary organic aerosol (SOA) particles was investigated at temperatures between 253 and 205 K in the Aerosol Interaction and Dynamics in the Atmosphere cloud simulation chamber. Pristine SOA particles were nucleated and grown from pure gas precursors and then subjected to repeated expansion cooling cycles to compare their intrinsic ice nucleation ability during the first nucleation event with that observed after ice cloud processing. The unprocessed α-pinene SOA particles were found to be inefficient ice-nucleating particles at cirrus temperatures, with nucleation onsets (for an activated fraction of 0.1%) as high as for the homogeneous freezing of aqueous solution droplets. Ice cloud processing at temperatures below 235 K only marginally improved the particles' ice nucleation ability and did not significantly alter their morphology. In contrast, the particles' morphology and ice nucleation ability was substantially modified upon ice cloud processing in a simulated convective cloud system, where the α-pinene SOA particles were first activated to supercooled cloud droplets and then froze homogeneously at about 235 K. As evidenced by electron microscopy, the α-pinene SOA particles adopted a highly porous morphology during such a freeze-drying cycle. When probing the freeze-dried particles in succeeding expansion cooling runs in the mixed-phase cloud regime up to 253 K, the increase in relative humidity led to a collapse of the porous structure. Heterogeneous ice formation was observed after the droplet activation of the collapsed, freeze-dried SOA particles, presumably caused by ice remnants in the highly viscous material or the larger surface area of the particles.

1. Introduction

The ice nucleation ability of organic aerosol particles is a rapidly developing field of research. This is exemplified by the large number of experimental and theoretical investigations on that issue, which have been published since the release of the latest comprehensive review on laboratory measurements of ice nucleation on atmospheric aerosols [*Hoose and Möhler*, 2012]. A key question of the recent studies was the identification of organic compounds that are able to contribute to the abundance of ice-nucleating particles (INPs) in the atmosphere, i.e., particles that are responsible for heterogeneous ice nucleation [*Vali et al.*, 2015].

Some organic compounds, like various monocarboxylic and dicarboxylic acids, exist in the crystalline solid state and were shown to promote heterogeneous ice nucleation via deposition nucleation when prevalent as bare substances [*Baustian et al.*, 2010; *Schill and Tolbert*, 2012; *Shilling et al.*, 2006; *Wagner et al.*, 2010] or via immersion freezing when embedded as crystalline inclusions in water or aqueous solution droplets [*Wagner et al.*, 2011, 2015; *Zobrist et al.*, 2006]. Organic compounds also frequently form amorphous semisolid or amorphous solid (glassy) states at low temperature and/or relative humidity [*Koop et al.*, 2011; *Virtanen et al.*, 2010; *Zobrist et al.*, 2008]. In such cases, the glass transition relative humidity (RH_g) and the timescale for water diffusion in the particles will control the mode of ice nucleation during an atmospheric updraft [*Berkemeier et al.*, 2014]. Depositional ice nucleation on the surface of the particles may occur before passing the RH_g line during humidification of the air upon an adiabatic expansion, as first experimentally evidenced with glassy citric acid aerosol particles [*Murray et al.*, 2010]. The RH_g threshold denotes the onset of the humidity-induced phase transition from the glassy into the liquid region, also termed as amorphous deliquescence [*Mikhailov et al.*, 2009]. In an updraft with fast relative humidity increase, the water diffusion in the glassy organic particles may be too slow for immediately transforming them into entirely liquid solution droplets above RH_g, resulting in core-shell morphologies with glassy cores and liquid outer layers [*Berkemeier et al.*, 2014]. Such partially deliquesced particles can trigger ice nucleation via immersion

freezing. Further humidification leads to a continuous shrinkage of the glassy core, until entirely liquid particles are finally formed at the full deliquescence relative humidity [*Berkemeier et al.*, 2014]. Above that limit, homogeneous freezing remains the only feasible ice nucleation mechanism [*Koop et al.*, 2000].

After the first measurements of heterogeneous ice nucleation on glassy materials using citric acid [*Murray et al.*, 2010], further experimental work was performed with other proxies for atmospherically abundant organic aerosol particles, e.g., with single compounds like raffinose, levoglucosan, HMMA (4-hydroxy-3-methoxy-DL-mandelic acid), sucrose, and glucose [*Baustian et al.*, 2013; *Wilson et al.*, 2012] and with multicomponent mixtures like raffinose/M5/AS (M5: mixture of five dicarboxylic acids, AS: ammonium sulfate), citric acid/AS, glucose/AS, sucrose/AS, and 1,2,6-hexanetriol/2,2,6,6-tetrakis(hydroxymethyl)cyclohexanol [*Baustian et al.*, 2013; *Schill and Tolbert*, 2013; *Wilson et al.*, 2012]. In an attempt to categorize the ice nucleation abilities of amorphous organic (semi)solids, the latter compounds were grouped into the class "simple sugars/acids" to differentiate them from organic aerosol components that are formed by chemical reactions in the atmosphere (secondary organic aerosol, SOA) [*Schill et al.*, 2014]. Ice nucleation studies with SOA compounds include the reaction products from the gas phase oxidation of naphthalene with OH radicals [*Wang et al.*, 2012], the aqueous phase reaction of methylglyoxal with methylamine [*Schill et al.*, 2014], and the ozonolysis of alkenes and α-pinene [*Ignatius et al.*, 2016; *Ladino et al.*, 2014; *Möhler et al.*, 2008; *Prenni et al.*, 2009], the latter being one of the most abundant monoterpene SOA precursor compounds [*Hallquist et al.*, 2009].

The organic compounds belonging to the class of simple sugars/acids reveal a higher ability to act as INPs at cirrus temperatures compared to the SOA species. This is illustrated by comparatively low onset ice saturation ratios, S_{ice}, for heterogeneous ice nucleation, which are typically in the range from 1.1 to 1.4 for temperatures between 235 and 200 K and thereby clearly fall below the homogeneous freezing threshold that ranges from about 1.45 to 1.6 in the same temperature regime [*Schill et al.*, 2014]. With freezing onsets in terms of S_{ice} between about 1.4 at 235 K and 1.5 at 200 K, the ice nucleation data for the naphthalene + OH and methylglyoxal + methylamine SOA particles can still be unambiguously assigned to the heterogeneous nucleation regime. This assignment is less definite for the α-pinene SOA particles where the experimental findings are partly inconsistent. The currently most extensive data set for the ice nucleation ability of freshly generated α-pinene SOA particles from *Ladino et al.* [2014] shows freezing onsets at or even slightly above the homogeneous freezing line at temperatures between 233 and 213 K. This poor ice nucleation ability for α-pinene SOA is substantiated by the measurement from *Möhler et al.* [2008] conducted at a temperature of 205 K, where the onset of ice nucleation only occurred at an ice saturation ratio as high as 1.7. In contrast, one of the most recent ice nucleation studies with α-pinene SOA particles revealed freezing onsets below the homogeneous freezing limit at temperatures around 235 K [*Ignatius et al.*, 2016]. Specifically, ice saturation ratios between 1.3 and 1.4 for the nucleation onset as well as ice-active fractions of up to 20% were found [*Ignatius et al.*, 2016].

These experimental findings can be compared to recent measurements of the low-temperature water diffusion coefficients in SOA material generated from the oxidation of α-pinene with OH radicals and ozone [*Lienhard et al.*, 2015; *Price et al.*, 2015]. As outlined above, kinetic limitations in water diffusion would favor the particles' ability to act as heterogeneous ice nuclei during humidification because the process of amorphous deliquescence would be slowed down. Data and model calculations from *Lienhard et al.* [2015] suggest that for temperatures above 220 K the SOA particles equilibrate with the ambient relative humidity for an updraft velocity as high as 3 m s^{-1}, meaning that heterogeneous ice nucleation is unlikely under such conditions. Below 220 K, a glassy or highly viscous core might persist when the particles' trajectory reaches the regime of ice supersaturation, thereby enabling heterogeneous ice nucleation in the immersion freezing mode. At very cold temperatures below 195 K, water diffusion could be limited to such a degree that homogeneous ice nucleation of the particles would be delayed, even for small updrafts of 0.1 m s^{-1} [*Lienhard et al.*, 2015]. *Price et al.* [2015] conclude that at a starting temperature of 220 K and an updraft speed in the range of 0.02–2 m s^{-1} or at a starting temperature of 230 K and an updraft speed of 2 m s^{-1}, the core of the α-pinene SOA particles might still prevail in an amorphous solid state when the relative humidity of the environment exceeds ice saturation.

Obviously, there is a need to reconcile the water diffusion measurements in α-pinene SOA with at least part of the ice nucleation experiments, as, e.g., *Ignatius et al.* [2016] observed heterogeneous ice nucleation at a temperature where the particles are supposed to be fully equilibrated with the gas phase humidity

[*Lienhard et al.*, 2015]. However, the comparison between various studies is not straightforward because the chemical composition of the generated SOA materials (as, e.g., expressed by their elemental oxygen-to-carbon and hydrogen-to-carbon ratios) may vary due to different oxidants (OH radicals and ozone), precursor concentrations, residence times, and oxidation temperatures employed [*Grayson et al.*, 2016]. Also, particle processing like precooling was shown to have an influence on the ice nucleation ability [*Ladino et al.*, 2014].

A drawback of most laboratory studies is that the determination of the onset conditions for ice nucleation in the case of SOA particles does not automatically disclose the underlying ice nucleation mechanism because it is difficult to probe the particle morphology in situ during the trajectory of humidification. Let us, e.g., consider the results from *Ladino et al.* [2014] who found freezing onsets close to the homogeneous freezing line for α-pinene SOA. This could mean (i) that the particles had completely been liquefied and frozen homogeneously; (ii) that the particles had a core-shell morphology at the freezing onset, with the glassy core just being inefficient in triggering ice nucleation by immersion freezing before the homogeneous freezing limit was reached and the surrounding liquid layer nucleated ice; and (iii) that the particles had remained entirely in the glassy state during humidification, and the onset of ice nucleation via deposition nucleation on the glassy surface just accidentally coincided with the homogeneous freezing threshold. Recently, the use of in situ, near-backscattering depolarization measurements was explored to detect temperature- and humidity-induced viscosity transitions in α-pinene SOA particles [*Järvinen et al.*, 2016]. The applicability of this technique, however, is limited to laboratory experiments with very high number concentrations and particle sizes above 0.6 μm, where nonspherical SOA particle aggregates can be formed, whose transition to less viscous and thereby spherical particle morphologies can be detected by a decrease in the depolarization ratio.

An indirect measure to infer the ice nucleation mechanism for glassy SOA particles could be the degree of morphology change during ice cloud processing (atmospheric freeze drying) [*Adler et al.*, 2013; *Wagner et al.*, 2012]. Provided that the glassy particles liquefy during the updraft and homogeneous freezing occurs, the ice growth within the liquefied droplets will lead to a revitrification of the freeze-concentrated organic solution, and the subsequent sublimation of ice will leave behind highly porous aerosol particles. Evidence for such porous aerosol formation comes from freeze-drying experiments with particles generated from a reference sample for natural organic matter (Suwannee River Natural Organic Matter, International Humic Substances Society), where the particle morphology before and after the freeze-drying step was inferred from electron microscopy [*Adler et al.*, 2013]. The formation of a porous structure with potential surface defects and a larger surface area compared to a smooth sphere could also explain experimental findings from previous Aerosol Interaction and Dynamics in the Atmosphere (AIDA) measurements with amorphous organic aerosol particles of the simple sugars/acids category [*Wagner et al.*, 2012], where an increase in the ice nucleation efficiency of the aerosol particles was detected after a preceding homogeneous ice freezing experiment. Such structural change will not occur if the organic particles remain glassy in the course of an ice nucleation event and act as INPs in the deposition mode. Repeated ice nucleation experiments with the same load of organic aerosol particles, together with the analysis of associated changes in the morphology and the ice nucleation ability of the particles, could therefore be a valuable tool to gain further information about the ice nucleation mechanism.

In the present study, we first provide a new temperature-dependent data set for the ice nucleation ability of pristine SOA particles generated from the ozonolysis of α-pinene. The ice nucleation experiments were performed in the AIDA (Aerosol Interaction and Dynamics in the Atmosphere) cloud chamber, which has already successfully been employed in previous studies with glassy materials [*Möhler et al.*, 2008; *Murray et al.*, 2010; *Saathoff et al.*, 2009; *Wagner et al.*, 2012; *Wilson et al.*, 2012]. Specifically, our new study extends the former ice nucleation measurement for α-pinene SOA at 205 K [*Möhler et al.*, 2008] to a temperature range from 243 to 205 K, which immediately allows the comparison of the new data with those from *Ladino et al.* [2014] and *Ignatius et al.* [2016] for the same SOA precursor compound.

In addition to the ice nucleation measurements with pristine α-pinene SOA particles, the second main goal of this work is to explore to what extent freeze drying and porous aerosol particle formation occur at different temperatures and what the associated effect on the particles' ice nucleation efficiency would be. Our paper is structured as follows: After describing the instrumentation and technical operation of the AIDA chamber in section 2, we analyze in section 3 the ice nucleation experiments with pristine, unprocessed SOA particles from the ozonolysis of α-pinene, compare our results to previous literature studies, and discuss the

potential freezing mechanisms. Section 4 investigates the ice cloud processing of the α-pinene SOA particles and the modification of their ice nucleation ability in repeated ice nucleation experiments. We then conclude our article with a summary and an outlook on future experiments in section 5.

2. Experimental

2.1. General Setup

The AIDA facility consists of two aerosol vessels, (i) an 84.3 m^3-sized aluminum chamber, referred to as the AIDA chamber and (ii) a 3.7 m^3-sized stainless steel chamber, referred to as the aerosol preparation and characterization (APC) vessel (Figure 1) [*Möhler et al.*, 2008]. The APC vessel can only be operated at ambient temperature (295 K) and was used to generate the α-pinene SOA particles in a reproducible manner (section 2.2). A fraction of the SOA particles was then transferred through a stainless steel tube into the AIDA vessel for the ice nucleation experiments. The AIDA chamber is located in an isolating containment and can be cooled to any temperature between ambient and 183 K. Supersaturations with respect to ice are achieved by expansion cooling, as conducted by a controlled reduction of the chamber pressure with a mechanical pump that is typically operated at volume flow rates between 1.5 and 3 m^3/min (section 2.3). During the freeze-drying experiments, the evacuated APC vessel served as additional expansion volume to induce a rapid increase in the ice supersaturation (section 2.4).

2.2. Aerosol Generation and Characterization

Before aerosol preparation, the APC vessel was evacuated to a pressure below 1 hPa and then filled with particle-free synthetic air to ambient pressure. SOA particles were generated by reacting (1S)-(−)-α-pinene (99%, Aldrich) and ozone (Semozon 030.2 discharge generator, Sorbios) in the dark at low relative humidity with respect to water (RH$_w$ < 10%). First, 2 ppmv of ozone was added to the APC vessel, followed by the addition of 2 ppmv of α-pinene. A few experiments were also conducted with (S)-(−)-limonene (>97%, Merck) instead of α-pinene as the SOA precursor compound. The number concentration of the nucleated SOA particles was measured with condensation particle counters (CPC3010 and CPC3022, TSI) and their size distribution recorded with a scanning mobility particle sizer (SMPS, TSI) and an aerodynamic particle spectrometer (APS, TSI). After a reaction and growth period of 1 h, the SOA particles had a number concentration of ~$3 \cdot 10^5$ cm^{-3} and formed a unimodal size distribution that could accurately be fitted with a lognormal function, yielding a median mobility-equivalent diameter, d_{me}, of ~300 nm and a mode width, σ_g, of ~1.3. A fraction of the SOA particles from the APC vessel was then transferred through a stainless steel tube into the cooled AIDA chamber. The connection between APC and AIDA was closed when the number concentration of particles in the AIDA chamber reached a value of 1500 cm^{-3}. The size distribution of the SOA particles in AIDA was recorded with a second set of SMPS and APS instruments. An exemplary size distribution as measured in the AIDA chamber is shown in the top left part of Figure 1. The AIDA chamber was held at temperatures between 243 and 205 K, representing the starting conditions for the ice nucleation experiments described in section 2.3. RH$_w$ in AIDA was controlled by an ice layer on the chamber walls and varied between ~70% at 243 K and ~55% at 205 K. For each individual ice nucleation experiment at a different AIDA temperature, a fresh load of α-pinene SOA particles was generated in the APC vessel using the same experimental procedure and transferred to AIDA, guaranteeing reproducible and uniform particle properties in terms of number concentration, size, and chemical composition. The composition of the SOA particles in AIDA was characterized with a high-resolution time-of-flight aerosol mass spectrometer (HR-ToF-AMS, Aerodyne). For all experiments, the mean oxygen-to-carbon (O/C) and hydrogen-to-carbon (H/C) ratios of the SOA particles as inferred from the AMS measurements were 0.35 and 1.55, respectively.

The ice nucleation experiments discussed in this article were part of an extended measurement campaign on the chemical and physical properties of α-pinene SOA particles in the temperature range from 298 to 205 K. Further information about the individual organic compounds in the SOA particles, as inferred from high-resolution time-of-flight chemical ionization mass spectrometer measurements (FIGAERO-HR-ToF-CIMS, Aerodyne) [*Lopez-Hilfiker et al.*, 2014], will be discussed in a forthcoming article. In addition to the CIMS analyses, the bounce characteristics of the SOA particles were measured by the Aerosol Bounce Instrument (ABI) [*Pajunoja et al.*, 2015]. The ABI, however, could only be operated down to a temperature of 258 K inside the isolating containment of the AIDA chamber (Figure 1), thereby probing the particles at conditions as prevalent in the AIDA chamber itself. Below 258 K, the ABI had to be removed from the cold housing, meaning that
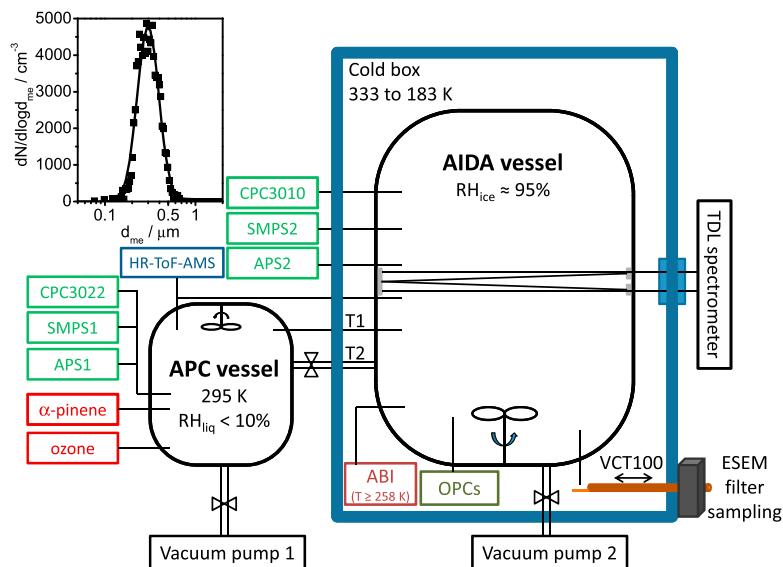
Figure 1. Simplified scheme of the AIDA aerosol and cloud chamber facility with the relevant scientific instrumentation used in this study. Both the volumes of the AIDA and the APC chamber are stirred by mixing fans mounted at the bottom and at the top of the vessels, respectively. T1 is a 25 mm stainless steel connection tube to transfer the α-pinene SOA particles from the APC to the AIDA aerosol vessel. T2 is a 100 mm stainless steel connection tube between the two aerosol vessels, whose valve is opened during the freeze-drying experiments to provoke an additional expansion of the AIDA volume into the evacuated APC vessel (section 2.4). All instruments and abbreviations are discussed in sections 2.1 to 2.4. The insert in the top left shows a typical number size distribution of the SOA particles after having them transferred from the APC into the AIDA chamber at 243 K. The SMPS data points (squares) could be accurately fitted with a unimodal lognormal distribution function, yielding $\sigma_g = 1.32$ and $d_{me} = 0.30$ μm.

it was not possible to measure the bounced fraction of the particles in the temperature regime covered by the ice nucleation experiments. Also, the specific demands with respect to particle number concentration and size for depolarization measurements to be sensitive to probe the phase state of the SOA particles, as estimated to be 10,000 cm^{-3} particles with a diameter of at least 600 nm [*Järvinen et al.*, 2016], were not met in our study.

We have therefore no direct information about the phase state of the α-pinene SOA particles after injecting them into the AIDA at $T \leq 243$ K and RH$_w \leq 70\%$. From a particular freeze-drying experiment conducted at an initial temperature of 243 K, however, we obtained unambiguous evidence that the SOA particles resided in a highly viscous state even at 243 K and 70% RH$_w$, i.e., at the highest temperature and relative humidity conditions before starting the expansion cooling experiments. This could be concluded because the freeze-dried SOA particles adopted and conserved a highly porous structure under these conditions and did not immediately collapse into spherical, less viscous particles. For the sake of clarity, we will discuss this experiment only later in this article (section 4.1) and presume for the discussion in section 3 that at the starting conditions of the ice nucleation experiments, highly viscous or glassy α-pinene SOA particles were present. This assumption is also in agreement with the temperature-and humidity-dependent parameterization of the viscosities of α-pinene SOA [*Wang et al.*, 2015].

2.3. Standard Ice Nucleation Experiments

Figure 2 (left) shows time series of the most important AIDA data during a typical ice nucleation experiment with α-pinene SOA particles at an initial temperature of 233 K, where the start of expansion cooling is denoted by time zero. Panel A depicts the evolution of the AIDA pressure (black line) and mean gas temperature (red line, computed from the average of a series of vertically arranged thermocouple sensors, uncertainty ± 0.3 K). The controlled reduction of the chamber pressure leads to a decrease in the gas temperature and an increase in the ice saturation ratio, S_{ice}, and the saturation ratio with respect to supercooled water, S_{liq} (panel
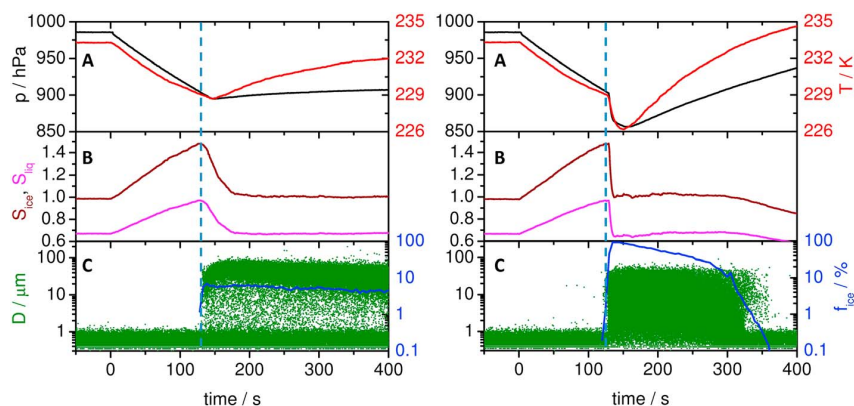
Figure 2. Ice nucleation characteristics of α-pinene SOA particles during (left) a standard ice nucleation and (right) a freeze-drying experiment. Panel A: AIDA pressure (black line) and mean gas temperature (red line). Panel B: Saturation ratio with respect to ice (S_{ice}, brown line) and liquid supercooled water (S_{liq}, magenta line). Panel C: Aerosol and cloud particle size distribution (green dots) and ice-active fraction of the aerosol population (f_{ice}, blue line).

B, brown and magenta lines, respectively). The latter two quantities were computed from the equations by *Murphy and Koop* [2005], based on water vapor concentrations that were measured in situ in the AIDA chamber by a tunable diode laser (TDL) spectrometer with an uncertainty of ±5% [*Fahey et al.*, 2014]. The onset of ice nucleation was measured with two optical particle counters (OPC, type welas 2000, Palas, overall size range 0.3–240 μm) that were mounted inside the isolating containment of the AIDA chamber (Figure 1). The OPC data are illustrated as a scatterplot (green dots in panel C), where each dot represents the signal of an individual particle that was categorized into a specific size channel of the OPC according to its scattering intensity. Initially, only the smaller-sized seed aerosol particles with optical diameters up to 1 μm are visible in the OPC records. The onset of ice formation at about $t = 130$ s (vertical line) is then clearly defined by the appearance of the nucleation mode of larger particles with optical diameters above 10 μm. By introducing an optical threshold size, the nucleated ice crystals can be separately counted, and by dividing the ice particle number concentration through the number concentration of the α-pinene SOA seed aerosol particles, the ice-active fraction of the aerosol population can be inferred (f_{ice}, blue line in panel C, estimated uncertainty ±20%). From each expansion cooling run, a data pair consisting of temperature and ice saturation ratio at the nucleation onset can be inferred, such as $T = 229.1$ K and $S_{ice} = 1.47$ for the experiment shown in Figure 2.

2.4. Freeze-Drying Experiments

In order to detect changes in the ice nucleation ability of the α-pinene SOA particles in repeated expansion cooling cycles, it is a prerequisite to activate and process as many seed aerosol particles as possible in the first ice nucleation run. As can be seen from the AIDA records of the standard ice nucleation experiment (Figure 2, left), only a small fraction of 6% of the particle ensemble was activated. This is because the ice supersaturation was rapidly depleted after the onset of ice nucleation so that no further ice crystals could nucleate. We therefore employed a special procedure to activate a larger fraction of the seed aerosol population (Figure 2, right). The freeze-drying experiment was started with a similar pumping speed as in the preceding standard ice nucleation run, but then, just when reaching the afore determined nucleation threshold ($S_{ice} = 1.47$, vertical line), a valve to the evacuated APC vessel was opened. The additional expansion provoked a further, almost instant decrease of the gas temperature by 2.5 K and led to the formation of a strong nucleation mode with an ice-active fraction close to 100%. After a short observation period of about 30 s, the AIDA vessel was refilled with dry synthetic air to ambient pressure, leading to the rapid sublimation of the nucleated ice crystals and leaving behind the population of ice cloud processed α-pinene SOA particles. In a subsequent ice nucleation experiment, we could then probe whether freeze drying had modified the ice nucleation ability of the seed aerosols compared to the behavior of the unprocessed particles shown in Figure 2 (left).

Two methods were used to probe a potential morphology change of the freeze-dried α-pinene SOA particles. Necessarily, these methods have to keep the SOA particles at cold temperatures as prevalent in the AIDA

chamber in order to not modify their phase state upon warming. On the one hand, the records from the optical particle counters, mounted in the thermostated housing of the AIDA chamber, proved to be useful to discriminate between compact and highly porous particle morphologies, in accordance with previous findings that the optical properties of these two particle types are substantially different [*Adler et al.*, 2014]. On the other, we developed a method to obtain electron microscope images of the aerosol particles before and after freeze drying. For that purpose, we used a vacuum cryotransfer system (EM VCT100, Leica) to ensure an unbroken cold chain from particle sampling to electron microscopic analysis. The cryotransfer unit includes a liquid-nitrogen cooled transfer shuttle with a silicon substrate mounted on a copper sample holder. For particle sampling, the Si substrate was introduced through a pneumatic lock into a sampling chamber located inside the isolating containment of the AIDA chamber. To achieve efficient sampling of SOA particles, the aerosol flow from AIDA was directed through a neutralizer (model 3077A, TSI) onto the sampling substrate connected to a high-voltage power supply set to 2 kV. After sampling, the substrate was retracted into the precooled shuttle. Thereafter, under continuous supply of liquid nitrogen, the shuttle was detached from the AIDA lock, transferred to a nearby laboratory, and attached to the lock of an environmental scanning electron microscope (ESEM, Quanta 650 FEG, FEI). This newly developed technique was successfully deployed during a freeze-drying experiment performed at 243 K. We plan to refine its operation in order to establish it as a standard diagnostic tool for future AIDA measurement campaigns. In the context of this work, we are limited to the results from this single experiment.

3. Ice Nucleation Experiments With Pristine, Unprocessed α-Pinene SOA Particles

3.1. Ice Nucleation Onsets and Potential Nucleation Mechanisms

Figure 3a shows the ice saturation ratios required to activate 0.1% of the unprocessed α-pinene SOA particles (dark green squares), as inferred from the standard ice nucleation experiments described in section 2.3. The error bars represent the 5% uncertainty of the water vapor measurements with the TDL spectrometer. A single expansion cooling run was conducted with limonene SOA particles at a starting temperature of 223 K. Its corresponding ice nucleation onset is shown as the dark green circle in Figure 3a. The data are compared to several nucleation onsets for various aerosol types reported previously, two of which we first want to take into consideration in our discussion: (i) the previous AIDA measurement with α-pinene SOA particles at 205 K (dark green diamond) [*Möhler et al.*, 2008] and (ii) the homogeneous freezing of aqueous sulfuric acid solution droplets (cyan stars), as also inferred from previous AIDA expansion cooling experiments [*Möhler et al.*, 2003]. *Möhler et al.* [2008] had also used the APC vessel to generate the SOA particles from α-pinene and ozone at room temperature in the dark. Hence, the α-pinene SOA particles should have been of similar, albeit unspecified, composition as those generated in the present study. The good agreement of the formerly derived nucleation onset for α-pinene SOA at 205 K with that from the present study supports this assumption and illustrates the excellent repeatability of the AIDA ice nucleation experiments.

The most striking observation from the data in Figure 3a is the similarity of the freezing onsets for α-pinene SOA particles and aqueous H_2SO_4/H_2O solution droplets. The latter are in reasonable agreement with the parameterization of the homogeneous freezing threshold from *Koop et al.* [2000], although the AIDA measurements tend to follow a slightly steeper slope, as already discussed in *Möhler et al.* [2003]. As mentioned in section 2.4, we postulate that the α-pinene SOA particles are initially in a highly viscous or glassy state before the expansion cooling runs are started. A possible explanation for the observed freezing behavior is thus the fast equilibration of the SOA particles with the increasing relative humidity during expansion cooling, meaning that the thickness of the diluted outer particle layer was at least equal to or larger than the diameter of the critical ice nucleus before the homogeneous freezing threshold was reached [*Lienhard et al.*, 2015]. In case the particles were only partially liquefied and still contained a glassy core, the absence of ice formation before the homogeneous freezing threshold would indicate the immersion freezing mode to be rather inefficient. Further conclusions on the prevailing ice nucleation mechanism cannot be drawn from the measurements of the ice nucleation onsets only, a drawback that has already been mentioned in section 1.

As an additional step in the analysis, we therefore investigated the ice-active fractions of the seed aerosol population during the expansion cooling cycles, as shown in Figure 3b (see also *Murray et al.* [2010, Figure 2] for a similar graphical representation). The black curves are the measured T-S_{ice} trajectories of the ice

255
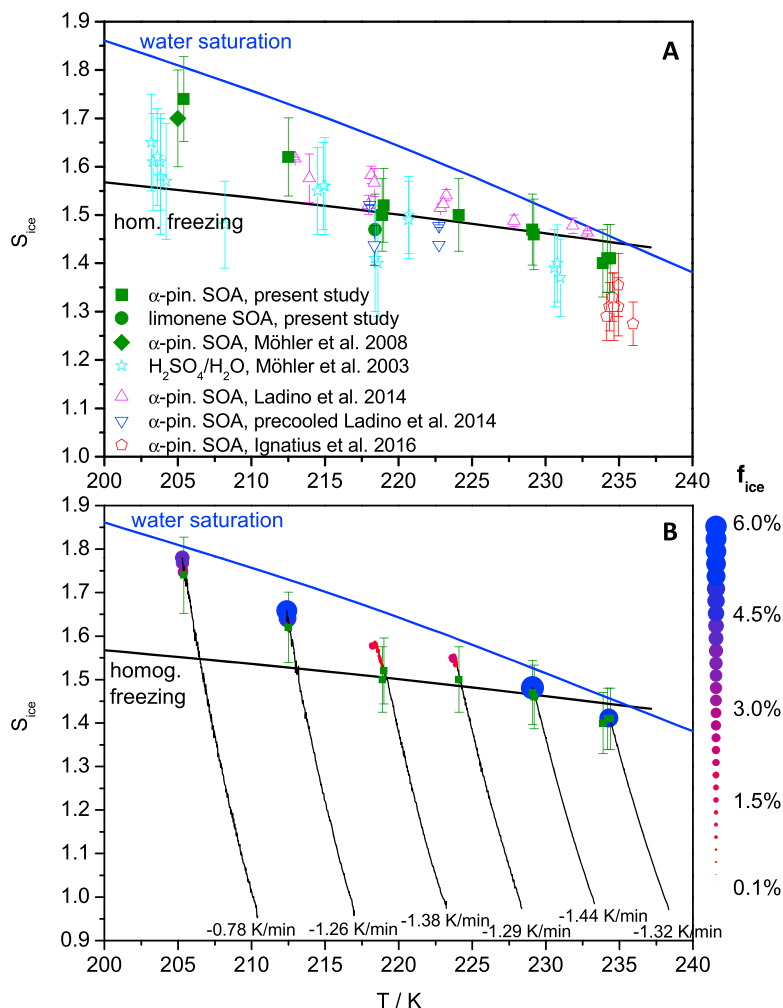
Figure 3. (a) Ice nucleation onsets of α-pinene and limonene SOA particles from this study in comparison with previously reported nucleation onsets for α-pinene SOA particles and aqueous sulfuric acid solution droplets, which are discussed in detail in section 3. The blue line is the saturation curve with respect to liquid supercooled water, and the black line represents the homogeneous freezing threshold [*Koop et al.*, 2000]. (b) T-S_{ice} trajectories of the expansion cooling experiments with the α-pinene SOA particles from this study (black curves), superimposed with the detected freezing onsets (dark green squares, same data as in Figure 3a) and the fractions of aerosol particles that activated to ice (size of the colored circles). The number at the bottom of each trajectory denotes the cooling rate at the ice nucleation onset. See section 3 for further discussion of this panel.

nucleation experiments with α-pinene SOA particles, covering the period from the start of expansion cooling at slightly ice-subsaturated conditions until the time when the maximum ice saturation ratio was reached. The numbers at the bottom of each trajectory denote the respective cooling rates at the ice nucleation onsets, the latter again marked by the dark green squares (same data as in Figure 3a). The size of the colored dots superimposed on the trajectories represents the ice-active fraction of the seed aerosol particles. For starting temperatures of 238, 233, and 223 K, two separate ice nucleation experiments were conducted, and for each of those, a fresh load of α-pinene SOA particles, afore generated in the APC vessel, was used. As can be seen from Figure 3a, the ice nucleation onsets for these pairs of expansion cooling experiments closely agree. The same is true for the time evolution of the ice-active fractions, and hence, for the sake of clarity, only a single trajectory is shown in Figure 3b for these temperatures. The selected experimental trajectory for the starting temperature of 233 K corresponds to the data shown in Figure 2 (left).

At initial temperatures of 238 and 233 K, the temporal development of the f_{ice} data displays the expected behavior for liquid or liquefied aerosol particles in which ice nucleates homogeneously. As soon as the homogeneous freezing threshold is reached, f_{ice} rapidly increases and the growth of the nucleated ice crystals almost immediately quenches the supersaturation and prevents further nucleation. As a result, the peak ice saturation ratio almost coincides with the nucleation onset. Such behavior is commonly observed for AIDA expansion cooling experiments with aqueous sulfuric acid solution droplets when similar cooling rates as in the α-pinene SOA experiments are employed. More importantly, the sharply defined homogeneous nucleation threshold with the immediate, strong increase in f_{ice} is also observed at temperatures down to about 200 K. Only when the expansion cooling runs are conducted at temperatures below 200 K, a nonequilibrium effect may delay the burst of homogeneously nucleated ice crystals, because the supercooled liquid particles do not reach their equilibrium water activity due to the small absolute amount of water vapor prevalent in the gas phase [*Haag et al.*, 2003]. This implicates that there is not such a sharp, sudden increase in f_{ice} at the homogeneous freezing threshold at $T < 200$ K. In addition, the nucleated ice crystals only slowly grow into the detection range of the OPCs at these low temperatures [*Möhler et al.*, 2003], thereby leading to an artificial delay in the measured evolution of f_{ice}. These two factors, however, do not count in the temperature regime of the SOA experiments considered in Figure 3. As an example, a sudden burst of homogeneously nucleated ice crystals was also detected for aqueous citric acid aerosol particles at a starting temperature of 215 K and contrasted with the behavior observed at lower temperatures in the glassy regime [*Murray et al.*, 2010]. Here the much more gradual increase in f_{ice} after the nucleation onset was attributed to a heterogeneous nucleation mode. For the α-pinene SOA particles, there is also a clear change in the evolution of f_{ice} with temperature (Figure 3b). At intermediate starting temperatures of 228 and 223 K, the number concentration of ice crystals that nucleate after exceeding the homogeneous freezing threshold is much smaller compared to the experiments at higher temperatures, even though similar cooling rates were encountered at the nucleation onsets. As a result, the ice supersaturation is not instantly depleted but rises clearly above the value of the nucleation onset, in which course f_{ice} gradually increases. Overall, the maximum ice-active fractions are by a factor of 3 to 4 smaller than at 238 and 233 K. Interestingly, the nucleation characteristics change again at even lower temperatures. At starting temperatures of 217 and 211 K, f_{ice} again more rapidly increases after the nucleation onset, limiting the peak ice supersaturation to a value only slightly above the nucleation onset. Also, the maximum ice-active fractions are again as high as during the experiments that started at 238 and 233 K; although particularly at the lowest starting temperature of 211 K the cooling rate at the nucleation onset is clearly reduced.

These variations in the evolution of f_{ice} are an indirect but robust indication for a change in the underlying ice nucleation mechanisms over the considered temperature range. Most likely, the nucleation modes observed at starting temperatures of 238 and 233 K can be attributed to homogeneous freezing, without being able to clarify whether the entire particle or just a sufficiently thick outer layer of the α-pinene SOA particles liquefies during expansion cooling. The retarded evolution of f_{ice} during the 228 and 223 K experiments can be interpreted as delayed homogeneous freezing, meaning that the glassy SOA particles just start to soften in the vicinity of the homogenous freezing limit. A slow formation of liquid layers would explain the observed gradual increase of the number concentration of nucleated ice crystals at elevated humidities above the homogeneous freezing limit [*Lienhard et al.*, 2015]. The again different behavior at lower temperatures could be due to the transition to yet another nucleation regime. According to our line of reasoning that condensed-phase diffusion is already slowed down during the expansion cooling experiments that started at 228 and 223 K, it seems unlikely that the α-pinene SOA particles would liquefy at all at even lower temperatures. This suggests deposition nucleation to be the prevailing ice formation mechanism for SOA particles at these temperatures, with just the accidental situation that the heterogeneous nucleation onsets for the SOA particles coincide with the homogeneous freezing thresholds for aqueous solution droplets.

3.2. Comparison With Literature Data

We now turn toward the comparison of our freezing onsets with those measured in preceding ice nucleation studies, thereby addressing the additional data displayed in Figure 3a. Our interpretation of a homogeneous freezing mode during the expansion cooling experiments at 238 and 233 K is in contradiction to the results of *Ignatius et al.* [2016], who observed heterogeneous ice nucleation when probing the ice nucleation ability of α-pinene SOA particles in a continuous flow diffusion chamber (CFDC) at 238 K (red pentagons in Figure 3a,

representing the onset values for f_{ice} = 10%). The SOA particles were also generated from the reaction of α-pinene with ozone, which, however, was carried out at lower temperatures (263–235 K) and under irradiation with UV light. The average specified O/C ratio of the α-pinene SOA particles was lower than in our study (0.25 compared to 0.35), which could affect the particles' viscosity and response to a change in relative humidity [*Berkemeier et al.*, 2014; *Pajunoja et al.*, 2015]. An important issue could also be the abrupt humidification and short residence time (about 10 s) of the aerosol particles in the nucleation region of the CFDC chamber. Compared to these conditions, the α-pinene SOA particles probed in a typical AIDA expansion cooling experiment have more time to adjust to the increasing relative humidity, thus making liquefaction and homogeneous freezing more likely.

Nonetheless, our reported freezing onsets for α-pinene SOA are in good agreement with a different ice nucleation study that was carried out with a CFDC chamber [*Ladino et al.*, 2014]. *Ladino et al.* [2014] have used a flow tube and a smog chamber set up to generate SOA particles from the ozonolysis of α-pinene at room temperature. The O/C ratio of the particles was not specified. The pink, upward pointing triangles in Figure 3a denote the reported ice saturation ratios to activate 0.1% of the particles, comprising experiments with freshly formed α-pinene SOA, as well as studies where samples of the water-soluble fraction of filter-collected particles were atomized and probed in the CFDC chamber. Similar to the AIDA results, the S_{ice} onsets are located at or slightly above the homogeneous freezing threshold. In a different type of experiment, the particles generated from the samples of the water-soluble organic fraction were precooled for 30 s at 233 K in a cooling flow tube prior to the injection into the CFDC chamber. The concomitant onset S_{ice} values, shown as the blue, downward pointing triangles in Figure 3a, are slightly lower than those determined for the particles that were not precooled. Precooling could lead to hardening of the organic material, thereby favoring the particles' ability to promote heterogeneous ice nucleation. However, the authors could not exclude that the improved ice nucleation ability of the precooled particles was due to preactivation in the cooling flow tube [*Ladino et al.*, 2014].

The discussion makes clear that measured onset values for ice nucleation by highly viscous or glassy materials will crucially depend on the humidification conditions of the specific experiment. The cooling rates shown along the T-S_{ice} trajectories in Figure 3b correspond to dry adiabatic cooling rates at 1.3 to 2.5 m/s updraft velocities in the troposphere, representing values at the high end of atmospheric updrafts taken into account in the recent model simulations of the water uptake by α-pinene SOA particles [*Lienhard et al.*, 2015; *Price et al.*, 2015]. With our interpretation of a delayed homogeneous freezing mode during the expansion cooling experiments that started at 228 and 223 K, we are in agreement with the simulations by *Price et al.* [2015] who predicted kinetically limited water diffusion already at these temperatures. According to *Lienhard et al.* [2015], homogeneous ice nucleation should only be delayed at very cold conditions (195 K) near the tropical tropopause. Concerning the reliability of the model simulations, one should state that the underlying measurements of the water diffusion coefficients were only performed at relative humidities below ice saturation and, in the case of the *Price et al.* [2015] study, only down to a temperature of 240 K. Therefore, the model simulations rely on an extrapolation of the water diffusion coefficient parameterization to higher relative humidities and, in part, to lower temperatures.

4. Atmospheric Freeze-Drying Experiments

4.1. Freeze-Drying Experiments Simulating a Convective Cloud System

4.1.1. Formation of Highly Porous Aerosol Particles

We have introduced the freeze-drying experiments as a tool to gain further insights into the ice nucleation mechanism of the α-pinene SOA particles at cirrus temperatures. Before addressing this subject in section 4.2, we want to explore whether the observations from the atmospheric freeze-drying cycle of the Suwannee River NOM particles [*Adler et al.*, 2013], namely, the formation of highly porous aerosol particles, can be reproduced for the α-pinene SOA particles. The laboratory freeze-drying cycles performed by *Adler et al.* [2013] were not started in the cirrus regime but mimicked a deep convective cloud system, entailing droplet activation of the aerosol particles at warm temperatures, homogeneous freezing of the cloud droplets below 237 K, and release of the freeze-dried particles after the sublimation of ice in an ice-subsaturated environment. To simulate such a process in AIDA, we have started an expansion cooling run with the α-pinene SOA particles at 243 K, following the usual procedure of particle
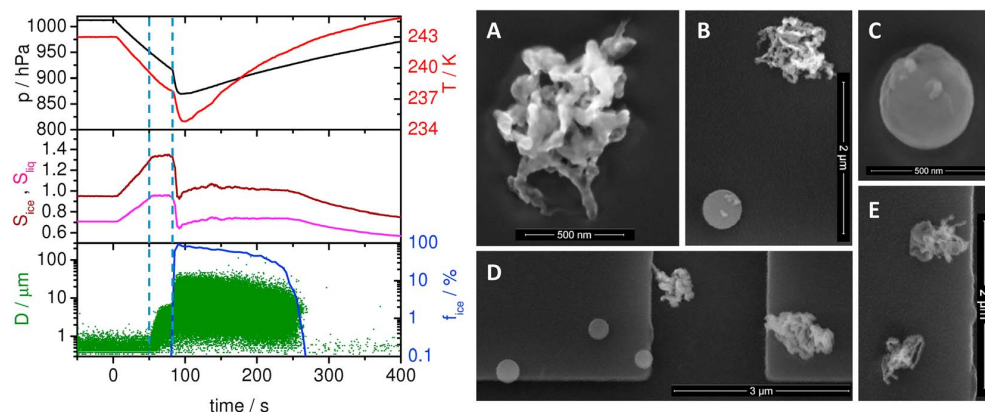
Figure 4. (left) Ice nucleation characteristics of α-pinene SOA particles during a freeze-drying experiment that started at 243 K. The data types are the same as shown in Figure 2. (right) Selection of ESEM images of α-pinene SOA particles collected on a Si substrate before and after the freeze-drying step, following the experimental procedure described in section 2.4. Note that both the unprocessed and the freeze-dried α-pinene SOA particles were deposited on the same substrate.

generation in the APC chamber at room temperature and transfer to the AIDA vessel. The AIDA records of the freeze-drying experiment are shown in Figure 4 (left). During expansion cooling, the α-pinene SOA particles were first activated to a cloud of supercooled water droplets (first vertical line) when the relative humidity exceeded water saturation. At the time of droplet activation, the gas temperature had dropped to about 239 K. After two further degrees of cooling during continued pumping, the gas temperature approached the homogeneous freezing temperature of micron-sized supercooled water droplets (second vertical line). No heterogeneously formed ice crystals were detected until reaching the homogeneous freezing limit. At that moment, we induced an extra expansion by opening the valve to the evacuated APC chamber. The intention of this action was the same as in the freeze-drying experiment that started at 233 K (Figure 2, right), namely, to ensure that the complete population of seed aerosol particles, respectively, cloud droplets, was involved in the freeze-drying step. The additional expansion led to an almost instant decrease of the gas temperature by additional 2.5 K, causing the whole cloud of supercooled water droplets to freeze with f_{ice} close to 100%. Thereafter, the nucleated ice crystals were rapidly sublimed by refilling the AIDA chamber with dry synthetic air, thereby minimizing sedimentation losses of large ice crystals and releasing the freeze-dried α-pinene SOA particles in an ice-subsaturated environment.

As an immediate consequence of the freeze-drying experiment, the ice cloud processed α-pinene SOA particles almost completely disappeared from the records of the optical particle counters. Before the start of the expansion cooling cycle at $t < 0$, the OPC measurements have captured about 5% of the overall aerosol particle number concentration. This fraction corresponds to the largest α-pinene SOA particles of the size distribution shown in Figure 1, which are detected at optical diameters below 1 μm by the OPCs. After the freeze-drying step, the dilution-corrected fraction of seed aerosol particles that are still captured by the OPCs is less than 0.25%. This points to a severe change of the optical properties of the freeze-dried compared to the unprocessed α-pinene SOA particles, given that the size classification of the OPCs is based on the particles' light scattering intensities at scattering angles of 90 ± 12 ° [*Benz et al.*, 2005]. Such large modification of the optical properties upon freeze drying, apparent as a reduction of the extinction efficiencies of the freeze-dried NOM aerosols compared to those of the nonporous particles, was also observed by *Adler et al.* [2013, 2014]. The fact that the freeze-dried α-pinene SOA particles appear "less visible" than the unprocessed particles in the OPC records is therefore a first indication for the formation of highly porous aerosol particles. The porosity of the freeze-dried α-pinene SOA particles is confirmed by the ESEM images of SOA particles collected on the Si substrate as shown in Figure 4 (right). Collection of SOA particles with the liquid-nitrogen cooled transfer shuttle was performed in a way that both the unprocessed and the freeze-dried α-pinene SOA particles were deposited on the same substrate, with sampling periods of 30 min at $t < 0$ before the start of expansion cooling and another 30 min at $t > 300$ s after the sublimation of the ice crystals. The ESEM images B and D show proof of

259
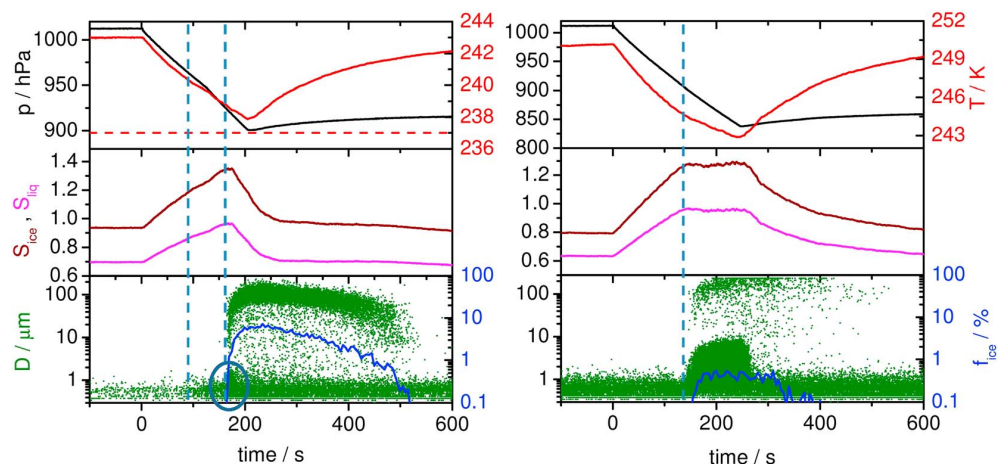
Figure 5. Ice nucleation characteristics of α-pinene SOA particles after the freeze-drying experiment shown in Figure 4. (left) expansion cooling run started at the same temperature as the freeze-drying experiment (243 K). The horizontal dashed line in the first panel represents the onset of homogeneous freezing observed in the ice nucleation experiment with the unprocessed α-pinene SOA particles (Figure 4, left). (right) Expansion cooling run started after warming the freeze-dried SOA particles to 250 K. The data types are the same as shown in Figure 2.

two different particle morphologies: compact, near-spherical particles (see also image C), representing the unprocessed particle ensemble, and highly irregular, porous particles (see also images A and E), representing the freeze-dried population of α-pinene SOA particles.

4.1.2. Ice Nucleation Ability of the Highly Porous Aerosol Particles

Adler et al. [2014] have performed a detailed analysis of the optical properties of the highly porous aerosol particles. The AIDA facility represents an ideal extension for the characterization of such aerosols, insofar as we can immediately probe whether the freeze-dried particles reveal a modified ice nucleation ability compared to the nonporous SOA particles. For that purpose, we performed a subsequent ice nucleation experiment with the porous α-pinene SOA particles at 243 K, which was started 1 h after the initial freeze-drying experiment. Its records are shown in Figure 5 (left). In the course of expansion cooling, there is clear indication for a humidity-induced collapse of the porous structure of the freeze-dried SOA particles. Starting at about 240 K and RH_w = 85% (first vertical line at t = 90 s), there is a rapid increase in the count rate of the OPCs at optical diameters below 1 μm, as visually evident from a much denser scatterplot in the OPC records than before the beginning of pumping. Taking into account particle dilution due to pumping, the fraction of seed aerosol particles that is detected by the OPCs again approaches the initial value from before the freeze-drying experiment. Such increase in the OPC count rate upon humidification was not observed in the expansion cooling experiments with the unprocessed α-pinene SOA particles at 243 K, i.e., it cannot simply be related to the hygroscopic growth of the aerosol particles. Similar to the depolarization method explored by *Järvinen et al.* [2016], also, the OPC measurements thereby prove to be a tool for detecting a morphology change of the α-pinene SOA particles which is related to a change of the particles' viscosity. For the particles probed by *Järvinen et al.* [2016], whose ice nucleation characteristics were investigated by *Ignatius et al.* [2016], the detected viscosity transition RH_w (55–62% at 243 K and 69–79% at 235 K) was somewhat lower than in our study, pointing to a different chemical composition of the generated SOA materials. We only detected a small structural change of the freeze-dried α-pinene SOA particles while they were suspended in the AIDA chamber for 1 h at T = 243 K and S_{ice} = 0.95 (RH_w = 70%) between the two expansion cooling cycles shown in Figures 4 and 5 (left). During that time, the fraction of aerosol particles detected by the OPCs slightly increased from about 0.25% to 0.5% but remained 1 order of magnitude lower than before the freeze-drying experiment, where a 5% fraction of the SOA particles was captured in the OPC records.

With the further increase of the relative humidity in the course of expansion cooling, the collapsed, freeze-dried α-pinene particles finally acted as cloud condensation nuclei (CCN) (second vertical line in Figure 5, left). The evolving cloud droplet mode, however, is barely visible in the OPC records and only persists for a short
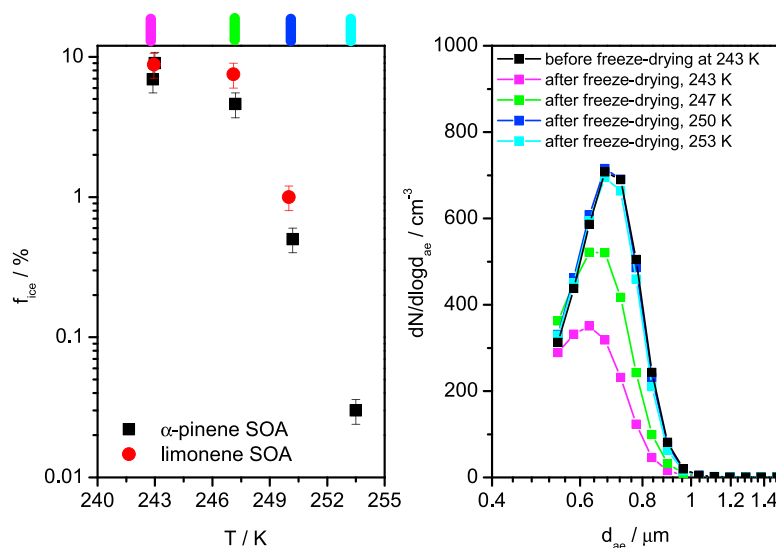
Figure 6. (left) Temperature-dependent ice-active fractions of freeze-dried α-pinene and limonene SOA particles in the CCN-induced ice growth mode. The colored bars on the top axis denote the times of individual size distribution measurements with the APS, which are shown with the same color coding in the right panel. In addition to the size distributions that were recorded after freeze drying, the initial APS distribution from before the freeze-drying experiment is also shown (black squares). As explained in the text, the maximum in the APS size distributions is only artificial and arises due to the decreasing detection efficiency at d_{ae} smaller than 0.7 μm (see also exemplary SMPS size distribution of the α-pinene SOA particles shown in the top left of Figure 1).

time period of about 20 s (as highlighted by the blue circle in Figure 5), because instantaneously with the CCN activation of the seed aerosol particles a large number concentration of ice crystals was formed with f_{ice} close to 10%. At the time of CCN activation, the gas temperature was still 2 K above the homogeneous freezing temperature of supercooled water droplets at about 237 K where the homogeneous ice nucleation of the CCN-activated, unprocessed α-pinene SOA particles was observed (Figure 4, left, second vertical line). This homogeneous freezing threshold for the unprocessed SOA particles is shown as the horizontal dashed line in the first panel of Figure 5 (left). It can be seen that during the expansion run with the freeze-dried SOA particles the temperature has never dropped below the homogeneous freezing line, meaning that the observed ice nucleation mode must be due to a heterogeneous freezing mechanism. Heterogeneous ice formation upon CCN activation was also detected when the freeze-dried particles were probed at warmer temperatures. Figure 5 (right) shows an experiment where a fresh load of α-pinene SOA particles was generated in the APC chamber, transferred to the AIDA vessel, subjected to a freeze-drying cycle at 243 K as shown in Figure 4, and then directly warmed to 250 K to probe the ice nucleation ability of the freeze-dried particles at that temperature. The expansion cooling run at 250 K was started about 3 h after the freeze-drying cycle at 243 K. Upon warming, there was a full recovery of the OPC count rate for the seed aerosol particles, which, similar to the data shown in Figure 4, had decreased by a factor of 20 immediately after the freeze-drying step. This observation points to a complete collapse of the porous structure of the freeze-dried α-pinene SOA particles during warming to 250 K. After CCN activation of the seed aerosol particles (vertical line, Figure 5, right), the droplet cloud evolves more clearly in the OPC records and persists for a much longer time period in comparison with the expansion cooling cycle started at 243 K (Figure 5, left). Nonetheless, there is still a distinct number concentration of ice crystals heterogeneously formed after CCN activation with an ice-active fraction of about 1%. Figure 6 (left) summarizes the f_{ice} values of the freeze-dried SOA particles as a function of temperature. Each data point corresponds to an individual experiment with freshly generated SOA particles, freeze dried at 243 K, and then probed for their heterogeneous ice nucleation ability in an expansion cooling experiment that started at the indicated temperature. In addition to the freeze-drying cycles with α-pinene SOA, we conducted three such experiments with limonene SOA, whose results, as evidenced by the data from Figure 6, closely agree with those for α-pinene SOA. Note again that all ice nucleation data displayed in Figure 6 represent

heterogeneous freezing modes that were exclusively observed for the freeze-dried SOA particles after CCN activation at temperatures above 237 K. CCN-activated, unprocessed SOA particles only promoted homogeneous ice nucleation at $T < 237$ K.

In the following, we refer to the improved ice nucleation ability of the freeze dried compared to the unprocessed SOA particles as preactivation. The term "preactivation" has been introduced in the context of repeated ice nucleation experiments with insoluble INPs like mineral dust where the particles do not significantly change their morphology during ice-cloud processing [*Pruppacher and Klett*, 1997; *Vali et al.*, 2015]. One might therefore be tempted to discuss the ice nucleation ability of the freeze-dried particles as a separate class of particles, i.e., unrelated to the properties of the compact SOA particles. On the other hand, the occurrence of the ice nucleation modes of the freeze-dried SOA particles displayed in Figure 5 inevitably requires a preceding ice nucleation event with the compact SOA particles, which suggests applying the concept of preactivation in the interpretation of our results. The preactivation efficiency of the freeze-dried SOA particles gradually decreases with increasing temperature (Figure 6, left), but preactivation is still detectable even for a temperature at or slightly above 250 K, where the OPC records point to a collapse of the porous network of the freeze-dried particles due to their reduced viscosity at higher temperatures. But obviously, the particles' viscosity is still sufficiently high that a memory effect from the preceding ice nucleation event is conserved in the viscous medium, which allows for the immediate growth of ice crystals after the droplet activation of the SOA particles at ice-supersaturated conditions. Whether the heterogeneous freezing mode of the freeze-dried SOA particles is induced by genuine, microscopic ice germs that are trapped in the viscous material during revitrification in the freeze-drying step, by a residual imprint of the ice lattice, or just by the particles' enhanced surface area even in the collapsed state remains a matter of speculation. Due to the observation of the ice nucleation mode only appearing after the droplet activation of the SOA particles, we propose to term the preactivation mode as "CCN-induced ice growth mode."

During the experiments depicted in Figure 6 (left), we were able to assess a different technique to at least qualitatively probe the morphology change of the α-pinene SOA particles after freeze drying and subsequent warming. *Adler et al.* [2013] have detected a clear increase of the mode diameter of the NOM particles in the SMPS size distribution measurement after freeze drying. Our SMPS instrument is located outside of the cold housing of the AIDA chamber, and the overall residence time of the particles in the sampling line, electrostatic classifier, and subsequent CPC is about 16 s. This gives the freeze-dried particles sufficient time for potential restructuring at warm temperatures and might be the reason why we could not detect a systematic change in the SMPS size distributions in the course of the freeze-drying experiments. This was different for the APS instrument, which is also situated outside the isolating containment but keeps the residence time of the particles in the warm environment at less than 1 s. Figure 6 (right) shows exemplary number size distributions as a function of the aerodynamic diameter, which were recorded before and after freeze drying of α-pinene SOA at 243 K (black and magenta squares, respectively), as well as after subsequent warming to 247, 250, and 253 K (green, blue, and cyan squares, respectively). All size distributions were corrected for the overall dilution of the particle number concentration during the experiment. Similar to the OPC records, the APS only detects the largest particles of the size distribution, and the apparent maximum at $d_{ae} = 0.7$ μm is due to the decreasing detection efficiency at smaller diameters. After freeze drying, there is clear decrease of the number concentration of SOA particles that are captured in the detection range of the APS instrument, pointing to the reduced settling velocities and aerodynamic diameters of the porous particles. Upon warming to 250 K and above, the initially detected size distribution is fully recovered as a result of the collapse of the particles' porous network.

4.1.3. Estimating the Viscosity of the α-Pinene SOA Particles

The porous particle morphology of the freeze-dried α-pinene SOA particles shown in Figure 4 results from the vitrification of the freeze-concentrated organic solution on the nucleated ice crystals and the subsequent sublimation of the ice pockets. Freezing must occur at a temperature in the region of the so-called T_g', denoting the temperature where the glass transition curve and the ice melting point curve in the SOA/water phase diagram intersect [*Zobrist et al.*, 2008]. Even at a temperature slightly above T_g', a porous particle morphology could be formed provided that the viscosity is high enough to prevent a structural rearrangement on the experimental time frame. For a generic SOA material, T_g' was estimated to be about 233 K [*Koop et al.*, 2011]. The freezing of the CCN-activated α-pinene SOA particles during the freeze-drying cycle performed in the AIDA chamber occurred at a similar temperature (Figure 4). We also observed that the investigated

262
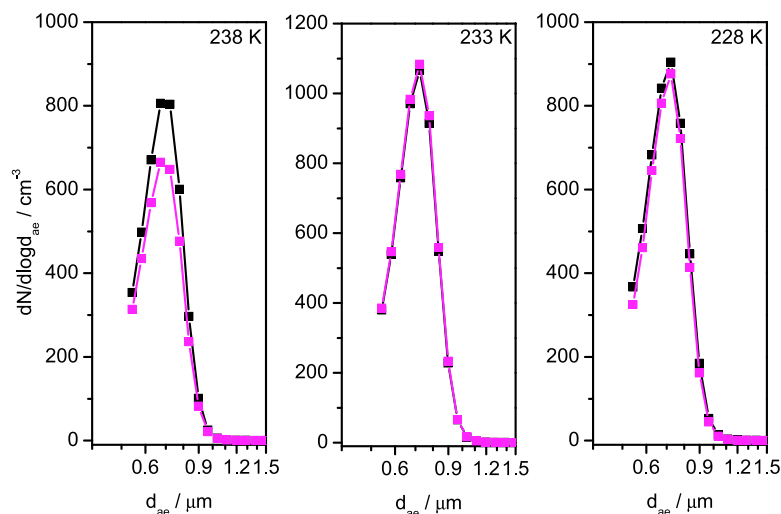
Figure 7. APS size distribution measurements of the unprocessed (black squares) and the freeze-dried (magenta squares) populations of α-pinene SOA particles during the freeze-drying experiments conducted at 238, 233, and 228 K.

particles were still highly viscous at 243 K in an almost ice-saturated environment (corresponding to about 70% RH_w), because the OPC records only indicated a minor structural rearrangement of the freeze-dried particles over a timescale of 1 h. We can use the OPC data for a rough estimate of the viscosity of the α-pinene SOA particles under these conditions, following an approach that relates the relaxation time of coalescing amorphous particles to their viscosity [*Pajunoja et al.*, 2014]. Quantitatively, the decrease in the OPC count rate of the SOA particles immediately after freeze drying was only recovered by about 5% within of an observation period of 1 h at 243 K and 70% RH_w. Assuming that this translates into a total relaxation time of 20 h for the full recovery of the OPC count rate, and approximating the porous SOA particles as aggregates with a primary particle size of 100 nm and a surface tension of 35 mN m^{-1} [*Pajunoja et al.*, 2014], the estimated viscosity would be in the range of 10^{10} Pa s. Accordingly, the particles' phase state would fall into the highly viscous, semisolid regime [*Koop et al.*, 2011]. A recent temperature-dependent parameterization of the viscosities of α-pinene SOA even predicted the transition into the solid state with a viscosity of 10^{12} Pa s at 243 K and 70% RH_w [*Wang et al.*, 2015]. Based on these data, we conclude that the unprocessed α-pinene SOA particles, which were probed on their ice nucleation ability at even lower temperatures in the cirrus regime (Figure 3), were initially also in the highly viscous, semisolid or even glassy solid state before the expansion cooling cycles were started.

4.2. Freeze-Drying Experiments at Cirrus Temperatures

An immediate question is whether the dominant morphological change of the α-pinene SOA particles after freeze drying at 243 K is also evident when the freeze-drying experiments are performed at cirrus temperatures. This would be a hint at the underlying ice nucleation mechanism, as it would indicate whether liquefaction of the aerosol particles has occurred during humidification or not. The AIDA data from one freeze-drying experiment that started at 233 K are already displayed in Figure 2 (right). In obvious contrast to the respective experiment at 243 K (Figure 4), there is no reduction of the number concentration of aerosol particles counted by the OPCs after the freeze-drying step. The same behavior was observed at starting temperatures below 233 K. Only for freeze-drying experiments that started at 238 K, the dilution-corrected count rate of the OPCs was lowered by a small factor of 1.2 compared to the unprocessed α-pinene SOA particles. This factor, however, is much smaller than the factor of 20 observed during the corresponding experiment that started at 243 K. Obviously, there is much less structural change during the trajectories in the cirrus regime compared to a simulated convective-cloud system where the SOA particles are processed at warmer temperatures. Also, the APS measurements substantiate this conclusion. Similar to Figure 6 (right), Figure 7 shows the dilution-corrected number size distributions of the SOA particles as a function of the aerodynamic diameter from before (black squares) and after the freeze-drying experiments (magenta squares)
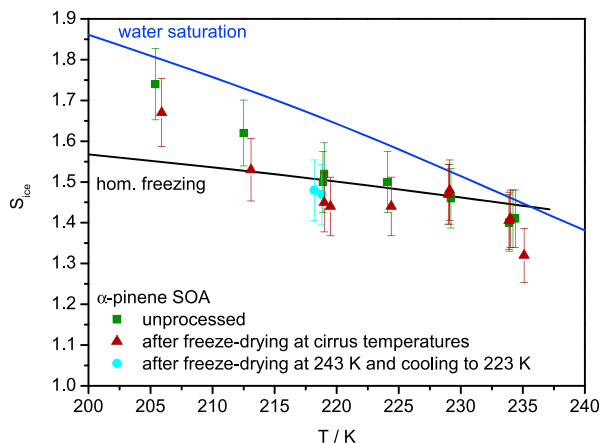
Figure 8. Comparison of the ice nucleation onsets for unprocessed and freeze-dried α-pinene SOA particles at cirrus temperatures. See text for details.

that started at 238, 233, and 228 K. Only for the experiment that started at 238 K, there is a slight reduction of the number concentration measured with the APS after freeze drying, which is due to a decrease of the aerodynamic diameter of the ice cloud processed SOA particles.

These observations can now be linked to the tentative assignment of the temperature-dependent ice nucleation mechanism of the α-pinene SOA particles detailed in section 3. For the experiment that started at 238 K, we assumed that ice has nucleated homogeneously. At least a small degree of structural change of the SOA particles could be indirectly evidenced from the observation of the freeze-dried particles having a slightly reduced count rate in the OPC and APS records at this temperature in comparison with the unprocessed particles. Most likely, the particles adopted a core-shell morphology at the freezing onset, with the solid core being inefficient in triggering ice formation by immersion freezing before the homogeneous freezing threshold of the liquefied outer layer was reached. The formation of porous material by vitrification and ice sublimation was then restricted to the particles' outer layer and could not lead to the formation of such highly porous particles as displayed in Figure 4, which explains the less pronounced changes in the OPC and APS measurements after freeze drying at 238 K. The sharp nucleation onset observed for the experiment that started at 233 K (Figure 3) was also interpreted as a homogeneous nucleation mode. If true, homogeneous freezing would be limited to a very thin liquefied layer because there was no indication for a morphological change of the particles upon freeze drying at this temperature. Following this interpretation, the onset of the homogeneous freezing mode should likely be delayed when the starting temperature of the expansion cooling cycle is further decreased. This reasoning is in good agreement with the more gradually evolving ice nucleation modes observed at starting temperatures of 228 and 223 K (Figure 3), which were already tentatively assigned as delayed homogeneous freezing modes.

The remaining question is how the ice nucleation ability of the SOA particles that were freeze dried at cirrus temperatures changes with respect to that of the unprocessed particles. Figure 8 again shows the onset conditions for ice nucleation of 0.1% of the unprocessed α-pinene SOA particles as the dark green squares and compares them to the respective S_{ice} thresholds after the particle ensembles were subjected to freeze-drying cycles at cirrus temperatures as described in section 2.4 (brown triangles). For starting temperatures of 228 K and below, there is a systematic, albeit small decrease in the onset S_{ice} value of the freeze dried compared to the unprocessed α-pinene SOA particles. As we do not expect a substantial change of the overall particle morphology during freeze drying at these temperatures, the small preactivation ability can be attributed to a memory effect of ice from the preceding nucleation event on the glassy material. The slightly reduced ice nucleation onsets observed for precooled α-pinene SOA particles by *Ladino et al.* [2014] could therefore also be due to preactivation in their cooling flow tube setup. For most experiments at starting temperatures above 228 K, we did not observe any change in the particles' ice nucleation ability after freeze drying. This indicates that the memory effect on the glassy material is small, meaning that at warmer temperatures preactivation cannot compete with the liquefaction of the outer particle layers during humidification and homogeneous freezing is also the dominant ice nucleation mechanism after freeze drying. There was only one exception to this general behavior, where we observed a small heterogeneous ice nucleation mode after freeze drying at 238 K. Ice formation initiated at $S_{ice} = 1.32$ but involved less than 1% of the overall particle population. In two other freeze-drying experiments conducted at 238 K, we did not observe this early preactivation mode and also the freeze-dried α-pinene SOA particles nucleated ice homogeneously. The temperature of 238 K is just the threshold where the APS and OPC measurements still indicate

a small morphological change of the SOA particles during freeze drying. This could explain why the ice nucleation behavior of the freeze-dried SOA particles is more complex and variable at 238 K than at colder temperatures.

Figure 8 also includes the ice nucleation onsets for two experiments where the freeze-drying cycle was conducted at 243 K, and the highly porous α-pinene SOA particles were then cooled to 223 K to probe their ice nucleation ability in the cirrus regime (cyan circles). The freezing onsets remain almost unchanged compared to the compact, unprocessed SOA particles, indicating that the larger surface area of the porous particles alone does not make them better INPs. This substantiates the interpretation that the CCN-induced ice growth mode of the porous particles at warmer temperatures is induced by ice pockets that are enclosed in the glassy matrix. Such ice pockets can be released and trigger ice formation upon liquefaction at warm temperatures but will remain completely shielded and do not enhance the particles' ice nucleation ability during expansion cooling experiments at colder temperatures. We want to emphasize that this interpretation is only valid provided that the SOA particles probed at 223 K have conserved their highly porous morphology from the freeze-drying cycle performed at 243 K. Due to the cooling of the AIDA chamber from 243 to 223 K, there was a time delay of about 6 h between the freeze-drying cycle at 243 K and the succeeding expansion cooling run at 223 K, during which the OPC measurements detected a small structural change of the freeze-dried α-pinene SOA particles. The fraction of aerosol particles detected by the OPCs, which had dropped from 5 to 0.25% immediately after the freeze-drying step at 243 K, increased to 0.6% during cooling to 223 K. In an ideal experiment, as, e.g., feasible by the joint operation of the AIDA chamber with a continuous flow diffusion chamber (see section 5), highly porous aerosol particles could be generated in AIDA at 243 K and immediately probed for their ice nucleation ability at cirrus temperatures by the CFDC chamber.

5. Conclusions and Outlook

Our results suggest that monoterpene SOA particles are of minor importance for heterogeneous ice nucleation in the cirrus cloud regime of the upper troposphere. Although we assigned the ice nucleation mode that is dominant at temperatures below 218 K to deposition nucleation, its efficiency is very low in view of the high values for the ice saturation ratio which are needed to initiate ice formation ($S_{ice} > 1.6$). Other abundant INPs like mineral dust require much lower values for S_{ice} to trigger heterogeneous ice formation at these temperatures [*Hoose and Möhler*, 2012]. For example, two types of mineral dust particles from the Takla Makan desert in Asia and the Sahara with median diameters between 0.35 and 0.40 μm showed ice-active fractions in the deposition nucleation mode of at least 25% at $T < 223$ K and $S_{ice} < 1.35$ in previous AIDA measurements [*Möhler et al.*, 2006]. For the present SOA ice nucleation experiments, we estimate to be sensitive to an ice-active fraction of 0.01%, when assuming a detection limit of 0.1 cm^{-3} for the ice particle number concentration in combination with a seed aerosol number concentration of around 1000 cm^{-3}. This means that a very small fraction of the SOA particles could have nucleated ice at lower ice saturation ratios, but we would have been unable to detect this nucleation mode. The ratio of the ice-active fraction observed for mineral dust (25%) and the detection limit for the SOA particles (0.01%) yields a value of 2500, meaning that the number concentration of SOA particles must be higher by at least 3 orders of magnitude than that of the mineral dust particles to obtain a similar number concentration of nucleated ice crystals at lower ice saturation ratios. Aircraft-based single-particle mass spectrometer measurements of the aerosol composition for several altitude ranges indicated that the TTL region was enriched in organic material and depleted in mineral dust [*Froyd et al.*, 2009]. However, the number fraction of dust particles was only reduced by a factor of about 5 in the TTL region above 12 km compared to the convective region with altitudes from 4 to 12 km [*Froyd et al.*, 2009]. So we expect that the higher abundance of organic aerosol particles in the TTL region only compensates to a small extent for their much lower ice nucleation activity compared to mineral dust particles.

At temperatures above 218 K, we ascribed ice formation to homogeneous or delayed homogeneous freezing of the partly liquefied SOA particles and did not find any indication for an immersion freezing ability of a potentially still existing glassy particle core. Our experiments substantiate the conclusion that SOA compounds reveal a lower ability to act as INPs at cirrus temperatures compared to organic species belonging to the class of simple sugars/acids, part of which were also investigated using the AIDA cloud chamber and showed clearly lower S_{ice} thresholds to initiate ice formation compared to the α-pinene and limonene

SOA particles [*Wilson et al.*, 2012]. The current study also supports the observation from previous AIDA experiments that the heterogeneous ice nucleation efficiency of mineral dust particles is greatly reduced by a coating with SOA material [*Möhler et al.*, 2008].

A particular pathway by which the SOA particles could be preactivated was atmospheric freeze drying and in particular freeze drying in a convective cloud system as first proposed by *Adler et al.* [2013]. This process could lead to the encapsulation of ice pockets in the revitrified glassy matrix. These ice pockets, however, seem to be completely shielded because we did not observe instant ice particle growth when the freeze-dried particles were again exposed to an ice-supersaturated environment. Heterogeneous ice formation only occurred after droplet activation via the so-called CCN-induced ice growth mode, which was observed up to a temperature of about 253 K in the mixed-phase cloud regime. These findings are again in contrast with repeated ice nucleation experiments conducted with organic species of the simple sugars/acids category, where ice cloud processing improved the particles' ice nucleation ability more significantly [*Wagner et al.*, 2012].

The most important objective for future experiments is the systematic investigation of the dependence of the ice nucleation ability of the SOA particles on their chemical composition. One could select a fixed starting temperature for a series of AIDA expansion cooling experiments, as, e.g., 228 or 223 K which are just in the transition regime where ice nucleation was ascribed to delayed homogeneous freezing. With varying SOA formation conditions like temperature, relative humidity, or reactants (e.g., different types of monoterpenes and oxidants), SOA particles with different O/C ratios could be generated and probed for their ability to nucleate ice heterogeneously. Less viscous particles than those probed in the current study could provoke a more distinct, sharply defined homogeneous freezing mode at 228 or 223 K, whereas hardening of the glassy matrix could favor the particles' ability to nucleate ice via deposition nucleation. The implementation of low-temperature filter sampling for ESEM analyses as a new standard measurement technique could help to ascertain the proposed ice nucleation mechanisms, as it would yield direct proof of a potential morphological change of the particles during freeze drying.

Similarly important, one could conduct a series of ice nucleation experiments at a fixed starting temperature where SOA particles with the same O/C ratio are probed at varying humidification rates, which can be controlled by adjusting the pumping speed in the adiabatic expansion experiments. Different humidification rates or updraft velocities would alter the time that the SOA particles have to adjust to the increasing relative humidity, which in turn could influence the ice nucleation characteristics (sharply defined versus delayed homogeneous freezing). A series of such experiments would also deliver a robust data set which could be fitted by model calculations with a kinetic multilayer model, using the water diffusion coefficient of the SOA material as a tunable parameter [*Lienhard et al.*, 2015].

Concerning the freeze-drying experiments, a major experimental step forward would be the joint operation of AIDA with a continuous flow diffusion chamber via a low-temperature connection line, in which the particles do not experience transient warm conditions and thereby preserve their morphology and preactivation ability. Freeze-dried SOA particles could so be routinely produced and maintained in the AIDA chamber and then systemically probed for their ice nucleation ability by the CFDC chamber over a wide range of temperatures.

References

Adler, G., T. Koop, C. Haspel, I. Taraniuk, T. Moise, I. Koren, R. H. Heiblum, and Y. Rudich (2013), Formation of highly porous aerosol particles by atmospheric freeze-drying in ice clouds, *Proc. Natl. Acad. Sci. U.S.A.*, 110(51), 20414–20419.

Adler, G., C. Haspel, T. Moise, and Y. Rudich (2014), Optical extinction of highly porous aerosol following atmospheric freeze drying, *J. Geophys. Res. Atmos.*, 119, 6768–6787, doi:10.1002/2013JD021314.

Baustian, K. J., M. E. Wise, and M. A. Tolbert (2010), Depositional ice nucleation on solid ammonium sulfate and glutaric acid particles, *Atmos. Chem. Phys.*, 10(5), 2307–2317.

Baustian, K. J., M. E. Wise, E. J. Jensen, G. P. Schill, M. A. Freedman, and M. A. Tolbert (2013), State transformations and ice nucleation in amorphous (semi-)solid organic aerosol, *Atmos. Chem. Phys.*, 13(11), 5615–5628.

Benz, S., K. Megahed, O. Möhler, H. Saathoff, R. Wagner, and U. Schurath (2005), T-dependent rate measurements of homogeneous ice nucleation in cloud droplets using a large atmospheric simulation chamber, *J. Photochem. Photobiol. A*, 176(1–3), 208–217.

Berkemeier, T., M. Shiraiwa, U. Pöschl, and T. Koop (2014), Competition between water uptake and ice nucleation by glassy organic aerosol particles, *Atmos. Chem. Phys.*, 14(22), 12513–12531.

Fahey, D. W., et al. (2014), The AquaVIT-1 intercomparison of atmospheric water vapor measurement techniques, *Atmos. Meas. Tech.*, 7(9), 3177–3213.

Froyd, K. D., D. M. Murphy, T. J. Sanford, D. S. Thomson, J. C. Wilson, L. Pfister, and L. Lait (2009), Aerosol composition of the tropical upper troposphere, *Atmos. Chem. Phys.*, *9*(13), 4363–4385.

Grayson, J. W., Y. Zhang, A. Mutzel, L. Renbaum-Wolff, O. Boge, S. Kamal, H. Herrmann, S. T. Martin, and A. K. Bertram (2016), Effect of varying experimental conditions on the viscosity of alpha-pinene derived secondary organic material, *Atmos. Chem. Phys.*, *16*(10), 6027–6040.

Haag, W., B. Kärcher, S. Schaefers, O. Stetzer, O. Möhler, U. Schurath, M. Krämer, and C. Schiller (2003), Numerical simulations of homogeneous freezing processes in the aerosol chamber AIDA, *Atmos. Chem. Phys.*, *3*(1), 195–210.

Hallquist, M., et al. (2009), The formation, properties and impact of secondary organic aerosol: Current and emerging issues, *Atmos. Chem. Phys.*, *9*(14), 5155–5236.

Hoose, C., and O. Möhler (2012), Heterogeneous ice nucleation on atmospheric aerosols: A review of results from laboratory experiments, *Atmos. Chem. Phys.*, *12*(20), 9817–9854.

Ignatius, K., et al. (2016), Heterogeneous ice nucleation of viscous secondary organic aerosol produced from ozonolysis of alpha-pinene, *Atmos. Chem. Phys.*, *16*(10), 6495–6509.

Järvinen, E., et al. (2016), Observation of viscosity transition in alpha-pinene secondary organic aerosol, *Atmos. Chem. Phys.*, *16*(7), 4423–4438.

Koop, T., B. P. Luo, A. Tsias, and T. Peter (2000), Water activity as the determinant for homogeneous ice nucleation in aqueous solutions, *Nature*, *406*, 611–614.

Koop, T., J. Bookhold, M. Shiraiwa, and U. Pöschl (2011), Glass transition and phase state of organic compounds: Dependency on molecular properties and implications for secondary organic aerosols in the atmosphere, *Phys. Chem. Chem. Phys.*, *13*(43), 19238–19255.

Ladino, L. A., S. Zhou, J. D. Yakobi-Hancock, D. Aljawhary, and J. P. D. Abbatt (2014), Factors controlling the ice nucleating abilities of alpha-pinene SOA particles, *J. Geophys. Res. Atmos.*, *119*, 9041–9051, doi:10.1002/2014JD021578.

Lienhard, D. M., et al. (2015), Viscous organic aerosol particles in the upper troposphere: Diffusivity-controlled water uptake and ice nucleation?, *Atmos. Chem. Phys.*, *15*(23), 13599–13613.

Lopez-Hilfiker, F. D., et al. (2014), A novel method for online analysis of gas and particle composition: Description and evaluation of a Filter Inlet for Gases and AEROsols (FIGAERO), *Atmos. Meas. Tech.*, *7*(4), 983–1001.

Mikhailov, E., S. Vlasenko, S. T. Martin, T. Koop, and U. Pöschl (2009), Amorphous and crystalline aerosol particles interacting with water vapor: Conceptual framework and experimental evidence for restructuring, phase transitions and kinetic limitations, *Atmos. Chem. Phys.*, *9*(24), 9491–9522.

Möhler, O., et al. (2003), Experimental investigation of homogeneous freezing of sulphuric acid particles in the aerosol chamber AIDA, *Atmos. Chem. Phys.*, *3*(1), 211–223.

Möhler, O., et al. (2006), Efficiency of the deposition mode ice nucleation on mineral dust particles, *Atmos. Chem. Phys.*, *6*(10), 3007–3021.

Möhler, O., S. Benz, H. Saathoff, M. Schnaiter, R. Wagner, J. Schneider, S. Walter, V. Ebert, and S. Wagner (2008), The effect of organic coating on the heterogeneous ice nucleation efficiency of mineral dust aerosols, *Environ. Res. Lett.*, *3*(2), 025007, doi:10.1088/1748-9326/3/2/025007.

Murphy, D. M., and T. Koop (2005), Review of the vapour pressures of ice and supercooled water for atmospheric applications, *Q. J. R. Meteorol. Soc.*, *131*(608), 1539–1565.

Murray, B. J., et al. (2010), Heterogeneous nucleation of ice particles on glassy aerosols under cirrus conditions, *Nat. Geosci.*, *3*(4), 233–237.

Pajunoja, A., J. Malila, L. Q. Hao, J. Joutsensaari, K. E. J. Lehtinen, and A. Virtanen (2014), Estimating the viscosity range of SOA particles based on their coalescence time, *Aerosol Sci. Technol.*, *48*(2), i–iv.

Pajunoja, A., et al. (2015), Adsorptive uptake of water by semisolid secondary organic aerosols, *Geophys. Res. Lett.*, *42*, 3063–3068, doi:10.1002/2015GL063142.

Prenni, A. J., M. D. Petters, A. Faulhaber, C. M. Carrico, P. J. Ziemann, S. M. Kreidenweis, and P. J. DeMott (2009), Heterogeneous ice nucleation measurements of secondary organic aerosol generated from ozonolysis of alkenes, *Geophys. Res. Lett.*, *36*, L06808, doi:10.1029/2008GL036957.

Price, H. C., et al. (2015), Water diffusion in atmospherically relevant alpha-pinene secondary organic material, *Chem. Sci.*, *6*(8), 4876–4883.

Pruppacher, H. R., and J. D. Klett (1997), *Microphysics of Clouds and Precipitation*, pp. 330–341, Kluwer Acad., Dordrecht, Sect. 9.2.3.5.

Saathoff, H., K. H. Naumann, O. Möhler, A. M. Jonsson, M. Hallquist, A. Kiendler-Scharr, T. F. Mentel, R. Tillmann, and U. Schurath (2009), Temperature dependence of yields of secondary organic aerosols from the ozonolysis of alpha-pinene and limonene, *Atmos. Chem. Phys.*, *9*(5), 1551–1577.

Schill, G. P., and M. A. Tolbert (2012), Depositional ice nucleation on monocarboxylic acids: Effect of the O:C ratio, *J. Phys. Chem. A*, *116*(25), 6817–6822.

Schill, G. P., and M. A. Tolbert (2013), Heterogeneous ice nucleation on phase-separated organic-sulfate particles: Effect of liquid vs. glassy coatings, *Atmos. Chem. Phys.*, *13*(9), 4681–4695.

Schill, G. P., D. O. De Haan, and M. A. Tolbert (2014), Heterogeneous ice nucleation on simulated secondary organic aerosol, *Environ. Sci. Technol.*, *48*(3), 1675–1682.

Shilling, J. E., T. J. Fortin, and M. A. Tolbert (2006), Depositional ice nucleation on crystalline organic and inorganic solids, *J. Geophys. Res.*, *111*, D12204, doi:10.1029/2005JD006664.

Vali, G., P. J. DeMott, O. Möhler, and T. F. Whale (2015), Technical note: A proposal for ice nucleation terminology, *Atmos. Chem. Phys.*, *15*(18), 10263–10270.

Virtanen, A., et al. (2010), An amorphous solid state of biogenic secondary organic aerosol particles, *Nature*, *467*(7317), 824–827.

Wagner, R., O. Möhler, H. Saathoff, M. Schnaiter, and T. Leisner (2010), High variability of the heterogeneous ice nucleation potential of oxalic acid dihydrate and sodium oxalate, *Atmos. Chem. Phys.*, *10*(16), 7617–7641.

Wagner, R., O. Möhler, H. Saathoff, M. Schnaiter, and T. Leisner (2011), New cloud chamber experiments on the heterogeneous ice nucleation ability of oxalic acid in the immersion mode, *Atmos. Chem. Phys.*, *11*(5), 2083–2110.

Wagner, R., O. Möhler, H. Saathoff, M. Schnaiter, J. Skrotzki, T. Leisner, T. W. Wilson, T. L. Malkin, and B. J. Murray (2012), Ice cloud processing of ultra-viscous/glassy aerosol particles leads to enhanced ice nucleation ability, *Atmos. Chem. Phys.*, *12*(18), 8589–8610.

Wagner, R., K. Höhler, O. Möhler, H. Saathoff, and M. Schnaiter (2015), Crystallization and immersion freezing ability of oxalic and succinic acid in multicomponent aqueous organic aerosol particles, *Geophys. Res. Lett.*, *42*, 2464–2472, doi:10.1002/2015GL063075.

Wang, B. B., A. T. Lambe, P. Massoli, T. B. Onasch, P. Davidovits, D. R. Worsnop, and D. A. Knopf (2012), The deposition ice nucleation and immersion freezing potential of amorphous secondary organic aerosol: Pathways for ice and mixed-phase cloud formation, *J. Geophys. Res.*, *117*, D16209, doi:10.1029/2012JD018063.

Wang, B. B., R. E. O'Brien, S. T. Kelly, J. E. Shilling, R. C. Moffet, M. K. Gilles, and A. Laskin (2015), Reactivity of liquid and semisolid secondary organic carbon with chloride and nitrate in atmospheric aerosols, *J. Phys. Chem. A*, *119*(19), 4498–4508.

Wilson, T. W., et al. (2012), Glassy aerosols with a range of compositions nucleate ice heterogeneously at cirrus temperature, *Atmos. Chem. Phys.*, *12*(18), 8611–8632.

Zobrist, B., C. Marcolli, D. A. Pedernera, and T. Koop (2008), Do atmospheric aerosols form glasses?, *Atmos. Chem. Phys.*, *8*(17), 5221–5244.

Zobrist, B., et al. (2006), Oxalic acid as a heterogeneous ice nucleus in the upper troposphere and its indirect aerosol effect, *Atmos. Chem. Phys.*, *6*(10), 3115–3129.